58th Shock and Vibration Symposium

Volume I

Compiled by
Walter and Barbara Pilkey
University of Virginia
Charlottesville, VA 22901

NASA

Symposium Management

Host Representatives

Jess H. Jones - Marshall Space Flight Center
James W. Daniel - U.S. Army Missile Command

Administrative Management

William W. Wassmann - Naval Surface Weapons Center

Contract Support

Advanced Technology & Research, Inc.
Laurel Technology Center
14900 Sweitzer Lane
Laurel, MD 20707

Project Manager

Henry C. Pusey, ATR, Inc.

58th Symposium Program Committee

James D. Cooper
Defense Nuclear Agency
SPSS
Washington, DC 20305

James W. Daniel
U.S. Army Missile Command
AMSMI-RD-TE-C
Redstone Arsenal, AL 35898

Jess H. Jones
NASA Marshall Space Flight Center
Structural Analysis Division
Huntsville, AL 35812

John H. Wafford
U.S. Air Force
ASD/ENF
Wright-Patterson AFB, OH 45433

William W. Wassmann
Naval Surface Weapons Center
Environments Branch Code H14
Silver Spring, MD 20902-5000

Proceedings Compilers

Walter D. Pilkey
Mechanical and Aerospace Engineering
University of Virginia
Charlottesville, VA 22901

Barbara F. Pilkey
Mechanical and Aerospace Engineering
University of Virginia
Charlottesville, VA 22901

Table of Contents

CONTRIBUTORS

R. J. Allemang
Structural Dynamics Research Laboratory
Department of Mechanical
  and Industrial Engineering
University of Cincinnati
Cincinnati, Ohio 45221

T. J. Baca
Sandia National Laboratories
Div. 7542A
P.O. Box 5800
Albuquerque, New Mexico 87185

V. I. Bateman
Modal and Structural Dynamics Division
Sandia National Laboratories
P.O. Box 5800
Albuquerque, New Mexico 87185

G. A. Becus
Department of Aerospace Engineering
  and Engineering Mechanics
University of Cincinnati
Cincinnati, Ohio 45221-0070

N. E. Bedewi
Advanced Technology and Research, Inc.
14900 Sweitzer Lane
Laurel, Maryland 20707

R. G. Bell
Sandia National Laboratories
P.O. Box 5800
Albuquerque, New Mexico 87185

P. Berthier
I.N.S.A.
Laboratoire de Mécanique des Structures
U.A. C.N.R.S. 862
20, avenue Albert Einstein
69621 Villeurbanne
France

C. W. Bobbitt
Department of Aerospace Engineering
Mississippi State University
Mississippi State, Mississippi 39759

J. J. Boehnlein
Rockwell International
Rocketdyne Division
6633 Canoga Avenue AC152
Canoga Park, California 91304

R. Brillhart
Structural Dynamics Research Corporation
11055 Roselle Street
San Diego, California 92121

D. L. Brown
Structural Dynamics Research Laboratory
Department of Mechanical
  and Industrial Engineering
Mail Location #72
University of Cincinnati
Cincinnati, Ohio 45221

H. L. Budweg
Department of Mechanical Engineering
Code 69Sg
Naval Postgraduate School
Monterey, California 93943

L. P. Davis
Honeywell Inc.
Sperry Space Systems Division
Glendale, Arizona 85308

J. B. Cheek
USAE Waterways Experiment Station
P.O. Box 631
Vicksburg, Mississippi 39180-0631

P. Conti
Structural Dynamics Research Corporation
2000 Eastman Drive
Milford, Ohio 45150

G. Ferraris
I.N.S.A.
Laboratoire de Mécanique des Structures
U.A. C.N.R.S. 862
20, avenue Albert Einstein
69621 Villeurbanne
France

M. Gross
Advanced Technology and Research Inc.
14900 Sweitzer Lane
Laurel, Maryland 20707

P. M. Guilhen
I.N.S.A.
Laboratoire de Mécanique des Structures
U.A. C.N.R.S. 862
20, avenue Albert Einstein
69621 Villeurbanne
France

U. Hollburg
I A B G
Einsteinstr. 20
8012 Ottobrunn
West Germany

C. B. Hopson
Rockwell International
Space Transportation Systems Division
555 Discovery Drive
Huntsville, Alabama 35806

D. L. Hunt
Structural Dynamics Research Corporation
11055 Roselle Street
San Diego, California 92121

B. M. Jensen
Morton Thiokol, Inc.
P.O. Box 524
Brigham City, Utah 84302

M. Lalanne
I.N.S.A.
Laboratoire de Mécanique des Structures
U.A. C.N.R.S. 862
20, avenue Albert Einstein
69621 Villeurbanne
France

J. Leifer
Advanced Technology and Research Inc.
14900 Sweitzer Lane
Laurel, Maryland 20707

P. E. Lewallen
Component Assessment Branch, Code ED23
Structures and Dynamics Laboratory
NASA/Marshall Space Flight Center
Huntsville, Alabama 35812

T. W. Lim
Department of Mechanical
  and Aerospace Engineering
University of Virginia
Charlottesville, Virginia 22901

T. C. Lin
Department of Mechanical Engineering
  and Applied Mechanics
The University of Michigan
Ann Arbor, Michigan 48109

W. J. Liou
Department of Mechanical Engineering
Feng-Chia University
Taichung
Taiwan, Republic of China

C. Y. Lui
Department of Aerospace Engineering
  and Engineering Mechanics
M.L. #70
University of Cincinnati
Cincinnati, Ohio 45221

D. R. Mason
Morton Thiokol, Inc.
P.O. Box 524
Brigham City, Utah 84302

L. Minnetyan
Department of Civil
  and Environmental Engineering
Clarkson University
Potsdam, New York 13676

B. Palmertree
Instrumentation Services Division
Waterways Experiment Station
Vicksburg, Mississippi 39180-0631

H. V. Panossian
Rockwell International
Rocketdyne Division
6633 Canoga Avenue AC15
Canoga Park, California 91304

P. N. Patel
Civil Engineering Department
West Virginia University
Morgantown, West Virginia 26506

R. I. Persh
Electronics Hardening Branch, H23
Naval Surface Weapons Center
Silver Spring, Maryland 20903-5000

A. G. Piersol
Astron Research and Engineering
3228 Nebraska Avenue
Santa Monica, California 90404

W. D. Pilkey
Department of Mechanical
  and Aerospace Engineering
University of Virginia
Charlottesville, Virginia 22901

J. C. Prucz
Department of Mechanical
  and Aerospace Engineering
West Virginia University
Morgantown, West Virginia 26506-6101

D. K. Rao
Mechanical Technology Inc.
Advanced Technology Operation
968 Albany Shaker Road
Latham, New York 12110

B. E. Reed
Instrumentation Services Division
Waterways Experiment Station
P.O. Box 631
Vicksburg, Mississippi 39180-0631

S. A. Robbins
Sandia National Laboratories
P.O. Box 5800
Albuquerque, New Mexico 87185

W. K. Rule
Structural Dynamics Research Corporation
2000 Eastman Drive
Milford, Ohio 45150

D. Schiff
Assurance Technology Corporation
84 South Street
Carlisle, Massachussetts 01741

R. A. Scott
Department of Mechanical Engineering
  and Applied Mechanics
The University of Michigan
Ann Arbor, Michigan 48109

Y. S. Shin
Department of Mechanical Engineering
Naval Postgraduate School
Monterey, California 93943

C. C. Spyrakos
Civil Engineering Department
West Virginia University
Morgantown, West Virginia 26506-6101

C. T. Sun
Department of Engineering Sciences
University of Florida
Gainesville, Florida 32611

A. O. Sykes
Acoustical Research and Applications
304 Mashie Drive S.E.
Vienna, VA 22180

V. A. Tischler
Air Force Wright Aeronautical Laboratories
Wright-Patterson Air Force Base, Ohio 45433

V. B. Venkayya
Air Force Wright Aeronautical Laboratories
Wright-Patterson Air Force Base, Ohio 45433

M. L. Wei
Structural Dynamics Research Laboratory
Department of Mechanical
  and Industrial Engineering
University of Cincinnati
Cincinnati, Ohio 45221

J. F. Wilson
Honeywell Inc.
Sperry Space Systems Division
Glendale, Arizona 85308

J. C. S. Yang
Department of Mechanical Engineering
University of Maryland
College Park, Maryland 20742

Q. Zhang
Structural Dynamics Research Laboratory
Department of Mechanical
  and Industrial Engineering
University of Cincinnati
Cincinnati, Ohio 45221

FEATURED PAPER

The Analysis of Nonstationary Vibration Data

Allan G. Piersol

Procedures for analyzing the random vibration environments of transportation vehicles and other machinery are well defined and relatively easy to accomplish, as long as the vibration data are stationary in character; i.e., the average properties of the vibration do not vary with time. There are cases, however, where a random vibration environment of interest is naturally nonstationary in character, for example, the vibrations produced during the launch of a space vehicle. A well developed methodology exists for the analysis of nonstationary random data, but the resulting analysis procedures require measurements from repeated experiments that often cannot be obtained in practice. The alternative then is to employ a parametric analysis procedure that can be applied to individual sample records of data, under the assumption that the data have a specific nonstationary character. This paper reviews the general methodology for the analysis of arbitrary nonstationary random data, and then discusses a specific parametric model, called the product model, that has applications to space vehicle launch vibration data analysis. Illustrations are presented using nonstationary launch vibration data measured on the Space Shuttle orbiter vehicle.

INTRODUCTION

The launch vibration environment of space vehicles is highly nonstationary in character due to a sequence of time-varying aeroacoustic events that govern the dynamic loads on the vehicle. The most important of these events and the excitations they produce are (a) the acoustic noise excitation from the rocket motors during lift-off, (b) the excitation due to shock wave/boundary layer interactions during transonic flight, and (c) the turbulent aerodynamic boundary layer excitation

during flight through the region of maximum dynamic pressure (max "q").
These three events are clearly apparent in the time history of the
typical Space Shuttle launch vibration measurement shown in Figure 1.
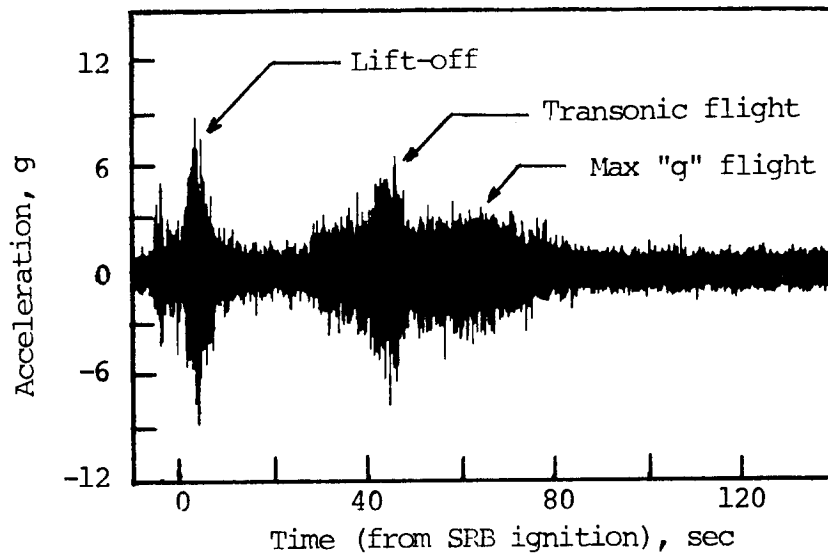
Figure 1. Typical Vibration Time History During A Space Shuttle Launch.

Traditionally, the vibration data measured on space vehicles during
launch are analyzed by selecting short time slices of data at those
times when the overall value of each measurement reaches a maximum
during each of the above noted events. Auto (power) spectral density
functions are then computed for each time slice, and are used to
describe the vibration spectra for those events. However, because space
vehicle launch vibration data are basically random in character, this
analysis procedure poses a serious problem. On the one hand, it is
clearly desirable to make the spectral analysis with a small frequency
resolution bandwidth B to properly extract the spectral variations in
the data, and also with a small averaging time T to properly define the
time variations in the data. On the other hand, because the data repre-
sent a random process, the spectral estimates will involve a statistical
sampling error [2, p. 283], which can be approximated in terms of a
normalized random error (coefficient of variation) by $\epsilon = [BT]^{-1/2}$.
Hence, as the bandwidth B is made smaller to obtain a better spectral
resolution, and the averaging time T is made smaller to obtain a better
time resolution, the random error in the estimate increases, often to
levels in excess of the bias errors that would have occurred if a wider
resolution bandwidth B and/or averaging time T had been used.
    Several studies of this nonstationary data analysis problem have
been performed dating back to the 1960's [3,4], and including a recent
study directed specifically at the analysis of the Space Shuttle launch
aeroacoustic and structural vibration environment [5]. This paper sum-
marizes the theoretical background for improved vibration data analysis
procedures recommended in [5], and illustrates applications using a
Space Shuttle launch vibration measurement. The suggested procedures
should also be applicable to expendable launch vehicle vibration data.

Many analytical methods have been proposed over the years for describing the spectra of nonstationary random data. From the viewpoint of describing mathematically rigorous input-output relationships for physical systems, including time-varying systems, the double frequency (generalized) spectral density function is broadly accepted as the most useful spectral description for nonstationary data. A full development and discussion of various forms of the double frequency spectrum are presented in [2, pp. 448-456]. For the purposes of applied data analysis, the instantaneous spectral density function (sometimes called the frequency-time spectrum or the Wigner distribution) is usually considered a more useful spectral description for nonstationary data. The instantaneous spectrum is detailed in [2, pp. 456-465], and will be used here as the starting point for the analytical discussions of improved spectral analysis procedures for launch vehicle vibration data.

The Instantaneous Spectrum

Consider a random process defined by an ensemble of sample functions $\{x(t)\}$, where individual measurements of the random process produce time history records $x_i(t)$; $i = 1,2,3,....,N$, as illustrated in Figure 2. The instantaneous autocorrelation function of the random process is given by [2, p. 445]

$$R_{xx}(\tau,t) = E[x(t-\tau/2)x(t+\tau/2)] \qquad (1)$$
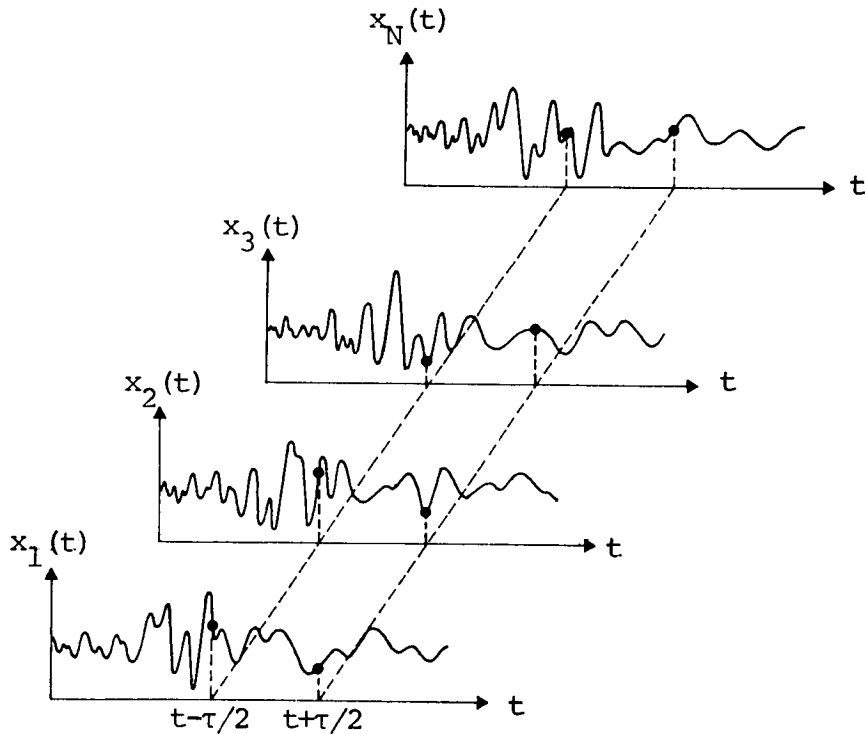
Figure 2. Sample Records Forming Nonstationary Random Process.

where E denotes an "expected value", which in practice would be approximated by an ensemble average over i = 1 to N sample records. The instantaneous autospectral density function is then defined by

$$W_{xx}(f,t) = \int_{-\infty}^{\infty} R_{xx}(\tau,t)\cos 2\pi f\tau \, d\tau \qquad (2)$$

In words, the instantaneous autospectral density function is the Fourier transform of the instantaneous autocorrelation function computed over τ. Since the instantaneous autocorrelation function is always real valued, the Fourier transform involves only the cosine term. This fact also leads to the following properties of the instantaneous autospectrum:

$$W_{xx}(f,t) = W_{xx}(-f,t) \qquad\qquad W_{xx}(f,t) = W_{xx}^{*}(f,t) \qquad (3)$$

$$\int_{-\infty}^{\infty} W_{xx}(f,t)\,df = E[x^2(t)] \qquad\qquad \int_{-\infty}^{\infty} W_{xx}(f,t)\,dt = E[|X(f)|^2] \qquad (4)$$

In Equation (3), the asterisk (*) denotes complex conjugate, and in Equation (4), X(f) is the Fourier transform of x(t) given by

$$X(f) = \int_{-\infty}^{\infty} x(t)e^{-j2\pi ft}\,dt \qquad (5)$$

where the integral in Equation (5) is assumed to exist. In words, Equation (4) says that the integral of the instantaneous autospectrum over frequency at any time yields the mean square value of the data at that time, while the integral over time at any frequency yields the "energy" spectral density of the data at that frequency. These two properties closely relate the instantaneous autospectrum to the ordinary autospectrum (also called the "power" spectrum) that is commonly computed for random data in practice, including launch vehicle vibration data.

Practical Measurement Considerations

The instantaneous autospectrum, $W(f,t)$ defined in Equation (2), provides a rigorous description of nonstationary vibration data that lends itself well to the formulation of design criteria and test specifications. However, the estimation of an instantaneous autospectrum theoretically requires an ensemble average over a collection of sample records to first obtain the instantaneous autocorrelation function defined in Equation (1). For the case of spacecraft launch vibration data, this means that measurements would have to be made at identical locations on numerous launches of the same spacecraft under identical conditions. For most space vehicles, this clearly is not feasible. For the special case of Space Shuttle, where the same launch vehicle is used many times and the outputs of certain vibration transducers have been recorded several times on at least one of the orbiter vehicles, an ensemble averaging analysis approach might be considered. Even here, however, the launch conditions have not been identical on the various Space Shuttle launches due to differences in payload weights and SSME thrust. Furthermore, there have not been a sufficient number of launches to date (with repeated measurements at identical locations) to provide

ensemble averaged estimates with acceptable sampling (random) errors. See [2, p. 285] for a discussion of the sampling errors in spectral estimates produced by ensemble averaging procedures.

The alternative to ensemble averaging is the short time averaging analysis procedure discussed in the Introduction. However, this approach involves an inherent conflict between the frequency resolution bandwidth B and the averaging time T needed to achieve spectral estimates with acceptable bias and random estimation errors. To elaborate on this problem, from [2], the bias error due to the finite frequency resolution bandwidth B used to compute the spectral density estimate at any time t is approximated by

$$b[\hat{W}(f,t)] \approx (B^2/24) \; d^2[W(f,t)]/df^2 \tag{6}$$

where the hat (^) denotes "estimate of". The approximation for the bias error due to the finite averaging time T used to compute the spectral density estimate at any frequency f has a similar form, namely,

$$b[\hat{W}(f,t)] \approx (T^2/24) \; d^2[W(f,t)]/dt^2 \tag{7}$$

In Equations (6) and (7), the second derivatives essentially represent the sharpness of peaks and notches in the variations of $W(f,t)$ with both frequency and time. Finally, as noted in the introduction, the random error due to the finite sample size used to compute the spectral density estimate is approximated in terms of the normalized standard deviation of the estimate (the coefficient of variation) by

$$\epsilon = \sigma[\hat{W}(f,t)]/W(f,t) \approx 1/[BT]^{1/2} \tag{8}$$

Since B and T appear in the denominator of Equation (8), but in the numerator of Equations (6) and (7), respectively, it is clear that there will be at least some frequencies and times when it is not possible to estimate a time varying spectrum by short time averaging procedures that will have an acceptable combination of bias and random errors. This problem can be circumvented only by assuming a specific model for the nonstationary character of the data, which can then be exploited for analysis purposes (a parametric procedure).

The Product Model

A special model for nonstationary data that has received considerable attention for applications to space vehicle launch vibration data [2-5], as well as nonhomogeneous atmospheric turbulence data [6], is the product model, which is defined as a nonstationary random process {x(t)} producing sample records of the form

$$x(t) = a(t)u(t) \tag{9}$$

where a(t) is a deterministic function, and u(t) is a sample record from a stationary random process {u(t)} with zero mean and unit variance; i.e., $\bar{u} = 0$ and $\overline{u^2} = 1$. For the special case where a(t) is restricted to positive values, it can be interpreted as the time varying standard deviation of {x(t)}. It follows from Equations (1) and (2) that the

instantaneous autocorrelation and autospectral density functions for the product model are given by

$$R_{xx}(\tau,t) = R_{aa}(\tau,t)R_{uu}(\tau) \qquad W_{xx}(f,t) = \int_{-\infty}^{\infty} S_{aa}(\beta,t)S_{uu}(f-\beta)d\beta \qquad (10)$$

where the S terms in the spectral result are two-sided spectral density functions defined as

$$S_{aa}(f,t) = \int_{-\infty}^{\infty} R_{aa}(\tau,t)e^{-j2\pi f\tau}\, d\tau \qquad S_{uu}(f) = \int_{-\infty}^{\infty} R_{uu}(\tau)e^{-j2\pi f\tau}\, d\tau \qquad (11)$$

Note in Equations (10) and (11) that the autocorrelation and auto-spectral density functions are nonstationary for a(t), but are stationary for {u(t)} since this is a stationary random process. Also note that it is common practice to work with one-sided spectra (defined for positive frequencies only), as opposed to two-sided spectra. The one-sided spectra are related to the two-sided spectra as follows:

$$
\begin{array}{ll}
W(f,t) = 2W(f,t) \;;0 \leq f & G(f) = 2S(f)\;;0 \leq f \\
\quad\quad\;\; = 0 \quad\quad\;\; ;f < 0 & \quad\quad\; = 0 \quad\quad\; ;f < 0
\end{array} \qquad (12)
$$

The Locally Stationary Model

An important special class of nonstationary random processes that fit the product model of Equation (9) are locally stationary data [2,7] (sometimes called uniformly modulated data [8]). Data are said to be locally stationary if they fit Equation (9) where a(t) varies slowly relative to u(t); i.e., the highest frequency component in $S_{aa}(f,t)$ is at a much lower frequency than the lowest frequency component in $S_{uu}(f)$. For this case, the instantaneous autospectral density function in Equation (10) can be approximated by

$$W_{xx}(f,t) \approx a^2(t)G_{uu}(f) \qquad (13)$$

where W(f,t) and G(f) are one-sided spectra, as defined in Equation (12), and $a^2(t)$ is the instantaneous mean square value of the data (the instantaneous variance if the mean value is zero). Hence, the instantaneous autospectrum for locally stationary data becomes a product of independent time and frequency functions that can be measured separately. Specifically, one can estimate the instantaneous autospectrum from a sample record of length T_r by two operations, as follows:

(1) Compute the autospectrum of the record by averaging over the entire record length T_r using a narrow spectral resolution bandwidth B.

(2) Compute the time varying mean square value over the entire record bandwidth B_r using a short averaging time T.

The above operations permit the estimation of the instantaneous spectrum with a good resolution in frequency and time, which suppresses the

frequency and time interval bias errors in the estimate, while still achieving a large bandwidth-averaging time product to suppress the random errors in the estimate.

Hard-Clipped Analysis

The locally stationary model in Equation (13) is valid only if $a(t)$ varies slowly relative to $u(t)$ in Equation (9). If this is not the case, $a(t)$ will act as a modulating function on $u(t)$, and cause the spectrum of $x(t)$ to spread [2]. It follows that the computed average autospectrum of $x(t)$ will not be proportional to the autospectrum of the fictitious stationary component $u(t)$ in the product model; i.e., $G_{xx}(f) \neq c\, G_{uu}(f)$ where c is a constant. However, the autospectrum of the stationary component $u(t)$ can still be estimated, even though $u(t)$ cannot be directly measured, by a special procedure suggested and illustrated in [6]. Specifically, since $a(t)$ represents a standard deviation which never takes on negative values, and assuming the mean values of $x(t)$ and $u(t)$ in Equation (9) are zero, it follows that the zero crossings of $x(t)$ will be identical to those of $u(t)$. Under the further assumption that the random process $\{u(t)\}$ has a normal (Gaussian) probability density function, the stationary autospectrum of $\{u(t)\}$ can be computed from a hard-clipped version of a sample record $x(t)$ by applying the "arc-sine" rule [9], as follows:

(1) Hard-clip the record $x(t)$ to obtain a new record $y(t)$ defined by

$$y(t) = \begin{array}{l} 1 \text{ for } x(t) \geq 0 \\ = -1 \text{ for } x(t) < 0 \end{array} \tag{14}$$

(2) Compute the autocorrelation function of $y(t)$ to obtain $R_{yy}(\tau)$.

(3) Compute the normalized autocorrelation function of $u(t)$ from

$$R_{uu}(\tau) = \sin[(\pi/2)R_{yy}(\tau)] \tag{15}$$

(4) Compute the autospectrum of $u(t)$ by Fourier transforming the autocorrelation function of $u(t)$ over a delay time $(1/B)$, where B is the desired spectral resolution, as follows:

$$G_{uu}(f) = 4\int_0^{(1/B)} R_{uu}(\tau)\cos(2\pi f\tau)\, d\tau \tag{16}$$

The computed spectrum of $u(t)$ in Equation (16) does not, of course, represent the actual autospectrum of the nonstationary vibration environment that was measured. It is simply the autospectrum of the fictitious $u(t)$ in the theoretical product model given by Equation (9). However, with this term, and an estimate for the time-varying term $a(t)$ in Equation (9), one could simulate the nonstationary spectrum $W_{xx}(f,t)$ in the laboratory by applying a nonstationary excitation produced by multiplying a signal with a stationary spectrum $G_{uu}(f)$ by a time-varying signal $a(t)$.

9

APPLICATIONS TO LAUNCH VIBRATION DATA

It is generally agreed that the desired spectral representation for the nonstationary vibration measurements made on space vehicles during launch is a spectrum that defines the maximum mean square value in each frequency resolution bandwidth during the nonstationary event, independent of the times when the maximum values in the various bandwidths occur. Such a spectral representation, referred to hereafter as the maximax spectrum, generally will not represent the instantaneous spectrum of the data at any specific instant of time, unless the data are stationary or locally stationary. However, since vibration induced malfunctions and failures of space vehicle structures and equipment tend to be frequency dependent, the maximax spectrum does provide a conservative measure of the environment from the viewpoint of damage potential and, hence, constitutes a rational basis for the derivation of test specifications and design criteria.

The issue at hand is whether the desired maximax spectrum of the space vehicle vibration response during a nonstationary launch event can be adequately approximated by the maximum of the instantaneous spectrum computed assuming the data are locally stationary during the event. This matter was empirically evaluated for Space Shuttle launch vibration and aeroacoustic data in [5]. The general conclusion from that reference is that, even though the launch vibration data do not always make a rigorous fit to the locally stationary model, the discrepancies of the maximum instantaneous spectrum (computed assuming local stationarity) from the maximax spectrum for each launch event are negligible compared to the errors that occur in a short time averaged spectral calculation. (It should be mentioned that this conclusion does not necessarily apply to aeroacoustic data). An illustration of the results from [5] is now presented for a vibration measurement on a Space Shuttle payload during the STS-2 launch.

Data Evaluation Procedures

To illustrate the data evaluation procedures, consider a vibration measurement made on the OSTA-1 payload during the second Space Shuttle launch (STS-2). The exact location of the measurement in terms of orbiter coordinates was x = 920, y = -73, and z = 413. The measurement is identified in [1] as V08D9248A (hereafter referred to as Accel 248). The short time averaged (T = 1 sec) overall rms value for this measurement is shown in Figure 3. Note that the three primary nonstationary launch events are clearly apparent in the overall level versus time. The maximum overall values during these events occur at about T+4 for lift-off, T+45 sec for transonic flight, and T+60 sec for max "q" flight.

To calculate an approximate maximax spectrum and facilitate other studies, the short time averaged spectra of this vibration measurement through the three primary nonstationary launch events were computed every sec (every 3 sec for max "q" data) from the beginning to the end of each event, considered to be as follows:

(a) Lift-off: T+2 to T+8 sec (6 sec duration).
(b) Transonic flight: T+40 to T+48 sec (8 sec duration).
(c) Max "q" flight: T+52 to T+70 sec (18 sec duration).

10
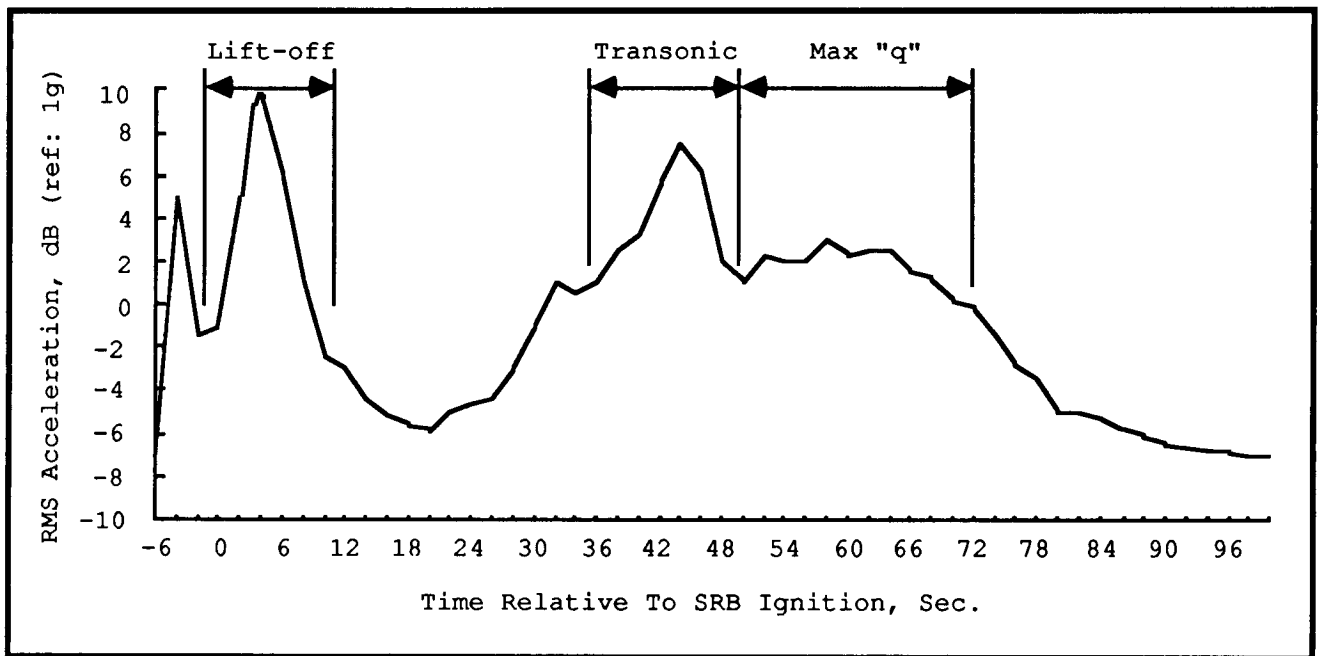
Figure 3. Overall Vibration level Versus Time Measured By Accel 248 During STS-2 Launch.

These durations were selected to avoid contamination of the data for each event by other events. For example, the transonic and max "q" events clearly overlap, but the selected 4 sec separation should be adequate to avoid serious contamination of the data for one event by the other. Also, the first 2 sec of lift-off were omitted to avoid contamination by the lift-off transient. The spectra were computed in 1/3 octave bands to enhance the BT product of the calculations and suppress random errors. The frequency range for the 1/3 octave band calculations was 16 to 1000 Hz. The results are presented in the appendix (Figures A1 through A3). To further facilitate data interpretations, all 1/3 octave band spectra were normalized to an overall mean square value of unity. These normalized results are also detailed in the appendix (Figures A4 through A6). If the data were locally stationary and there were no random sampling errors in the spectral estimates, these normalized spectral plots for each event would be identical. From Equation (8), the random error in the 1/3 octave band estimates is $\epsilon \approx 2.1/[f_o]^{1/2}$ ($\epsilon \approx 1.2/[f_o]^{1/2}$ for the max "q" data), where f_o is the center frequency of the octave band.

Average Spectra

There are two basic ways to calculate the spectral portion of locally stationary data, as given by $G_{uu}(f)$ in Equation (13). The first and most common way is simply to compute the average spectrum over the entire nonstationary event, or a sufficiently long portion of the event (providing a total record length T_r), to yield a BT_r product that will adequately suppress the random errors in the estimate. The values of the resulting spectrum can then be divided by the area under the spectrum to obtain a result with a mean square value of unity. This approach is hereafter referred to as the direct average procedure. It is clear that

11

the direct average procedure will give greatest weight to the spectral values at those times when the magnitudes are large.

The direct average spectra of the 1/3 octave band values in the appendix (Figures A1 through A3) were computed as follows. Let MS_{ij} denote the mean square value of the data measured during the ith time slice ($i = 1, 2, \ldots, k$) and in the jth frequency band ($j = 1, 2, \ldots, r$) during a given event. The average mean square value in each 1/3 octave band over the nonstationary event of interest is given by

$$MS_j = \sum_{i=1}^{k} MS_{ij}/k \qquad (20)$$

The direct average spectrum (without a normalization on bandwidth) is then given by

$$G_{uu}(j) = MS_j / \sum_{j=1}^{r} MS_j \qquad (21)$$

The second way to estimate $G_{uu}(f)$ in Equation (13) is to first normalize the instantaneous spectrum of the data to a mean square value of unity at all instances of time, and then compute the average of the normalized spectrum over the entire nonstationary event. This approach is hereafter referred to as the normalized average procedure. Unlike the spectra produced by the direct average approach, the normalized average procedure weights the spectral values at all times during the nonstationary event equally, independent of their magnitudes.

The easiest way to normalize the instantaneous spectrum of data is by the hard clipping procedure detailed in Equations (14) through (16). This permits the normalized average spectrum to be computed directly by Equation (16). However, for the Space Shuttle data, the normalized average spectra were approximated by averaging the normalized 1/3 octave band values given in the appendix (Figures A4b through A6b). Specifically, for the ith time slice and the jth frequency interval,

$$NMS_{ij} = MS_{ij} / \sum_{j=1}^{r} MS_{ij} \qquad (22)$$

The normalized average spectrum (without a normalization on bandwidth) is then given by

$$G_{uu}(j) = NMS_j = \sum_{i=1}^{k} NMS_{ij}/k \qquad (23)$$

Errors In Average Spectral Computations

The most direct way to assess the errors that would occur if the Space Shuttle vibration measurement were analyzed using the locally stationary assumption is first to compute its average spectrum by both the direct and normalized average procedures, and then to compare these results with the maximax spectrum after adjustments to make the mean square values of the different spectral computations equal. This was accomplished for each of the three primary nonstationary launch events. The discrepancies between each of the average spectra, $G_{ave}(f)$, and the

corresponding maximax spectrum, $G_{max}(f)$, were computed in dB using the formula

$$dB \ error(f) \ = \ 10 \ log_{10}[G_{ave}(f)/G_{max}(f)] \tag{24}$$

The dB errors between the average and maximax spectra determined using Equation (24) are plotted in Figure 4. The standard deviations for these errors are detailed in Table 1.

Table 1. Summary of Errors Between Average And Maximax Spectra.

Type of Average	Standard Deviation of Errors, dB		
	Lift-off	Transonic	Max "q"
Direct average	0.38	0.98	0.44
Normalized average	0.81	1.09	0.48

It is clear from Figure 4 and Table 1 that the direct average produces a smaller net discrepancy from the maximax spectrum than the normalized average. From [5], this was true for all the Space Shuttle vibration and aeroacoustic measurements considered. Hence, there is no question that the direct average provides the superior approach. This is a gratifying result, since the direct average is the easier of the two calculations to perform using current data analysis equipment and software. Specifically, one simply computes the autospectrum of the record as if it represented stationary data, except the ordinate scale of the resulting spectrum must be independently established.

Applications To Narrowband Autospectra

The previous results and conclusions are based upon the spectra of data measured in 1/3 octave bands under the assumption that the nonstationary trends observed in the 1/3 octave band data should be representative of the trends in narrowband auto (power) spectra data (PSD's). To check this assumption, the maximax and direct average autospectra for the data measured by Accel 248 during lift-off were computed using a 10 Hz frequency resolution bandwidth with the results shown in Figure 5. The analysis was conducted to only 500 Hz because, in terms of constant bandwidth autospectra, the spectral levels of the data from Accel 248 during lift-off were very small above this frequency. The errors between the average and maximax spectrum, as defined in Equation (24), are detailed in Figure 6. The standard deviation of the errors for the narrow bandwidth (10 Hz) analysis is 0.6 dB, somewhat larger than the net error of about 0.4 dB calculated from the 1/3 octave band data in Table 1 because of the larger random errors in the narrowband spectral estimates (the random error between the maximax and average spectra should be small since they are computed from the same data record, but there is some random error because the maximax spectra are computed over a shorter time interval).

13
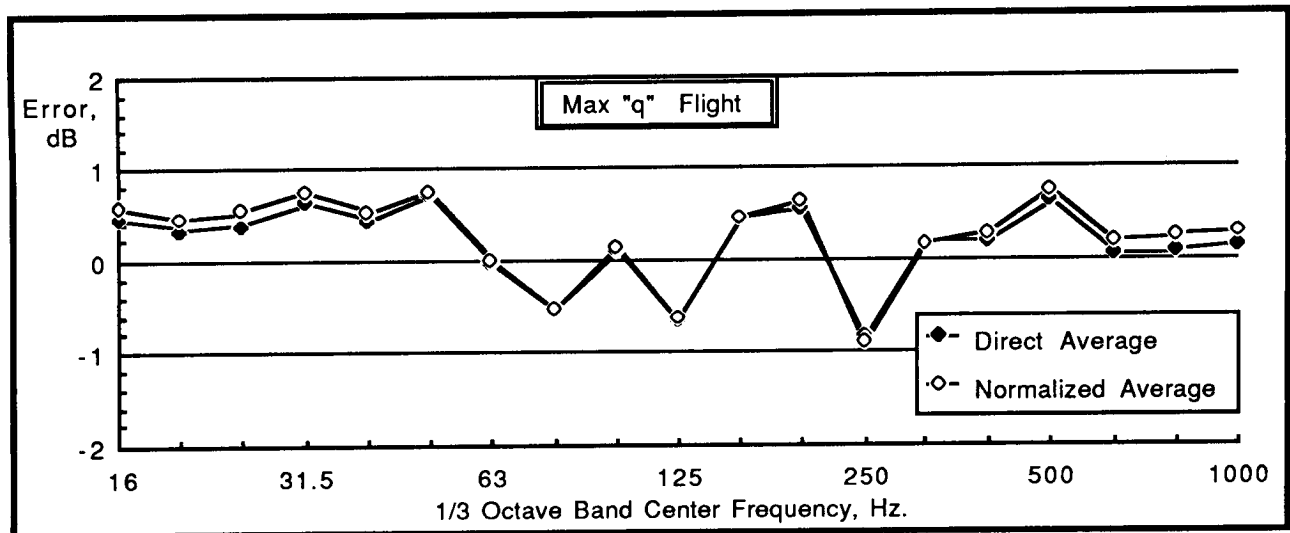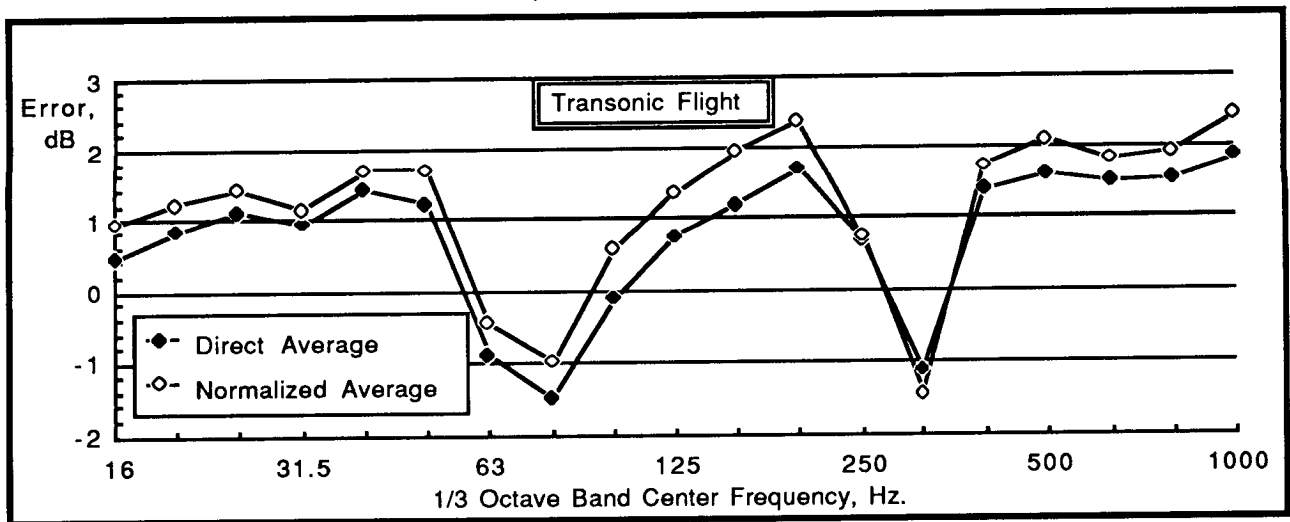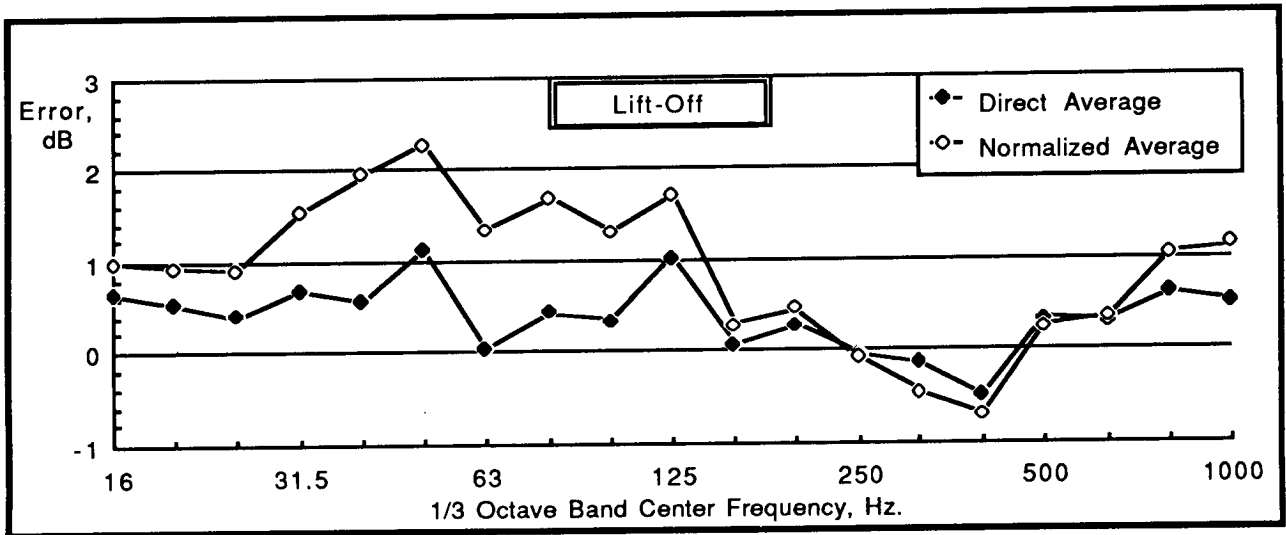
Figure 4. Errors Between Average And Maximax Spectra for Accel 248.
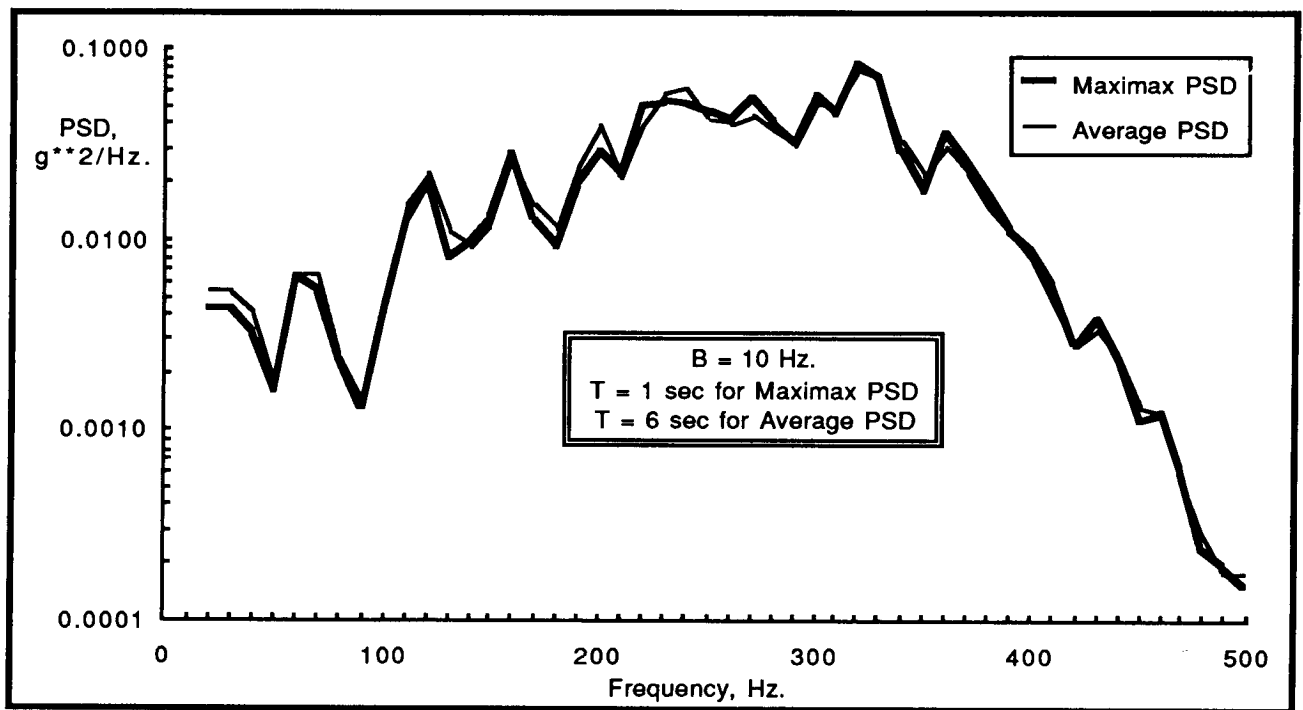
Figure 5. Average And Maximax Autospectra For Accel 248 During STS-2 Lift-Off.
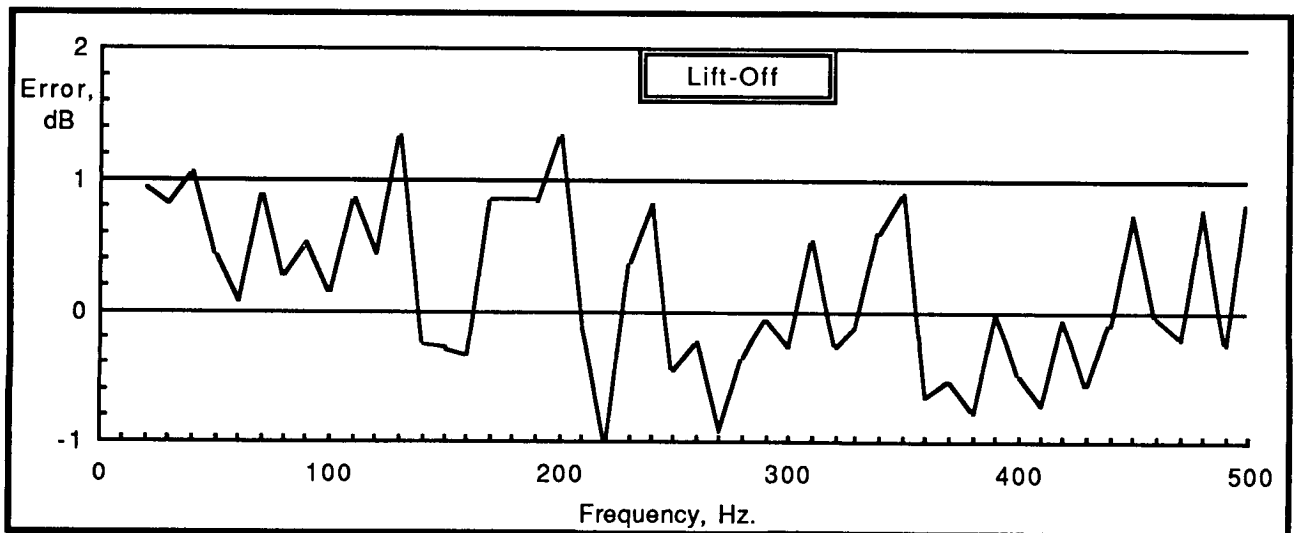
Figure 6. Errors Between Average And Maximax Autospectra Of Vibration Measured By Accel 248 During STS-2 Lift-Off.

Estimation of Maximax Overall Value

The computation of an average spectrum constitutes only half the analysis for data assumed to be of the locally stationary form. The second half of the required analysis involves the computation of the maximum overall value of the data during each nonstationary event of interest; i.e., the maximum value of $a(t)$ in Equation (13). As discussed

15

earlier, the desired overall value here is the overall for the maximax spectrum, and not the maximum instantaneous spectrum. Of course, for data which rigorously fit the locally stationary model, the maximax and maximum instantaneous overalls would be equal since the mean square values of locally stationary data reach their maximum values in all frequency bands at exactly the same time. However, from [5], much of the Space Shuttle launch vibration data do not rigorously fit the locally stationary model; the locally stationary assumption is being used here only as an approximation to be exploited for data analysis purposes. This fact poses a practical analysis problem since the maximum instantaneous overall value of nonstationary data is relatively easy to estimate, but a determination of the maximax overall value requires a knowledge of the maximum value in each individual frequency band independent of when that maximum value occurs.

The easiest way to approximate the overall value of the maximax spectrum is to use the maximum instantaneous overall value as an approximation. To assess the potential errors of such an approximation, the overall values of the maximax spectrum and the maximum instantaneous spectrum for Accel 248 during the three nonstationary launch events were computed with the results shown in Table 2. Also shown in Table 2 are the differences between the two overall values in percent and dB. The maximax overall values were determined by selecting the highest spectral value for each event in each 1/3 octave band in Figures A1 through A3, independent of the time it occurred, and summing these 1/3 octave values. The maximum instantaneous overall values were determined by short time averaging procedures with an averaging time of 1 sec for the lift-off and transonic data and 3 sec for the max "q" data, as shown in Figures A4a through A6a (the error associated with this calculation is discussed later).

Table 2. Summary of Errors Between Maximum Instantaneous and Maximax Overall Values.

Calculation	Lift-off	Transonic	Max "q"
Maximax overall, g	3.06	2.78	1.46
Max. instant. overall, g	2.99	2.61	1.37
Percent difference (rms), %	2.3	6.5	6.6
Percent difference (ms), %	4.7	13.4	13.6
Decibel difference, dB	0.2	0.6	0.6

It is seen from Table 2 that the maximax overall value always exceeds the maximum instantaneous overall value as expected, but generally by less than 15% of the mean square value (from [5], this appears to be a reasonable error bound for both vibration and aeroacoustic data, at least for Space Shuttle launches). Hence, to be conservative, it would be wise to multiply the computed maximum instantaneous overall mean square value of the vibration measured during each nonstationary event by a factor of 1.15 to estimate the maximax overall mean square value. Of course, there is still the problem of making an accurate estimate for the maximum instantaneous mean square value during each of the primary nonstationary launch events, which is discussed next.

Estimation Of Maximum Instantaneous Overall Values

The maximum instantaneous overall value of vibration data during a nonstationary event can be estimated in two general ways. The first and easiest way is to compute the time varying mean square value of the record during the nonstationary event using a short averaging time. The maximum instantaneous overall value is then given by the square root of the maximum mean square value calculated during the event. The short time average may be computed using either linear or exponentially weighted averaging procedures. The only problem is to select an appropriate averaging time.

The optimum averaging time to estimate the time-varying overall value of nonstationary data is the longest averaging time that can be used without smoothing the nonstationary trend in the overall value. In more quantitative terms, it is the longest averaging time that will not cause a significant bias error as defined by Equation (7). From the time-varying overall values presented for the Space Shuttle launch vibration data in [1], it appears that the most rapid variations in mean square value with time (using an averaging time of T = 1 sec) occur for the lift-off and transonic data, and resemble a half sine wave with a period of at least 5 sec; that is,

$$a^2(t) \approx \sin(\pi t/5) \qquad (25)$$

Using this criterion as the worst case for lift-off and transonic data, it follows from Equation (7) that the bias error in the estimate of $a^2(t)$ due to the finite averaging time T is given by

$$b[\hat{a}^2(t)] \approx -[(\pi T)^2/600] \sin(\pi t/5) \qquad (26)$$

The largest bias error occurs where t = 2.5 sec (the peak mean square value) and is approximated by

$$b_{max}[\hat{a}^2(t)] \approx -(\pi T)^2/600 \approx -0.0165 \ T^2 \qquad (27)$$

where the minus sign means the finite averaging time always causes an underestimate of the instantaneous overall value. Hence, an averaging time of T = 1 sec, as used in this study, produces maximum mean square value estimates that are biased on the low side by up to 1.7% or 0.07 dB (rms value estimates that are low by less than 0.9%). From [10], a linear averaging time of T = 1 sec is broadly equivalent to an exponentially weighted average with a time constant of about TC = 0.5 sec.

For the max "q" data in [1], the variations in the mean square value with time are slower, more closely fitting a half sine wave with a period of at least 12 sec. The maximum bias error due to the finite averaging time in this case is approximated by

$$b_{max}[\hat{a}^2(t)] \approx -0.00286 \ T^2 \qquad (28)$$

Plots of the finite averaging time bias errors defined in Equations (27) and (28) are shown in Figure 7.

17

It is seen in Figure 7 that the error in estimating the time-varying mean square value for Space Shuttle launch vibration data by short time averaging procedures will be about -0.1 dB with linear averaging times of T = 1 sec for the lift-off and transonic regions, and T = 3 sec for the max "q" region. These linear averaging times are statistically equivalent [10] to exponentially weighted averaging time constants of TC = 0.5 and 1.5 sec, respectively. An error of -0.1 dB corresponds to an underestimate of the maximum mean square value of 2.3%, which is considered an acceptable error.
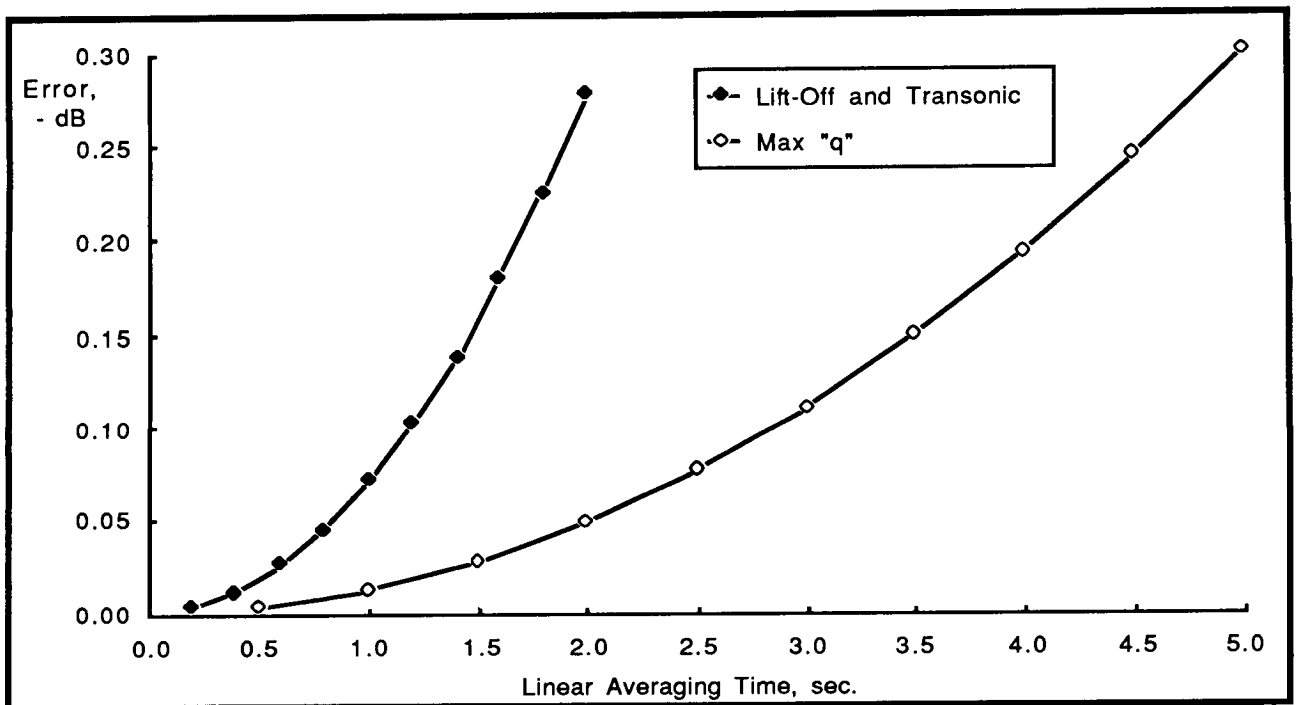
Figure 7. Maximum Bias Errors In Space Shuttle Overall Vibration Level Estimates Due Finite Averaging Time.

In closing on this subject, it must be emphasized that the bias errors in Figure 7 apply only to the Space Shuttle launch environment. Because of differences in the early launch acceleration of various space vehicles, the time durations for the primary nonstationary launch events will be different, meaning the averaging time required to suppress the bias errors in short time averaged mean square value estimates will also be different.

Now concerning the random errors in short time averaged mean square value estimates, Equation (8) applies where $B = B_r$, the equivalent total bandwidth of the data. The equivalent bandwidth B_r will equal the actual bandwidth of the data only for the case of "white noise"; i.e., data with a constant autospectrum. As a rule of thumb, B_r will usually be at least one-quarter of the actual bandwidth of random vibration data. Hence, even with the T = 1 sec averaging time, the normalized random error of the overall mean square value estimate at any instant for a 1 kHz bandwidth vibration record is given by Equation (8) as $\epsilon[\hat{a}^2(t)] \approx 0.063$ or about ±0.3 dB, which is considered an acceptable random error.

18

The second way to estimate the overall value of vibration data during a nonstationary event is by fitting an appropriate series function to the squared values of the individual data points using conventional regression analysis procedures. For relatively simple mean square value/time variations, where there is a single maximum with values falling monotonically on both sides of the maximum, a trigometric set will often provide a good fit with only a few terms (see [6] for an illustration). However, a more common approach is to fit the individual squared values of the data, $w_n = x^2(n\Delta t)$; $n = 1,2,\ldots,N$, with a Kth order polynomial,

$$\hat{a}^2(n\Delta t) = \sum_{k=0}^{K} b_k(n\Delta t)^k \; ; \; n = 1,2,\ldots,N \qquad (29)$$

where $3 \leq K \leq 5$ is usually adequate, as long as the time variation of the mean square value is of the relatively simple form described above. A least squares fit of the function in Equation (29) to the individual squared data values yields a set of equations of the form [2, p. 363]

$$\sum_{k=0}^{K} b_k \sum_{n=1}^{K} (n\Delta t)^{k+m} = \sum_{n=1}^{N} w_n(n\Delta t)^m \; ; \; m = 1,2,\ldots,K \qquad (30)$$

This set of K+1 simultaneous equations are solved for the regression coefficients, b_k, which are then substituted into Equation (29) to obtain the mean square value estimate versus time.

The regression analysis approach offers the advantage of potentially lower random errors than are achievable by the short time averaging analysis procedure described earlier, if the order of the fitted polynomial is low. This is true because, with a low order fit, more data are used to define the mean square value estimate at each instant of time. However, if the time variations of the mean square value are not relatively smooth through the maximum value, a significant bias error can occur in the calculated maximum mean square value with a low order polynomial fit. Increasing the order K of the fit to suppress this possible bias error will increase the random error of the estimate, exactly as reducing the averaging time T in the short time averaging approach will increase the random error of the estimate.

CONCLUSIONS

The maximax auto (power) spectral density functions for the nonstationary vibration data produced during a space vehicle launch can be closely approximated by separate time and frequency averaging procedures. This approach to the analysis of such data allows the estimation of spectral density functions with a much smaller combination of bias and random errors. Although developed for Space Shuttle applications, this same procedure, with appropriately modified averaging times, should apply to the analysis of the launch vibration data for expendable launch vehicles as well.

REFERENCES

1. W.F. Bangs, et al, "Payload Bay Acoustic and Vibration Data From STS-2 Flight: A 30-Day Report", NASA DATE Report 003, Jan. 1982.

2. J.S. Bendat and A.G. Piersol, RANDOM DATA: Analysis and Measurement Procedures, 2nd edition, Wiley, New York, 1986.

3. A.G. Piersol, "Spectral Analysis of Nonstationary Spacecraft Vibration Data", NASA CR-341, Nov. 1965.

4. A.G. Piersol, "Power Spectra Measurements for Spacecraft Vibration Data", J. Spacecraft and Rockets, Vol. 4, No. 12, pp.1613-1617, Dec. 1967.

5. A.G. Piersol, "Analysis Procedures For Space Shuttle Launch Aeroacoustic and Vibration Data", Astron Report No. 7072-02, July 1987.

6. W.D. Mark and R.W. Fischer, "Investigation of the Effects of Nonhomogeneous (or Nonstationary) Behavior on the Spectra of Atmospheric Turbulence", NASA CR-2745, Feb. 1976.

7. R.A. Silverman, "Locally Stationary Random Processes", IRE Trans.,Information Theory, Vol. IT-3, pp. 182-187, Mar. 1957.

8. G. Treviño, "The Frequency Spectrum of Nonstationary Random Processes", TIME SERIES ANALYSIS: Theory and Practice 2, pp. 237-246, North-Holland, Amsterdam, 1982.

9. J.I. Lawson and G.E. Uhlenbeck, Threshold Signals, McGraw-Hill, New York, 1950.

10. A.G. Piersol, "Estimation of Power Spectra by a Wave Analyzer", Technometrics, Vol. 8, No. 3, pp. 562-565, Aug. 1966.

APPENDIX

Figures A1-A3. 1/3 octave band spectra for OSTA-1 payload vibration mea-
surement (Accel 248) during Space Shuttle launch (STS-2).

Units: Mean square acceleration (MS Accel) in g^2 (g**2).

Averaging Time: 1 sec for lift-off and transonic flight; 3 sec for
max "q" flight (T+x is end of averaging interval).

Figures A4-A6. Overall values and normalized 1/3 octave band spectra for
OSTA-1 payload vibration measurement (Accel 248).

Units: Overall values - Mean square acceleration (MS Accel) in g^2
(g**2).
Normalized spectra - normalized mean square acceleration
(NMS Accel) relative to the overall
(OA) in linear units and dB.

Averaging Time: 1 sec for lift-off and transonic flight; 3 sec for
max "q" flight (T+x is end of averaging interval).
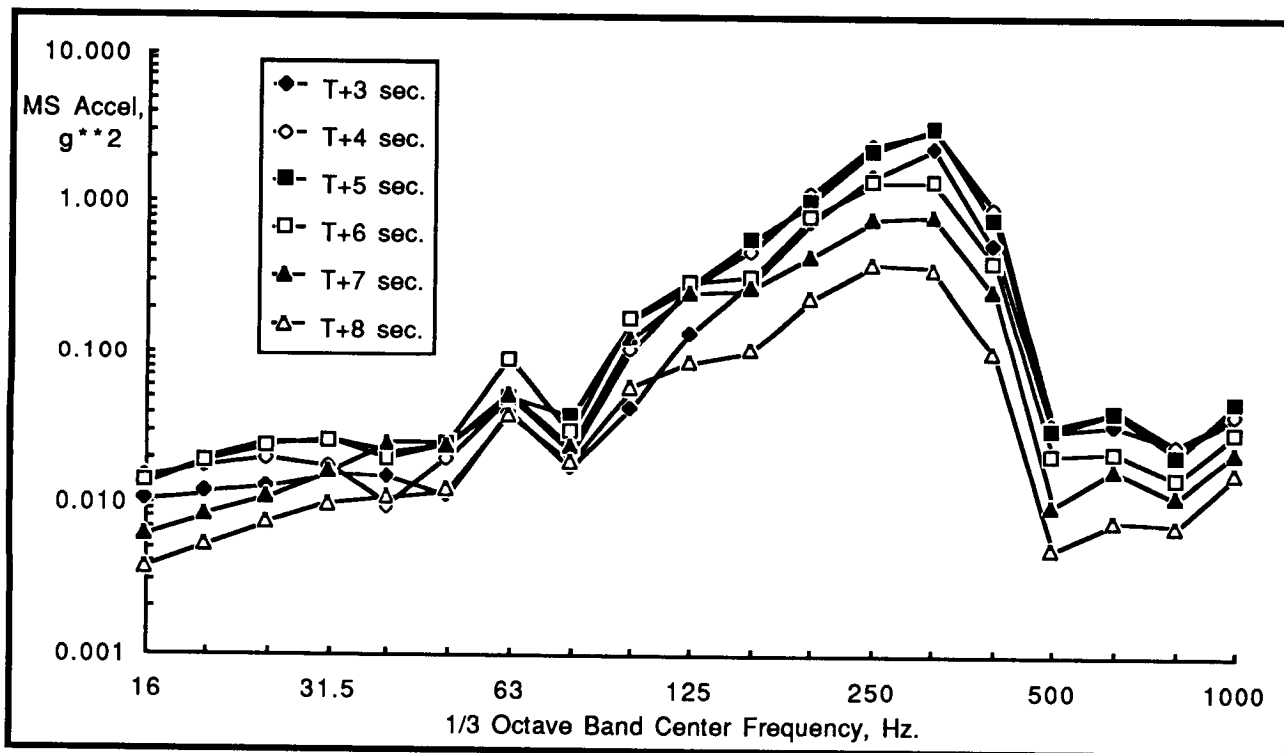
Figure A1. 1/3 Octave Band Vibration Levels During Space Shuttle
Lift-Off; STS-2 Accel 248.

21
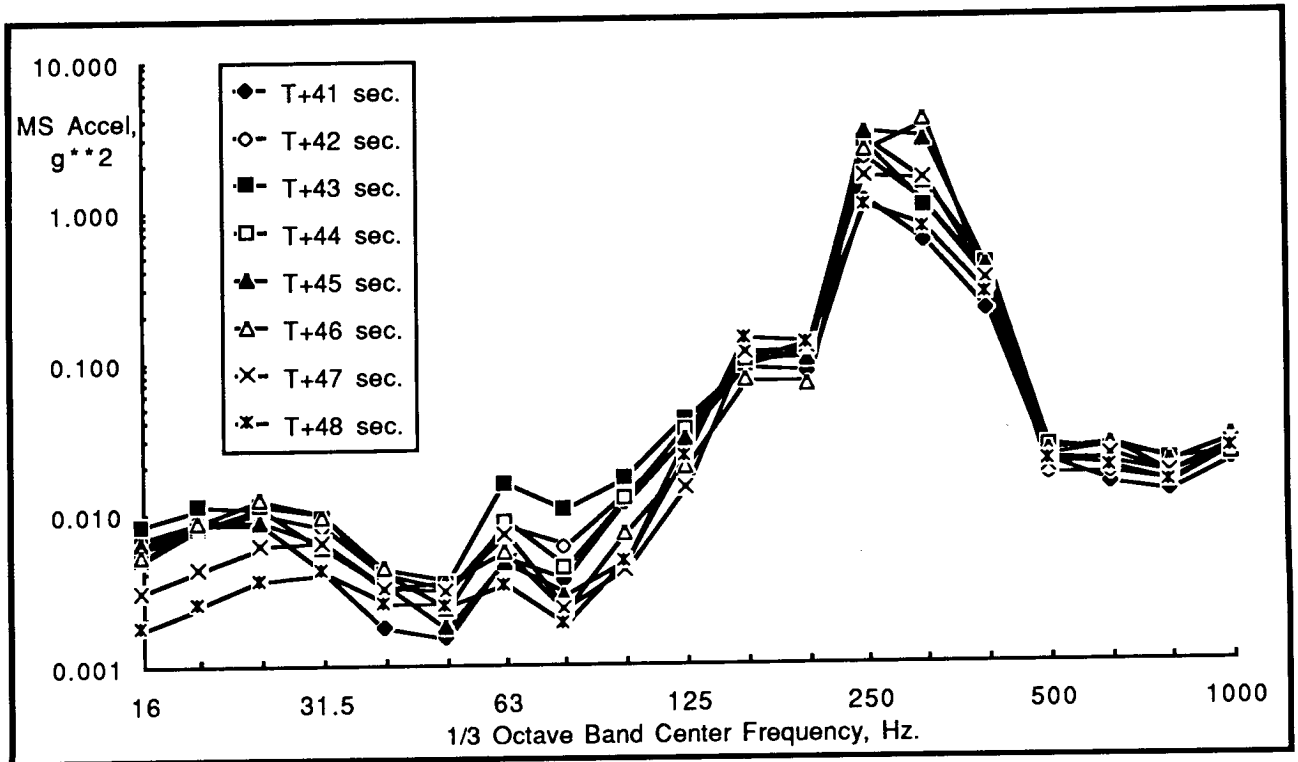
Figure A2. 1/3 Octave Band Vibration Levels During Space Shuttle
Transonic Flight; STS-2 Accel 248.
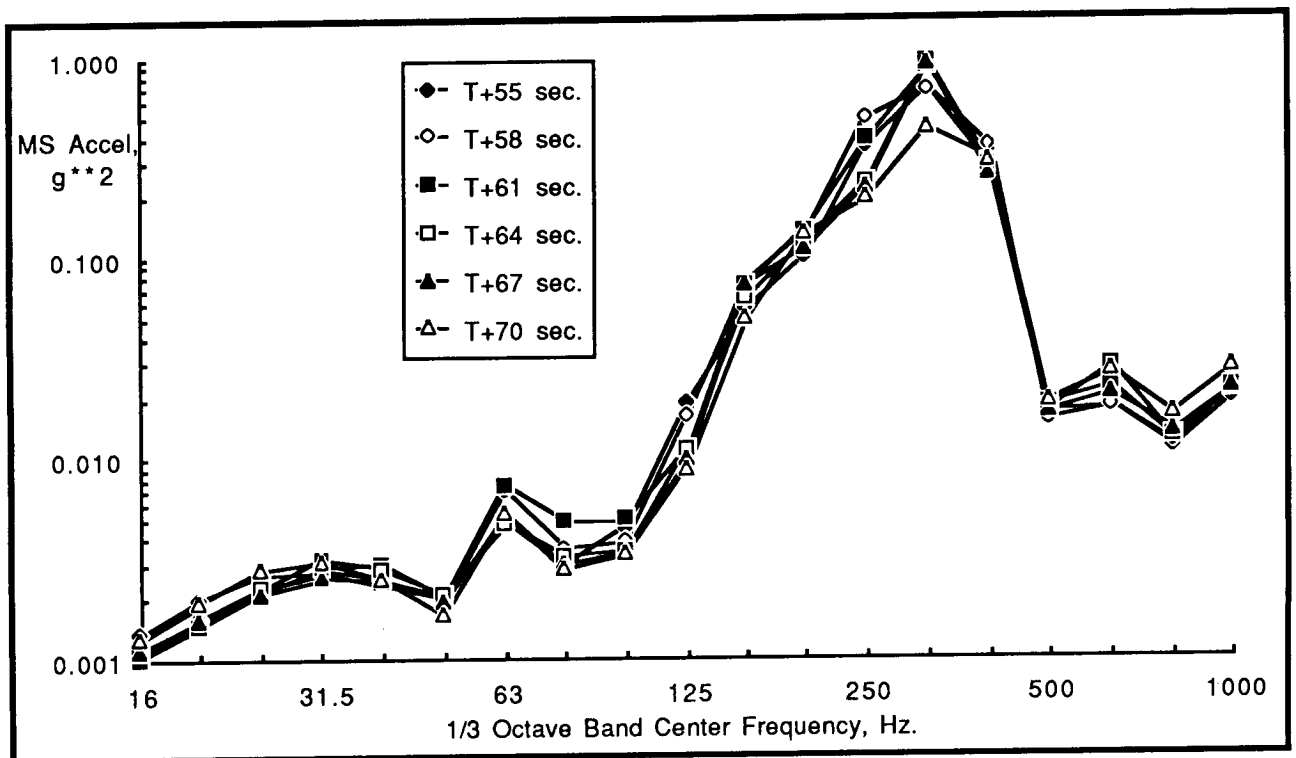
Figure A3. 1/3 Octave Band Vibration Levels During Space Shuttle
Max "q" Flight; STS-2 Accel 248.
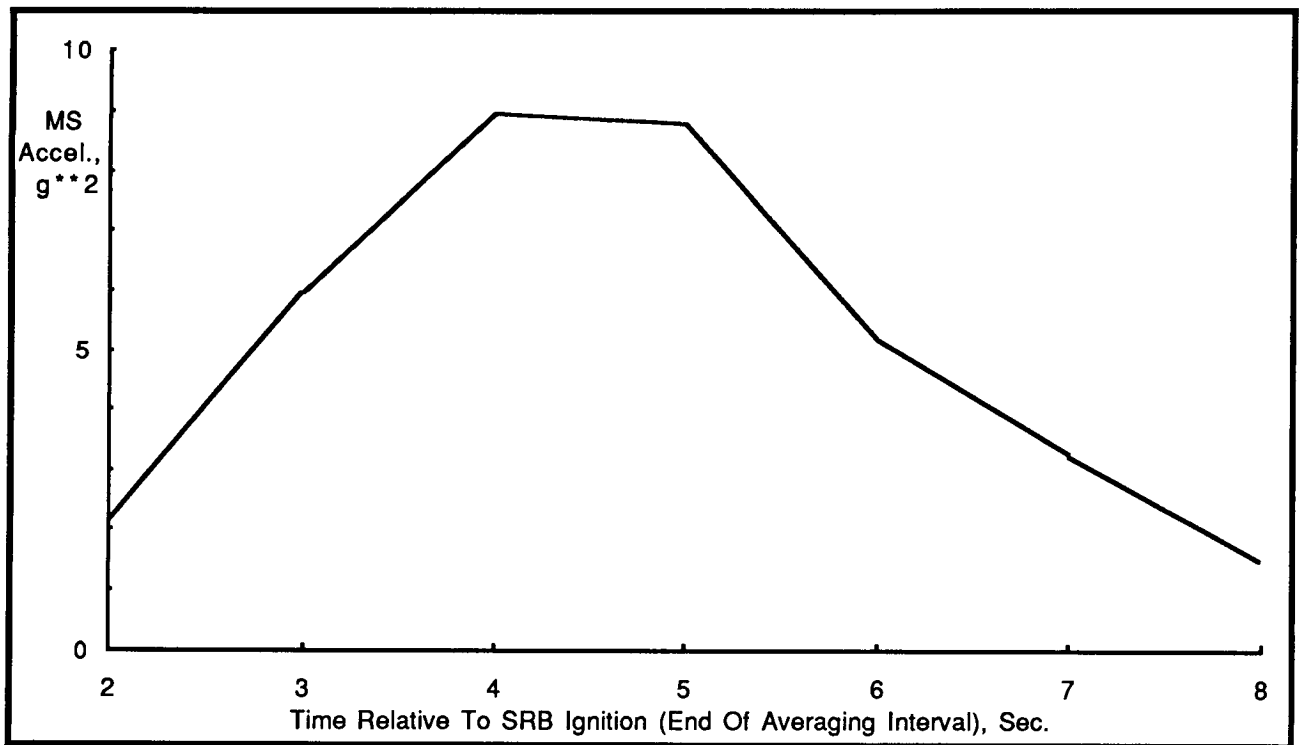
Figure A4a. Overall MS Vibration Level During Space Shuttle Lift-Off; STS-2 Accel 248.
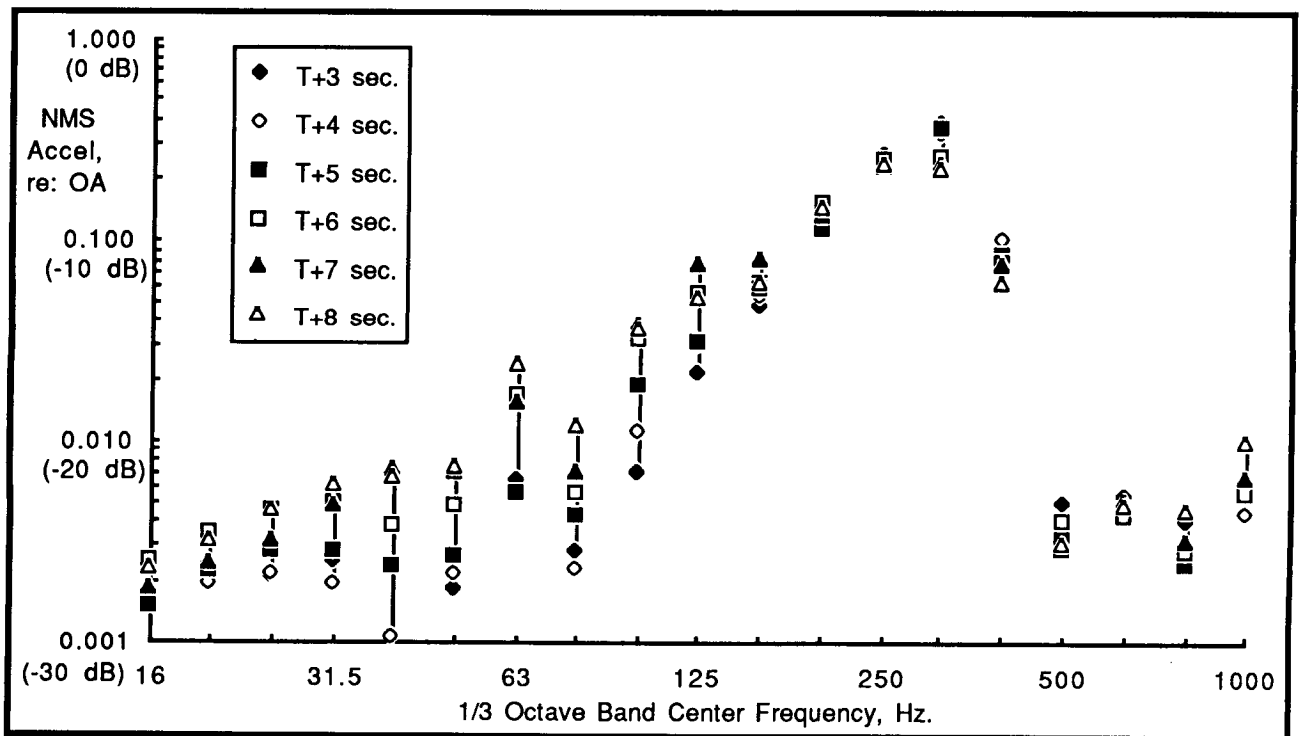
Figure A4b. 1/3 Octave Band Spectra Of Normalized MS Vibration Levels During Space Shuttle Lift-Off; STS-2 Accel 248.
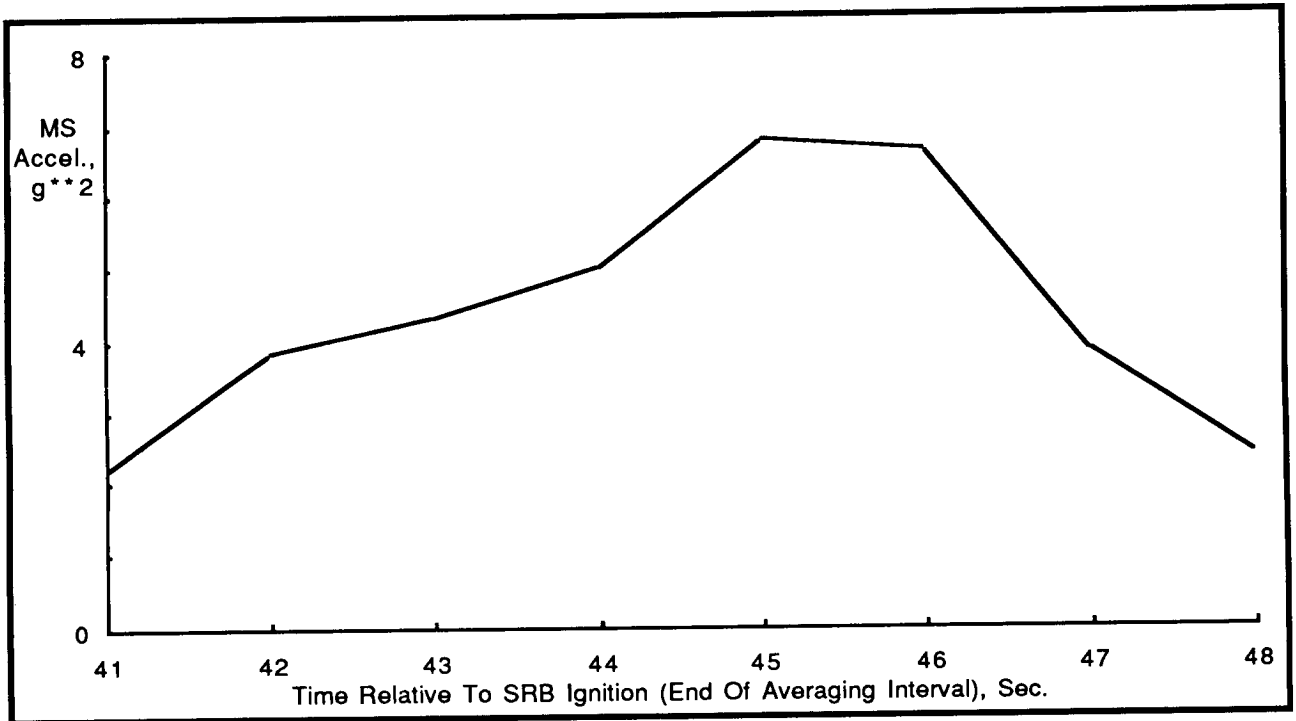
Figure A5a. Overall MS Vibration Level During Space Shuttle Transonic Flight; STS-2 Accel 248.
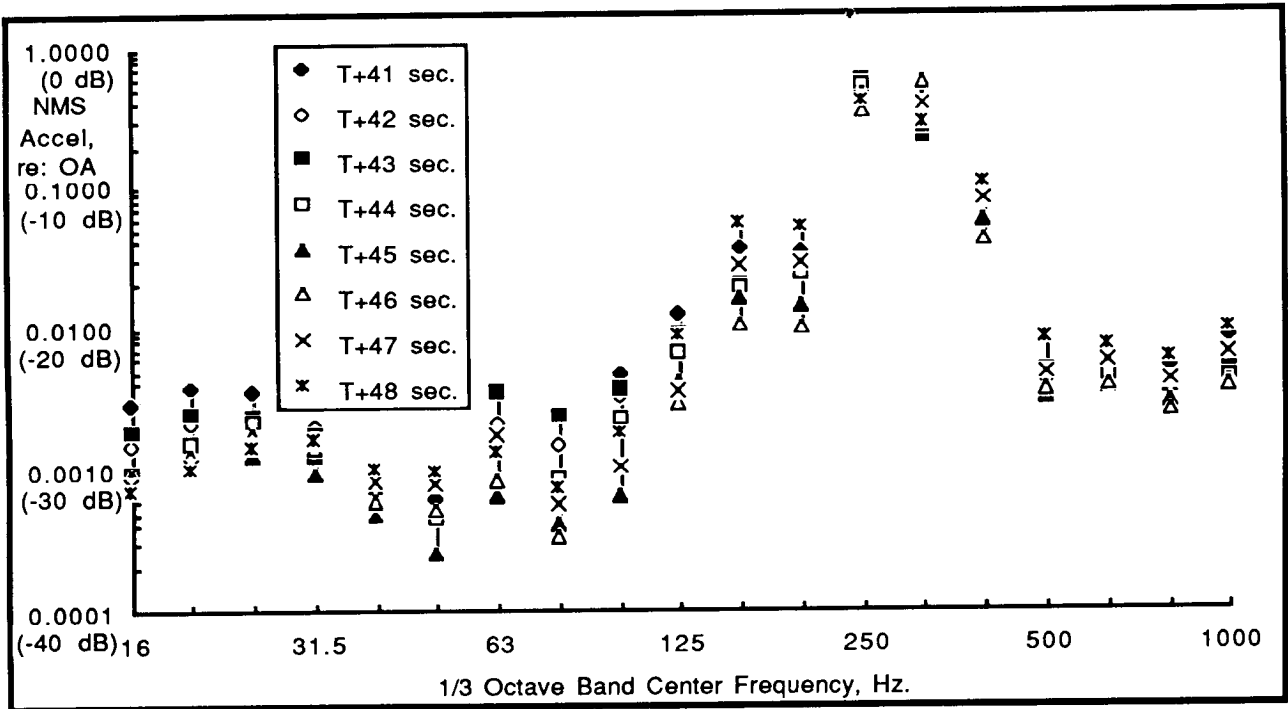
Figure A5b. 1/3 Octave Band Spectra Of Normalized MS Vibration Levels During Space Shuttle Transonic Flight; STS-2 Accel 248.
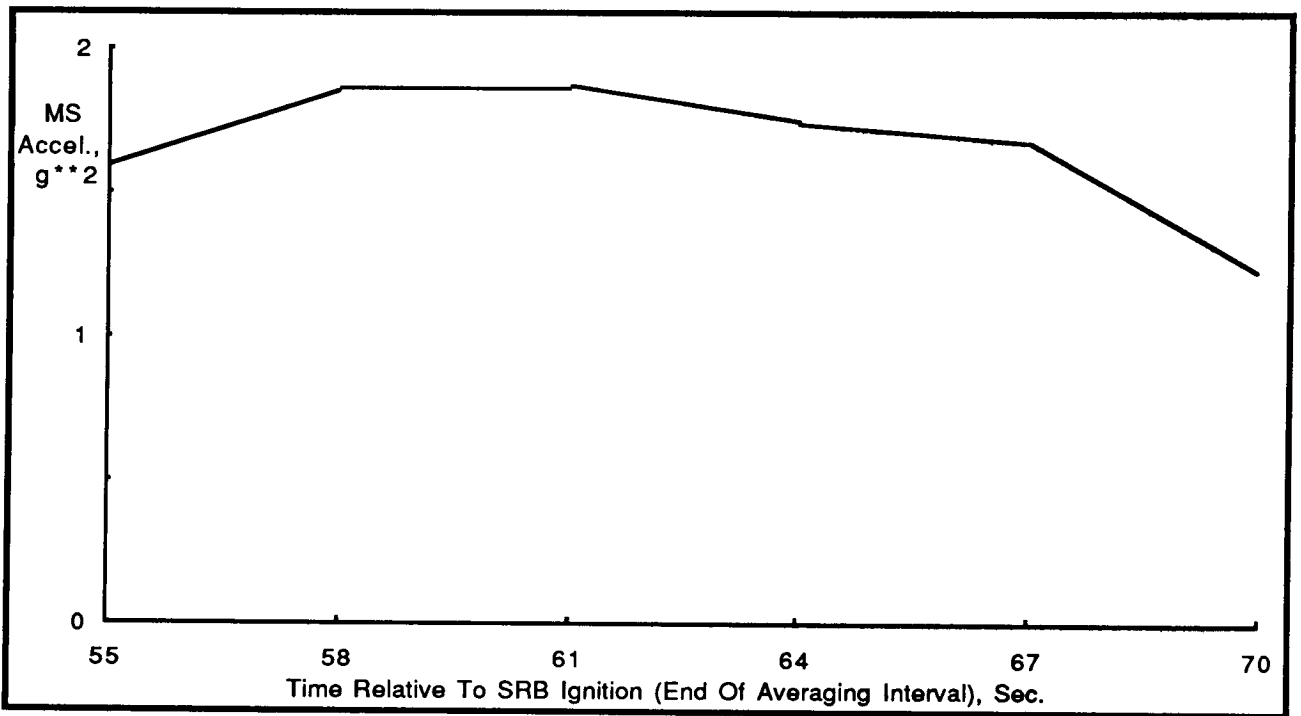
Figure A6a. Overall MS Vibration Level During Space Shuttle Max "q" Flight; STS-2 Accel 248.
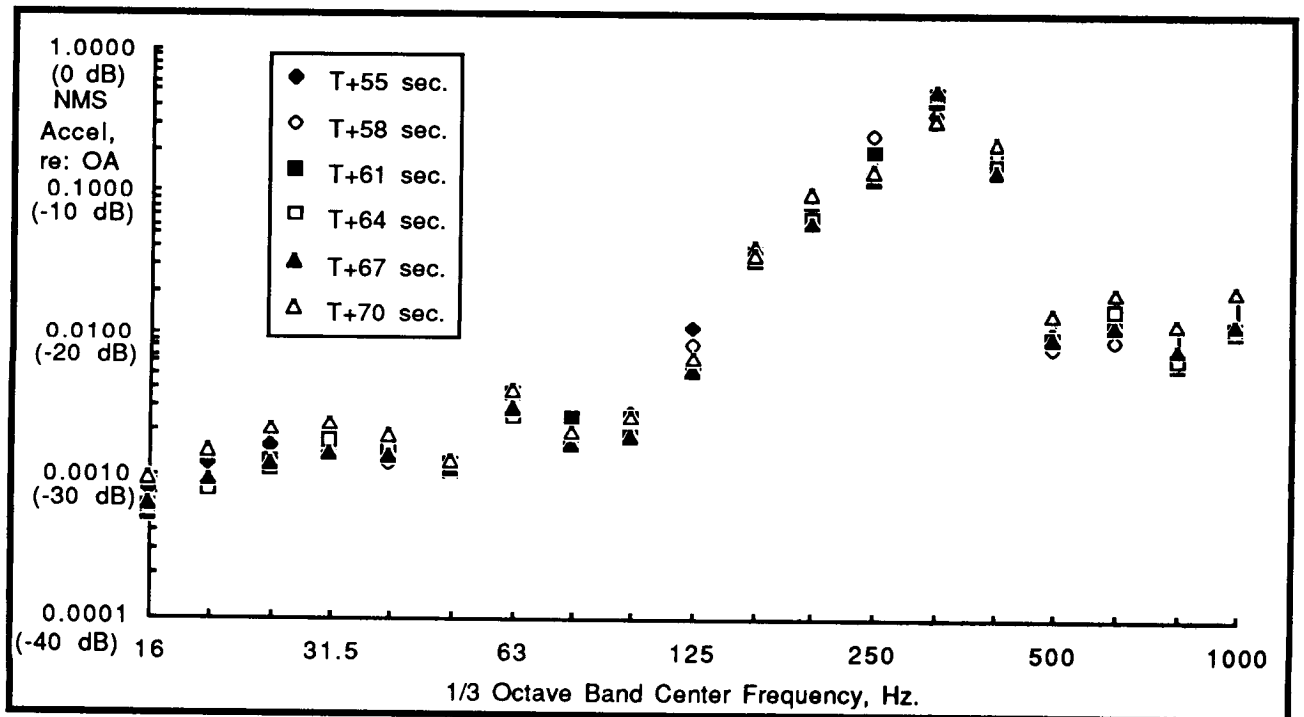
Figure A6b. 1/3 Octave Band Spectra Of Normalized MS Vibration Levels During Space Shuttle Max "q" Flight; STS-2 Accel 248.

MECHANICAL SHOCK

Conservatism Implications of Shock Test Tailoring for Multiple Design Environments

Thomas J. Baca
R. Glenn Bell
Susan A. Robbins

N88-13611

Specification of a mechanical shock test requires an en-
gineering decision concerning the relationship between the
laboratory and field shock environments. Once a method of
shock characterization is selected, test conservatism becomes
a measure of the degree to which the laboratory test is more
severe than the operational environment of the structure
being tested. This paper describes a method for analyzing
shock conservatism in test specifications which have been
tailored to qualify a structure for multiple design
environments. Shock test conservatism is quantified for
shock response spectra, shock intensity spectra and ranked
peak acceleration data in terms of an Index of Conservatism
(IQC) and an Overtest Factor (OTF). The multi-environment
conservatism analysis addresses the issue of both absolute
and average conservatism. The method is demonstrated in a
case where four laboratory tests have been specified to
qualify a component which must survive seven different field
environments. Final judgment of the tailored test
specification is shown to require an understanding of the
predominant failure modes of the test item.

INTRODUCTION

Tailoring test specifications for shock-hardened components requires an engineer
to relate the laboratory test environment to the field shock environment in the most
meaningful way possible. This process is critical since "overtesting" may require
expensive design modifications to the component, while "undertesting" will sustain
uncertainty regarding the survivability of the component in the field. The
fundamental problem becomes one of operationalizing the analyst's engineering
judgment about test conservatism into a consistent and quantitative methodology.
This process is complicated further when the component must survive more than one
field environment. An engineer typically utilizes data measured from the operational
shock environment as the basis for selecting the qualification test method and test
level. Test conservatism is a measure of the degree to which this tailored
laboratory shock environment exceeds the field environment. Even though it is rarely
evaluated in a quantitative manner, a level of test conservatism is implicit in every
test specification. In this paper, a method is presented and demonstrated for

---

assessing conservatism in shock test specifications tailored for multiple field environments.

Description of the conservatism analysis procedure will be presented by example. Shock data for an electronics package subjected to both operational and laboratory mechanical shock tests will be analyzed in the course of performing the conservatism assessment. The discussion will cover: 1) the original tailoring of the the test specification considering multiple environments; 2) the initial evaluation of conservatism; 3) the specification of a level of conservatism for judging an overtest condition; 4) the identification of overtest and undertest conditions; and 5) and the interpretation of the results in terms of possible failure modes of the component.

SHOCK TEST TAILORING

A common shock test tailoring procedure [1] is based on matching the absolute acceleration shock response spectra (SAA) [2] of the field data and a laboratory test input. If multiple field environments exist, then the test is specified to have a SAA spectrum which envelops the SAA of the field data. For the component being discussed in this paper, the field design environments consisted of six measured and one analytically predicted responses of the component in its longitudinal (X) and lateral (Y) axes. Figures 1A and 1B show the ensembles of SAA spectra for these environments. The field environments are denoted with regard to the fact that they are either derived from blast (B) or nonblast (NB) environments. These operating environments include: 1) three different impulsive shock tests (NB1, NB2, NB3); 2) one induced thermo-structural response (NB4); 3) two blast tests (B1 and B2); and one analytical prediction of a different type of blast loading (B3). Envelopes showing the distinction between the blast and nonblast environments are shown in Figures 2A and 2B. In general, the blast environments dominate the low frequency range (i.e., 100 Hz to 1000 Hz), while the nonblast environments control in the high frequency range (i.e., 1 KHz to 10 KHz). All of the data were lowpass filtered at 10 KHz and a 20 ms duration were analyzed for each record.

A resonant plate shock test technique [3] was chosen as the test method. This technique produces high level, two-sided shock inputs which are more similar to the field data than a one-sided haversine pulse which is generated using a drop table shock machine [4]. Two resonating plates were chosen with primary resonant frequencies of 250 Hz and 3000 Hz. The component test specification required that the component survive shocks on the low and high frequency plates in both the X and Y axes. Figures 3A and 3B show a comparison of SAA spectra for the field and test environments. The test designation is a three letter code denoting: the resonant plate used (H for the high frequency plate and L for the low frequency plate); the component axis aligned with the test input direction (X or Y); and the orientation of the accelerometer at the base of the component during the test (X or Y). For example. HYX is the measured X axis input during the Y axis high frequency plate test.

These tests were judged to be acceptably tailored given the constraints of seeking a minimum number of different test setups, and accepting partial enveloping of the X axis shock spectra in the high frequency range. Note that the X axis high frequency range controlled selection of the high frequency plate test while the Y axis low frequency data primarily influenced tailoring of the low frequency plate test.
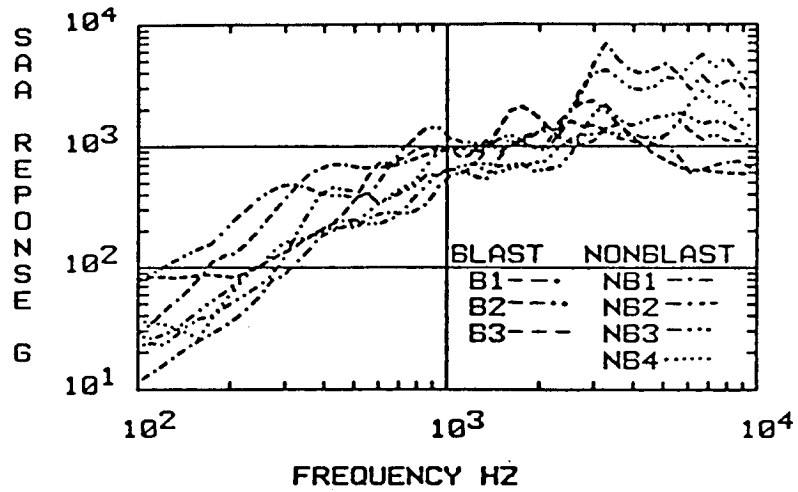
FIGURE 1A.
COMPARISON OF X AXIS SAA RESPONSE FIELD DATA
(DAMPING=0.05)
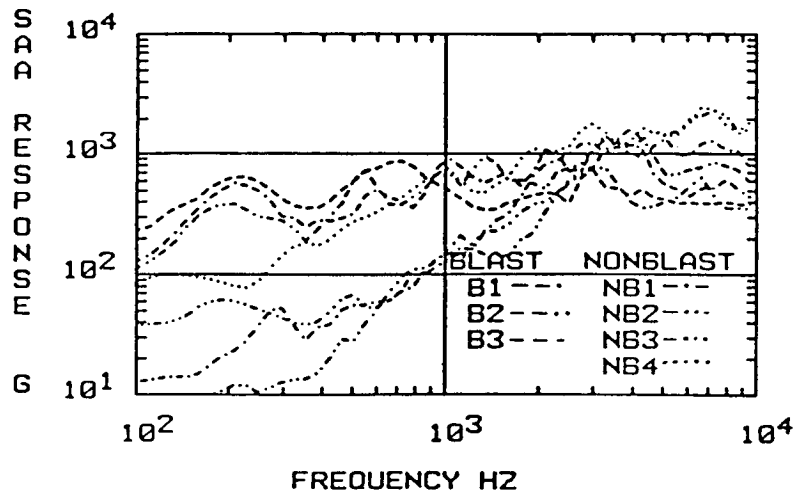
FIGURE 1B.
COMPARISON OF Y AXIS SAA RESPONSE FIELD DATA
(DAMPING=0.05)

FREQUENCY HZ
FIGURE 2A.
COMPARISON OF BLAST & NONBLAST X AXIS SAA FIELD DATA ENVELOPES
(DAMPING=0.05)

FREQUENCY HZ

FIGURE 2B.
COMPARISON OF BLAST & NONBLAST Y AXIS SAA FIELD DATA ENVELOPES
(DAMPING=0.05)
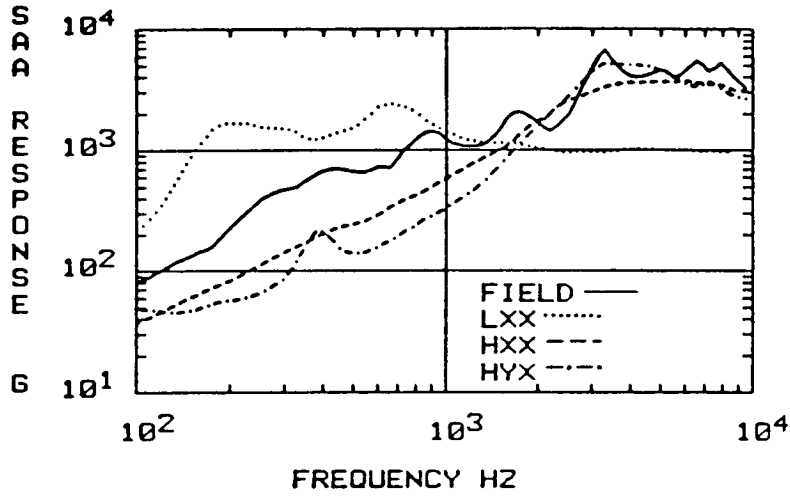
FIGURE 3A.
COMPARISON OF X AXIS SAA FIELD DATA ENVELOPE AND THREE TEST INPUTS
(DAMPING=0.05)
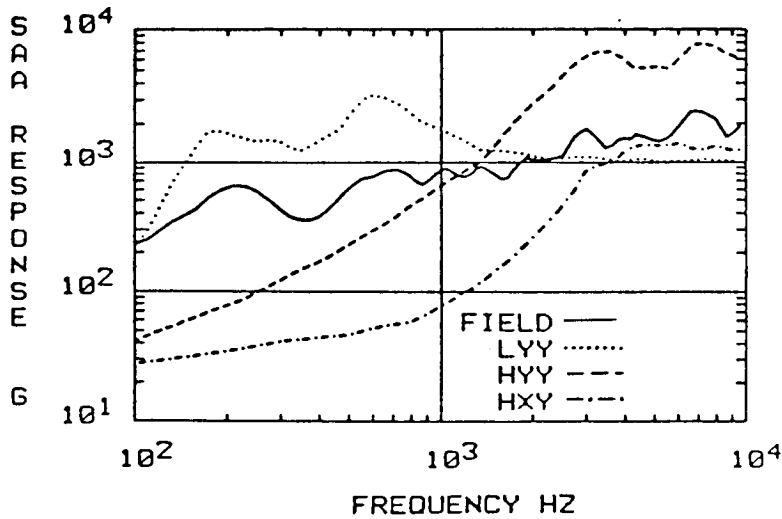
FIGURE 3B.
COMPARISON OF Y AXIS SAA FIELD DATA ENVELOPE AND THREE TEST INPUTS
(DAMPING=0.05)

33

MULTIPLE ENVIRONMENT SHOCK CHARACTERIZATION

Even if the shock test is specified on the basis of the SAA spectrum, it is not necessary to restrict the conservatism assessment to that sole shock characterization. The advantages of utilizing alternative shock characterizations have been demonstrated in previous studies of shock conservatism involving single field environments [5-8]. Primary attention will be focused on the shock intensity spectrum (SIS) which is a plot of the contribution of each frequency band shown to the overall rms acceleration of the shock transient [8]. The SIS has the advantage of being a direct indicator of frequency content of the shock signal, while the SAA represents the single degree of freedom response to the shock transient as a function of the natural frequency of the SDOF resonators. Additional mention will be made of the ranked acceleration peaks, with particular attention being paid to the highest peak value (TPK1) as a meaningful shock characterization.

These shock characterizations were computed using the SHARPE computer code [5.8] for all of the field and laboratory test data. The blast and nonblast envelopes of the X axis field test SIS spectra are given in Figure 4. Note the lack of frequency content in the blast data above 3000 Hz. A comparison between an envelope of all of the field data and the lab test data is shown in Figure 5. The predominant frequency of the low frequency plate is shown to actually be at 180 Hz. The question of statistical variation of a shock environment characterization must also be considered prior to the conservatism analysis. This is a difficult question because of the paucity of field data normally available at the time the test is specified, so it is rarely answered. Since all seven field environments considered in this study were different, each field environment characterization is considered as an average value having a coefficient of variation of 0.15. This introduces a variability factor into the field data which may be optimistic (i.e., it may be difficult to verify the accuracy of the measured or analytical data with this degree of refinement), but previous studies [8] indicate that this is a reasonable value. The statistical variation of the laboratory tests was dealt with by repeating each test ten times. Mean values and standard deviations were also calculated by the SHARPE code for the ensembles of laboratory test data.

CONSERVATISM CRITERIA

The index of conservatism (IOC) [5] provides a quantitative criterion for evaluating shock conservatism. Calculating the IOC for a particular shock characterization C requires that the mean and standard deviations of the field and test be provided by the analyst. Representing the mean values as $\overline{C}_T$ and $\overline{C}_F$, and the standard deviations as σ_T and σ_F, where T and F denote the lab test and field environments, respectively, the IOC is defined as:

$$IOC = \frac{\overline{C}_T - \overline{C}_F}{\sqrt{\sigma_T^2 + \sigma_F^2}} = \frac{\overline{M}}{\sigma_M} \qquad (1)$$

where $\overline{M}$ is the mean margin of conservatism and σ_M is the standard deviation of the margin of conservatism. Figures 6 and 7 depict the relationship between these field and test environment parameters. These figures also emphasize the fact that when the mean margin of conservatism is zero, the mean field and test environments are the same on the average, but some of the time there is an overtest or an undertest.
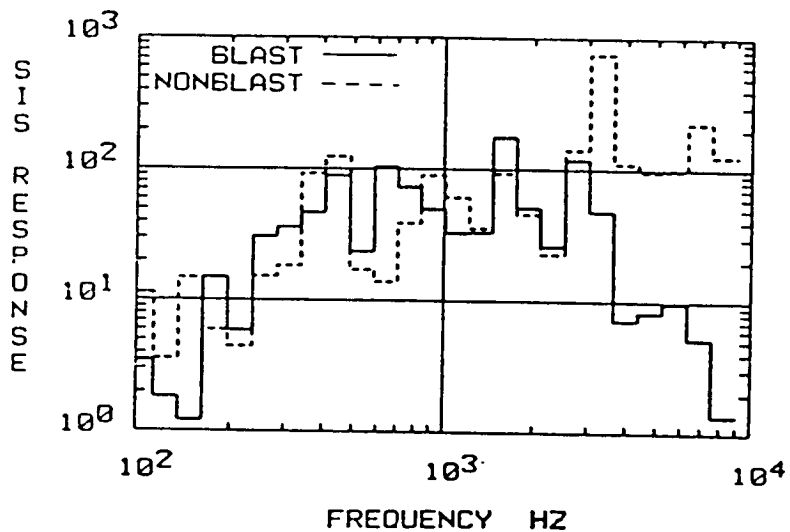
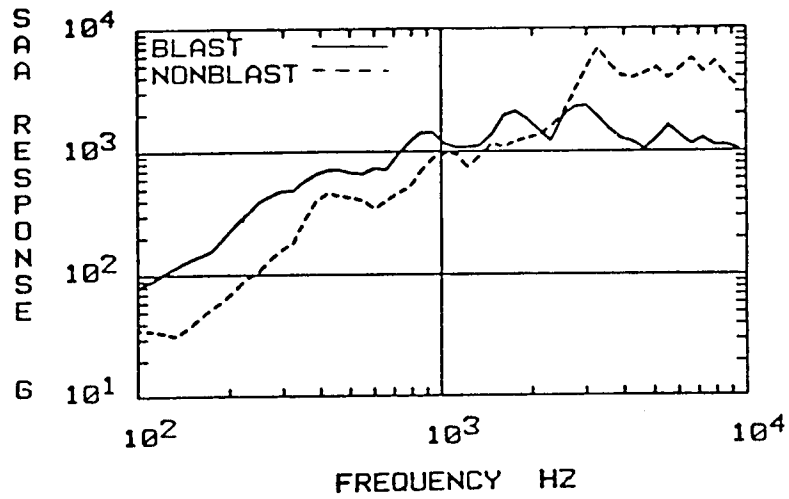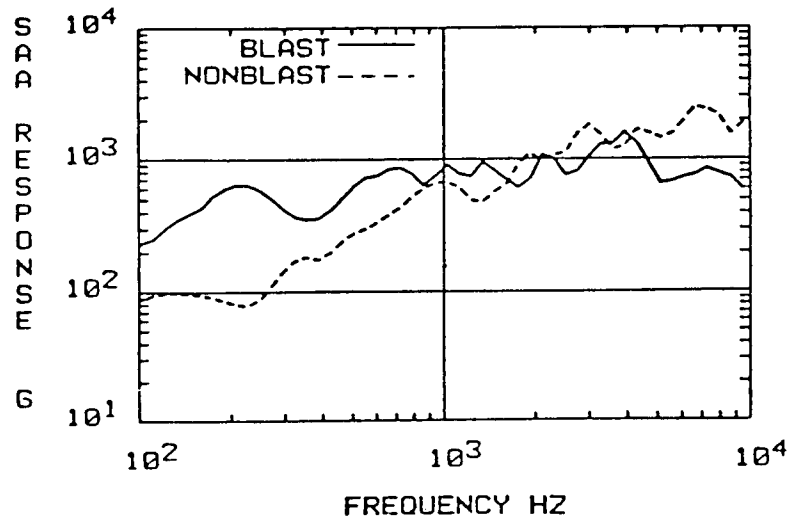FIGURE 4.
COMPARISON OF BLAST & NONBLAST X AXIS SIS FIELD DATA ENVELOPES
(DURATION=0.02)
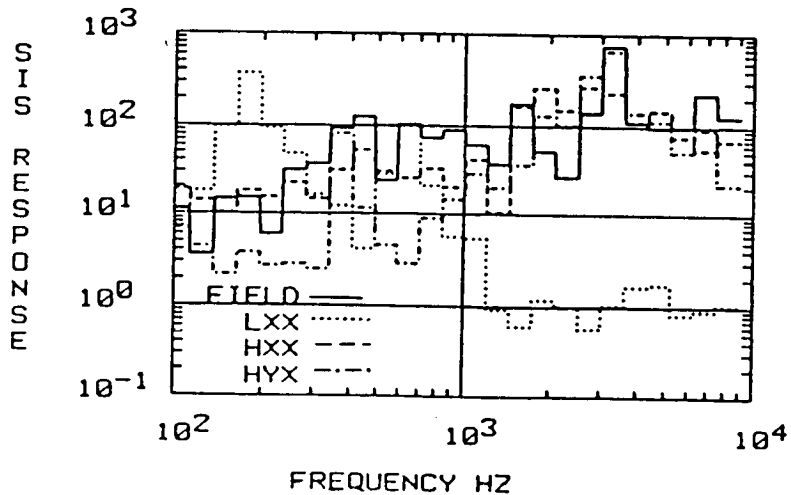
FIGURE 5.
COMPARISON OF X AXIS SIS FIELD DATA ENVELOPE AND THREE TEST INPUTS
(DURATION=0.02)

35

$P_C(c)$
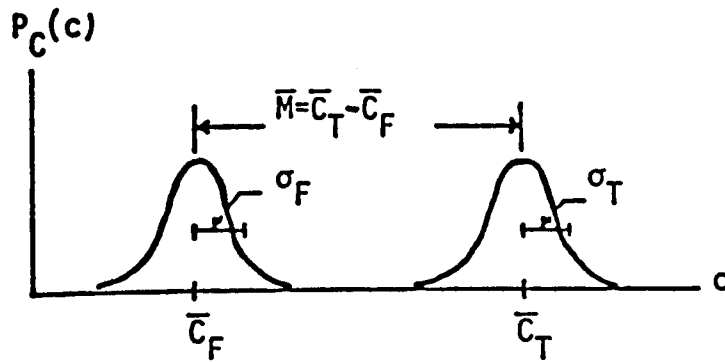
Figure 6 Probability Density Functions of Field and Laboratory Test Shock Environments

$P_M(m)$
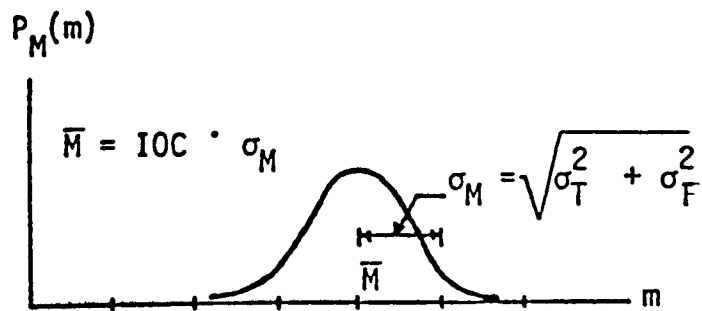
Figure 7 Probability Density Function of the Margin of Conservatism M

Initially in this study, a test is considered conservative if the IOC is greater than zero. This criterion is the basis of a conservatism binary index (CBI_j) which is defined for N different field tests under study:

$$CBI_j = \begin{cases} 0, & IOC_j < 0 \\ 1, & IOC_j \geq 0 \end{cases} \qquad j = 1,N \qquad (2)$$

Once the CBIj is calculated, these values are combined in a quantity called the multiple environment conservatism ratio (MECR) given by:

$$MECR = \frac{\sum\limits_{J=1}^{N} CBI_j}{N} \qquad (3)$$

Thus, a MECR value of one indicates that the test was always conservative, and a zero value would indicate that the laboratory test was never conservative for any of the field environments. The MECR ratios were computed for SAA and SIS data collected as X axis inputs to the component in the three lab tests and the seven field tests. This data is shown in Figures 8A and 8B. Figure 8A shows that the low frequency test covers the field data up to 1300 Hz. The high frequency tests are conservative for only 70 to 80 percent of the tests at frequencies above 1500 Hz. The MECR for SIS in Figure 8B reveals a frequency range between 950 and 1100 Hz where none of the tests were conservative. Both plots indicate that the Y axis test is comparable to the X axis test in providing an X axis input to the component.

SPECIFYING CONSERVATISM REQUIREMENTS

While the MECR ratio indicates whether the test was nominally conservative, it does not indicate the degree to which an overtest or an undertest was experienced during the test. This can only be done once the analyst has selected a desired level of conservatism for the test. Specifying the desired level of conservatism involves selecting an IOC value and then calculating an overtest factor (OTF) [8] defined as:

$$OTF = \frac{\overline{C}_T}{\overline{C}_{T,I}} \qquad , IOC = I \qquad (4)$$

where $\overline{C}_{T,I}$ is the mean characterization of the test data which will produce the desired IOC value of I. In other words, the OTF indicates how many times greater the mean test characterization was than it had to be to satisfy the conservatism criterion. The OTF is calculated assuming that $\overline{C}_T$ varies linearly and that σ_T

37
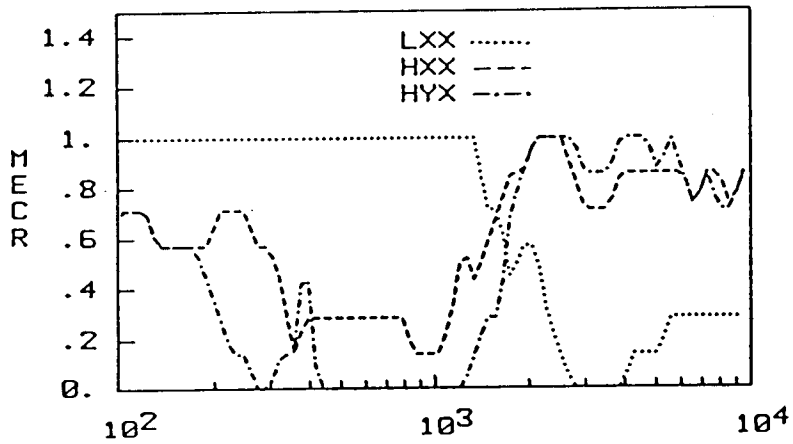
FREQUENCY HZ
FIGURE 8A.
MERC FOR X AXIS SAA RESPONSE
(DAMPING=0.05)
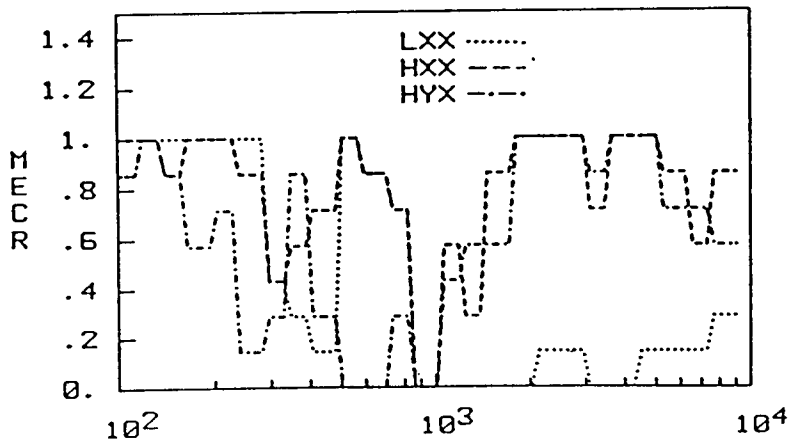
FREQUENCY HZ
FIGURE 8B.
MECR FOR X AXIS SIS RESPONSE
(DURATION=0.02)

remains constant regardless of a change in $\bar{C}_T$. An overtest occurs if OTF is greater than one. An OTF less than one indicates an undertest.

OVERTEST ANALYSIS

Assuming that an IOC of one is the desired degree of shock test conservatism, the OTFs for SAA and SIS were computed for each combination of field test and lab test. The minimum of these OTF curves are shown in Figures 9A and 9B. Significant overtesting is apparent in both plots at the resonant frequencies of the high and low frequency plates.

In order to get a closer look at where the overtest and undertest is occurring, a multiple environment overtest ratio (MEOR) can be defined:

$$MEOR = \frac{\sum\limits_{j=1}^{N} OBI_j}{N} \tag{5}$$

where N is the number of field environments and the overtest binary index is given by:

$$OBI_j = \begin{cases} 0, & OTF_j < 1 \\ 1, & OTF_j \geq 1 \end{cases} \qquad j = 1,N \tag{6}$$

The MEOR plots for SAA and SIS are shown in Figures 10A and 10B, respectively. Note the general similarity between Figures 10A and B and the MECR plots in Figures 8A and 8B. The plot amplitudes have decreased in the MEOR curve where the lab tests are only marginally conservative. Figures 11A and 11B portray the SAA and SIS MEOR ratios for the Y axis tests. The Y axis tests indicate that the desired level of conservatism was reached for nearly the entire SAA spectrum (Figure 11A). The Y axis SIS spectrum MEOR ratio, however, reveals a significant area of undertest in the 900 to 1000 Hz region.

FAILURE MODEL BASIS FOR INTERPRETING RESULTS

Final interpretation of the conservatism analysis results obtained so far requires the analyst to assume a failure model for the component being tested. For example, if the component has a failure mode in the X axis associated with a certain frequency, the analyst looks at Figures 9A or 9B to determine the value for the minimum overtest factor at that frequency. If an overtest occurs, consideration might be given to modifying the test input accordingly. If an undertest is observed, then Figures 10A or 10B indicate what percentage of the field tests experience an undertest at this frequency.

FREQUENCY HZ
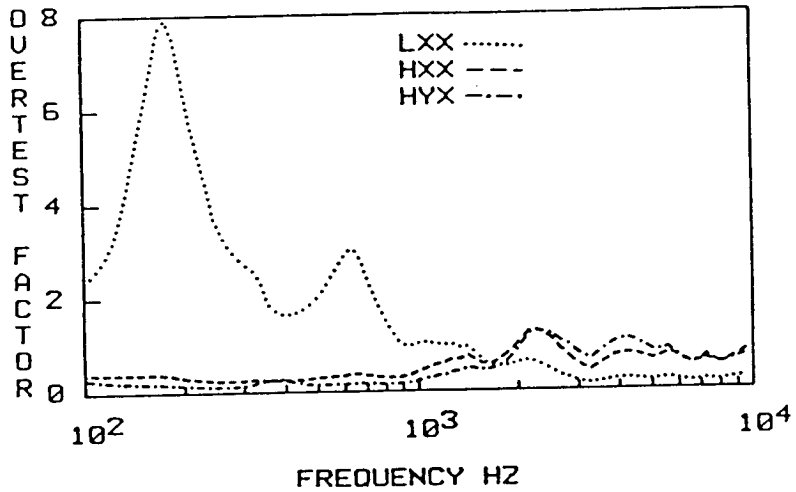
FIGURE 9A.

COMPARISON OF X AXIS SAA OTF MINIMUMS FOR THREE TEST INPUTS
(DAMPING=0.05)
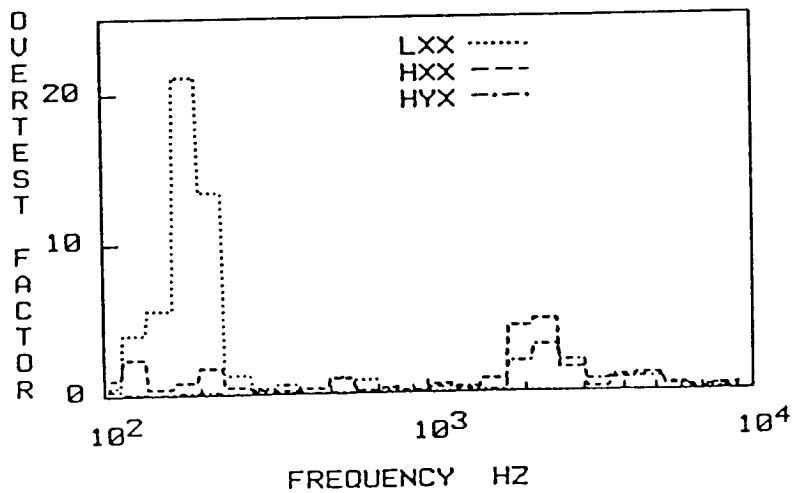
FREQUENCY HZ

FIGURE 9B.

COMPARISON OF X AXIS SIS OTF MINIMUMS FOR THREE TEST INPUTS
(DURATION=0.02)
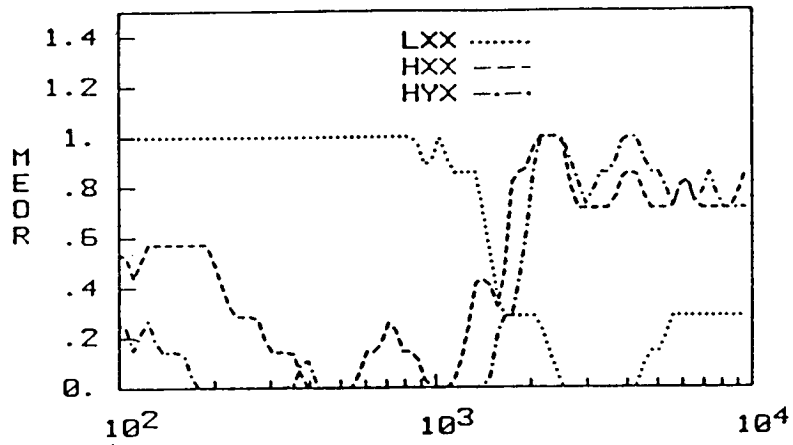
FREQUENCY HZ
FIGURE 10A.
MEOR (IOC=1) FOR X AXIS SAA RESPONSE
(DAMPING=0.05)
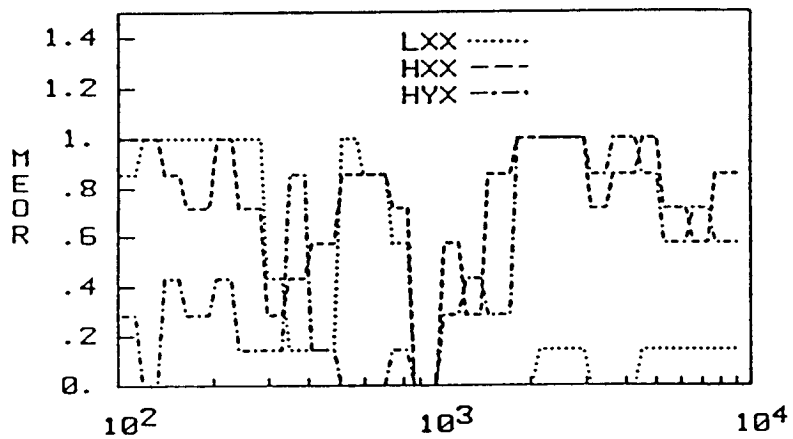
FREQUENCY HZ

FIGURE 10B.
MEOR (IOC=1) FOR X AXIS SIS RESPONSE
(DURATION=0.02)

41
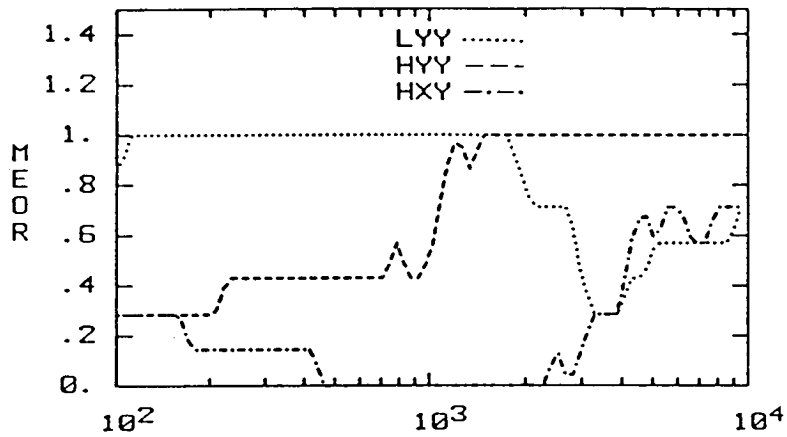
FREQUENCY   HZ
FIGURE 11A.
MEOR (IOC=1) FOR Y AXIS SAA RESPONSE
(DAMPING=0.05)
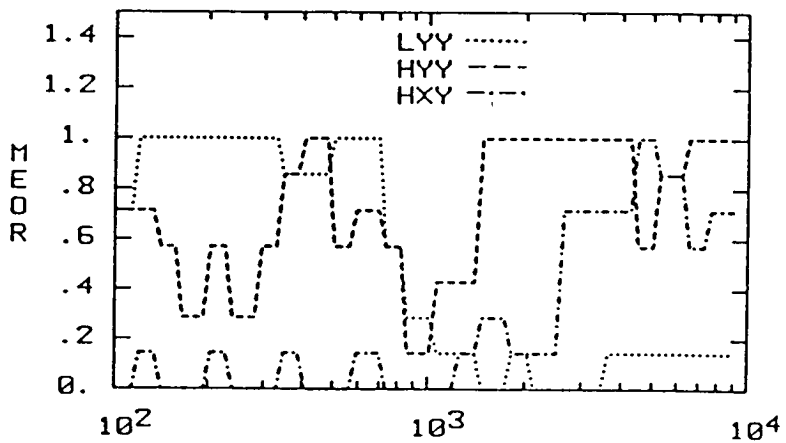
FREQUENCY   HZ

FIGURE 11B.
MEOR (IOC=1) FOR Y AXIS SIS RESPONSE
(DURATION=0.02)

When the sensitivity of the component is not well understood, another approach is to summarize the conservatism data by assuming a general type of failure model, such as a brittle displacement sensitive structure or a fatigue/multicycle sensitive structure. The conservatism analysis in the X axis is summarized in Tables I and II for each of these failure models. Table IA and Table IIA present overtest and undertest weights as bar charts and weighted OTF numerical values for each of the field/lab test comparisons. The overtest weight WTO is given by:

$$WTO = \frac{\sum\limits_{i=1}^{K} D_{oi}}{\sum\limits_{j=1}^{L} D_{aj}} \qquad (7)$$

where:

D_{oi} = ith abcissa delta increment where an overtest condition exists for the shock characterization

D_{aj} = jth abcissa delta increment for the shock characterization

K = total number of abcissa overtest delta increments

L = total number of abcissa delta increments.

For discrete characterizations like ranked peaks, the WTO is the ratio of the number of ranked peaks which were an overtest to the total number of ranked peaks under study. For frequency domain characterizations, the WTO is the ratio of the cumulative frequency range where an overtest condition occurred to the total frequency range being considered. An undertest weight WTU is defined in a parallel manner. Note that WTO and WTU must sum to one. The shaded rectangle is positioned in the bar depending on the relative values of WTO and WTU. Complete undertest is indicated by a shaded box shifted entirely to the left, and complete overtest is indicated by a shaded box situated on the right end of the bar chart. This display of the data offers the analyst the opportunity to see the range of test conservatism. The weighted OTF values OTFw are shown on each side of the bar chart and are defined as:

$$OTFw = \begin{cases} WTO * \dfrac{\sum\limits_{i=1}^{K} OTF_i}{K} & OTF_i \geq 1 \\[4ex] WTU * \dfrac{\sum\limits_{i=1}^{L-K} OTF_i}{L-K} & OTF_i < 1 \end{cases} \qquad (8)$$

43

TABLE IA.

SUMMARY OF OVERTEST FACTOR WEIGHTS AND WEIGHTED OTFS BRITTLE AND DISPLACEMENT SENSITIVE STRUCTURES

LXX ▬   HXX ▥   HYX ▨

	MAX PEAK G		SAA 100–1000 HZ		SIS 100–1000 HZ	
	UNDER TEST	OVER TEST	UNDER TEST	OVER TEST	UNDER TEST	OVER TEST
B1	0.00	1.51	0.00	6.32	0.10	14.87
	0.00	3.29	0.47	0.01	0.25	5.18
	0.00	3.39	0.28	0.00	0.19	0.63
B2	0.00	1.15	0.09	3.35	0.14	12.37
	0.00	2.51	0.35	0.00	0.26	1.95
	0.00	2.56	0.21	0.00	0.20	0.16
B3	0.00	1.55	0.00	7.79	0.17	20.00
	0.00	3.25	0.65	0.00	0.25	12.06
	0.00	3.45	0.37	0.00	0.24	1.29
NB1	0.55	0.00	0.00	17.22	0.16	20.00
	0.00	.121	0.40	0.97	0.12	9.92
	0.00	1.24	0.59	0.16	0.13	1.13
NB2	0.00	1.14	0.00	11.73	0.16	7.20
	0.00	2.49	0.49	0.30	0.14	1.70
	0.00	2.57	0.50	0.02	0.24	0.00
NB3	0.45	0.00	0.00	10.61	0.19	20.00
	0.98	0.00	0.57	0.37	0.25	4.43
	0.00	1.01	0.57	0.00	0.40	0.36
NB4	0.00	1.09	0.00	11.22	0.16	17.93
	0.00	2.36	0.68	0.17	0.32	2.22
	0.98	0.00	0.57	0.37	0.25	4.43

TABLE IB.

SUMMARY OF OVERTEST FACTOR WEIGHTED AVERAGES BRITTLE AND DISPLACEMENT SENSITIVE STRUCTURES

LXX ▬   HXX ▥   HYX ▨

	MAX PEAK G		SAA 100–1000 HZ		SIS 100–1000 HZ	
	UNDER TEST	OVER TEST	UNDER TEST	OVER TEST	UNDER TEST	OVER TEST
ALL	0.14	0.92	0.01	9.61	0.16	16.05
	0.14	2.16	0.51	0.26	0.23	5.36
	0.14	2.04	0.44	0.08	0.23	1.14
B	0.00	1.40	0.03	5.49	0.14	15.74
	0.00	3.02	0.49	0.00	0.25	6.41
	0.00	3.14	0.29	0.00	0.21	0.69
NB	0.26	0.56	0.00	12.69	0.16	16.28
	0.25	1.52	0.53	0.45	0.21	4.57
	0.25	1.21	0.56	0.14	0.25	1.48

44

TABLE IIA.

SUMMARY OF OVERTEST FACTOR WEIGHTS AND WEIGHTED OTFS
FATIGUE AND MULTICYCLE SENSITIVE STRUCTURES

Legend: LXX ▬ HXX ▥ HYX ▨

		MAX 5 PEAK G		RMS OVERALL		ALL SIS	
		UNDER TEST	OVER TEST	UNDER TEST	OVER TEST	UNDER TEST	OVER TEST
B1	LXX	0.33	0.83	0.00	1.50	0.24	1.33
	HXX	0.19	1.56	0.00	2.79	0.05	9.93
	HYX	0.00	2.10	0.00	3.05	0.05	8.86
B2	LXX	0.49	0.44	0.00	1.14	0.20	1.28
	HXX	0.18	1.21	0.00	2.12	0.05	8.68
	HYX	0.00	1.70	0.00	2.32	0.05	7.94
B3	LXX	0.19	1.10	0.00	1.55	0.06	20.00
	HXX	0.00	1.87	0.00	3.25	0.06	20.00
	HYX	0.00	2.29	0.00	3.45	0.05	20.00
NB1	LXX	0.43	0.00	0.55	0.00	0.12	5.71
	HXX	0.41	0.24	0.00	1.02	0.21	5.13
	HYX	0.54	0.25	0.00	1.12	0.17	1.64
NB2	LXX	0.18	0.96	0.00	1.13	0.17	0.64
	HXX	0.00	1.66	0.00	1.23	0.05	5.07
	HYX	0.00	2.04	0.73	0.00	0.05	5.28
NB3	LXX	0.43	0.00	0.45	0.00	0.18	3.01
	HXX	0.63	0.00	0.83	0.00	0.35	2.14
	HYX	0.56	0.20	0.91	0.00	0.25	0.99
NB4	LXX	0.30	0.64	0.00	1.10	0.19	1.83
	HXX	0.17	1.22	0.00	2.05	0.15	5.30
	HYX	0.63	0.00	0.83	0.00	0.35	2.14

TABLE IIB.

SUMMARY OF OVERTEST FACTOR WEIGHTED AVERAGES
FATIGUE AND MULTICYCLE SENSITIVE STRUCTURES

Legend: LXX ▬ HXX ▥ HYX ▨

		MAX 5 PEAK G		RMS OVERALL		ALL SIS	
		UNDER TEST	OVER TEST	UNDER TEST	OVER TEST	UNDER TEST	OVER TEST
ALL	LXX	0.34	0.57	0.14	0.92	0.17	4.83
	HXX	0.23	1.11	0.12	1.78	0.13	8.03
	HYX	0.26	1.23	0.35	1.42	0.14	6.69
B	LXX	0.34	0.79	0.00	1.40	0.18	7.53
	HXX	0.12	1.55	0.00	2.72	0.05	12.87
	HYX	0.00	2.03	0.00	2.94	0.05	12.27
NB	LXX	0.33	0.40	0.25	0.56	0.17	2.80
	HXX	0.30	0.78	0.21	1.07	0.19	4.41
	HYX	0.43	0.62	0.62	0.28	0.21	2.51

where L and K are defined above. The weighted OTF reflects both the amplitude of the OTF and the range over which either an undertest or an overtest occurs. Zero values of OTFw indicate that either WTO or WTU was zero for that range of the shock characterization. It should be noted that nonzero weighted overtest factors have been limited to values between 0.05 and 20 in an effort to keep extremely large overtest values from dominating summary averages of the weighted OTFs in Tables IB and IIB. These summary averages provide a measure of overall overtest or undertest characterized into three summary groups: all of the tests, the blast tests. and the nonblast tests. A review of these tables indicates that even though absolute conservatism is not achieved for all of the shock characterizations, the analyst is in a position to make a quantitative statement about the degree of overtest or undertest in an average sense. The low frequency X axis shock test is quite conservative for brittle and displacement sensitive structures as indicated in Table IB.

The high frequency content of the X and Y axes tests results in their achieving the desired level of conservatism for fatigue and multicycle sensitive components.

CONCLUSION

Conservatism analysis techniques have been described and demonstrated in this paper which address the complication of trying to make a laboratory test qualify a component for use in multiple field environments. Quantitative measures are introduced which show when tests are conservative in both an absolute and average sense. Both the degree of undertest and the degree of overtest are tracked in this procedure. Alternatives to shock spectra are shown to give additional conservatism information to the engineer which may be crucial in determining the suitability of a shock test specification. The desired level of conservatism used in the analysis is always clearly stated, and can be modified to meet the requirements of the design engineer. Specifically, knowledge about the failure modes of a component may lead to lower level test specifications which do not meet the original criterion of enveloping shock spectra, but which can be rigorously shown to be conservative in terms of another shock characterization. Greater insight into the significance of the functional outcome of the test (i.e., did it break because the design is too weak or because the test specification is too conservative ?) and detailed knowledge of how the test specification can be altered to achieve a desired level of test conservatism are two significant benefits of performing a conservatism analysis. Future use of these techniques will produce qualification test inputs which venture beyond the realm of engineering judgment, and enter the state of soundly tailored test specifications founded on quantifiable measures of conservatism.

REFERENCES

1. S. Rubin, "Concepts in Shock Data Analysis," Shock and Vibration Handbook, Second Edition, C. M. Harris and C. E. Crede, eds., New York: McGraw-Hill, 1976, pp. 23-1,30.

2. R. D. Kelly and G. Richman, Principles and Techniques of Shock Data Analysis, The Shock and Vibration Information Center, USDOD, SVM-5, 1969.

3. N. Davie, "The Controlled Response of Resonating Fixtures Used to Simulate Pyroshock Environments," Shock and Vibration Bulletin, Vol. 56, Part 3, 1986, pp. 119-124.

4. I. Vigness and J. R. Sullivan, "Shock Testing Machines," Shock and Vibration Handbook, Second Edition, C. M. Harris and C. E. Crede, eds., New York: McGraw-Hill, 1976, pp. 26-1,19.

5. T. J. Baca, "Characterization of Conservatism in Mechanical Shock Testing of Structures," SAND82-2186, Sandia National Laboratories, 1983.

6. T. J. Baca, "Evaluation and Control of Conservatism in Drop Table Shock Tests," Shock and Vibration Bulletin, Vol. 53, Part 1, 1983, pp. 163-176.

7. T. J. Baca, "Alternative Shock Characterizations for Consistent Shock Test Specifications," Shock and Vibration Bulletin, Vol. 54, Part 2, 1984, pp.109-130.

8. T. J. Baca and T. D. Blacker, "Relative Conservatism of Drop Table and Shaker Shock Tests," Shock and Vibration Bulletin, Vol. 56, Part 1, 1986, pp. 289-298.

Scaling the Electromagnetically Driven Explosive Shock Simulator

Robert I. Persh

A heavy payload electromagnetically driven explosive shock
simulator, referred to as EDESS-3, has been assembled and
characterized at the Naval Surface Weapons Center. EDESS-3
is the logical outgrowth of the earlier EDESS 1 and 2
simulator work which explored the use of electrical pulse
power technology for the generation of explosive like
shocks. This paper presents the features of EDESS-3,
reviews the shock generation concept, and introduces designs
for the next generation of EDESS machines.

INTRODUCTION

EDESS-3 (the third generation of Electromagnetically Driven Explosive Shock
Simulator), has been successfully evaluated at the Naval Surface Weapons Center.
EDESS-3 has a twenty ton payload and is the culmination of a NAVSEA Program to
develop and demonstrate an alternate technology for shock testing equipment to
MIL S 901C type shocks over a wider range of payload weights. EDESS technology
holds the promise of providing the mechanical designer and equipment qualifier
with the means to perform shock developmental and qualification testing in a
laboratory setting over the full MIL S 901C range of equipments.

The groundbreaking EDESS 1 and 2 established the engineering practicality of
using pulse-power for generating explosive like shocks in significant payloads.
The 2 ton payload EDESS-1 and 5 ton EDESS-2 laid the groundwork for many of the
techniques integrated into EDESS-3. These earlier machines pioneered the use of
pancake drive coils, high energy density capacitor banks, triggered backstrap
switching, and air suspension and isolation of the reaction mass.

The shock output of EDESS-3 has been carefully characterized from a large
number of acceleration measurements. The resulting shock signatures strongly
correlate with floating shock platform signatures for similar loads. Shocks
measured in a 20-ton armor plate load at full rated bank energy are routinely in
excess of 100 g's with velocities of 11 ft/sec and center of mass displacements of
13 inches.

CONCEPT OF OPERATION

EDESS develops explosive like shocks in subject test objects, as a result of the magnetic repulsive force between pairs of spiral pancake magnetic coils that are positioned between a large reaction mass and the test carriage upon which the test object is mounted. The driving energy is supplied from the electrostatic energy stored in capacitor banks and is transferred to the coil pairs by the closure of a high voltage/high current triggered switch.

The concept is illustrated in Figure 1. The figure shows a cross section of a typical pair of single layered, spirally wound pancake coils connected in series opposition. When a pulse of current flows from terminals A to B through the spiral paths of the two coils, a large magnetic repulsive force is developed between the coils as a result of the opposite flow through each of the nearly touching circular coils. A (+) refers to current flow into the plane of the drawing; while a (.) refers to flow out of the plane. The series inductance and capacitance can be varied to generate a variety of single shock pulses. The design details are developed in some detail in Reference 2. In general, once the system capacitance is established by the capacitance of the energy storage banks, the time constant and associated rise time of the driving pulse can be defined through the suitable selection of driving coil inductance.
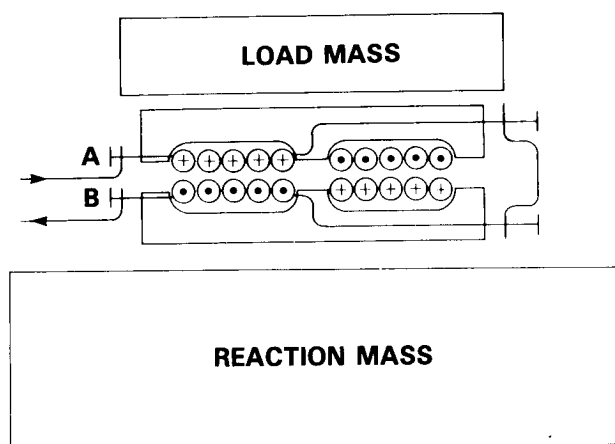
Figure 1. Shock Generation Concept

TECHNICAL DETAILS

EDESS-3 capacitor banks utilize high energy density capacitors which result in net energy densities of 2.78kJ/cu ft, with a system capacity of 1.5MJ. The banks are assembled with 20 each 125ufd, 20kVDC capacitors; Maxwell Laboratories, Inc. part No. 32289. Each of the three resulting 500kJ energy storage banks in the current system is a forklift manageable, modular steel construction weighing approximately three tons and occupying 108 cu ft. Reference is made to Figures 2 and 3. Figure 2 shows the internal details of the standard 500kJ bank. The schematic of Figure 3 outlines the electrical details of the EDESS-3 machine. For internal protection the banks utilize series current limiting resistors and protective fuses. Referring to Figure 3, the current limiting resistors (1) limit the discharge current that the individual capacitors (2) can achieve in case of a shorted load. The protective fuses (3) are specified to prevent destructive discharge of the entire bank or banks into a shorted capacitor. The twenty parallel capacitors feed a low inductance triaxial transmission line (4), designed to minimize the bank time constant and rise time. Each bank contains integral charge current limiting resistors and protective fuses (5), dump resistor networks (6) and associated remote controlled contactors (7), for the charge disconnect and

dump modes of operation. The triaxial feed lines join at the forward end of the banks where they are serviced by a single triggered switch.

Switching of the electrical energy is accomplished through a pin triggered backstrap type high voltage/current switch, utilizing canted graphite electrodes which operate in a plasma quenching atmosphere. The switch design has emphasized long life/low maintenance electrodes with a wide, no adjustment, operating voltage range. The EDESS machine is designed to offer the user wide latitude and ease of selection of

Figure 2. 500 kJ Capacitor Bank

peak shocks. To this end, the switch has undergone an evolutionary process culminating in the current radial trigger pin configuration which offers reliable triggering over the entire useful EDESS charge voltage range. The radial trigger pin, which supplanted the earlier coaxial pin design, is triggered by the discharge of a five stage, 100kV marx type high voltage trigger generator. This combination of radial trigger pin and high trigger voltage allows wide main switch gapping with consistent triggering which is generally independent of the capacitor bank's charge voltage.

Figure 3. EDESS-3 Electrical

The switch electrodes are machined graphite cylinders of four-inch diameter and six-inch length. The discharge end of each electrode is hemispherically shaped to minimize any pre-fire enhancing sharp geometries. Earlier switch designs demonstrated self-destructive tendencies due to plasma growth associated

with the switch geometry and backstrap displacement of the plasma. To overcome this, the EDESS-3 switch utilizes a canted geometry and a plasma quenching sulfur hexaflouride operating atmosphere which reduces electrode and mounting bracket damage. The resulting switching arrangement shown mechanically in Figure 4 has demonstrated a life to date in excess of several hundred shots with no damage and minimal maintenance. Operationally the switch features dependable, no adjustment, triggering over the entire usable operating range of the simulator.

The mechanical design of EDESS-3 depicted in Figure 5, utilizes twelve air springs (1) to effectively shock isolate the reaction mass from the concrete laboratory floor. The reaction mass (2) consists of 80 tons of steel armor plate and provides a four to one mass ratio with the maximum capacity of the machine. The test carriage (3), a 20 ton armor plate in the current machine is supported on four bi-directional hydraulic cylinders. The cylinders in combination with accumulators and one-way bypass valves (4) (and shown in detail in Figure 6) form a passive load catcher system, which serves the dual purpose of preventing rebound

Figure 4. Triggered Backstrap Output Switch

shock to the coil pairs and elimination of rebound shock to the test object. The hydraulics in conjunction with the four guide pins (5), maintain the alignment between the test carriage and the reaction mass, thereby insuring the maximum force between the coil pairs. EDESS-3 utilizes four driving coil pairs, Figure 7, the coils being of the single layer spiral wound design, that has been established in earlier simulators. The four pairs of 30 inch diameter coils, backed with G-10 fiberglass forms, are veterans of over 300 shock shots and have demonstrated only superficial wear.

OPERATIONAL RESULTS

Subsequent to developmental testing, a characterization test series was performed to highlight shock performance as a function of operating voltage and spacial parameters. The EDESS was tested at charge voltages of 10-20kV which translates to 25-100 percent of the stored energy capacity of the 1.5MJ capacitor banks. For the purpose of these tests the machine was loaded with a twenty ton armor plate. Operational shock data was acquired from two accelerometer arrays, each utilizing five ENDEVCO model no. 2262-2000 accelerometers. The first array mapped corner-to-corner variations, while the second highlighted variations along a typical diagonal. The location of the accelerometer arrays is shown in Figure 5.
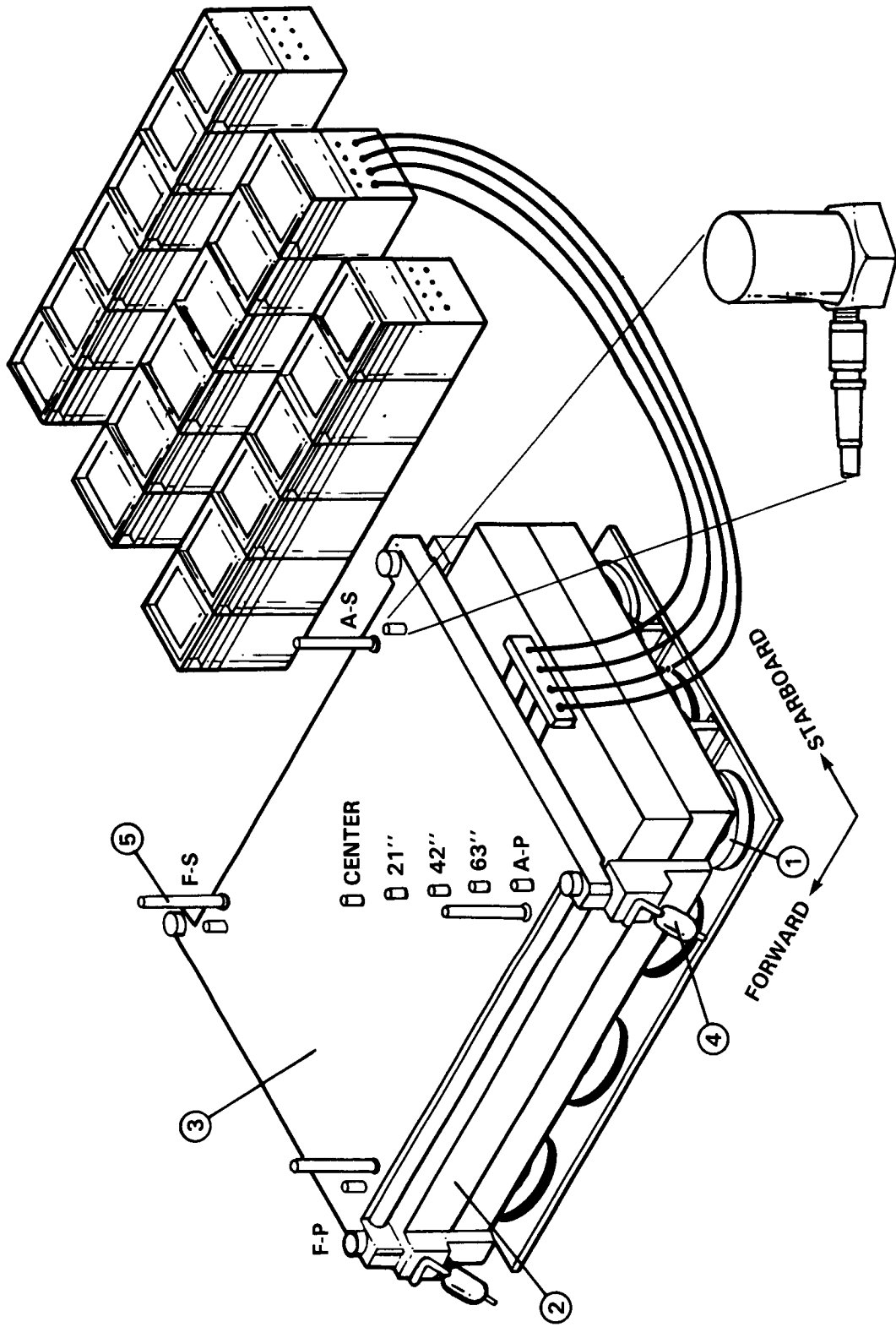
Figure 5. EDESS-3

Figure 8 reproduces a typical shot data sheet reduced from data acquired during the characterization test series. This particular example is of a 20kV (100 percent energy) shot with measurements from the accelerometer located at the center of the test mass. The upper left trace shows measured acceleration in g's which has been low pass filtered with a cutoff frequency of 2kHz. The second trace is of digitally integrated acceleration - velocity in ft/sec. The third left trace is of 200 Hz filtered acceleration data, while the second integral or displacement is shown at bottom left in units of inches. For each of these plots the time base is in units of seconds. At upper right, a pictorial view of the test mass locates the accelerometer from above. The lower right shock spectrum is plotted on a four-coordinate system with frequency on the abscissa and spectral acceleration on the ordinate.
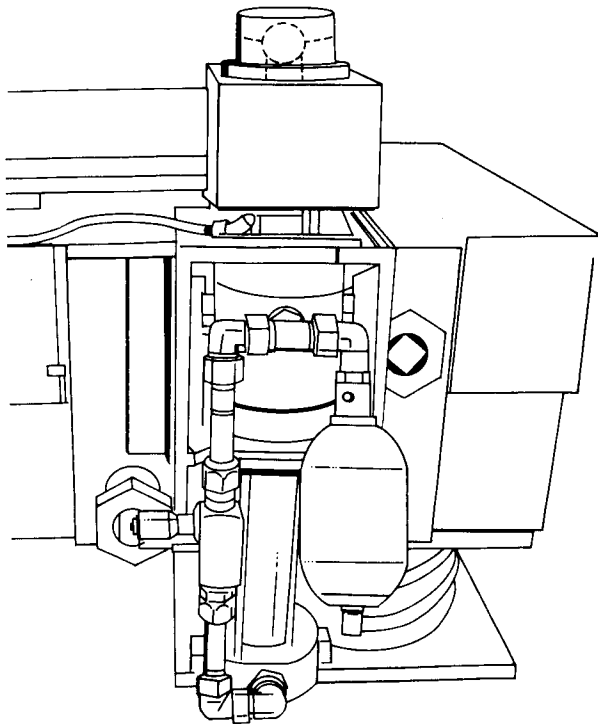
Figure 6. Hydraulic Load Catcher System

Tables 1 and 2 give summarized acceleration and velocity data respectively versus position on the test load and operating voltage of the simulator. Figures 9a-d present the data of Tables 1 and 2 in a graphical form.

FUTURE WORK

NSWC has developed designs for EDESS type machines capable of producing multi-axis shocks such as the vertical and athwartship motion, associated with underwater explosion (UNDEX). A preliminary
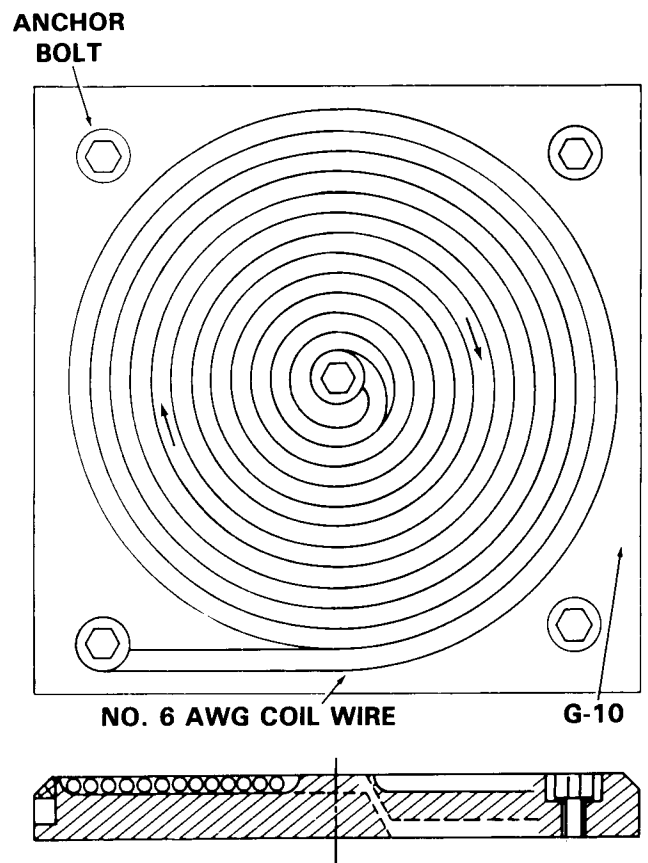
Figure 7. Pancake Drive Coils
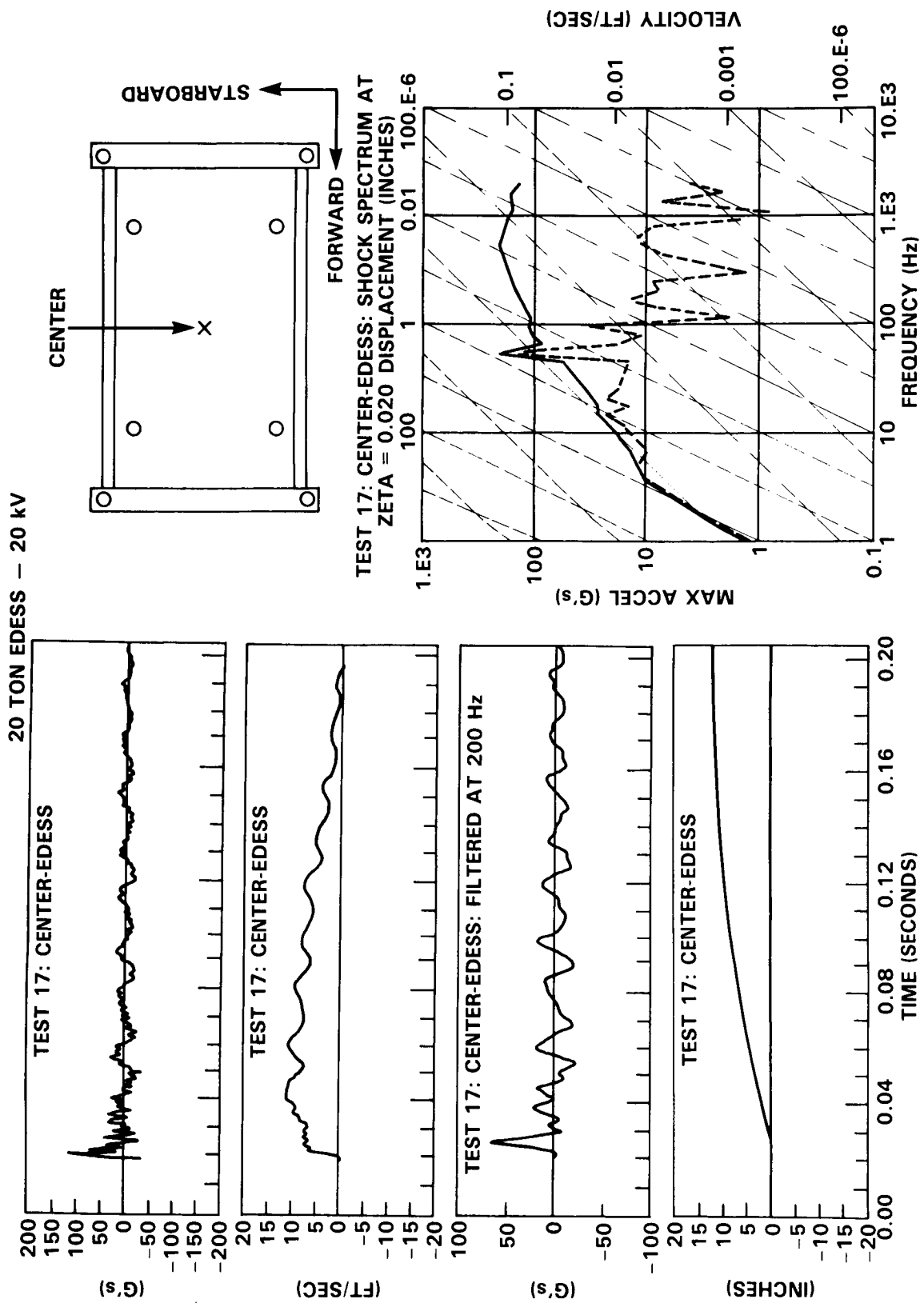
Figure 8. 20KV Characterization Data

ACCELERATION[1] g's-FOR VARIOUS LOCATIONS[2]

OPERATING VOLTAGE (KV)	AP	FP	FS	AS	C	21"	42"	63"
10	13.9	13.0	12.6	13.4	18.4	20.8	14.3	11.6
12	18.1	18.0	17.6	18.1	26.1	27.9	19.0	15.0
14	24.0	25.0	24.4	26.4	35.8	37.0	25.0	19.9
16	30.4	31.1	32.0	31.7	45.3	46.1	31.1	25.2
18	38.0	37.0	34.0	38.0	56.0	54.7	36.1	28.4
20	44.2				65.0	66.5	44.6	34.0

1. Peak measured acceleration filtered at 200 Hz
2. Accelerometer locations are shown in Figure 5

Table 1. Peak acceleration versus position and operating voltage

VELOCITY[1] FT/SEC-FOR VARIOUS LOCATIONS[2]

OPERATING VOLTAGE (KV)	AP	FP	FS	AS	C	21"	42"	63"
10	3.6	3.1	3.1	3.2	2.9	3.3	3.1	3.0
12	4.7	4.5	4.5	4.1	4.2	4.7	4.3	4.0
14	7.0	6.5	6.6	5.9	5.5	6.3	5.8	5.5
16	8.7	8.0	9.8	7.8	7.5	8.2	7.7	7.3
18	10.7	10.1	10.4	9.9	9.1	10.1	9.2	8.8
	13.1				11.0	12.4	11.2	10.8

1. Peak calculated velocity
2. Accelerometer location from which velocities are calculated is shown in Figure 5.

Table 2. Peak velocity versus position and operating voltage
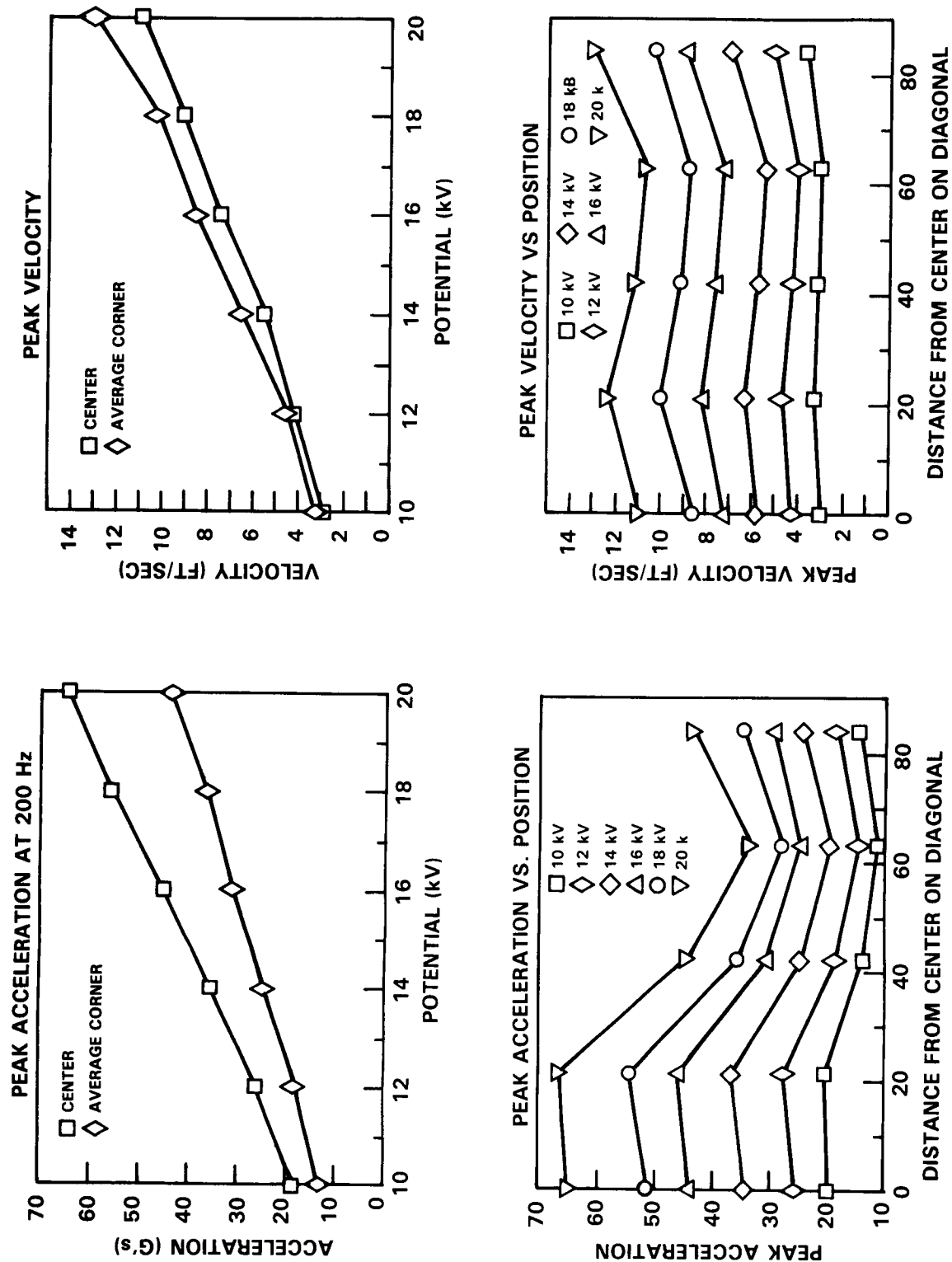
Figure 9. Acceleration and Velocity Data Summaries

57

design for an EDESS configured to simulate air blast induced shock (ABIS) has been proposed, as have designs for vertical axis machines with significantly larger payloads. The multi-axis UNDEX design incorporates EDESS-3 in conjunction with the additional electrical and mechanical components needed to generate as much as 30 percent athwartship motion. Figure 10 shows such a simulator, utilizing two additional coil pairs, horizontal bracing and hydraulic load control components.

Figure 11 is a preliminary design for an ABIS EDESS. This design uses a novel rolling reaction mass in lieu of a large reinforced buttress to absorb the horizontal motion. The ABIS machine translates the horizontal reaction force into rolling motion which is absorbed by a conventional braking system. This design makes use of solenoidal type coil to achieve the somewhat longer duration, lower peak shock associated with ABIS. The test carriage allows simulated deck and bulkhead mounting of a full range of subject equipments. This five ton capacity machine is capable of testing a large majority of the equipments that will be subjected to the ABIS phenomena.

CONCLUSIONS

EDESS-3 has demonstrated the up-size scaling of the smaller EDESS 1 and 2. The perfection of mechanical and electrical techniques, in conjunction with the application of higher energy density capacitors, readily suggest the development of larger and/or multi-axis EDESS machines. With payload capacities and shock simulations equaling or exceeding current shock test capabilities, along with the benefits of testing in a laboratory setting unaffected by inclement weather, the EDESS can make a major contribution towards the goal of shock hardening and qualification.

The success achieved with EDESS-3 strongly encourages future development of these programs and the verification and acceptance of the simulators as shock testing standards.

BIBLIOGRAPHY

1. E. W. Elements, "Shipboard Shock and Navy Devices For It°s Simulation," NRL Report 7396, July 1972.

2. F. J. Sazama, V. L. Kenyon, R. L. Martin, "EDESS: An Electromagnetically-Driven Explosive-Shock Simulator for Heavy Payload Shock Testing," 54th Shock and Vibration Bulletin, 4 April 1984.

3. F. J. Sazama, J. B. Whitt, "EDESS: An Electromagnetically-Driven Explosive Shock Simulator," The Shock and Vibration Bulletin, Bulletin 51, May 1981.

4. "Military Specification - Shock Tests, H.I. (High Impact); Shipboard Machinery, Equipment and Systems, Requirements for," MIL-S-901C (NAVY), 15 January 1963.

5. F. J. Sazama, V. L. Kenyon, J. M. Butner, "Progress on the EDESS Generator for Heavy Payload Shock Testing,"
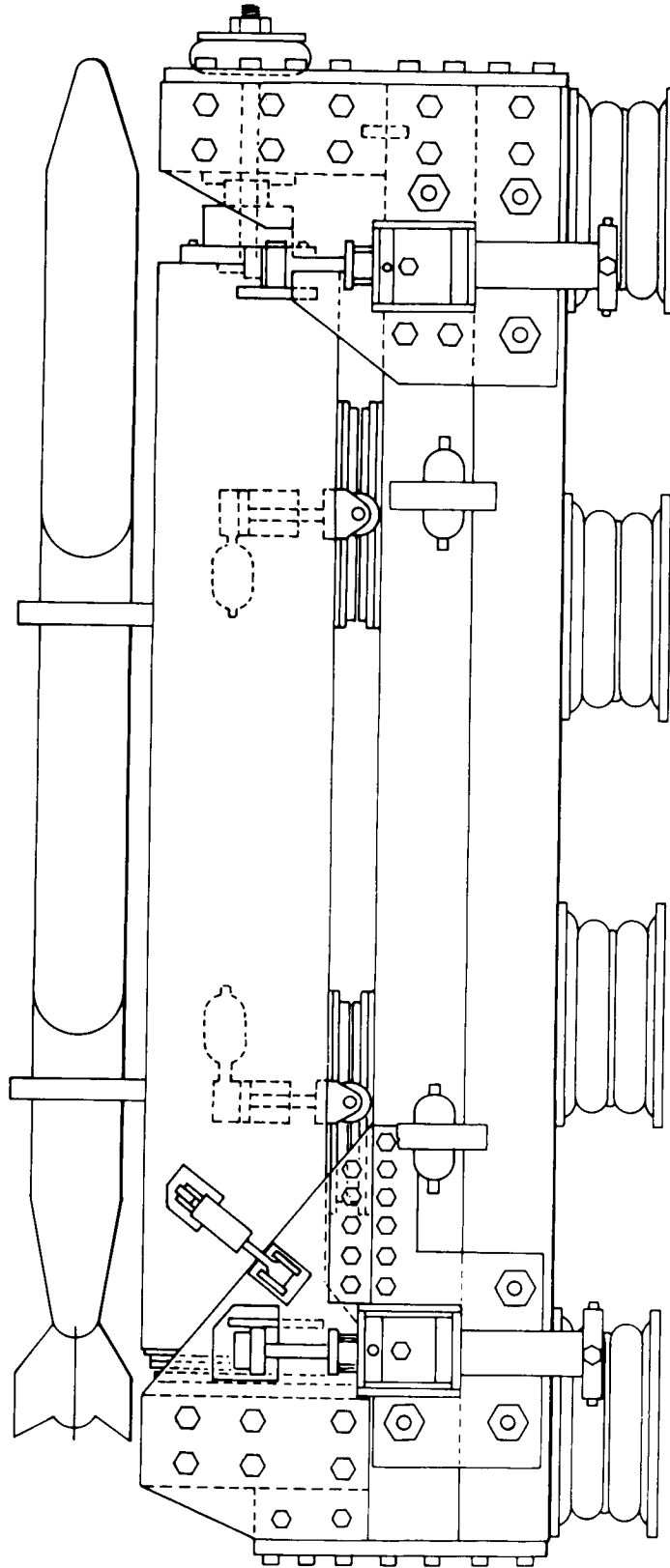
Figure 10. Multi-axis UNDEX EDESS
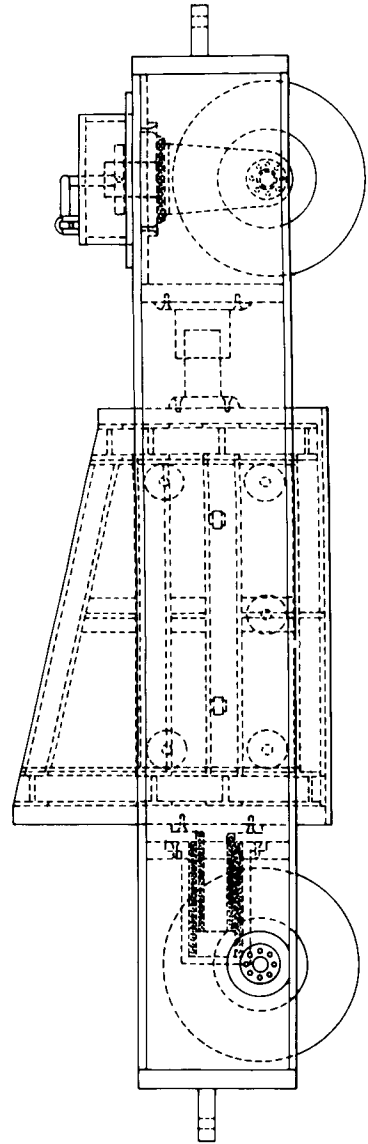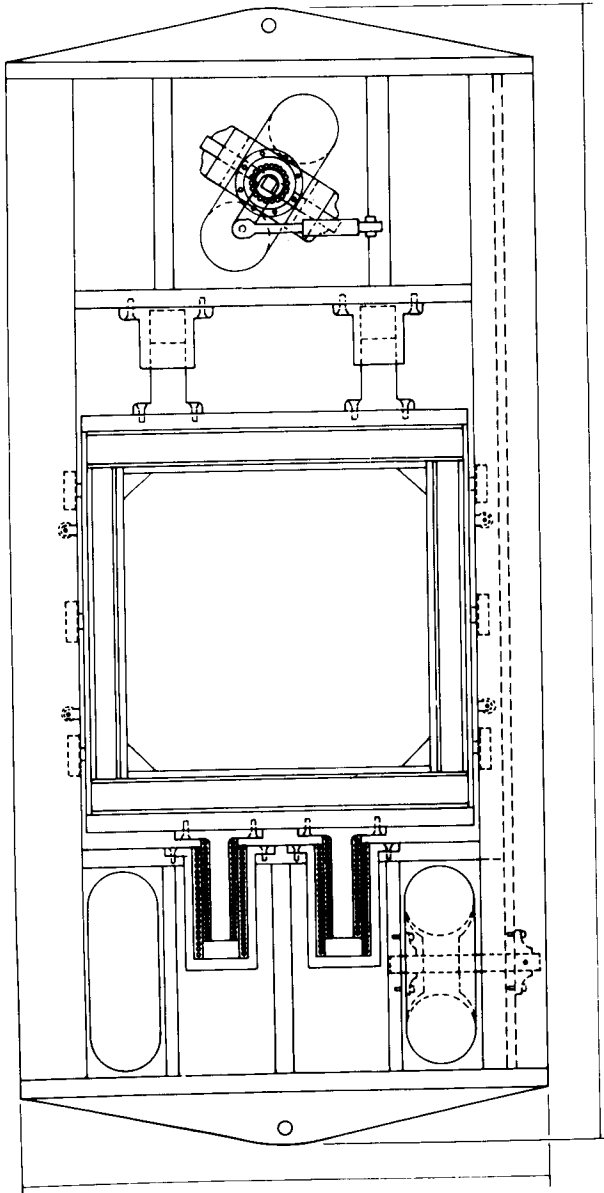
Figure 11. ABIS EDESS

Experimental Studies on the Tripping Behavior of Narrow T-Stiffened Flat Plates Subjected to Hydrostatic Pressure and Underwater Shock

H. L. Budweg
Y. S. Shin

An experimental investigation was conducted to determined the static and dynamic responses of a specific stiffened flat plate design. The air-backed rectangular flat plates of 6061-T6 aluminum with an externally machined longitudinal narrow-flanged T-stiffener and clamped boundary conditions were subjected to static loading by water hydropump pressure and shock loading from an eight pound TNT charge detonated underwater. The dynamic test plate was instrumented to measure transient strains and free-field pressure. The static test plate was instrumented to measure transient strains, plate deflection, and pressure. Emphases was placed upon forcing static and dynamic stiffener tripping, obtaining relevant strain and pressure data, and studying the associated plate-stiffener behavior.

INTRODUCTION

Military submarine hull design has concentrated on the basic structural element, a stiffener reinforced shell. The submarine shell/stiffener form is the ring stiffened cylinder. The cylinder construction, which is the least expensive and the simplest form of shell construction, takes advantage of the high strength levels in high-strength materials through the use of ring stiffeners allowing higher load bearing capacities without the cylinder becoming unstable. Additionally, high-strength material is used for its toughness (due to low temperature requirements) and resistance to high dynamic loads (e.g., depth charge attack) [1].

The submarine ring stiffened cylinder is designed with generous safety margins against overall collapse triggered by frame yielding or tripping [1]. Tripping, a lateral-torsional buckling of stiffeners which have low lateral-torsional rigidity, has been identified as a potential form of catastrophic collapse which may take place with but a single application of load. The stiffener tripping form of collapse is a sudden and drastic reduction in load-carrying ability, a damage mechanism which occurs through compression plastic instability affecting a large critical region of cross-section. Predictions of this prime modeof failure need to be supported by good test data that is inside the current ship design range. To date, supporting experimental data gor this panel and grillage behavior is extremely scarce. Generous safety margins have been the accepted practice to avoid premature sideways tripping rather than to predict it. However, avoidance design is really an extension of design based on acceptable risk, where additional strength is necessary to provide a certain level of safety against extreme conditions [2]. Avoidance designs may not be the answer since stiffeners (i.e. frames) may over play their part and, because of excess rigidity, actually cause

premature failure of the shell by inducing in it additional components of stress. It has been observed that the cause of ultimate collapse in the plating of a "thin-walled" shell is excessive circumferential stress rather than longitudinal stress and there may be excessive yielding of the shell at the toes of frame flanges (before collapse finally occurs) due to high circumferential stress [3]. The alternative approach is then: how weak may the frame rings be and still be adequate? It has been generally recognized that a stronger, more resilient type of construction is that in which frames and shell are nearly equal in strength as opposed to a hard-framed structure.

Frame dimensions are also of concern; using high web height- to-thickness ratios could lead to designs for which local stiffener tripping becomes important since excessively slender frame proportions make the frame sensitive to any tilt. Also, internal frames are equally sensitive to the effects of any tilt in bringing about tripping of frames under load. This mode of failure is usually a result of coupled flexural and torsional modes of buckling. The result in any of these cases being the same (i.e., general instability of the frame and shell in unison causing failure of the submarine hull under external pressure).

Submarine hulls require the high structural efficiency which can be achieved by reducing the excess rigidity of frames, (i.e., minimizing stress concentration). Accordingly, if frame weight can be reduced in the process and that amount of weight used in additional thickness of the shell, the cylinder's collapse strength will effectively be increased. The careful choice of ring-stiffened geometry can have a significant influence on shell performance, but there is a general lack of agreement on what the "appropriate" general collapse loads for ring-stiffened cylinders are [4].

OBJECTIVE

Submarine hull failure is a complex process involving stages of failure including initial yielding, large displacments, local instability, and finally collapse. Analysis of grillage failure and knowledge of plating behavior throughout the load range is necessary, both statically and dynamically. It is therefore of considerable importance to be able to predict the safe buckling behavior through general and reliable methods of analysis which provide necessary correlations between sea loads and their effects on a structure. According to A. E. Mansour [5], no satisfactory analysis method exists for inelastic tripping of stiffeners welded to continuous plating or for the prediction of the inelastic collapse strength. Therefore, it is more than a matter of being able to predict stresses, but the way in which the stresses are used to anticipate failure.

This investigation and analysis will follow the guideline that in many physical problems, resort to experiment is often the shortest cut to a decision as to which analyses need be made and what effects are important in those analyses [6]. Employing this guideline, data obtained on specific model design of a longitudinally narrow-flanged T-stiffened rectangular flat plate under static and dynamic (i.e., underwater charge detonation) conditions, will be investigated and analyzed.

STRUCTURE BEHAVIOR

STATIC TRIPPING PHENOMENA

Tripping (or compound failure), as shown in Figure 1, will be discussed here qualitatively in terms of a rectangular flat plate stiffened by a T-stiffener.

Generally speaking, stiffener bending stress arises from the reaction of a plating-stiffener combination to a loading (i.e. water pressure) normal to the plating, while the plating itself acts as one flange of this system. In the case of a ship hull, the shell plating performs functions of contouring and sealing in addition to sharing the load carrying requirement with the stiffeners, (ring stiffeners in the case of submarines) [7].
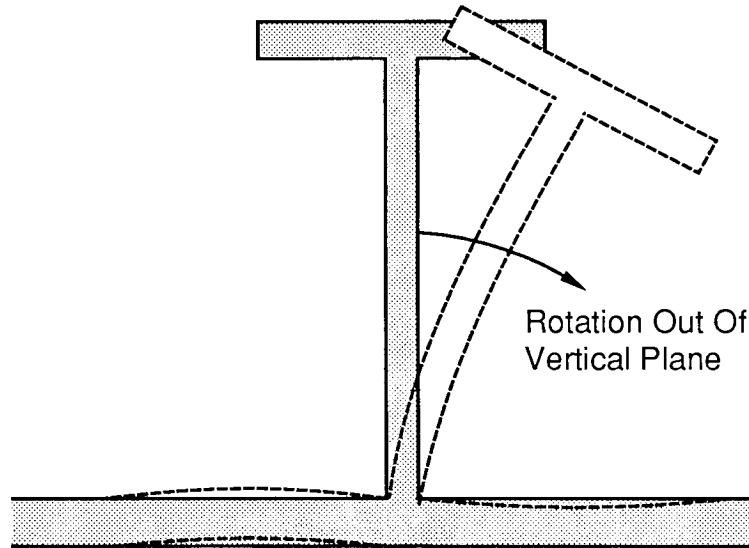
Figure 1   Stiffener Triping

The web of the T-stiffener can be considered a plate restrained against rotation (hinged) along one edge, free and elastically supported by the flange on the other one (the restraining effect of the web on the flange being small). Also, the flange can be thought of as a plate simply supported by the web along one side and free on the other [8]. In an actual structure, a stiffener welded to one side of a plate results in a considerable increase in the flexural rigidity of the stiffener since the adjacent zones of the plate take part in the bending of the deflected stiffener, that is, the stiffeners not only carry a portion of the load but subdivide the plate into smaller panels, thus increasing the critical stress at which the plate will buckle [8]. Additionally, there occurs an incompatibility of the buckling patterns (as favored by the web and the flange) which tends to make the buckling load higher than it would be for either the web or the flange of the stiffener alone [9]. Therefore, such combinations maybe able to support loads well above the load for local buckling of the plate.

Even though there is a substantial restraining effect of the plate on the stiffener and of the stiffener on the plate, there are also plate-stiffener destabilizing influences on each other. The fact that the plate prevents the stiffener from moving laterally in any other way except by rotation around the toe of the web, dictates the form of failure called tripping. This mode of failure involves the twisting of the stiffener about its line of attachment to the plating, a coupled displacement combination of sideways flexure and stiffener rotation. For example, as the load orthogonal to the plate increases, the

effectiveness of the plate decreases until at some limiting stress the stiffener-plate combination fails and as the plate buckles, the rotational constraint provided by the plate at the line of attachment of the stiffener changes, thus increasing the stiffener's sensitivity to tripping. Once the stiffener starts lateral torsional buckling, any increase in deformation will cause an unloading which is triggered by yielding after considerable deformation. [2]

There is the possibility that under extreme conditions a submarine hull ring stiffener may trip. If such deformations were to become large, the support furnished by the ring to the cylinder hull would be impaired and there would be a redistribution of pressure resistance to adjacent rings resulting in a rapid deterioration in the general capacity of the shell to resist pressure.

DYNAMIC RESPONSE

Under static loading, stresses and strains are generally distributed throughout the entire body and every part of the body has an opportunity to participate. However, under impulsive loading, transient and highly localized stresses and strains exist in the rapidly changing stress system. This dynamic phenomenon involves interactions between inertial, hydrodynamic, and elastic forces which can arise as a consequence of the detonation of an explosive charge. The structural response to a plain step shock wave has attracted considerable interest since steep-fronted shock waves are characteristic of underwater explosions (UNDEX) and have similar properties [10].

The large amount of energy that is transmitted to a structure (when it is dynamically loaded) distributes itself within the metal and much of the absorbed energy is observed in the form of macroscopic and microscopic inelastic deformations. It has been noted that the critical value of the equivalent static pressure in dynamic loading is considerably higher than the static buckling pressure. The critical load is so high that buckling is plastically initiated (i.e., an unstable behavior called dynamic plastic buckling) [11]. This is a consequence to two uniquely dynamic effects. First, the shape of the structure impulsively loaded and constraints imposed upon it frequently determine both the location and the amount of plastic flow that will take place. Secondly, the intense transient stress disturbances and the extremely high pressures and rapid loading rates of impulsive loads may markedly influence the following mechanical properties of the metal being loaded: the hardness may increase, the tensile strength may go up, and yield and plastic flow characteristics are altered. Metal behavior is strongly contingent upon stress level. That is, metal possesses rigidity when elastic, but at very high stress levels it completely loses its rigidity. [12,13]

EXPERIMENT AND MODEL DESIGN

BASIC MODEL

The intention to this investigation and the several preceding it [14,15,16] has been to use one basic flat plate model and vary the stiffener types and plate thicknesses so that the UNDerwater EXplosion (UNDEX) shock response of these different geometries could be studied. But, due to several equipment failures, stiffener design geometries which showed no instability, and strain gage over-ranging, there was not a significant amount of dynamic tripping information compiled. However, each attempt was an invaluable step in the process of developing the proper model and the necessary experimental expertise.

It was clear that the model should be redesigned since no obvious tripping behavior was demonstrated in any of the previous four underwater shock tests. Also, as a preventive measure against equipment failure and strain gage over-ranging, a static test was performed (on a model of the same geometry as the redesigned test panel) to field test the same type of strain gages and same equipment used in the undex test.

The new test panel was designed after closely examining the physical deformations of each of the previous undex test panels. The objective was to combine the greatest plate deflection with the most sensitive stiffener. The model plate thickness used in the Rentz and Shin investigation [14] exhibited the most favorable plate deformation, while the rectangular stiffener behavior in the Langan investigation [16] gave the most promise of showing instability. Based on this, the model established was a 0.1875 inch thick test panel, 18 inches in length by 12 inches in width, machined out of the center of a 6061-T6 aluminum blank measuring 27 inches by 33 inches and two inches thick. One free-standing longitudinal narrow-flanged external T-stiffener (vice a rectangular stiffener) was machined as an integral part of the plate. The T-stiffener web slenderness ratio (i.e., web height divided by its thickness) was also increased to enhance the stiffener's sensitivity to plate deflection. Additionally, to avoid the stiffener end tensile fractures observed in previous tests, the T-stiffener ends were detached from the boundaries of the cavity as shown in Figure 2.

STATIC TEST

In order to verify the reliability (under more controlled conditions) of all the electronic equipment, cabling, and strain gage type (and attachment) that would be used for the underwater shock test, a static test was performed. The static test also was expected to provide valuable insight into the behavior of the redesigned test panel and the opportunity of comparing the static and the dynamic responses of a specific plate-stiffener geometry.

The experimental procedure was intentionally kept as simple as possible with the desire to collect only strain and deflection data as the stiffened plate (i.e., test panel) was deformed by increasing water pressure from zero psi to 350 psi. This pressure range was selected to cause approximately a four plate thickness deflection (deflection predictions calculated using the finite element/finite central difference computer code, EPSA, Elasto Plastic Shell Analysis) [14]. It was expected that this amount of deflection would produce tripping behavior in the stiffener. The test configuration was as shown in Figure 3.

The strongback used to enclose the test panel cavity, see Figure 4, was machined from a one inch thick high strength steel sheet and was drilled and tapped for standard three-quarter inch pipe fittings for a low point filling connection and a high point vent. Between the inlet valve and strongback there was installed a zero to 400 psig Ashcroft pressure gage and the high point vent was fitted with a standard three-quarter inch gate valve. To provide an adequate pressure seal, the strongback and test panel mating surfaces were coated with a Permatex high pressure sealant and separated by a precut one-eighth inch thick cork gasket. The test panel and strongback were then secured together by 28, one inch in diameter, A325 high strength structureal steel bolts and torqued to 500 ft-lbs. The test medium was potable water and was used to gradually fill the test panel cavity and purge it of all air. The source of applied pressure was a manually operated, single piston, reciprocating hydropump rated for 1000 psi. A check valve and gate valve arrangement was used to regulate the pressure in 25 psi increments from zero psi to 350 psi. Several minutes (2 to 3 minutes) were needed at each increment to allow deflection readings to be obtained. The strain
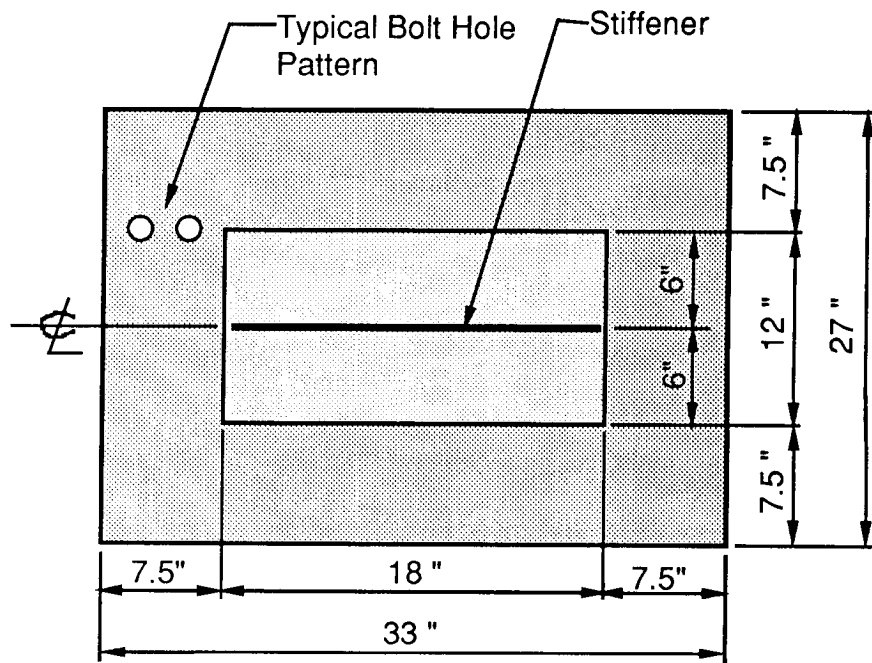
TOP VIEW OF TEST PANEL
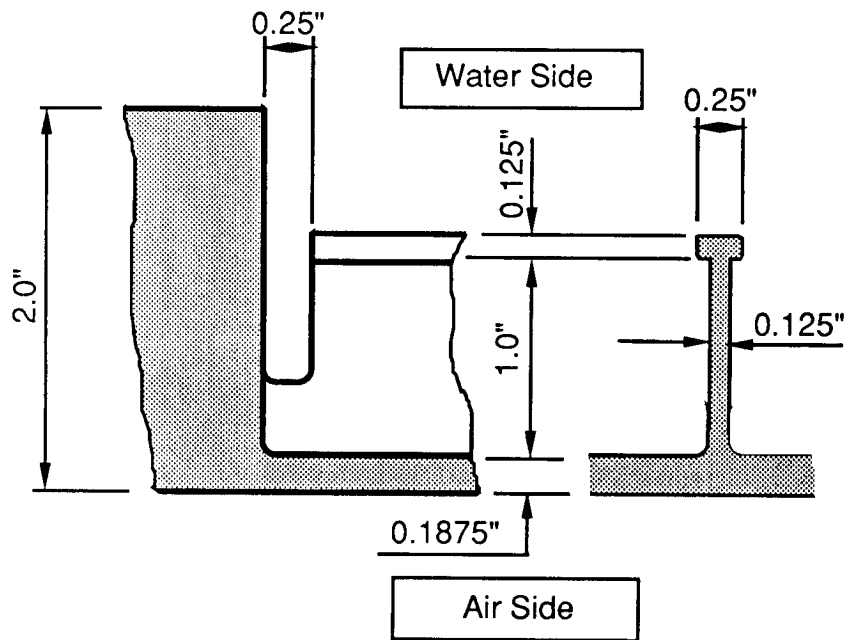
SIDE-VIEW OF STIFFENER

Figure 2. Test Panel with Longitudinal Narrow-Flanged T-Stiffener
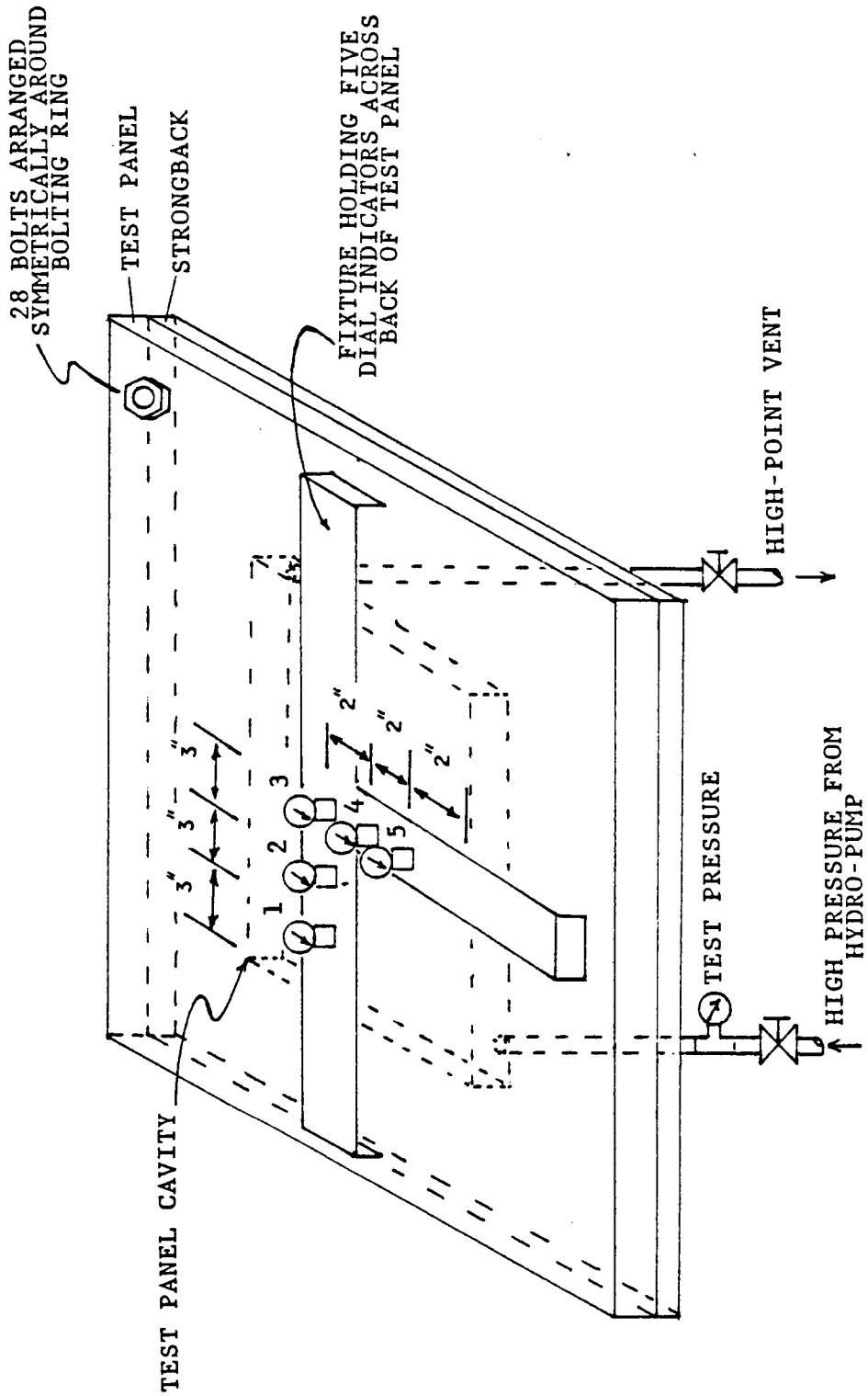
Figure 3 Static Test Configuration
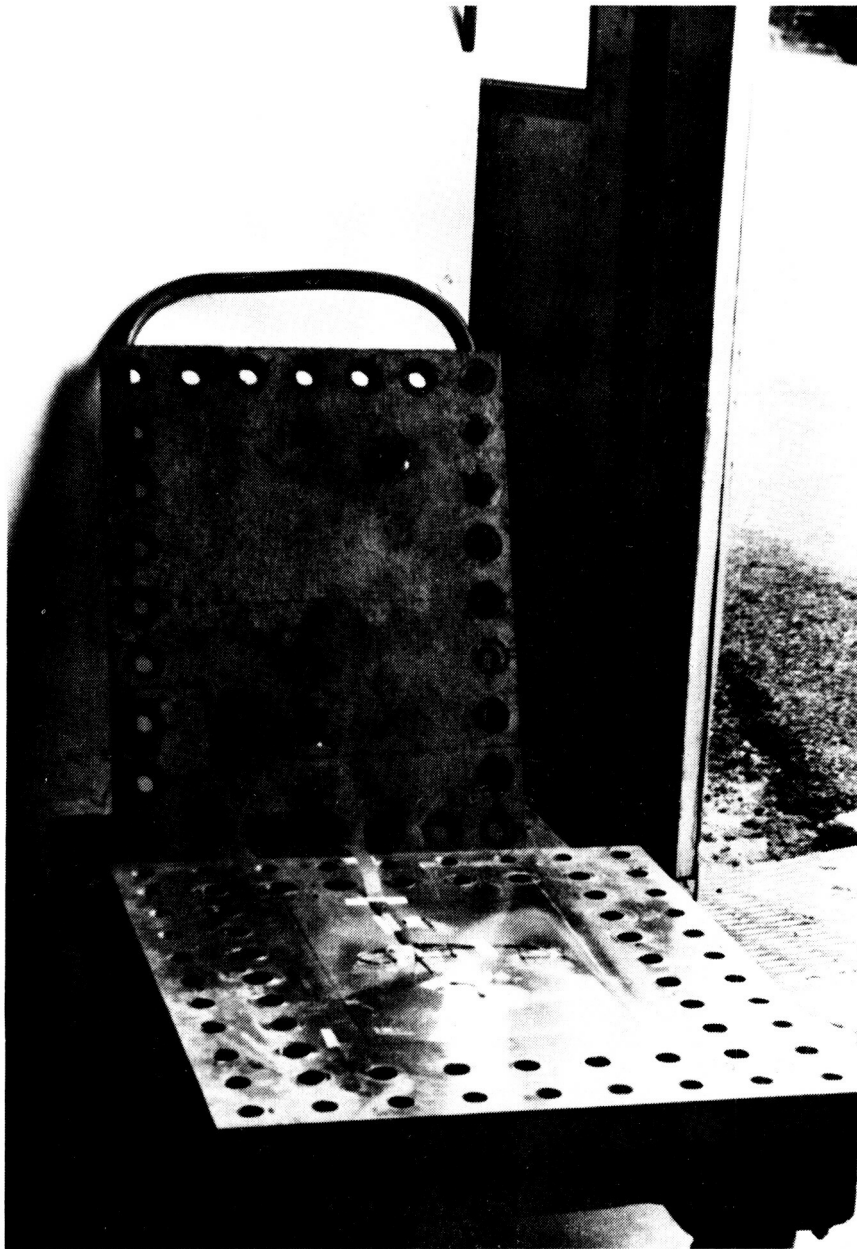
Figure 4. Static Test Strongback(Upper) and Test Panel(Lower)

measurments were recorded continuously on a magnetic tape recorder. Strain gage arrangement and details of the electronic instrumentation will be discussed in the underwater shock test section.

UNDERWATER SHOCK TEST

UNDEX EXPERIMENT DESIGN

It is well known that the shock wave loading of a body by an underwater explosion is complicated considerably by the secondary effects of the explosion phenomena. Therefore, as in previous studies [14,15,16], by using the correct test configuration and sample time window, the data sampling can essentially be limited to the response of the test panel to the incident shock wave emanating from the charge. Consequently, the secondary effects from bulk cavitation, cavitation closure, reloading from the explosive gas bubble and bubble migration, surface cutoff, and bottom reflections can be avoided or ignored [17].

The initial studies mentioned used eight pounds of TNT at a depth of four feet with a ten foot stand-off in an attempt to produce the necessary plate deflection to force stiffener tripping. Post-shot analysis of the four undex tests' pressure data [14,15,16] indicated that the TNT charges were not of a calibrated type and were reacting typically thirty percent greater in charge size (i.e., 8 lb charge was exploding with the force of a 10.4 lb TNT charge even though no booster charge was used). Under the assumption that all other eight pound TNT charges used would continue to react as larger sized charges, all test panel standoff and explosive charge depth calculations were made on the basis that the explosive charge would react approximately as a 10 pound TNT charge. Accordingly, it was determined that the charge depth be 4.5 feet with a test panel standoff of 10 feet. Using this test configuration and a four millisecond sample windown, the response expected would be that of a test panel experiencing an approximately plane shock wave.

TEST CONFIGURATION

All undex testing was performed at the West Coast Shock Facility (WCSF), Hunter's Point Naval Shipyard, San Francisco, California.

In order to simulate a hull configuration and to ensure fully clamped boundary conditions, the test panel was securely bolted to the air-back chamber shown in Figure 5, designed by Rentz and Shin [14]. Note that the stiffener is exposed so that the loading conditions at the plate center will be compressive (i.e., enhancing the possibility of tripping).

For the actual testing the test panel and chamber combination was suspended as shown in Figure 6 by steel cables attached to two pneumatic fenders. The critical dimensions of the test configuration are: charge depth set at 4.5 feet, test panel/chamber standoff of 10 feet, and two free-field pressure gages set to measure incident pressure at a ten foot standoff radius. A pressure gage was also attached to the test panel exposed surface to measure fluid pressure at the plate.

Strain measurements were taken on both the water exposed side and the air-backed side of the test panel as shown by Figure 7. The strain gage placement was determined on the basis of symmetry and the stiffener position. Consequently, the strains observed should be consistent with their position on the plate and would approximate the values and trends exhibited by symmetrically equal positions on other portions of the plate. Additionally, gages on the stiffener flange should be the first to show tripping effects, with the longitudinal array of three gages on the airside centerline soom mimicking the same trend.
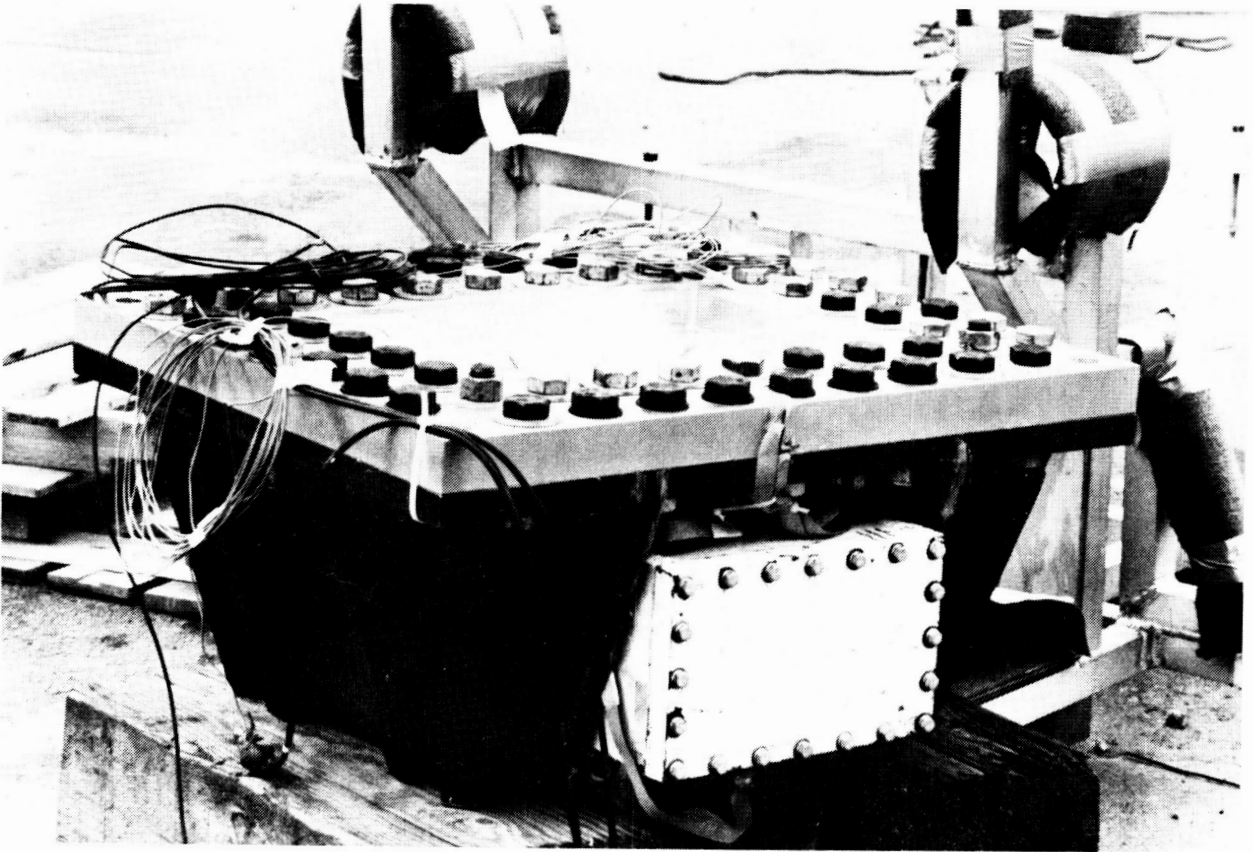
Figure 5. Test Panel Bolted to Air-Back Chamber
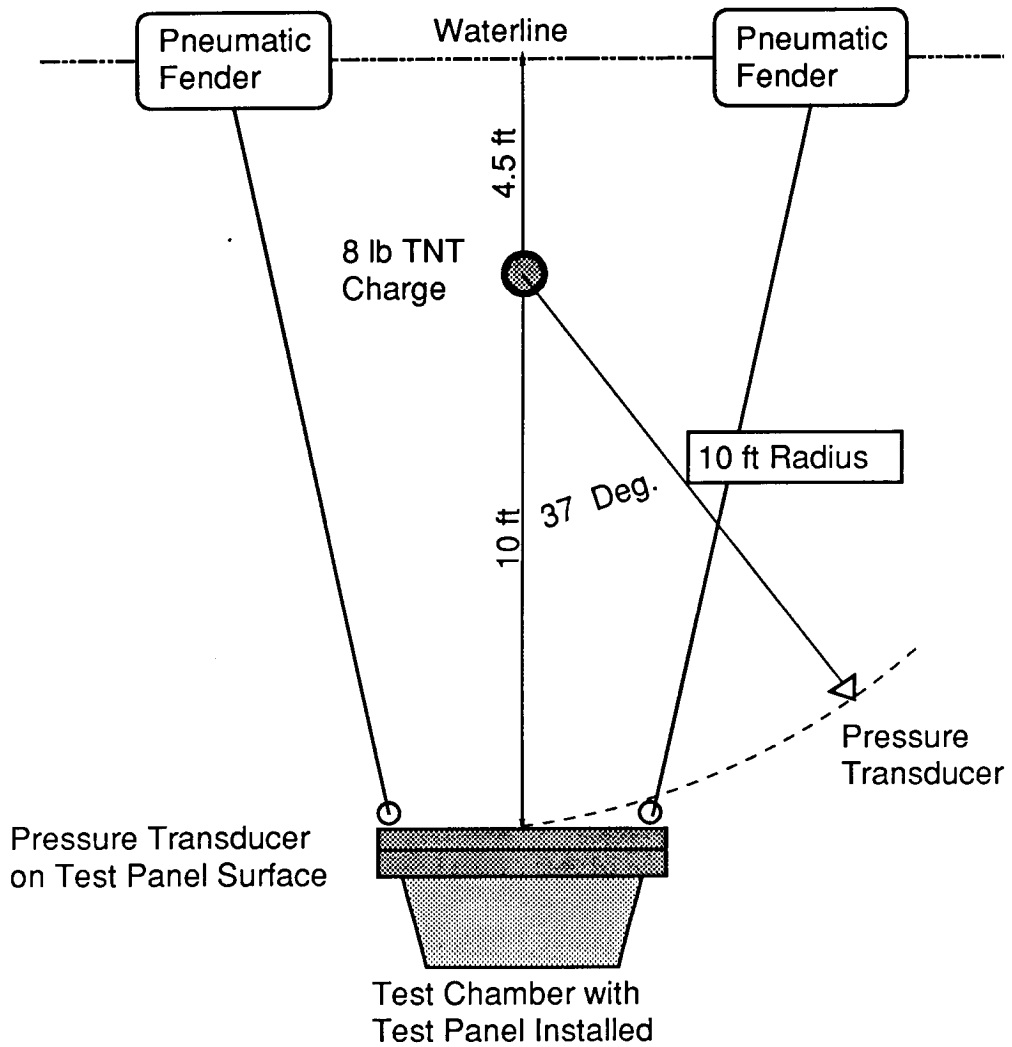
Figure 6. Schematic of UNDEX Test Geometry

AIR SIDE
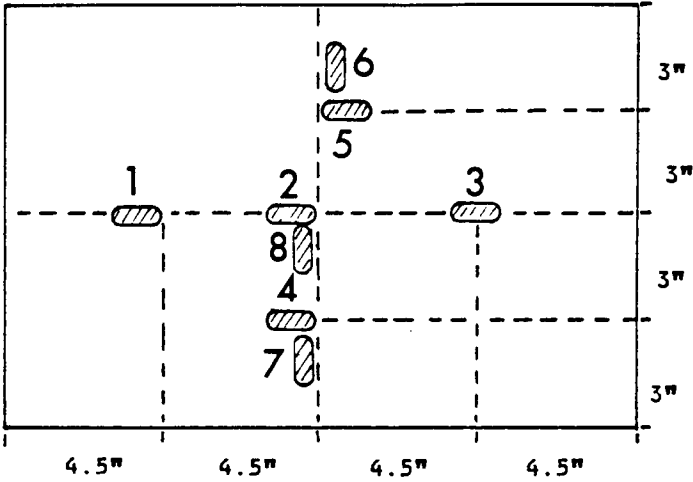
WATER SIDE
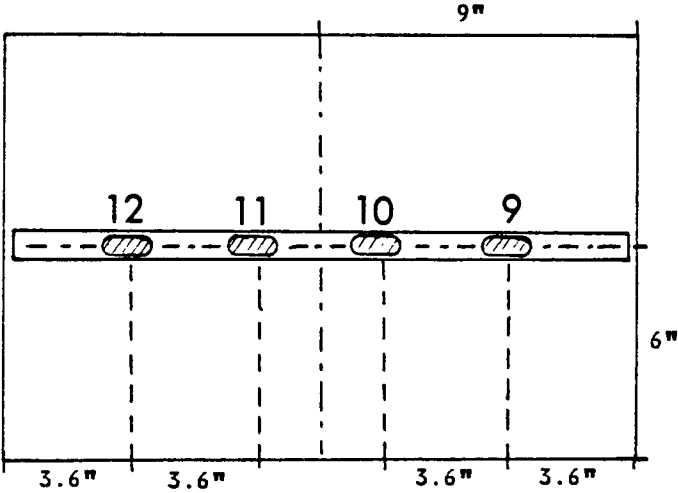
Figure 7   Diagram of Strain Gage Placement

72

INSTRUMENTATION

Twelve strain gages and three pressure transduces were placed as previously discussed and depicted in Figure 7. The strain gages were attached as described in [14] and coated with silicone sealant to ensure water tight integrity. The tourmaline pressure transducers were tied in their respective positions.

SPECIFICATIONS OF EQUIPMENT

EQUIPMENT	TYPE	RANGE
strain gages	CEA-350 ohms	50k microstrain
pressure transducers		.25" Tourmaline 10 ksi, 97% response ratio
amplifiers	Ektron 563F J	------------------

Two Honeywell MD-101 Wideband II (direct record) tape units were used to record all data channels at a tape speed of 120 inches-per-second. Post-shot processing of the recorded strain and pressure data was through the NPS Vibrations Laboratory's HP-5451C Fourier Analyzer. Equipment specifications are listed above.

RESULTS AND DISCUSSION OF DATA

STATIC TEST RESULTS

The static pressure deflection test of the panel machined for this purpose, proved to be a source of very good strain and deflection data showing the plate/stiffener behavior building up to elastic tripping as increasing water pressure deformed the plate. Deflections were measured by dial indicators at positions 1 through 5 as shown in Figure 3, the results of which appear in Table 1 and Figure 8. Deflections are again represented in Figure 9, but here deflection has been normalized to pressure at each 25 psi increment. Note the well defined regions for plastic, formation of fully plastic hinge, and elastic tripping behaviors.

Strain data was continuously recorded on the Honeywell MD-II at a tape speed of 1.87 inches per second, over the entire forty minute period needed to perform the test. Ten strain gages performed very satisfactorily while two (SG-5 and SG-11) failed for unknown reasons. The recorded strain history for each surviving gage was then displayed by a strip-chart recorded, thus providing the traces seen in Figures 10 through 13. Table 2 contains the strain values recorded at each pressure increment for each strain gage.

The effect of stiffener unloading and stress redistribution as the stiffener began to elastically trip can be clearly seen in Figures 10 and 11. The region of the plate most sensitive to symmetrical stiffener tripping would be the area near the toe of the web, accordingly strain gage SG-2 would and did first sense the stiffener unloading. Additionally the center of the plate and the stiffener continued to be areas of largest strain (SG-2 and SG-10) until elastic tripping was observed at approximately 225 psi, at which point the stiffener web was elastically buckling and unloading as was demonstrated in all other regions of the plate (Figures 12 and 13). Also note that strains monitored at the far ends of the stiffener (SG-1, 3, 9, 10 and 12) continued to increase until elastic tripping occurred, at which point the rate of strain-increase became greater at these

73
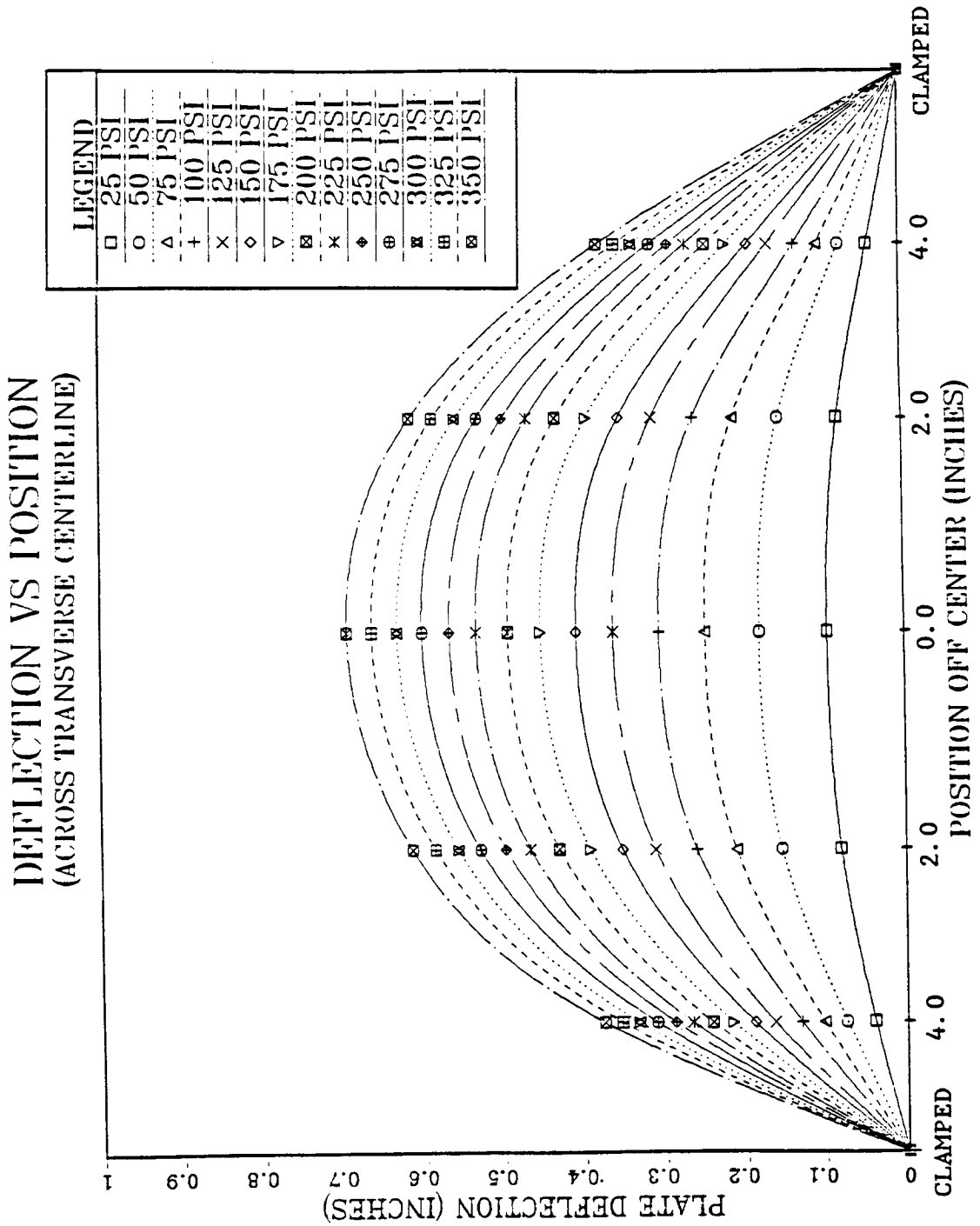
Figure 8   Plot of Static Deflection Test Results

74
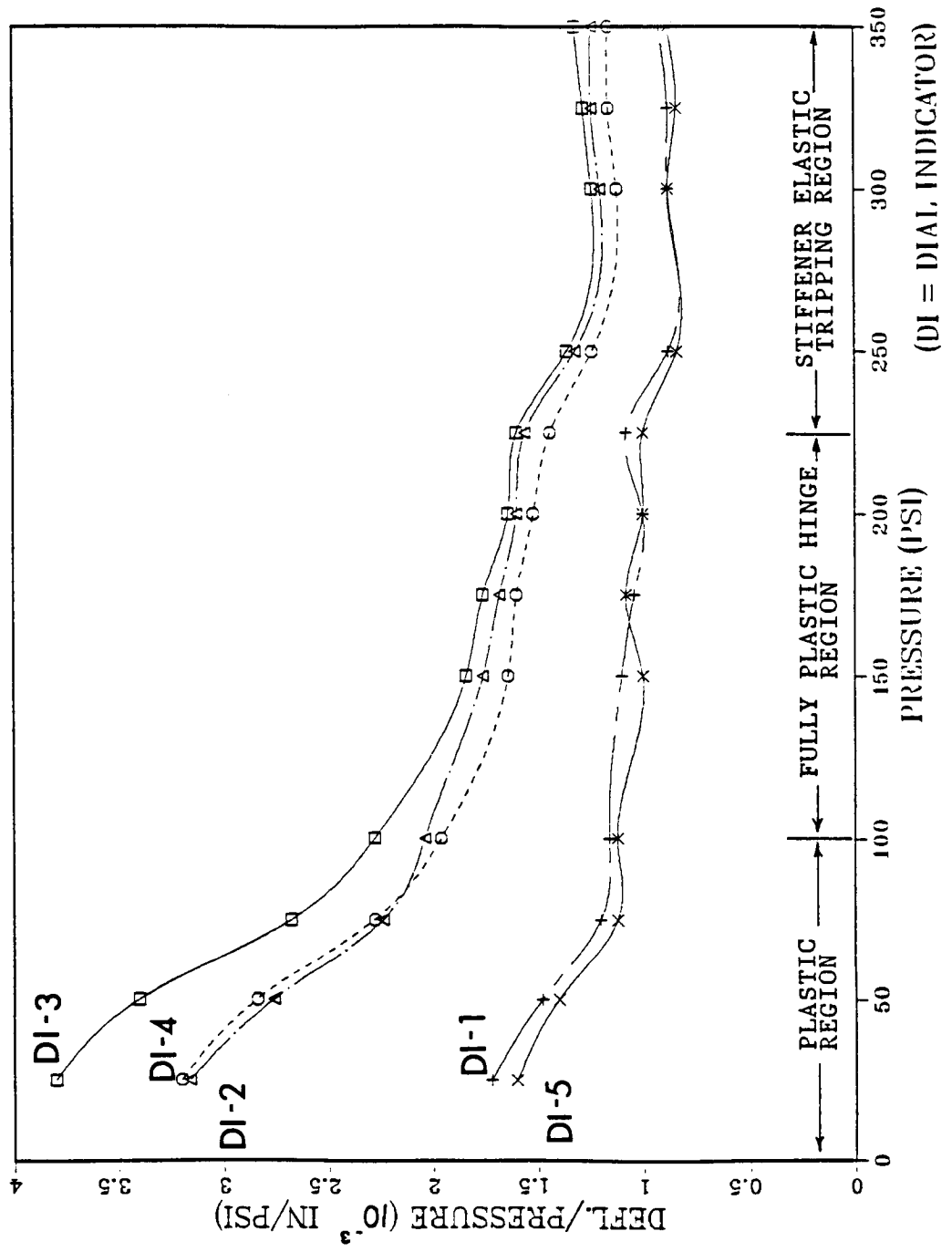
Figure 9   Plot of Static Deflection Normalized to Pressure

75
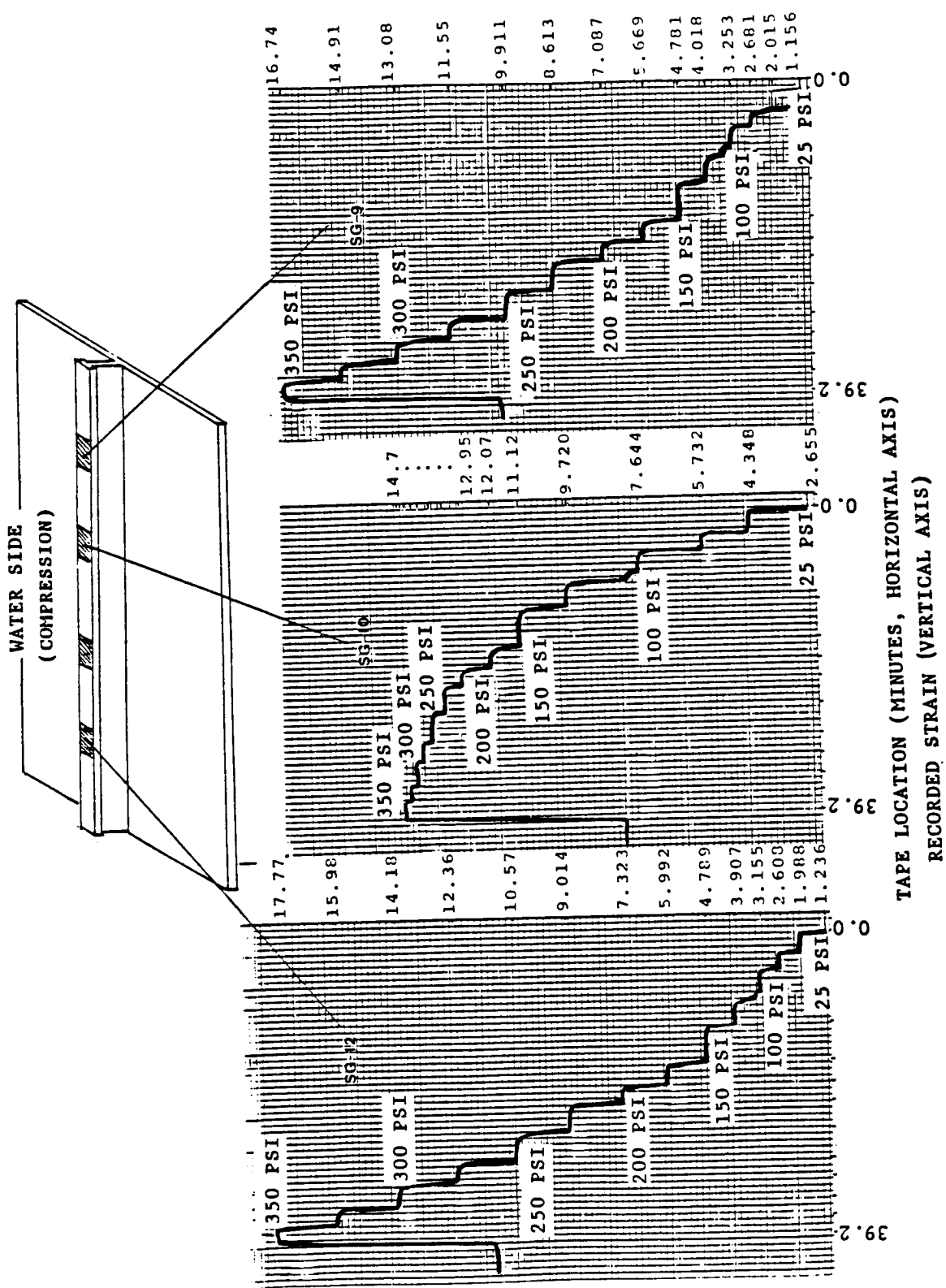
Figure 10   Static Strain History Recorded Longitudinally

Across Flange of T-Stffener
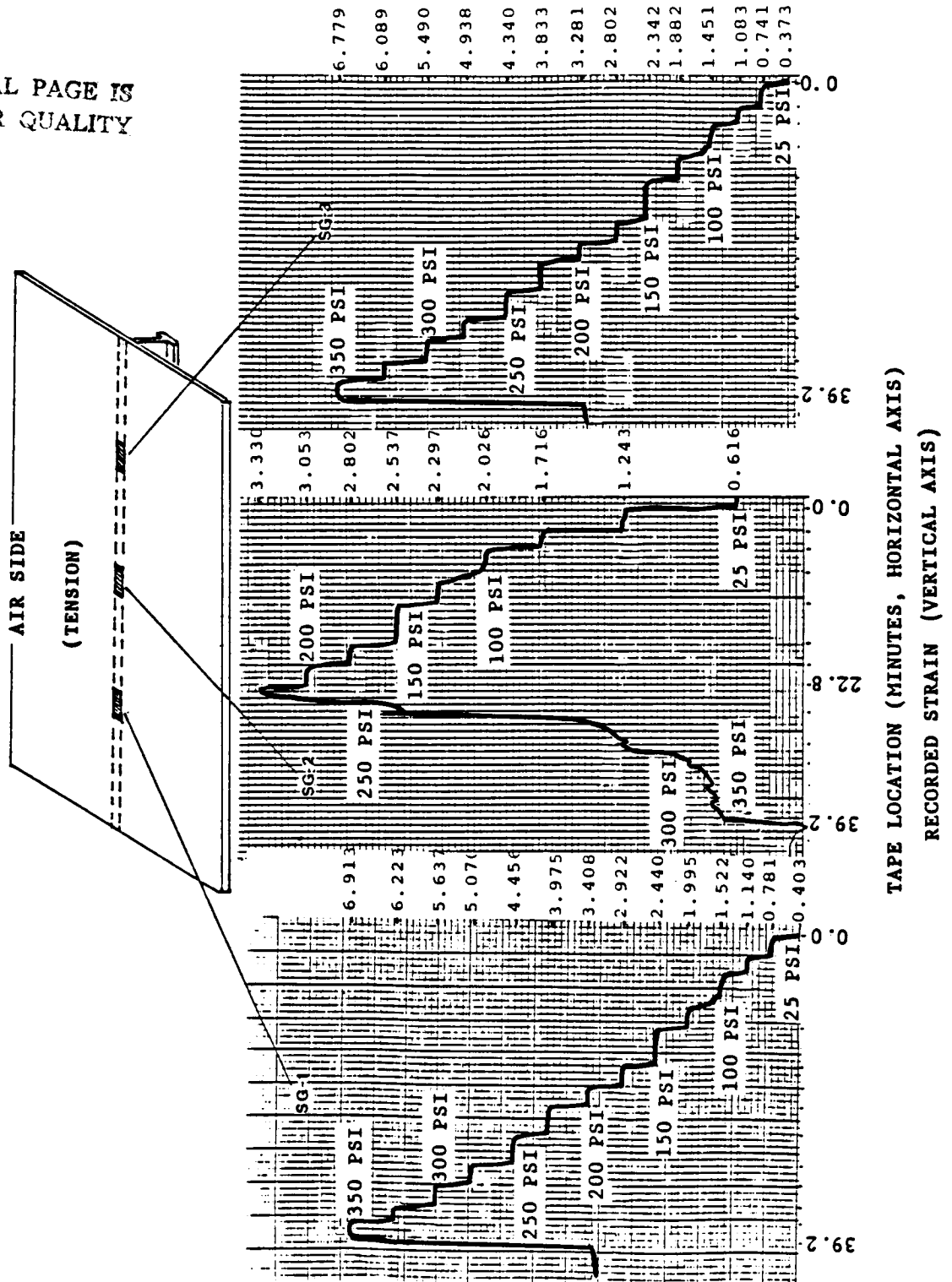
Figure 11   Static Strain History Recorded Longitudinally

Across Centerline of Plate Back
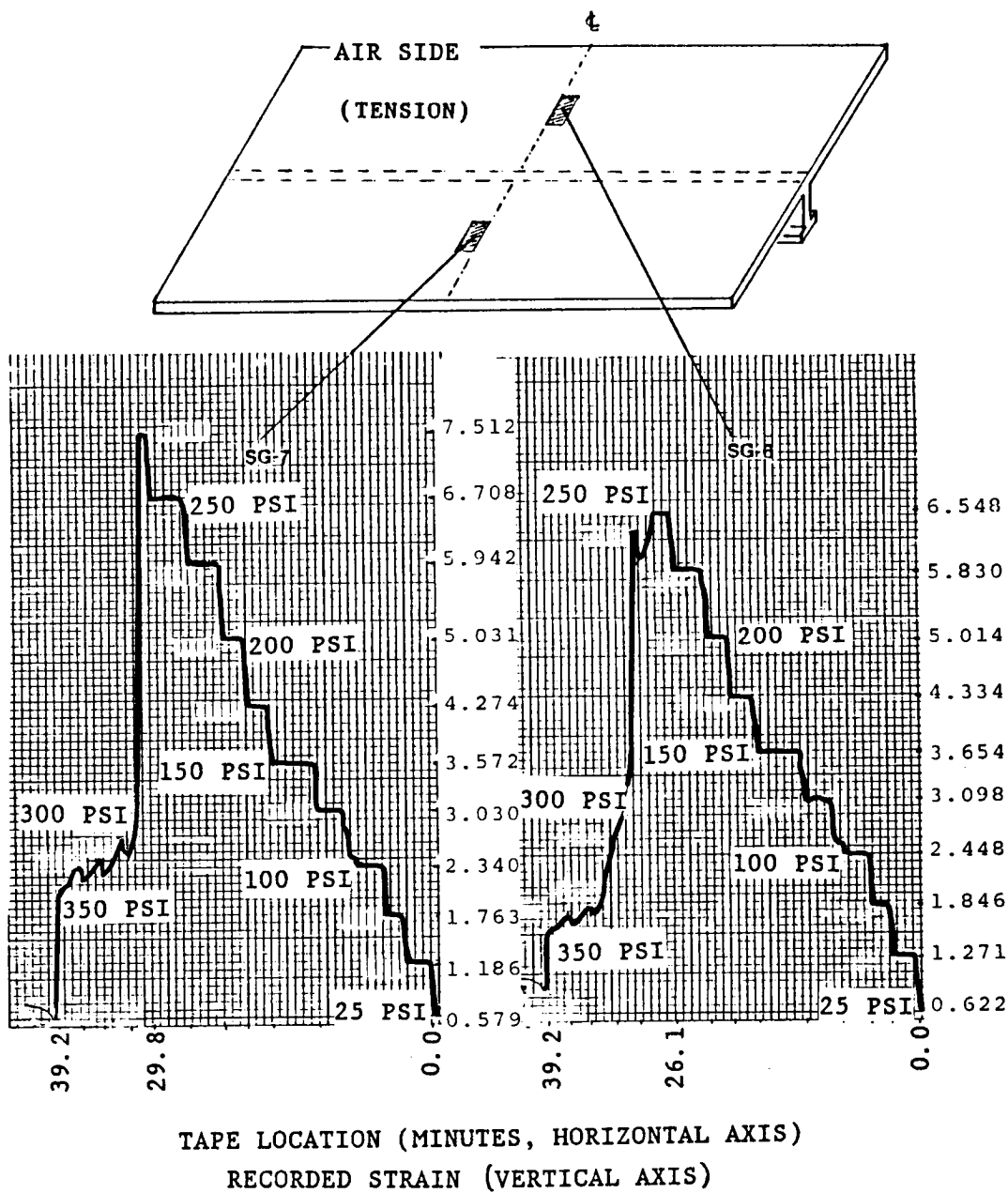
Figure 12   Static Strain History Recorded Across

Transverse Centerline of Plate Back

AIR SIDE

(TENSION)

250 PSI SG-4

200 PSI

300 PSI

150 PSI

350 PSI

100 PSI

25 PSI

1.542
1.515
1.359
1.231
1.100
0.977
0.841
0.694
0.509
0.242

39.2
22.8
0.0

250 PSI SG-3

200 PSI

150 PSI

300 PSI 100 PSI

350 PSI

25 PSI

7.901
7.351
6.778
6.183
5.550
4.769
4.025
3.314
2.595
1.697
0.745

39.2
29.8
0.0

TAPE LOCATION (MINUTES, HORIZONTAL AXIS)
RECORDED STRAIN (VERTICAL AXIS)
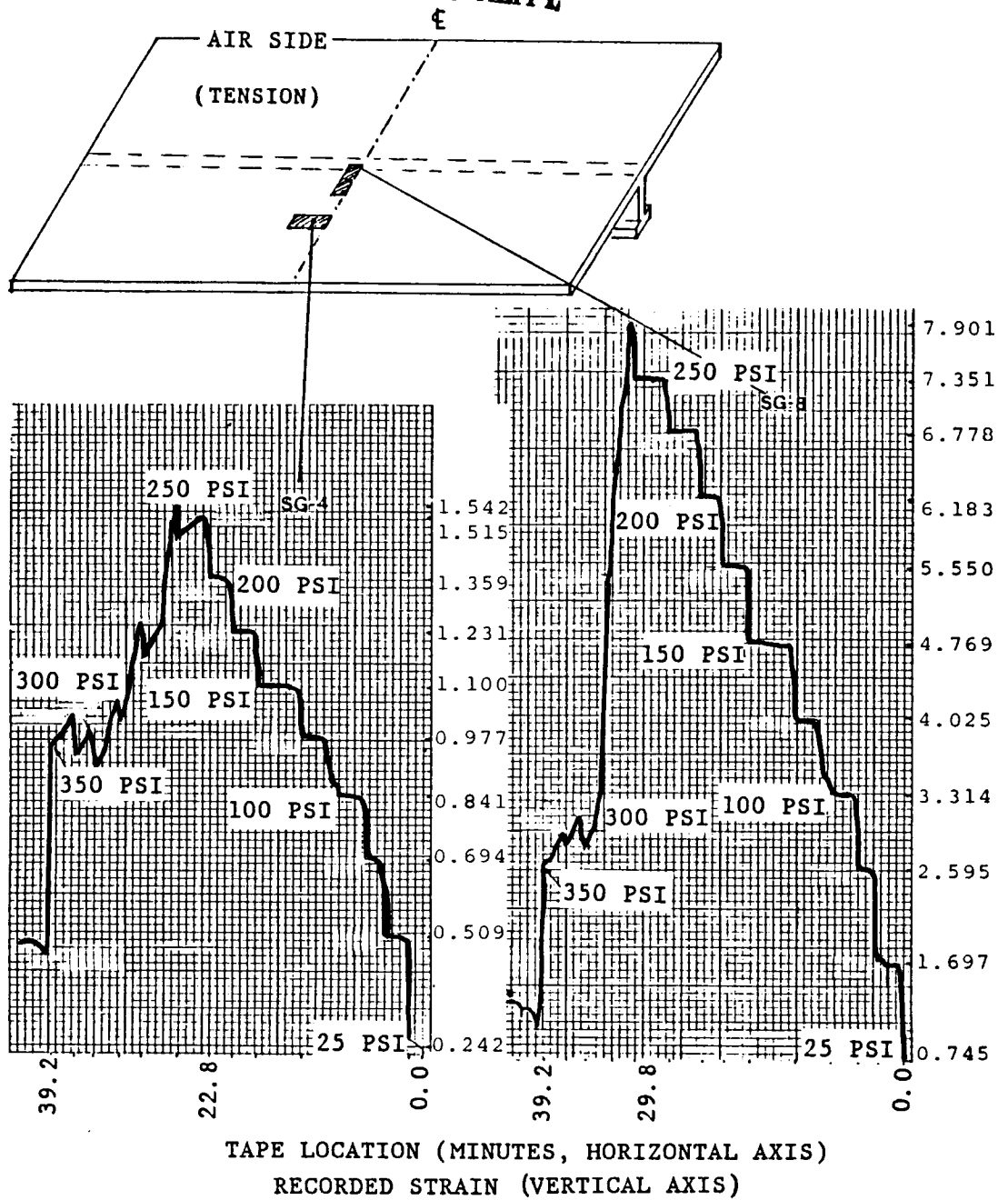
Figure 13   Static Strain History Recorded on Lower Half

of Transverse Centerline of Plate Back

79

TABLE 1

STATIC DEFLECTION AND PRESSURE DATA

PRESSURE (PSI)	1	2	3	4	5
25	.043	.079	.095	.080	.040
50	.080	.148	.180	.154	.075
75	.110	.204	.247	.211	.103
100	.139	.255	.304	.260	.131
125	.180	.308	.361	.311	.165
150	.197	.352	.407	.352	.190
175	.223	.394	.451	.392	.217
200	.248	.434	.492	.430	.242
225	.275	.473	.532	.466	.267
250	.297	.506	.566	.497	.288
275	.321	.540	.601	.529	.311
300	.342	.570	.632	.557	.333
325	.364	.601	.664	.586	.354
350	.387	.632	.695	.615	.376

NOTE: AFTER PRESSURE WAS VENTED OFF, A PERMANENT SET OF 0.408 INCHES REMAINED AT NODE (16,13).

TABLE 2

STATIC TEST STRAIN AND PRESSURE DATA

STRAIN GAGE DATA (MICROSTRAIN)
-STRAIN GAGE POSITIONS

PRESSURE (PSI)	1	2	3	4	5	6	7	8	9	10
25	403	616	373	242	662	579	745	1156	2655	1236
50	781	1243	741	509	1271	1186	1697	2015	4348	1988
75	1140	1716	1083	694	1846	4763	2595	2681	5132	2608
100	1522	2026	1451	841	2448	2340	3314	3235	7644	3155
125	1995	2297	1882	977	3098	3030	4025	4018	9720	3907
150	2440	2537	2342	1100	3654	3572	4769	4781	11122	4789
175	2922	2802	2802	1231	4334	4274	5550	5669	12074	5992
200	3408	3053	3281	1359	5014	5031	6183	7081	12948	7323
225	3975	3330	3833	1515	5830	5942	6778	8613	13458	9014
250	4456	2633	4340	1542	6548	6708	7351	9911	13877	10574
275	5070	1261	4938	1258	6288	7512	7901	11552	14132	12359
300	5637	871	5490	1073	2754	2686	5401	13078	14314	14181
325	6223	760	6089	1030	1873	2462	3091	14910	14496	15985
350	6913	734	6779	996	1743	2377	2964	19742	14678	17770
VENT	3266	284	3189	485	10748	691	1236	10102	8190	11137

NOTE: STRAIN GAGES SG-5 AND SG-11 FAILED PRIOR TO TEST, ALSO STRAIN VALUES IN THE VENT ROW INDICATE STRAIN REMAINING AFTER PRESSURE WAS VENTED OFF (I.E. AT ATMOSPHERIC PRESSURE).

positions. This was not typical in the case of SG-10 (located 1.8 inches off the center of the point of maximum vertical deflection of the flange) where strain continued to increase but at a decreasing rate, demonstrating that the stiffener load was being redistributed to the regions of the stiffener where the web had not yet begun to rotate out of the vertical plane. The redistribution of the stresses throughout the stiffener is best illustrated in Figure 14 which is strain normalized at each 25 psi increment for strain gages SG-1, 3, 9, 10 and 12. None of these plate and stiffener gage locations showed the same elastic tripping "unloading" as did SG-2, 4, 5, 7, and 8. Accordingly SG-1, 3, 9, 10, and 12 best represented the response of the stiffener flange (SG-9, 10, and 12) and web toe (SG-1 and 3) to elastic tripping. In Figure 14 it again can be seen how the center of the stiffener flange (SG-10) begins to unload as the web rotates elastically out of the vertical plane (symmetrical tripping) and the remaining portion of the stiffener assumes the load. The strain histories also indicate that the stiffener was rotating out of the vertical plane towards strain gage SG-6, since SG-7 values were not sensitive to the initial tripping action until 275 psi, versus 250 psi for SG-6 (Figure 12). It should also be noted that the transverse centerline strain gages placed longitudinally (SG-2 and SG-4) were more sensitive to initial tripping action than those placed transversely in the same regions (SG-7 and SG-8).

As a consequence of this test it was determined that more than four plate thicknesses deflection would be required to initiate inelastic tripping. Lateral measurements of the stiffener (after the 0.695 inch centerline vertical deflection of the test planel, i.e., approximately four plate thicknesses) indicated no permanent deformation of the flange or web out of the vertical plane. Additionally, the progressive behavior of this specific plate- stiffener combination when loaded was found to be well difined, qualif\tatively predictable, and sensitive to tripping. The static field test had shown also that the equipment to be used in the underwater explosion data collection was reliable and performed well.

UNDERWATER SHOCK TEST RESULTS

The shot went off as planned and, as predicted, the 8 lb charge reacted as a 10 lb charge (determined by post-shot calculations). The dome and plume from the explosion were symmetrical, as was expected for the cylindrical charge used. Also, as had happened during the Langan test [16], the pneumatic fenders were ruptured from the force of the explosion.

As the chamber was pulled from the water immediately after the shot it was readily obvious that over three-quarters of the test plate surface area was blown free from the rest of the test panel. Upon closer inspection it was discovered that the missing section had been cleanly torn along the boundaries of the test panel and was lying in the bottom of the air-back chamber. As can be seen in Figure 15, the stiffener exhibited an anti-symmectric displacement configuration (i.e., the stiffener remains vertical) as described in [8]. This type of deformation is the initial stage of inelastic tripping before collapse of the stiffener. The web had begun to buckle at the point of attachment to the flange in three separate areas spaced symmetrically along the length of the stiffener: the center and four inches on either side as shown in Figure 15. The stiffener, though it had not rotated out of the vertical plane, was showing indications of doing so and collapsing to the left side of the plate. The center-most position of the plate retained a permanent vertical deflection of approximately 1.30 inches, a deflection of sever plate thicknesses. Even at this extreme amount of deformation there was not a total collapse of the stiffener. The strain histories
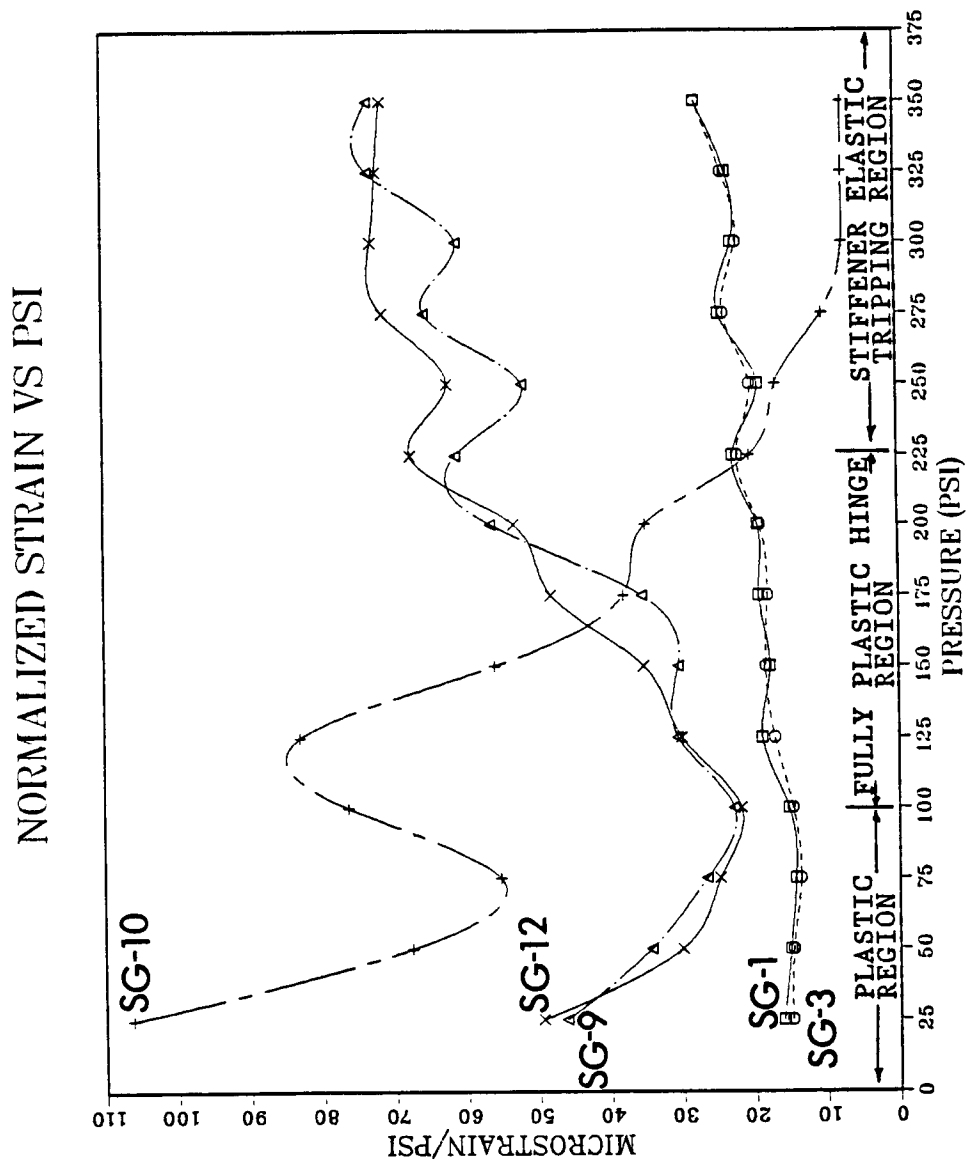
Figure 14 Plot of Static Strain Normalized to Pressure

82
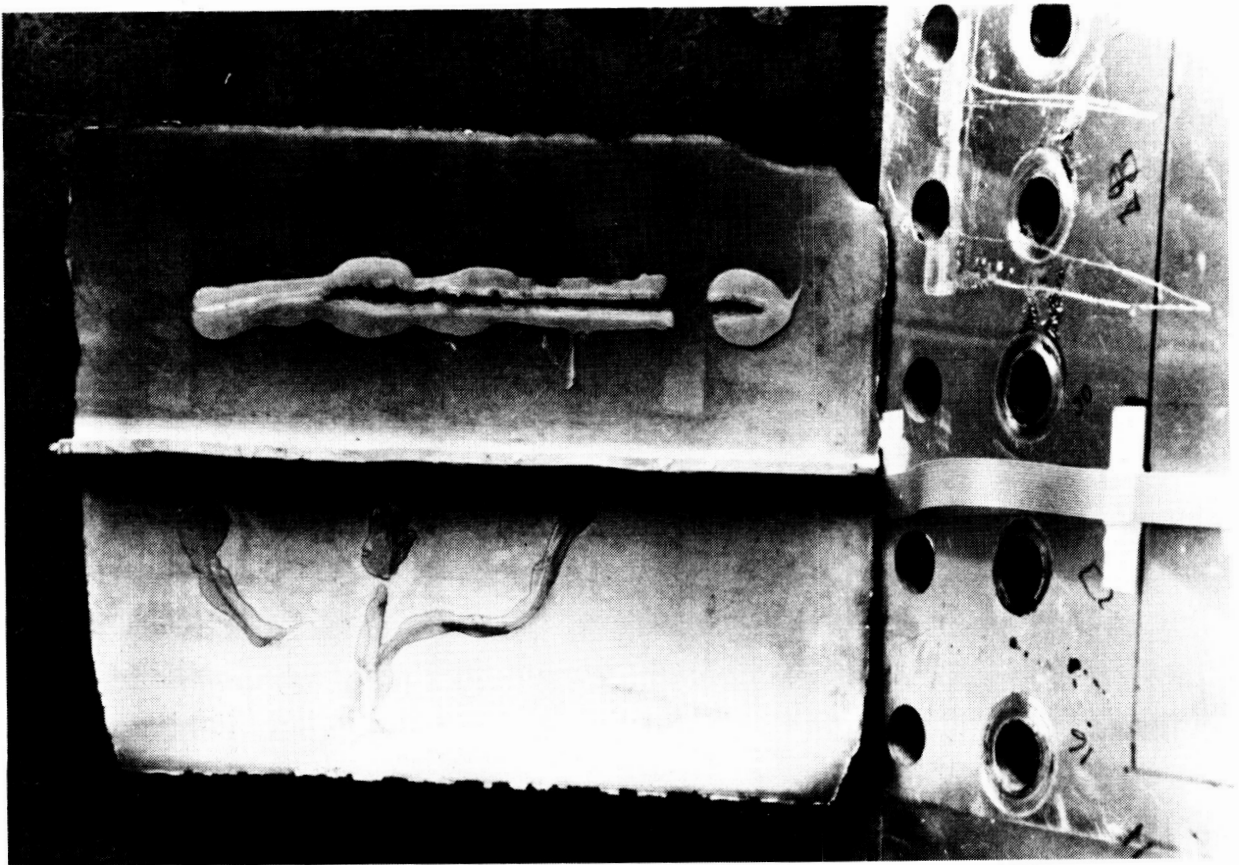
Figure 15. View of Plate Section Showing Anti-Symmetrical
Section

were expected to follow the same symmetry and trends experienced in the static test, even though now the free field pressure was 3780 psi (Figure 16) and was generated by a shock wave which peaked 17.3 microseconds after arrival at the ten foot standoff radius.

The recorded peak strain values and arrival times are listed in Table 3 and associated strain histories are shown in Figures 17 through 20. Each strain gage history had been transferred from the high speed tape to disk storage on the HP-5451C Fourier Analyzer, where individual records were reviewed and outputted graphically. Typically, one strain gage history would cover fourteen records (approximately 4.48 milliseconds). Note that the voltage values on the vertical axis were multiplied by each strain gage's calibration factor to obtain the peak strain values which are annotated in each strain gage history. The strain gage histories are also marked at the time of arrival of the wave front.
A characteristic of every strain history was an eventual peak strain drop-off to a negative value. This represented the plate detaching from the water (due to cavitation at the plate surface) allowing the plate to come to rest until it was

TABLE 3

SENSOR	ARRIVAL TIME (MILLISECONDS)	RECORDED PEAK (MICROSTRAIN)
SG-1	2.53	20.2 k
SG-2	2.50	30.0 k
SG-3	2.56	44.0 k
SG-4	2.18	17.0 k
SG-5	2.44	23.0 k
SG-6	2.50	25.2 k
SG-7	2.18	40.0 k
SG-8	2.56	35.o k
SG-9	2.24	36.0 k
SG-10	2.24	16.0 k
SG-11	FAILED	
SG-12	2.24	36.0 k
P-XDCR-1	2.10	3780 psi
P-XDCR-2	2.08	3500 psi
P-XDCR-3	FAILED	

reloaded microseconds later by an onrush of water from the explosion [13]. A summary of strain gage shockwave arrival times, peak times before reloading (multiple peaks in many cases), times to cavitation (i.e., last peak time less arrival time), and reload times is provided in Table 4. Note that reload times for all strain histories in the center of the plate and across the stiffener (SG-1, 2, 3, 8, 9, and 12) were consistent at approximately 3.12 to 3.17 milliseconds. Additionally, the time period prior ro the onset of surface cavitation was also uniform in the plate center (SG-1, 2, 3, and 8) at 540 to 590 microseconds.

84
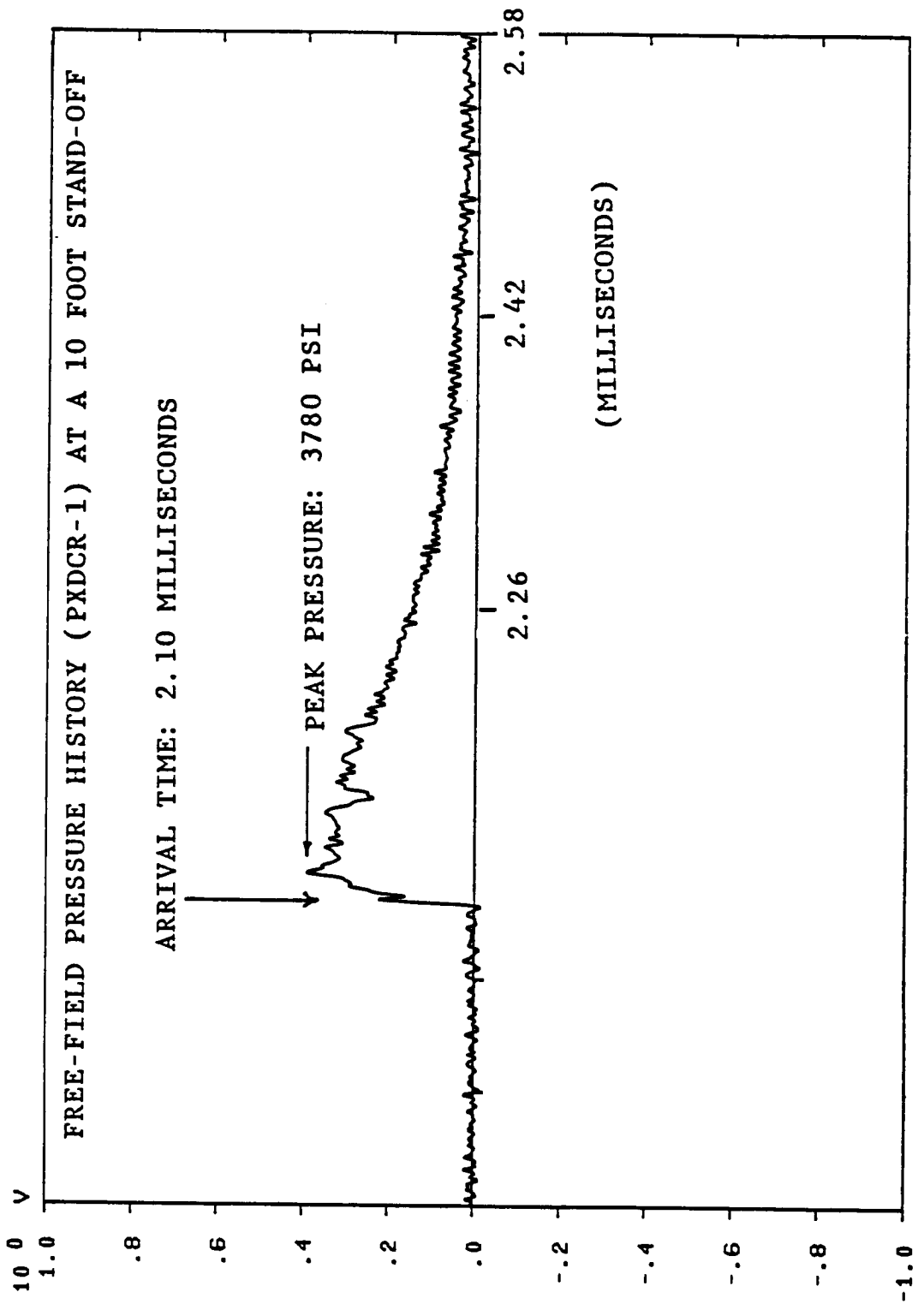
Figure 16   Free-Field Pressure and Arrival Time

85

comparison of observed symmetry and trends was made in Figures 17 through 20. Initially after making a general overview of all the strain histories, it became evident that the upper left end of the plate (Figure 15) was exposed to the shock wave earliest and experienced the highest strain values. The shock wave arrival time for the left side gages SG-4 and SG-7 was 2.18 msec., while the arrival time for the stiffener gages SG-9, 10, and 12 was 2.24 msec and for the gages on the opposite side of the plate it was even later (i.e., 2.44 msec and 2.50 msec). The information suggests that the test panel and air-back chamber were not parallel relative to the shock front but slightly canted to one side. The left side of the plate was apparently higher than the right, which is why all other plate strain gage arrival times were approximately 0.3 milliseconds later. This confirmed the belief that the cabling and junction box mounted to the side of the air-back chamber could possibly tilt the chamber once it was lowered into the water and only supported by the pneumatic fenders.

TABLE 4

SUMMARY OF SHOCK WAVE ARRIVAL TIMES, PEAK
TIMES, TIME TO CAVITATION, AND RELOAD TIMES

SENSOR	ARRIVAL TIME (MILLISEC)	*PEAK TIMES (MILLISEC)	ELAPSED TIME PRIOR TO CAVITATION (MICROSEC)	RELOAD TIME (MILLISEC)
SG-1	2.52	3.03/3.07/3.09	560	3.13
SG-2	2.50	2.98/2.99/3.07 3.09	590	3.12
SG-3	2.56	3.07/3.10	540	3.12
SG-4	2.18	2.32/2.42	240	2.43
SG-5	2.44	2.76	320	2.77
SG-6	2.50	2.77/2.81	310	2.84
SG-7	2.18	2.35	120	2.38
SG-8	2.56	3.00/3.08/3.12 3.14	580	3.17
SG-9	2.24	2.33/2.53/2.65 2.73/2.95	710	3.17
SG-10	2.24	2.45/2.60/2.70	550	2.86
SG-11		FAILED		
SG-12	2.24	2.36/2.43/2.59 2.71/3.07	830	3.17

UNDERLINED PEAK TIME INDICATES TIME OF MAXIMUM
STRAIN VALUE.

The plate rectangular geometry additionally dictated that all longitudinally measured strains would be less than those measured transversely across the width of the plate in the same positions. This proved to be the case in the undex test (as well as the satic test) where the peak values of strains for SG-6, 7, and 8

(measured 90 degrees from the longitudinal gages SG-2, 4, and 5) were higher. As expected, except for the region of the plate affected by the chamber tilt, all arrival times measured on the plate were later than those for the stiffener. Additionally, it can be seen that the general shapes of the recorded strain histories in regions which are symmetrically equal are very similar (specifically Figure 18 (SG-1 and SG-3), Figure 19 (SG-6 and SG-8), and Figure 20 (SG-9 and SG-12)). As far as determining the correlation between strain histories and the physical deformation of the stiffener, it can only be speculative. For illustrative purposes Figure 20 containing SG-9, SG-10, and SG-12 strain histories will be used. Again in comparison to static test trends, it would be expected that the strain values experienced at SG-10 would never get quite as large as elsewhere on the stiffener, but build up, unload, and build up again as the stiffener experiences its progressibe deformations. Undoubtedly, the three areas of stiffener deformation shown in Figure 15 occured progressively starting with the region initially of highest compressive stress (the center of the plate) and then progressed to the next highest, probably the SG-9 portion of the stiffener, and lastly SG-12. This sequence seems to follow escpecially well the strain history undulations depicted in the curves for SG-9 and SG-12, and somewhat for all the other strain histories.

GEOMETRY AND MATERIAL CONSIDERATIONS

The results of the underwater shock test are unique for the specific test panel geometry and material used. To put this "uniqueness" in the correct perspective, a discussion of the impulsive load effects on geometry and materials follows.

The deformation of the test panel is more than just a property of the material, it also depends on the geometry of the test panel and the process used to deform it. It has been found [13] that dynamic yielding occurs only at pressures 3 to 10 times the static yield values. This is due to the fact that materials which undergo a transition from ductile to brittle behavior at lowered temperatures will generally undergo a similar transition when the loading has changed from static to dynamic.

Additionally, materials which are ductile at low temperatures tend to remain ductile under dynamic loading [12]. The flow characteristics of most metals will be influenced by the high strain-rates involved, especially in iron which has a very noticeable loss of ductility at high strain-rates. This strain-rate sensitivity determines the magnitude of the permanent deflections. It was because of materials' typical strain-rate sensitivity that a relatively strain-rate independent metal was selected for the test panel material, since the less strain-rate sensitive the material is, the less explosive charge required to cause the necessary deformations. Aluminum 6061-T6 was believed to be almost strain-rate insensitive compared to steel plate at the same strain-rates and was a readily available material. Accordingly, 6061-T6 aluminum was used for all the test panels.

The anatomy of a shock front interaction with a plate is shown in Figure 21. The reflected incident wave is compressive and is the reactive force which causes the plate to deform. additionally, the amplitude and shape of the incident wave changes rapidly as it passes through the plate. The stready decrease in the amount of permanent deformation is due primarily to the decay of the wave. The transmitted incident wave, which is microseconds later, reaches the backside reff surface of the plate and is reflected as a tensile rarefaction wave. The free surface reflected wave in many cases can lead to the development of tension
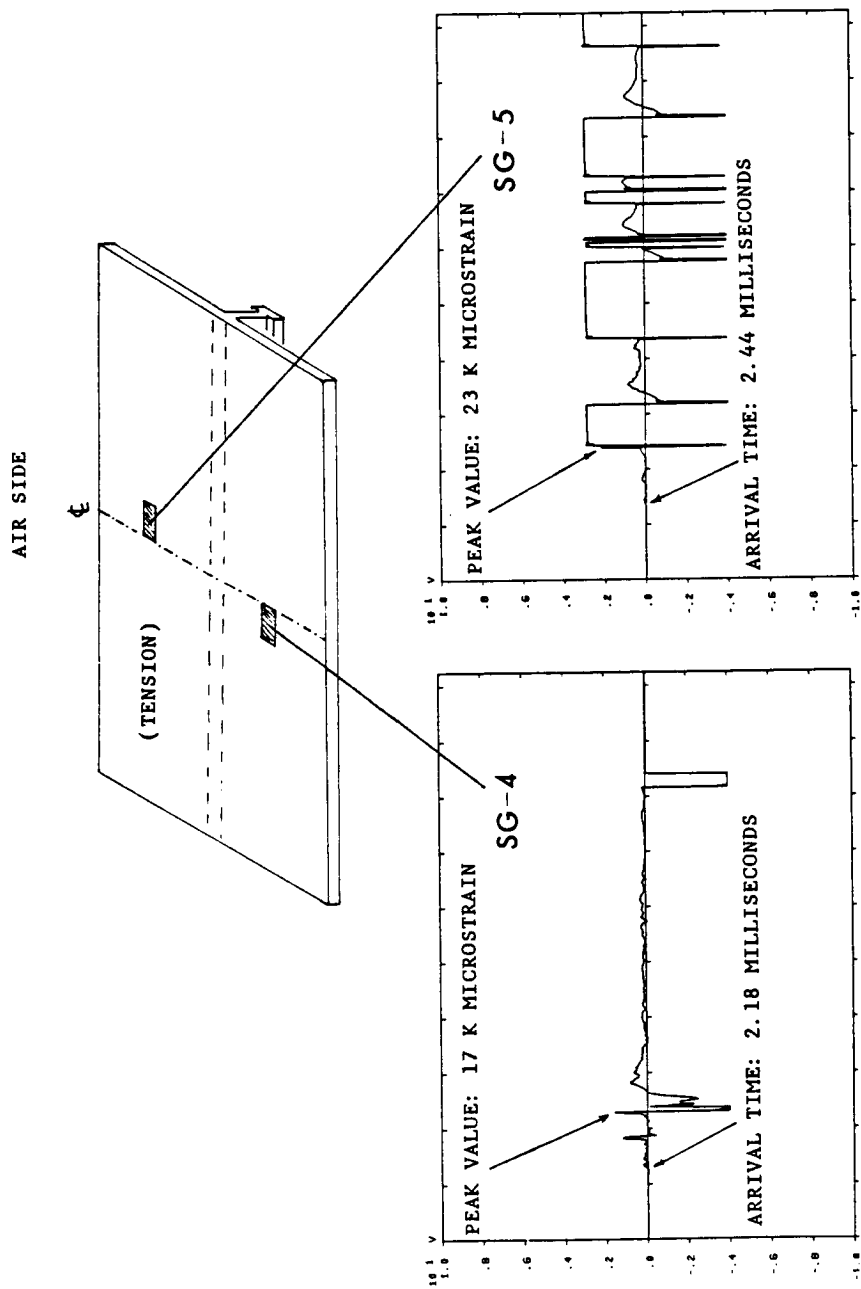
Figure 17 Dynamic Strain History Recorded Across

Transverse Centerline of Plate Back

C-2
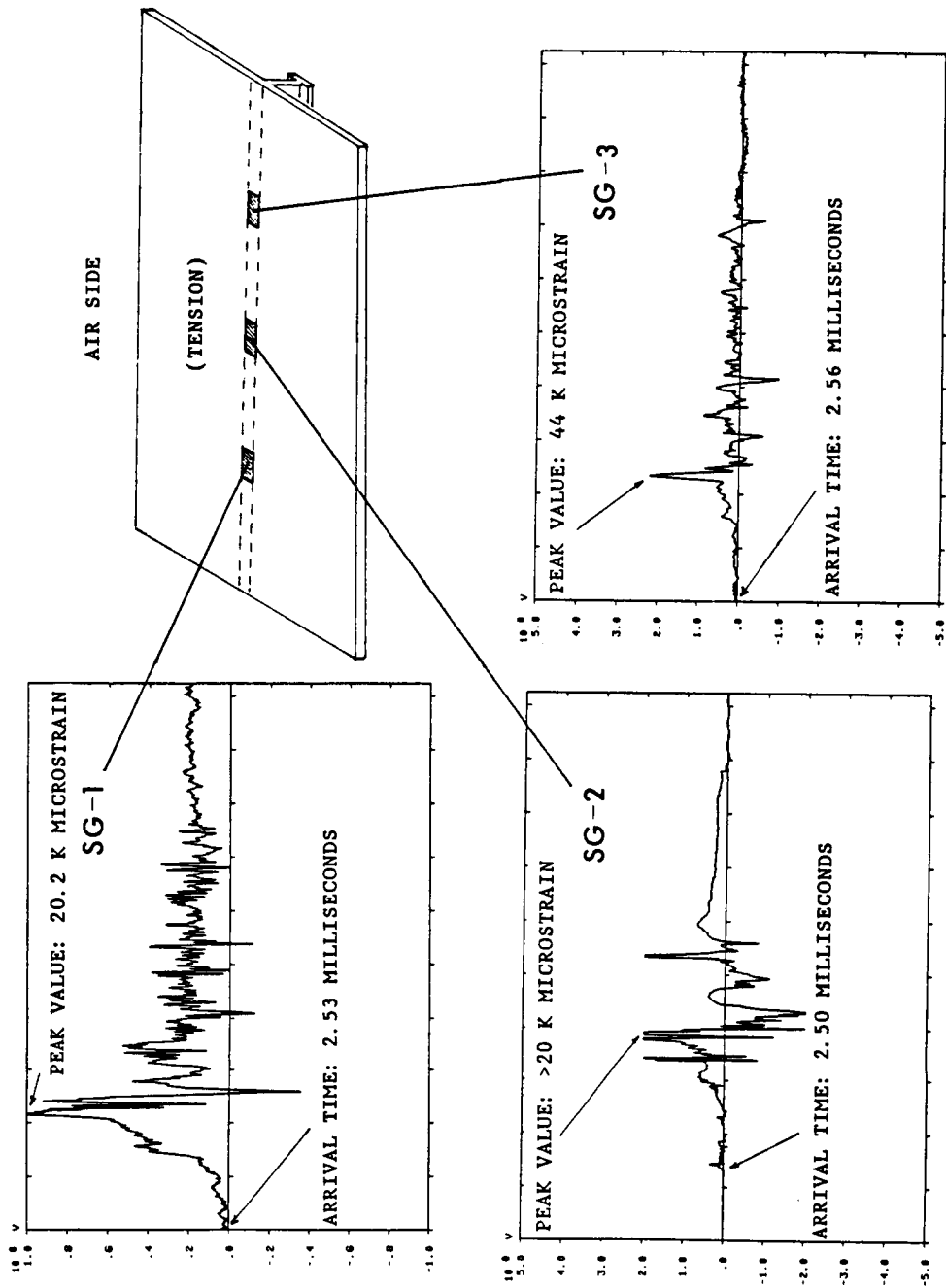
Figure 18   Dynamic Strain History Recorded Across
Centerline of Plate Back (Longitudinally)
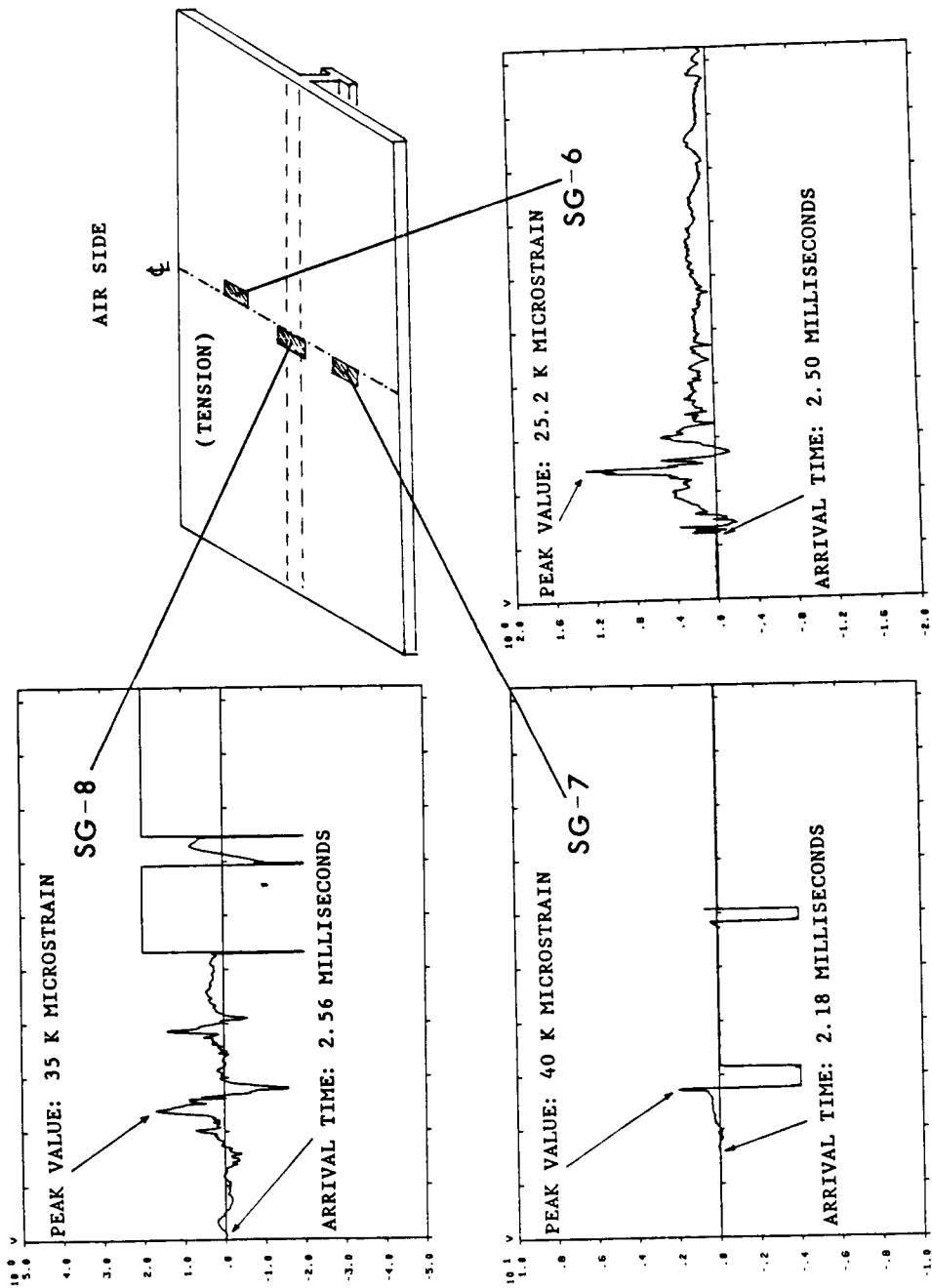
Figure 19   Dynamic Strain History Recorded Across Transverse

Centerline of Plate Back (Transversely)
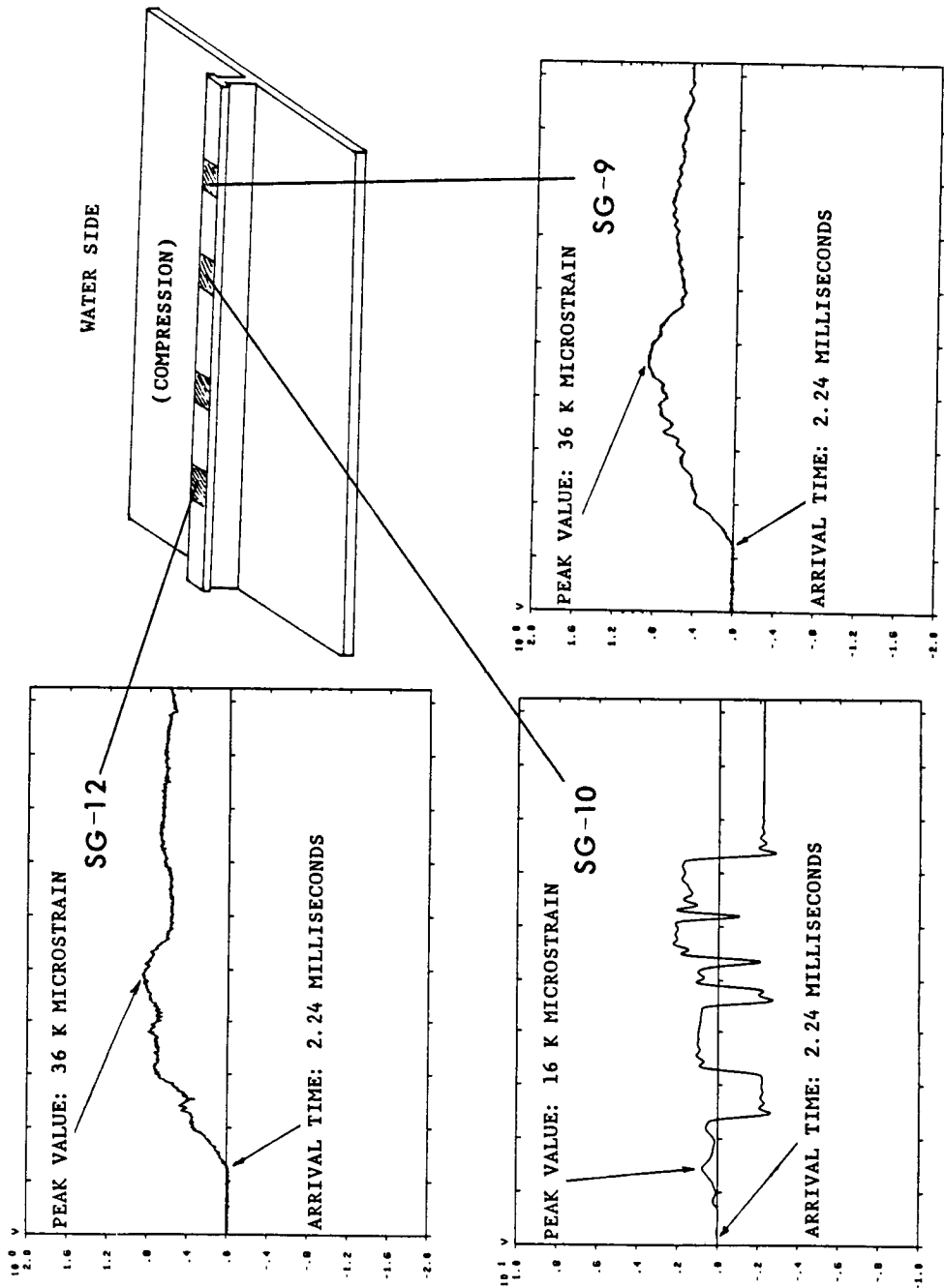
Figure 20   Dynamic Strain History Recorded Longitudinally
Across Flange of T-Stiffener

fractures. Finally, the reflected tension wave is partly transmitted back into the water. [13,21]

The shock front interaction with the plate can be complicated extensively by the shape of the test panel since the geometry of a body and its constraints determine both the location and the amount of plastic flow that will take place. In most cases, interpreting the deformation and fractures that occur can be facilitated by considering the effects that the geometrical shape has on the stress waves. For example, fracturing may occur at a corner dur to the reinforcement between two (or more) tension waves that eat in simultaneously from the edge of the corner. Additionally, entrapment of the incident shock wave by the corner causes multiple reflections from the walls of the corner (pressire increasing stepwise with each further reflection), leading to a significant increase in the pressure at the corner. This combination of reinforced tension waves and pressure amplification is undoubtedly the source of the initiation of the fracturing observed in the test panel and eventual 360 degree tearing of the plate from the test panel, Figures 15 and 22.

Energy Source

Reflected
Compression
Wave

6062-T6 Aluminum

Waterside

Tensile
Rarefaction
Wave

Transmitted
Wave

Airside
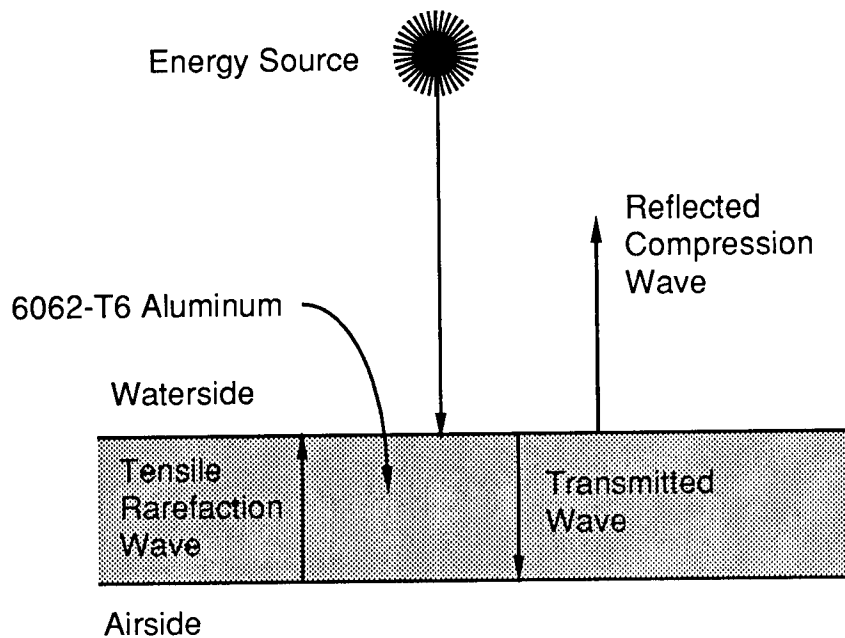
Figure 21. Shock Front Interaction with a Plate

As a closing remark to this section, it should be mentioned that the test panel incurred two surface gouges (less than three thirty-secondths of an inch deep) near the plate edge while being machined. One was weld repaired and one was left as is, and after exposure to the underwater explosion neither defect showed any involvement in the plate fracturing or deformation and apparently were not stress concentrators in this situation. This was also observed in [12],". . . the presence of notches may have little effect in impulsive load situations." However, spalling (or scabbing) was observed in the weld repaired defect.

Spalling, an unusual type of fracturing, occurs near a free-surface relatively far removed from the area of application of a pressure impulse [12]. The spalling observed was a consequence of the applied load generating both longitudinal and transverse waves which progressively struck the weld fusion boundary creating additional waves giving rise to highly localized stresses which were sufficient to cause localized fracturing in the center of the weld repair.

CONCLUSIONS

The static pressure deflection test of the panel machined for this purpose proved to be a source of very good strain and deflection data quantitatively representing the plate and stiffener behavior up to and into the elastic tripping region. Additionally, the progressive behavior of this plate-stiffener combination when loaded hydroststically was found to be well defined, quantitatively predictable, and sensitive to tripping. As a consequence of this test, it was also determined that more than four plate thicknesses deflection would be required to initiate static inelastic tripping.

The dynamic response test, though complicated by the rapidly changing nature of the variables and the complex relationship between stress, strain, and strain-rate, provided strain histories clearly depicting: the initial interaction between the shock front and the test panel, the cavitation times, and the reload times. Additionally, the shock front arrival times measured at eleven different plate locations were precise enough to indicate (through calculation) that the test chamber was not parallel to the shock front emenating from the eight pound TNT charge, but was inclined to the cable junction box side. It was also determined from post UNDEX measurements of plate deflection that even at an extreme deformation of seven plate thicknesses there was not a total collapse of the narrow-flanged T-stiffener. Additionally it has become obvious that the geometry of the test panel machined "cavity" and its constraints determined both the location and the amount of plate racturing which took place.

In summary, narrow-flanged T-stiffener tripping has been observed demonstrating both the static elastic and dynamic inelastic behaviors. Also the underlying cause of the fracturing observed in the UNDEX test plate has been attributed to the design geometry of the test panel.

It is not apparent how much effect the amplified corner pressures had on the plate deformation and strain histories, but to ensure strain histories representative of only the shock front and plate interaction, the test panel warrants redesign so as to eliminate the cavity walls surrounding the stiffened plate, thus removing boundaries which may cause shock wave pressure amplification.

As a by-product of this investigation (shock wave efects on welds), spalling of a weld repair should be of interest for any future studies evaluating the physical and metallurgical effects of an underwater explosion shock wave front on a metal panel containing multiple welds or weld repairs (e.g., spalling noted in the dynamic test plate). The importance of this is self-evident since the hull integrity of every Naval vessel is dependent upon the reliability of the welds bonding the plating together.

93

REFERENCES

1. Faulkner, D., <u>The Collapse Strength and Design of Submarines</u>, paper presented at the Symposium on Naval Submarines, London, May 1983.

2. Evans, J.H., <u>Ship Structural Design Concepts</u>, Cornell Maritime Press, 1975.

3. Evans, J.H. and Adamchak, J.C., <u>Ocean Engineering Structures</u>, vol. 1, The MIT Press, 1969.

4. Thompson, J.M.T. and Hunt, G.W., <u>Collapse</u>, Cambridge University Press, 1982.

5. Mansour, A.E., Gross Panel Strength Under Combined Loading, Project SR-225, Department of the Navy, Naval Ship Engineering Center, 1977.

6. Flax, A.H., "<u>Aero and Hydro-Elasticity</u>," Structural Mechanics, Pergamon Press, 1960.

7. Gerard, G., <u>Introduction to Structural Stability Theory</u>, McGraw-Hill Book Company, 1962.

8. Bleich, F., <u>Buckling Strength of Metal Structures</u>, McGraw-Hill Book Company, 1952.

9. Kennard, E.H., Tripping of T-shaped Stiffening Rings of Cylinders Under External Pressure, Report 1079, NS 731-038, 1959.

10. Weertman, J., "<u>Dislocation Mechanics at High Strain Rates</u>," Metallurgical Effects at High Strain Rates, Plenum Press, 1973.

11. Jones, N., Dumas, J.W., Giannotti, J.G., and Grossit, K.E., "<u>The Dynamic Plastic Behavior of Shells</u>", Dynamic Response of Structures, Pergamon Press, 1972.

12. Rinehart, J.S. and Pearson, J., Behavior of Metals Under Impulsive Loads, The American Society for Metals, 1954.

13. Rinehart, J.S. and Pearson, J., <u>Explosive Working of Metals</u>, Pergamon Press, 1963.

14. Rentz, T.R. and Shin, Y.S., On the Field Experiences of UNDEX Testing For A Stiffened Flat Plate Model, <u>The Shock and Vibration Bulletin</u>, Bulletin 55, part 2, June 1985.

15. King, N.R., Underwater Shock-Induced Responses of Stiffened Flat Plates: An Investigation Into the Predictive Capabilities of the USA-STAGS Code, Master's Thesis, Naval Postgraduate School, Monterey, California, December 1984.

16. Lagan, J.R., An Investigation Into the Comparisons of the Underwater Shock Effects on a Stiffened Flat Plate to the Predictive Nature of a Computer Model, Master's Thesis, Naval Postgraduate School, Monterey, California, March 1985.

17. Cole, R.H., <u>Underwater Explosions</u>, Princeton University, Princeton, New Jersey, 1948.

18. Gilot, A. and Clifton, R.J., "Pressure-Shear Waves in 6061-T6 Aluminum and Alpha-Titanium", <u>J. Mech. Phys. Solids</u>, No. 3, pp. 263-284, 1985.

19. Carden, A.E., Williams, P.E., and Karpp, R.R., "Comparison of the Flow Curves of 6061 Aluminum Alloy", Shock Waves and High Strain Rated Phenomena in Metal, Plenum Press, 1981.

20. Nicholas, T., "Tensiles Testing of Materials at High Rates of Strain", <u>Experimental Mechanics</u>, pp. 177-185, May 1981.

21. American Society of Tool and Manufacturing Engineers, <u>High-Velocity Forming Metals</u>, Prentice-Hall, 1964.

Non-Linear Shipboard Shock Analysis of the TOMAHAWK Missile Shock Isolation System

Joel Leifer
Michael Gross

The identification, quantification, computer modeling and verification of the TOMAHAWK non-linear liquid spring shock isolation system in the surface ship Vertical Launch System (VLS) are discussed. The isolation system hardware and mode of operation is detailed in an effort to understand the non-linearities. These non-linearities are then quantified and modeled using the MSC/NASTRAN finite element code. The model was verified using experimental data from the Naval Ordnance Systems Center (NOSC) MIL-S-901 medium-weight shock tests of Aug. 1986. The model was then used to predict the TOMAHAWK response to the CG-53 USS MOBILE BAY shock trials of May-June 1987. Results indicate that the model is an accurate mathematical representation of the physical system either functioning as designed or in an impaired condition due to spring failure.

INTRODUCTION

This paper presents the analysis and predicted response of the TOMAHAWK CG53/VLS shock isolation system during shipboard shock. The analysis was complicated by the need to identify and quantify several non-linearities. The heart of the shock isolation system analyzed is an assembly of liquid springs. The function of each assembly was non-linear due to geometric clearance (gapping) and loading as a non-linear function of displacement and velocity. These springs work in conjunction with the sixteen friction pads that are attached to the MK-14 canister and grip the AUR.

The VLS is a modular construction consisting of eight cells. Seven of the cells contain eight encanistered missiles each. The eighth cell contains five encanistered missiles and a strikedown crane. The missiles are TOMAHAWK cruise, Standard Missile Two and Vertical Launch ASROC. The isolation system study applies only to the TOMAHAWK missile in the MK 14 Canister.

LIQUID SPRING HARDWARE

The liquid spring system considered in this paper is designed to isolate the TOMAHAWK missile in the surface ship Vertical Launch System from shipboard shock caused by nearby underwater explosions. Each missile/All-Up Round (AUR) configuration has its own integral shock isolation system containing four liquid spring assemblies. Each assembly has a primary and secondary liquid spring working in opposite directions. The secondary spring has the ability to isolate itself from the system during the initial pulse by lifting off of its bearing surface (gapping). Each spring has a resetting spring force that is a quadratic function of the relative displacement and a damping force (that varies depending on whether the spring is in compression or extension). This damping force is a function of the velocity to a power of .7 as specified on the procurement drawings.

MODE OF OPERATION

The liquid spring assembly experiences four distinct conditions or modes of operation as it performs its job. These conditions are :

1) Primary in compression and compressing, secondary gapped - condition 1
2) Primary in compression but extending, secondary gapped - condition 2
3) Primary in compression but extending, secondary in compression and compressing - condition 3
4) Primary in compression and compressing, secondary in compression but extending - condition 4

A plot of a typical spring assembly response is shown in Figure 1 with the occurrence of each condition labeled. The four conditions are discussed in more detail in the following paragraphs.

The secondary spring is preloaded by pressurizing the cylinder. This forces the piston to its full one inch displacement. The two springs are then loaded into the strut and the primary spring is preloaded by torquing the bolt that bears on the secondary spring (see Figure 2) to a one inch displacement. The two springs are in series, but, since the secondary is so much stiffer than the primary, it acts as a semi-rigid bar and transfers most of the load (and hence the deflection) into the primary spring. The AUR is then installed, reducing the preload in the primary spring by an amount equal to its weight of 3600 lbs. This is the steady state condition.

Condition 1 (see Figure 3) commences when the system is subjected to a transient excitation in the vertical or X direction. The

98

FIGURE 1   TYPICAL SPRING ASSEMBLY RESPONSE
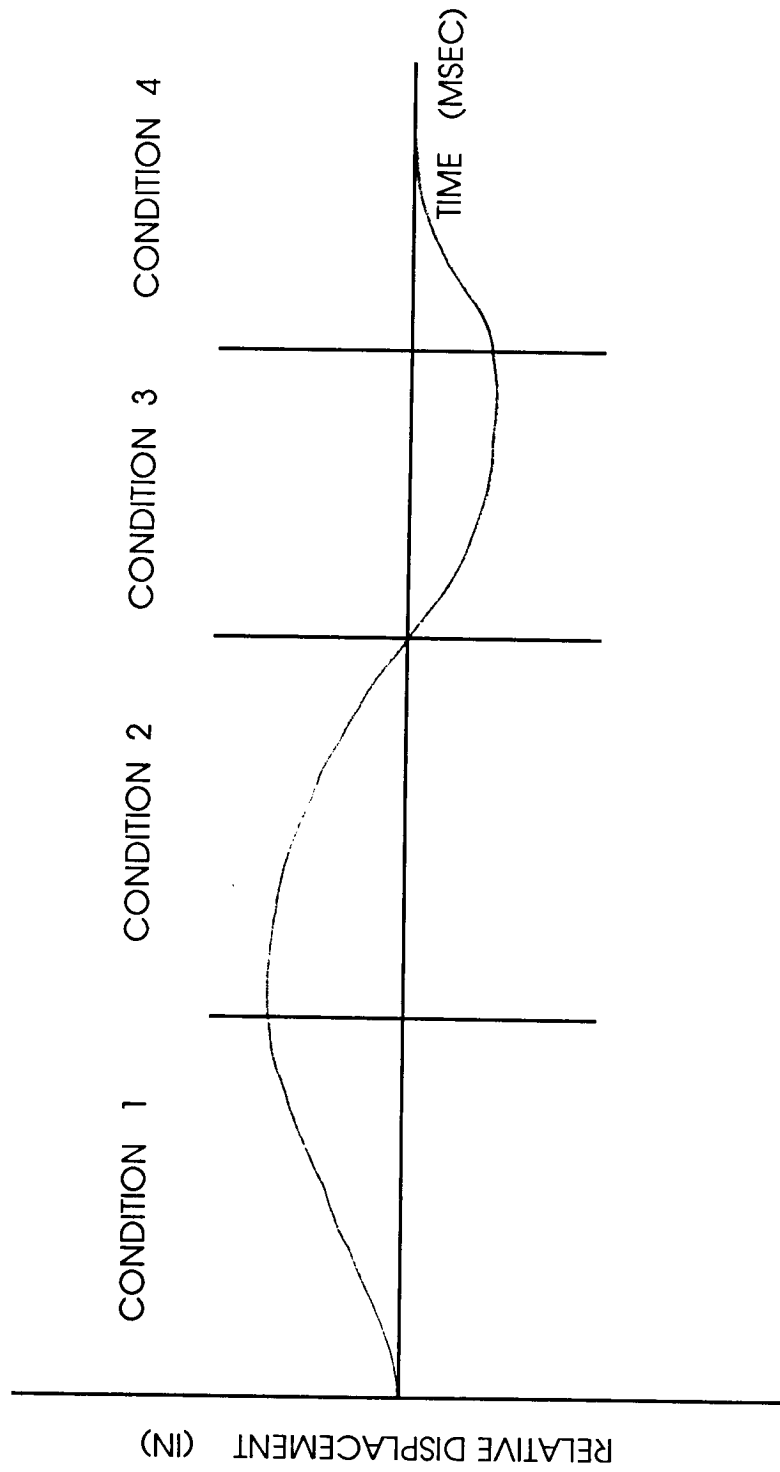
FIGURE 2 LIQUID SPRING ASSEMBLY GEOMETRY

PRELOAD BOLT

GRID 1

MK-14 CANISTER

GRID 5

X^+

GRID 2

SECONDARY SPRING

SPRING STRUT

DAMPER

PRIMARY SPRING

ROD

AUR

GRID 3

GRID 4

AUR BASEPLATE
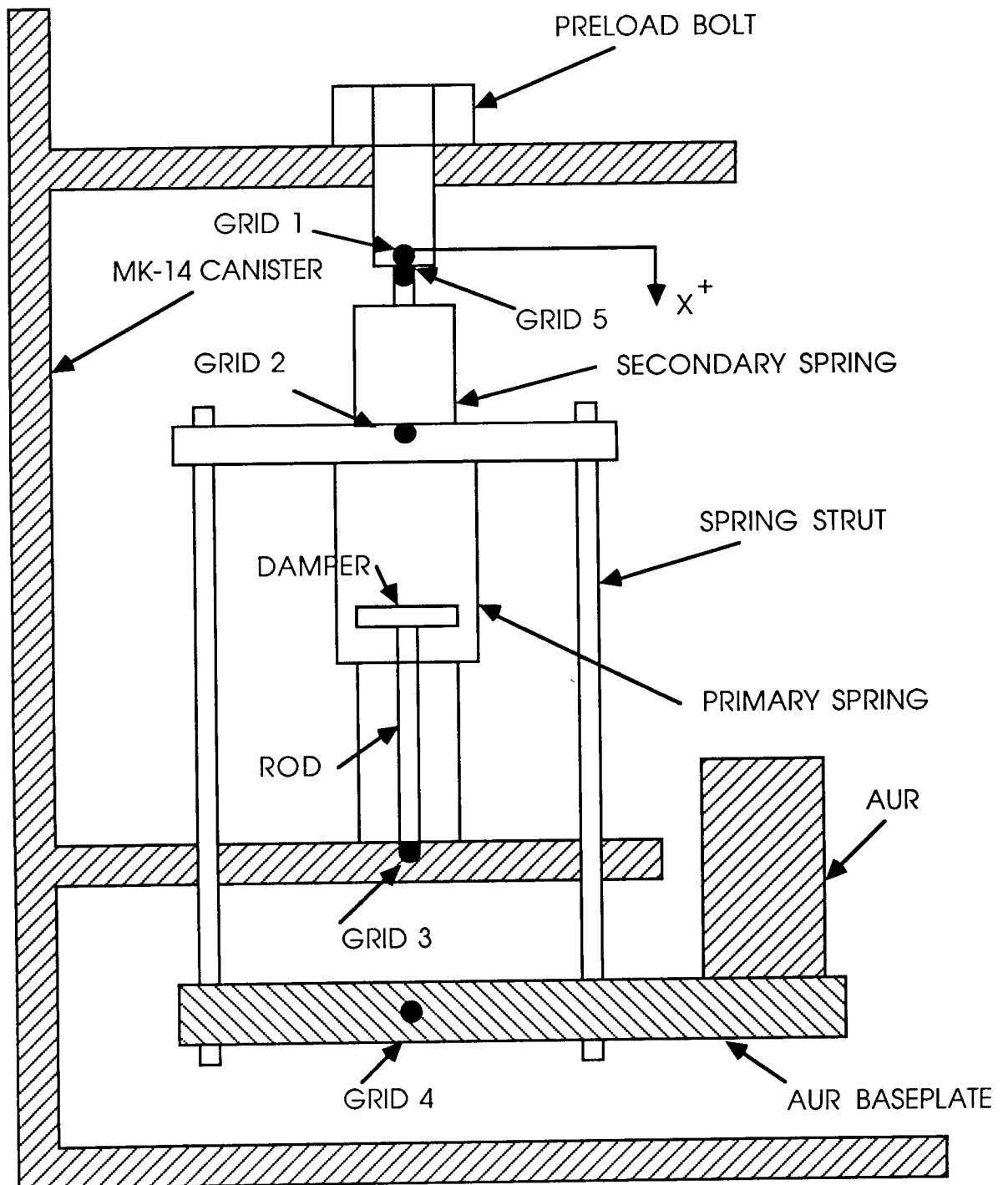
FIGURE 3   PRIMARY IN COMPRESSION AND COMPRESSING,

SECONDARY GAPPED
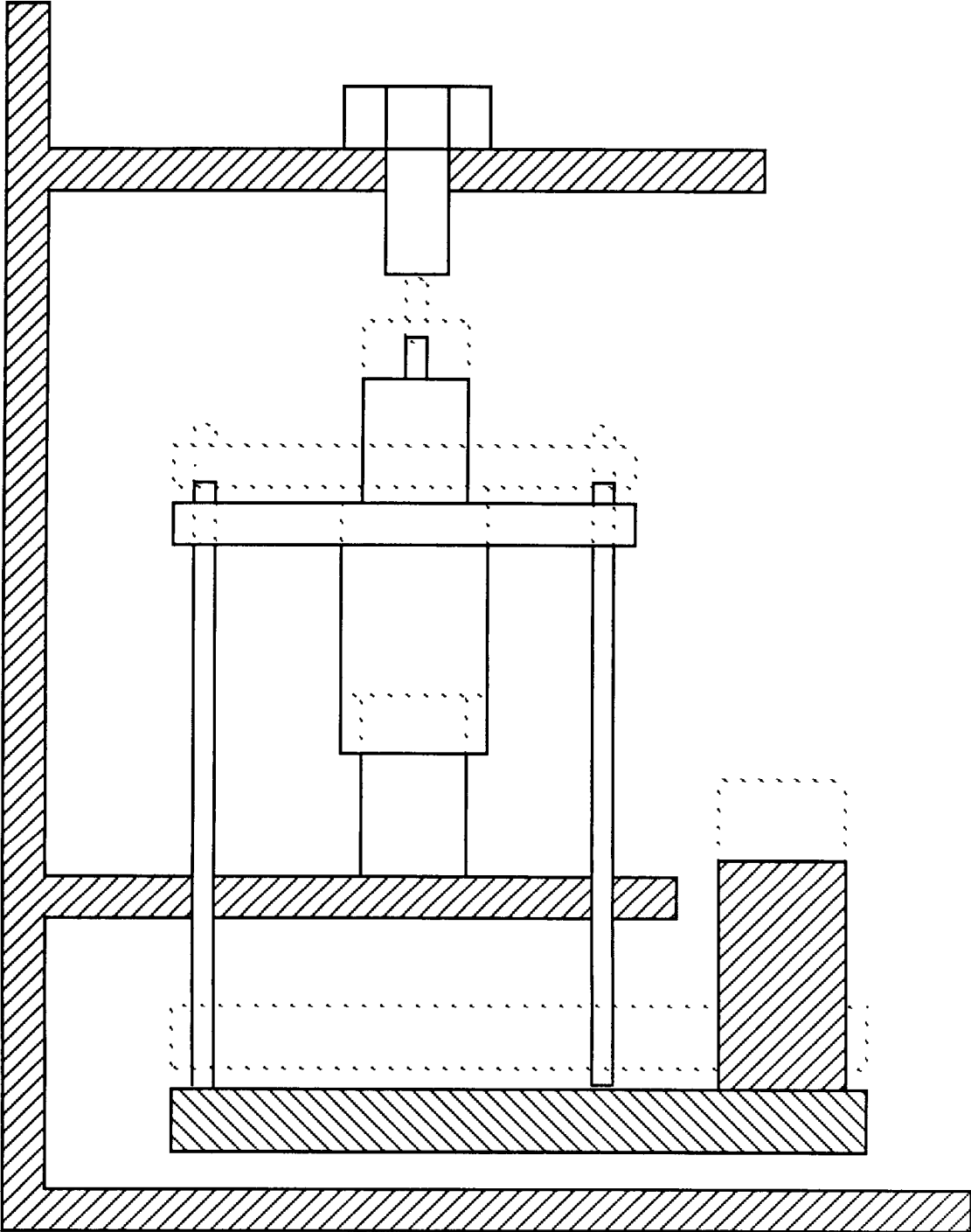
resulting load path is from the MK-14 Canister, thorough the liquid spring assemblies and into the AUR. Initially, the MK-14 Canister will move in the X- direction (see Figure 2 for coordinate system definition), compressing the primary spring. The secondary spring will gap when the compression force generated in the primary spring overcomes the remaining primary preload. This remaining preload is the difference between the initial preload caused by the one inch compression and the weight of the AUR.

When the acceleration in the X+ direction is of sufficient force to overcome the momentum in the opposite direction the relative displacement will have peaked and will begin to decline. This signals the start of condition 2 (see Figure 4). At this time the primary spring (which has been compressed) will start to extend. The spring force stored in the primary spring will add to the acceleration generated force. The secondary spring will remain gapped until the primary spring releases its stored spring force by extending to its original length. The gap will close at the same condition it opened at, ie, when the force generated in the primary spring by the applied load is equal to the remaining preload.

The momentum continues in the same direction as in the previous condition causing the primary to pass to its equilibrium position and try to extend. At its equilibrium position, however, the secondary will have closed its gap and will attempt to bear the load. At this point (the start of condition 3, Figure 5) any compression of the secondary is accompanied by an equal extension of the primary. The total load on the secondary is the sum of the applied force and the stored spring force in the primary. For this analysis, any impact forces generated by the gap closing are ignored.

At the start of condition 4 (Figure 6) the momentum has shifted to the X- direction, and the extension in the primary and compression in the secondary have peaked. The secondary will start to extend, releasing its stored spring energy in the form of a force which adds to the acceleration developed force. The sum of these forces is absorbed by the compressing of the primary spring.

FINITE ELEMENT MODEL

The MSC/NASTRAN [1] finite element computer code was used to analyze the missile response. MSC/NASTRAN employs the finite element method to assemble a mathematical model based on user supplied parameters describing the structure and loading. This model is solved using a numerical integration technique that steps through time. The code requires the user to define physical hardware locations (grid points) and connections (elements) that will result in a mathematical model representing the system under analysis. The associated geometry, element selection, and loading are discussed in the following paragraphs.

The grid points are located using the geometry shown in Figure 2. Grid point one is located on the end of the preload bolt above the secondary spring. Grid point five is at the end of the secondary

FIGURE 4 PRIMARY IN COMPRESSION BUT EXTENDING, SECONDARY GAPPED
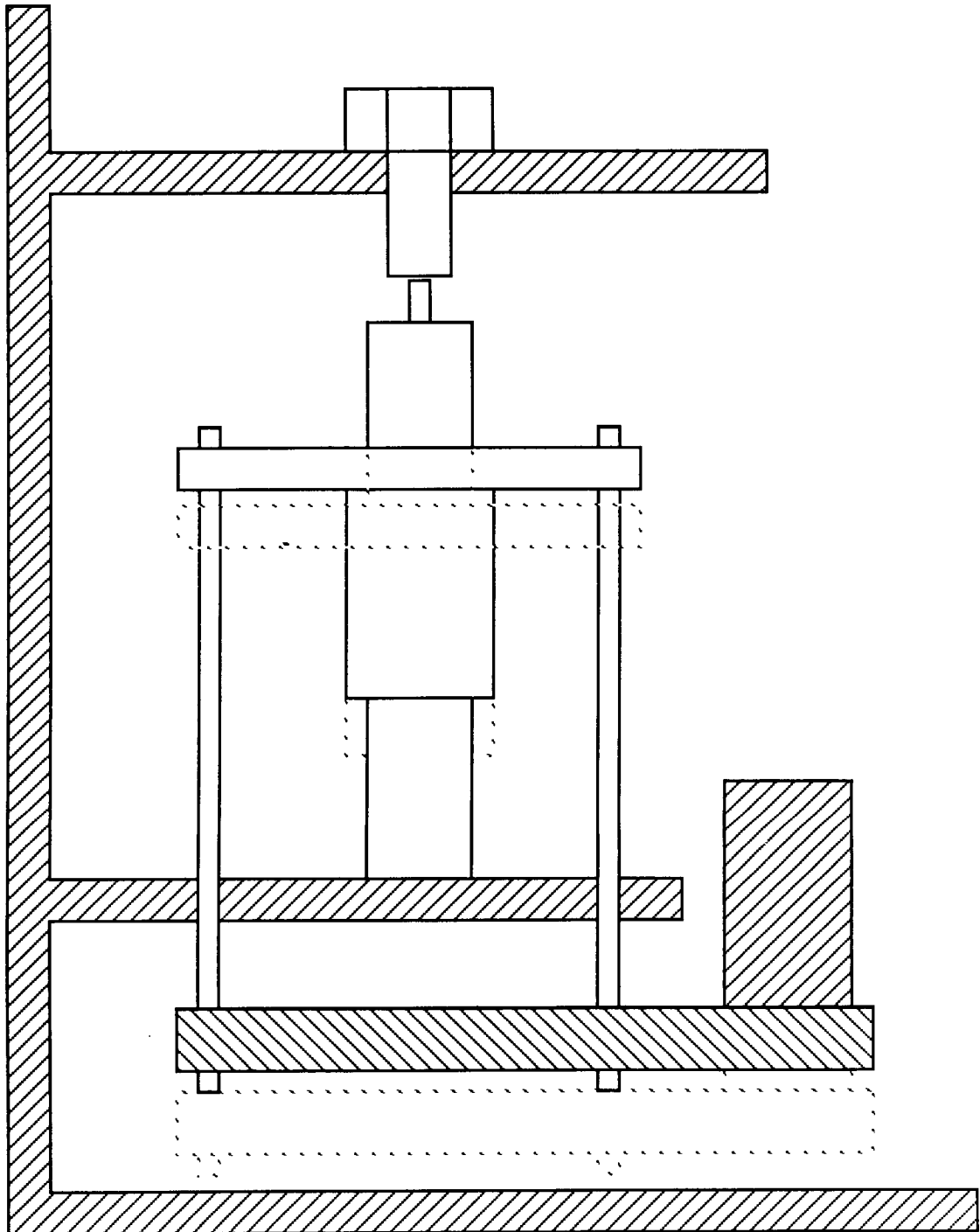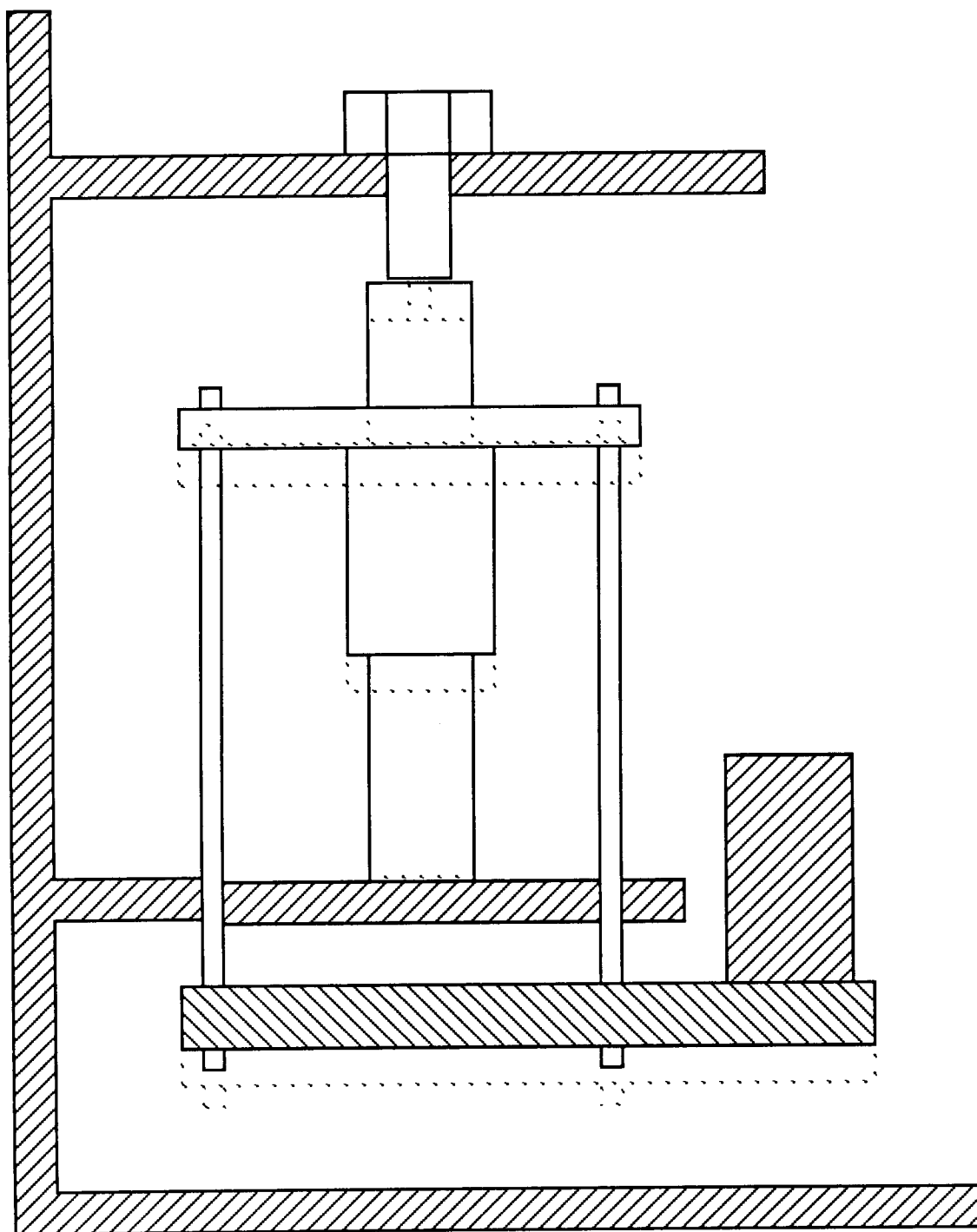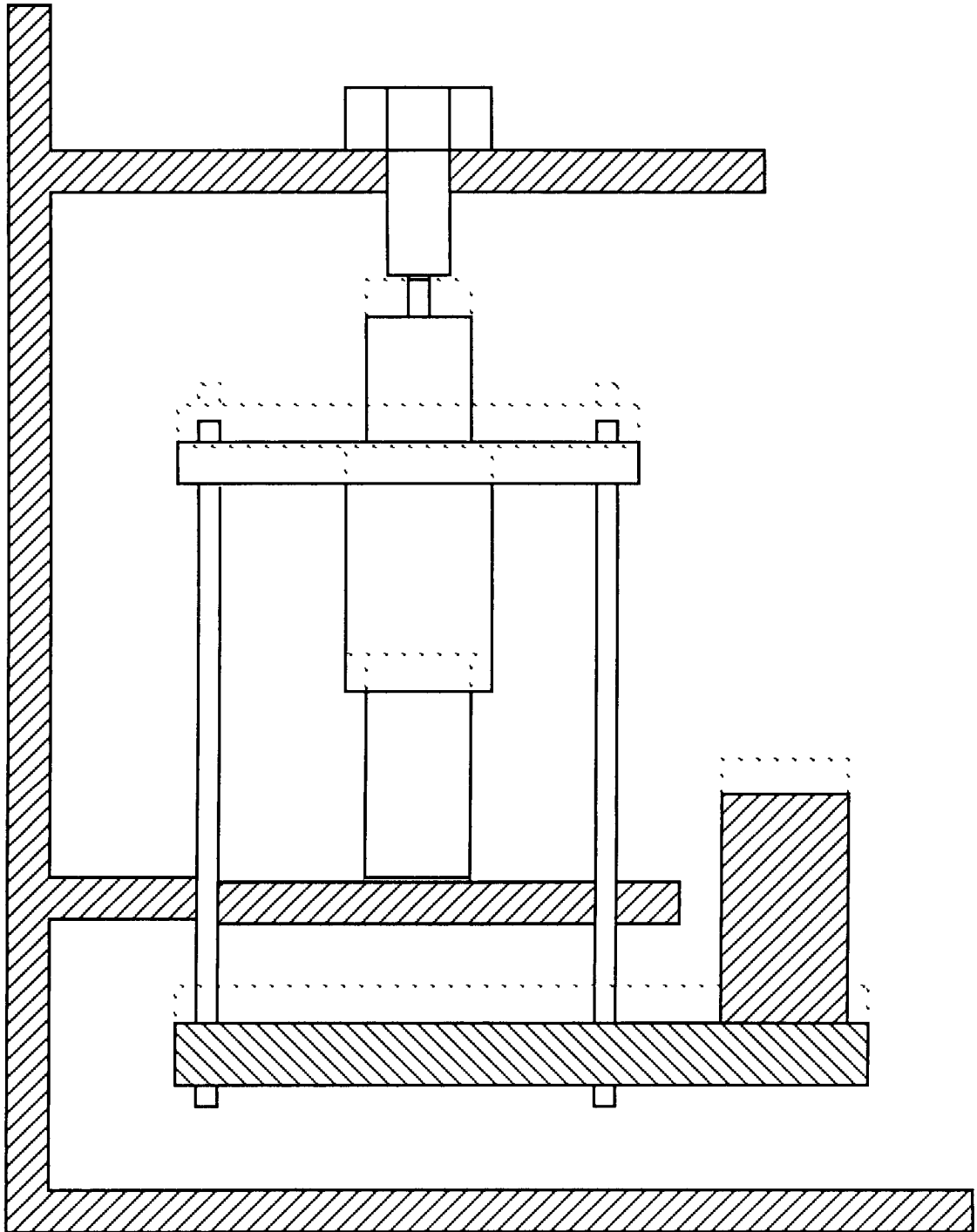
spring piston. Its geometric location is identical to grid point one. Grid point two is located on the plate that bolts the two springs together. Grid point three is located at the intersection of the primary spring and the MK-14 Canister. The base plate adapter is represented by grid point four.

The grid and element numbering system is shown schematically in Figure 7. The X axis is positive downward, and the origin is located at grid point one. The orientation of the Y-Z axes is immaterial for this model.

The gap element is used to simulate the ability of the secondary spring (at grid point 5) to separate from the MK-14 Canister (at grid point 1). When the gap is closed (which occurs at steady state and conditions 3 and 4), the element acts like a rigid bar and causes the secondary spring to work. During conditions 1 and 2, the gap is open, and the secondary spring is isolated. The gap condition during operation is illustrated in Figures 3 through 6.

The rod element is used to model the linear part of the static spring force. The non-linear part is handled as a non-linear load (see further discussion below). The static spring force is used as a reset mechanism to return the assembly to its original position. As such, it will absorb force when it is being compressed and release the force when it is extending from the compressed position. The stiffness is set equal to the linear part of the spring force for both the primary and secondary springs.

For simplicity, a viscous damper element is used to characterize the coulomb damping resulting from the MK-14 Canister pads contacting the AUR. The correct value was determined using an iterative process of running the model and comparing the results to the experimental data.

The non-linear load applied to the model consists of the non-linear static spring force and the velocity dependent spring damping. The non-linear static spring force consists of a preload and a term that is a function of the spring displacement squared. The damping is a function of the velocity to .7 power.

The preload for both springs is ignored. This could be done since the model was constructed at the steady state assembled condition.

The squared term for the primary spring is input according to the liquid spring drawing specifications. The squared term for the secondary spring is ignored. This is done since the anticipated secondary spring displacement is about one inch and after squaring and scaling the resulting force is negligible.

The primary spring damping acts in compression and extension and removes force from the system in either case. The force was generated as a function of the relative velocity of the end points of the spring in accordance with the liquid spring drawing specifications. It was

FIGURE 7   LIQUID SPRING ASSEMBLY FINITE ELEMENT MODEL
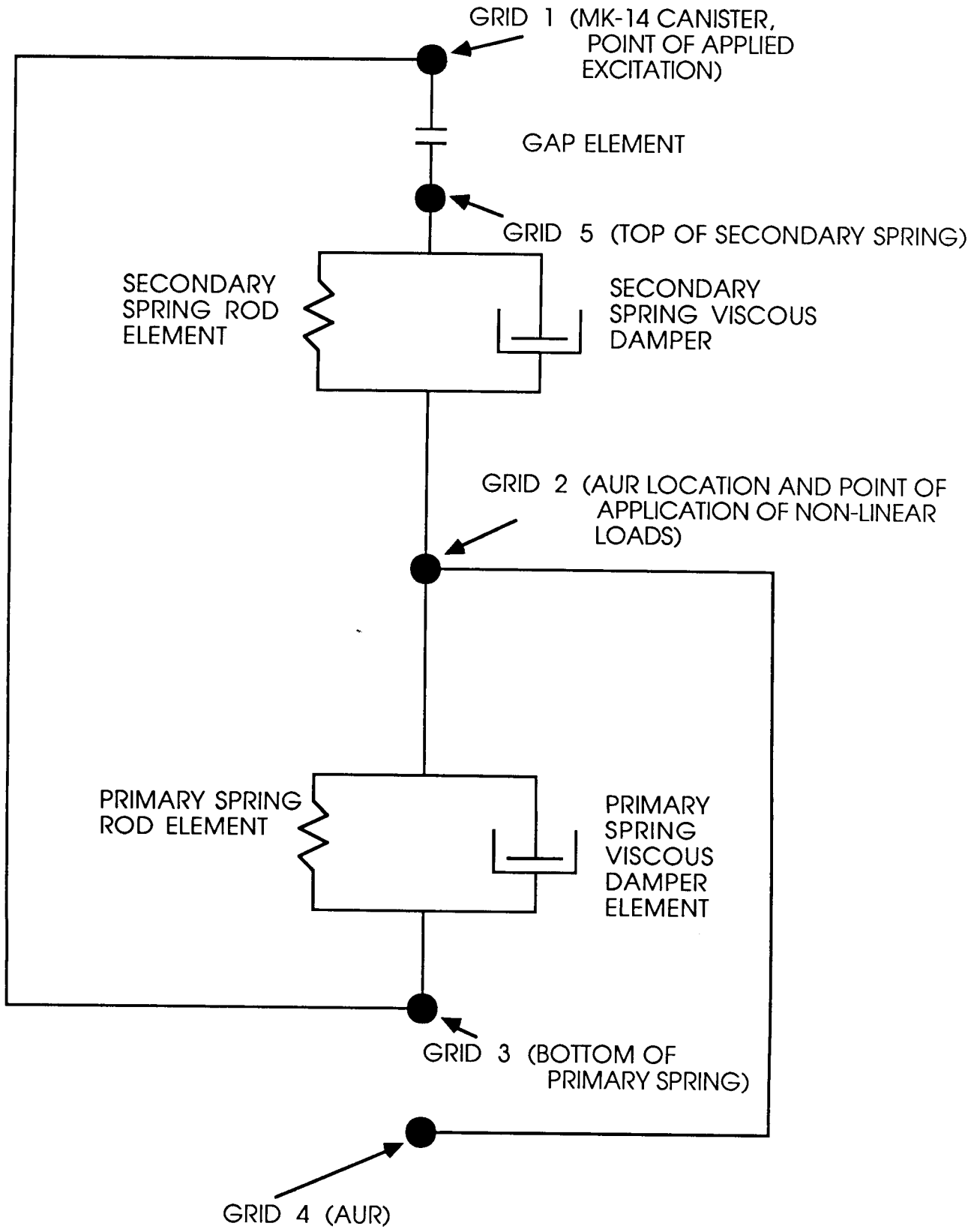
anticipated that a spring failure would result in the loss of extension damping and so the model was constructed to be able to zero this term. The damping of the secondary spring was ignored. This was done since the damping force range specified in the liquid spring drawing is negligible.

The excitation consisted of the MK-14 Canister acceleration. The response in the X or vertical direction was used since it was the primary load direction.

RESPONSE TO NOSC MIL-S-901 MEDIUM-WEIGHT MACHINE SHOCK TESTS

Tests 75 through 86 corresponding to the second canister Launch Test Inert Vehicle (LTIV) series [2] were chosen to validate the finite element model. Selected displacement results are shown in Figures 8 and 9. Model parameters indicate a degradation of the primary compression damping occurring over tests 75 and 76 (see Table 1) with zero effective primary extension damping. This is an indication that the springs were malfunctioning. The post test inspection revealed that three of the four springs had sustained a tension failure at the attachment of the piston rod to the damper plate.

The presence of the compression damping can be explained when one considers how the springs operate as detailed in the preceding section. At the initial pulse the primary spring is compressed, hence the compression damping. As the spring starts to expand, the damper plate (which has broken off from the piston rod, see Figure 2) will be suspended in the fluid as the piston moves away resulting in zero extensional damping. At the conclusion of the test the damper plate will settle onto the piston rod as gravity and time take effect. This provides compression damping at the start of the next test.

Table 1 Optimized Model Parameters for each Test

test no	extension damping (-)	compression damping (-)	initial gap (in)	primary viscous damping (lb/in-sec)	secondary viscous damping (lb/in-sec)
75	5	-2200	0.02	200	50
76	5	-1800	-0.02	100	80
77	5	-1800	-1.1	100	400
78	5	-1800	-0.9	200	200
79	5	-1800	-0.3	200	200
80	5	-1800	-1.6	400	400
81	5	-1800	-1.0	150	50
82	5	-1700	-2.2	20	10
83	5	-1700	-0.5	200	400
84	5	-1700	-1.0	10	50
85	5	-1700	-1.0	10	50
86	5	-1700	-0.5	150	10

Figure 8 NOSC Test 77 Displacement
Theoretical Prediction vs Test Data

Time (seconds)
—— EXP. + MSC/NASTRAN
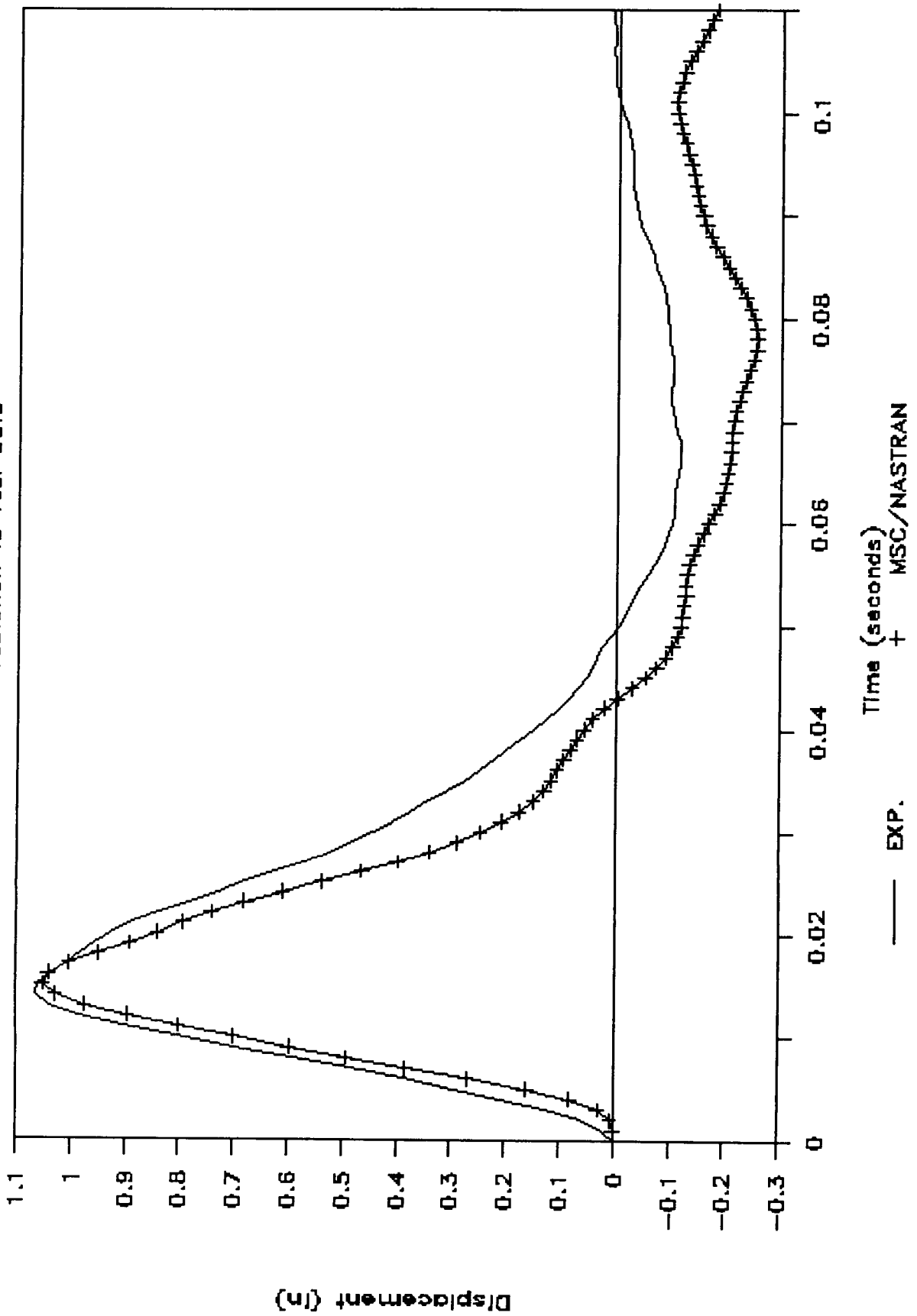
Displacement (in)

Figure 9   NOSC Test 81 Displacement

Theoretical Prediction vs Test Data
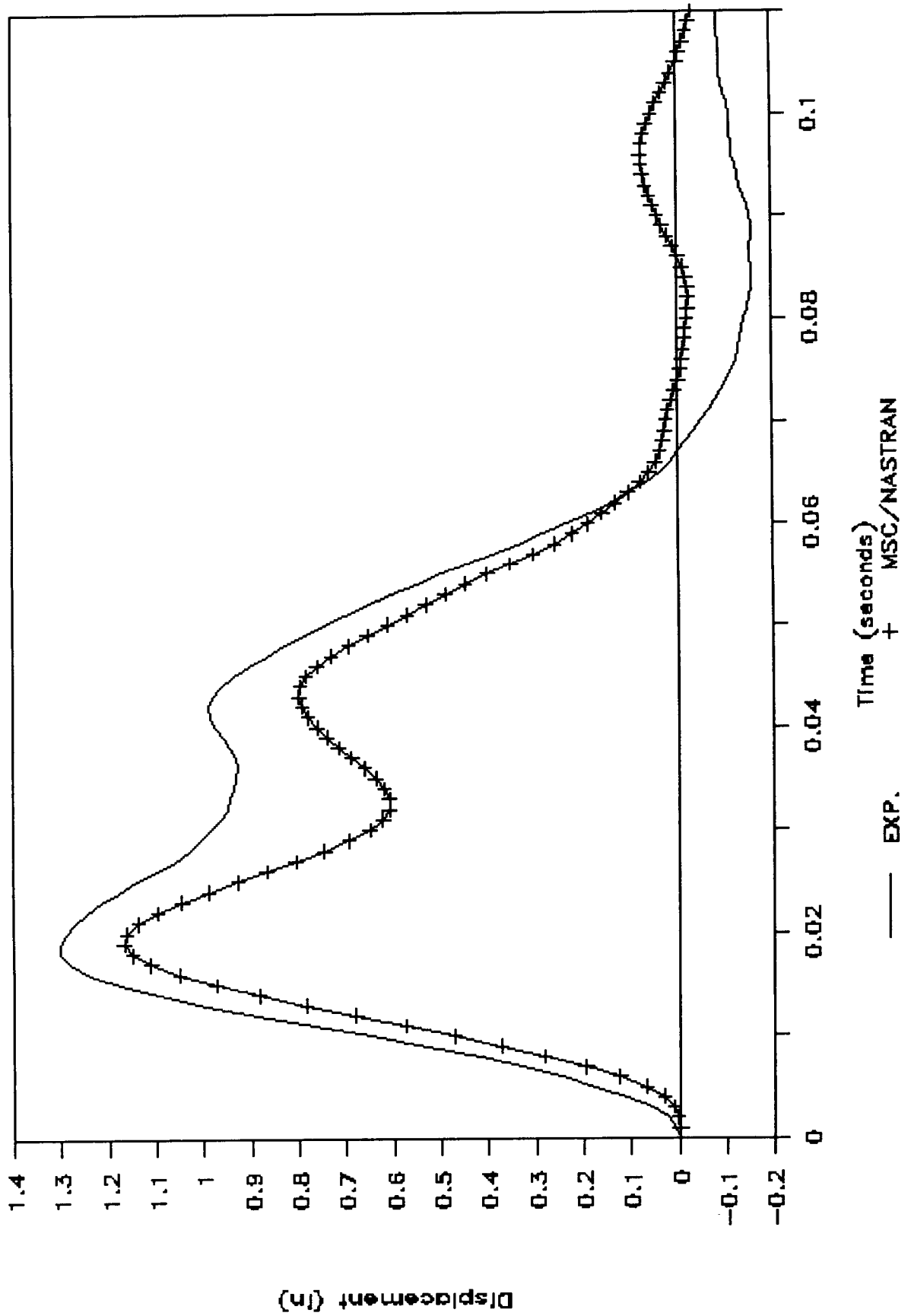
Test 77 (Figure 8) provides an ideal response in that it is relatively easy to divide the MSC/NASTRAN generated curve into the four conditions described previously. Condition one occurs between time zero and fifteen msec and peaks at 1.05 inches. This is a primary spring displacement (the secondary having gapped and so isolated itself at this time) and results in a stored force of 6000 lbs for four springs. The velocity at this time is 0.518 fps which translates into 6500 lbs of force reduced by the springs. Additional force is removed by the friction pads.

Condition 2 occurs between 15 and 42 msec. At 42 msec the 6000 lb spring force has been returned to the MK-14 Canister and the secondary spring gap has closed. No additional force has been removed from the system by the springs. All damping is due to the friction pads.

Condition 3 occurs between 42 and 78 msec. The 0.25 in. peak displacement at this time is an extension of the primary spring and an equal compression of the secondary spring. The deviation from the experimental data during this and the next condition is due to the modeling of the friction pads (coulomb damping) as a viscous damper element. At low velocities, the viscous damper removes less energy while the friction pads ,in reality, are removing more energy due to higher forces.

Condition 4 starts at 78 msec and continues until the displacement returns to zero. This analysis was stopped at 120 msec when most of the energy from the shock had been dissipated. This condition corresponds to a resetting of the spring in preparation for the next test. The system does not return to the pretest condition. This can be seen from Table 1 which shows an initial gap corresponding to the system condition at the end of the previous test. This gap is caused by the friction pads.

RESPONSE TO CG-53 SHOCK TRIAL

After NOSC test validation the model was used to predict TOMAHAWK response to the CG-53 shock trial loading. Predictions and validation were done for TOMAHAWK test missiles designated IOM-A (Inert Operational Missile), IOM-B, IOM-C, LTIV-1, AND LTIV-3. After the first shot, the procedure was to validate the model using the previous shot data (MK-14 Canister and AUR baseplate accelerations and relative displacement across the liquid springs), scale up this data by a ratio obtained from analysis of the YORKTOWN shock test series to make a prediction for the next shot and, at the conclusion of the next shot, compare predictions with actual data. The YORKTOWN test series was analyzed due to the ship's similar specifications and identical shock geometry to the MOBILE BAY's. The procedure was performed for shots 2 through 4.

Figures 10 through 13 compare the model predictions and subsequent validations with test data. These results are representative of the results for all TOMAHAWK test vehicles. The

FIGURE 10 CG53 SH#4 IOM B
RELATIVE DISPLACEMENT
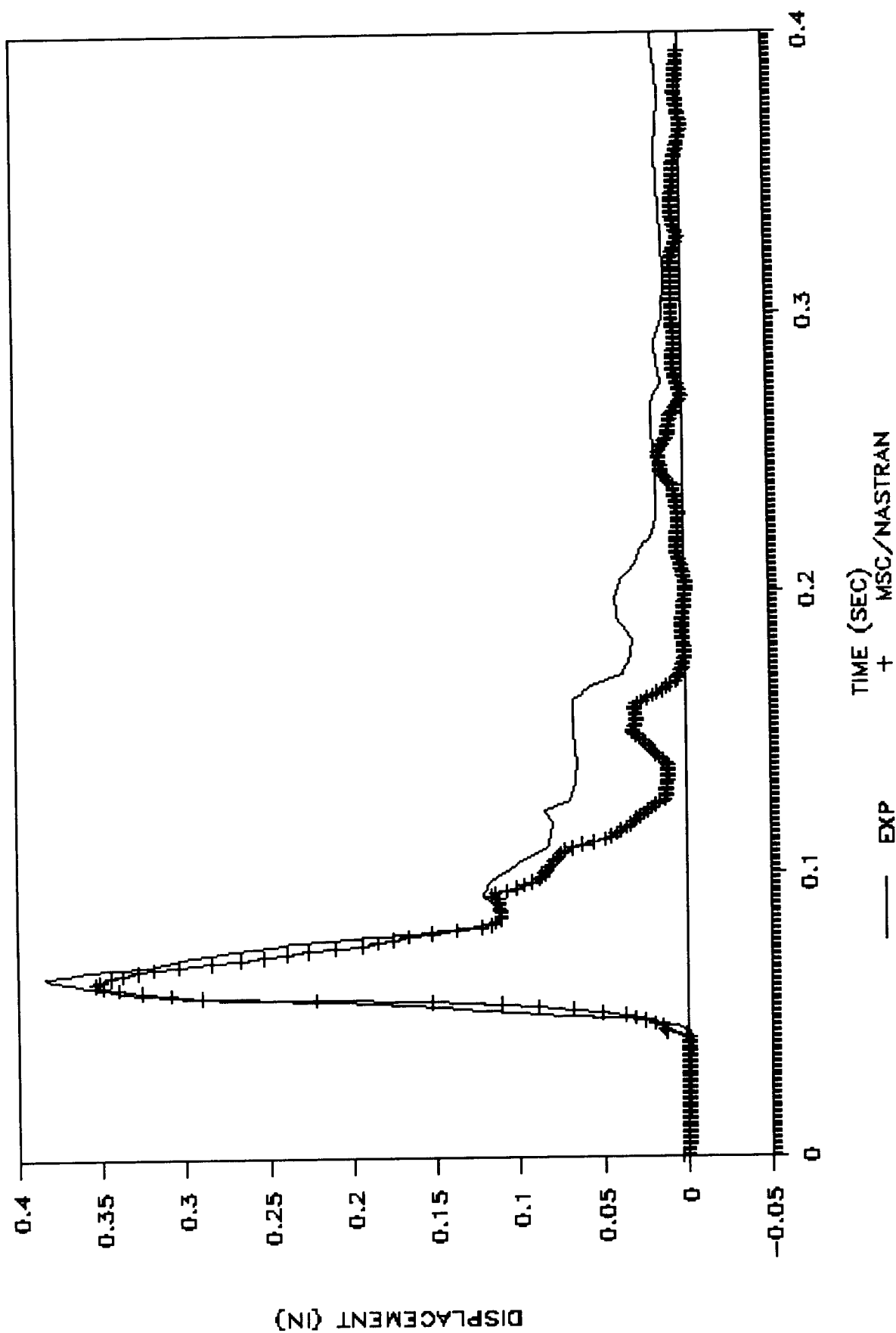
FIGURE 11 CG-53 SH#4 IOM-B
FAST FOURIER TRANSFORM

MAG (G)

FREQUENCY (HZ)

EXP. ———
MSC/NASTRAN +
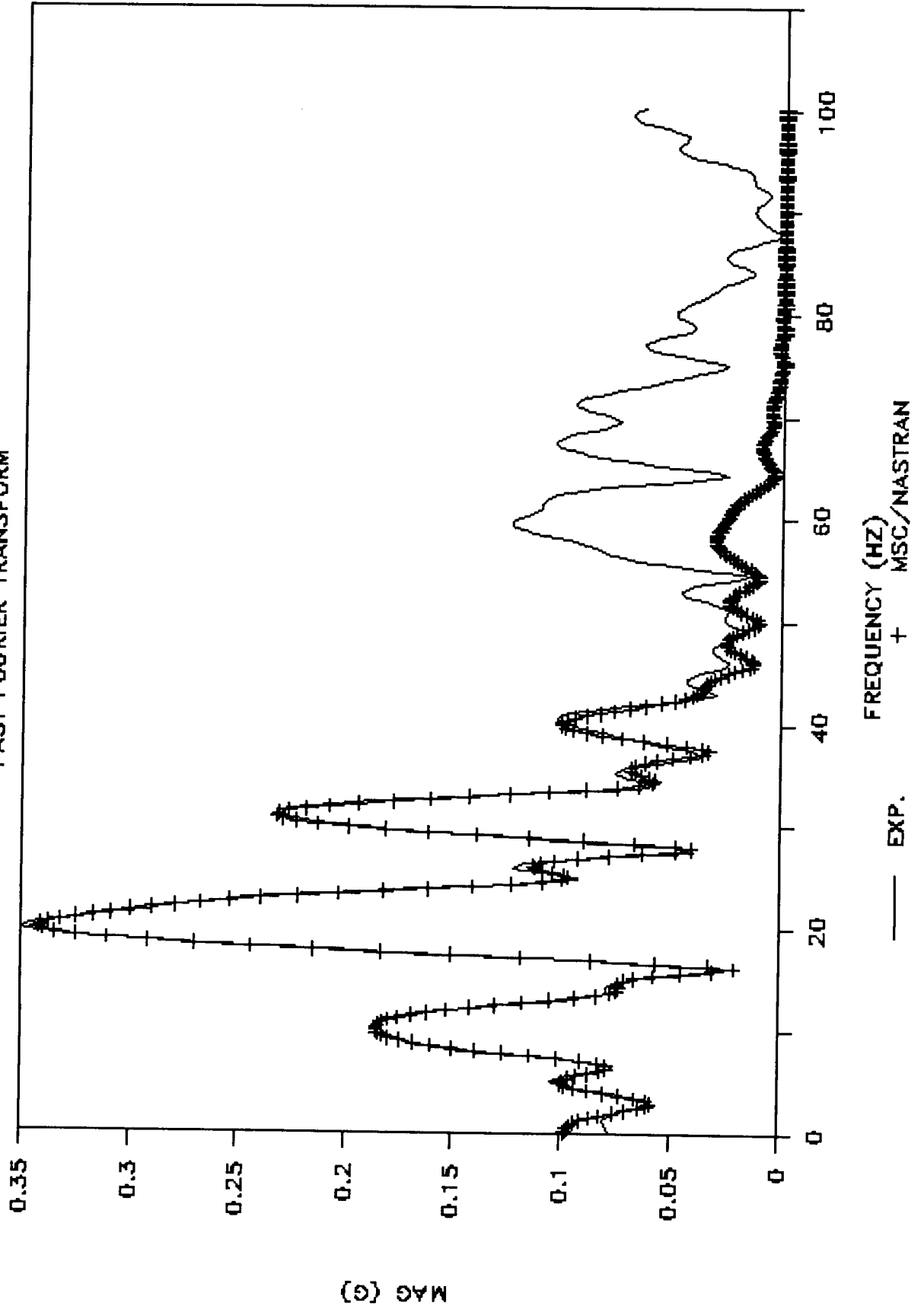
FIGURE 12   CG53 SH#5 IOM B   Shock Spectrum (Zeta=.02)
Theoretical Prediction vs Test Data
Displacement (inches)

114
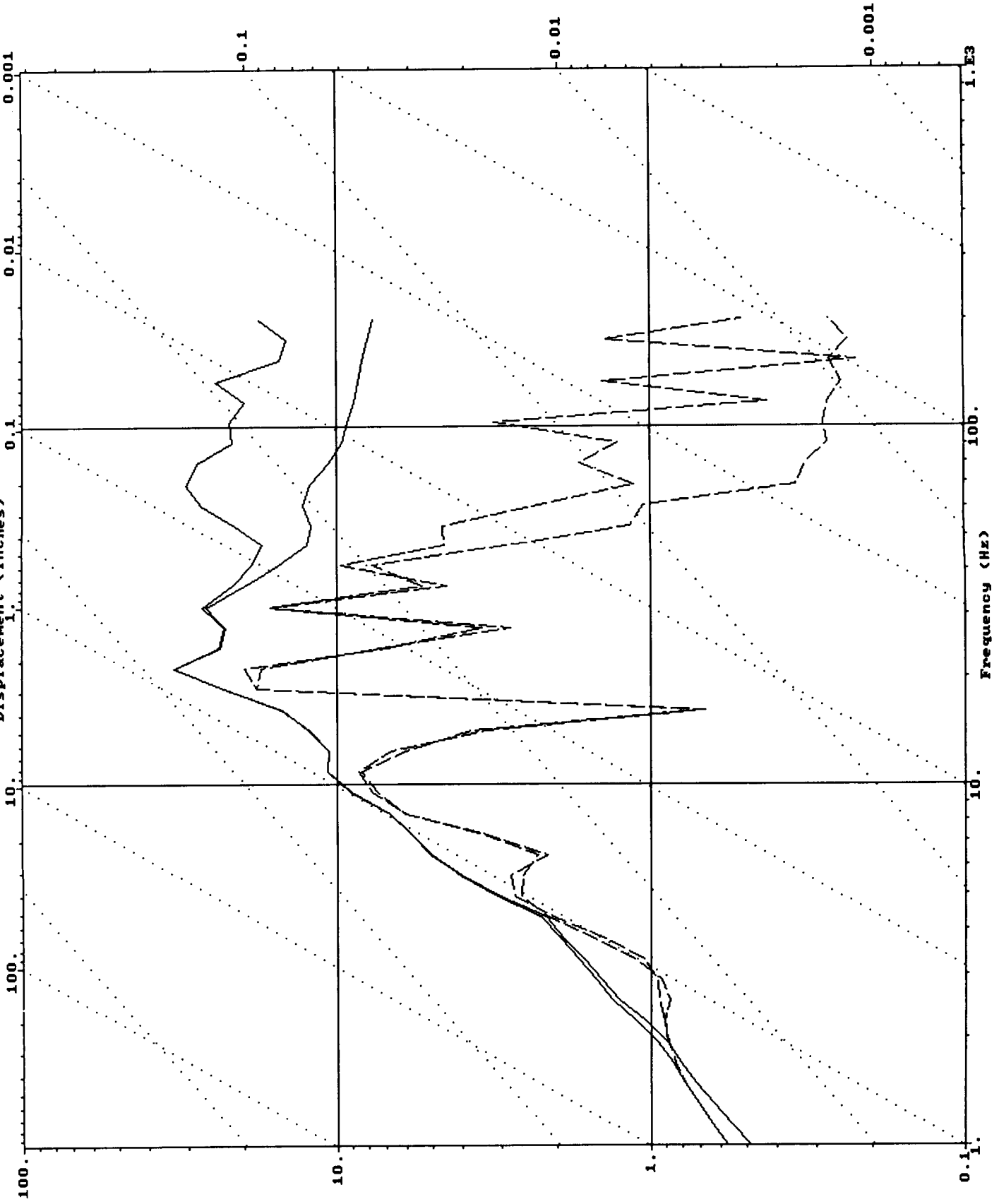
FIGURE 13 CG53 SH#2 LTIV 3

AUR GROSS ACCELERATION 50 HZ FILTER

TIME (SEC)

— EXP   + MSC/NASTRAN

ACCELERATION (g.s)
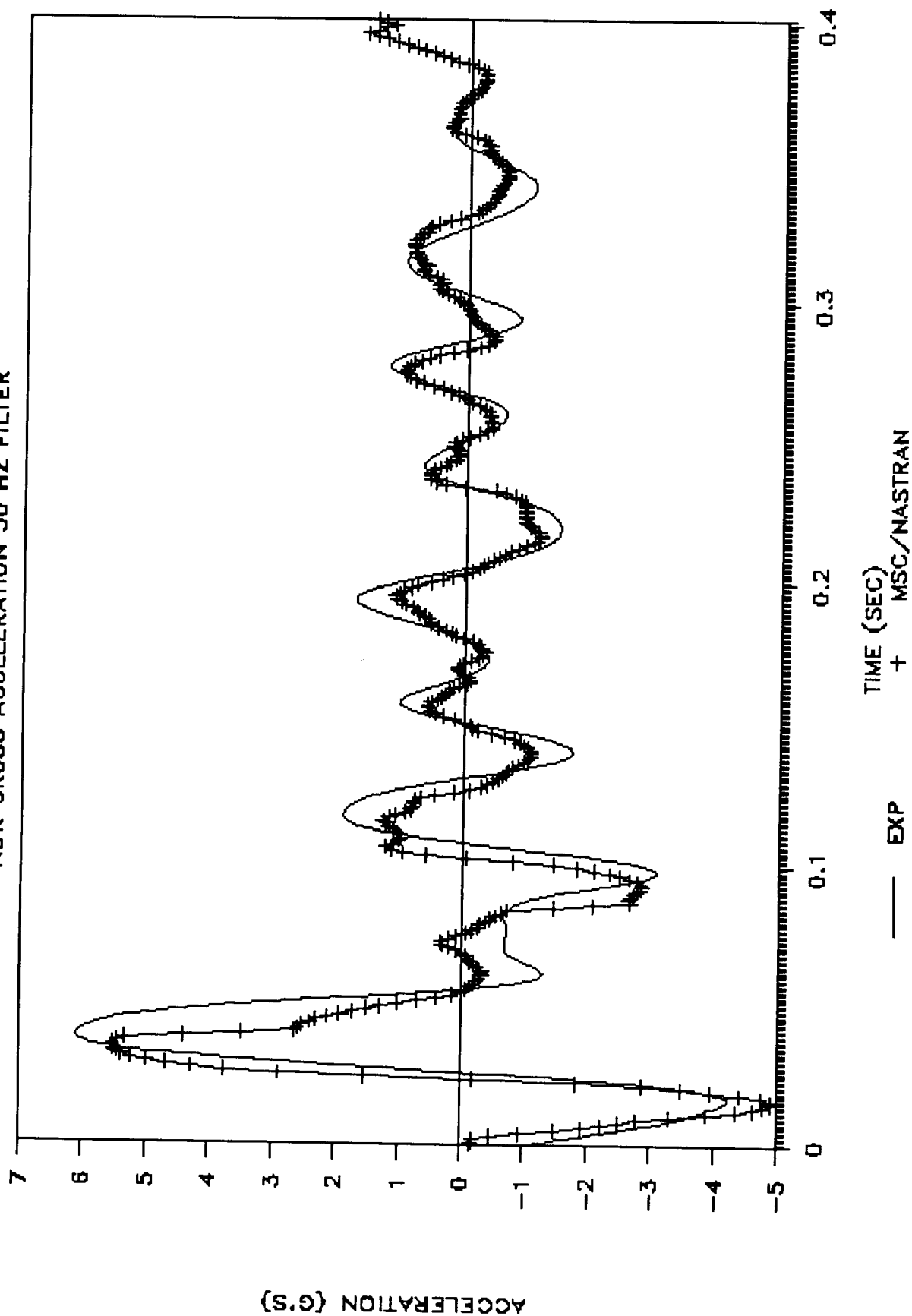
model parameters indicated that the springs provided adequate shock isolation with only a slight degradation of primary spring extensional damping.

Figure 10 is a plot of model verification for shot 4 IOM-B relative displacement. Note that conditions 3 and 4 are not as pronounced as in the NOSC tests. This is due to the availability of extensional damping (since the spring is not broken) on the primary spring. Conditions 3 and 4 can be considered as occurring after 100 msec when the system is settling down after its response to the shock.

Figure 11 is a plot of the fast fourier transform of the gross acceleration (experimental and model prediction) for shot 2 LTIV-3 model verification. Figure 12 is a plot of the shock spectrum of the gross acceleration (experimental and model prediction) for shot 4 IOM-B model verification. These figures demonstrate that the majority of energy is concentrated below 50 Hz and the model response is valid to 50 Hz. Therefore, the experimental data is low-pass-filtered at 50 Hz. and compared to the model response (Figure 13) for verification. Based on Figures 10 thru 13 it is concluded that the finite element model accurately represents the physical system.

Figure 14 compares the prediction made for shot 4 with the actual shot results for LTIV-1 relative displacement. This model was first verified for shot 3 before being used for the shot 4 prediction. This comparison indicates that the scaling ratio obtained from analysis of the YORKTOWN test series is reasonable.

Displacement and acceleration predictions agree well with experimental results indicating that the model can successfully track the actual TOMAHAWK performance and that the response from shot to shot is a linear function of the previous shot.

CONCLUSIONS

Successful analysis of non-linear systems is a three step process. First the non-linearities must be identified and quantized. Step two is the selection of an analysis technique and/or computer code that addresses the identified non-linearities. The final step is the validation of the model using system data and the subsequent use of the model in prediction and validation of test results. This technique was illustrated using the TOMAHAWK shock isolation system and MSC/NASTRAN finite element computer code with excellent agreement between model and test results.

REFERENCES

1. MSC/NASTRAN USER'S MANUAL version 65, November 1985.
2. QUICK LOOK REPORT, VLS CANISTER/MISSILE CONFIDENCE SHOCK TEST, TEST 75-86, NOSC, August 1986.

FIGURE 14 CG53 SH#4 LTIV 1 REL. DISPL.
EXPERIMENTAL DATA VERSUS PREDICTION

DISPLACEMENT (IN)

TIME (SEC)

— EXP   + MSC/NASTRAN

117
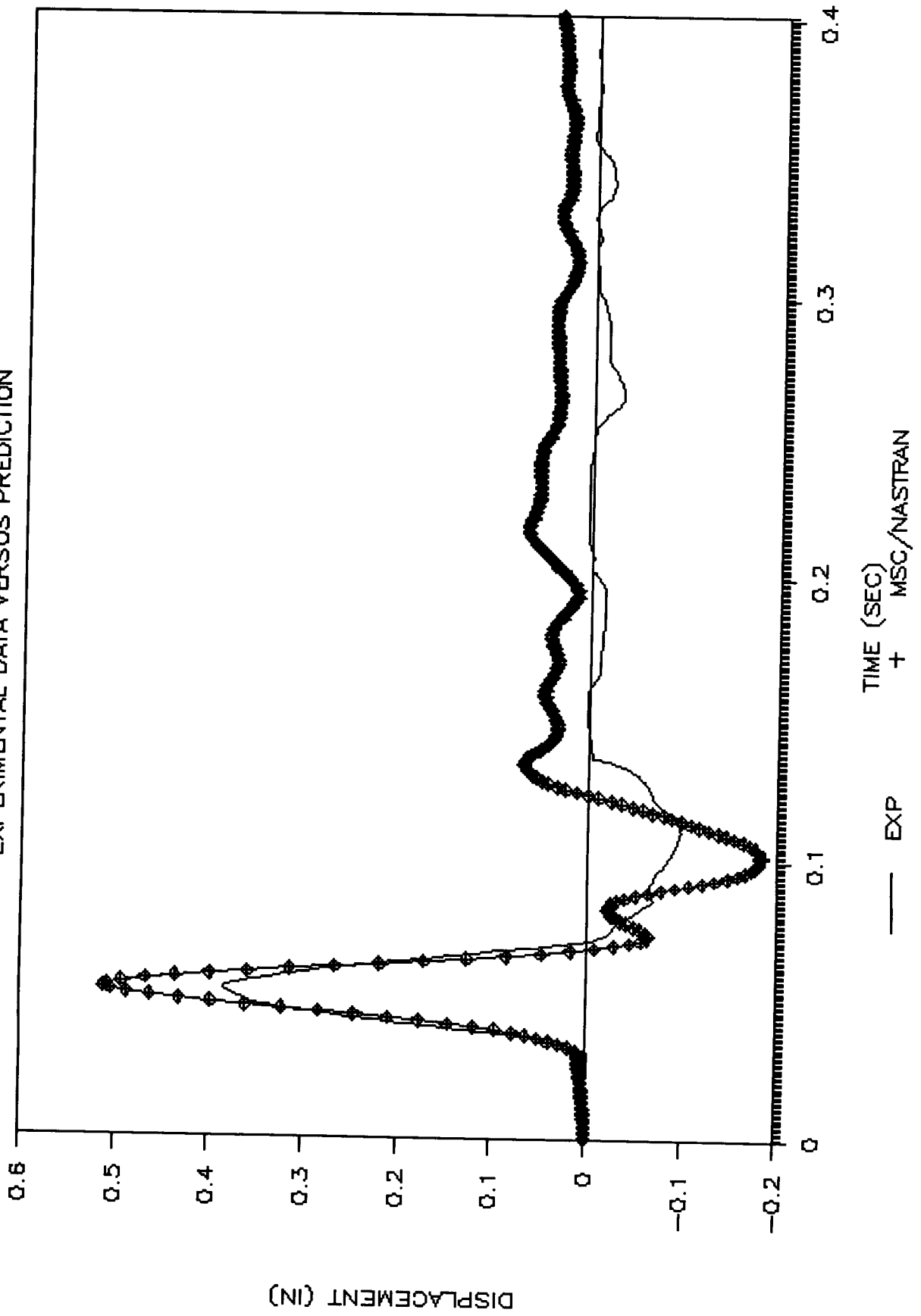
On the Simulation of Ballistic Shock Loads

Uwe Hollburg

Blast or penetrator-impact induced shocks are pre-
sented by high acceleration levels particularly in
the higher frequency range and for a short time
duration. These shocks are dangerous for the equip-
ment of combat vehicles, airplanes, ships or space-
structures. As ballistic shock loads are insufficient
simulated by laboratory test machines a ballistic
shock simulator has been designed.
The impact induced shocks are simulated by an explo-
sive and the vehicle to be bombarded is replaced by
a simplified structure. This structure is suitable
to accomodate any equipment which can be tested up
to their loads limits.

INTRODUCTION

Ballistic shock loads are mostly produced by non-penetrating
projectiles. Near the impact point the shock is presented by an
one-side directed impulse excitation of very short time duration,
shown in figure 1. In general the velocity jump of such a shock is
small. At a distance from the impact point the shock response has an
oscillatory character, figure 2. Usually the hard fixed optical
sightings of armored vehicles are exposed to these very high dynamic
strains which can produce shock related equipment failures as
disadjustments of the line of sight, damages of prisms and even me-
chanical destruction of components. The dynamic reliability of fire
control systems are described in the technical regulations,
MIL-STD-810D, ISO/DIS 8568, DEF STAN 07-55, TL 1240, for instance.
Usually the test shocks are produced by impact shock machines, multi-
shaker systems, electrodynamic exciters and acoustic excitations.
The ballistic shock loads generated by an impact projectile or an
explosive exceed considerably the acceleration amplitudes which are
produced by laboratory simulation test machines. A comparison between
the shock spectra determined from half-sine pulses, produced by an im-
pact machine, with the acceleration time data, caused by an non-pen-
trating projectile, shows that a considerably higher dynamic strain is
generated by the shot, figure 3.
Using half-sine pulses for shock testing, the low frequency range of
the equipment is overstressed while the higher frequency range is un-
derloaded. From realistic bombardments against armored vehicles it is
known that the shocks can lead to defects in such equipment which had
previously been tested by conventional test facilities.

REQUIREMENTS TO A SUITABLE SHOCK SIMULATION TECHNIQUE

In order to qualify any equipment of combat vehicles a realistic method, for the simulation of ballistic shock loads is needed. For that purpose high standards are demanded of a suitable simulation technique. The shock loads to be simulated should :

- provide high acceleration levels in a wide frequency range

- have a short time duration

- be reproducible

- be easily tunable to a given spectrum

- be nearly non-destructive

- be economical.

In addition to a realistic shock excitation, the environment of the equipment must be considered. There is an interaction between the equipment and the dynamic behavior of the carrier structure.
An important point is the check of the individual built-in unit after the shock test is finished. Usually function tests are carried out and the disadjustments of the line of sight are detected if the object was an optical device.
Therefore in addition to the requirements for a realistic shock excitation the used carrier structure should :

- have enough space to accomodate the built-in units and their electronic components. The performance of operational tests must be possible

- have an easily changeable dynamic behavior

- be resistant to blast-induced shocks.

Concerning these requirements the straightforward way for shock testing built-in units would be: the bombardment of a fully equipped tank, for example, with different types of ammunition.
Bombarding tests performed on realistic vehicles for the purpose of analysing the vulnerability of actually equipments include, in addition to the economic reasons, a series of disadvantages.

Therefore suitable techniques for the simulation of ballistc shock loads have to be developed with the aim of proving the equipment of armored vehicles, ships or spacecraft structures and give design proposals for the improvement of their shock resistance.
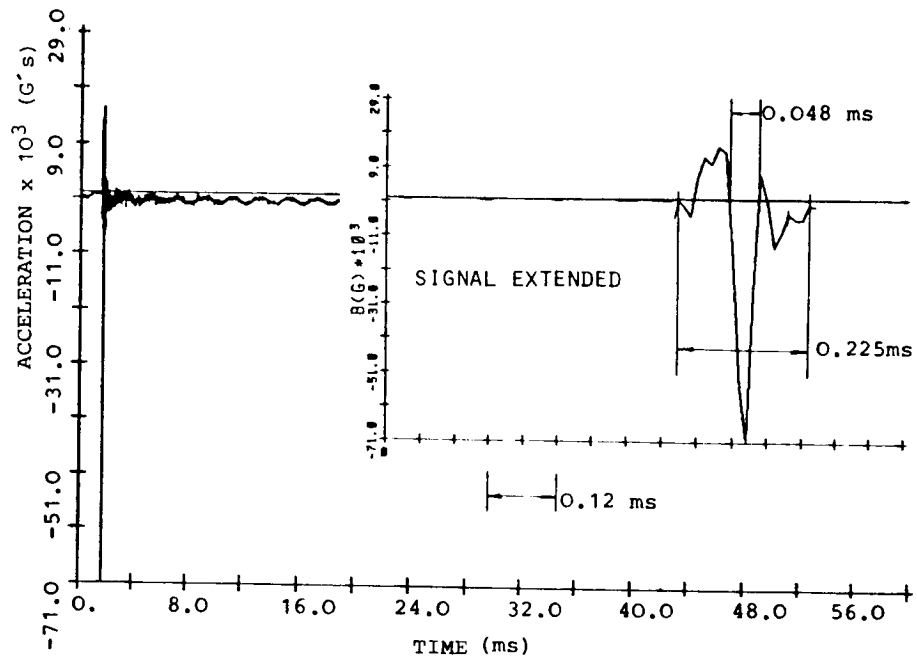
Fig. 1- Shock excitation near the impact point

Fig. 2- Shock response

Fig. 3- Comparision of penetrator-impact induced shocks
with half-sine pulses produced by impact shock
machines

SIMULATION OF BALLISTIC SHOCK LOADS

The shock tests described in the technical regulations are mainly based on one directed shocks like half-sine pulses, rectangular pulses, initial- or terminal-peak sawtooth pulses.
They are good reproducible and suitable to simulate rough handling and travelling loads.
Shock loads produced by non-penetrating hits are not simulatable by conventional laboratory tests.

In order to simulate ballistic shock loads related to the requirements a simple structure based on plates was selected. As the shock propagation depends on mass and stiffnes a carrier structure should have similar dynamic properties like the real vehicle. For that purpose a finite element model, based on the STARDYNE-computer code, of a simplified plate structure, as shown in figures 4 and 6, was created to calculate frequencies and modes up to 2 kHz.
In order to change the dynamic parameters several configurations were considered :

* equal wall-thickness, free installed

* equal wall-thickness, with baffle, free installed

* different wall-thickness, free installed

* different wall-thickness, one side fixed

* equal wall-thickness, with baffle, one side and bottom fixed

* different wall-thickness, with two baffles, one side and bottom fixed

* different wall-thicknes with three baffles one side and bottom fixed

* different wall-thicknes with three baffles one side and bottom fixed and partly closed cover.

To evaluate the particular design alternatives for each variant the modal density was calculated up to 2 kHz.
In figure 5 the modal densities for each variant are represented versus the first eigenfrequency, figure 5.

Starting from the parameters

M_{jk} : Mass matrix of the structure

K_{jk} : Stiffness matrix of the structure

C_{jk} : Damping matrix

123

x_k : Displacement vector

q_k : Generalized parameters

F_j : Force vector

ψ_{jk} : Eigenvectors, summarized in a modal matrix

ω_j : Undamped natural frequencies

m_j : Generalized masses

α_j : Estimated modal damping values

Ω : Frequency of excitation

a complex transfer function model of the simplified structure was calculated.

Equation of motion:

$$M_{jk} \cdot \ddot{x}_k + C_{jk} \cdot \dot{x}_k + K_{jk} \cdot x_k = F_j(t) \cdot e^{i\Omega t} \tag{1}$$

modal transformation:

$$x_k = \psi_{kl} \cdot q_l \tag{2}$$

transformed equation of motion:

$$m_j \cdot \ddot{q}_j + m_j \cdot \alpha_j \cdot \omega_j \cdot \dot{q}_j + m_j \cdot \omega_j^2 q_j = \psi_{kj} \cdot F_k(t) \cdot e^{i\Omega t} \tag{3}$$

using:

$$q_j = \hat{q}_j e^{i\Omega t} \tag{4}$$

$$\eta_j = \Omega / \omega_j$$

response acceleration:

$$\ddot{x}_1 = \frac{-\eta_j^2}{m_j(1 - \eta_j^2 + i \cdot \alpha_j \cdot \eta_j)} \psi_{1j} \cdot \psi_{kj} \cdot F_k(t) e^{i\Omega t} \tag{5}$$

transfer function:

$$H_{lk}(\Omega) = \frac{\eta_j^2}{m_j(1-\eta_j^2 + i\cdot\alpha_j\cdot\eta_j)}\ \psi_{lj}\cdot\psi_{kj} \qquad (6)$$

Then the response acceleration $\ddot{x}_1$ to a fourier transformed impact force $f(\Omega)_k$ is given by:

$$\ddot{x}_1 = H_{lk}(\Omega)\cdot f_k(\Omega)\ . \qquad (7)$$

The next step is the estimation of a loading function which represents the impact of a projectile. To get realistic loading functions the penetration process must be calculated in detail.
For a simple estimation of the force time history it is sufficient to consider the ballistic parameter of the projectile, mass, final velocity and angle of impact.
Due to experience in the field of bombardment of armored vehicles it is possible to make assumptions concerning the time duration and the deceleration of the penetrator.
In addition to that the shape of the loading function is of interest. For a rough estimation it is sufficient to use triangular or saw-tooth shapes. In general the compression phase is characterized by a steep gradient.

Example:

Mass of the projectile: $m = 0,85$ kg

Final velocity   : $v = 800$ m/s

Deceleration law   : $a(t) = -\hat{a}(1 - t/T)$

Depth of penetration : $s = 160$ mm

Acceleration   : $\hat{a} = 0,67\cdot v^2/s = 2,67\cdot 10^6$ m/s²

Time duration   : $T = 3\cdot s/v = 0,6$ ms

Force amplitude   : $F = m\cdot\hat{a} = 2,27\cdot 10^6$ N.

In addition it is assumed that the impact force is represented by a saw-tooth shape, figure 7.

From equation (7) the response spectrum of the analytical model was calculated. These responses were compared with actual shock data from bombarding tests.
The result of such preliminary investigations is the simplified structure as shown in figure 4.
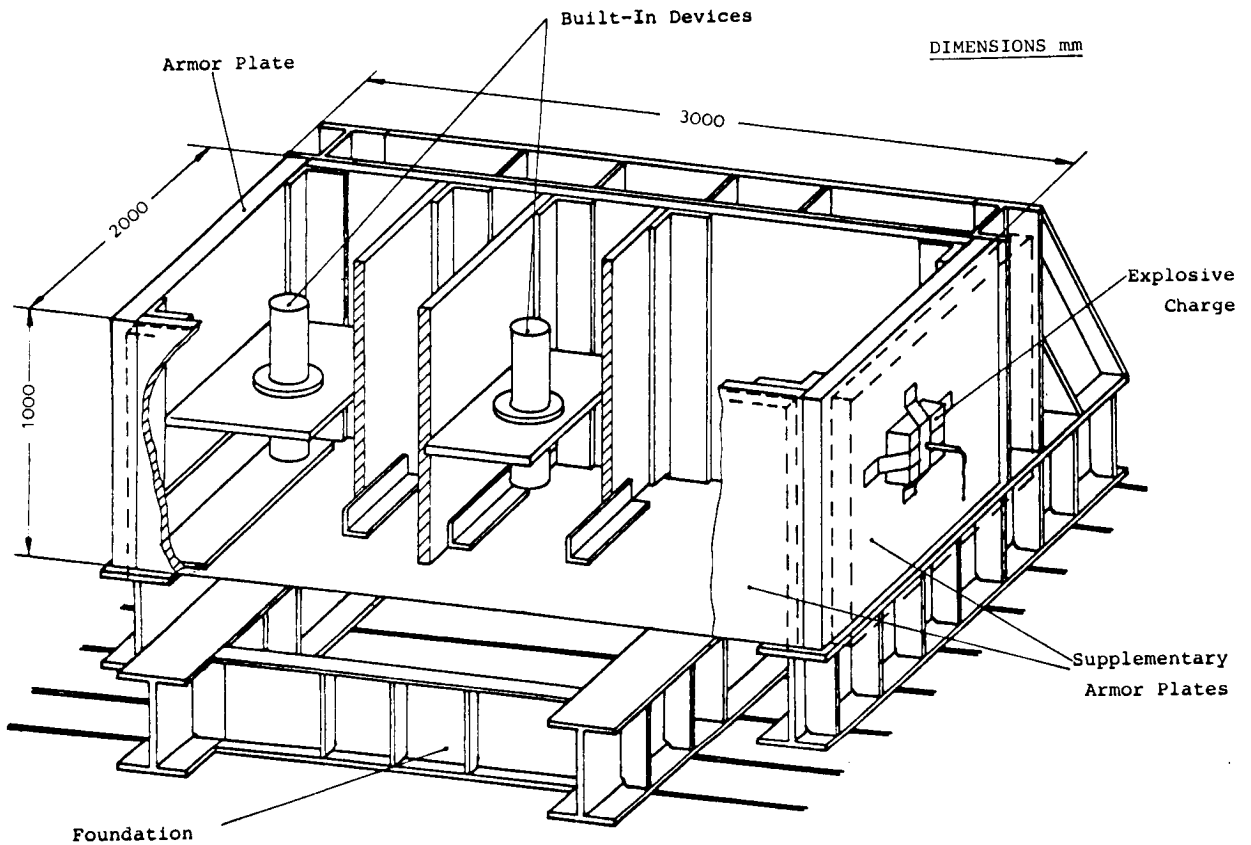
DIMENSIONS mm

Fig. 4- Ballistic shock simulator (SBS)

1 - EQUAL WALL-THICKNESS, FREE INSTALLED
2 - EQUAL WALL-THICKNESS, WITH BAFFLE, FREE INSTALLED
3 - DIFFERENT WALL-THICKNESS, FREE INSTALLED
4 - DIFFERENT WALL-THICKNESS, ONE SIDE FIXED
5 - EQUAL WALL-THICKNESS, WITH BAFFLE, ONE SIDE
    AND BOTTOM FIXED
6 - DIFFERENT WALL-THICKNESS, WITH TWO BAFFLES,
    ONE SIDE AND BOTTOM FIXED
7 - DIFFERENT WALL-THICKNESS WITH THREE BAFFLES ONE
    SIDE AND BOTTOM FIXED
8 - DIFFERENT WALL-THICKNESS WITH THREE BAFFLES AND
    PARTLY CLOSED COVER
□ - REAL TURRET STRUCTURE

Fig. 5- Design alternatives of the SBS

126
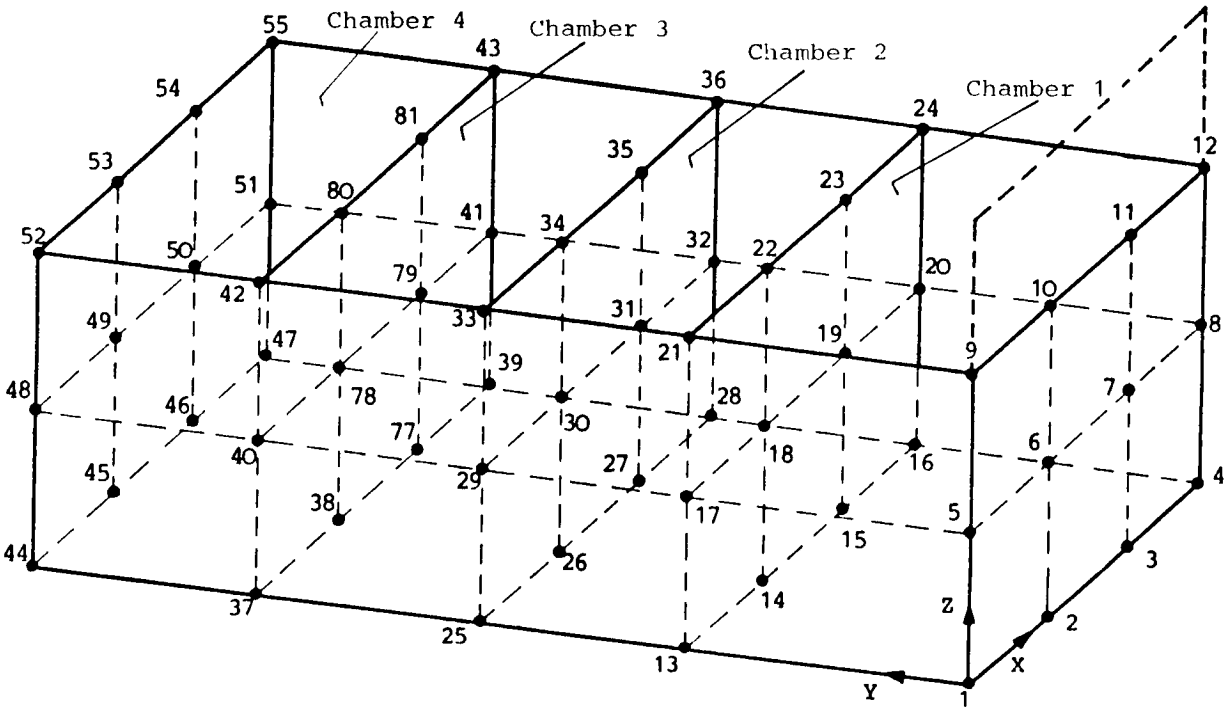
Fig. 6- Nodal points of the SBS
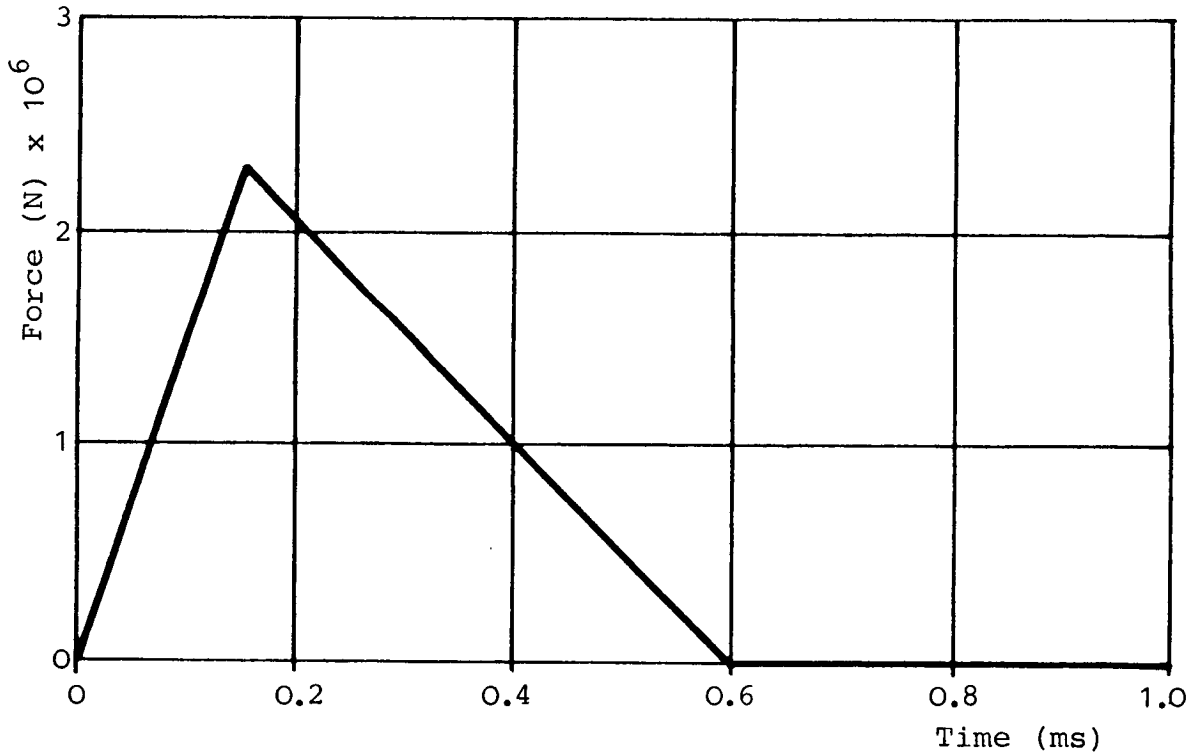
Fig. 7- Estimated force time history of an impact

127

The structure consists of armored plates of a thickness of 120 mm and has the dimensions 1000 * 2000 * 3000 mm. The plates are bolted and partly welded. The simulator is bolted to an elastic foundation.
The interior is divided into seperate chambers in which the equipment to be tested is installed. The dynamic properties of the structure are variable based on changing mass and stiffness. In addition to the analytical assessment of the modal parameter, experimental modal anlysis had been carried out using GENRAD 2515 for data acquisition and SDRC software for evaluation.
The mass of the simulator is changeable from 6500 kg to 12 000 kg the lowest eigenfrequency from 9 Hz to 186 Hz.
In order to simulate ballistic shock loads the knowledge of the stiffness of the carrier structure is important as the stiffer the equiment is mounted the higher are the shocks.

The shocks to be simulated are produced by an explosive formed to a cube and free deplaced to the structure.

The responses due to blasting the shock simulator are measured by piezoelectric and piezoresistive accelerometers which are bolted or glued to the structure and to the test object.
From the oscillatory acceleration, time histories are calculated shock spectra which are a useful tool for evaluating shock loads.

PARAMETER IDENTIFICATION

In order to simulate penetrator-impact induced shock loads the essential parameters must be known. For that purpose accelerometers had been attached at those points as shown in figure 6. Then the SBS had been blasted at different locations. These experimental investigations give information about the influence of the:

- explosive charge

- kind of explosive

- point of excitation

- dynamic properties of the SBS.

Finally these investigations are required to get knowledge about the reproducibility of the shock tests carried out with the SBS and their stability and resistance against blasting.

The results ot these preparatory investigations are:

* The influence of the amount of the explosive to the induced shocks
----

The shock level in the entire frequency range depends on the explosive charge. An increase of the quantity of the explosive results in a rising gradient of the shock spectrum, figure 8.
The relationship between the quantity and the induced shocks is non-linear and can approximately be described by a cubic function in a particular frequency range.
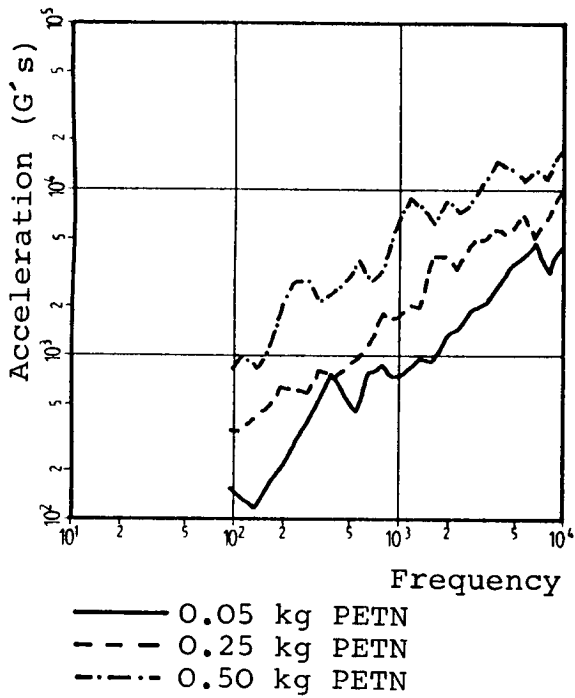
Fig. 8 - Influence of the
explosive charge

— 0.05 kg PETN
− − − 0.25 kg PETN
−·−·· 0.50 kg PETN

Fig. 9 - Influence of the
point of excitation
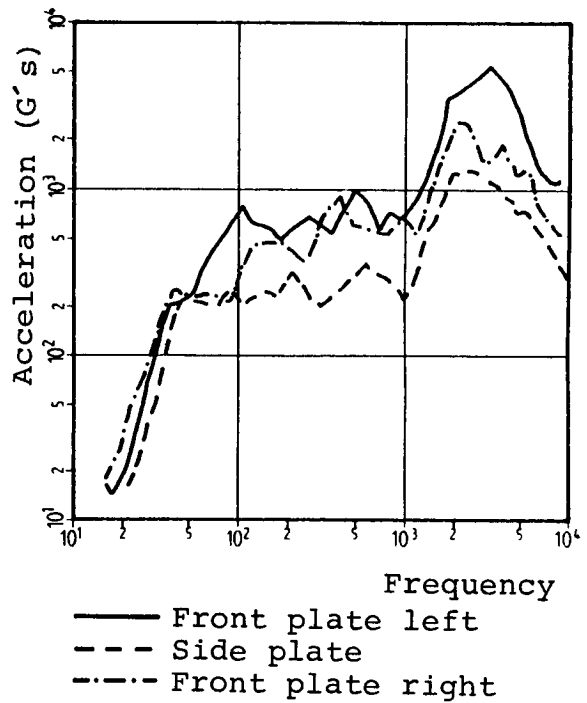
— Front plate left
− − − Side plate
−·−·· Front plate right
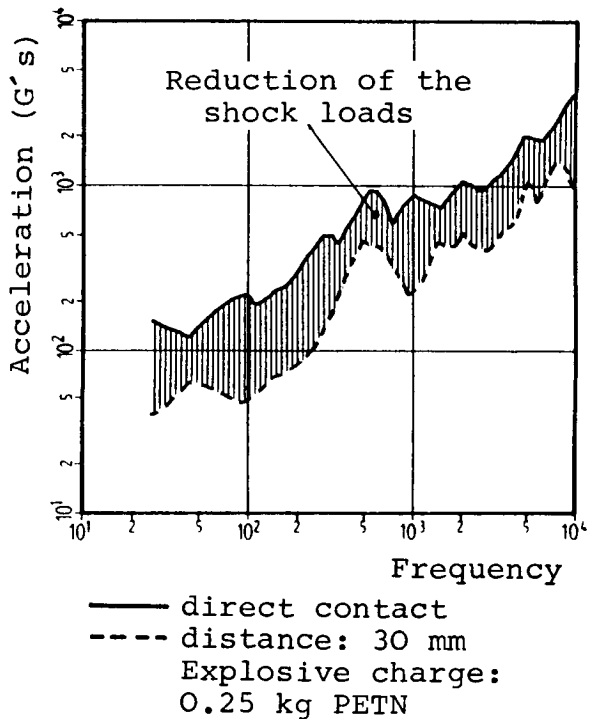
Fig. 10 - Influence of the
distance between
front plate and
explosive

— direct contact
− − − distance: 30 mm
Explosive charge:
0.25 kg PETN
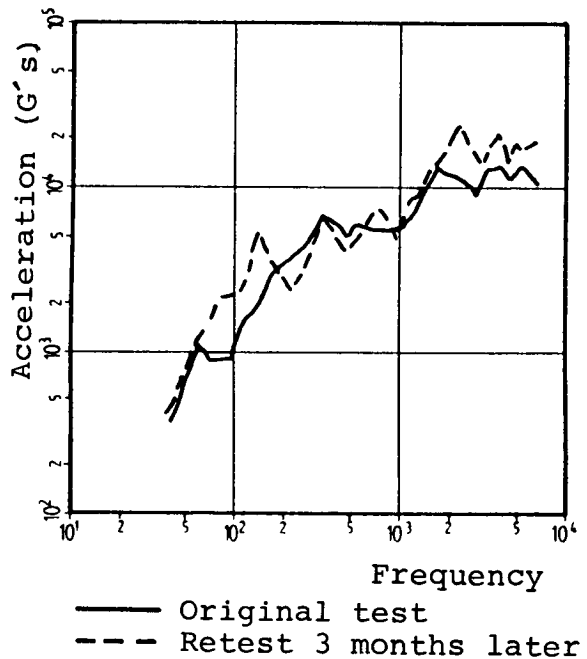
Fig. 11 - Reproducibility of
blast test

— Original test
− − − Retest 3 months later

*   The influence of the kind of explosive to the induced shocks
----

    In general the shock loads depend on the detonation velocity of the
    explosive used. A mining explosive like AMMONGELIT with a detona-
    tion velocity of about 2,4 km/s results in a sufficient excitation
    of the lower frequency range but is unable to produce high shock
    loads in the higher frequency range.
    High explosives like NITROPENTA, HEXOGEN,both have a detonation ve-
    locity of 8,4 km/s, or OCTOGEN with 9 km/s produce shock loads
    which are comparable with penetrator-impact induced shocks in the
    entire frequency range.

*   The influence of the point of excitation to the induced shocks
----

    The changing of the point of excitation influences the shock loads,
    figure 9. In this case the SBS had been blasted by an explosive
    charge of 0,25 kg PETN at the locations 50, 29 and 7, figure 6. The
    travelled shocks were measured at a built-in unit installed at
    chamber 3. The g-loads are different as the shock propagation de-
    pends on the dynamic properties of the SBS. The structure in the x-
    direction is more elastic than in the y-direction. To get very high
    dynamic strains the equipment to be tested must be mounted in cham-
    ber 1 or chamber 4 and blasted at the locations 6/7 or 49/50.

    In many chases it is desirable to reduce the shock loads to be si-
    mulated. In general the equipment is protected against the blast.
    The excitation is mainly caused by the stress wave. In order to
    damp the stress wave amplitude the distance between the armor
    plate of the SBS and the explosive was changed. The influence of
    the change of the distance is presented in figure 10.

*   The reproducibility of shock tests using the SBS

    The reproducibility of the simulated shock loads at the equipment
    is of importance and depends mainly on the state of the used ex-
    plosive. A long time of storage can result in a change of the den-
    sity and the detonation velocity respectively.
    The dynamic properties of the SBS are unimpared against the blast-
    tests as door plates are used.
    From a multitude of shock tests carried out with the SBS the repro-
    ducibility lies in a band width of about 15 to 20%. An example of
    the reproducibility is given in figure 11.

*   The influence of the dynamic properties to the induced shocks
----

    The shock propagation and the g-loads depend on the stiffness of
    the structure. In order to raise shock loads the test object must

130

be hard fixed.
Figure 12 shows the mounting of a base plate carrying a test object. The base plate is bolted by an angle shape to the front plate. In addition the base plate contacts the front plate by a groove. After blasting by an explosive charge of 1 kg PETN the elastic restraint was distorted.
In order to maintain the closing shape a stretching device was installed as shown in figure 13. After blasting with the same explosive charge the mounting was unchanged.
The comparison of the shock propagation in y- and z-direction of the mountings is presented in the figures 14 and 15. In the entire frequency range a considerable higher dynamic strain is transferred using the mounting b).

RESULTS

The method introduced is applied to produce penetrator-impact induced shock loads. By use of the described parameters it is possible to increase the simulated shock level up to the individual load limit of the test object. In order to evaluate the shock resistance of the equipment shock measurements are necessary at the suspension points where the shocks are initiated, at the equipment itself and into the device. This knowledge is required to find out critical areas and to provide design proposals for improvements.

The comparisons of shocks produced by a non-penetrating projectile with simulation results are shown in the figures 16 and 17. At the suspension points the shocks differ in a wide frequency range. In general it is difficult to simulate initiation shocks because the dynamic properties of the bombarded structure differs from the simulator. The shock responses at the equipment itself are sufficiently simulated in the entire frequency range.
Usually the initiation shocks are higher than the shock response outside or inside the built-in units, figure 18. The difference between the shocks is absorbed by the suspension.
For the improvement of the shock resistance the shock distribution inside the equipment is of main interest, figure 19. Critical shocks are detectable if the shock distribution is different.
An important point is the check of the individual built-in unit. In addition to an operational test the change of the position of the line of sight is measured. This shows a relationship between shock loads and possible equipment failures and enables a finale valuation of the test object.

SUMMARY

Shocks produced by non-penetrating projectiles are very dangerous for the equipment of combat vehicles, airplanes, ships or space structures. Usually these shock loads are not simulatable by laboratory test machines. As the hard fixed optical sightings of armored vehicles are exposed to very high dynamic strains shock related failures like disadjustments, damage of prisms and even mechanical destructions
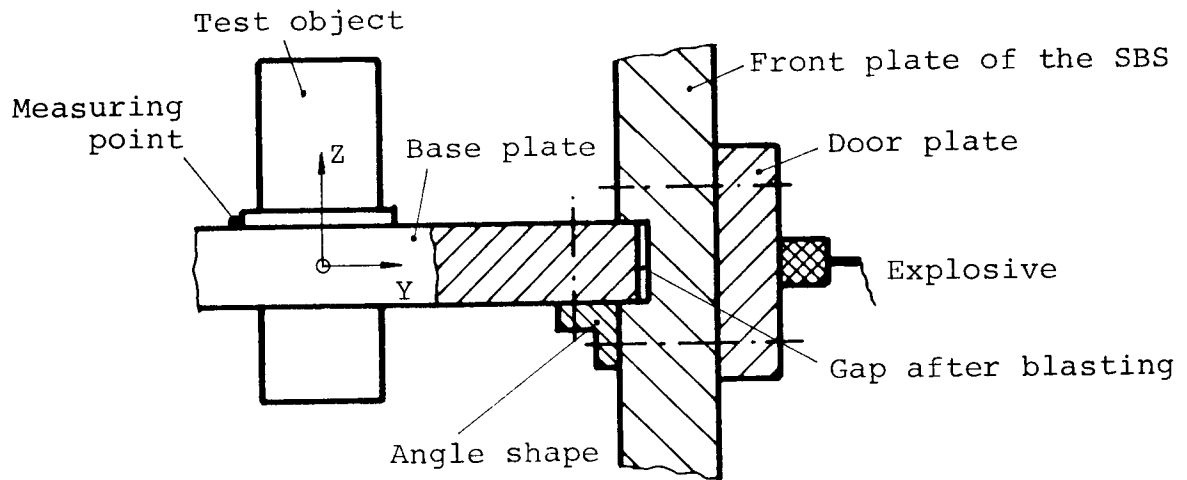
Fig. 12 - Mounting a): Elastic fixed base plate
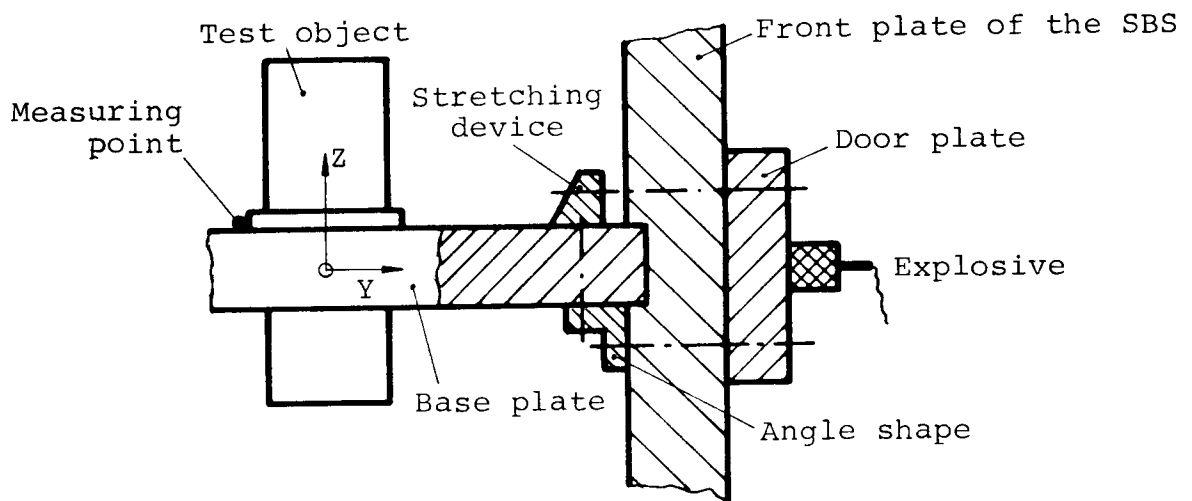
Fig. 13 - Mounting b): Hard fixed base plate
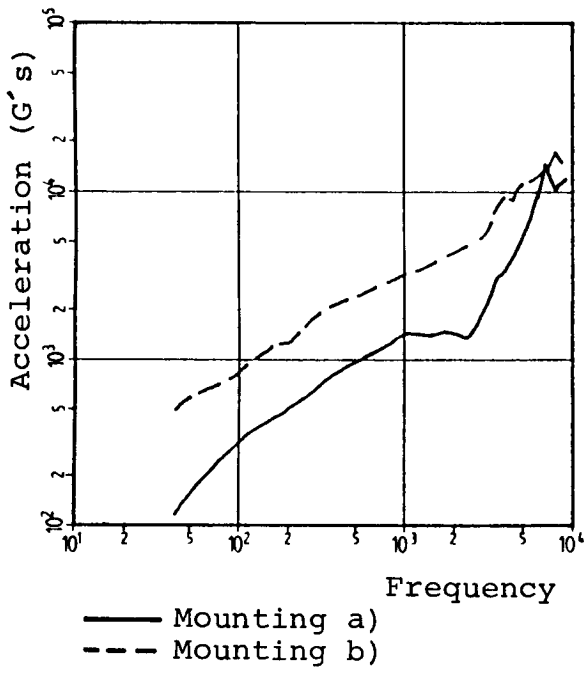
Fig. 14 - Influence of the
structure to the
shock propagation
in y-direction
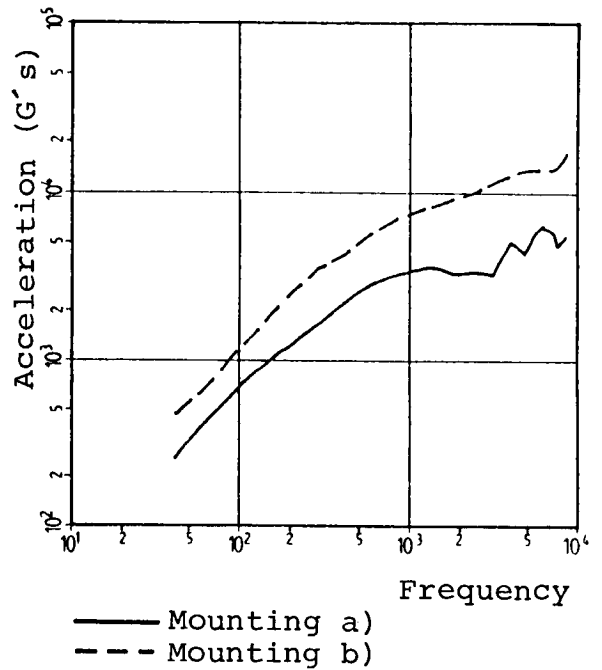
Fig. 15 - Influence of the
structure to the
shock propagation
in z-direction
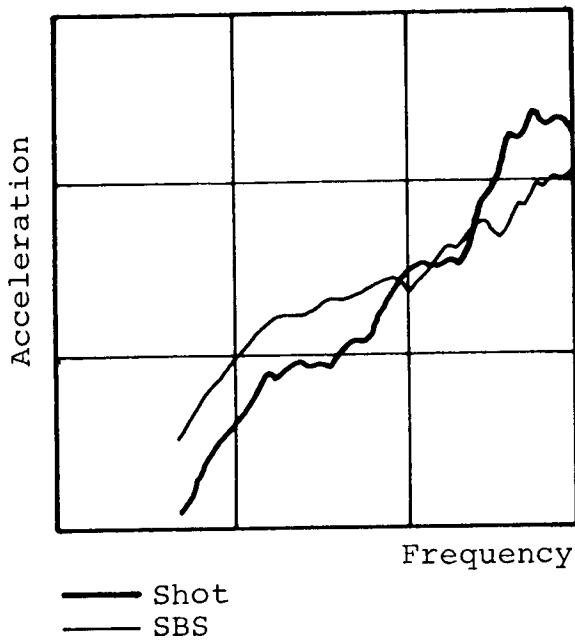
Fig. 16 - Comparision of ini-
tiated shocks between
real bombardment and
simulation

Legend:
— Shot
— SBS
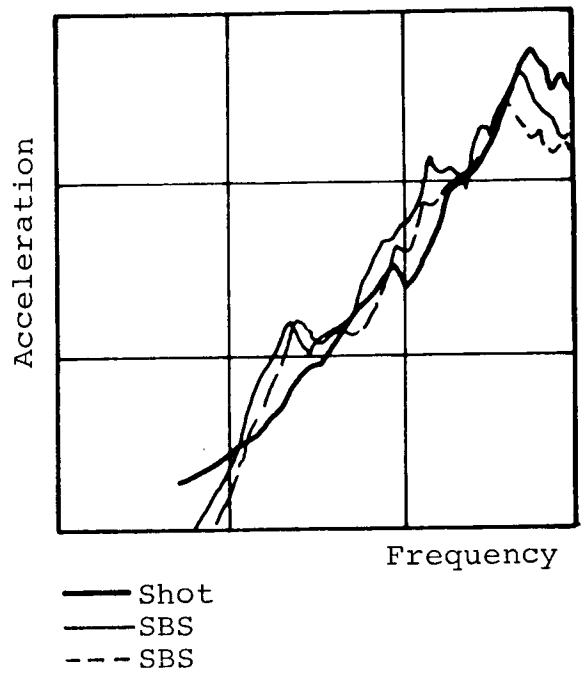
Fig.17 - Comparision of shock
responses between real
bombardment and simu-
lation

Legend:
— Shot
— SBS
- - - SBS
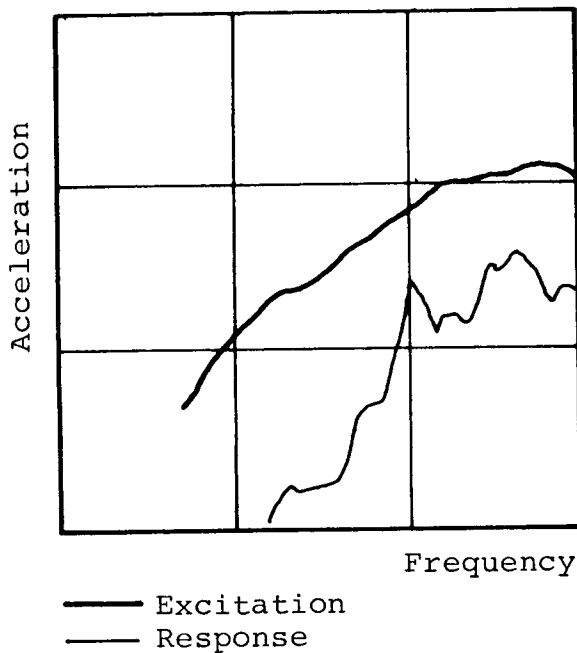
Fig. 18 - Comparision between
initiated shock and
shock response at
the equipment

Legend:
— Excitation
— Response

Critical Load
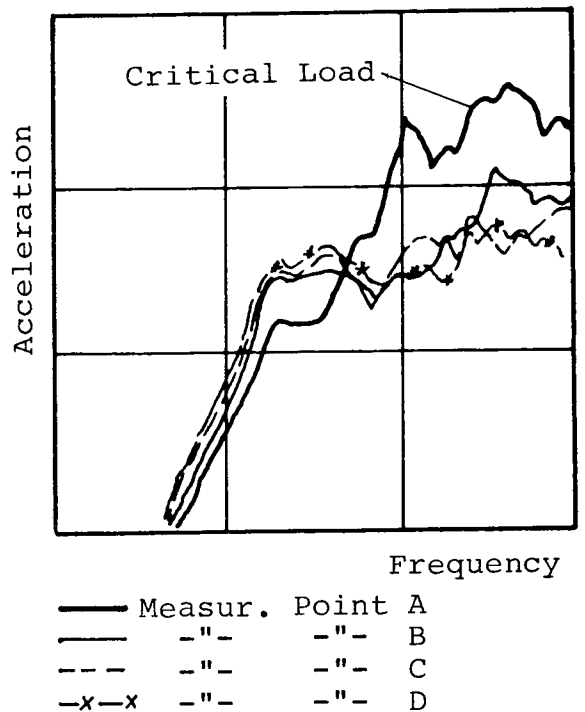
Fig.19 - Shock distribution
inside the equipment
to find out critical
areas

Legend:
— Measur. Point A
— -"- -"- B
- - - -"- -"- C
—x—x -"- -"- D

134

of components are possible.
From realistic bombardments against armored vehicles it is known
that the shocks can lead to defects in such equipment which previous-
ly been tested by conventional test systems.
There is a need for a realistic test method for verification of equip-
ment. For that purpose a suitable shock simulation technique is intro-
duced. The armored vehicle is replaced by a simplified structure with
similar dynamic properties. The shocks are produced by a high explo-
sive. The shock simulator has the dimensions 1m * 2m * 3m, consists of
armor plates and is bolted to an elastic foundation. The interior is
divided into seperate chambers in which the equipment to be tested can
be installed. Mass and stiffness can be varied to adjust the dynamic
properties to real vehicles. Due to the dimensions of the simulator it
is possible to accommodate complete firing control systems.
This is important for operational tests of the equipment.
The produced shocks are tuned to given shock spectra by dosing the
quantity of the explosive, by changing the point of excitation and
by varying the stiffness of the simulator.
The method can be used for verification of equipment which is in rea-
ity exposed to high g-levels by short time durations.
Additionally the equipment can be tested to its load limit. The
weakest points are then recognizable. The knowledge of the load
limits is required to increase the protection against shock.
As the Simulator is unimpaired against the blastings a multitude of
shock tests can be executed with the same test set up. The handling is
easy and ballistic shock tests are carried out economically.

REFERENCES

[1] H.N. Luhrs
    Pyrotechnic Shock Testing - Past and Future
    The Journal of Environmental Sciences, 1981.

[2] R.J. Thornhill, C.C. Smith
    Impact Force Prediction Using Measured Frequency
    Using Response Functions
    Journal of Dynamic Systems, Measurement and Control, 1983

[3] S.N. Prescott
    Pyrotechnic Shock Reduction
    Jet Propulsion Laboratory, California Institue of Technology
    NAS7-100

[4] U. Hollburg
    Experimentelle Methoden zur Simulation von Sekundäreffekten
    infolge Beschuß von Strukturen ohne Durchschlag
    C C G - Lehrgang B1.21, 1986

Analysis of Photopole Data Reduction Models

James B. Cheek

An estimate of the total impulse obtained from a buried
explosive charge can be calculated from displacement versus
time points taken from successive film frames of high-speed
motion pictures of the explosive event. The indicator of
that motion is a pole and baseplate ("photopole"), which is
placed on or within the soil overburden. This paper is
concerned with the precision of the impulse calculation and
ways to improve that precision. Typically, a general cubic
power series in time is fitted to the deflection versus time
data points that describe the explosive-induced motion of
photopoles. The resulting equation fails to meet the
initial conditions of the actual test. This paper examines
the effect of each initial condition on the curve-fitting
process and shows that the zero initial velocity criteria
should not be applied due to the linear acceleration versus
time character of the cubic power series. It points out the
role of the nonzero initial velocity in helping the linear
model deal with the effects of the highly nonlinear pressure
versus time conditions in the explosive test bed. Last,
this paper illustrates the applicability of the new method
to photopole data records whose early-time motions are
obscured. It describes how and why the early-time data
serve to degrade the data fit in the region of the maximum
velocity as does any constraint on initial conditions. It
concludes that future photopole data processing must not
include the early-time data points, that constraints should
not be applied to the initial conditions modeled by the data
fit, and that the photopole data should include points well
beyond the explosive cavity venting time.

INTRODUCTION

This report is about processing the data obtained from high-speed photographs
of "photopoles." For those unfamiliar with the use of photopoles to estimate the

total impulse produced by a buried explosive, the following overview is provided. Photopoles typically consist of a length of pipe (several feet long) attached to a circular baseplate. The pole is placed on or within the soil (overburden) that covers the explosive charge and the specimen being tested. Each pole is painted a background color. A contrasting colored horizontal band is painted around the vertical pole. This band serves as a witness mark for subsequent measurements. When the explosive charge is initiated (zero time), the photopole and the mass of soil beneath its baseplate are assumed to be lifted as a unit by the force of the blast. Prior to the test event, several 1,000 frames per second motion-picture cameras are sited so as to have the photopoles positioned near the bottom of the cameras' field of view. The high-speed photographs taken by each camera provide a position versus time history for each pole. That record covers the time period from before zero time and continuing until the pole is out of the cameras' field of view or is obscured by flash, smoke and/or dust.

Using a photographic film reader, measurements are made on each film frame of the vertical position of each pole with respect to a single reference point whose elevation remains essentially constant during test event. These data, together with a scale factor to convert the film measurements to engineering units, are processed to produce a deflection (S) versus time (t) history for each pole. Those data are further processed to obtain the maximum velocity of the photopole (V_m). With that value, the impulse is calculated as the product of the sum of the soil and photopole mass times V_m.

The best way to estimate the soil mass is by no means agreed upon by all researchers. Nevertheless, once the mass value is established, the impulse calculation depends entirely on the value calculated for V_m. For that reason, the dependability and the accuracy of the data-processing procedure are very important issues in the overall testing process. Those issues are the focus of the remainder of this paper.

CALCULATING THE MAXIMUM VELOCITY, CURRENT PROCEDURE

The first step in calculating V_m is a curve-fitting process. In order to fit a curve to data, a function form must first be chosen. Past experience indicates that the displacement versus time history of photopoles is satisfactorily modeled by the function:

$$S = At^3 + Bt^2 + Ct + D \tag{1}$$

Using Equation 1, the maximum velocity is at the time when $\dfrac{d^2S}{dt^2}$ is zero. Thus:

$$V_m = C - \frac{B^2}{3A} \tag{2}$$

Current practice is to estimate the time at which the pole first begins to move (lift-off time, T) by examining the plot of the S versus t as shown on Figure 1. Points prior to T are deleted and the values for the constants A, B, C, and D are then determined by the least squares curve-fitting procedure. The points and fitted curve are shown in Figure 2.

The procedure just described has been used for several years. The calculated impulse values agree within the limits of experimental error with the results obtained by other means. However, there are a few bothersome details relating to

138

the photopole's initial conditions. Specifically, the nature of a least squares fit to a data set assures that the coefficients obtained result in the best fit of the chosen function to the data. Since the graph of that function may not pass through some of the data points, this leads to the potential for violations of known initial conditions. Thus, the equation may have a nonzero deflection at zero time, wrongly indicating that the photopole moved before the test began. The slope of the equation at zero time may be nonzero, again, wrongly indicating that the pole was moving when the test began. Finally, when the lift-off is not at zero time, the velocity may also be nonzero. This is also incorrect. While all those errors in the initial condition specification are part of the current procedure, it is important to note that they appear not to degrade the process of finding V_m. How can this be so? How can one ignore known initial conditions?

One answer to those questions is that the actual task is not to fit a curve to all of the data. Instead the task is to get a good fit to the data on each side of the point in time at which V_m is developed. Then V_m is calculated from the curve fitted to that region alone. One might conclude that the early-time data should be deleted from the curve fit since only the maximum velocity region is important. The need to examine the merit of that conclusion presented itself when a test failed to produce any early-time photopole data. Efforts to obtain a good fit to those incomplete data sets required a detailed analysis of the role of initial conditions in the curve-fitting process.

MODELING THE INITIAL CONDITIONS

A study of the high-speed photographs shows that the lift-off time appears to occur several milliseconds after zero time, see Figure 1. As noted previously, this forces the user to choose T and delete points prior to that time. This choice is not always an easy one to make. Consequently, it was decided to let the program select the best value for T. In order to meet the S = 0 at t = T condition, Equation 1 was transformed from S as a function of t, to S as a function of U, where U is zero at lift-off time. This results in U = t-T, dU = dt, and $V = \dfrac{dS}{dt} = \dfrac{dS}{dU}$, which when substituted into Equation 1 gives:

$$S = AU^3 + BU^2 + CU \tag{3}$$

That expression forces S to zero when U is zero, thereby meeting one of the two initial conditions. The second condition is met by differentiating Equation 3 with respect to U, which gives:

$$V = 3AU^2 + 2BU + C \tag{4}$$

Since V is zero when U is zero, C is zero and that allows Equation 3 to be written as:

$$S = AU^3 + BU^2 \tag{5}$$

This displacement versus shifted time expression meets both initial conditions.

Unfortunately, Equations 5 and 3 are in terms of three and four unknowns, respectively. This is apparent when they are expressed in terms of t as:

$$S = A(t-T)^3 + B(t-T)^2 + C(t-T) \tag{6}$$

$$S = A(t-T)^3 + B(t-T)^2 \tag{7}$$

139

The problem with those equations is that the coefficients and T parameter cannot be obtained directly by the least squares procedure. In order to overcome that difficulty, a minimum search program was used to find the T value that yields the best of the "best fits." However, T can be calculated directly from a fit with Equation 1 by setting S to zero and solving the resulting cubic equation for t (which is T since t = T when S = 0).

INITIAL CONDITIONS FOR MISSING EARLY-TIME DATA CALCULATIONS

In order to test the effects of the initial conditions on the curve-fitting process, all combinations of constraints on initial velocity and T were tried. However, the requirement that deflection be zero at T was applied to all calculations. During this study, quite a few runs were made using the four initial conditions with data sets having various combinations of total number of points and time of first point. The results presented in Figures 3 through 6 are typical of those obtained for each initial condition during the study. Data for the four examples presented are taken from the original data set, Figure 1, with the time of the first point set to ten milliseconds (data prior to that time are ignored).

The results shown in Figure 3 are with lift-off at zero time and lift-off velocity constrained to zero. It was expected that those results would be the best because the specified initial conditions agree with the known conditions in the test. They are not. The curve fit to the data points both in the early- and the late-time regions is unsatisfactory. From this we conclude that either the lift-off at zero time or the zero velocity at lift-off constraint is improper.

With that in mind we look at calculations wherein the velocity at lift-off is unconstrained while lift-off is at zero time. Those results, shown in Figure 4, show a slightly better fit of the curve to the data.

The third example, Figure 5, presents the results of forcing lift-off velocity to zero and allowing the program to find the T value that best fits the data. We expected the lift-off to take place a few milliseconds after zero time, thereby agreeing with the observation of the photopole performance. Such is not the case; T is negative.

Since constraining either the velocity at lift-off or the lift-off time produces undesirable effects, the results of the unconstrained case are presented in Figure 6. We find, much to our liking, that T is positive and close to the time indicated by the original data, Figure 1.

DELETING EARLY-TIME DATA

Since the curve fit shown in Figure 6 is better than the fit to the time shifted data shown in Figure 2, we wonder just how many points should be deleted in order to get the best results. For this test, the criteria for goodness of fit is the smallest error mean square. This value (labeled EMS on each plot) is computed as:

$$\text{EMS} = \frac{1}{N} \sum_{i=1}^{N} [S_i - f(t_i)]^2 \tag{8}$$

where t_i, S_i are the coordinates of the ith data point, $f(t_i)$ is the value of the equation at the time coordinate of the data point, and N is the number of data

points. Note that the number of points need not be the same for each data set in order to use these criteria.

Also in question is how does V_m change as the early-time data points are deleted. Those points are addressed in the two plots shown in Figure 7. The curves were produced by making a series of curve fits. First, to all of the data points, then all but the first point, then all but the first two points and so on until only a few data points remain. Plotting the EMS and V_m as a function of the time of the first point produces the curves shown. In all cases tested, the curves show the slight decline in V_m and a rapid decline in EMS out to 5 to 10 milliseconds. From that point on, both V_m and EMS hold almost constant values until the EMS and/or V_m begin to show sensitivity to removing a single point (the points in this data set are at intervals of 1 millisecond). This sensitivity is due to the decrease in the total number of points in the data set and the fact that points are being removed from the region that defines V_m.

LATE-TIME POINTS

The need for points well beyond the time (T_m) at which V_m occurs is illustrated in Figure 8. The original data set was used for this test, except all points beyond 55 milliseconds were deleted. Here we see the degrading in the fit because of the poor definition of the region beyond T_m. As mentioned previously, dust and the pole's motion limit the total number of points that can be obtained. Nevertheless, this series of calculations well illustrates the importance of those late-time points and justifies the extra effort expended in obtaining them.

ANALYSIS AND CONCLUSIONS

It may seem trite to observe, "When one chooses a model, one also takes the first step in reducing the accuracy and precision with which we model the effects in question." However, grasping the implications of that observation is critical to understanding the seemingly strange results produced during this series of computational experiments. At this point, a close examination of strongly held beliefs regarding the role and importance of initial conditions is in order. As the results demonstrate, forcing the fit to meet the known initial conditions produces the least satisfactory results. Why?

Responding to that question, we look to the general form of the displacement versus time model, Equation 1. From that model we extract the underlying acceleration (a) model:

$$a = 6At + 2B \qquad (9)$$

That model describes the photopole motion as being the result of an acceleration that is a linear function of time. On the other hand, our knowledge of the explosive test environment tells us that the pressure on the soil mass beneath the photopole's baseplate is highly nonlinear. From its initial peak value, the pressure declines exponentially and falls to zero shortly after venting. Assuming constant pole-soil mass and base area, this means that the actual acceleration of the photopole is highly nonlinear in the early time portion of the test. However, as the pressure declines during the late time portion of the test, the exponential decay curve has only a slight nonlinearity. Thus, the acceleration experienced by the pole is more or less linear as the blast-induced acceleration matches the gravitational acceleration at t_M. This is why the model produces a good fit in the maximum velocity region. But why a negative T value as shown in Figure 5?

141

The model is doing what we told it to do, and in so doing, it is "talking" to us. It says, "If you force acceleration to be linear and the initial velocity and displacement to be zero, then the photopole must get an early start in order to gain enough momentum to best fit the data in the maximum velocity region." As first thought, this seems too much to ask of us. How can we accept initial conditions and a model that produce pole movement before the blast is initiated?

We can and we must accept the conditions if we accept the model. While it is silly to say that the photopole actually moved before the blast was initiated, it is equally silly to say that the initial velocity was not zero (as is done in the current curve-fitting procedure). In either situation, we are in effect helping our linear model deal with the nonlinear part of its forcing function by relaxing the constraints on the initial conditions. Purely from the standpoint of modeling the data to obtain the maximum velocity in the (almost) linear acceleration region, one must view the negative lift-off time as reasonable, provided the initial velocity must be zero. In like manner, the nonzero initial velocity must be accepted. For the complete relaxation of all constraints, the nonzero displacement at zero time must be allowed. Thus, the concept of valid initial conditions at zero time has no meaning in this sense. Only when the task is to accurately describe the entire displacement versus time function must we focus on initial conditions.

In the light of the above discussion, one is pressed to conclude that the early-time data points serve no useful purpose. Instead of improving the data-fitting process, they poison it.

As mentioned previously, the pressure versus time relationship is almost linear at t_M, which is to imply a low pressure level. But how low? Since the blast pressure is a decreasing function of time, the photopole will reach its maximum velocity when the air drag force and the force induced on the pole-soil mass by the gravitational acceleration are equal to the force induced by the effective pressure on the pole's base area. For a typical pole-soil mass, the force balance pressure is around 1.5 pounds per square inch. One may therefore conclude that t_M will not be 1 or 2 milliseconds after cavity venting, but quite a few more milliseconds later. This further substantiates the need for late-time data points.

RECOMMENDATIONS

Using a linear-in-time acceleration model on photopole data forces us to restrict its application to deflection versus time data taken somewhat before and after the time at which the maximum velocity is anticipated. The specification of the pole's initial conditions at t = 0 has no meaning in this application. If those conditions are forced, the fit tends to degrade the maximum velocity result. Consequently, this study recommends that we ignore the initial conditions without having bad feelings about the failure to model every aspect of the actual situation.

Beyond being comforted, this study recommends that the best maximum velocity results are produced from photopole data having no definition of the early-time deflections, provided enough late-time data points are included to model the photopole's decrease in velocity from its maximum.

CAUTIONS ON MODELING THE COMPLETE DEFLECTION VERSUS TIME HISTORY

There is a growing interest in being able to model the entire deflection versus time history of photopole data. Here, the early-time points become important as do some, if not all, of the initial conditions. However, using a cubic power series to

model all of the initial conditions and subsequent motion in the early-time data region is nothing less than wrong. Efforts are under way to apply proper models to the several regions of the photopole data that exhibit unique effects and properly link those models in the transition zones.

ACKNOWLEDGMENT

POLE NUMBER = 1

PHOTOPOLE DATA PROCESSING TEST CASE 14

Figure 1. Original data.

Figure 2. Time shifted data.

PROG JPPFZ,   S = A x U:x3 + B x U:x2,   U = t - T

POLE NUMBER = 1   PHOTOPOLE DATA PROCESSING TEST CASE 14

Lift-off time = T = 0

EMS- 2 257489E-01

A= -7 943992E-05
B= 9 525614E-03

INITIAL CONDITIONS.
T = 0 0
S(T) = 0 0
U(T) = 0 0

TIME AT UMAX = 39.97
    UMAX = 380 74
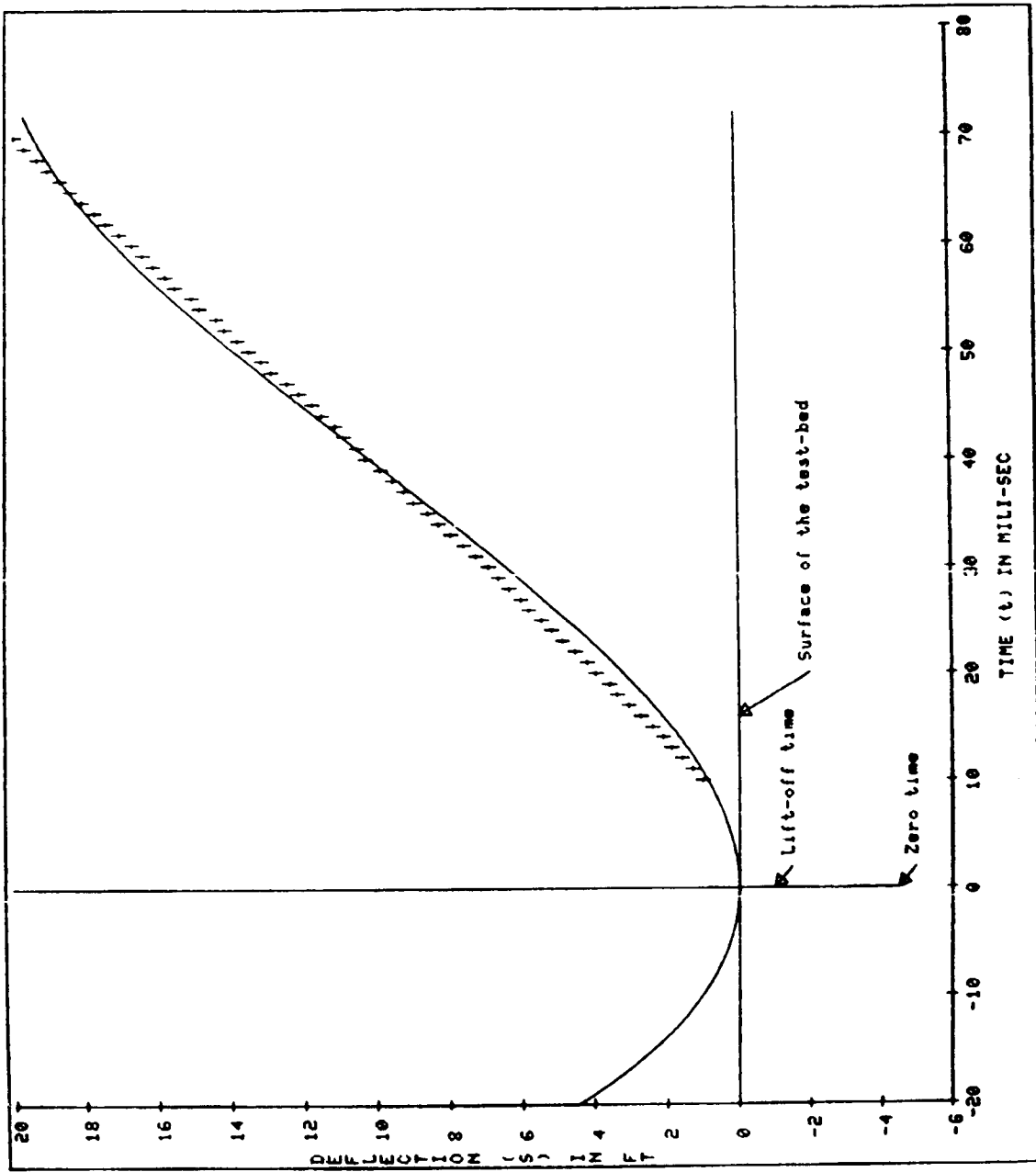
Figure 3.   Initial conditions satisfied.

146

PROG JPP3Z,   S = A x U**3 + B x U**2 + C x U,   U = t - T

POLE NUMBER = 1   PHOTOPOLE DATA PROCESSING TEST CASE 14

Lift-off time = T = 0

EMS = 2.705044E-02

A: -3.732499E-05
B: 5.157079E-03
C: 1.058439E-01

INITIAL CONDITIONS:
T = 0.0
S(T) = 0.0
V(T) IS UNCONSTRAINED

TIME AT VMAX = 46.06
VMAX = 343.36

Surface of the test-bed

Lift-off time

Zero time

DEFLECTION (S) IN FT

TIME (t) IN MILI-SEC
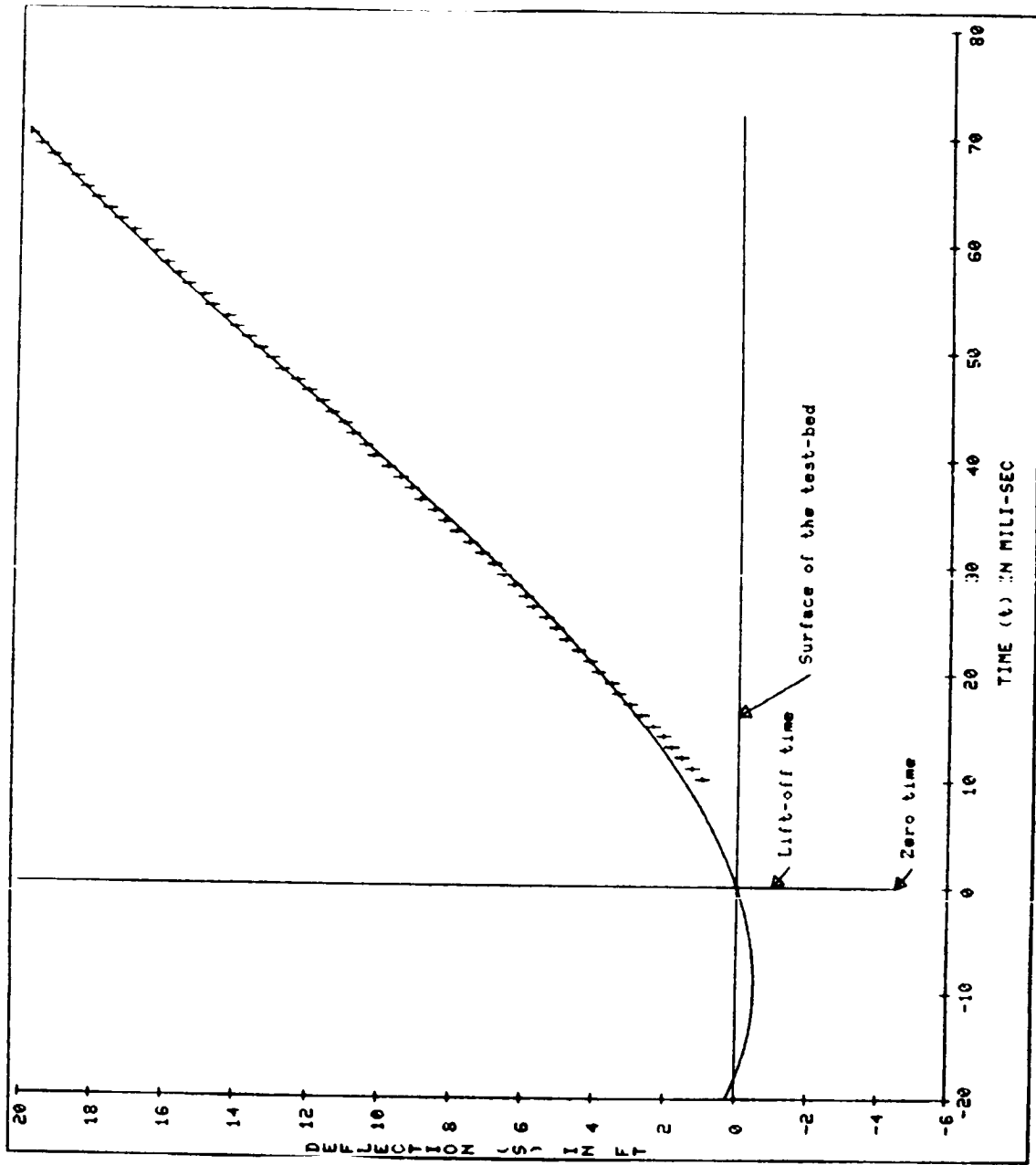
Figure 4. Nonzero initial velocity.

147
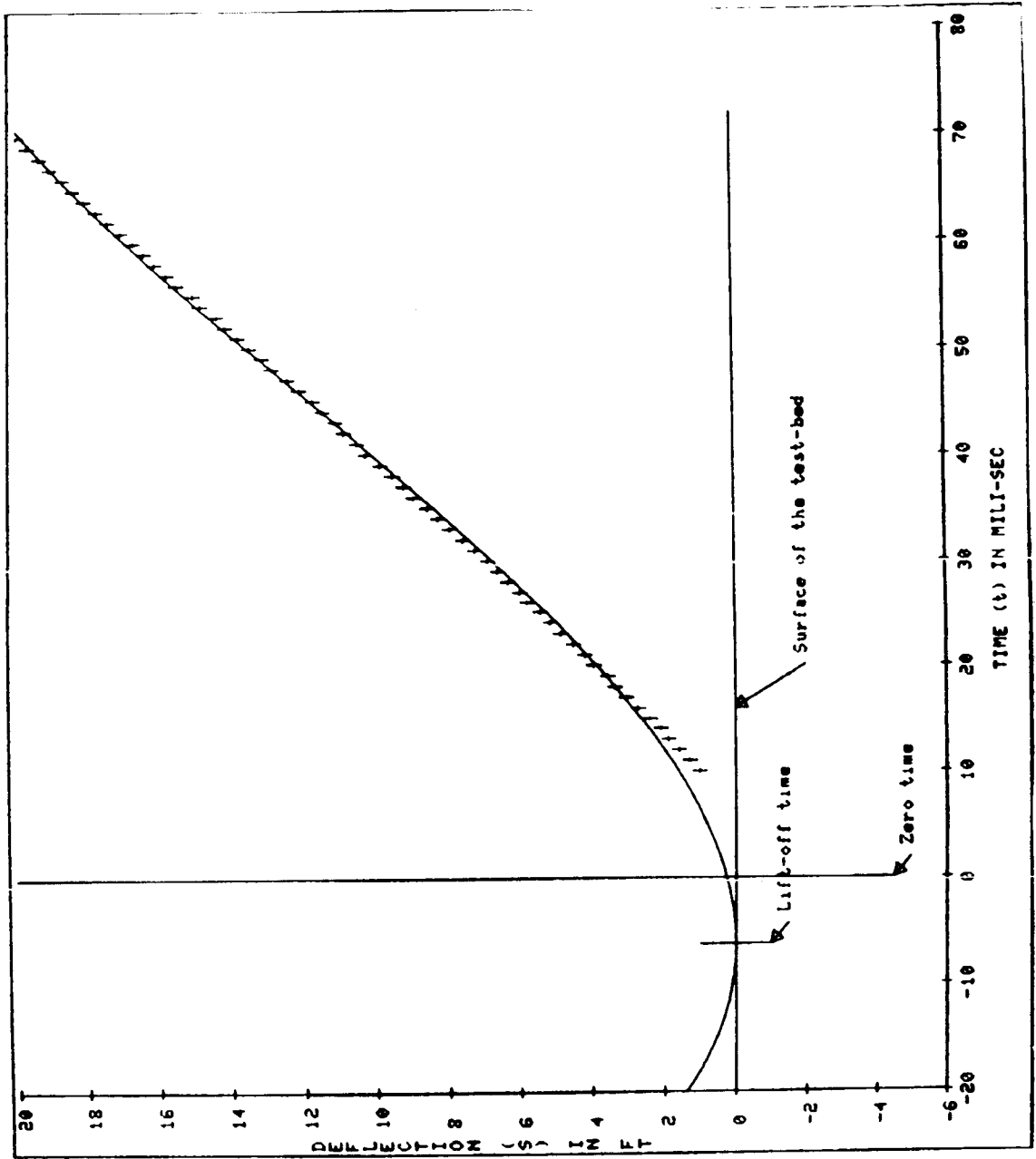
Figure 5. Volocity zero at lift-off, best lift-off time.

148
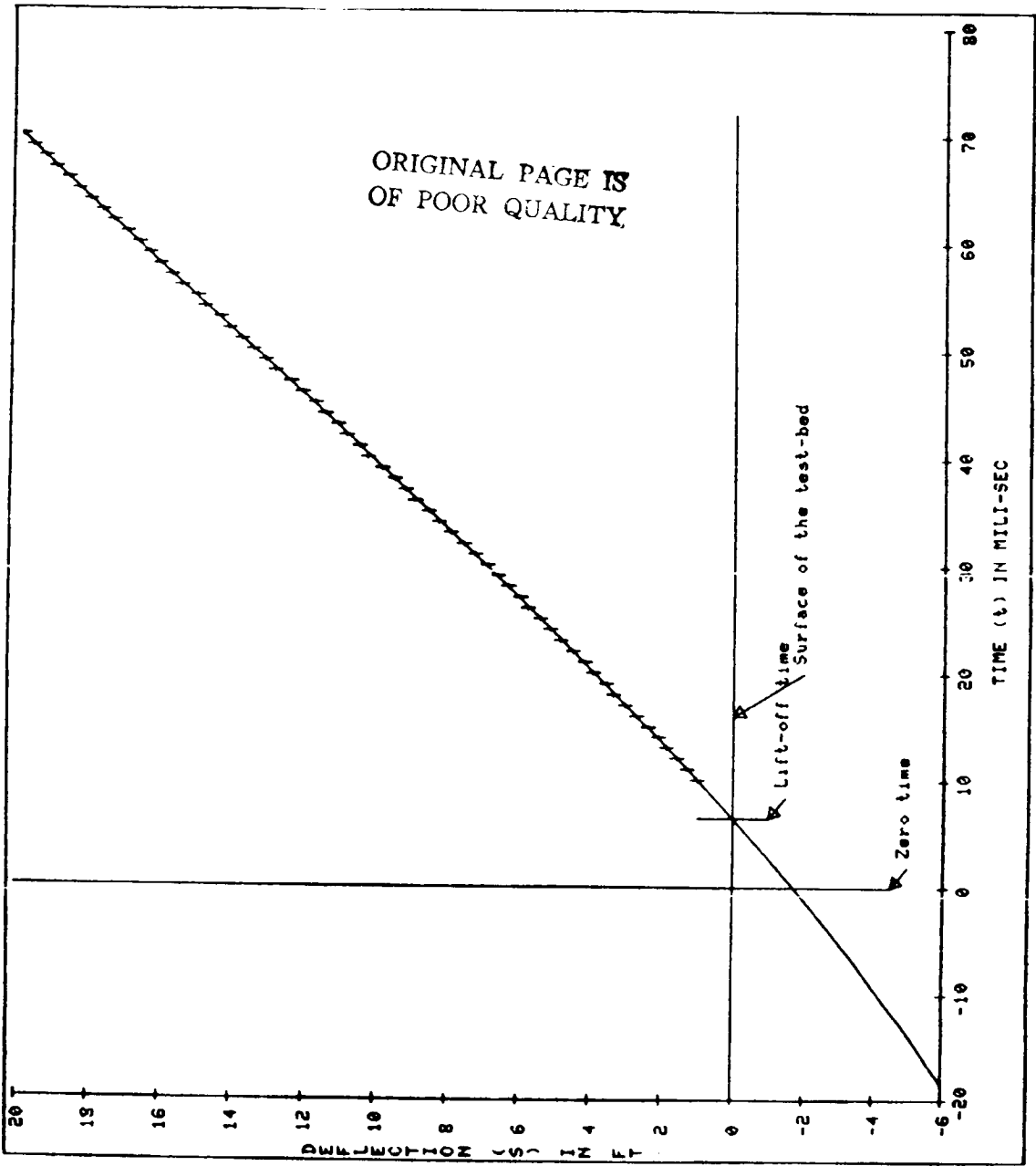
Figure 6. Best fit to data, no time or velocity constraints.

Time	EMS	VMX
0	025036	339 46
1	018892	337 54
2	013450	335 75
3	008303	334 01
4	005409	332 49
5	004222	331 80
6	003147	331 05
7	002298	330 43
8	001919	329 88
9	001488	329 56
10	001454	329 57
11	001473	329 63
12	001488	329 49
13	001497	329 47
14	001497	329 44
15	001508	329 36
16	001512	329 47
17	001538	329 61
18	001558	329 61
19	001514	329 21
20	001518	329 62
21	001508	329 41
22	001526	329 41
23	001570	329 42
24	001535	329 17
25	001527	328 97
26	001546	330 28
27	001401	324 77
28	001382	312 32
29	001450	329 15
30	001500	325 21
31	001424	324 52
32	001424	329 38
33	001570	330 12
34	001541	330 47
35	001676	332 30
36	001552	329 63
37	001575	326 50
38	001732	330 39
39	003419	328 52
40	002422	331 14
41	002412	327 43
42	004751	328 81
43	005086	329 73
44	002078	330 28
45	007424	331 07
46	005267	328 59
47	027574	333 84
48	062165	340 07
49	076508	335 16
50	001874	319 21

TIME OF LAST POINT IS
72.00 MILI-SEC

VELOCITY MAX FT/SEC

TIME OF FIRST POINT IN MILI-SEC

ERROR MEAN SQUARE

TIME OF FIRST POINT IN MILI-SEC

Figure 7. Sensitivity to time of first point, 72 point data set.

150
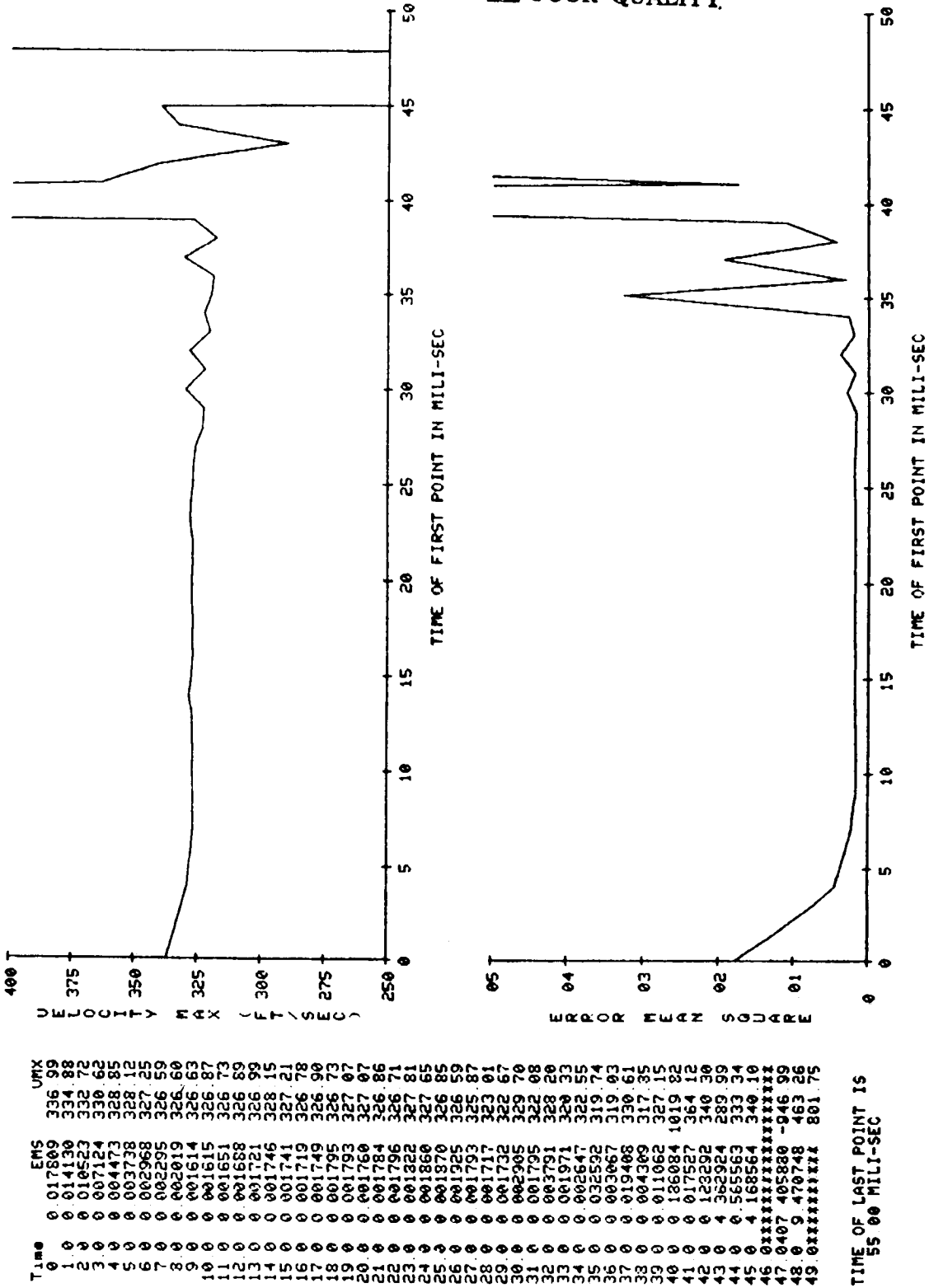
Figure 8. Sensitivity to time of first point, 55 point data set.

151

DYNAMIC ANALYSIS

Modal Survey of the Space Shuttle Solid Rocket Motor Using Multiple Input Methods

Ralph Brillhart

David L. Hunt

Brent M. Jensen

Donald R. Mason

The ability to accurately characterize propellant in a finite element model is a concern of engineers tasked with studying the dynamic response of the Space Shuttle Solid Rocket Motor (SRM). The uncertainties arising from propellant characterization through specimen testing led to the decision to perform a modal survey and model correlation of a single segment of the Shuttle SRM. Multiple input methods were used to excite and define case/propellant modes of both an inert segment and, later, a live propellant segment. These tests were successful at defining highly damped, flexible modes, several pairs of which occurred with frequency spacing of less than two percent.

INTRODUCTION

Morton Thiokol, under contract to the NASA Marshall Space Flight Center, has developed detailed finite element models for studying the behavior of the Space Shuttle SRM. These models are being used to assess both SRM response to a variety of load cases including stacking, static firing, and liftoff as well as the impact of SRM design changes. An important parameter in these highly refined models is the material properties of the solid propellant grain. The propellant is a viscoelastic material whose properties vary with temperature, frequency, and strain rate. Since the solid propellant has a noticeable influence on the structural characteristics and behavior of the SRM, the accurate determination of its properties is very important to the modeling and analysis effort.

Traditionally, propellant dynamic modulus was characterized through rheometric dynamic spectrometer (RDS) specimen testing. The major benefits of RDS testing are associated with the specimen's compact geometry and ease of data acquisition. The major drawbacks occur in relating the specific propellant stress-strain state being modeled to the specimen pre-strain and dynamic strain state during RDS testing.

Based upon the uncertainties of specimen testing and the importance of having an experimentally validated model, Morton Thiokol investigated the use of modal testing as a means to accurately determine propellant properties and improve

PRECEDING PAGE BLANK NOT FILMED

confidence in the results from the specimen testing. Modal tests of SRMs per-
formed a few years earlier demonstrated difficulty in exciting propellant modes
and in correlating the analytic model with the experimental results. It was felt,
however, that the advances in modal testing and system identification techniques
that had taken place since the earlier tests could overcome the limitations
encountered before. In particular, multiple input random excitation [1] and
improved parameter estimation techniques [2,3] had been shown to be capable of
handling the difficulties associated with symmetric, complex structures [4,5].
Recent improvements in system identification and model correlation methods [6,7]
gave confidence that the SRM analytic model could be adjusted to match the results
from a modal test. The decision was made to perform a modal survey on both an
inert and a live propellant SRM segment.

The choice of testing a single segment rather than multiple segments or an
entire motor was based upon maximizing the chances to obtain useful data for
determining propellant behavior, while minimizing the unwanted and unneeded
effects of joints and other SRM components. Modal testing of a complete SRM,
which defined case and joint characteristics, had been performed previously on an
empty case after static firing. Additionally, a test of a complete SRM would
require significantly more time to plan and prepare, which would delay the date
when a correlated model would be available.

The important elements that comprised the SRM modal survey were (1) choice of
test article, (2) boundary conditions, (3) location and type of exciters,
(4) instrumentation locations, and (5) excitation and data analysis methods.
These five elements are discussed in this paper, along with the significant
results and conclusions that arose during the modal survey.

TEST SETUP

In order to improve the likelihood of exciting propellant modes, an exciter
location directly on the solid propellant was desired. Safety considerations
dictated that an inert segment be used if propellant excitation was planned. A
simulated free-free boundary condition was chosen with the segment oriented hori-
zontally and supported underneath with an air bag system. The goal of the support
system was to have the highest rigid body mode at least 2.5 times lower than the
lowest flexible mode.

A single Shuttle SRM segment with propellant weighs approximately 297,000
pounds. The pretest finite element model was used to study various test require-
ments. A set of exciter locations that would define the modes felt to be most
important for post-test model correlation was determined using the model. The
analysis also indicated that excitation levels in the 200 to 2,000 pound (RMS)
range were required in order to produce response levels that could be measured
with high sensitivity accelerometers. To meet this requirement, as well as fre-
quency content and exciter displacement requirements, electrohydraulic exciters
were chosen. The model was also used to determine the optimum transducer loca-
tions which would ensure measurement of the important modes. A new finite element
model reduction method [8] that employs the analytic mode shapes was used to
define a mass matrix corresponding to the transducer locations. The mass matrix
was used to calculate orthogonality and cross-orthogonality. This analysis
resulted in 230 accelerometers distributed at 136 locations—64 on the segment
case, 16 on the propellant faces, and 56 inside the segment along the bore.

Sixteen of these were actually imbedded in holes drilled into the inert propellant.

TEST PERFORMANCE

The SRM segment was instrumented with a fixed set of accelerometers to avoid the problems associated with relocating transducers during the test. The hydraulic exciters equipped with load cells were attached to rigid supports and large masses to eliminate their interaction with the segment. A photo of the test setup is shown in Figure 1.
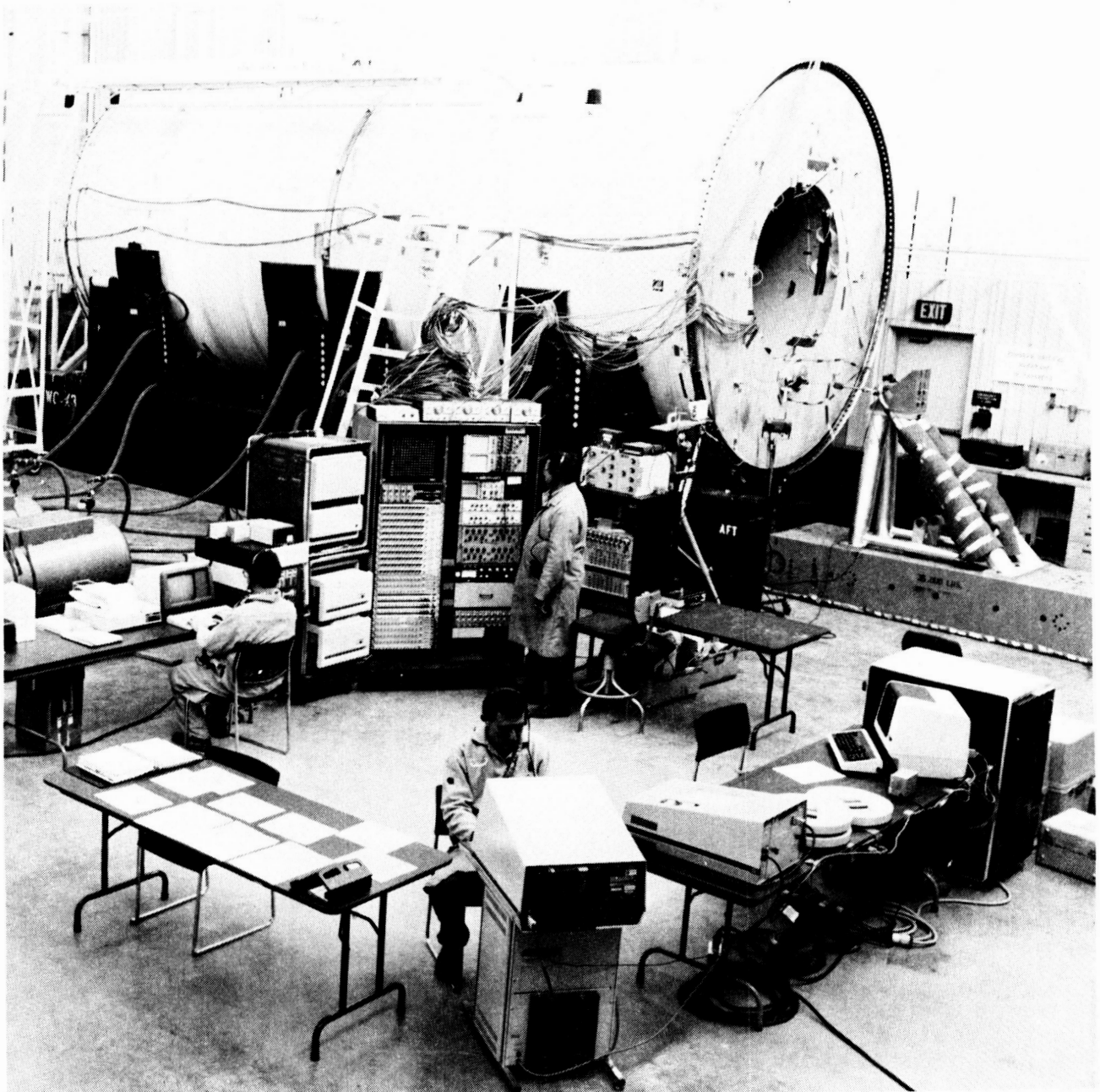
Figure 1. Test setup for modal survey of inert SRM center segment.

The data collection system, as diagrammed in Figure 2, included the capability for performing multiple input random excitation testing using 16 simultaneous channels and multiple input sine excitation using 244 simultaneous channels. The sine excitation part of this system has a number of advanced features, such as closed-loop exciter control, which have improved this traditional aerospace method [9].
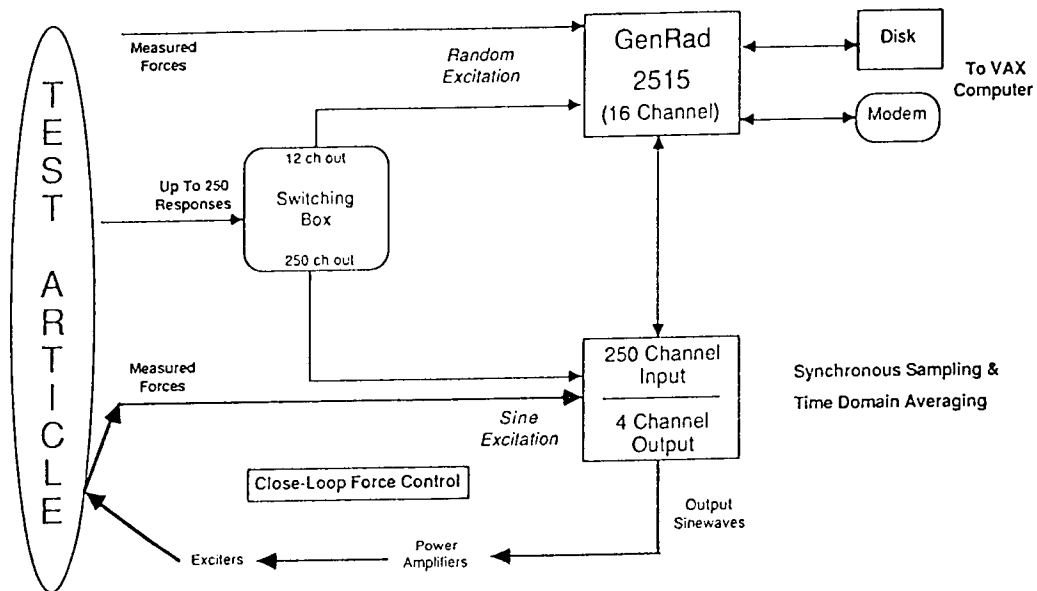
Figure 2. Data collection system for
multiple input random and multiple input sine excitation.

Initial random excitation of the SRM was performed to determine which combination of exciter locations would define the modes. Four exciter locations, depicted in Figure 3, were investigated. Three of these were on the SRM case; one was attached directly to the inert propellant. The initial frequency range for the test, based upon the pre-test model, was planned for 0 Hz to 16 Hz. It was discovered immediately that the flexible modes of the segment were much higher than expected, and the frequency range was increased to 64 Hz. This initial testing also indicated that the axial propellant location was not a good place for an exciter because of local flexibility. A large portion of the excitation energy was absorbed locally, which resulted in poor excitation of global modes. This can be seen in the frequency response function, plotted in Figure 4, where the response in the 5 Hz to 60 Hz range is dominated by the flexibility of a mode near or above 60 Hz.
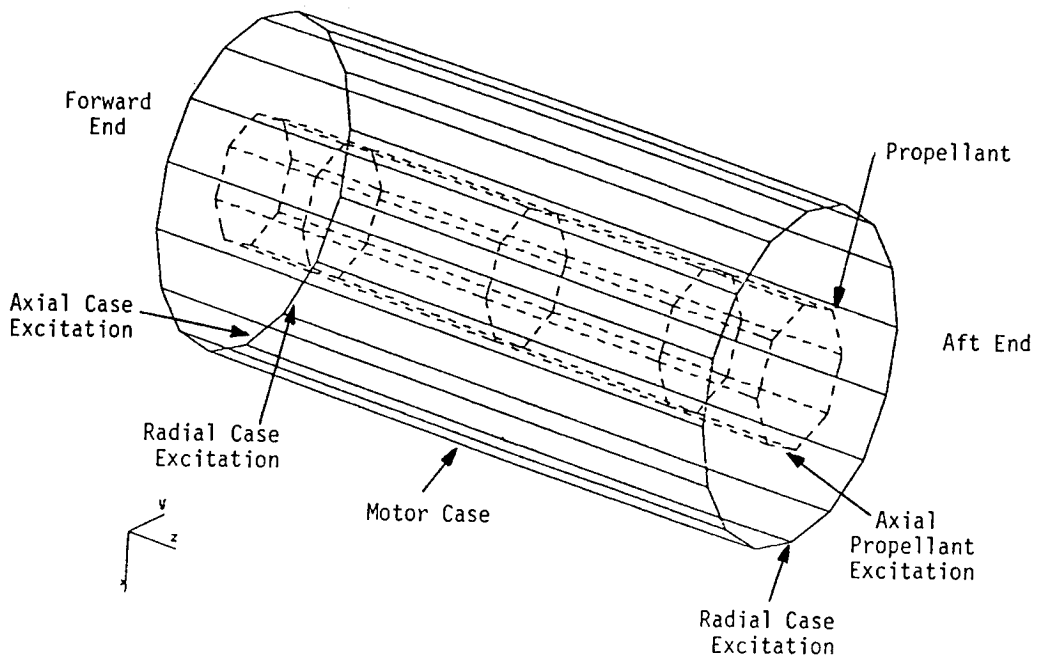
Figure 3. Exciter locations and subset of measurement locations.
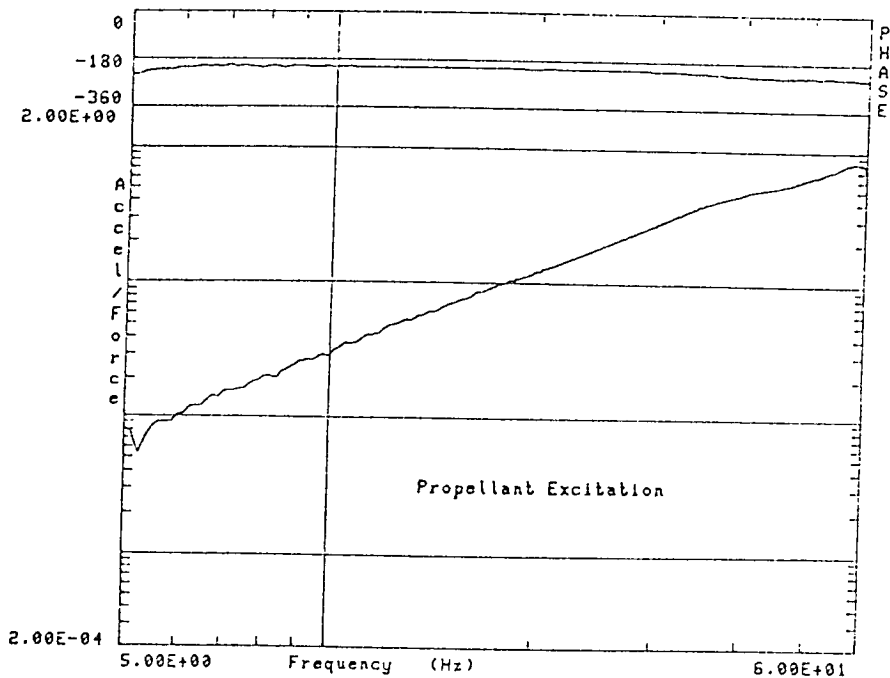
Figure 4. Driving point frequency response function for
propellant excitation shows a large amount of local flexibility.

The three SRM case exciter locations, one axial and two radial, were chosen
for a multiple input broadband survey. This multiple input random test was
performed to assess quickly the modal frequencies, shapes, and damping of the
SRM. The survey produced 690 frequency response functions (frf) and was completed

in less than four hours. A typical frf from the survey is shown in Figure 5. It shows the characteristics of both the rigid body modes, below 10 Hz, and the more highly damped flexible modes above 10 Hz. The multivariate mode indicator function [10] was used to determine more precisely the number and frequency of the modes in both ranges. See Figure 6.

SRM MODAL SURVEY - MULTIPLE INPUT RANDOM EXCITATION
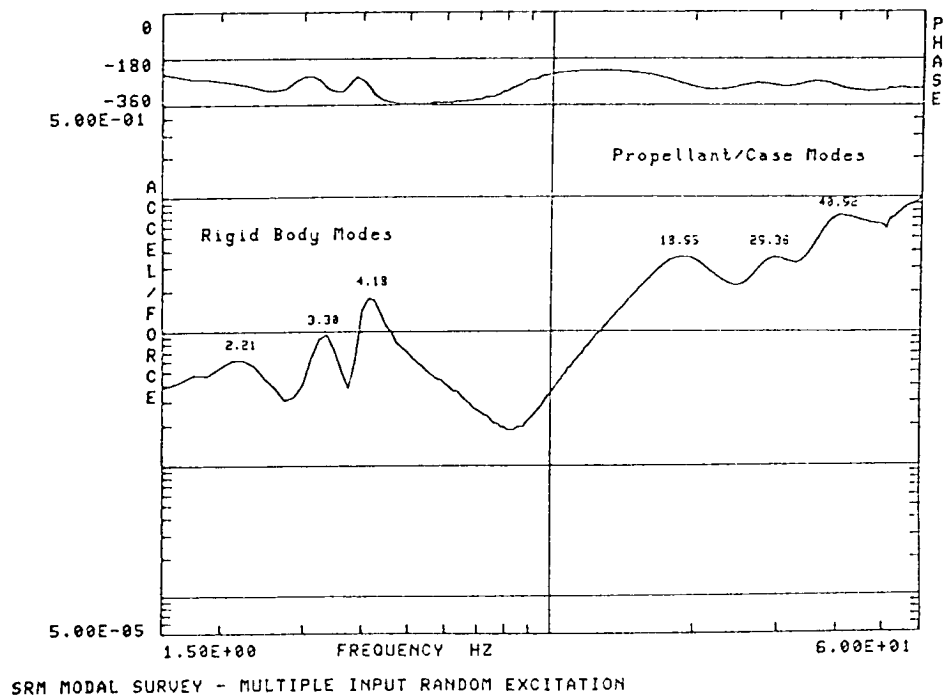
Figure 5. Typical frequency response function from the three exciter random survey on the inert segment.
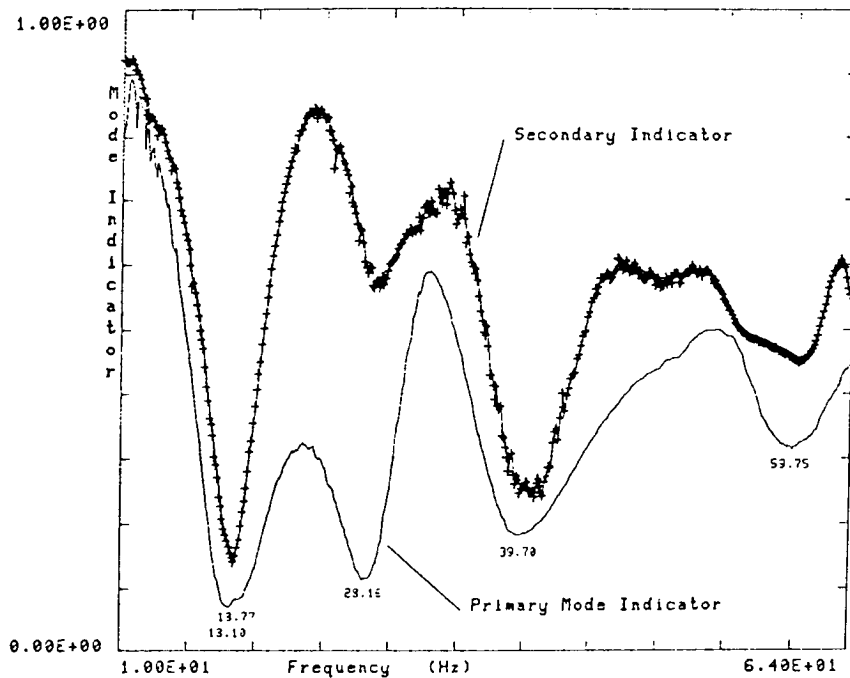
Figure 6. Multiple input frf are used to compute indicator functions which show approximately six modes between 10 Hz and 64 Hz.

160

The frf were analyzed first using a fairly straightforward "weighted total response" technique [11] to see if the modes made sense and to spot any malfunctioning or erroneously scaled transducers. Inspection of the mode shapes showed that, while this method identified the basic mode shape, it did not work well for transducers in the vicinity of the exciter locations. At these locations, there was enough local flexibility to give large errors in the mode shape coefficients computed using the total response method. This can be seen in the comparison of mode shapes depicted in Figure 7. The solid lines plot the mode shape for the 29 Hz saddle mode, computed using the weighted total response method. The dashed lines plot the same mode computed using the "direct estimate" method, described later in this paper. Two of the exciter locations are identified. The end view plot of the shapes clearly shows that these are the locations where the differences exist. The total response method uses the value of the frf at the resonant frequency as the mode shape coefficient. At these exciter locations, this results in an overestimate of the modal coefficient because the contribution of the response from the higher frequency, locally flexible mode exceeds that of the 28 Hz mode.

Isometric View   End View
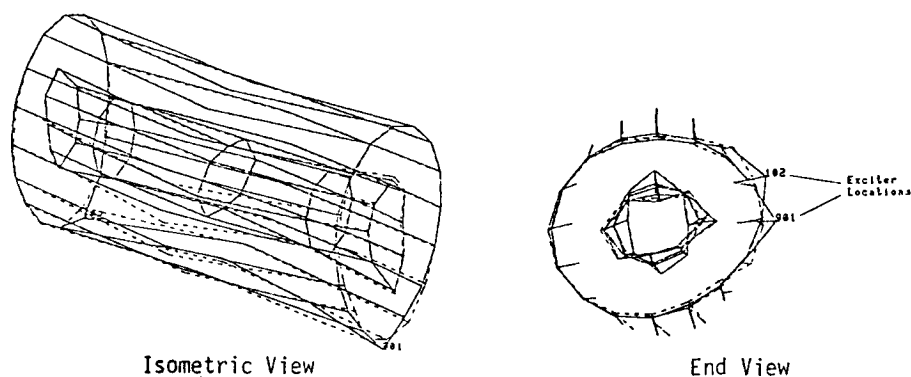
Figure 7. Shape comparison for 29 Hz mode computed using
weighted total response (solid line) and
direct estimate method (dashed line).

The frf were next analyzed using the polyreference parameter estimation technique [2]. The polyreference method had performed well on many lightly damped structures with high modal density, including structures with symmetry. Because the SRM data was considered high quality, it was expected that the polyreference method would produce good results. Unfortunately, it seemed to have a great deal of trouble with this data. In retrospect, several possibilities for the problems became clear. The polyreference method that was employed was a time domain version (frequency domain polyreference versions were not available at the time). This means the frf are transformed to the time domain before the modal extraction begins. Because of the highly damped nature of the modes, the time domain (impulse response) data rapidly decays to zero. A second reason for the problems was the effect of the local flexibilities of the structure. Local flexibilities are usually seen in the form of higher frequency modes outside the range of interest. The formulation of the polyreference method does not allow for an accurate treatment of these residual modes.

The next method applied to the frf was the frequency domain "direct estimate" method [3]. Besides operating in the frequency domain, it directly handles residual modes outside the analysis range. This method produced very consistent

and sensible results. It overcame the difficulties associated with the total response method for mode shape calculation, described earlier. It also enabled the separation of closely spaced modes. Table 1 lists all of the modes identified in the inert modal survey. The Forward Oval and Aft Oval modes are separated by less than 0.2 Hz. The direct estimate method was able to clearly identify these two heavily damped, closely spaced modes, as shown in Figure 8.

Table 1. Modes identified in the center segment inert propellant test.

Mode Number	Frequency (Hz)	Damping (C/Cr)	Mode Description
1	2.137	0.148	Rigid body pitch about bottom
2	3.322	0.052	Rigid body bounce
3	4.142	0.035	Rigid body pitch about top
4	4.998	0.035	Rigid body roll about top
5	18.681	0.172	Forward Oval (n=2,m=1)
6	18.806	0.161	Aft Oval (n=2,m=1)
7	28.980	0.090	Saddle (n=2,m=2)
8	40.867	0.139	Forward Triangular (n=3,m=1)
9	41.524	0.118	Axial Propellant (driven on propellant)
10	42.489	0.097	First Bending
11	60.249	0.104	Local Propellant

18.7 Hz
Forward Oval

18.8 Hz
Aft Oval
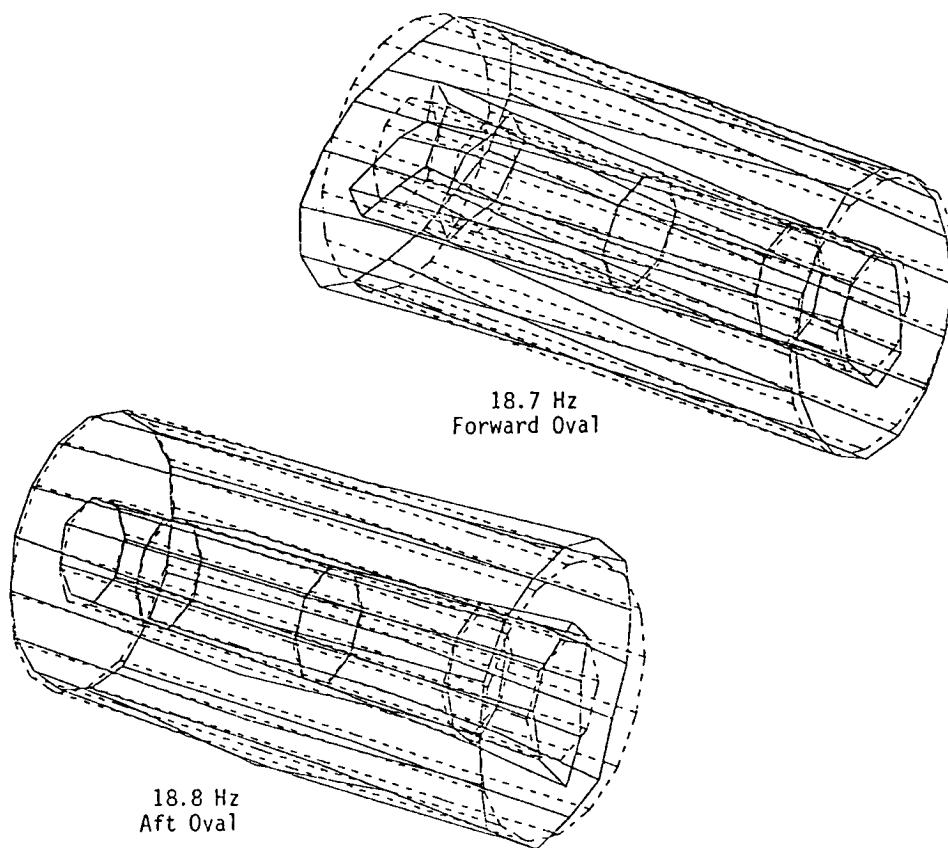
Figure 8. The direct estimate method was used to compute and separate these two closely spaced modes.

Because of the large differences between the predicted and measured mode frequencies, Morton Thiokol personnel felt that a modal test of a segment with live propellant was needed to ascertain the true properties of the solid propellant. Additionally, questions were raised about the effect of aging since the inert segment was several years old. A second test would add confidence in the propellant properties determined through the modal survey.

The inert survey had established that high quality results could be obtained using excitation on the segment case and that the test could be performed safely. A test of a live segment was planned and performed along the lines of the inert segment. The case exciter locations were the same, which eliminated the need for additional fixturing. The propellant exciter location was deleted for safety reasons. Measurement locations were very similar, with the deletion of the interior propellant measurements. The inert test indicated that these measurements did not give any additional relevant data.

The live propellant modal survey was performed several weeks after the inert test. A three-input random survey identified a set of modes which were very similar to the inert segment. The similarity in the two segments is evidenced by the frf comparison shown in Figure 9. The rigid body mode frequencies did not shift while the flexible modes of the live propellant segment appear 5% to 10% lower than those of the inert segment. This suggested that the live propellant has a lower modulus than the inert. The complete set of modes identified in this second modal survey is shown in Table 2.
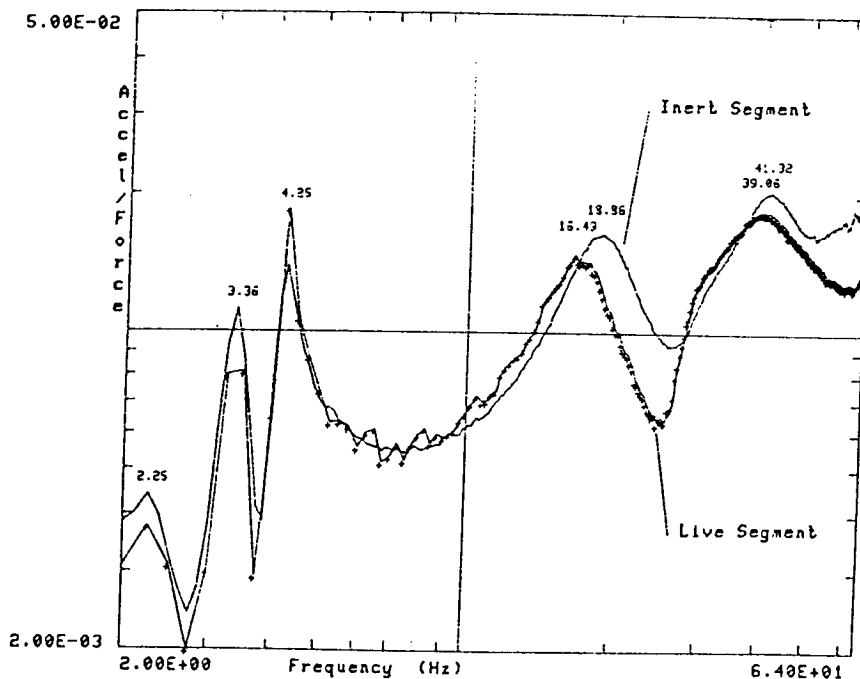
Figure 9. Comparison of frf for the inert and
live propellant segment tests indicates
the live propellant is more flexible.

163

Table 2. Modes identified in the center segment live propellant test.

Mode Number	Frequency (Hz)	Damping (C/Cr)	Mode Description
1	1.944	0.139	Rigid body pitch about bottom
2	3.198	0.068	Rigid body bounce
3	3.762	0.071	Rigid body pitch about top
4	4.752	0.036	Rigid body roll about top
5	14.647	0.210	Forward Oval (n=2,m=1)
6	16.726	0.174	Aft Oval (n=2,m=1)
7	28.163	0.097	Saddle (n=2,m=2)
8	29.131	0.177	Combined Forward Triangular and Saddle
9	38.634	0.209	Unclear mode
10	40.163	0.189	Aft Triangular and Case Bending
11	44.711	0.060	Case Bending mode
12	49.090	0.143	Propellant Axial
13	63.878	0.067	Propellant Axial
14	97.919	0.103	Local case mode

In both center segment modal surveys sinusoidal excitation was used to excite the segment to higher force levels to see if the modal frequencies, and possibly the propellant modulus, would change as a function of force. Additionally, mode shapes were computed using sine excitation for comparison to the results achieved using random excitation. Force patterns for tuning and exciting individual modes were computed from the random survey frf using the multivariate mode indicator approach [9,10]. This approach uses force patterns associated with each minimum of the indicator function. In the case of two closely spaced modes, the force pattern associated with the secondary indicator function was used. In general, the force patterns predicted by the indicator functions were quite good at isolating individual modes. Variations on these force patterns were also tried but were not found to offer any additional improvement.

The data from sinusoidal excitation of individual modes was acquired by holding the force pattern constant during a frequency sweep around the resonance. The force pattern was maintained via the closed loop control system, diagrammed in Figure 2. An incremental sine sweep was then performed, and frequency response functions were computed. The benefit of the short sweep as opposed to a single frequency dwell is that the direct estimate parameter estimation method could be used to further remove the effects of modes other than the one being tuned. Mode shape comparisons between the random and sine tests for the live segment are shown in Figures 10 and 11. These are two closely spaced modes with distinctly different shapes that occur near 29 Hz.
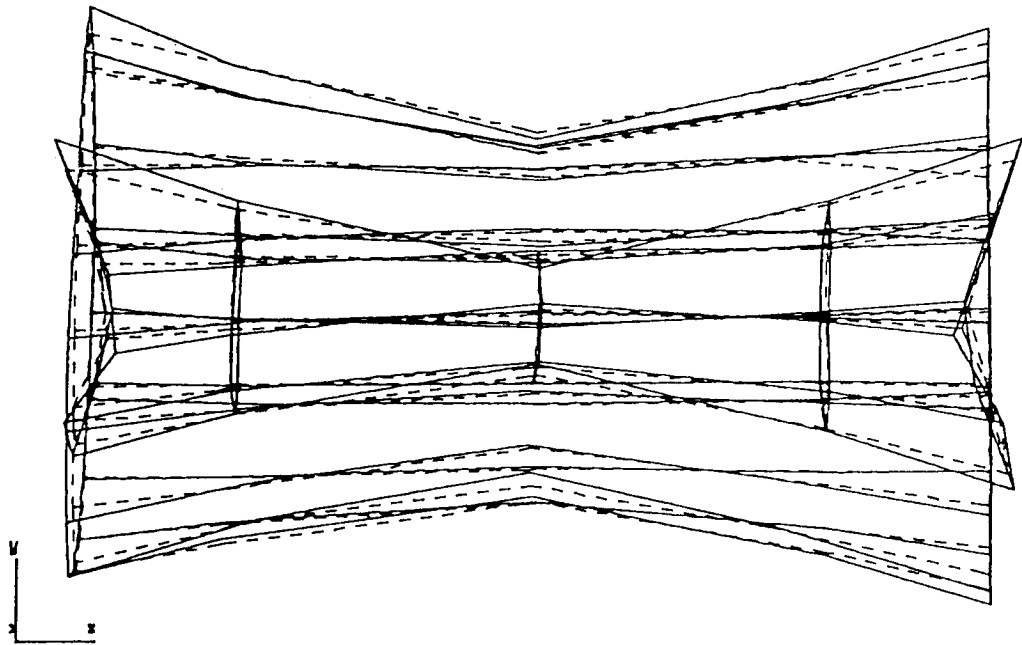
Figure 10. Comparison of 28.2 Hz saddle mode computed from sine and random excitation shows very good agreement.
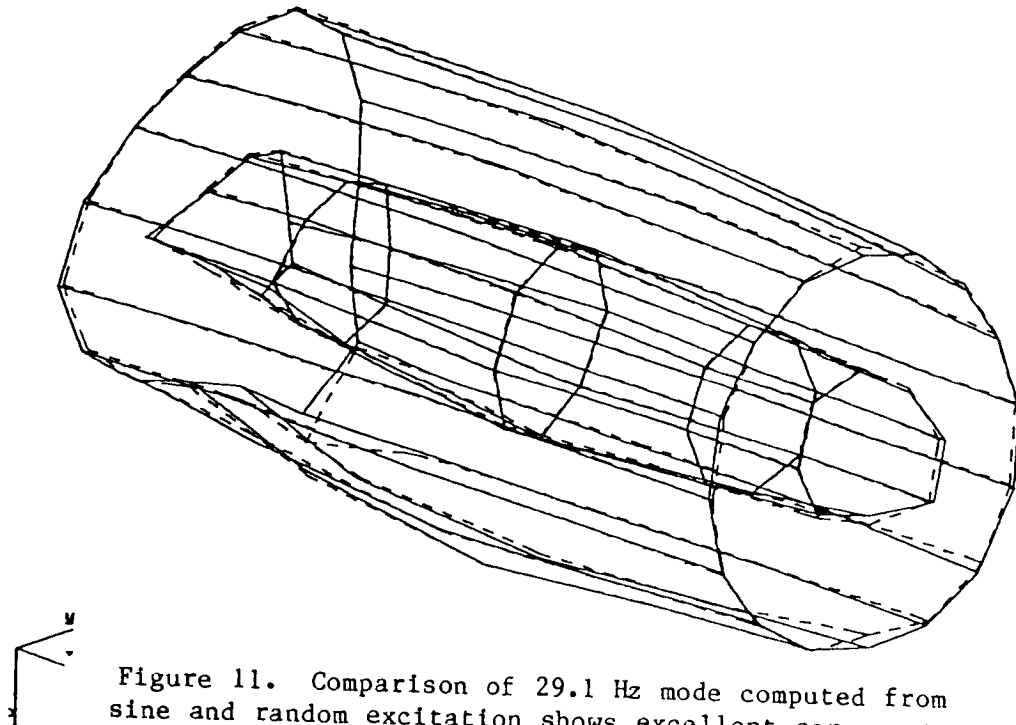
Figure 11. Comparison of 29.1 Hz mode computed from sine and random excitation shows excellent agreement.

After each mode was tuned and the frequency sweep completed, excitation was performed at several force levels to see if the mode frequency would change. Force levels from 50 pounds to 2000 pounds were used. Although frequency shifts

had been expected due to the nature of solid propellant, only minor changes on the order of 2% or less were observed.

The modal data from these two modal surveys was used in a correlation and system identification process that resulted in an updating of the finite element model. This part of the project and model update results will be documented in an upcoming paper [12]. As a result of these tests Morton Thiokol was able to obtain better agreement between propellant properties determined from RDS specimen testing and those determined from the model updating process. Three-dimensional models of the entire SRM, including joints, nozzle, and skirts, are being built and analyzed using the propellant modeling methods and properties that were identified as a result of these modal surveys.

SUMMARY AND CONCLUSIONS

The results of modal surveys performed on two SRM center segments show that single segment SRM case/ propellant modes can be defined using multiple input excitation on the segment case. These modes have damping on the order of 10% to 20% (equivalent viscous damping), which is characteristic of solid propellant articles. Accurate estimation of mode shapes from frequency response functions requires the use of a frequency domain estimation algorithm capable of representing residual modes. Although many pure propellant modes (modes with no case deflection) were predicted by the finite element model, very few were identified, even though a propellant excitation location was used. We conclude that these modes are extremely heavily damped and are not contributors to overall SRM behavior.

Close agreement in frequency and mode shape was found between sinusoidal and random excitation. Mode frequencies as a function of force level did not vary noticeably. Closed loop force control allowed a force pattern to be maintained during a sine sweep. Force patterns predicted using frf from the random survey via the multivariate mode indicator approach were successful in exciting individual modes using sine excitation and multiple exciters.

The results of this test were used to update finite element models, improve confidence in the results from RDS specimen testing, and improve the accuracy of full SRM models being used in the SRM redesign program.

REFERENCES

1. Hunt, D.L., and E.L. Peterson, "Multishaker Broadband Excitation for Experimental Modal Analysis," SAE, Aerospace Congress and Exposition, Long Beach, California, October, 1983.

2. Crowley, J.R., D.L. Hunt, G.T. Rocklin, and H. Vold, "The Practical Use of the Polyreference Modal Parameter Estimation Method," Third International Modal Analysis Conference, January, 1985.

3. Vold, H., J. Leuridan, "A Generalized Frequency Domain Matrix Estimation Method for Structural Parameter Identification," 7th Seminar on Modal Analysis Journal of AIAA, 1982.

4. Hunt, D.L., B. Wendler, and S. Soule, "A Normal Mode Identification Test Using Multiple Inputs," SAE, Aerospace Technology Conference & Exposition, Long Beach, California, October, 1985.

5. Chen, J.C., and D.L. Hunt, "Application of Multiple Input Random and Polyreference Analysis Techniques to the Galileo Spacecraft Modal Test," AIAA/ASME/ASCE/AHS, 25th Structures, Structural Dynamics & Materials Conference, Palm Springs, California, May, 1984.

6. Flanigan, C.F., "Test/Analysis Correlation of the STS Centaur Using Design Sensitivity and Optimization Methods," 5th International Modal Analysis Conference, April, 1987.

7. Kammer, D.C., "An Optimum Approximation for Residual Stiffness in Linear System Identification," presented at the 28th AIAA/ASME/ASCE/AHS SDM Conference, Monterey, California, April, 1987.

8. Kammer, D.C., "Test-Analysis Model Development Using an Exact Modal Reduction," submitted for publication to International Journal of Analytical and Experimental Modal Analysis.

9. Hunt, D.L., R. Williams, and J. Mathews, "A State-of-the-Art Implementation of Multiple Input Sine Excitation," 5th International Modal Analysis Conference, April, 1987.

10. Williams, R., J. Crowley, and H. Vold, "The Multivariate Mode Indicator Function in Modal Analysis," Third International Modal Analysis Conference, January, 1985.

11. Brillhart, R.D., and D.L. Hunt, "Computation of Total Response Mode Shapes Using Tuned Frequency Response Functions," Fourth International Modal Analysis Conference, Los Angeles, 1986.

12. Brillhart, R.D., D.L. Hunt, and D.C. Kammer, "Modal Survey and Test-Analysis Correlation of the Space Shuttle SRM," to be presented at the 6th International Modal Analysis Conference, Orlando, Florida, February, 1988.

A New Method to Real-Normalize Measured Complex Modes

Max L. Wei
Randall J. Allemang
Qiang Zhang
David L. Brown

A time domain subspace iteration technique is presented to compute a set of normal modes from the measured complex modes. By using the proposed method , a large number of physical coordinates are reduced to a smaller number of modal or principal coordinates. Subspace free decay time responses are computed using properly scaled complex modal vectors. Companion matrix for the general case of nonproportional damping is then derived in the selected vector subspace. Subspace normal modes are obtained through eigenvalue solution of the $[M_N]^{-1}[K_N]$ matrix and transformed back to the physical coordinates to get a set of normal modes. A numerical example is presented to demonstrate the outlined theory.

INTRODUCTION

Experimental modal analyses are carried out to extract a set of modal parameters from the measured time or frequency domain data of the structure under test. These identified eigenvectors are in general damped complex modes due to several possible reasons [1,2]:

1. The damping is nonproportional, i.e., [C] matrix is not proportional to [K] and [M] matrices.

2. Measurement errors due to mass loading effects, noise, nonlinearities, etc.

3. Digital signal processing errors due to finite frequency resolution, leakages, high modal density, and frequency response functions estimation procedure (H_1, H_2, H_v).

4. Modal parameter estimation errors due to invalid estimation of number of degrees of freedom.

Identified complex modes can be used directly in the applications of modal modeling, structural dynamic modification and sensitivity analysis[3,4], or validation and optimization of an analytical model[5,6]. On the other hand, real normal modes are sometimes more desired in the similar applications due to the facts that (i) normal modes are numerically easier to handle than complex modes and (ii) analysts usually computes normal modes rather than complex modes in the finite element analysis due to the lack of information of physical damping matrix. If normal modes are desired from a set of identified complex modes, a real-normalization procedure is needed to be implemented. Several methods have been proposed[7-13]in the past to derive normal modes from identified complex modes. In this paper, a time domain subspace iteration technique (an improved approach from the method described in Reference 12) developed by the Structural Dynamics Research Laboratory (SDRL) is proposed to real-normalize identified complex modes originated from systems with nonproportional damping.

THEORY AND FORMULATION: in the physical coordinates

Assume there exists a set of measured modal parameters from a modal test. These modal parameters consists of N complex modes (and their complex conjugates), λ_r, r=1,....,N and $\{\psi\}_r$, r=1,$\cdots$,N. Each modal vector has dimensions N_m and in general $N_m >> N$. To compute a set of normal modes from the given complex modes, a time-domain approach developed in the physical coordinates is formulated.

Formulation of Free Decay Time Responses

For the given modal parameters, displacement, velocity and acceleration responses can be expressed as

$$\{x(t)\} = \sum_{r=1}^{2N} \{\psi\}_r e^{\lambda_r t} \tag{1}$$

$$\{\dot{x}(t)\} = \sum_{r=1}^{2N} \lambda_r \{\psi\}_r e^{\lambda_r t} \tag{2}$$

$$\{\ddot{x}(t)\} = \sum_{r=1}^{2N} \lambda_r^2 \{\psi\}_r e^{\lambda_r t} \tag{3}$$

Computation of Companion Matrix [E]

The equations of motion for the general case of nonproportional damping is

$$\begin{bmatrix} [C] & [M] \\ [M] & [0] \end{bmatrix} \begin{Bmatrix} \dot{x}(t) \\ \ddot{x}(t) \end{Bmatrix} + \begin{bmatrix} [K] & [0] \\ [0] & -[M] \end{bmatrix} \begin{Bmatrix} x(t) \\ \dot{x}(t) \end{Bmatrix} = \begin{Bmatrix} [f] \\ [0] \end{Bmatrix} \tag{4}$$

Another form of the homogeneous Equation 4 can be written as

$$\begin{Bmatrix} \dot{x}(t) \\ \ddot{x}(t) \end{Bmatrix} = \begin{bmatrix} [0] & [I] \\ -[M]^{-1}[K] & -[M]^{-1}[C] \end{bmatrix} \begin{Bmatrix} x(t) \\ \dot{x}(t) \end{Bmatrix} \tag{5}$$

Let

$$[E] = \begin{bmatrix} [0] & [I] \\ -[M]^{-1}[K] & -[M]^{-1}[C] \end{bmatrix} \tag{6}$$

Equation 5 can then be written as

$$\{\dot{y}(t)\} = [E]\{y(t)\} \tag{7}$$

where $\{y(t)\}$ is now the system's state vector containing the displacement response $\{x(t)\}$ and velocity responses $\{\dot{x}(t)\}$

and [E] is called the companion matrix. In the physical coordinates, by repeating Equation (7) $2N_m$ time instants and dropping vector notation, the following equation is satisfied

$$[\dot{y}(t_1), \cdots, \dot{y}(t_{2N_m})] = [E][y(t_1), \cdots, y(t_{2N_m})] \tag{8}$$

where $t_1, t_2, \cdots, t_{2N_m}$ represent $2N_m$ time instants. From Equation 8, the companion matrix [E] can be computed

$$[E] = [\dot{Y}][Y]^{-1} \tag{9}$$

where [E], [Y] and [$\dot{Y}$] are all $2N_m \times 2N_m$ matrices.

Computation of Normal Modes

By computing the companion matrix [E], $[M]^{-1}[K]$ matrix gives the normal modes according to the eigenvalue solution

$$\left[[M]^{-1}[K]\right][\Phi] = \omega_r^2[\Phi], \quad r = 1, \cdots, N \tag{10}$$

In the physical coordinate, [Y] is always singular due to the number of measurement degrees of freedom N_m is much larger than the number of measured modes N. In other words, it is numerically difficult and unstable to solve [E] in the physical coordinates[7,11]. Therefore, it is proposed to compute the companion matrix [E] in the principal or modal coordinates in the following way.

NORMAL MODES SOLUTION: subspace iteration technique

Based on a set of identified complex modes, a time domain subspace iteration technique is developed to obtain a set of normal modes in the following way:

Hypothesis

Define $[\hat{\Phi}]$ = transformation matrix of the identified complex modal matrix [Ψ], it is assumed that [Ψ] can be expressed as

$$[\Psi] = [\hat{\Phi}][W] \tag{11}$$

where [W] is a $N \times N$ complex matrix and can be obtained through pseudo inverse technique

$$[W] = [\hat{\Phi}]^+[\Psi] \tag{12}$$

For the proposed method, the selection of the transformation matrix $[\hat{\Phi}]$ can not be arbitrary since it represents a N-dimensional subspace of the physical N_m-dimensional vector space from which the companion matrix $[E_N]$ and the normal modes are derived. Therefore, the following method to determine the transformation matrix $[\hat{\Phi}]$ is proposed and justified.

Determination of the Transformation Matrix $[\hat{\Phi}]$

Using the proposed method, it can be shown that choice of the $[\hat{\Phi}]$ has significant effects on the calculated normal modes. Since the transformation matrix $[\hat{\Phi}]$ can be considered as a N-dimensional vector subspace (column space of $[\hat{\Phi}]$), into which the physical system matrices and the identified complex modes are transformed, therefore, it must be so chosen such that the following conditions are satisfied:

1. $[\hat{\Phi}]$ must not be orthogonal to the normal modal matrix $[\Phi]$ of the undamped system, and

2. $[\hat{\Phi}]$ should be selected that it is as close to $[\Phi]$ as possible.

3. $[\hat{\Phi}]$ must has rank N.

A logical way to select $[\hat{\Phi}]$ is based on the identified complex modal matrix $[\Psi]$.

1. Fillod[14] proved that if the complex modal vector is normalized according to the following equation

$$2\lambda_r\{\psi\}_r^T[M]\{\psi\}_r + \{\psi\}_r^T[C]\{\psi\}_r = 2j\omega_r \qquad (13)$$

,the imaginary part of $\{\psi\}_r$ is minimized. This indicates that the real part of $\{\psi\}_r$ is maximized and contains maximum useful information of the identified complex modes.

2. It can be proved (see Appendix) that if a undamped system is perturbated to the first order by a nonproportional damping matrix, and the calculated complex modes are normalized according to Equation 13, then the real parts of the normalized complex modes are very close to the normal modes of the undamped system.

3. The transformation matrix obtained by taking the real part of a set of complex modes normalized according to Equation 13, has rank N due to the fact that (i) the identified complex modes are independent of each other, and (ii) norms of the columns of $[\hat{\Phi}]$ have the same order of magnitude, i.e, eigenvalues found in Equation 19 using singular value decomposition technique also have the same order of magnitude.

From the above observations, it can be concluded that real part of the complex modes normalized to $2j\omega_r$ according to Equation 13 is the best choice of the transformation matrix $[\hat{\Phi}]$.

Computation of Free Decay Time Responses in Subspace

In order to derive the companion matrix $[E_N]$ in the selected subspace $[\hat{\Phi}]$, free decay time responses in the physical coordinates needs to be transformed into the selected vector subspace using one of the following two approaches:

Modal Space Approach

The displacement vectors in the physical and modal coordinate systems are related by the following transformation:

172

$$\{x(t)\} = [\hat{\Phi}]\{p(t)\} \tag{14}$$

or

$$\{p(t)\} = [\hat{\Phi}]^+\{x(t)\} \tag{15}$$

where $[\hat{\Phi}]^+$ is the pseudo inverse of $[\hat{\Phi}]$.

Substitute Equation 1 and 11 into 15, for the given modal parameters, free decay displacement in the modal coordinate can be written as

$$\begin{aligned}\{p(t)\} &= [\hat{\Phi}]^+ 2\operatorname{Re}\{[\Psi]\{e^{\lambda t}\}\}\\ &= 2[\hat{\Phi}]^+[\Phi]\operatorname{Re}\{[W]\{e^{\lambda t}\}\}\\ &= 2\operatorname{Re}\{[W]\{e^{\lambda t}\}\}\end{aligned} \tag{16}$$

where "Re" represents the real part of a matrix.

Similarly, velocity and acceleration responses in the modal coordinates can be expressed as

$$\{\dot{p}(t)\} = 2\operatorname{Re}\{[W]\{\lambda e^{\lambda t}\}\} \tag{17}$$

$$\{\ddot{p}(t)\} = 2\operatorname{Re}\{[W]\{\lambda^2 e^{\lambda t}\}\} \tag{18}$$

Principal Response Analysis (PRA) Approach

Using singular value decomposition technique and assuming $[\hat{\Phi}]$ has full rank N, $[\hat{\Phi}]$ can be decomposed as

$$[\hat{\Phi}] = [P]\,\lceil\Sigma\rfloor\,[S]^H \tag{19}$$

where

$[P]$ = orthonormal matrix $(N_m \times N)$
$\lceil\Sigma\rfloor$ = diagonal matrix consists of
  eigenvalues of $[\hat{\Phi}]^H[\hat{\Phi}]$ $(N \times N)$
$[S]$ = unitary matrix consists of
  eigenvectors of $[\hat{\Phi}]^H[\hat{\Phi}]$ $(N \times N)$

Using matrix [P] as the transformation matrix, displacement in the physical coordinates can be transformed into the principal coordinates according to

$$\{x(t)\} = [P]\{p(t)\} \tag{20}$$

or

$$\{p(t)\} = [P]^H\{x(t)\} \tag{21}$$

Substitute Equation 1 and 19 into Equation 21, $\{p(t)\}$ can be expressed as

$$\begin{aligned}
\{p(t)\} &= [P]^H 2 \, \mathrm{Re}\{[\Psi]\{e^{\lambda t}\}\} \\
&= 2 [P]^H [\hat{\Phi}] \, \mathrm{Re}\{[W]\{e^{\lambda t}\}\} \\
&= 2 [P]^H [P] \, \lceil \Sigma_\rfloor [S]^H \, \mathrm{Re}\{[W]\{e^{\lambda t}\}\} \\
&= 2 \, \lceil \Sigma_\rfloor [S]^H \, \mathrm{Re}\{[W]\{e^{\lambda t}\}\}
\end{aligned} \tag{22}$$

Similarly, velocity and acceleration responses can be written as

$$\{\dot{p}(t)\} = 2 \, \lceil \Sigma_\rfloor [S]^H \, \mathrm{Re}\{[W]\{\lambda e^{\lambda t}\}\} \tag{23}$$

$$\{\ddot{p}(t)\} = 2 \, \lceil \Sigma_\rfloor [S]^H \, \mathrm{Re}\{[W]\{\lambda^2 e^{\lambda t}\}\} \tag{24}$$

Computation of companion matrix $[E_N]$

Similar to the derivations (Equation 4 to Equation 6) in the physical coordinates, the companion matrix E_N can be computed in the selected vector subspace using the time responses in equations 16-18 (modal space approach) or 22-24 (PRA approach)

$$\{q(t)\} = [E_N]\{\dot{q}\} \tag{25}$$

where $\{q(t)\}$ is now the system's state vector in the selected subspace containing the displacement response $\{p(t)\}$ and velocity responses $\{\dot{p}(t)\}$, and

$$[E_N] = \begin{bmatrix} [0] & [I] \\ -[M_N]^{-1}[K_N] & -[M_N]^{-1}[C_N] \end{bmatrix} \tag{26}$$

where $[M_N]$, $[K_N]$ and $[C_N]$ are the reduced system mass, stiffness and damping matrix respectively and can be written as

$$[M_N]_{N \times N} = [\hat{\Phi}]^T [M] [\hat{\Phi}] \quad \text{(modal space)} \tag{27a}$$
$$[M_N]_{N \times N} = [P]^H [M] [P] \quad \text{(PRA)} \tag{27b}$$

$$[K_N]_{N \times N} = [\hat{\Phi}]^T [K] [\hat{\Phi}] \quad \text{(modal space)} \tag{28a}$$
$$[K_N]_{N \times N} = [P]^H [K] [P] \quad \text{(PRA)} \tag{28b}$$

$$[C_N]_{N \times N} = [\hat{\Phi}]^T [C] [\hat{\Phi}] \quad \text{(modal space)} \tag{29a}$$
$$[C_N]_{N \times N} = [P]^H [C] [P] \quad \text{(PRA)} \tag{29b}$$

174

Once $\{q(t)\}$ and $\{\dot{q}(t)\}$ are computed at 2N time instants, companion matrix $[E_N]_{2N \times 2N}$ can then be computed in the modal or principal coordinates accordingly

$$[\dot{q}(t_1), \cdots, \dot{q}(t_{2N})] = [E_N][q(t_1), \cdots, q(t_{2N})] \tag{30}$$

and

$$[E_N] = [\dot{Q}][Q]^{-1} \tag{31}$$

Since $[Q]$ is a matrix with full rank 2N, it is always invertible.

Computation of Normal modes: first iteration

From the companion $[E_N]$, the N by N $[M]^{-1}[K]$ matrix gives the normal mode solutions $[\Phi]$ in the modal or principal coordinates according to the eigenvalue solution

$$\left[[M_N]^{-1}[K_N]\right][\Phi] = \Omega_r^2 [\Phi], \quad r = 1, \cdots, N \tag{32}$$

where Ω_r is the r-th undamped natural frequency.

From the modal space method, it is noticed that (i) if $[\hat{\Phi}]$ is selected as the normal modal matrix $[\Phi]$ of the undamped system, then $[M_N]$, $[K_N]$ and consequently, $[M_N]^{-1}[K_N]$ are all diagonal matrices by the orthogonality conditions, and (ii) Generalized damping matrix $[C_{gen}]$ can also be obtained from the companion matrix $[E_N]$ as $[M_N]^{-1}[K_N]$. Generalized damping matrix is defined as

$$[C_{gen}] = [\Phi]^T [C] [\Phi] \tag{33a}$$

and $[\Phi]$ must also satisfies the following relationship

$$[\Phi]^T [M] [\Phi] = [I] \tag{33b}$$

First estimation of the normal modes $\{\psi\}_r, r=1, \cdots, N$ of the undamped system can then be obtained through the coordinate transformation

$$[\Phi_1] = [\hat{\Phi}][\Phi] \quad (modal \ space) \tag{34a}$$

or

$$[\Phi_1] = [P][\Phi] \quad (PRA) \tag{34b}$$

where $[\Phi_1]$ is the first estimation of the normal modal matrix.

In order to improve (if possible) and check the accuracy of $[\Phi_1]$, $[\Phi_1]$ is compared with $[\hat{\Phi}]$ column by column to check the convergence. If not convergent, then $[\Phi_1]$ will substitute $[\Phi]$ in Equation 11,14 and 19 and a new iteration will start to find a $[\Phi_2]$. This process continues until $[\Phi_m]$ converges to $[\Phi_{m-1}]$, where m is the number of iterations. In general, m is usually 2 or 3, i.e., the transformation matrix $[\hat{\Phi}]$ converges very fast because all iterations are done in the same vector subspace which is defined by the initially estimated transformation matrix $[\hat{\Phi}]$.
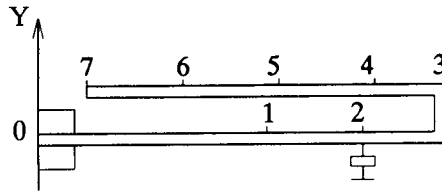
Figure 1. Folded Beam Used as Test Structure

CASE STUDY

The proposed method is applied to the identified complex modes of a simple structure as shown in Figure 1 (For comparisons, this example is the same as the one presented in Reference 11). This structure is a folded beam excited on its bending modes along the y axis. Its dynamic characteristics shows the existence of pairs of eigenvectors at very closely spaced eigenvalues (quasi multiplicity of order 2). The eigenvectors are described by seven measurement degrees of freedom as indicated in Figure 1. The first two complex modes are identified from a set of frequency response functions measured using slow sine sweep excitation technique. The identified complex modes scaled according to Equation 13 are listed in Table 1. The companion matrices $[E_N]$ calculated in the selected subspace using both the modal space and the PRA approaches are listed in Table 2. Two undamped natural frequencies and their corresponding normal modes based on the proposed method and the three methods proposed in Reference 11 are listed in Table 3. Modal Assurance Criteria (MAC)[15] are computed for these two normal modes between those obtained from the proposed method and those obtained from the methods described in Reference 11.

From Table 3, both the modal space and the PRA approaches calculate the same undamped natural frequencies and normal modes of the associated undamped system.

From Table 2, companion matrix $[E_N]$ obtained from the second iteration of the modal space approach shows (i) the $[M_N]^{-1}[K_N]$ matrix is fairly diagonalized and (ii) the $[M_N]^{-1}[C_N]$ matrix is fairly symmetrical. These indicate that the calculated normal modes are very close to the true real modes of the associated undamped system. Therefore, the calculated $[M_N]^{-1}[C_N]$ matrix listed in Table 5 is also very close to the generalized damping matrix derived in Reference 11.

From Table 3 and 4, two normal modes derived from the proposed method stay very close to those derived in Reference 11.

TABLE 1. Measured Complex modes

Point No.	First Mode $\lambda_1 = -1.992 + j\ 209.55$		Second Mode $\lambda_2 = -2.547 + j\ 213.40$	
	real	imaginary	real	imaginary
1	-0.144	0.118	0.266	.0683
2	-0.303	0.203	0.457	0.138
3	-0.498	0.267	0.598	0.228
4	-0.179	0.231	0.519	0.0847
5	0.210	0.207	0.464	-0.0942
6	0.618	0.192	0.433	-0.280
7	1.060	0.192	0.416	-0.483

TABLE 2. Calculated Companion Matrix $[E_N]$

Iteration No.	Modal Space Approach				PRA Approach			
1	0.0000	0.0000	1.0000	0.0000	0.0000	-.0001	1.0000	0.0000
	0.0000	0.0001	0.0000	1.0000	0.0000	0.0000	0.0000	1.0000
	-43507.2	-120.312	-3.7156	4.3521	-43970.09	-1182.15	-0.8233	2.9472
	-117.281	-45973.5	4.3826	-5.3629	-796.414	-45510.59	2.0166	-8.2553
2	0.0000	-.0001	1.0000	-.0000	-.0000	0.0001	1.0000	0.0000
	0.0000	0.0000	0.0000	1.0000	0.0000	-.0000	0.0000	1.0000
	-43501.49	0.0000	-4.1383	4.3492	-43921.51	-1142.37	-0.9521	3.1301
	-0.0156	-45979.18	4.5045	-4.9402	-756.586	-45559.18	2.1995	-8.1294

TABLE 3. Calculated Normal Modes

Point No.	First Mode					Second Mode				
	Method 1	Method 2	Method 3	Modal Spa.	PRA	Method 1	Method 2	Method 3	Modal Spa.	PRA
	natural frequency (rad/sec)					natural frequency (rad/sec)				
	208.38	208.59	208.68	208.58	208.58	214.22	214.45	214.32	214.43	214.43
1	.161	.153	.153	.151	.151	.458	.454	.454	.451	.451
2	.333	.312	.318	.312	.312	.774	.769	.771	.771	.771
3	.535	.506	.515	.506	.506	1.0	1.0	1.0	1.0	1.0
4	.215	.198	.200	.196	.196	.905	.890	.892	.889	.889
5	.169	.179	.178	.181	.181	.867	.830	.836	.827	.827
6	.571	.572	.577	.574	.574	.873	.810	.826	.815	.815
7	1.0	1.0	1.0	1.0	1.0	.901	.82	.832	.815	.815

TABLE 4. MAC for the Calculated Normal Modes

Modal Assurance Criteria						
	First Mode			Second Mode		
	Method 1	Method 2	Method 3	Method 1	Method 2	Method 3
PRA	.999122	.9999906	.9999941	.998605	.999992	.999913

TABLE 5. Generalized Damping Matrix $[C_{gen}]$

Method 2		Method 3		Proposed Method	
4.86	-4.72	4.14	-4.27	4.14	-4.35
-4.72	5.50	-4.27	4.94	-4.50	4.94

CONCLUSION

The proposed method described in this paper has the following advantages:

1. This method is numerically very efficient and stable because all computations are performed in the selected vector subspace and it requires very few iterations.

2. Since this method uses a time domain approach, it can be proved that the calculated normal modes are not sensitive to the norm or scaling errors existing in the identified complex modes.

The drawbacks of this method are:

1. It can not improve the norm or scaling errors existing in the identified complex modes.

2. The calculated normal modes are subject to modal truncation errors since an incomplete set of modes are identified.

It can be concluded that the success of the proposed method is dependent on the selection of the transformation matrix $[\hat{\Phi}]$ and the quality of the measured complex modes. It seems to be a reliable method that can be used as a post-processing procedure of the identified complex modes for further applications.

REFERENCES

[1] Deblauwe, F., Allemang, R. J., "A Possible Origin of Complex Modal Vectors", Proceedings of the 11th International Seminar on Modal Analysis, K. U. L., Leuven, September 1986, pp. A2-3

[2] Hopton, G. W., Deblauwe, F., "Relationships between Analysis Errors and Complex Mode Shapes", Proceedings of the 5th International Modal Analysis Conference, London, 1987, pp. 381-388

[3] O'Callahan, J., Avitable, P.,"A Structural Modification Procedure Using Complex Modes", Proceedings of the 1st International Modal Analysis Conference, Orlando, Florida, 1983, pp. 418-422

[4] Vanhonacker, P., "Sensitivity Analysis of Mechanical Structures, Based on Experimentally Determined Modal Parameters", Proceedings of the 1st International Modal Analysis Conference, Orlando, Florida, 1983, pp. 534-541

[5] Ibrahim, S. R., "Dynamic Modeling of Structures from Measured Complex Modes", AIAA Journal, Vol. 21, No. 6, 1982

[6] Heylen, I. W., "Model Optimization with Measured Modal Data by Mass and Stiffness Changes", Proceedings of the 4th International Modal Analysis Conference, Los Angeles, CA., 1986, pp. 94-100

[7] Ibrahim, S. R., "Computation of Normal Mode from Identified Complex Modes", AIAA Journal, Vol. 21, No. 6, 1983

[8] Natke, H. G., Rotert,D., "Determination of Normal Modes from Identified Complex Modes", Z. Fluguiss, Weltranmforsch, 9, 1985, Heft 2, pp. 82-88

[9] SDRC, "User Manual for Modal Analysis", Version 9.0, 1985, Section 6.2.5

[10] Zhang,Q.,Lallement G., "New Method of Determining the Eigensolutions of the Associated Conservative Structure from the Identified Eigensolutions", Proceedings of the 3rd International Modal Analysis Conference", Orlando, Florida, 1985, pp. 322-328

[11] Zhang, Q., Lallement, G., "Comparison of Normal Eigenmodes Calculation Methods based on Identified Complex Eigenmodes", J. of Spacecraft, Jan.-Feb., 1987, pp. 69-73

[12] Wei, M. L., Allemang, R. J., Brown, D. L., "Real-Normalization of Measured Complex Modes", Proceedings of the 5th International Modal Analysis Conference, London, 1987, pp. 708-712

[13] Zhang, Q., Lallement, G., "Simultaneous Determination of Normal Modes and Generalized Damping Matrix from Complex Modes", Proceedings of the 2nd ISASD, Aachen, Germany, April 1-3, 1985

[14] Fillod, R., "Contribution on Identification of Linear Mechanical Structure", Doctor of Sciences Physics Dissertation, University of Besançon , France, 1980

[15] Allemang, R. J., Brown, D. L., "A Correlation Coefficient for Modal Vector Analysis", Proceedings of the 1st International Modal Analysis Conference, Orlando, Florida, 1982, pp. 110-116

APPENDIX

The characteristics equations of a undamped and a damped system can be written as

$$[K][\Phi] - [M][\Phi] \ulcorner \Omega^2 \lrcorner = 0.$$ (35)

$$[M][\Psi] \ulcorner \Lambda^2 \lrcorner + [C][\Psi] \ulcorner \Lambda \lrcorner + [K][\Psi] = 0$$ (36)

It can be proved that in the case of a lightly damped system, i.e, $[C] = \varepsilon [\underline{C}]$, where ε is a small perturbation parameter, the natural frequencies and the normal modes of the associated undamped system can be approximated by taking the damped natural frequencies and the real part of the complex modal vectors respectively.

Assuming:

$$[\Phi]^T [\underline{C}][\Phi] = [\Gamma]$$ (37)

$$\ulcorner \Lambda \lrcorner = j \ulcorner \Omega \lrcorner + \varepsilon \ulcorner U \lrcorner$$ (38)

$$[\Psi] = [\Phi] \left[[I] + \varepsilon j [V] \right]$$ (39)

and recalling that complex modal vectors satisfy the following orthogonality conditions: (Note that both the Equation 13 and 40 are scaled to $2j\,\omega$)

$$[\Psi]^T[M][\Psi] \ulcorner \omega \lrcorner + \ulcorner \omega \lrcorner [\Psi]^T[M][\Psi] + \varepsilon [\Psi]^T[\underline{C}][\Psi] = 2j \ulcorner \omega \lrcorner \tag{40}$$

$$[\Psi^*]^T[M][\Psi] \ulcorner \omega \lrcorner + \ulcorner \Lambda^* \lrcorner [\Psi^*]^T[M][\Psi] + \varepsilon [\Psi^*]^T[\underline{C}][\Psi] = 0 \tag{41}$$

where "*" represents the complex conjugate of a matrix.

Substitute Equation 35,36 and 37 into Equation 40 and 41, equating the first order terms of ε:

$$[\Gamma] = -2 \ulcorner U \lrcorner + \ulcorner \Omega \lrcorner [V + V^T] + [V + V^T] \ulcorner \Omega \lrcorner \tag{42}$$

$$[\Gamma] = -2 \ulcorner U \lrcorner + \ulcorner \Omega \lrcorner [V - V^T] + [V - V^T] \ulcorner \Omega \lrcorner \tag{43}$$

and then

$$[\Gamma] = -2 \ulcorner U \lrcorner + [V] \ulcorner \Omega \lrcorner + \ulcorner \Omega \lrcorner [V]^T \tag{44}$$

$$0 = \ulcorner \Omega \lrcorner [V] + [V]^T \ulcorner \Omega \lrcorner \tag{45}$$

From Equation 45, the matrix $\ulcorner \Omega \lrcorner [V]$ is anti-symmetrical, therefore the diagonal elements of this matrix are all zero.

Since $[\Gamma]$ is a real matrix. From Equation 44, it can be concluded that:

1. $\ulcorner U \lrcorner$ is a real diagonal matrix. This indicates that the effect of the first order perturbation damping matrix on the eigenvalues is purely real.

2. $[V]$ is a real matrix. This indicates that the effect of the first order perturbation damping matrix on the eigenvectors is purely imaginary.

The Matrix Exponential in Transient Structural Analysis

Levon Minnetyan

The primary usefulness of the presented method is in the ability to represent the effects of high frequency linear response with accuracy, without requiring very small time steps in the analysis of dynamic response. The matrix exponential contains a series approximation to the dynamic model. However, unlike the usual modal analysis procedure which truncates the high frequency response, the approximation in the exponential matrix solution is in the time domain. By truncating the series solution to the matrix exponential short, the solution is made inaccurate after a certain time. Yet, up to that time the solution is extremely accurate, including all high frequency effects. By taking finite time increments, the exponential matrix solution can compute the response very accurately. .Use of the exponential matrix in structural dynamics is demonstrated by simulating the free vibration response of multi degree of freedom models of cantilever beams.

INTRODUCTION

The matrix exponential has been known in matrix theory as a method of solution for systems of differential equations. However, it has not been applied to the solution of structural dynamics problems. This method may be useful in some types of structural problems where modal decomposition is not practical or the number of modal vectors that can be accurately determined do not represent the true structural response. The matrix exponential contains a series approximation to the dynamic model. However, unlike the usual modal analysis procedure which truncates the high frequency response, the approximation in the exponential matrix solution is in the time domain. The exponential matrix method simulates the complete structural response, including the high frequency effects, but only for not too large values of the time parameter t. These properties make the exponential matrix method ideally suitable to complement the direct time-history integration of the equations of motion; to improve accuracy and to increase the integration stepsize. An updated Lagrangian formulation may be used at each integration step to recompute the matrix exponential with reference to the current state variables.

MATHEMATICAL BACKGROUND

Before examining the implementation of the matrix exponential in the solution of structural dynamics equations, it is helpful to consider the homogeneous systems of differential equations.

$$[\dot{X}] = [A][X] \tag{1}$$

with the initial conditions

$$[X(0)] = [I] \tag{2}$$

where $[A]$ is an $n \times n$ constant matrix, $[X]$ is an $n \times n$ matrix, the columns of which are individual unknown vectors and $[I]$ is the $n \times n$ identity matrix. It can be shown that the fundamental solution $[X]$ to Eq. (1) can be written as [1]

$$[X] = e^{[A]t} = \sum_{k=0}^{\infty} \frac{1}{k!} [A]^k t^k \tag{3}$$

where

$$[A]^k = [A] \cdots [A] \quad (k \ terms) \tag{4}$$

It can also be shown that the infinite series given by Eq. (3) converges uniformly and absolutely for t in any bounded interval [1]. Eq. (3) is referred to as the exponential matrix function.

To summarize the use of the matrix exponential in structural dynamics consider the equations of motion of a structure, written in the physical coordinates:

$$[M]\{\ddot{x}\} + [C]\{\dot{x}\} + [K]\{x\} = \{F(t)\} \tag{5}$$

where the symbols have their usual meanings. By defining

$$\left\{ \begin{array}{c} y_1 \\ y_2 \end{array} \right\} = \left\{ \begin{array}{c} x \\ \dot{x} \end{array} \right\} \tag{6}$$

the equations of motion, Eq. (5), can be writttten as a system of first order differential equations as

$$\left\{ \begin{array}{c} \dot{y}_1 \\ \hline \dot{y}_2 \end{array} \right\} = \left[\begin{array}{c|c} [0] & [I] \\ \hline -[M]^{-1}[K] & -[M]^{-1}[C] \end{array} \right] \left\{ \begin{array}{c} y_1 \\ \hline y_2 \end{array} \right\} + \left\{ \begin{array}{c} \{0\} \\ \hline [M]^{-1}\{F(t)\} \end{array} \right\} \tag{7}$$

or in short notation redefining new symbols for the overall matrices and vectors in Eq. (7), we represent them as

$$\{\dot{y}\} = [A]\{y\} + \{f(t)\} \tag{8}$$

Introducing a new unknown vector $\{z(t)\}$, defined by the equation

$$\{y(t)\} = [X(t)]\{z(t)\} \tag{9}$$

182

where $[X(t)]$ is the fundamental solution defined by Eqns. (1) and (3), we can write the time derivative of $\{y\}$ as

$$\{\dot{y}\} = [\dot{X}]\{z\} + [X]\{\dot{z}\} \tag{10}$$

Substituting Eq. (10) into Eq. (8):

$$[\dot{X}]\{z\} + [X]\{\dot{z}\} = [A][X]\{z\} + \{f\} \tag{11}$$

Combining Eq. (1) with Eq. (11) we obtain

$$[X]\{\dot{z}\} = \{f\} \tag{12}$$

The solution of which can be written as [1]

$$\{z(t)\} = \{z(0)\} + \int\limits_0^t [X(\tau)]^{-1}\{f(\tau)\}d\tau \tag{13}$$

and consequently

$$\{y(t)\} = [X(t)]\{y(0)\} + [X(t)]\int\limits_0^t [X(\tau)]^{-1}\{f(\tau)\}d\tau \tag{14}$$

with $\{z(0)\} = \{y(0)\}$ since $\{y\} = [X]\{z\}$ and $[X(0)] = [I]$. It can be shown that

$$[X(t)][X(\tau)]^{-1} = [X(t-\tau)] \tag{15}$$

if the matrix $[A]$ is independent of t. Thus

$$\{y(t)\} = [X(t)]\{y(0)\} + \int\limits_0^t [X(t-\tau)]\{f(\tau)\}d\tau \tag{16}$$

where $\{y(t)\}$ is the list of structural coordinate displacements and velocities as defined by Eq. (6)

EXAMPLES

Eq. (16) would give the correct solution for all t if the structure properties were independent of t and if $[X(t)]$ could be computed with sufficient accuracy. In general, it is not practical to compute $[X(t)]$ to a sufficient level of accuracy for Eq. (16) to be valid for all t. However, if t is not large, then Eq. (16) is expected to yield good results with relatively crude approximations of $[X(t)]$. For example, Fig. 1 shows a comparison of the true free vibration response of a single degree of freedom system with the response computed by Eq. (16) when only 4 terms are included in Eq. (3). Eq. (16) matches the true response exactly, but only for approximately 1/2 period of vibration. Fig. 2 shows the same comparison when 16 terms are included in Eq. (3). In this case the exact simulation lasts for two periods of vibration.
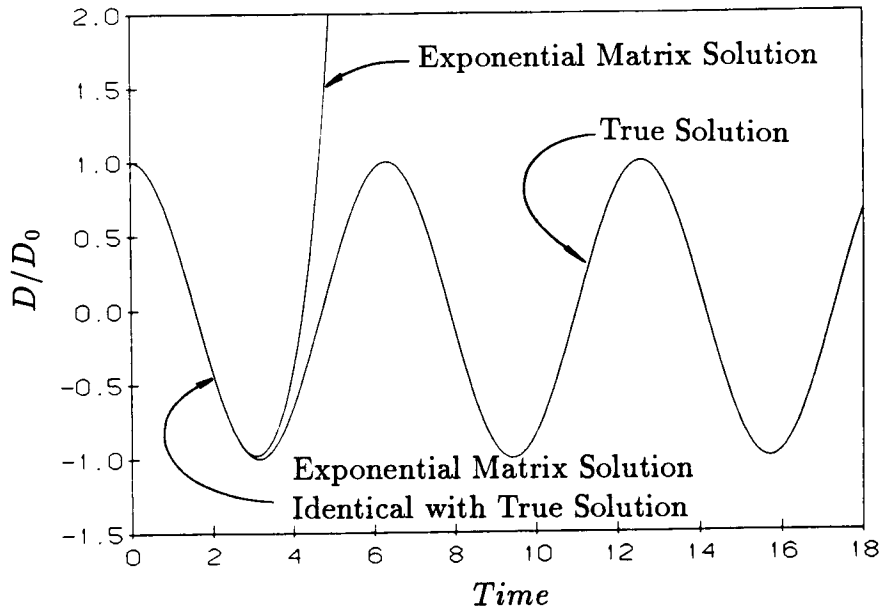
Fig. 1.– Free Vibration Response of a Simple Oscillator
(exponential series truncated after 4 terms)
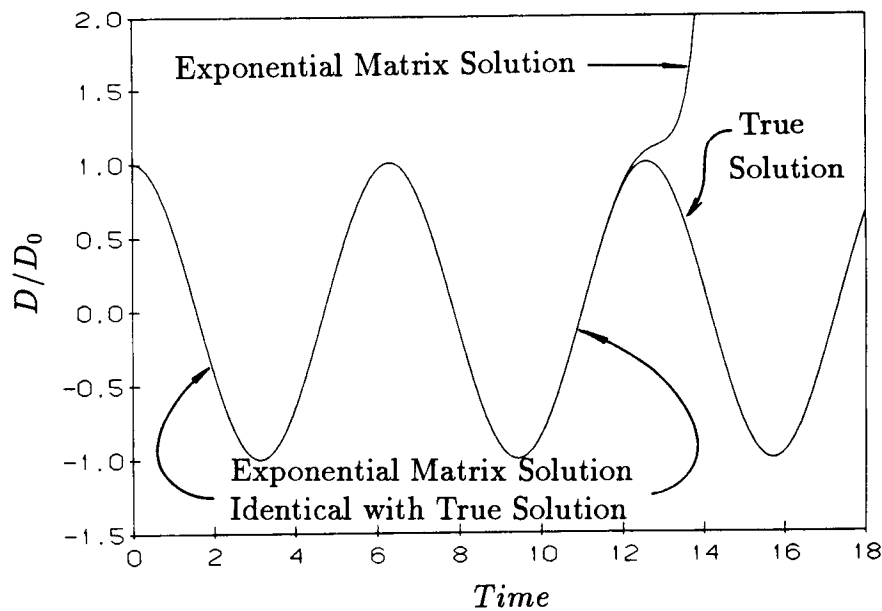
Fig. 2.– Free Vibration Response of a Simple Oscillator
(exponential series truncated after 16 terms)

Example with Two Degrees of Freedom

As a two-degree-of-freedom physical example, consider a steel cantilever beam, two meters long, with a 0.1 meter square cross section, with discretized degrees of freedom as numbered in Fig. 3.

184
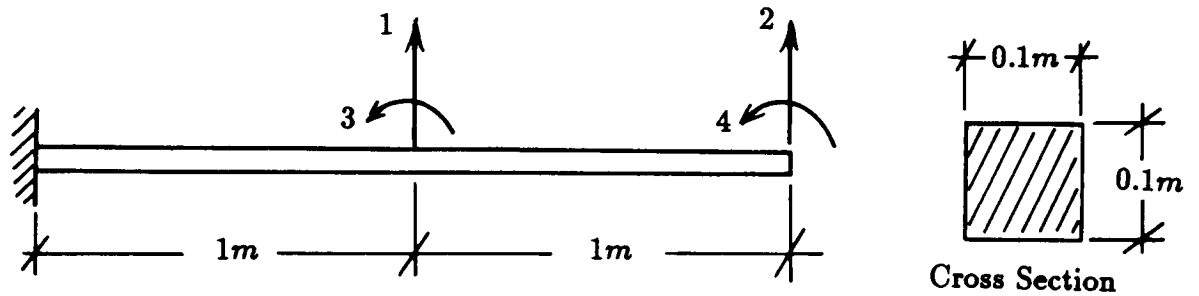
Fig. 3.– Example Beam with Coordinates

The stiffness matrix for the numbered coordinates is assembled from beam element stiffnesses as:

$$[K] = EI \begin{bmatrix} 24 & -12 & | & 0 & 6 \\ -12 & 12 & | & -6 & -6 \\ --- & --- & - & --- & --- \\ 0 & -6 & | & 8 & 2 \\ 6 & -6 & | & 2 & 4 \end{bmatrix} \tag{17}$$

Or, we can represent the stiffness matrix $[K]$ in terms of the submatrices as outlined by the dashed lines in Eq. (17) as

$$[K] = \begin{bmatrix} K_{11} & | & K_{12} \\ --- & - & --- \\ K_{21} & | & K_{22} \end{bmatrix} \tag{18}$$

Using matrix condensation [2], the condensed stiffness matrix $[K^*]$ corresponding to the first two coordinates is written as:

$$[K^*] = [K_{11}] - [K_{12}][K_{22}]^{-1}[K_{21}] \tag{19}$$

or

$$[K^*] = \frac{EI}{7} \begin{bmatrix} 96 & -30 \\ -30 & 12 \end{bmatrix} \tag{20}$$

Substituting $E = 200GPa$ for steel and dropping the star from our notation for the condensed stiffness matrix, we obtain the stiffness matrix for the structure degree-of-freedom coordinates shown in Fig. 4 as

$$[K] = \frac{20 \times 10^6}{(7)(12)} \begin{bmatrix} 96 & -30 \\ -30 & 12 \end{bmatrix} N/m \tag{21}$$

C - 3

185
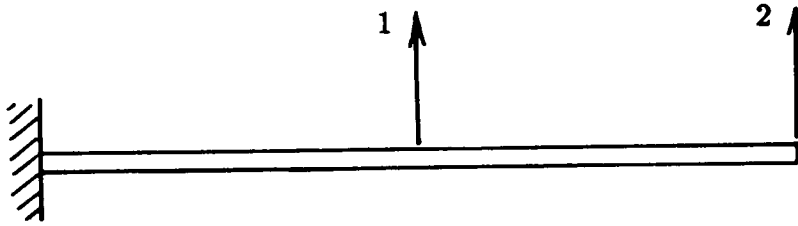
Fig. 4.– Coordinate numbering with condensed degrees-of-freedom

Substituting $\rho = 8,000 kg/m^3$ for the mass density of steel and considering only the transverse inertia of the beam, the lumped mass matrix for the two coordinates shown in Fig. 4 is written as:

$$[M] = \begin{bmatrix} 80 & 0 \\ 0 & 40 \end{bmatrix} kg \tag{22}$$

Substituting these values for $[M]$ and $[K]$ in Eq. (5) and assuming that $[C]$ and $\{f\}$ are null, we define the undamped free vibration problem for this cantilever beam as:

$$\begin{bmatrix} 80 & 0 \\ 0 & 40 \end{bmatrix} \begin{Bmatrix} \ddot{x}_1 \\ \ddot{x}_2 \end{Bmatrix} + 10^6 \begin{bmatrix} 22.86 & -7.143 \\ -7.143 & 2.857 \end{bmatrix} \begin{Bmatrix} x_1 \\ x_2 \end{Bmatrix} = \begin{Bmatrix} 0 \\ 0 \end{Bmatrix} \tag{23}$$

The time history response due to a set of initial conditions can be obtained by a direct numerical integration procedure, such as the central difference method. In the following examination the central difference method is used to compare the performance of various exponential matrix solutions.

Fig. 5 shows a comparison of the exact solution and a single step exponential matrix solution for the free vibration response of this example. In Fig. 5, only the first fifteen terms are included for the series solution of the matrix exponential as defined in Eq. (3). Fig. 6 shows the same comparison between the one step exponential matrix solution and the exact solution, but in this case thirty terms are used in the series definition of the matrix exponential. The solution depicted in Fig. 6 follows the exact solution for twice the time length as compared to the solution shown in Fig. 5, demonstrating the linear convergence of the exponential series. It is significant that the exponential matrix solution is identical to the true solution until very close to the divergence time. A second interesting point is that the simulation for both physical coordinates diverges simultaneously but in opposite directions. Fig. 7 shows the same comparison but considering twenty-nine terms in the series solution. When Fig. 7 is compared to Fig. 6, it is noted that divergence of the exponential simulation in these two figures go in opposite directions. It can be verified that divergence is always in a predictable direction, depending on having an odd or even number of terms in the series. The true benefit of the exponential matrix solution can be utilized when, for a given structural problem, the relationship between the accuracy of the exponential

186
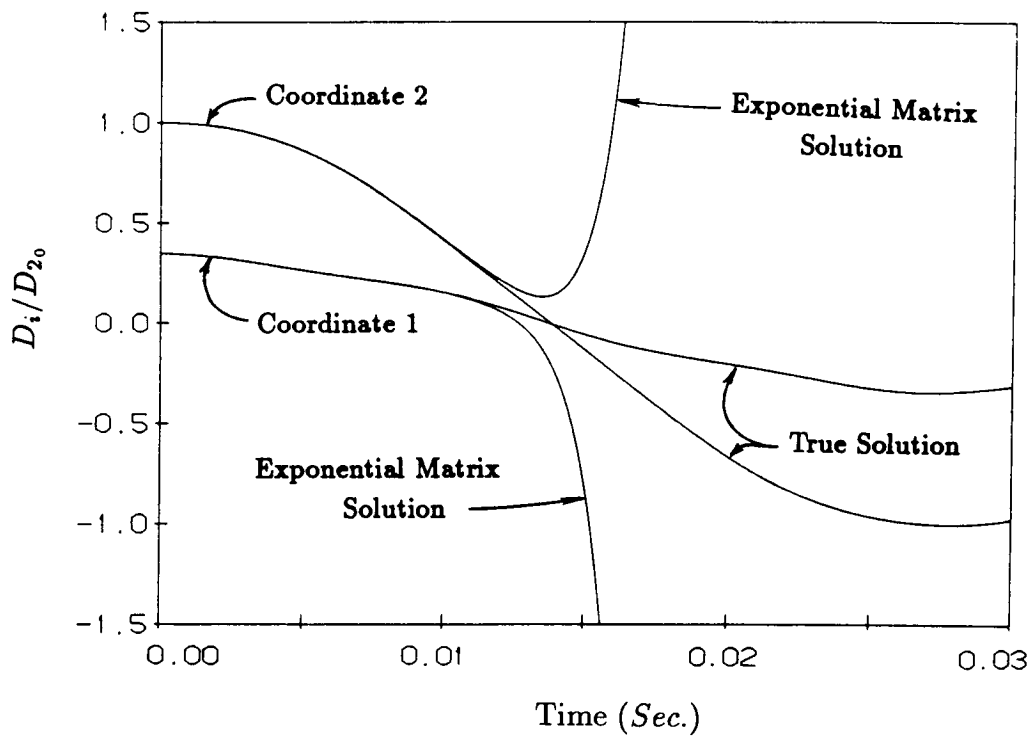
Fig. 5.– Coordinate Displacements during Free Vibration.
(Exponential Matrix Solution is Based on 15 Terms.)
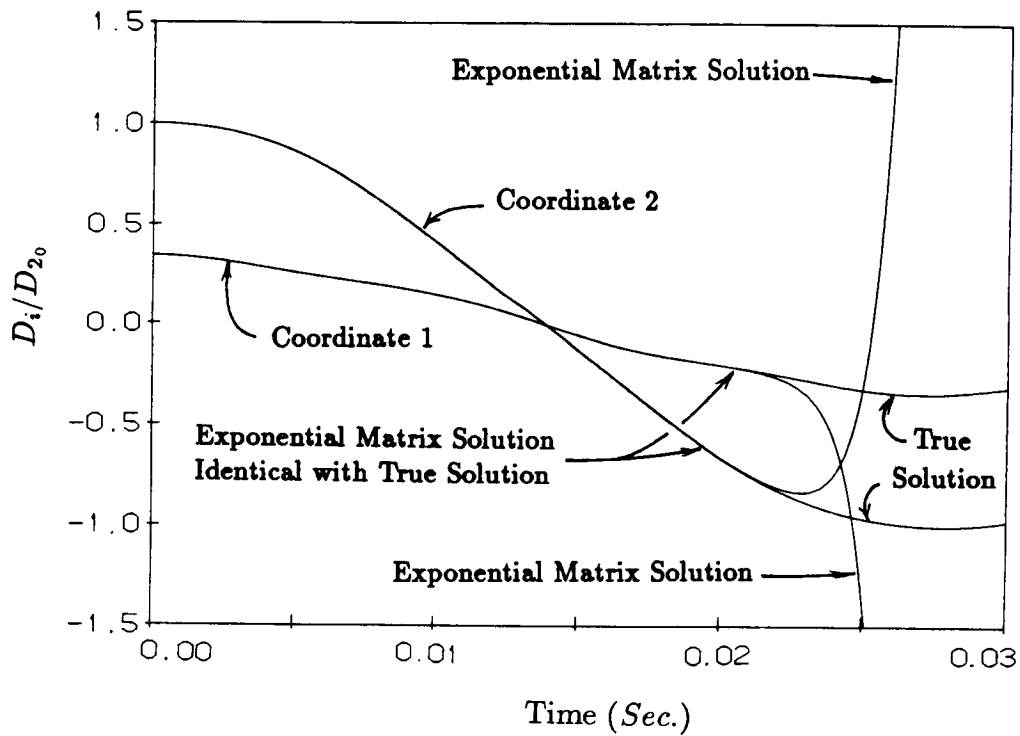
Fig. 6.– Coordinate Displacements during Free Vibration.
(Exponential Matrix Solution is Based on 30 Terms.)
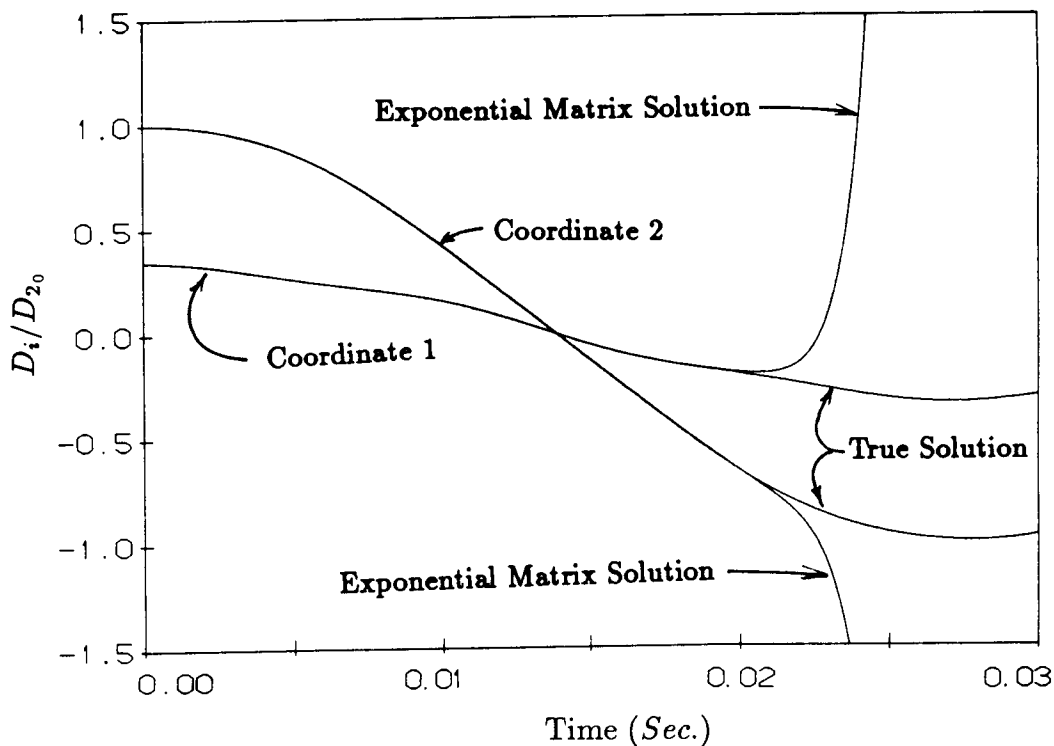
Fig. 7.– Coordinate Displacements during Free Vibration.
(Exponential Matrix Solution is Based on 29 Terms.)

matrix and the time duration of the accuracy of the solution can be predicted. Once the numerical technique for making this prediction is established, the exponential matrix solution can be used in discrete steps for extremely accurate time history analysis of dynamic systems.

Next, it is informative to study the same problem, during a longer time interval. This time, exponential matrix solutions are combined, step by step, to render an extraordinarily accurate solution of the system. The step by step exponential matrix solution can be used to obtain an exact solution of a dynamic system, even if an extremely large stepsize is used.

Figs. 8 and 9 show the exponential matrix solution and the central difference solution, respectively. In both figures the solid lines represent the "true" solution based on a central difference solution using a time increment of 0.0001 sec. The total simulation time is 0.1 sec. The exponential matrix solution is based on thirty terms in the series approximation. This exponential matrix solution with thirty terms diverges if the time interval is taken to be more than 0.021 sec., as depicted in Fig. 6. Accordingly, 0.020 sec is selected as the stepsize for the exponential matrix solution. The exponential matrix solution at each 0.02 sec time increment is plotted in Fig. 8 using square markers. The central difference solution diverges if the time interval is taken more than 0.0033 sec. In Fig. 9 the stepsize in the central difference solution is taken as 0.003 sec. In comparing Figs. 8 and 9, the dramatic difference between the exponential matrix and the central difference step-by-step solutions illustrate the relative effectiveness of the exponential matrix method. In this example, even though the exponential matrix solution stepsize in Fig. 8 is approximately seven times the central difference stepsize in Fig. 9, the exponential matrix solution is much more accurate in predicting the true response.

188
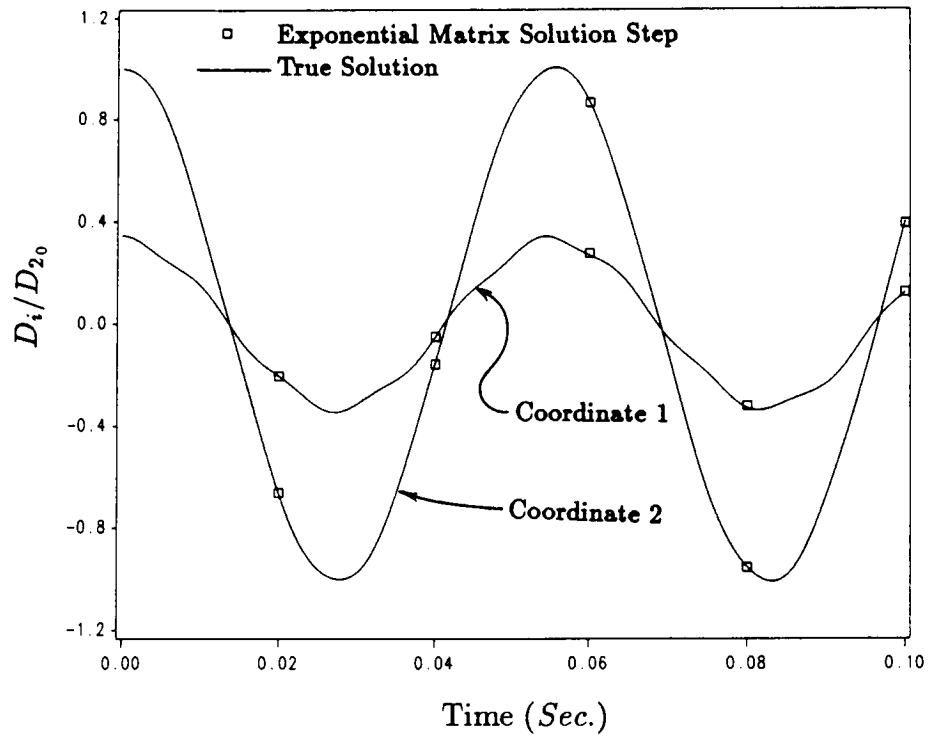
Fig. 8.– Comparison of Exponential Matrix Solution Steps with the True Solution.
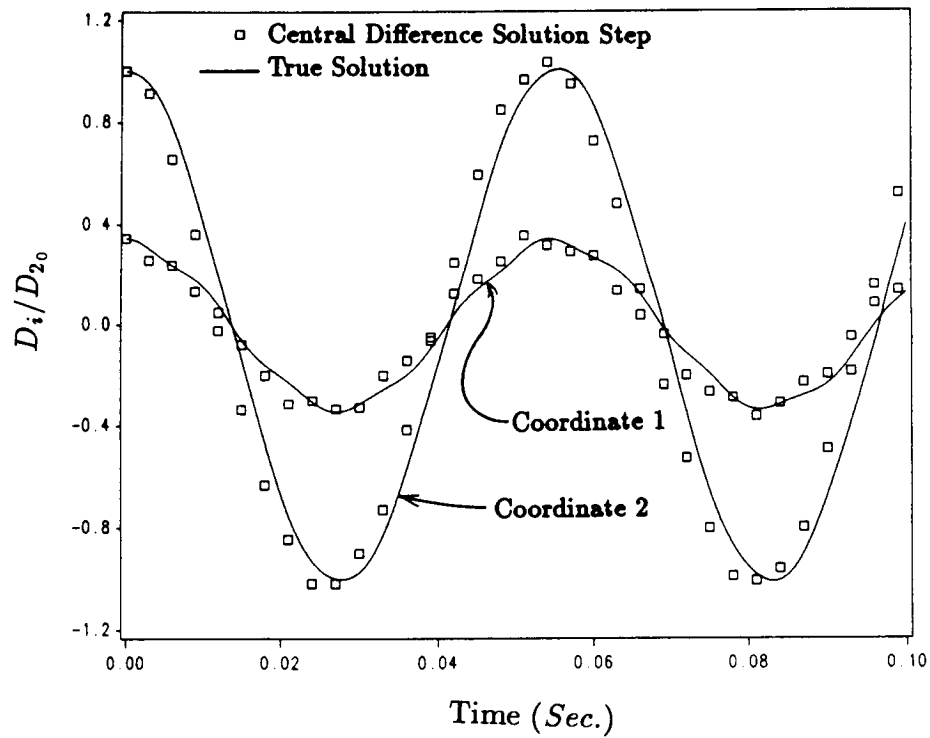
Fig. 9.– Comparison of Central Difference Solution Steps with the True Solution.

Example with Three Degrees of Freedom

Analogous to the two-degree-of freedom example, consider a cantilever beam with the same 0.1 m square cross section, 3 meters long, with the three condensed coordinates as shown in Fig. 10, using the same material constants as in the previous example, the equations of motion for the shown coordinates are written as:

$$\begin{bmatrix} 80 & 0 & 0 \\ 0 & 80 & 0 \\ 0 & 0 & 40 \end{bmatrix} \begin{Bmatrix} \ddot{x}_1 \\ \ddot{x}_2 \\ \ddot{x}_3 \end{Bmatrix} + \frac{10^6}{7.8} \begin{bmatrix} 240 & -138 & 36 \\ -138 & 132 & -48 \\ 36 & -48 & 21 \end{bmatrix} \begin{Bmatrix} x_1 \\ x_2 \\ x_3 \end{Bmatrix} = \begin{Bmatrix} 0 \\ 0 \\ 0 \end{Bmatrix} \tag{24}$$

As in the previous example, first a single step exponential matrix solution is compared with the true solution for the free vibration response. The results are depicted in Fig. 11. It is seen that increasing the number of degrees of freedom does not diminish the usefulness of the exponential matrix solution. However, as may be expected, a more accurate computation of the matrix exponential is required to keep the same time increment as the number of degrees of freedom is increased.

DISCUSSION AND CONCLUSION

The presented simple examples represent only the specific case of undamped free vibrations of a structure. However, the demonstrated benefits are also applicable to the analysis of dynamic systems under transient loading. In that case using the exponential matrix solution, the solution stepsize would depend only upon the discretization requirements of the applied transient loading. One could always include a sufficient number of terms in the computation of the exponential matrix to satisfy the time-history solution requirements of the high frequency structural response, using a time increment of any size. Eq. (16) can be used in the direct integration of the equations of motion to increase the practical stepsize and to improve the solution accuracy. Using Eq. (16) it is possible to keep the numerical integration stepsize at a practical time increment without losing the effects of high frequency structural response.

The exponential matrix solution may also prove useful for the time-history dynamic analysis of nonlinear structures under transient loading. In particular, the exponential matrix method would be useful when nonlinear structureal behavior does not significantly affect the high frequency response. In this case the exponential matrix solution stepsize can be selected to accommodate the nonlinear response characteristics of the structure as well as the accurate representation of the transient loading.

There has been a significant number of publications by computer scientists on the effective computation of the matrix exponential [2,3,4,5]. Algorithms using the Padé approximations appear to be the most successful ones from a survey of the literature [6,7,8,9,10]. It is possible to make a realistic estimate of the accuracy of the fundamental solution at a given time t. Again, it is easier to achieve higher levels of accuracy near the origin $t = 0$.

The exponential matrix solution should be further evaluated as a tool to improve the solution accuracy at a practical stepsize in the direct integration of equations of motion in structural dynamics. The stepsize is limited only by structural nonlinearities and the computational accuracy
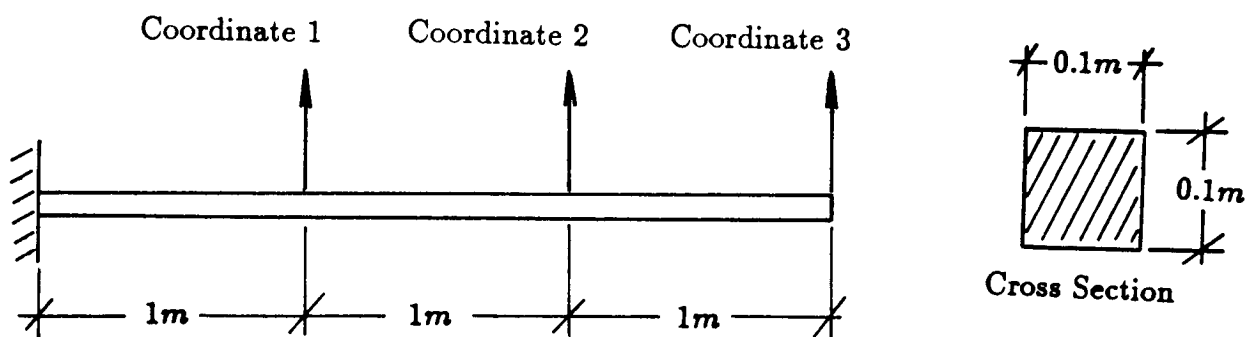
Fig. 10.– Example Beam with Three Coordinates.
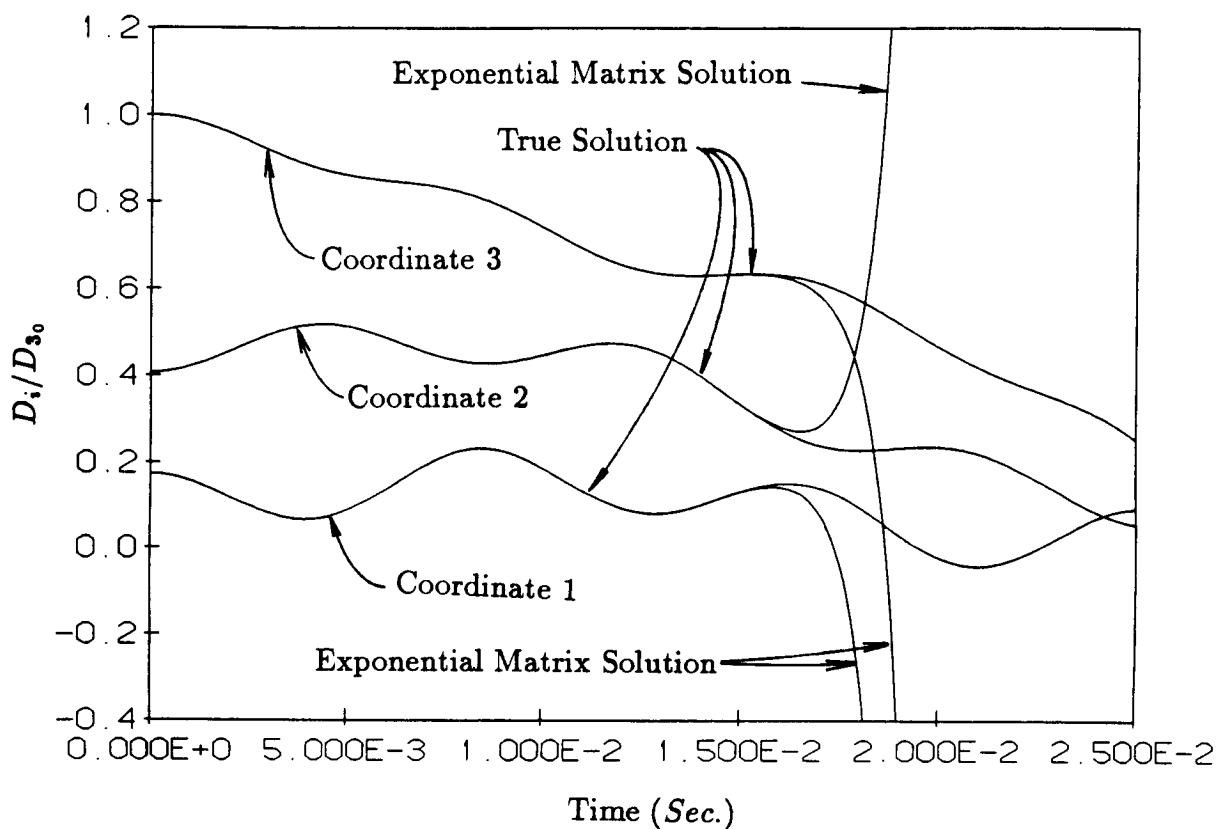
Fig. 11.– Comparison of Exponential Matrix Solution Steps with the True Solution
for Example Beam with Three Degrees of Freedom.
(Exponential Matrix Solution is Based on 30 Terms.)

191

of the matrix exponential. The relationship between the accuracy of the matrix exponential and the maximum stepsize needs to be quantified in general.

Having a method that can take larger intervals in the time domain would pave the way for more efficient finite time element algorithms to become practical in the simulation of dynamic response, enabling the use of different time intervals and/or different time quadrature rules to be used as needed at different locations of the structure and at different points on the time coordinate.

REFERENCES

1. J.N. Franklin (1968). *Matrix Theory*, Prentice-Hall.

2. G.H. Golub and C.F. Van Loan (1983). *Matrix Computations*, The Johns Hopkins University Press.

3. C.B. Moler and D.F. Van Loan (1978). "Nineteen Dubious Ways to Compute the Exponential of a Matrix," *SIAM Review* 20, 801-36.

4. C.F. Van Loan (1977). "The Sensitivity of the Matrix Exponential," *SIAM J. Num Anal.* 14, 971-81.

5. B. Kagstrom (1977). "Bounds and Perturbation Bounds for the Matrix Exponential," *BIT* 17, 39-57.

6. W. Fiar and Y. Like (1970). "Padé Approximations to the Operator Exponential," *Numer. Math.* 14, 379-82.

7. C.F. Van Loan (1977). "On the Limitation and Application of Padé Approximation to the Matrix Exponential," in *Padé and Rational Approximation*, ed. E.B. Saff and R.S. Varga, Academic Press, New York.

8. R.C. Ward (1977). "Numerical Computation of the Matrix Exponential with Accuracy Estimate," *SIAM J. Num. Anal.* 14, 600-14.

9. A. Wragg (1973). "Computation of the Exponential of a Matrix I: Theoretical Considerations," *J. Inst. Math. Applic.* 11, 369-75.

10. A. Wragg (1975). "Computation of the Exponential of a Matrix II: Practical Considerations," *J. Inst. Math. Applic.*, 15, 273-78.

Improvement of Modal Scaling Factors Using Mass Additive Technique

Qiang Zhang
Randall J. Allemang
Max L. Wei
David L. Brown

This paper presents a general investigation into the improvement of modal scaling factors of an experimental modal model using mass additive technique. Data base required by the proposed method consists of an experimental modal model (a set of complex eigenvalues and eigenvectors) of the original structure and a corresponding set of complex eigenvalues of the mass-added structure. Three analytical methods, i.e., first order and second order perturbation methods, and local eigenvalue modification technique, are proposed to predict the improved modal scaling factors. Difficulties encountered in scaling closely spaced modes are discussed. Methods to compute the necessary rotational modal vectors at the mass additive points are also proposed to increase the accuracy of the analytical prediction.

INTRODUCTION

For most applications of experimental modal database, the identified modal vectors are expected to be normalized according to $\{y_r\}^T[U]\{y_r\} = 1$. But in practice, this relation is rarely satisfied and it becomes $\{y_r\}^T[U]\{y_r\} = 1/\alpha_r^2$, where α_r is an unknown scaler of the rth modal vector.

Modal scaling errors, characterized by α_r, are disastrous for certain applications of experimental modal model, such as substructure synthesis, structural modification and adjustment finite element model[1-3]. Wei[4] analyzed the sources of modal scaling errors which are summarized as follows :

1. Local and global calibration errors.

2. Digital signal processing and FFT leakage errors.

3. Improper orientation of the force or response transducer at the driving point.

4. Low signal to noise ratio in the driving point measurement data.

Another possible cause of modal scaling errors is non-linearities of structures. A typical nonlinear example given by Lallement[5] showed that for a beam with nonlinear stiffness, lower natural frequencies and their corresponding mode shapes of a non-linear beam are very close to those of the same beam without the prescribed non-linear characteristics. However, α_r could vary from 0.4 to 1.3 .

From the above discussions, it can be concluded that modal scaling errors are almost inevitable in the applications of the prevailing modal testing techniques on practical structures. It is intended in this paper to determine the unknown scaler α_r by a supplementary testing technique, i.e., mass additive technique. Some of the work in correcting modal scaling errors using mass additive technique[6] has been done in the past using modal modeling technique. In this

paper, three analytical methods: first order and second order perturbation methods, and local eigenvalue modification technique are presented to predict the unknown modal scaling factors.

FIRST ORDER PERTURBATION APPROACH

The equation of motion for the general case of nonproportional damping is :

$$M \ddot{y}(t) + C \dot{y}(t) + K y(t) = f(t) \tag{1}$$

and its associated eigenvalue problem can be written as :

$$\lambda_r \begin{bmatrix} C & M \\ M & 0 \end{bmatrix} \begin{Bmatrix} \psi_r \\ \lambda_r \psi_r \end{Bmatrix} = \begin{bmatrix} -K & 0 \\ 0 & M \end{bmatrix} \begin{Bmatrix} \psi_r \\ \lambda_r \psi_r \end{Bmatrix} \tag{2}$$

or in the condensed form :

$$\lambda_r [U]\{y_r\} = [V]\{y_r\} \tag{3}$$

where :

$$\{y_r\} = \begin{Bmatrix} \psi_r \\ \lambda_r \psi_r \end{Bmatrix}, \quad \{y_r\} \in C^{2N}$$

$$[U] = \begin{bmatrix} C & M \\ M & 0 \end{bmatrix}, \quad [U] \in R^{2N}, \quad [U] = [U]^T$$

$$[V] = \begin{bmatrix} -K & 0 \\ 0 & M \end{bmatrix}, \quad [V] \in R^{2N}, \quad [V] = [V]^T$$

Defining a perturbated system :

$$\hat{\lambda}_r [U + \varepsilon \underline{U}]\{\hat{y}_r\} = [V + \varepsilon \underline{V}]\{\hat{y}_r\} \tag{4}$$

Where ε is the perturbation parameter, and the elements of matrices $\underline{V}$ and $\underline{U}$ are of the same order as those of matrices [U] and [V] respectively.

The eigenvalue $\hat{\lambda}_r$ may be expanded as power series in ε :

$$\hat{\lambda}_r = \lambda_r + \varepsilon \lambda_r^{(1)} + \varepsilon^2 \lambda_r^{(2)} + \cdots \tag{5}$$

In the case of small perturbations ($\varepsilon \ll 1$), the higher order terms of ε can be neglected, therefore Equation 5 can be written as :

$$\hat{\lambda}_r = \lambda_r + \varepsilon \lambda_r^{(1)} + O(\varepsilon^2) \tag{6}$$

The expression of $\lambda_r^{(1)}$ is given in numerous lectures [7,8] :

$$\lambda_r^{(1)} = \{y_r\}^T[\underline{V} - \lambda_r \underline{U}]\{y_r\} \tag{7}$$

Equation 7 is based on the assumption :

194.

$$\{y_r\}^T[\ U\ ]\{y_r\} = 1. \tag{8}$$

Considering the modal scaling errors, Equation 7 can be rewritten as :

$$\lambda_r^{(1)} = \{y_r\}^T[\ \underline{V}\ -\ \lambda_r \underline{U}\ ]\{y_r\}\alpha_r^2 \tag{9}$$

Where $\{y_r\}$ is the identified modal vector with modal scaling errors:

$$\{y_r\}^T[\ U\ ]\{y_r\} = 1/\alpha_r^2 \tag{10}$$

If the structural perturbation consists of only the mass matrix, $\Delta M = \varepsilon \underline{M}$, Equation 9 can be written as :

$$\lambda_r^{(1)} = -\lambda_r^2\{\psi_r\}^T\underline{M}\{\psi_r\}\alpha_r^2 \tag{11}$$

In the present problem, the mass added structure is considered as the perturbated system and the perturbated eigenvalues $\hat{\lambda}_r$ and both eigenvalues and eigenvectors of the original system have been identified. Using small added masses, the unknown scaler α_r can be directly derived from the first order approximation of $\hat{\lambda}_r$:

$$\Delta\lambda_r = \hat{\lambda}_r - \lambda_r = \varepsilon\lambda_r^{(1)} = -\lambda_r^2\{\psi_r\}^T\Delta M\{\psi_r\}\alpha_r^2 \tag{12}$$

Thus :

$$\alpha_r = \sqrt{\Delta\lambda_r/(-\lambda_r^2\{\psi_r\}^T\Delta M\{\psi_r\})} \tag{13}$$

SECOND ORDER PERTURBATION APPROACH

It is important to note that the first order perturbation approach is applicable only in the case of small perturbations. However, from a practical point of view, it is desirable to hold $\Delta\lambda_r$ from 5% to 10% of λ_r. Therefore, the second order perturbation approach is introduced to improve the accuracy of the estimated modal scaling factors :

$$\Delta\lambda_r = \hat{\lambda}_r - \lambda_r = \varepsilon\lambda_r^{(1)} + \varepsilon^2\lambda_r^{(2)} + \bigcirc(\varepsilon^3) \tag{14}$$

The expression of $\lambda_r^{(2)}$ is :

$$\lambda_r^{(2)} = \sum_{j=1,j\neq r}^{2N} [-\lambda_r^2\{\psi_j\}^T[\underline{M}]\{\psi_r\}\alpha_r\alpha_j]^2/(\lambda_r - \lambda_j) - 2\lambda_r\{\psi_r\}^T[\underline{M}]\{\psi_r\}\lambda_r^{(1)}\alpha_r^2 \tag{15}$$

Obviously Equation 14 is nonlinear in ε_r. Therefore an iterative process is applied to calculate ε_r. This iterative process consists of three steps :

1) Determining initial estimation of $\alpha_r^{(0)}$:

$$\alpha_r^{(0)} = \sqrt{(\hat{\lambda}_r - \lambda_r)/(-\lambda_r^2\{\psi_r\}^T\Delta M\{\psi_r\})} \tag{16}$$

2) Calculating $\varepsilon^2\lambda_r^{(2)}$:

$$\varepsilon^2\lambda_r^{(2)} = \sum_{j=1,j\neq r}^{2N} [-\lambda_r^2\{\psi_j\}^T[\Delta M]\{\psi_r\}\alpha_r^{(0)}\alpha_j^{(0)}]^2/(\lambda_r - \lambda_j) - 2\lambda_r^3[\{\psi_r\}^T[\Delta M]\{\psi_r\}(\alpha_r^{(0)})^2]^2 \tag{17}$$

3) Recalculating $\alpha_r^{(1)}$:

$$\alpha_r{}^{(1)} = \sqrt{(\hat{\lambda}_r - \lambda_r - \varepsilon^2\lambda_r{}^{(2)})/(-\lambda_r^2\{\psi_r\}^T\Delta M\{\psi_r\})} \tag{18}$$

Steps 2 and 3 are repeated until the convergence condition :

$$\left| \alpha_r{}^{(k)} - \alpha_r{}^{(k-1)} \right| < \sigma$$

is satisfied by the kth iteration, where σ is a given positive quantity. In general, $\alpha_r{}^{(k)}$ converges to a stable value very quickly.

LOCAL EIGENVALUE MODIFICATION

In most practical cases, the second order perturbation approach gives a reasonable estimation of modal scaling factors α_r . But if the structure under study possesses very closed eigenvalues ($|(\lambda_r - \lambda_{r+1})/\lambda_r| < 1\%$), the perturbation method is no longer valid. Zhang and Lallement[9] proposed a method based on modal space representation which would be suitable in this delicate case. This method requires not only the eigenvalues of the mass-added structure but also the modified eigenvectors. In this section, a method which does not require the eigenvectors of the mass added structure is presented : a method based on the local eigenvalue modification technique.

Recall[10] that if the structure is perturbated only at a single degree of freedom, the eigenvalues of the perturbated structure are of the roots of the following equation :

$$1/m = \sum_{r=1}^{N} (\hat{\lambda} \lambda_r^2 \psi_{kr}^2)/(\lambda_r - \hat{\lambda}) \tag{19}$$

Where :

λ_r and $\hat{\lambda}$ are respectively the eigenvalues of the initial structure and the perturbated structure.
ψ_{kr} is the kth component of the rth modal vector of the initial structure.
m is the mass attached at the degree of freedom k.

Because of the modal scaling error, Equation 19 becomes :

$$1/m = \sum_{r=1}^{n} (\hat{\lambda} \lambda_r^2 \psi_{kr}^2 \alpha_r^2)/(\lambda_r - \hat{\lambda}) \tag{20}$$

Since the eigenvalues of the perturbated structure $\hat{\lambda}_j$,j $= 1,2,\cdots,N$, are known, substitution of these values into Equation 20 yields :

$$\begin{Bmatrix} 1/m \\ \cdot \\ \cdot \\ \cdot \\ 1/m \end{Bmatrix} = \begin{bmatrix} (\hat{\lambda}_1 \lambda_1^2 \psi_{k1}^2)/(\lambda_1 - \hat{\lambda}_1) & \cdots & (\hat{\lambda}_1 \lambda_N^2 \psi_{kN}^2)/(\lambda_N - \hat{\lambda}_1) \\ & \cdot & & \cdot & & \cdot \\ & \cdot & & \cdot & & \cdot \\ & \cdot & & \cdot & & \cdot \\ (\hat{\lambda}_N \lambda_1^2 \psi_{k1}^2)/(\lambda_1 - \hat{\lambda}_N) & \cdots & (\hat{\lambda}_N \lambda_N^2 \psi_{kN}^2)/(\lambda_N - \hat{\lambda}_N) \end{bmatrix} \begin{Bmatrix} \alpha_1^2 \\ \cdot \\ \cdot \\ \cdot \\ \alpha_N^2 \end{Bmatrix} \tag{21}$$

or in the condensed form :

$$\{1/m\} = [Q]\{\alpha^2\} \tag{22}$$

and then the unknown modal scaling factors $\{\alpha^2\}$ are determined by solving Equation 22 :

$$\{\alpha^2\} = [Q]^{-1}\{1/m\} \tag{23}$$

196

There are several comments needed to be made on the proposed local eigenvalue modification technique:

1. Equation 20 implies the normalization relations :

$$\{y_r\}^T[U]\{y_r\} = 1/\alpha_r^2 , \quad \{y_r\}^T[V]\{y_r\} = \lambda_r/\alpha_r^2$$

where :

$$[U] = \begin{bmatrix} -C & 0 \\ 0 & K \end{bmatrix}, \quad [V] = \begin{bmatrix} C & K \\ K & 0 \end{bmatrix}, \quad [V] \in R^{2N} , \quad [V] = [V]^T$$

2. The major numerical difficulty in dealing with closely spaced modes is due to the following facts :

   • The difference between two adjacent eigenvalues $\lambda_r - \lambda_j$ appears in the denominators as shown in Equation 17.

   • It is difficult to make the correspondence between eigenvalues of the original structure and those of the mass-added structure.

   From Equation 21, it is noted that (i) the term ($\lambda_r - \lambda_j$) does not appear in this equation, and (ii) the interchange of two modified eigenvalues does not affect the solution $\{\alpha^2\}$. Therefore, this method is very effective in dealing with closely spaced modes.

3. The disadvantage of this method is that it is only applicable in the case of a single point and a single degree of freedom modification. In practice, this implies that the dynamics effect of the added mass must be dominant by only one of the six degrees of freedom at the mass attachement point. This theoretical restriction can cause real difficulty in choosing the proper location of the added mass.

To avoid this problem, one of the options is to replace the additive mass by a feedback device , i.e., a device which can provide a force proportional to the acceleration at the mass attachment point i ($f_i = m\ddot{x}_i$). Another alternative is to modify the structure by adding a single spring instead of a mass. In case of adding a spring, Equation 20 becomes :

$$-1/k = \sum_{r=1}^{n} (\psi_{kr}^2 \alpha_r^2)/(\lambda_r - \hat{\lambda}) \tag{24}$$

where k is the spring constant.

PRACTICAL CONSIDERATIONS: Effective Mass

Rotational degrees of freedom information at the mass attachment point(s) is also important in the application of the mass additive technique when the moment of inertia of the added mass(es) is not negligible. Various methods have been proposed to measure or predict the rotational degree of freedom frequency response functions or modal coefficients at a point on the structure[11,12], but all methods have their technical limitations.

In this section, the concept of effective mass is introduced to include the dynamics effect of the unmeasured rotational degree of freedom information. Define the effective mass associated with the rth mode m_{ef} as :

$$m_{ef} = m_{ad} + \Delta m_r \tag{25}$$

where m_{ad} is the added mass and Δm_r represents the additional mass due to the effect of the rotational degrees of freedom of mode r.

The estimation of Δm is based on the assumption that the kinetic energy due to rotation ($J\dot{\Theta}^2$) can be replaced by

an equivalent translational kinetic energy ($\Delta m \, \dot{z}^2$) along the z axis.

For a one dimensional problem, total kinetic energy due to the added mass at point k can be written as :

$$E = m_{ad}\dot{z}_k^2 + J\dot{\Theta}_k^2$$

where J is the moment of inertia of the added mass.

The angle of rotation Θ_k as shown in Figure 1 can be approximately calculated :

$$\Theta_k \approx tangent\Theta_k = (z_a - z_b)/l_{ab} \tag{26}$$

where l_{ab} is the distance between points a and b .
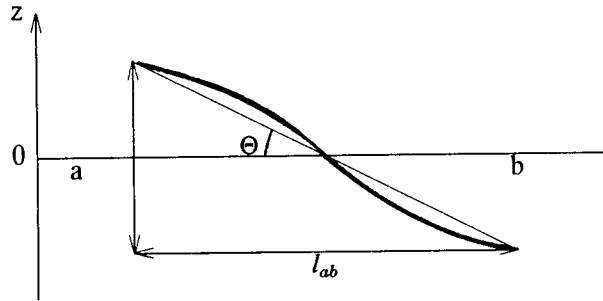
Figure 1. Estimation of Rotational DOF from Translational DOF

Equating $\Delta m\dot{z}_k^2$ to $J\dot{\Theta}_k^2$, i.e., E = ($m_{ad} + \Delta m$)$\dot{z}_k^2$, the scaler Δm is determined :

$$\Delta m = J\dot{\Theta}_k^2/\dot{z}_k^2 = J(\dot{z}_a - \dot{z}_b)^2/(l_{ab}\dot{z}_k)^2 \tag{27}$$

Denoting E_r as the total kinetic energy of the added mass associated with the rth mode :

$$E_r = \lambda_r^2(m_{ad} + \Delta m_r)\psi_{kr}^2$$

where :

$$\Delta m_r = J(\psi_{ar} - \psi_{br})^2/(l_{ab}\psi_{kr})^2 \tag{28}$$

Equation 28 shows that the effective mass $m_{ef} = m_{ad} + \Delta m_r$ is different for each mode.

CASE STUDY

In order to demonstrate the effectiveness of the proposed methods, a case study was performed on a lightly damped steel T plate shown in Figure 2. The Polyreference time domain modal parameter estimation method[13] was used to identify the eigenvalues and the eigenvectors of the unmodified T plate (4 references and 24 measurement points). Eigenvalues of the modified structure with two additive masses,i.e, mass 1: 97 grams at point 3 and mass 2: 43 grams at point 22, were extracted from the frequency response functions measured at four reference and mass attachment points. The first mode shapes of the original T plate are plotted in Figure 3.
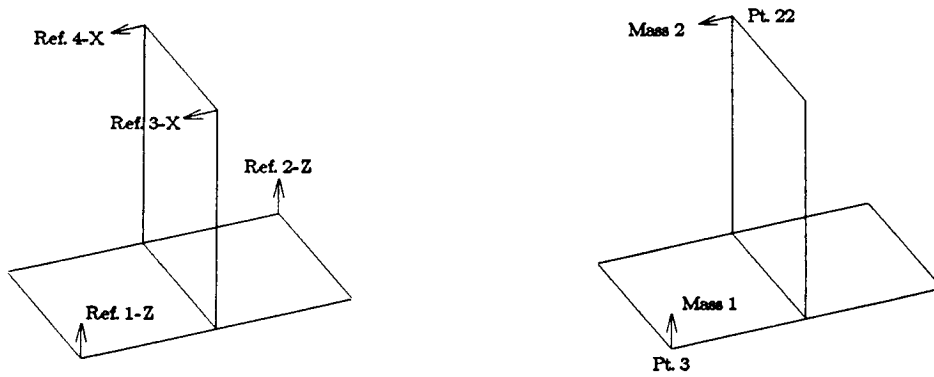
Figure 2. Test Structure: A Steel T Plate

Mode No. 1   Mode No. 2

Mode No. 3   Mode No. 4
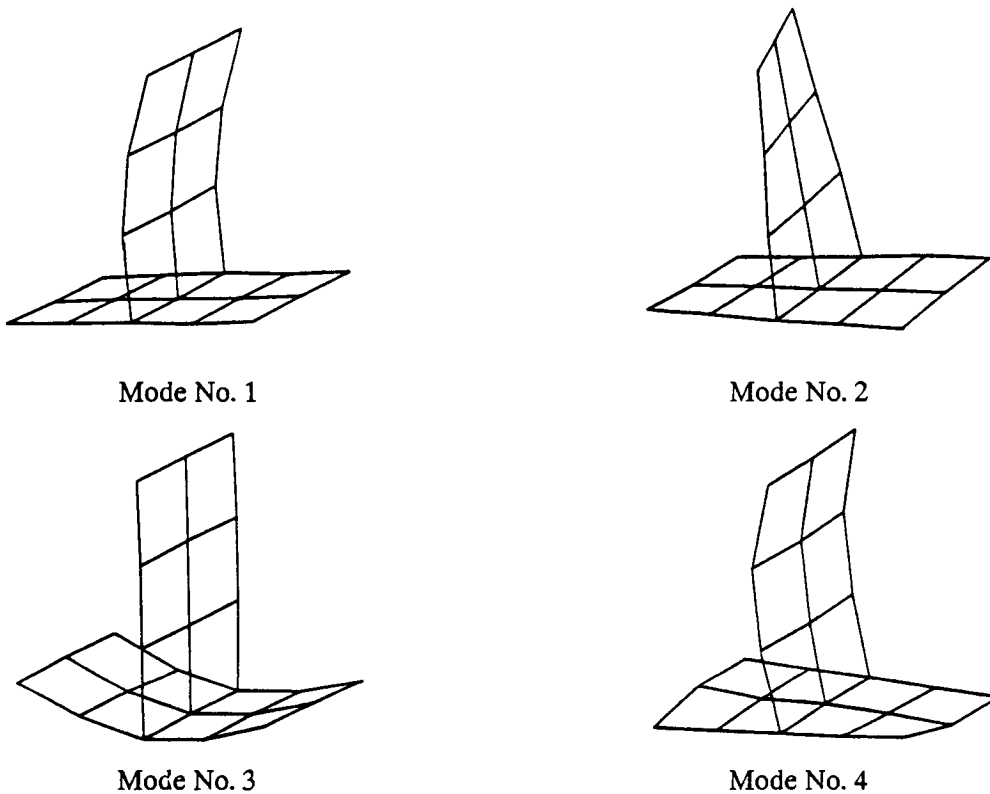
Figure 3. First Four Mode Shapes

The first four damped natural frequencies and modal damping ratios of the original and the modified T plate are listed in Table 1. The identified complex modal vectors of the original T plate were normalized according to Equation 8. The modal scaling factors α_r calculated by using the first and second order perturbation methods are listed in Table 2.

In order to verify the calculated modal scaling factors listed in Table 2, a structural modification software (DYNOP developed by U.C. SDRL) is used to predict the eigenvalues of the modified T plate with a single mass added at point 3. Modified eigenvalues were derived for both the original and rescaled (using the modal scaling factors listed in Table 2) experimental modal model. The predicted eigenvalues and the measured data are listed in Table 3.

TABLE 1. Measured Complex Eigenvalues

Mode No.	Original Structure		Modified T Plate(2 masses)	
	f(Hz)	$\varsigma(\%)$	f(Hz)	$\varsigma(\%)$
1	177.37	.984	171.07	1.322
2	334.20	.441	322.50	.566
3	411.10	.487	392.02	.558
4	581.7	.286	550.94	.503

TABLE 2. Calculated Modal Scaling Factors

Calculated Modal Scaling Factors, α_r

Mode No.	First Order Approach		Second Order Approach	
	real	imaginary	real	imaginary
1	0.95	0.05	0.96	0.06
2	1.05	0.02	1.09	0.01
3	0.98	0.04	1.01	0.03
4	0.76	-0.002	0.68	0.002

TABLE 3. Complex Eigenvalues of the Modified T Plate

Eigenvalues of the Modified T Plate(1 mass)

Mode No.	Measured Eigenvalues		Predicted Eigenvalues Using Original $\{\psi_r\}$				Predicted Eigenvalues Using Rescaled $\{\psi_r\}$			
	f(Hz)	$\varsigma(\%)$	f(Hz)	Err(%)	$\varsigma(\%)$	Err(%)	f(Hz)	Err(%)	$\varsigma(\%)$	Err(%)
1	172.8	1.289	173.1	.16	.894	-30.6	172.8	0	1.166	-9.5
2	331.8	.521	333.2	.41	.469	-10.0	333.4	.48	.468	-10.0
3	392.5	.594	389.7	-.72	.284	-52.0	392.0	-.13	.483	-18.7
4	556.5	.529	550.5	-1.06	.437	-17.3	563.9	1.34	.305	-42.3

From the results of this case study, it is noticed that:

1. Since all modal testings of the T plate were very carefully conducted, and the structure is perfectly linear, therefore, all but the last α_r are relatively small and within ±10% of 1.0 as shown in Table 2.

2. It was pointed out in Reference[14] that the analytical predictions of modified eigenvalues using modal modeling technique could be corrupted due to modal truncation error. It was also indicated that the last few predicted damped natural frequencies are usually greater than the true ones.

From Table 3, the 4th damped natural frequency derived from the original modal vectors is less than the measured data. On the contrary, the one from the rescaled modal vectors is greater. This indicates that the damped natural frequencies based on the rescaled modal vectors are more reliable.

CONCLUSIONS

The three analytical methods proposed in this paper can be used to improve the modal scaling factors of the measured modal vectors from the structure with or without close-spaced modes. The main advantage of these methods is that it only requires complex eigenvalues of the mass-added structure as additional information, i.e., only a few additional measurements are needed to obtain the complex eigenvalues of the mass-added structure.

The concept of the effective mass is introduced to include the rotational effects of the additive mass(es) due to the lack of test data at the rotational degrees of freedom. Case studies based on this concept can be found in Reference [15].

The proposed methods also have the following limitations:

1. The perturbation technique is applicable only in the absence of closely spaced modes.

2. The local eigenvalue modification technique is limited to a single degree of freedom modification.

REFERENCES

[1]   Hallquist J., "Modification and synthesis of large dynamic structural system", Ph. D. Dissertation, Michigan Technological University, 1974

[2]   Herbert, M. H., Kientzy, D. W., "Application of structural dynamic modification", SAE Technical Paper Series No. 801125, 1980

[3]   Zhang, Q., Lallement, G., "Dominant error localisation in a finite element model of a mechanical structure", Mechanical System and Signal Processing , Vol. 1, No. 2, pp. 141-149, 1987

[4]   Wei, M. L., Allemang, R. J., Brown, D. L., "Modal Scaling Considerations for structural modification application", Proceedings of the 5th International Modal Analysis Conference, pp. 1531-1537, London, U. K., 1987

[5]   Lallement, G., Fillod, R., Piranda, J., "Identification des structures non lineaires", Rapport final No. 82.S.1083, Laboratoir de Mecanique Appliquee, Univercite de Besancon, France, 1982

[6]   Wei, M. L., Allemang, R. J., Brown, D. L., "Structural Dynamic Modifications Using Mass Additive Technique", Proceedings of the 4th International Modal Analysis Conference, pp. 691-699, Los Angeles, CA, 1986

[7]   Noor, A. K., Lowder, H. E., "Approximate techniques of structural reanalysis" , Int. J. Comp. and Structure, Vol. 4, No. 4, pp. 801-812, 1974

[8]   Fox, R.L., Kapoor, M. P., "Rates of change of eigenvalues and eigenvectors" ,Journal of AIAA, Vol. 6, No. 1, 1976

[9]   Zhang, Q., Lallement, G., Fillod, R., "Modal Identification of Self-adjoint and Non Self-adjoint Structures by Additional Masses Technique", ASME Paper No. 85-det-109, 1985

[10] Palazzolo, A. B., "Vibration of locally modified structural system", Ph. D. Dissertation, University of Virginia, 1981

[11] Yasuda, C., Riehle, P., Brown, D. L., Allemang, R. J., "An Estimation Method for Rotational Degrees of Freedom Using Mass Additive Technique", Proceedings of the 2nd International Modal Analysis Conference, Orlando, Florida, pp. 877-886, 1984

[12] O'Callahan, J. C., Avitabile, P., "An efficient method of determining rotational degrees of freedom from analytical and experimental modal data", Proceedings of the 4th International Modal Analysis Conference, Los Angeles, CA, pp. 50-58, 1986

201

[13] Deblauwe, F., "Application of the polyreference time domain technique", Master of Science Thesis, Department of Mechanical and Industrial Engineering, University of Cincinnati, 1986

[14] Deel, J. C., Luk, Y. W., "Modal testing considerations for structural modification applications", Proceeding of the 3rd International Modal Analysis Conference, Orlando, Florida, 1985, PP.46-52.

[15] Zhang, Q., "Identification modal et parametrique de structures mecaniques auto-adjointes et non auto-adjointes", These es Sciences, Universite de Franche-comte, France, 1987

Initial Dynamic Load Estimates During Configuration Design

N88-13621

Daniel Schiff

Dynamic analysis of aerospace systems is required to insure that the structures will maintain their integrity and provide predictable and acceptable mechanical performance throughout the mission profile of specified acceleration environments. This analysis includes the structural response to shock and vibration and evaluates the maximum deflections and material stresses and the potential for the occurrence of elastic instability, fatigue and fracture. The required computations are often performed by means of finite element analysis (FEA) computer programs in which the structure is simulated by a finite element model which may contain thousands of elements. The formulation of a finite element model can be time consuming, and substantial additional modeling effort may be necessary if the structure requires significant changes after initial analysis. This paper presents rapid methods for obtaining rough estimates of the structural response to shock and vibration, for the purpose of providing guidance during the intial mechanical design configuration stage.

INTRODUCTION

Structures are often made up of simple components such as beams, rings, arcs, plates and shells. The natural frequencies of such a structure cannot usually be found from the frequencies of these components. However, the stiffness, damping and mass of these components, the stiffness and damping of the connections between components, and the type of attachment of the structures to mounting surfaces will determine the natural frequencies of the structure. Estimates of natural frequencies can only be made for simple structures without developing an FEA (finite element analysis) model and utilizing an FEA computer program. But even rough estimates of natural frequency can provide a relatively rapid means of comparing maximum acceleration, stress and fatigue in different design approaches, and identifying potential problem areas in a structure. This type of information can help to avoid excessive modification of the FEA model when a comprehensive computer analysis is done.

The methods presented here for evaluating natural frequencies of simple structures will typically have a frequency error on the low side, which will result in a conservative (larger than actual) estimate of stress.

Composite Beams

Beams may be made of two or more layers of different materials adhered to one another, with each layer running the length of the beam. In this section, the layers are assumed to have constant, rectangular cross sections. The layers may be oriented so that the direction of vibration is parallel to the layer interfaces or normal to the layer interfaces.

Vibration Parallel to Layer Interfaces

Figure 1 shows the case where the direction of vibration is parallel to the layer interfaces. The term EI/L is referred to as the stiffness of a beam. Defining EI as the stiffness factor of a beam, the stiffness factor of the composite beam of Figure 1 is

$$EI = \sum_{i=1}^{n} E_i I_i = (1/12) \sum_{i=1}^{n} E_i b_i h_i^3 \quad \text{lbf·in}^2 \tag{1}$$

where E_i = modulus of elasticity of layer i, lbf/in^2,
b_i = width of layer i, inch,
h_i = height of layer i, inch,
I_i = area moment of inertia of layer i about neutral (Z) axis, in^4.
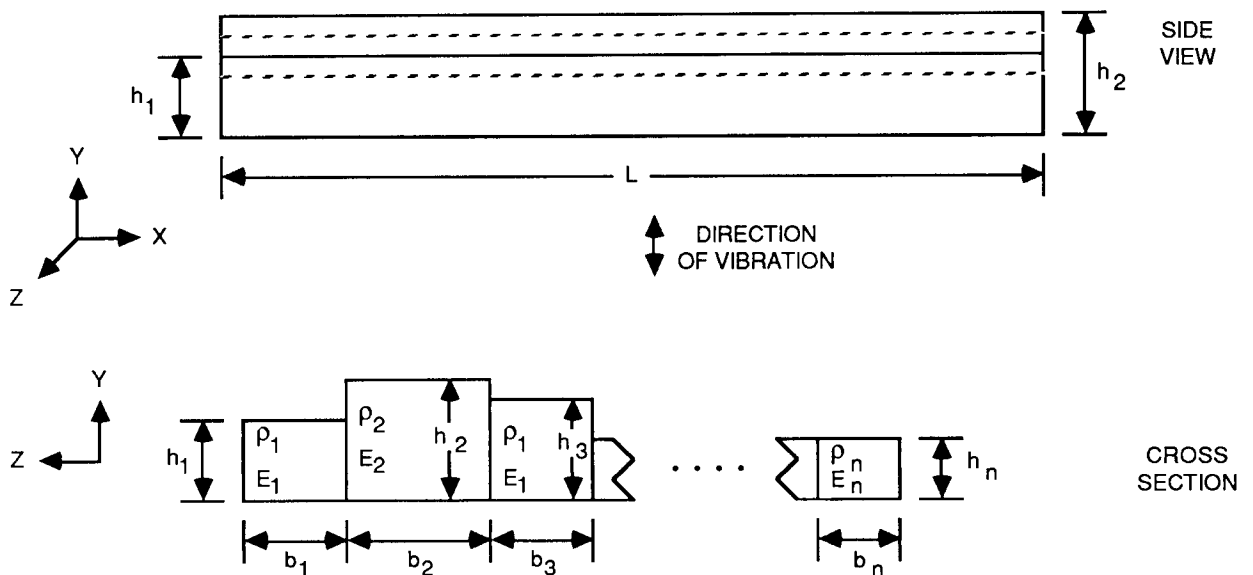
Fig. 1 Layered Beam, Vibration Parallel To Layer Interfaces

The weight per unit length of the composite beam is

$$W = \sum_{i=1}^{n} \rho_i b_i h_i \quad \text{lbf/in}$$

(2)

where ρ_i = weight density of layer i, lbf/in^3

Equations (1) and (2) may be used with slender beam frequency formulas when the composite beam is uniformly loaded and the neutral axis through the beam cross section, parallel to the Z axis, remains undeflected (no bending along the Z axis).

Vibration Normal to Layer Interface

Figure 2 shows the case where the vibration is normal to the layer interfaces. The stiffness factor of the composite beam of Figure 2 is

$$EI = \sum_{i=1}^{n} b_i h_i E_i [(\overline{Y}-Y_i)^2 + (1/12)h_i^2] \quad \text{lbf.in}^2$$

(3)

where $Y_i = \sum_{j=0}^{i-1} h_j + (1/2)h_i$ inch, where $h_0 = 0$,

and $\overline{Y} = \sum_{i=1}^{n} b_i h_i E_i Y_i \Big/ \sum_{i=1}^{n} b_i h_i E_i$ inch

See Equation 1 for definitions.
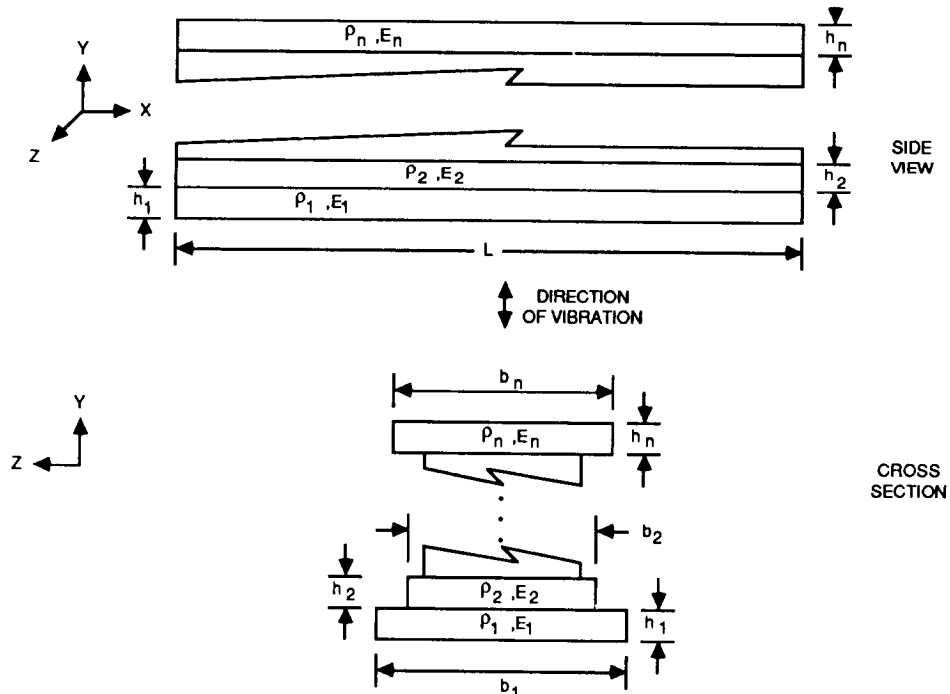
Fig. 2 Layered Beam, Vibration Normal to Layer Interfaces

The weight per unit length of the composite beam, W, is given by Equation (2). Equations (2) and (3) may be used with slender beam frequency formulas to obtain approximate values of natural frequency. Accuracy is improved when the layer widths, b_i, approach equality with one another.

Stepped Beams

Stepped beams have two or more different cross sections along their span, resulting in two or more different moments of inertia. Figure 3 shows two examples of stepped cantilever beams. In Figure 3a the beam has two different cross sections and the average moment of inertia for the beam is[1]

$$I_A = L^3 I_1 I_2 \Big/ [3(a^2 b + b^2 a + b^3/3)I_1 + a^3 I_2] \text{ in}^4 \tag{4}$$

In Figure 3b the beam has three different cross sections and the average moment of inertia for the beam is

$$I_A = L^3 I_1 I_2 I_3 \Big/ \Big\{ 3[(a+b)^2 c + (a+b)c^2 + c^3/3]I_1 I_2 \tag{5}$$
$$+ 3(a^2 b + ab^2 + b^3/3)I_1 I_3 + a^3 I_2 I_3 \Big\} \text{ in}^4$$
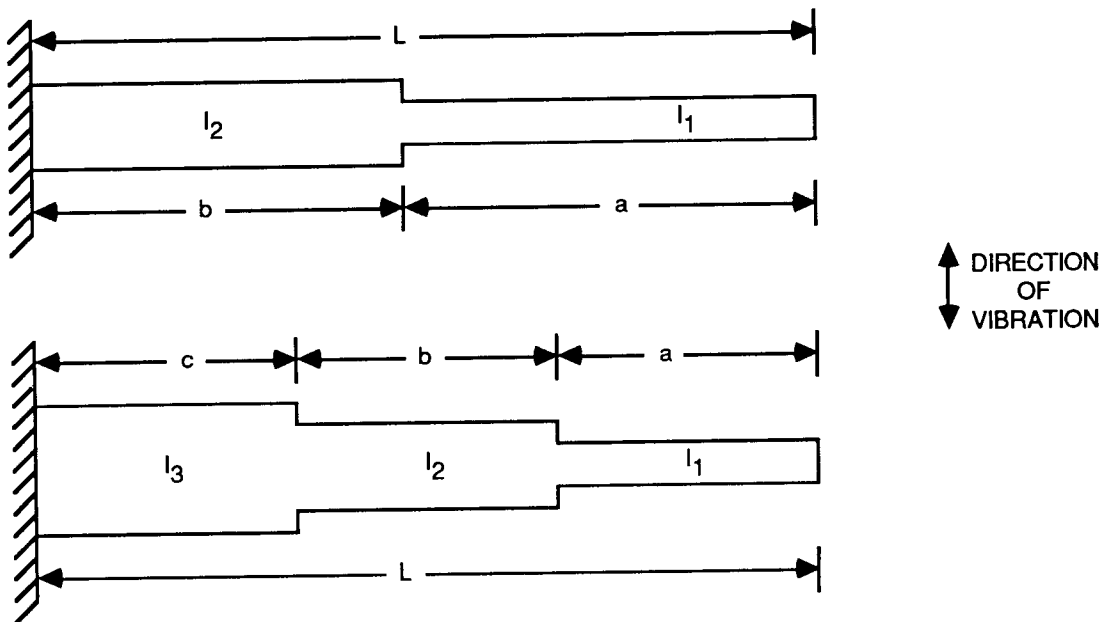
Fig. 3 Stepped Cantilever Beams With a) Two Different Cross Sections, and b) Three Different Cross Sections

206

In general, for a beam with n different cross sections, an approximate value for the average moment of inertia is

$$I_A = (1/L) \sum_{i=1}^{n} x_i I_i \quad in^4 \tag{6}$$

where x_i = spanwise length of cross section i, inch,
  I_i = moment of inertia of cross section i, in^4,
  L = Σx_i = full span of beam, inch.
     i

Equations (4), (5) and (6) may be used in standard frequency formulas to obtain values of natural flexural frequencies of stepped beams. Equations (4) and (5) are only for cantilever beams and should provide accurate results for slender beams. Equation (6) may be used for any end support conditions, and will usually yield a natural frequency roughly 5% to 10% lower than the correct value.

Slender Right Angles and U Bends

Figure 4 shows a right angle and a U bend with intermediate supports. The ends, E, may have any combination of pinned, P, or clamped, C, boundary conditions. The intermediate supports, S, prevent transverse motion (perpendicular to the beam axis) at the support but allow the beam to move parallel to its own axis and to rotate about any axis. The fundamental natural frequency for vibration in the plane of the figures (in-plane vibration) is[2]

$$F = (\lambda/2\pi R^2) \cdot (EI_y g/W)^{\frac{1}{2}} \quad Hz \tag{7}$$

where λ = dimensionless frequency parameter in Table 1,
  R = radius of curvature shown in Figure 4, inches,
  E = modulus of elasticity of beam material, lbf/in^2,
  I_y = area moment of inertia about axis perpendicular to the plane of the figures, in^4,
  g = gravitational acceleration at surface of earth = 386 in/sec^2,
  W = weight per unit length of beam, lbf/in.

The fundamental natural frequency for vibration perpendicular to the plane of the figures (out-of-plane vibration) is

$$F = (\lambda/2\pi R^2) \cdot (GI_p g/W)^{\frac{1}{2}} \quad Hz \tag{8}$$

where R, E, g and W are as defined for Equation (7),

and λ = dimensionless frequency parameter in Table 2,
  G = shear modulus = $E/2(1+\nu)$ lbf/in^2,
  ν = Poisson's ratio, dimensionless,
  I_p = polar area moment of inertia = $I_x + I_y$, in^4,
  I_x = area moment of inertia about axis in the plane of the figure and perpendicular to the local beam axis, in^4,
  I_y is as defined for Equation 7.
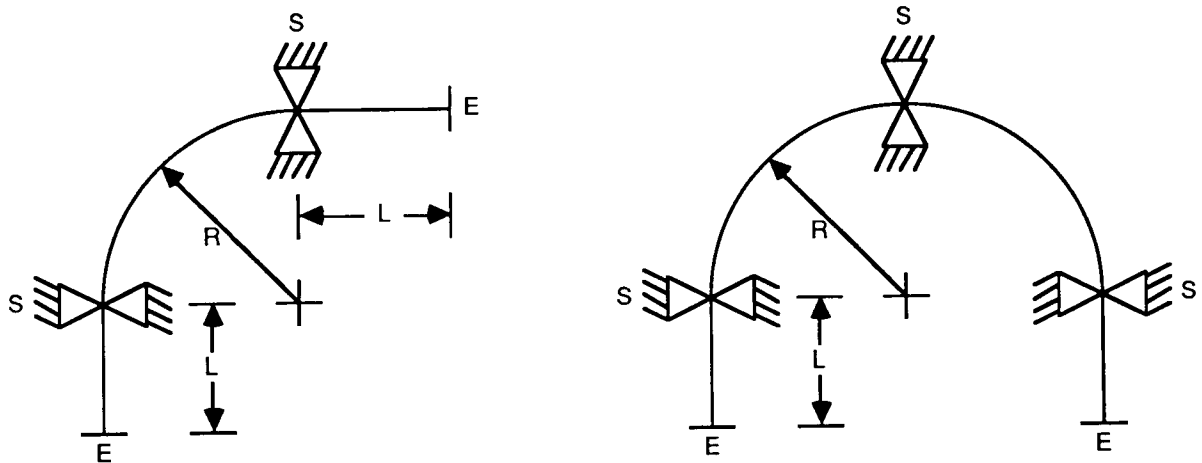
Fig. 4 Slender a) Right Angle Bend, and b) U Bend

Table 1 In-Plane Vibration of Right Angles and U Bends

	λ FUR USE IN EQUATION (7)					
	RIGHT ANGLES (FIGURE 4a)			U BENDS (FIGURE 4b)		
L/R	P-P	P-C	C-C	P-P	P-C	C-C
0	22.8	22.8	22.8	4.5	4.5	4.5
0.4	18.3	18.5	19.0	3.7	3.8	3.8
0.8	14.5	15.5	16.8	3.4	3.5	3.5
1.2	8.3	8.3	11.8	3.2	3.3	3.3
1.6	5.0	5.0	7.5	2.8	2.9	3.1
2.0	3.5	3.5	5.0	2.4	2.6	2.9

NOTES: 1. L = length of legs, inch
2. R = radius of curvature, inch
3. P = pinned end condition
4. C = clamped end condition
5. Vibration in the plane of Figures 4a and 4b

Table 2 Out-of-Plane Vibration of Right Angles and U Bends

| L/R | λ FUR USE IN EQUATION (8) | | | | | |
| | RIGHT ANGLES (FIGURE 4a) | | | U BENDS (FIGURE 4b) | | |
	P-P	P-C	C-C	P-P	P-C	C-C
0	9.5	9.5	9.5	5.8	5.9	5.9
0.4	7.5	7.6	7.8	5.1	5.3	5.3
0.8	6.0	6.4	6.8	4.7	4.8	4.9
1.2	5.0	5.4	5.9	4.3	4.4	4.6
1.6	3.5	4.1	5.0	3.6	3.8	4.2
2.0	2.6	3.0	3.8	2.7	2.9	3.6

NOTES: 1. See notes 1-4 of Table 1
2. Vibration perpendicular to the plane of Figures 4a and 4b
3. λ values for $\nu = 0.3$

Equations (7) and (8) do not take into account shear deformation, cross sectional distortion due to torsion, or coupling of rotation and displacement. The rotary inertia of the beam twisting about its own axis is not included in Equation (7) but is included in Equation (8). However, the values of λ given in Table 2 are only valid for circular beams or tubes with a value of $\nu = 0.3$.

Simple Frames

The simple frames shown in Figure 5 are also called portal frames in structural applications or bents in electronic applications. The following formulas provide approximate values for the fundamental natural frequencies in the specified vibration modes.[3]
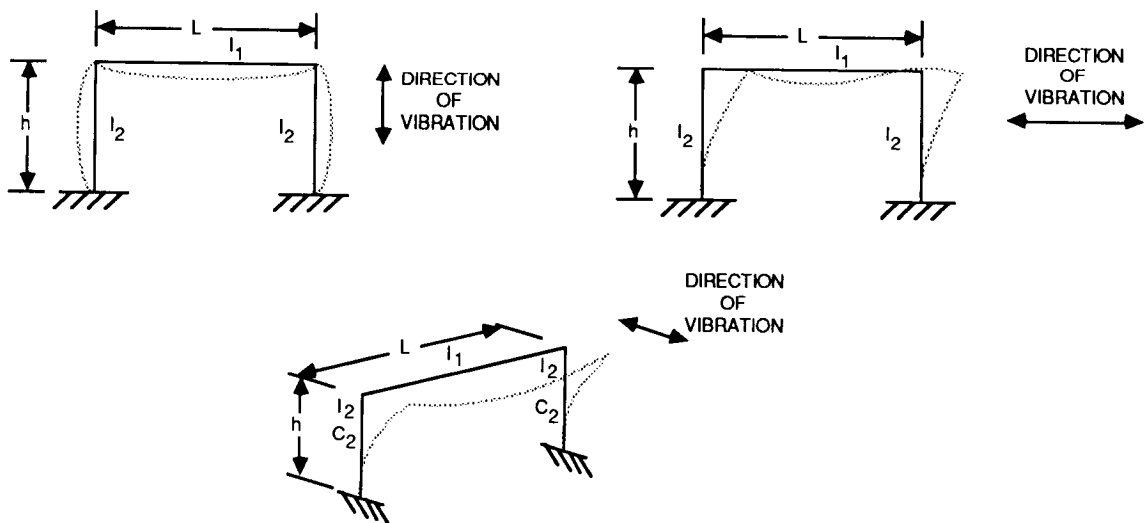
Fig. 5   A Simple Frame in a) In-Plane Vertical Vibration,
b) In-Plane Lateral Vibration, and c) Out-of-Plane Transverse Vibration

209

For in-plane vertical vibration with legs hinged at the supports, Figure 5a,

$$F = (1/2\pi)\left\{48EI_1g/WL^3[1-2.25/(2K+3)]\right\}^{\frac{1}{2}} \text{ Hz} \tag{9}$$

where E = modulus of elasticity of frame material, lbf/in^2,
I_1 = area moment of inertia of top of frame about neutral axis, in^4,
g = gravitational acceleration at surface of earth = 386 in/sec^2,
W = total weight of frame, lbf,
L = length of top (span of frame), inch,
K = hI_1/LI_2, dimensionless,
h = height of frame (length of leg), inch,
I_2 = area moment of inertia of frame legs about neutral axis, in^4.

For in-plane vertical vibration with legs fixed at the supports, Figure 5a,

$$F = (1/2\pi)\left\{48EI_1g/WL^3[1-3/(2K+4)]\right\}^{\frac{1}{2}} \text{ Hz} \tag{10}$$

For in-plane lateral vibration with legs fixed at the supports, Figure 5b,

$$F = (1/2\pi)\left\{24EI_2g/Wh^3[1+3/(6K+1)]\right\}^{\frac{1}{2}} \text{ Hz} \tag{11}$$

For out-of-plane transverse vibration with legs fixed at the supports, Figure 5c,

$$F = (g^{\frac{1}{2}}/2\pi)\left\{(W/2)[L^3/24EI_1 + h^3/3EI_2\right.$$
$$\left. - L^4GC_2/32EI_1(2hEI_1+LGC_2)]\right\}^{-\frac{1}{2}} \text{ Hz} \tag{12}$$

where C_2 = torsional constant, in^4.

The approximate fundamental natural frequency for a rigid body of mass M_o supported by n slender, uniform legs of length L, all in the same plane, clamped at their feet and at the rigid body, as shown in Figure 6, for vibration in the plane of the legs, is given by[4]

$$F = (1/2\pi)[(12\Sigma E_iI_i)/L^3(M_o+0.37\Sigma M_i)]^{\frac{1}{2}} \text{ Hz} \tag{13}$$

where M_o = rigid body mass, lbs.mass,
M_i = mass of leg i, lbs.mass,
E_i = modulus of elasticity of leg i, lbf/in^2,
I_i = area moment of inertia of leg i about its neutral axis, in^4,
Σ = sum over all legs, i = 1, 2, 3, ..., n,
n = number of legs $\geq$ 2.

Housings

Housings may be analyzed to estimate their fundamental natural frequencies. These frequencies may include flexural vibration along one or more axes of the structure, torsional vibration, and coupled modes of vibration. The frequencies will depend on the geometry and material properties of the

DIRECTION OF
VIBRTATION
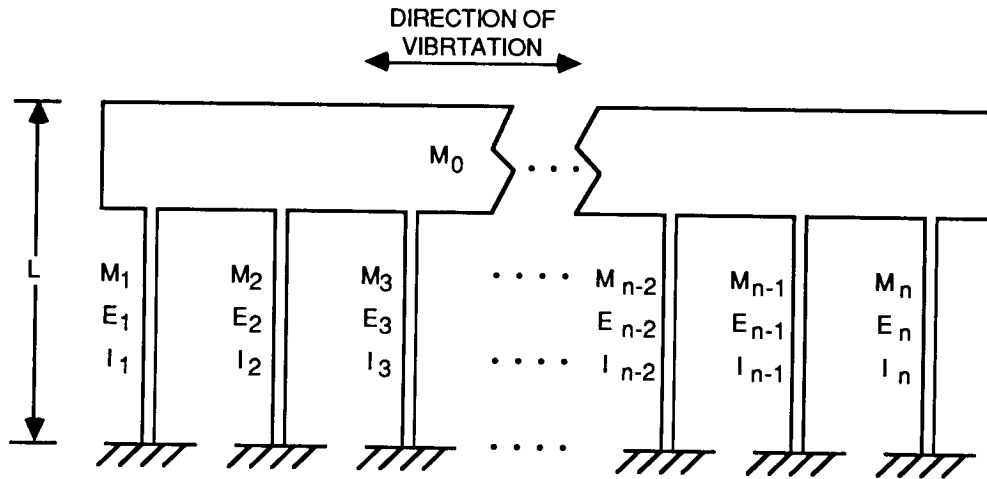
Fig. 6   Rigid Body on Slender Legs

structure[5], the attachment efficiency factor between parts of the structure and the connection of the structure to mounting surfaces (the boundary conditions).

Flexure

Figure 7 shows a housing composed of several structural elements. It is mounted by means of brackets attached at each end of the longer dimension, near the bottom (Figure 7b). It will be analyzed as a simply supported beam which can vibrate in flexure in the X direction and in the Y direction, and which can vibrate in torsion about the Z axis. Evaluation of the flexural frequencies requires an estimate of the stiffness factors of the structure, $E_x I_x$ and $E_y I_y$. These are determined as follows.

$$E_x I_x = \sum_{i=1}^{6} \eta_i E_i [A_i (\overline{X} - X_i)^2 + I_{x,i}] \quad \text{lbf.in}^2 \tag{14}$$

where η_i = attachment efficiency factor for element i, dimensionless,
  E_i = modulus of elasticity of element i, lbf/in^2,
  A_i = cross sectional area of element i in the x-y plane, in^2,
  X_i = distance from left edge of structure to neutral axis (or mid-point) of element i, inch,
  Ix,i = area moment of inertia of element i about the neutral axis parallel to the Y direction at X_i, in^4,
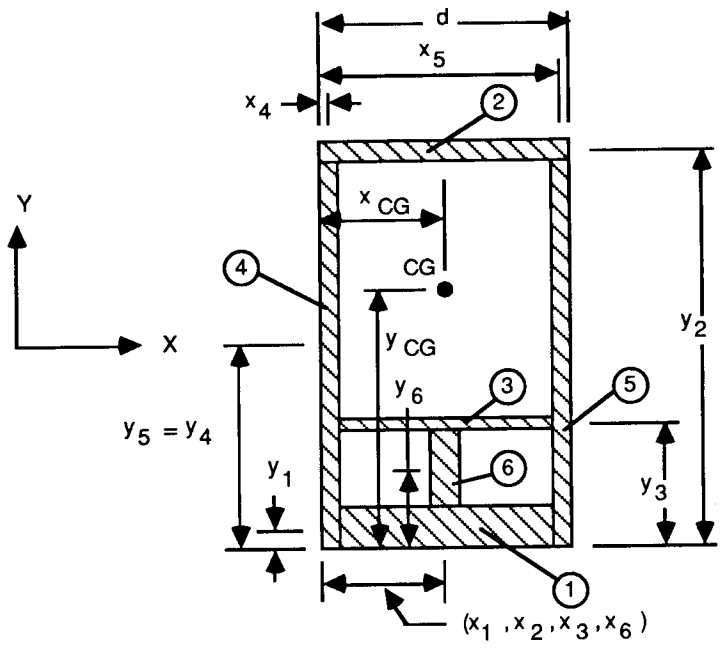
A) SIDE VIEW CROSS SECTION
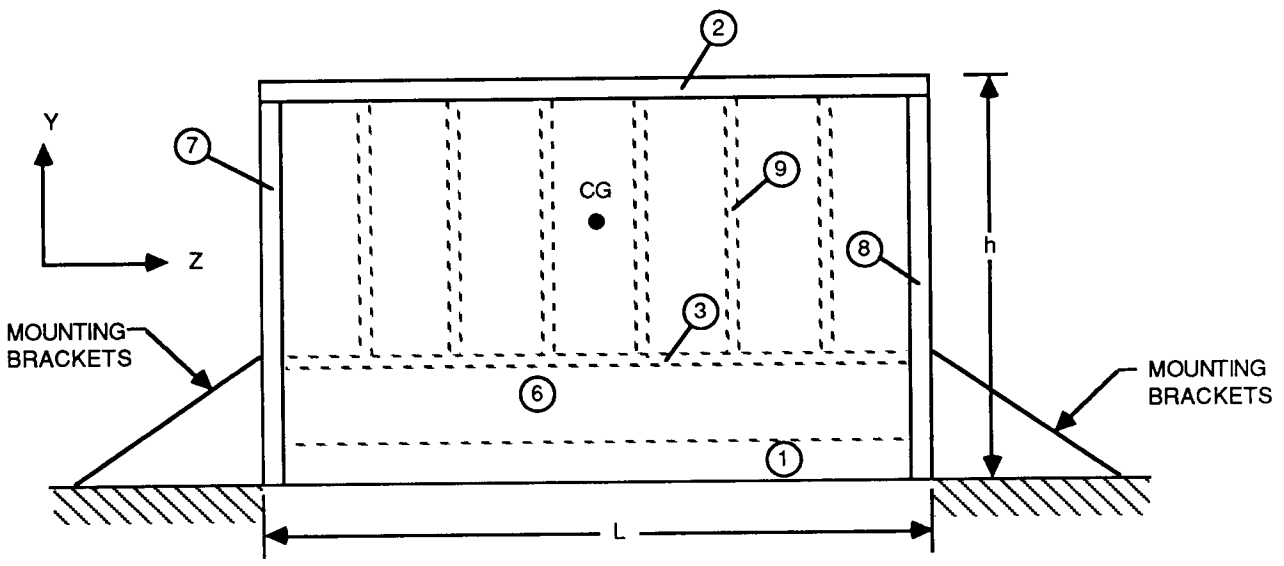
B) FRONT VIEW

Fig. 7 Housing

and

$$\overline{X} = \sum_{i=1}^{6} \eta_i A_i E_i X_i / \sum_{i=1}^{6} \eta_i A_i E_i \quad \text{inch.} \tag{15}$$

$$E_y I_y = \sum_{i=1}^{6} \eta_i E_i [A_i (\overline{Y} - Y_i)^2 + I_{y,i}] \quad \text{lbf.in}^2 \tag{16}$$

where η_i, E_i and A_i are defined following Equation (14),

and Y_i = distance from bottom of structure to neutral axis (or mid-point) of element i, inch,

$I_{y,i}$ = area moment of inertia of element i about the neutral axis parallel to the X axis at y_i, in^4,

and

$$\overline{Y} = \sum_{i=1}^{6} \eta_i A_i E_i Y_i / \sum_{i=1}^{6} \eta_i A_i E_i \quad \text{inch} \tag{17}$$

Note that structural elements 7, 8 and 9 are not included in Equations (14) through (17) because they are not subjected to bending but are either fixed to the mounting brackets or displaced parallel to their own plane. The fundamental natural frequencies for flexural vibration in the X and Y directions are

$$F_x = (\pi/2L^2)(E_x I_x g/W)^{\frac{1}{2}} \quad \text{Hz} \tag{18}$$

and

$$F_y = (\pi/2L^2)(E_y I_y g/W)^{\frac{1}{2}} \quad \text{Hz}$$

where L = length of housing, Figure 7b, inches,
g = acceleration of gravity at surface of earth = 386 in/sec^2,
W = weight of housing per unit length, lbf/inch (Total weight = WL)
$E_x I_x$ and $E_y I_y$ are found from Equations (14) and (16).

If the ends of the housing, structural elements 7 and 8, were mated with and fixed to mounting surfaces, then the constant in Equation (18) would be $(22.373/\pi)$ instead of π.

Torsion

Acceleration in the X direction will produce torsion as well as bending since the housing is supported near its bottom and the center of gravity (CG) is located above the support (Figure 7b). The axis of rotation for torsion will be at the bottom of the housing parallel to the Z axis. See Figure 8. Since the CG is not on the axis of rotation, the torsional natural frequency of the housing will be coupled to the flexural natural frequency, F_x.
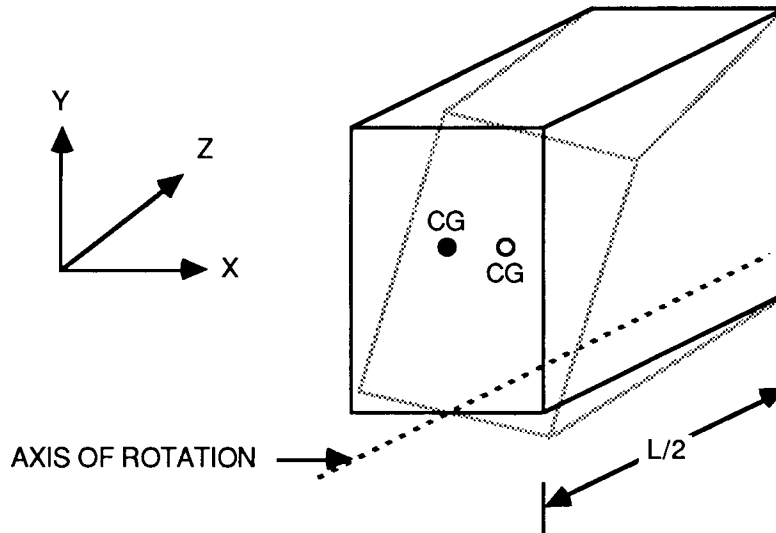
Fig. 8 Torsional Deflection, With One-Half of Housing Shown

The frequency formula for torsional vibration is

$$F_\theta = (\lambda/2\pi L) \cdot (CGg/\mu I_p)^{1/2} \, Hz \qquad (19)$$

where C = torsional constant of beam cross section, in^4
   G = shear modulus of beam material, lbf/in^2
   μ = weight density of beam material, lbf/in^3
   I_p = polar area moment of inertia of beam cross section about the beam axis of torsion, in^4.

The polar mass moment of inertia, J, about the axis of rotation is an important factor in the present case. The half-housing shown in Figure 8 may be analyzed with the frequency constant λ found by solving the transcendental equation which includes the parameter J:

$$cot\lambda = (Jg/\mu LC)\lambda \qquad (20)$$

For the half-housing, L must be replaced by L/2 in Equations (19) and (20), and J must be the polar mass moment of inertia about the axis of rotation for the half-housing. The same results may be obtained by using the formula

$$F_\theta = (1/2\pi) \cdot (4CG/LJ)^{1/2} \, Hz \qquad (21)$$

instead of Equation (19) when $(\mu L I_p/gJ)^{1/2} \ll 1$. In Equation (21), L is the full length of the housing and J is the polar mass moment of inertia about the axis of rotation for the full housing. C and G have the same values as in Equations (19) and (20). Using the relation $\mu = Mg/LA$ lbf/in^3, where M is the total mass of the housing and A is the housing cross sectional area in the X-Y plane, and equating Equations (19) and (21) yields:

214

$$I_p/A = \lambda^2 J/M \quad in^2 \tag{22}$$

where the radius of gyration is $(I_p/A)^{\frac{1}{2}}$. In arriving at Equation (22), L was replaced by L/2 in Equation (19).

The value of the polar area moment of inertia about the axis of rotation, I_p, may be estimated by

$$I_p = (E_x I_x + E_y I_y)/E_a \quad in^4 \tag{23}$$

where E_a is an appropriate average value for the structure. In the case where the structure is composed primarily of a single structural material, E_a is the modulus of elasticity for that material.

The value of J is given by

$$J = \sum_{i=1}^{9} [J_{z,i} + m_i(x_i^2 + y_i^2)] \quad lbmass.in^2 \tag{24}$$

where $J_{z,i}$ = polar mass moment of inertia about axis through the neutral axis of element i and parallel to the axis of rotation, $lbmass.in^2$,
   m_i = mass of element i, lbmass,
   x_i, y_i previously defined.

A more rapid but less accurate approximation for J is

$$J = (M/12)(4h^2 + d^2) \quad lbmass.in^2 \tag{25}$$

where M is the total mass of the housing. (See Figure 7.)

If J is calculated for the entire housing, then only half of its value must be used in Equation (20).

The torsional constant C is much more difficult to accurately estimate, even for a simple structure. The following rough approximation may be used:[6]

$$C \cong [1/2]I_p \quad in^4 \tag{26}$$

Coupled Modes
   As pointed out previously, acceleration in the X direction produces both bending at a frequency F_x and torsion at a frequency F_θ. These vibration modes will be coupled to produce a fundamental natural mode of the structure which can be approximated by Dunkerley's method[7]

$$F_c = (F_x^{-2} + F_\theta^{-2})^{-\frac{1}{2}} \quad Hz \tag{27}$$

where F_x and F_θ are found from Equations (18) and (19). The coupling of modes of vibration always results in a natural frequency lower than the coupled frequencies, and a consequent increase in deflection and stress. In the example given in the preceeding two sections, this coupling of modes may be

avoided by mounting the housing so that the center of gravity (CG) lies on the mounting plane. Torsional modes may still occur but they will not be coupled with the bending mode. Figure 9 is an example of a CG mount.
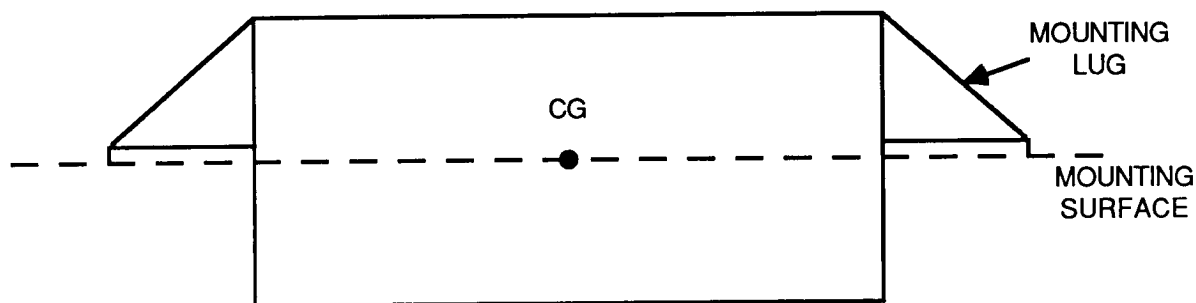
Fig. 9   A CG Mount

Other Housing Configurations

There are other housing geometries and mounting configurations where the housing may be modeled as a beam or a plate with boundary conditions which approximate the mounting attachments. In these cases the standard frequency formulas may be used to estimate the fundamental natural frequency of the housing. The flexural stiffness factors, EI, and the torsional frequency parameters C, I_p and J must be estimated as in Section 5.3.

The examples shown in Figure 10 could be analyzed as follows.

Figure 10a.
   1) For L > h,t: A beam with simply supported ends.
       Flexural vibration in X and Z directions.
       Torsional vibration about the axis through centroid, parallel to Y axis.
       Flexural and torsional modes not coupled.

   2) For L ≅ h > t: A plate with two opposite sides simply supported, other two sides free.
       Flexural vibration in Z direction.

216
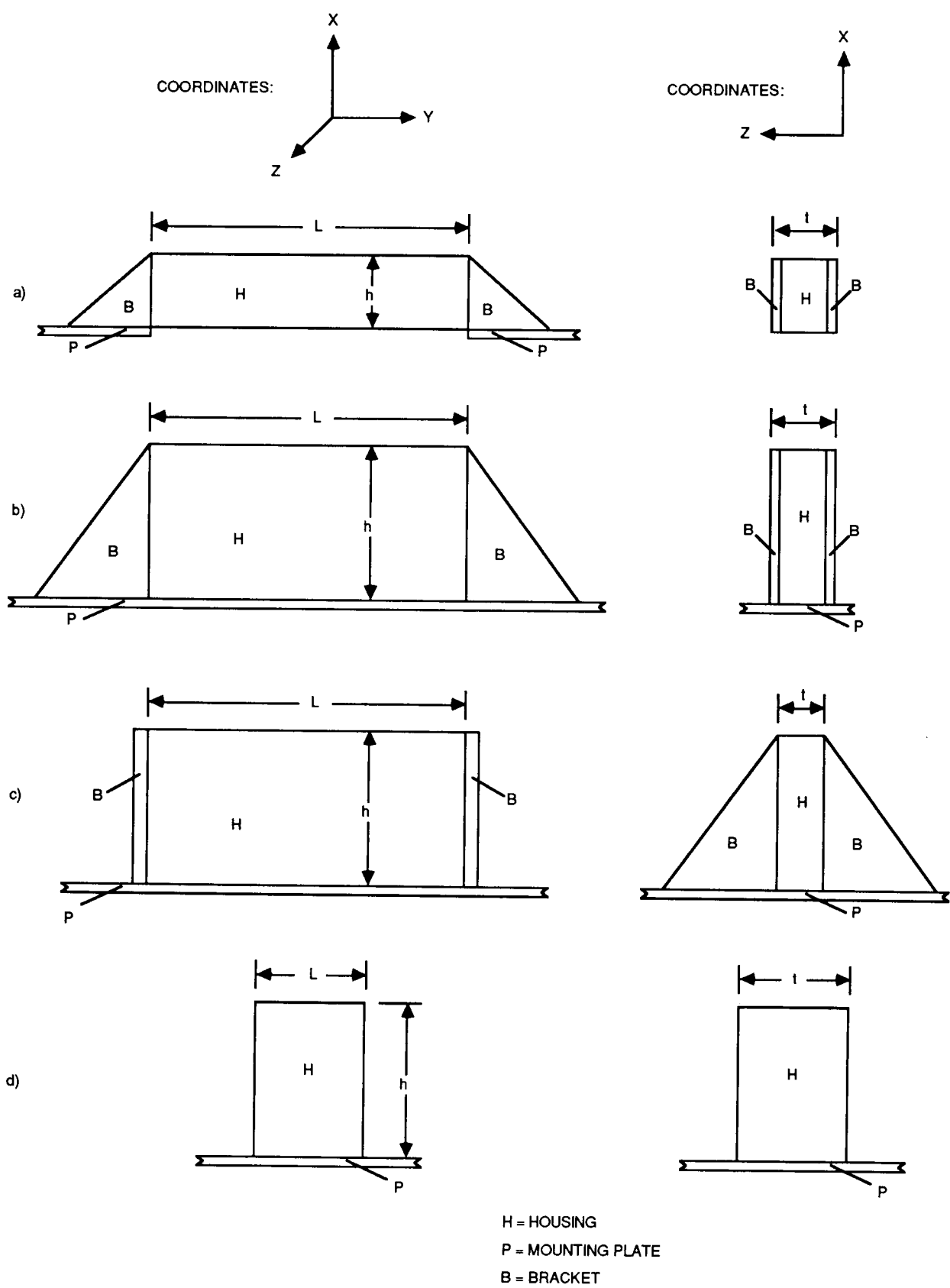
Fig. 10 Examples of Housing and Mounting Configurations

3) For L ≅ t > h: A plate with four corner supports.
   Flexural vibration in X direction.

Figure 10b.
   For L ≅ h > t: A plate with three simply supported sides.
   Flexural vibration in Z direction.

Figure 10c. Same as 10b.

Figure 10d.
   1) For h > L,t: A cantilever beam.
      Flexural vibration in Y and Z directions.
      Torsional vibration about the axis through centroid, parallel to X axis.
      Flexural and torsional modes coupled if CG is not at the mid-point of the L and the t dimensions.

   2) For L ≅ h > t: A plate simply supported on one side with other three sides free.
      Flexural vibration in Z direction.
      Torsional vibration about the axis through centroid parallel to X axis.
      Flexural and torsional modes coupled if CG is not at the mid-point of the L dimension.

Lumped Elements

One type of model that may be used to represent structures is the lumped element model. In this approach, parts of the structures are treated as masses and other parts as springs. Rigid, heavy components may be treated as masses, while flexible, light weight components may be treated as springs. The spring elements may be some of the same structural components that make up the masses, even though they are treated as massless in the analysis. The combined weight of the masses must add up to the total weight of the complete structure.

Figure 11 shows a three degree-of-freedom structure composed of a transformer mounted on a bracket which is attached to a PWB mounted in a housing. The bottom of the housing is fixed to a mounting plate. When the acceleration is parallel to the mounting plate and normal to the PWB, the housing will vibrate as a cantilever, the PWB will vibrate as a loaded plate, and the bracket will vibrate in the direction shown. Figure 12 is a lumped element model of the structure shown in Figure 11. The values of the spring constants, K, may be determined by use of the following equation:

$$K = (W/g) \cdot (2\pi F)^2 \text{ lbf/inch} \tag{28}$$

where   W = weight of element, lbf,
        g = acceleration of gravity at surface of earth = 386 in/sec^2,
        F = fundamental natural frequency of the element, Hz.

The frequency formulas for finding the values of F in Equation (28) are given by Equation (9) for the bracket and by standard formulas for the PWB and the cantilever housing. The static deflections, for a one-g acceleration, are

218
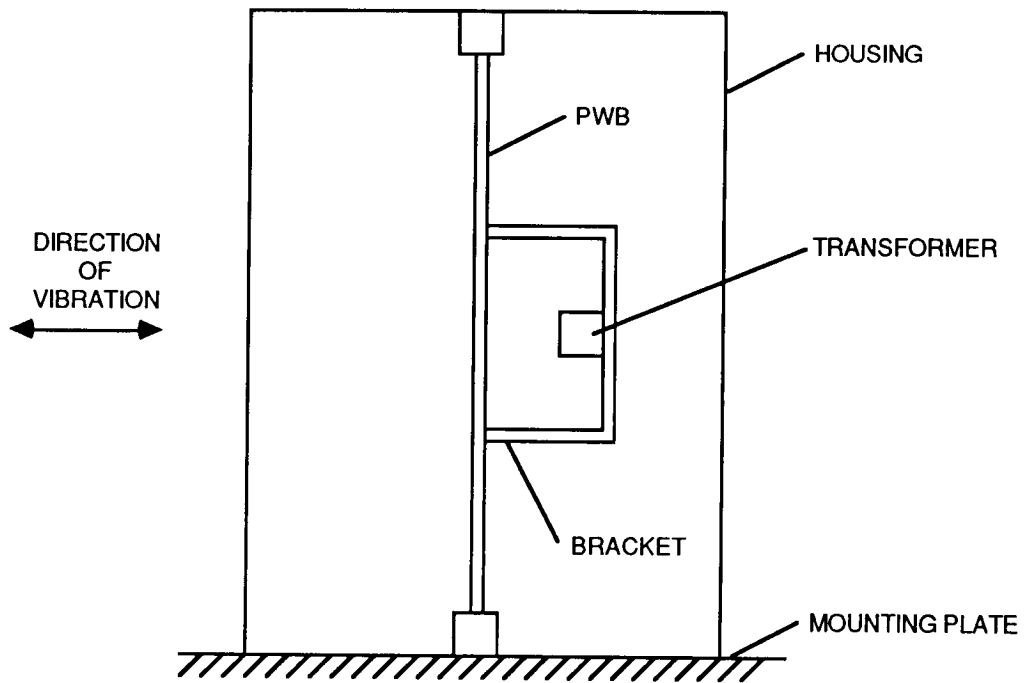
Fig. 11 Example of Three Degree-of-Freedom Structure
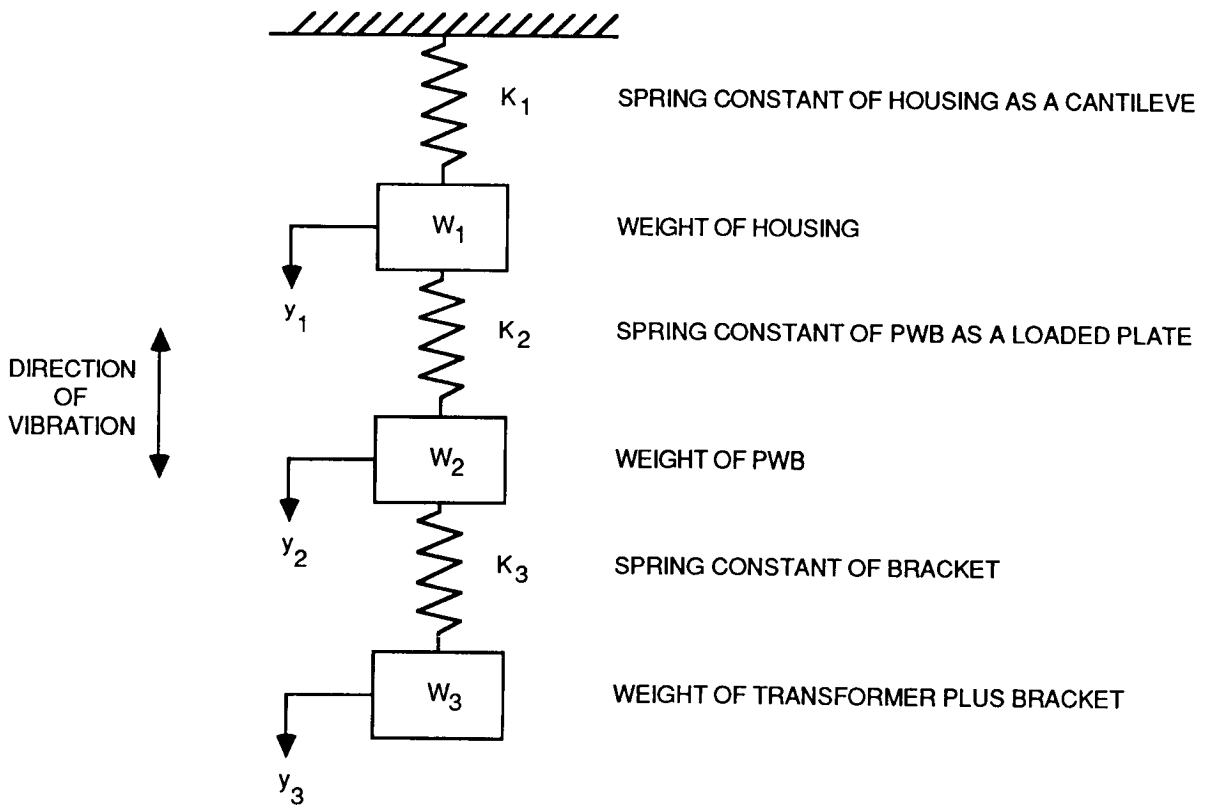
Fig. 12 Lumped Element Model of Three Degree-of-Freedom Structure

$$y_1 = (W_1 + W_2 + W_3)/K_1 \text{ inch} \tag{29}$$

$$y_2 = y_1 + (W_2 + W_3)/K_2 \text{ inch}$$

$$y_3 = y_1 + y_2 + W_3/K_3 \text{ inch}$$

The fundamental natural frequency of the structure shown in Figures 11 and 12 is[8]

$$F = (1/2\pi)\left[g \sum_{i=1}^{3} W_i y_i / \sum_{i=1}^{3} W_i y_i^2\right]^{\frac{1}{2}} \text{ Hz} \tag{30}$$

For a structure with n degrees of freedom, which can be represented by n spring/mass elements in series,

$$y_i = \sum_{j=1}^{i-1} y_j + \sum_{j=i}^{n} W_j/K_i \text{ inch} \tag{31}$$

and

$$F = (1/2\pi)\left[g \sum_{i=1}^{n} W_i y_i / \sum_{i=1}^{n} W_i y_i^2\right]^{\frac{1}{2}} \text{ Hz} \tag{32}$$

Accelerations and Stresses

The natural frequency of a structure will determine what will be its acceleration response in a shock or vibration environment. Two different structural designs with two different natural frequencies will generally experience different accelerations, resulting in different stresses when exposed to the same shock or random vibration spectrum. The estimates of natural frequency allow comparison of structural designs in terms of dynamic loads due to the specified acceleration environments.

Figure 13 shows the shock acceleration response spectrum for an NSI ordinance, one-inch separation nut. The acceleration response is the three-sigma peak value (exceeded only 0.28% of the time) in units of the gravitational acceleration at the earth's surface, and it peaks at 15,000g and 10,000Hz. A structure with a natural frequency of 200Hz will experience a 215g shock, while one with a natural frequency of 250Hz will experience a 310g shock. The acceleration ratio is 310/215 = 1.44.

Figure 14 shows a typical random vibration power spectral density (PSD) to which a space structure would be exposed during launch. The three-sigma peak acceleration response is approximated by

$$G_{pk} = 3[(\pi/2) \cdot \text{PSD} \cdot Q_o \cdot F_o]^{\frac{1}{2}} \text{ g} \tag{33}$$

where Q_o = transmissibility at the structure's natural frequency, F_o. Assuming the same value of Q_o for the two structures with natural frequencies of 200Hz and 250Hz, the acceleration ratio will be 1.12.
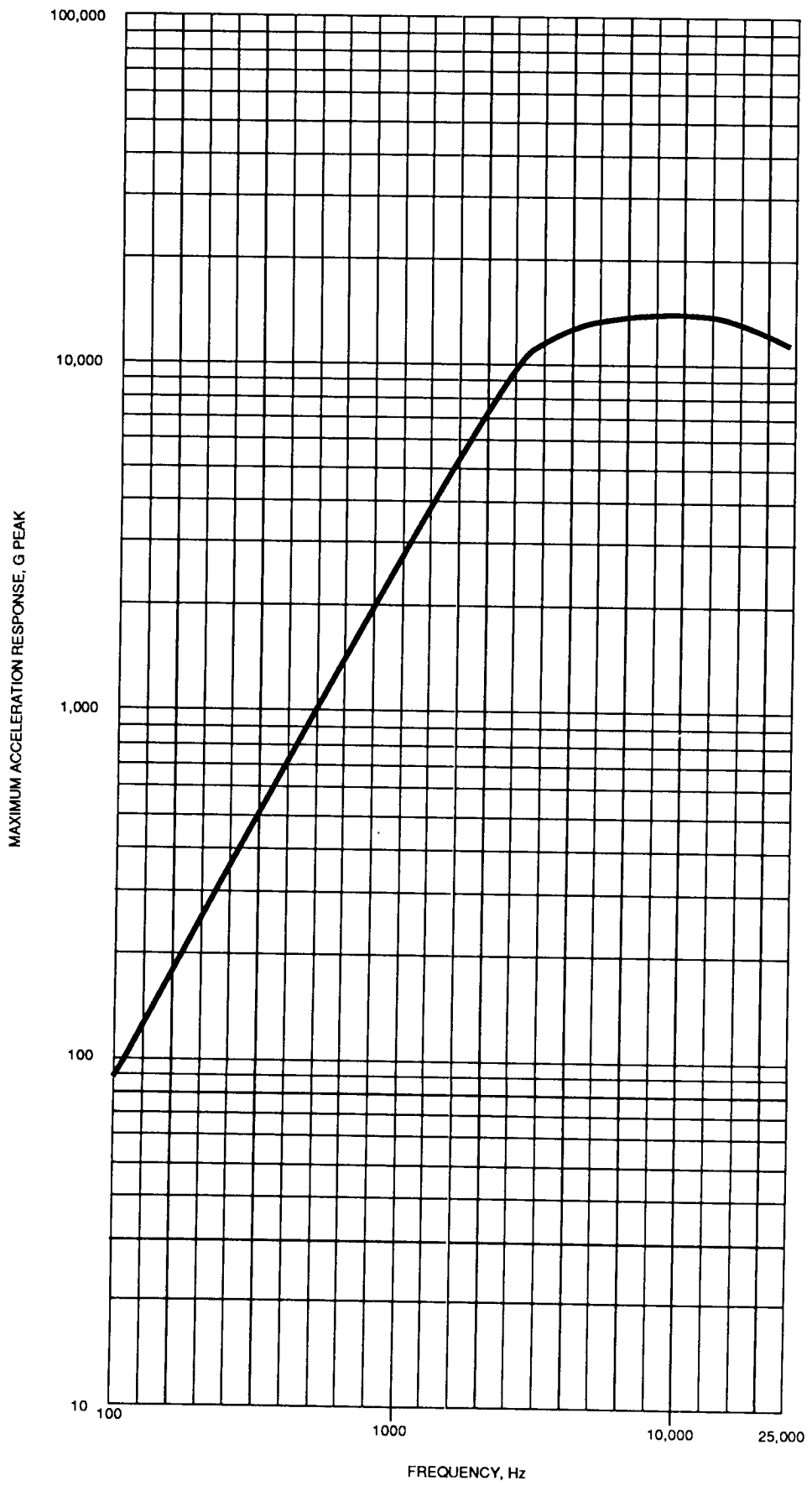
Fig. 13 Separation Nut Source Shock Spectrum (Reference 9)
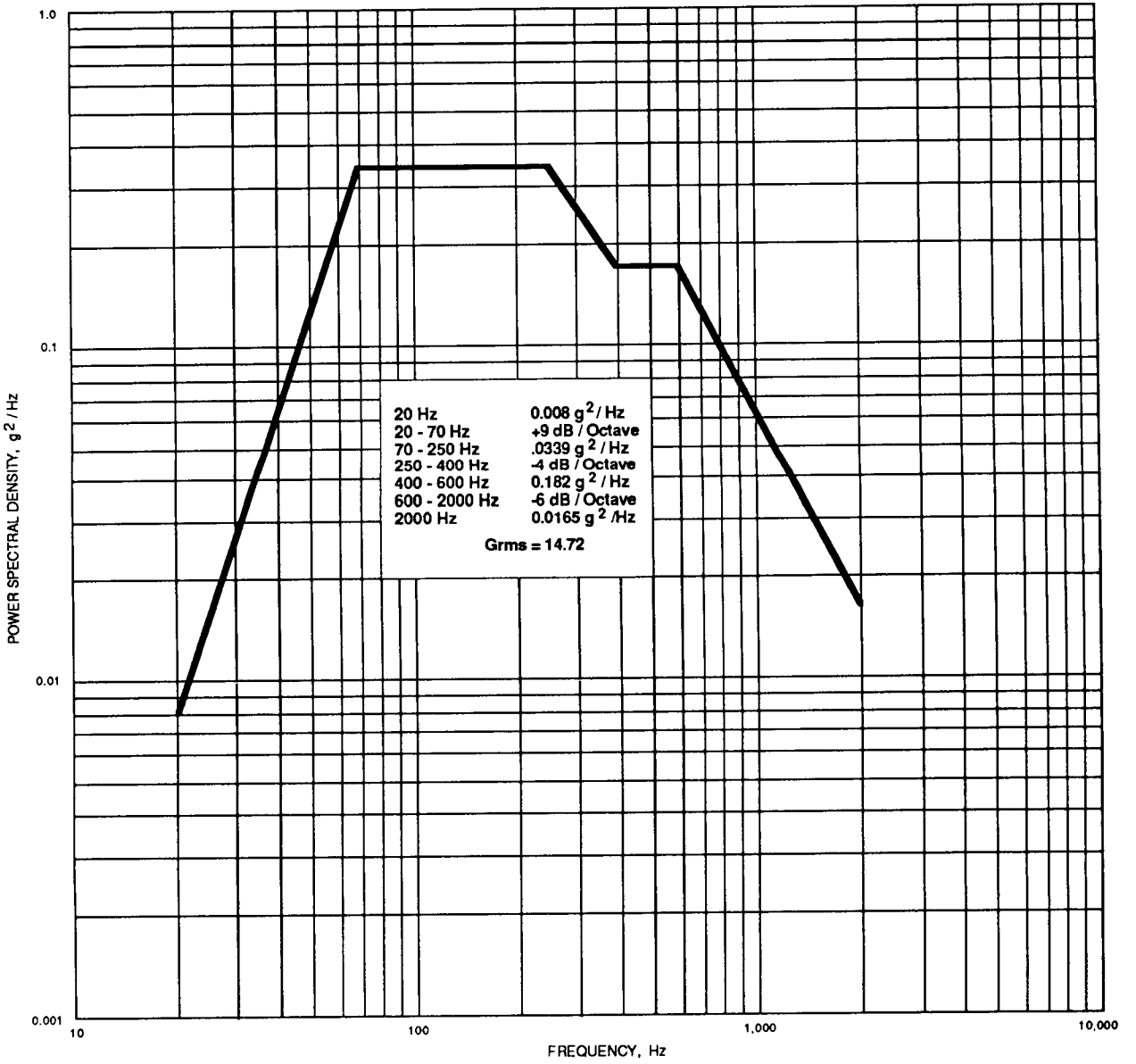
Fig. 14   A Typical Random Vibration Power Spectral Density (PSD)

In the above example, it is seen that the accelerations, and consequently the dynamic loads, between different structural designs may be compared when estimates of natural frequency can be made.

REFERENCES

1. D.S. Steinberg, _Vibration Analysis For Electronic Equipment_, pp. 127-136. Wiley-Interscience, New York, 1973

2. L.S.S. Lee, _J. Eng. Industry_ Vol. 97, pp. 23-32, 1975

3. Steinberg, op. cit., pp. 246-249

4. R.D. Blevins, _Formulas for Natural Frequency and Mode Shape_, p. 221. Van Nostrand Reinhold, New York, 1979

5. Steinberg, op. cit., pp. 304-306

6. R.J. Roark and W.C. Young, _Formulas for Stress and Strain_, 5th ed., pp. 290-303. McGraw-Hill, New York, 1975

7. Steinberg, op. cit., pp. 63-64

8. Steinberg, op. cit., p. 50

9. S. Barrett, "A Discussion of Pyrotechnic Shock Criteria," _Shock and Vibration Bulletin_, Vol. 41, No. 5, pp. 5-10, Dec. 1980

Simultaneous Structural and Control Optimization via Linear Quadratic Regulator Eigenstructure Assignment

G. A. Becus

C. Y. Lui

V. B. Venkayya

V. A. Tischler

This paper presents a method for simultaneous optimal structural and control design of large flexible space structures (LFSS) to reduce vibration generated by disturbances. Desired natural frequencies and damping ratios for the closed-loop system are achieved by using a combination of linear quadratic regulator (LQR) synthesis and numerical optimization techniques. The state and control weighting matrices (Q and R) are expressed in terms of structural parameters such as mass and stiffness. The design parameters are selected by numerical optimization so as to minimize the weight of the structure and to achieve the desired closed-loop eigenvalues. An illustrative example of the design of a two bar truss is presented.

INTRODUCTION

Large structural systems in general and large space structures in particular present new challenges to the structural dynamicist and the control engineer as well. Indeed, such large systems may exhibit well over a thousand vibrational modes usually closely spaced and with little, if any, damping. Some form of active control is likely to be necessary in order to meet exacting stability and pointing requirements. In fact, structural requirements (primarily low mass) increase the need for active control. Some optimal trade off between structural and control criteria has to be achieved.

Until recently, the design of control systems for large structural systems was a two-step procedures: first the structure was designed based on structural criteria (primarily total weight); then in a second step a control system (satisfying some desired control objectives) was designed for the structure obtained in the first step. Inasmuch as a low weight (and thus low stiffness) structure will require high control energy, the design objectives of the two steps are to some extent contradictory so that an optimal control design for an optimally designed structure will not in general result in an overall control-structure optimal design. Both designs need to be carried out simultaneously.

LITERATURE REVIEW

The optimal structural and control design of large flexible space structures was recently investigated by several researchers. Venkayya and Tischler [1-2] have suggested that the performance index (PI) in optimal control of structural systems be a measure of the system total mechanical energy. By appropriately choosing the state and control weighting matrices, the PI can be expressed as the (weighted) sum of the kinetic, strain and potential (including control) energies. Khot and Venkayya [3-4] tackled the structural and control optimization problem by minimizing the weight of the structure with constraints on structural frequencies and the minimum Frobenious norm of the gain matrix. This process has to be carried out in an iterative fashion.

Becus and Lui [5] have proposed a general method to choose state and control weighting matrices in optimal control design so as to satisfy desired closed-loop eigenvalues. This was further extended by Becus and Sonmez [6] to allow for eigenvector assignment. In this paper we combine both ideas in order to obtain a method to carry out simultaneous optimal structural and control design.

Desired dynamic structural requirements (natural frequencies and damping ratios for example) can be expressed both in terms of desired closed-loop eigenstructure (eigenvalues and/or eigenvectors) and structural parameters (mass and stiffness for example). Using a PI of the form suggested in [1], the elements of the state and control weighting matrices (Q and R respectively) are also expressed in terms of structural parameters. Thus, when choosing the Q and R matrices (using the method of [5-6]) to satisfy a desired closed-loop eigenstructure (i.e. dynamic structural requirements), one in fact chooses new strucutral parameters and therefore carries out a simultaneous optimal control structure design.

In this paper a new design algorithm is developed so that a minimum weight structure with desired damping and natural frequency of the closed-loop system can be obtained. We compare the results with [3] in the last section.

SIMULTANEOUS STRUCTURAL AND CONTROL OPTIMIZATION

Consider a controlled structural dynamic system described by the discrete (finite element) model

$$M\ddot{r} + Kr = Du \tag{1}$$

where r is a vector of n physical displacements and the number of control inputs (forces) u is m. M, K and D are the mass, stiffness and applied load distribution matrices of appropriate dimensions respectively. Assume that M and K are positive definite.

The state space representation of Eq. (1) can be written as

$$\dot{x} = Ax + Bu \tag{2}$$

where
$$x = [\dot{r}^T \quad r^T]^T \tag{3}$$

$$A = \begin{vmatrix} 0 & | & -M^{-1}K \\ \text{---------} \\ I & | & 0 \end{vmatrix} = A(p) \quad , \tag{4}$$

and

$$B = \begin{vmatrix} M^{-1}D \\ \text{------} \\ 0 \end{vmatrix} = B(p) \quad , \tag{5}$$

where p is a vector of structural parameters of dimension 1.
The optimal steady-state control is a linear state feedback

$$\bar{u} = -Gx \quad . \tag{6}$$

The state feedback gain matrix G is obtained from LQR synthesis and the closed-loop system is given by

$$\dot{x} = (A - BG)x \quad . \tag{7}$$

LQR synthesis determines a control $\bar{u}$ which minimizes the quadratic performance index [1]

$$PI = \int_0^\infty [\Theta_m \dot{r}^T M \dot{r} + \Theta_k r^T K r + \Theta_r u^T D^T K^{-1} D u] \, dt \tag{8}$$

or in the state space coordinates

$$PI = \int_0^\infty [x^T Q x + u^T R u] \, dt \tag{9}$$

where

$$Q = \begin{vmatrix} \Theta_m M & | & 0 \\ \text{-----------} \\ 0 & | & \Theta_k K \end{vmatrix} = Q(p) \tag{10}$$

and

$$R = [\Theta_r D^T K^{-1} D] = R(p) \tag{11}$$

for positive scaling parameters Θ_m, Θ_k and Θ_r. In Eq. (8), PI is the absolute weighted sum of the kinetic, strain and potential energies.

The relationship between characteristic polynomial of the optimal system and weighting matrices is obtained as follows [7]

$$\det(sI - Z) = \begin{vmatrix} sI - A & | & BR^{-1}B^T \\ \text{------------------} \\ Q & | & sI + A^T \end{vmatrix} \tag{12}$$

or

$$\phi_c(s)\phi_c(-s) = \phi_0(s)\phi_0(-s)\det[I + R^{-1}H^T(-s)QH(s)] \tag{13}$$

where H(s) is the open-loop transfer function matrix

$$H(s) \overset{\Delta}{=} (sI - A)^{-1} B \ , \tag{14}$$

Z is the canonical system matrix, $\phi_c(s)$ and $\phi_0(s)$ are the closed-loop and open-loop characteristic polynomials respectively.

For a given desired closed-loop pole $s = s_d$ which is not an open-loop pole, the determinant in the right-hand side of Eq. (13) must equal zero when the weighting matrices Q and R take values which yield the desired closed-loop eigenvalues. In order to use numerical optimization techniques to solve Eq. (13) for Q and R, we, as in Ref. [8], set the objective function as

$$obj = \det\left[I + R^{-1}H^T(-s_d)QH(s_d)\right] = 0 \ . \tag{15}$$

The desired characteristic equation corresponding to Eq. (15) is

$$\overset{n}{\underset{j=1}{\Pi}} = (s - s_{d_j})(s + s_{d_j}) = 0 \tag{16}$$

where s_{d_j} is the j-th desired closed-loop eigenvalue.

Q and R are determined by equating coefficients of the terms involving equal powers of s in Eqs. (15) and (16). This yields

$$f_1(p) = 0$$
$$\cdot$$
$$\cdot \tag{17}$$
$$\cdot$$
$$f_k(p) = 0$$

where k is the number of equality constraints which involve equal powers of s in Eqs. (15) and (16).

The objective in structural and control optimization is to make the selection of design parameters so that the structure weight is a minimum and the specified closed-loop eigenvalues are satisfied. The optimization problem can be stated as

$$\text{Minimize the weight} \quad W = W(p)$$

subject to   Eq. (17)   (18)

and $P_s \geq \bar{P}_s, \ s = 1, \ \cdots, \ 1,$

where $\bar{P}_s$ denote minimum allowable values of the structural design parameters.

ILLUSTRATIVE EXAMPLE

In order to illustrate the feasibility of the above algorithm, the structural two bar truss model shown in Fig. 1 was considered as a simple design example. For the geometry shown, the dynamical equations of motion (Eq. (1)) are

$$
\begin{vmatrix} 2 & 0 \\ 0 & 2 \end{vmatrix}
\begin{vmatrix} \ddot{r}_1 \\ \ddot{r}_2 \end{vmatrix}
+ k_1
\begin{vmatrix} (A_1+A_2) & 2(A_1-A_2) \\ 2(A_1-A_2) & 4(A_1+A_2) \end{vmatrix}
\begin{vmatrix} r_1 \\ r_2 \end{vmatrix}
=
\begin{vmatrix} \cos(\theta) \\ \sin(\theta) \end{vmatrix} u
\qquad (19)
$$

thus
$$
M = \begin{vmatrix} 2 & 0 \\ 0 & 2 \end{vmatrix}
\qquad (20)
$$

and

$$
K = k_1 \begin{vmatrix} (A_1 + A_2) & 2(A_1 - A_2) \\ 2(A_1 - A_2) & 4(A_1 + A_2) \end{vmatrix}
\qquad (21)
$$

are the optimal mass and stiffness of the structure respectively. In Eq. (19), A_1 and A_2 are the cross-sectional areas of the bars and $k_1 = E/(5L)$ is a stiffness coefficient, E representing the elastic modulus of the bars and L the length of the members. A control force u is located at the vertex with θ being the angle between its line of action and the horizontal. r_1 and r_2 are the horizontal and vertical displacements of the vertex respectively.

The dimensions of the structure were given in unspecified consistent units. The elastic modulus of the members was assumed to be 1 and the density ρ of the structural material was assumed to be 0.001. A nonstructural mass of 2 units was attached at node 2 and the structural mass of the members was ignored for simplicity (thus the mass matrix of Eq. (20)). The actuator and sensor were located in element 1 connecting node 1 and 2. The minimum cross-sectional area was set equal to 10 units for both members.

Once the choice of the material is fixed, the design variables are the cross-sectional areas of the members A_1 and A_2, the scaling parameters θ_m, θ_k and θ_r, and the angle θ of the applied load with respect to the horizontal. The optimal closed-loop eigenvalues are specified as $s_{d_1} = -0.0228 \pm 1.17j$ and $s_{d_2} = -0.361 \pm 4.81j$. Arbitrary lower and upper values of θ were set at $30°$ and $60°$ respectively.

Analytical and numerical computations were carried out using MACSYMA[TM] [9] for symbolic algebraic manipulations, MATLAB [10] for matrix computations and LQR synthesis, and GRG2 [11] for numerical optimization. The numerical results for several representative optimal designs are listed in Table 1. A discussion of these results appears in the next section.

Table 1. Optimal Two Bar Truss Designs

DESIGN	A_1	A_2	WEIGHT	Θ_m	Θ_k	Θ_r	θ deg	ACHIEVED CLOSED-LOOP EIGENVALUES
1	101.98	889.88	22.18	1	1.12	2.78	60	$-0.5074 \pm 1.25j$ $-0.382 \pm 4.82j$
2	788.86	78.81	19.40	1	1.26	53.80	55	$-0.0702 \pm 1.17j$ $-0.361 \pm 4.81j$
3	531.74	53.02	13.08	1	1.87	73.68	60	
4	442.86	44.16	10.89	1	2.25	73.68	60	$-0.0393 \pm 1.17j$
5	311.18	31.03	7.65	1	3.20	73.68	60	$-0.361 \pm 4.81j$
6	115.36	11.50	2.84	1	8.64	73.68	60	
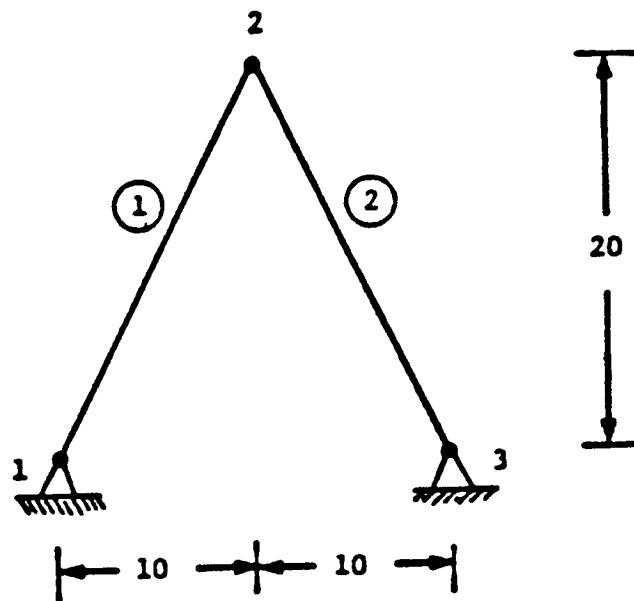
Fig. 1 Two Bar Truss

DISCUSSION OF RESULTS

For this simple example the six design variables were not independent. The scaling parameters Θ_m and Θ_k appeared in the constraint equations only as the combination $k_1\Theta_m/\Theta_k$. This combination was then used as one of five independent design variables. To obtain the values of Table 1, Θ_m was arbitrarily set equal to 1 then Θ_k was evaluated by multiplying the value obtained by numerical optimization by $k_1 = 0.0089$.

Since there are five independent design variables and only four equality constraints, there are many solutions to the optimization problem. In order to obtain a unique solution one could arbitrarily fix the value of one of the five independent design variables or equivalently introduce an additional constraint.

Of all designs presented in Table 1, Design 6 is the best since it leads to the lowest value for the weight. This "optimal" design leads to a weight of 2.84 which is less than half of the best design of Ref. [3] (6.417).

A closer examination of Table 1 leads to some interesting observations. Designs 3 through 6 have weights which are inversely proportional to Θ_k. In fact the product $\Theta_k \times$Weight is nearly constant for these four designs and equal to 24.45. In addition it can be seen that for these four designs the ratio A_1/A_2 is nearly constant and equal to 10. It is conjectured that many other designs could be obtained by choosing areas satisfying this relationship and calculating the corresponding Θ_k while keeping the other design variables constant.

Design 1 is representative of several designs for which the ratio A_1/A_2 is nearly constant and equal to 0.1 while Design 2 leads to an angle less than the upper bound value of $60°$. For all designs obtained the product $\Theta_k \times$Weight was nearly constant and equal to 24.45.

Finally it must be noted that as more weight is given to the control effort the achieved closed-loop eigenvalues are closer to the desired eigenvalues. As more weight is being given to the strain energy cost the total weight decreases.

CONCLUSION

An algorithm for simultaneous structural and control optimization design of a minimum weight structure with desired closed-loop eigenvalues was proposed. It has been shown that structural and control designs can be obtained by LQR assignment. The design parameters were appropriately selected by numerical optimization so as to minimize the weight of the structure and to achieve desired natural frequencies and damping ratios. The feasibility of the algorithm was demonstrated by applying it to a simple example. Further work is needed to investigate the application of the algorithm to large-order systems.

REFERENCES

1. V.B. Venkayya and V.A. Tischler, "Frequency Control and its Effect on the Dynamic Response of Flexible Structures," AIAA Journal, Vol. 23, pp. 1768-1774, 1985.

2. D.F. Miller, V.B. Venkayya and V.A. Tischler, "Integration of Structures and Controls - Some Computational Issues," Proceedings of 24th Conference on Decision and Control, Ft. Lauderdale, FL, Dec. 1985.

3. N.S. Khot, V.B. Venkayya, H. Oz, R.V. Grandhi and F.E. Eastep, "Optimal Structural Design with Control Gain Norm Constraint," AIAA-87-0019, AIAA 25th Aerospace Sciences Meeting, Reno, Nevada, Jan. 12-15 1987.

4. N.S. Khot, R.V. Grandhi and V.B. Venkayya, "Structural and Control Optimization of Space Structures," AIAA-87-0939-CP, AIAA/ASME/ASCE/AHS 28th Structures, Structural Dynamics and Materials Conference, Monterey, CA, Apr. 6-10 1987.

5. G.A. Becus and C.Y. Lui, "A General Methodology for Pole Placement in Linear Quadratic Regulator Design of Multivariable Control Systems," AIAA-87-2314, AIAA GNC Conference, Monterey, CA, Aug. 17-19 1987.

6. G.A. Becus and G. Sonmez, "Eigenstructure Assignment in LQR Design of Multivariable Control Systems," SIAM 35th Anniversary Meeting (to be presented).

7. H. Kwakernaak and R. Sivan, "Linear Optimal Control Systems," Wiley Interscience, New York, 1972.

8. W.K. Chow and D.J. Collins, "Automated Pole Placement Algorithm for Multivariable Optimal Control Synthesis," AIAA-86-2196, AIAA GNC Conference, 1986.

9. VAX UNIX MACSYMA^{TM} Reference Manual, Release 309.1, Document SMI0501030.011, Symbolics, Inc., 1985.

10. J. Little and A. Laub, "Control System Toolbox User's Guide," The MathWorks, Inc., Sept. 1985.

11. L.S. Lasdon and A.D. Waren, "GRG2 User's Guide," Univ. of Texas at Austin, May 1982.

Viscous Damped Space Structure for Reduced Jitter

James F. Wilson

L. Porter Davis

ABSTRACT

A technique to provide modal vibration damping in high
performance space structures has been developed which uses
less than 1 ounce of incompressible fluid. Up to 50 percent
damping can be achieved which can reduce settling times of
the lowest structural mode by as much as 50 to 1. This
concept allows designers to reduce the weight of the struc-
ture while improving its dynamic performance.

Damping provided by this technique is purely viscous and has
been shown by test to be linear over 5 orders of input
magnitude. Amplitudes as low as 0.2 microinch have been
demonstrated. Damping in the system is independent of
stiffness and relatively insensitive to temperature.

This high resolution damping technique also complements
active structural control systems by reducing the struc-
ture's amplification ratios (Q) so that active compensation
becomes practical.

INTRODUCTION

In the past, engineers have required the structural designer to set the funda-
mental vibration modes of the spacecraft above the control frequencies. As space
structures become larger, this is impractical because designers are having to deal
with greater structural flexibility and high Q vibrations; consequently active and
passive damping techniques are being explored. The active systems suffer from high
cost, lower reliability, less coupling between modes and poor low-level or threshold
performance. Passive systems, which to date are primarily viscoelastic, suffer from
low damping ratios, sensitivity to temperature, predictability problems and flight
qualification difficulties.

A new concept using an incompressible viscous fluid provides some immediate
solutions, -- very high damping, linear predictable performance, acceptable tempera-
ture sensitivity, very easy qualification for long life space application and
relatively low cost.

The concept involves integrating a purely viscous damper using incompressible fluid into the basic strut element of a truss structure. Viscous forces of very high value, roughly equal to the spring or structural compliance force in the strut or tube can be developed. One specific implementation uses a tube within a tube arrangement (see Figure 1). The outer tube provides the basic high stiffness-to-weight characteristic provided for any normal truss structure element. The inner tube is in series with an incompressible fluid which is squeezed through a long orifice that provides a pure velocity sensitive force. The force depends on the viscosity of the fluid and the geometry of the orifice, and can be changed over a wide range. The velocity-sensitive force can be made significant compared to the spring force, and thus provide relatively high damping ratios. It might appear that the dual tube would weigh twice that of the conventional single-tube arrangement, but a structure designed for dynamic performance using highly damped dual-tube struts (D-Strut) could be lighter, since overall static stiffness would be reduced.
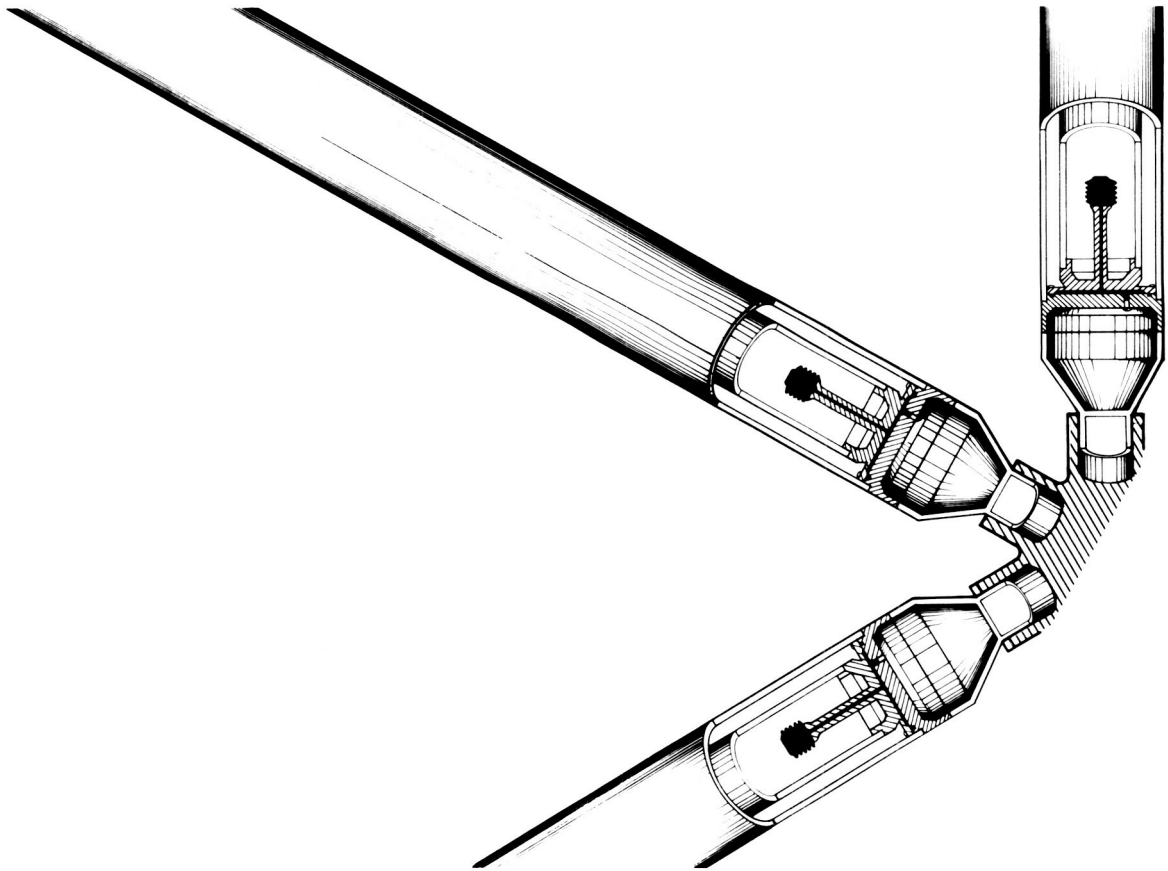
Fig. 1 D-Strut Shown in Truss Arrangement

A means is presented of implementing viscous fluid damping elements for optimal control of structure settling time. A heritage space-qualified damper design has been demonstrated to provide constant damping rate over measurable ranges of amplitude and frequency input. Its linear behavior and deterministic design characteristics allow the structural designer to truly optimize the spacecraft as a dynamically stable platform.

234

High structural damping concepts are an evolution of an existing space-qualified vibration-isolation design. This device was used to improve pointing performance of the Hubble Space Telescope (HST) by isolating the Reaction Wheel Assemblies (RWAs) from the space telescope structure. The satellite Attitude Control System employs four RWAs with approximately 220N (50 lb) rotors operating at variable speeds up to ±3000 rpm. Low level forces (millinewton) are produced at many harmonics of wheel speed so that all sensitive frequencies are swept by disturbances during RWA operation. During target acquisition the telescope must maintain precise alignment (<.007 arc sec rms) for periods up to 24 hours. Broadband isolation offered a solution but the application is unique in that performance is required at very low disturbance levels. This was achieved with the device shown in Figure 2. Metal springs act in parallel with a viscous fluid damping element. The spring and damper are physically independent and individually deterministic, permitting precise design for any desired dynamic parameters. Stiffness is provided by coil springs operating in parallel with metal bellows. The springs are positively preloaded to preclude deadband or nonlinearity around the null position. Damping is provided by viscous flow or silicon damping fluid through the annular damping chamber during payload motion. The damping rate is determined by the viscosity of the fluid and the dimensions of the damping chamber. Damping rate has been experimentally verified to be constant over at least five orders of input displacement magnitude. Damping rate is insensitive to input frequency in the region of interest and varies by approximately 2:1 over the qualification temperature range of -20 to +120 °F. The insensitivity to amplitude, frequency, and temperature is in marked contrast to more conventional means of passive damping and facilitates accurate dynamic modeling. Implementation of the isolation system on the HST resulted in approximately 130:1 reduction in peak RWA-induced disturbance in the 0-120 Hz region of interest. This is shown in Figures 3 and 4 where speed maps of RWA disturbances during wheel rundowns are plotted, with and without the isolation system.

THERMAL COMPENSATOR

SHAFT

PISTON

SKIRT

FLUID DAMPING GAP

SPRING (2)

BELLOWS (2)

BASE

AXIAL

FLUID

RADIAL

O

X

BELLOWS

SIMPLIFIED SCHEMATIC

● DAMPING PROPORTIONAL TO

$$\frac{\text{VISCOSITY} \times \text{LENGTH}}{(\text{GAP})^2}$$

● ANY DAMPING LEVEL DESIRED MAY BY PRECISELY OBTAINED
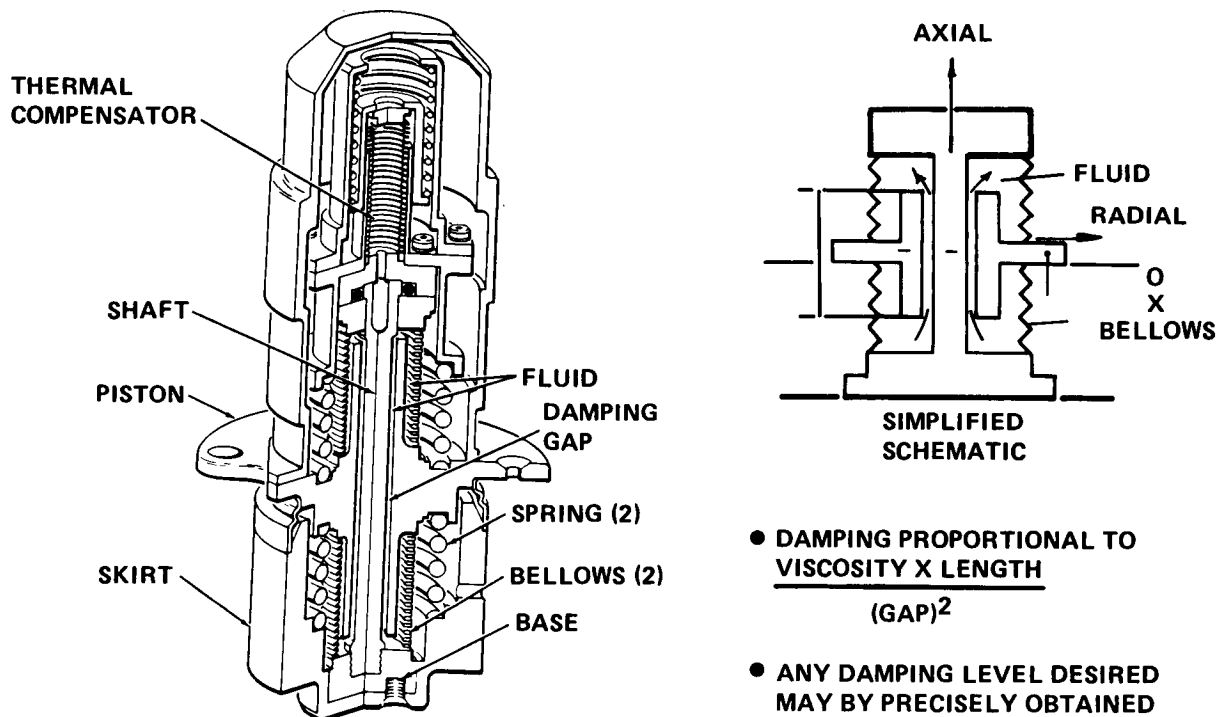
Fig. 2 Heritage Isolator Design

HARD MOUNTED
REACTION WHEEL AXIAL FORCE
(3.39 LB PEAK)

WHEEL
SPEED
ZERO

T
I
M
E

WHEEL
SPEED .0
3000 RPM .0
(50 Hz)

FREQUENCY (Hz)   120.0
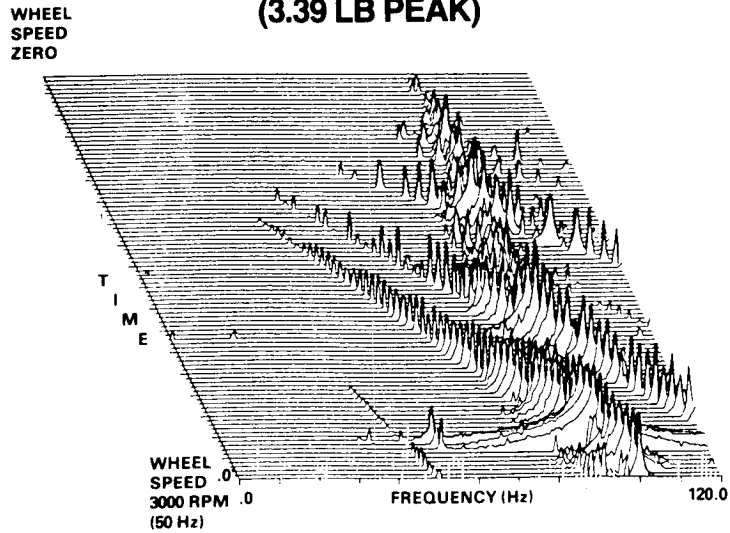
BEFORE

Fig. 3   RWA Disturbances Without Isolation

ISOLATED
(SPERRY VISCOUS ISOLATOR)
REACTION WHEEL AXIAL FORCE
(.025 LB PEAK)

WHEEL
SPEED
ZERO
0
SEC

T
I
M
E

WHEEL
SPEED .0
3000 RPM .0
(50 Hz)

FREQUENCY (Hz)   120.0

AFTER
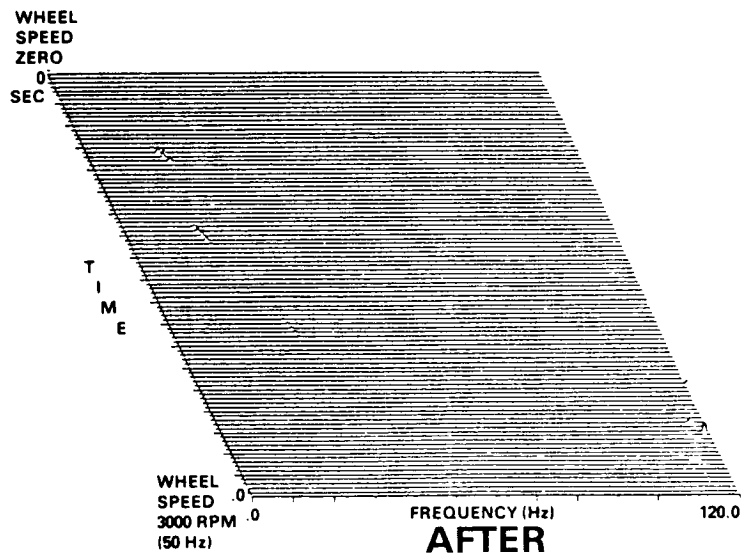
Fig. 4   RWA Disturbances With Isolation

VERY HIGH DAMPING IMPLEMENTATION

The deterministic performance of the HST damping element suggested application to the large space structures area, where very high damping rates at low excitation levels are desirable. An implementation for a standard truss element, the D-Strut, is shown in Figure 5. In this concept concentric truss tubes are connected by a fluid damping element. Design considerations for high damping rate include minimizing the fluid volume to limit compressibility effects and maximizing the ratio of plunger area to damping chamber area. Dampers of this design have demonstrated rates greater than 1000 lb-sec/in. in laboratory testing. A lumped-parameter model of the D-Strut is also shown in Figure 5. The springs k1 and k2 represent the outer and inner truss tubes and c represents the cylindrical damping chamber. The spring k3 represents the axial stiffness due to bending of the thin annular diaphragm. The spring k4 results from a combination of volumetric compression of the fluid and volumetric expansion of the fluid cavity. Due to the series/parallel arrangement of k3 and k4 in the damper, it is desirable to make k3 as small as possible and k4 as large as possible. Optimum sizing of the damper and truss tubes is determined by the structure dynamic requirements and is discussed in this paper. Although only k1 resists static loading, the complete system of dynamic elements resist dynamic loading. This leads to an optimum design since for a satellite on orbit the static loading arises from solar wind, gravity gradient, and other very low amplitude sources. The requirement of a satellite structure is to resist dynamic loading, providing a stable platform with maximum bandwidth and disturbance insensitivity. The optimum solution of this problem requires consideration of both stiffness and damping in the structural design.
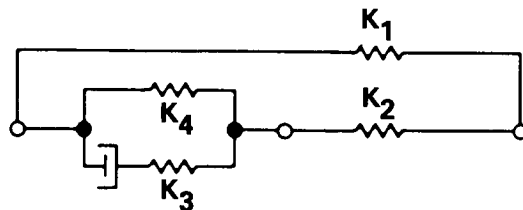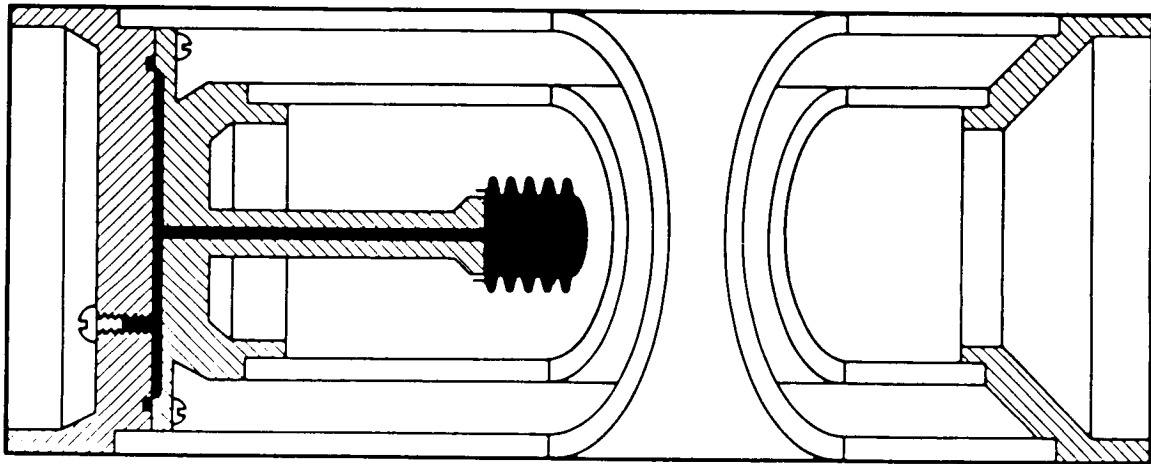
Fig. 5 D-Strut Truss Element

MODELING OF HIGHLY DAMPED STRUCTURES

When damping becomes a significant fraction of critical, its effect on a structure's natural frequencies and mode shapes is not negligible. Since damping on the order of 10 to 20 percent of critical is anticipated, special modeling techniques are required. Computer algorithms for solution of the complex eigenvalue problem

$$Kx + sCx + s^2Mx = 0 \qquad (1)$$

are available and the most direct approach would be to include all the dynamic elements. This would require using four nodes per truss element and would lead to fairly costly complex eigensolutions. If the interior nodes in the model in Figure 5 are assumed to be massless, the equations of motion for a damped strut become

$$Zo \begin{bmatrix} k & -k \\ -k & k \end{bmatrix} \begin{Bmatrix} x1 \\ x2 \end{Bmatrix} + s^2 \begin{bmatrix} M & o \\ o & M \end{bmatrix} \begin{Bmatrix} x1 \\ x2 \end{Bmatrix} = \begin{Bmatrix} o \\ o \end{Bmatrix} \qquad (2)$$

where Zok is the complex impedance of the strut and Zo is a dimensionless complex number. If a model is assembled from a number of these elements, each with approximately the same value of Zo, this term can be factored out of the equations. Under these assumptions the damping affects the natural frequencies but not the mode shapes of the model. The decoupled frequency equations become

$$Zo + s^2/pi = 0 \qquad (3)$$

where pi is the natural frequency obtained from the real eigenvalue solution obtained by setting $Zo = 1$. For the damped strut of Figure 5, if $k3 = 0$ and $k4 = \infty$;

$$Zo = \frac{a(1 - a) + \beta \, s/p}{1 - a + \beta \, s/p} \qquad (4)$$

where $k1 = a \, k$, $k2 = (1 - a)k$, and $\beta = cp/k$. The frequency equation becomes

$$0 = a(1 - a) + \beta(s/p) + (1 - a)(s/p)^2 + \beta(s/p)^3 \qquad (5)$$

Equation (5) always has one real negative root and one complex pair with a negative real component for physically-realizable parameters a and β. The complex pair is associated with normal exponentially-damped oscillation. The real root is associated with nonoscillating motion of the assumed massless internal node. The roots are plotted as a function of β for $a = 1/2$ in Figure 6. The time constraints associated with the mode are $1/rp$ for nonoscillating motion and $1/xp$ for oscillating motion. Since r is always greater than x, the minimum settling time design is where x is a maximum, $\beta = .5$. The optimal damper value is $c = .5k/p$ and the fraction of critical damping is $s/p = .175$.

238

$$s/p = -r, -x \pm jy$$
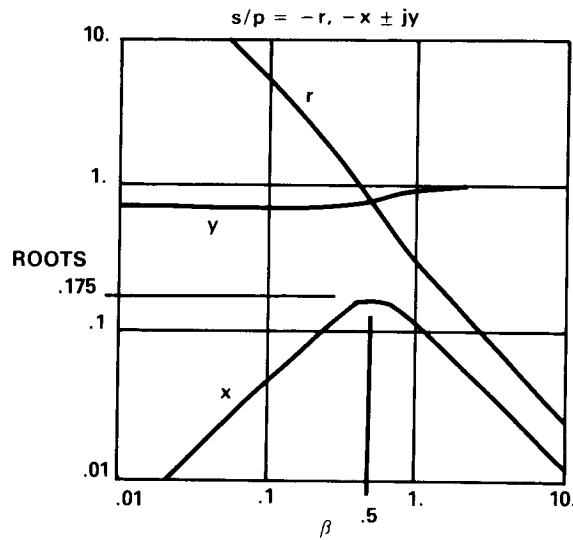
Fig. 6 Roots of Frequency Equation

GENERIC TRUSS EXAMPLE

In Figure 7 a generic truss structure is shown such as might be used for the Space Station or other large space structures. The frequencies of the first 20 modes are tabulated. The assumed goal of the structure designer is to make the longest system time constant as small as possible. The lowest mode is at 1.55 Hz for the lightly damped structure. If the damping associated with this mode is 1 percent (Q = 50), the time constant will be 1/.01x2x π x1.55 = 10 sec. If highly damped struts are used with a = 1/2 (1/2 of existing structure devoted to damping), the frequency of the mode will drop to 1.33 Hz but the time constant will become 1/.175x2x π x1.55 = .58 sec.
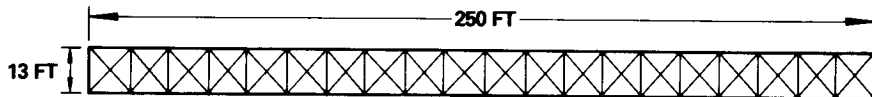
ROOT NUMBER	FREQUENCY (CYCLES/UNIT TIME)
1	1.5502
2	2.7361
3	3.6807
4	4.0358
5	5.3738
6	6.7065
7	7.3319
8	8.0105
9	9.2717
10	10.4813
11	10.9306
12	11.6318
13	12.7172
14	13.7304
15	14.6671
16	15.5136
17	16.2750
18	16.7708
19	17.2084
20	17.4099
21	18.0131

GRAPHITE EPOXY TUBING
2 IN OD × .06 WALL

Fig. 7 Generic Truss

239

To achieve the same time constant reduction by stiffening the structure would require raising the first mode to over 27 Hz, an improbable goal. In Figure 8 the time constant reductions for the lowest few modes are shown. Only the lower modes with long time constants are affected. Since the damping is applied in every member the result is insensitive to configuration changes that modify the mode shapes. The damping elements are sized to be most effective at 1.5 Hz and the system effectiveness would be compromised if the frequency of the lowest mode were to change significantly.
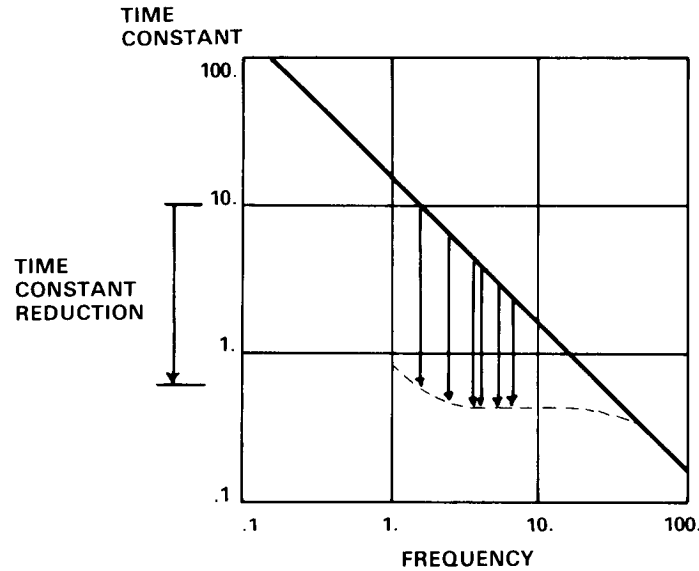
Fig. 8   Time Constant Reduction for Generic Truss

In Figure 9 the effect of high passive damping on structural control considerations is shown. Control bandwidth is often limited by the requirement to provide some level of margin, such as the 6 dB shown at the first structural resonance. Resonances with Qs of 3 and 50 are shown occurring at the same frequency. The very low Q system can implement approximately one order of magnitude higher bandwidth because of the greatly reduced gain at the first resonance.
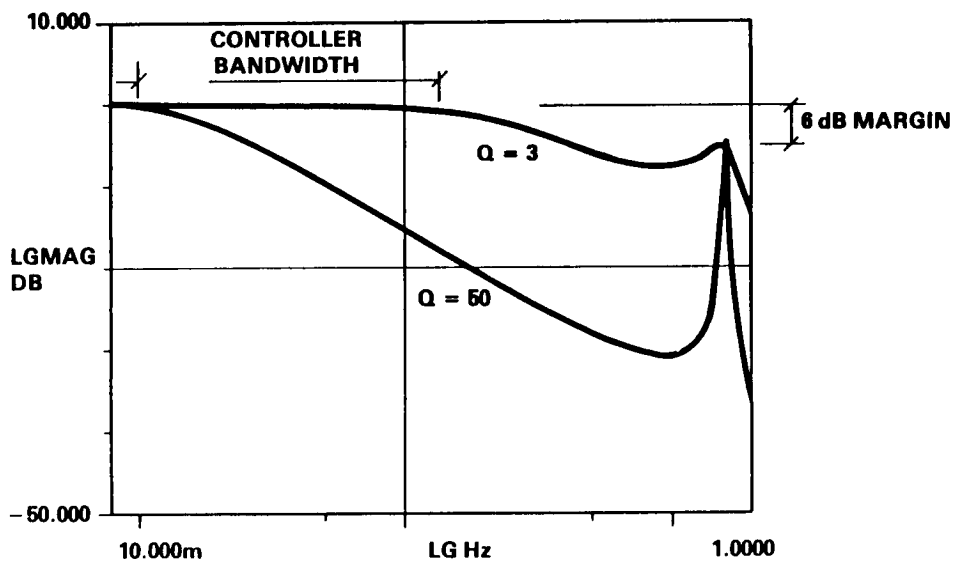
Fig. 9   Bandwidth Increase for Highly Damped Structure

SUPPLEMENTAL DAMPING IMPLEMENTATION

In some applications it may be desirable to merely add supplemental damping rather than build the entire structure from damped elements. One possible implementation of this is shown in Figure 10. Here a damping element is mounted in series with a stiff structural tube to provide damping along the axis of the strut. This strut may be derived from the one in Figure 5 by removing the outer tube. Such a strut might be used to limit response of a localized mode to the launch environment or on-orbit disturbance sources.
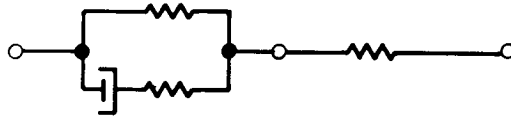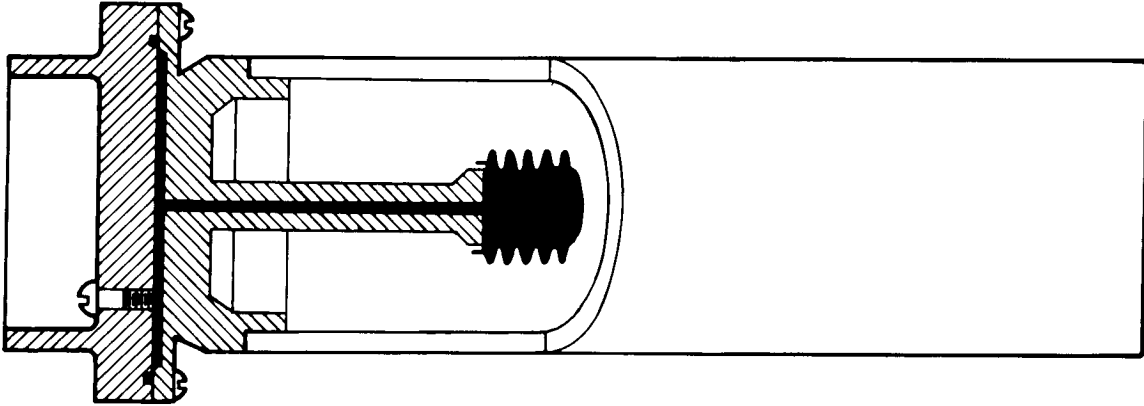
Fig. 10 Supplemental Damper

MODELING OF SUPPLEMENTAL DAMPING

It is assumed that a real eigenvalue solution has been performed for the lightly damped structure and natural frequencies p and mass-normalized mode shapes are available for the modes of interest. The complex impedance of the series spring damper is

$$Z = k \frac{cs/k}{1 + cs/k} \tag{6}$$

and at the frequency of interest

$$Z = k \frac{jcp/k}{1 + jcp/k} \tag{7}$$

The impedance may be expressed in real and imaginary components,

$$Z = k \frac{(cp/k)^2 + j(cp/k)}{1 + (cp/k)^2} \tag{8}$$

These are plotted in Figure 11. The optimal design is that for which the imaginary component is maximum, with $c = k/p$. The value of the imaginary impedance at this point is

$$Im\ (Z) = .5cpj = .5kj \qquad (9)$$

indicating the damper loses half its effectiveness due to the presence of the series spring. If ϕ is the mass-normalized modal displacement across the strut, the resultant modal damping ratio is

$$\zeta = c\phi^2/4p \qquad (10)$$
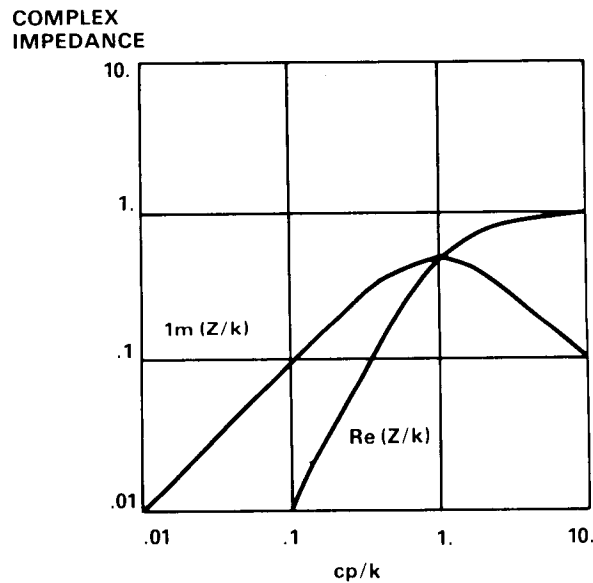
Fig. 11 Complex Impedance

CMG GIMBAL SUPPORT EXAMPLE

A proposed design for a CMG mounting application employed supplemental damping to reduce the CMG support loads during launch. Two stacks of two CMGs each were employed, as in Figure 12. Because of envelope restraints the stacks were canti-levered, although hard points were available near the top of the stacks. The stack consists of two 750N (170 lb) CMGs mounted in a cylindrical aluminum Gimbal Mounting Structure. The cylinders are approximately .6m in diameter and 1.3m high. Their fundamental rocking mode was predicted to be at 31 Hz. Consideration was given to structurally tie the tops of the stacks to the hard points to increase overall strength. This also has the effect of raising the frequency of the rocking mode and possibly increasing the input vibration level. It was decided to add a damping element rather than a stiffener to exploit whatever isolation may be obtained from the 31 Hz resonance while limiting its response. The proposed strut employed an aluminum tube with $k = 3.5 \times 10^6$ N/m (20,000 lb/in.), including joint flexibility. For optimum energy absorption the damper rate is

242
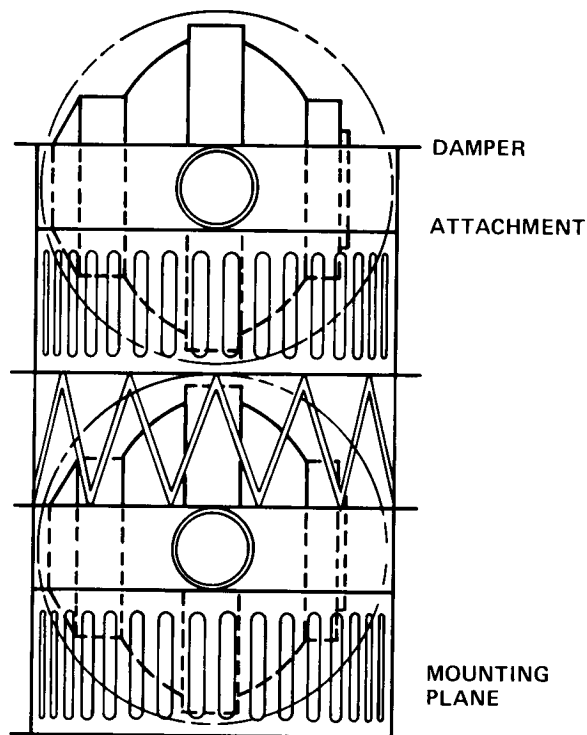
Fig. 12 CMG Mounting Application

$$c = k/p = 18,000 \text{ Ns/m (103 lb sec/in.)} \tag{11}$$

The modal displacement predicted across the strut is 1.21 and the increase in modal damping ratio is given by (10) as

$$\zeta = c\phi^2/4p = .19 \tag{12}$$

This solution produces a low frequency isolation mode with a Q of approximately 2.5 and appears to offer the optimum launch load reduction for the CMG stacks.

SUMMARY

The current concepts for large space-structure design are the evolution of a space-qualified precision isolation system design. Damper elements with very high damping rates, >170,000 N.S/m (1,000 lb-sec/in.), have been demonstrated in the laboratory. Analytical techniques for optimal implementation of these devices in large space structures are presented. Significant reductions in structure settling time appear feasible with optimal use of damping in the structural design. Means are presented for controlling the gains of all the modes in a given frequency region, facilitating active control techniques. A method for optimum implementation of supplemental damping for localized modes is also presented. These design approaches appear uniquely suited to satellite applications where static loading is virtually nonexistent and the requirement is for a dynamically stable mounting platform.

243

On the 'Glitches' in the Force Transmitted by an Electrodynamic Exciter to a Structure

Dantam K. Rao

Around resonance, the force transmitted by an exciter into a structure will be smaller or greater than a reference force generated by its coils due to electromechanical interaction. A simple analysis presented herein reveals how this phenomenon of force drop-off is controlled by three factors. The first factor, called Armature Mass Factor, describes a purely mechanical interaction between the structure and exciter. It signifies the value of armature-of-structure mass ratio relative to the modal loss factor. The electromechanical energy conversion and its interaction with the structure yields two additional factors, called Electrical Resistance and Electrical Inductance Factors. They describe the effects of coil resistance, inductance and magnetic field strength relative to structural damping and stiffness. Present analysis indicates that, under proper circumstances, more than 90% of the force drop-off can be eliminated if armature-to-structure mass ratio is smaller or equal to half of modal loss factor.

INTRODUCTION

Traditionally, in a typical measurement set-up, the force needed to vibrate a grounded structure is generated by an attached electrodynamic exciter. We usually assume that, in such set-up, a constant force is transmitted into the structure if a uniform sine voltage is inputted into the exiter via a power amplifier as shown in Fig. 1. But in reality, the amplitude and phase of transmitted force is substantially different from the force generated in the coils (around the resonance frequency) due to electromechanical interaction between exciter and structure, even if input voltage is constant. A Force Glitch describes these local differences in the force transmitted into a structure around its resonance frequency. (In contrast, a Motion Glitch describes local variations in the table base-motion excitation of a free structure. We do not intend to study them here). These glitches can be smoothened by a compressor loop, but we assume that our measurement setup does not have such a loop.

As shown in Fig. 2, a glitch consists of a Peak and a Notch in the plot of transmitted force vs frequency around the structural resonance. At the Notch frequency, this force drops to the lowest level, while at the Peak it rises to its highest value. The Notch frequency equals the resonance of the entire vibrating system.

Our major interest lies in analyzing the factors causing Force Drop-off viz. drop in level of force transmitted (from that generated in the coils) to the Notch value. We review below some (but not all) literature dealing with the force drop-off.

Historically, many "mechanical" models have been used to explain the force drop-off. They account only for the mechanical parts; they also presume that armature coil generates a constant-amplitude force. Ewins [1] used a 1-degree model to explain how the transmitted force becomes small at the structural resonance frequency. Earlier, Granick and Stern [2] analyzed a 2-degree model to show that the Notch frequency equals the structural resonance, while Bangs [3] analyzed the effect of structural nonlinearity. Rao [4] described a 3-degree model to include a force transducer.

A few researchers have also employed an "electromechanical" model. This model accounts for all vibrating parts, including electrical and electromechanical conversions; they presume that the armature coil generates a force proportional to current flow. An earlier review by Rao [5] recorded some pertinent literature on equations for exciters; these equations are identical to Crandall et al [6]. Extensive work by Tomlinson [7,8] showed that the transmitted force can be distorted if the table vibrations are so large that nonlinear solenoid effects come into play.

Recently Olsen [9] established that a "smaller" armature-to-structural mass ratio, viz., lighter armature, is required to reduce the force drop-off. (Research prior to 60's showed [10] that the motion glitch can be smoothened by selecting a heavier armature, i.e., a larger armature-to-structural mass ratio.)

Thus we know that a "smaller" armature-to-structural mass ratio reduces force drop-off. But, a question of practical interest to the experimenter is, how "small" should this ratio be? Should it be 1/100 or 1-in-million? This paper attempts to quantify this ratio. Another major aim of this paper is to identify and investigate the effect of any "electromechanical" factors that reduce the force drop-off (in addition to mechanical factors).
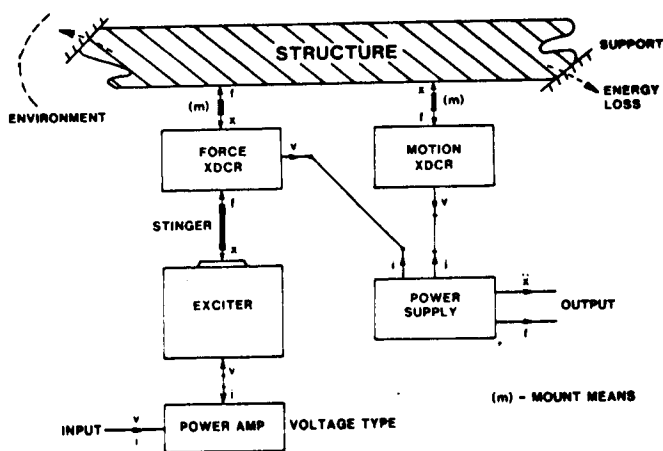
Fig. 1 Typical Setup for Measuring
        Frequency Response
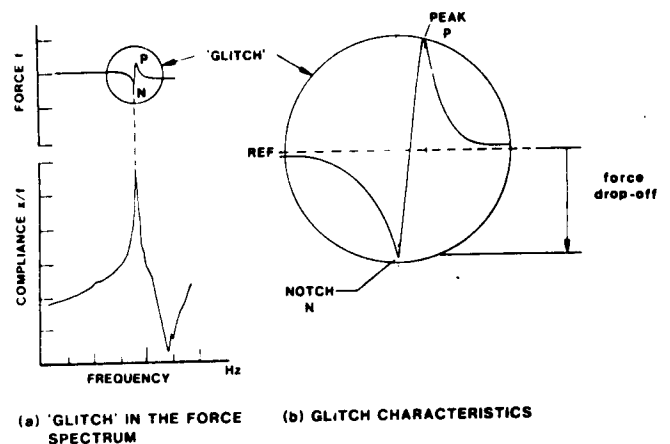
Fig. 2 Force Glitch Consisting of
        a Peak and a Notch.

246

NOTATION

e = input sine voltage
i = current flowing in the coils
f_c = ampl. of force ,, ,,
f_d = force drop-off
f_o = ampl. of force transmitted
j = $\sqrt{-1}$
k_g = force-to-current ratio
k^* = the complex modal stiffness
= $k(1 + j\eta)$
k = real part of modal stiffness
L = self-inductance of the coil
m = the modal mass of structure +
seismic part of force transducer
m_a = the eff. mass of armature +
part of force xdcr + stinger
R = resistance of coil + source
x = displacement of str. + armature
η = the structural modal loss factor
ω = frequency of excitation
ω_N = natural frequency of structure $\sqrt{k/m}$
d_t = time derivative d( )/dt
sub o = amplitude (real or complex)

Factors Controlling the Force Drop-off

M = Armature Mass Factor   (eq. 4)
C = Electrical Resistance Factor (eq. 9)
K = Electrical Inductance Factor (eq.10)
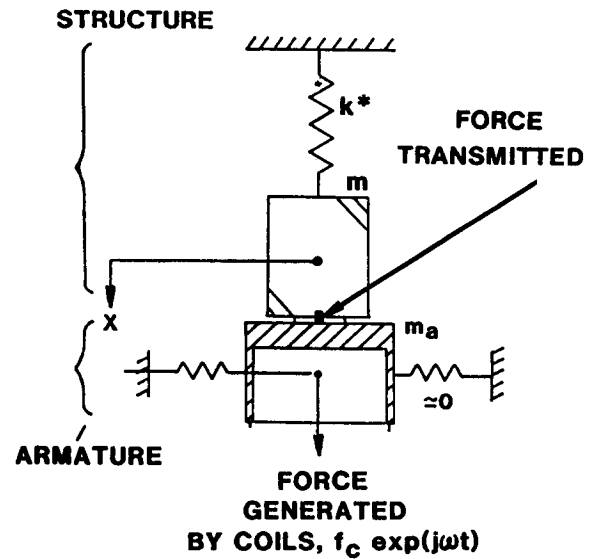
Fig. 3 "Mechanical" Model

"MECHANICAL" MODEL OF STRUCTURE ATTACHED TO AN EXCITER

Formula for Force Drop-off as a Function of Armature Mass

The equation of motion of a grounded structure attached rigidly to the armature of an exciter is (see Fig. 3 and Ref. [5] for assumptions)

$$(m + m_a)\ddot{x} + k^* x = f_c \exp(j\omega t) \qquad (1)$$

We rewrite this equation in the standard form $m\ddot{x} + k^* x = f_o \exp(j\omega t)$
where f_o, denoting the complex amplitude of force transmitted into the structure, is given by the difference [1] between the force generated in the coils and the inertial force needed to vibrate the armature,

$$f_o(\omega) = f_c + \omega^2 m_a x_o$$

$$= \frac{k^* - \omega^2 m}{k^* - \omega^2 (m + m_a)} f_c \qquad (2)$$

247

where the complex amplitude of displacement x_0 is obtained by solving (1). As shown in Fig. 2, we define the "force drop-off" f_d as the difference between the amplitude of reference force generated in the coils at zero-frequency, f_c, and the amplitude of the force transmitted into the structure at the natural frequency ω_N = $\sqrt{k/m}$. We use (2) to express the force drop-off in terms of a nondimensional factor M as given below:

$$f_d = f_o(0) - f_o(\omega_N)$$

$$= [1 - \frac{1}{\sqrt{\{1 + M^2\}}}] \; f_c \tag{3}$$

where the <u>Armature Mass Factor</u> M controlling force drop off is

$$M = \frac{m_a/m}{\eta} = \frac{\text{armature-to-structure mass ratio}}{\text{str. loss factor}} \tag{4}$$

Effect of Armature Mass on Amplitude and Phase of Transmitted Force

We display in Fig. 4 how armature mass influences transmitted force. This figure confirms the well known fact that a lighter armature beneficially reduces the force drop-off; but this also detrimentally reduces the frequency range between the Peak and Notch.

More significant is the additional phenomenon of <u>phase-drop</u> revealed by this Figure. The phase of the force signal (relative to that of force in the coils) drops to its lowest value at the Notch frequency and rises beyond it. This results in considerable fluctuations in the phase around the resonance frequency.
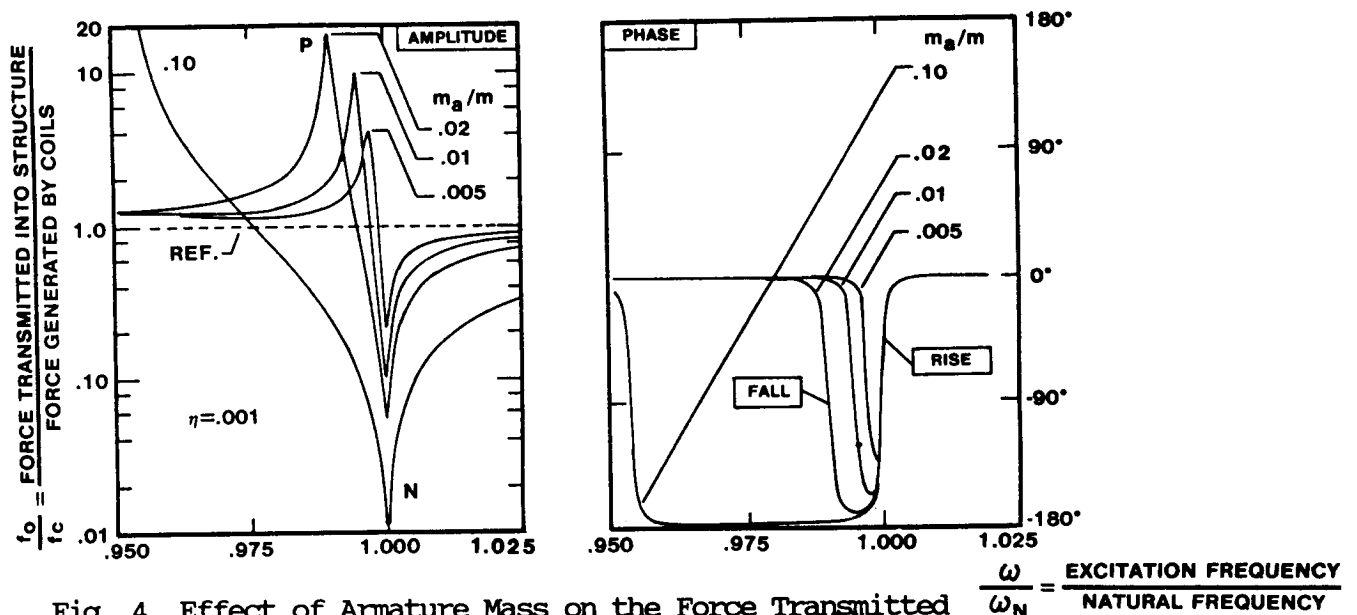
Fig. 4   Effect of Armature Mass on the Force Transmitted $\dfrac{\omega}{\omega_N} = \dfrac{\text{EXCITATION FREQUENCY}}{\text{NATURAL FREQUENCY}}$

For lighter armatures, this figure shows that the phase can fluctuate by as much as two full out-of-phase 180 deg. turns over a very narrow frequency range. The rate of rise in the Phase beyond Notch frequency appears, however, to be independent of armature mass. Hence although a lighter armature reduces the force drop-off and phase drop, we still need to use adequate frequency resolution to follow the sharp rise in the phase beyond the Notch frequency.

We display in Fig. 5 how the loss factor affects the force transmitted. This figure shows that heavier damping reduces the force drop off and widens the frequency range between the Peak and Notch. It also has the beneficial effect of reducing the phase drop; further the phase changes at a slower pace around the resonance.

$$\frac{\omega}{\omega_N} = \frac{\text{EXCITATION FREQUENCY}}{\text{NATURAL FREQUENCY}}$$
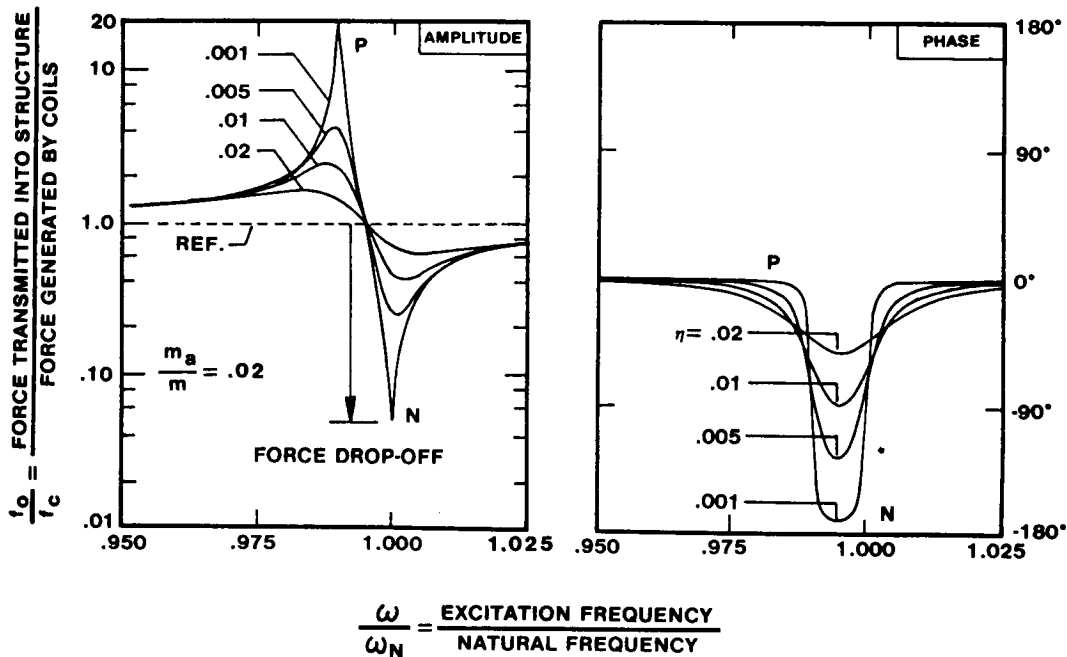
Fig. 5   Effect of Structural Loss Factor on Force Transmitted

Fig. 6 shows how the force drop-off is controlled by the Armature Mass Factor. From this figure, we conclude that 90% of coil-generated force can be transmitted into structure by choosing an armature-to-structure mass ratio that is less than half of the structural loss factor. This leads to a thumb rule, herein called the Half-Loss Factor Rule. Briefly stated, it recommends use of a light armature whose weight obeys the rule:

armature-to-structure mass ratio < half-of-loss factor   (5)

Then it is possible to transmit 90% of generated force into the structure at the frequency of resonance. For example, a structure with a modal mass = 10 kg and modal loss factor = 1/50 will require an armatur weighing 0.1 kg for the force drop-off to be 10%.

Formula for Force Drop-off Including Electromechanical Factors

Exciters work the principle of electromechanical conversion, an idealized version of which is shown in Fig. 7 as an conversion box. Ideal lossless electrical power inputted into it outputs mechanical force on a mass-less, frictionless push-rod. Fig. 8 shows how, in practical situations, the ideal electrical input is modified by the electrical resistance R and self-inductance L of the coil and the

$$M = \frac{\text{ARMATURE-TO-STRUCTURE MASS RATIO}}{\text{STRUCTURAL LOSS FACTOR}}$$
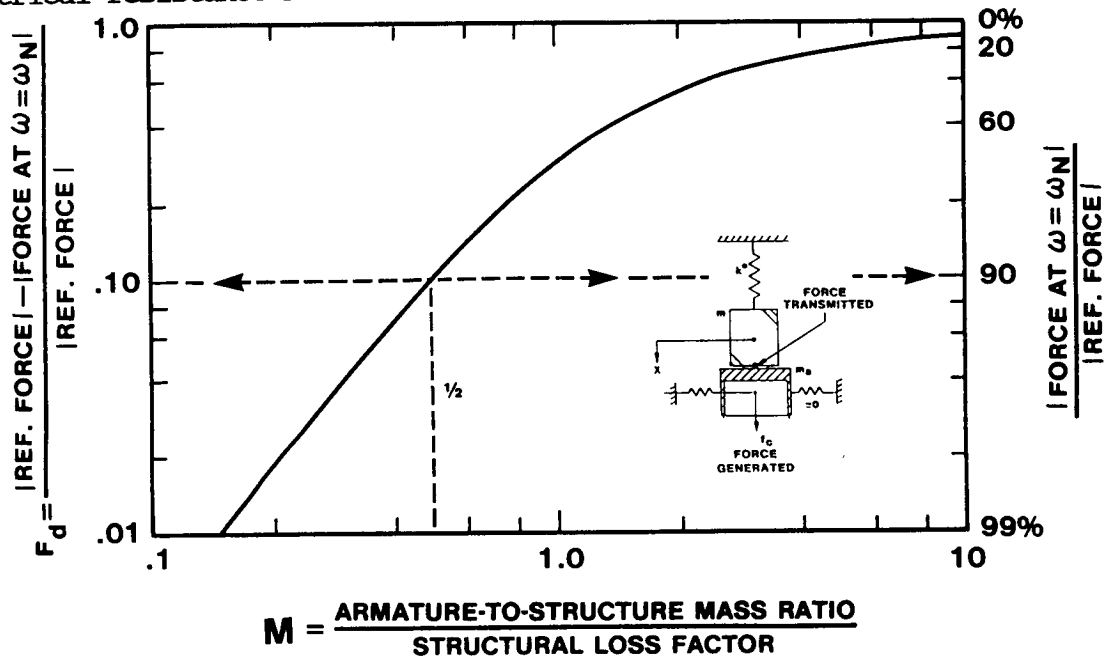
Fig. 6 Combined effect of Armature Mass and Str. Loss Factor on Force Drop-Off.

mechanical output by the mass of armature and structural properties. The equation of motion (1) thus modifies to (see [5] for details assumptions and derivation)

$$
\begin{aligned}
(m + m_a)\ddot{x} + k^* x - k_B i &= 0 \\
k_B x + (R + Ld_t) i &= e_0 \exp(j\omega t)
\end{aligned}
\tag{6}
$$

We rewrite first of this equation in the standard form $m\ddot{x} + k^* x = f_0 \exp(j\omega t)$ where f_0, denoting the complex amplitude of force transmitted into the structure, is given by the difference between the force generated in the coils (that is now proportional to the current) and the inertial force needed to vibrate the armature,

$$
\begin{aligned}
f_0(\omega) &= k_B i_0 + \omega^2 m_a x_0 \\
&= \frac{(k^* - \omega^2 m)R}{[k^* - \omega^2(m+m_a)][R+j\omega L] + j\omega k_B^2} f_c
\end{aligned}
\tag{7}
$$

250

BACK emf $e_b = -k_B \dot{x}$

B

N

FIELD DUE TO
CURRENT I
AWAY FROM
OBSERVER

S

$x(t)$

FORCE GENERATED
BY COILS $f_c = k_B i$

(a) ELECTROMECHANICAL TRANSDUCTION

COIL

$Fc = k_B i$

X

FRICTIONLESS
PUSH-ROD

k_B

i

$e_b = -k_B \dot{x}$
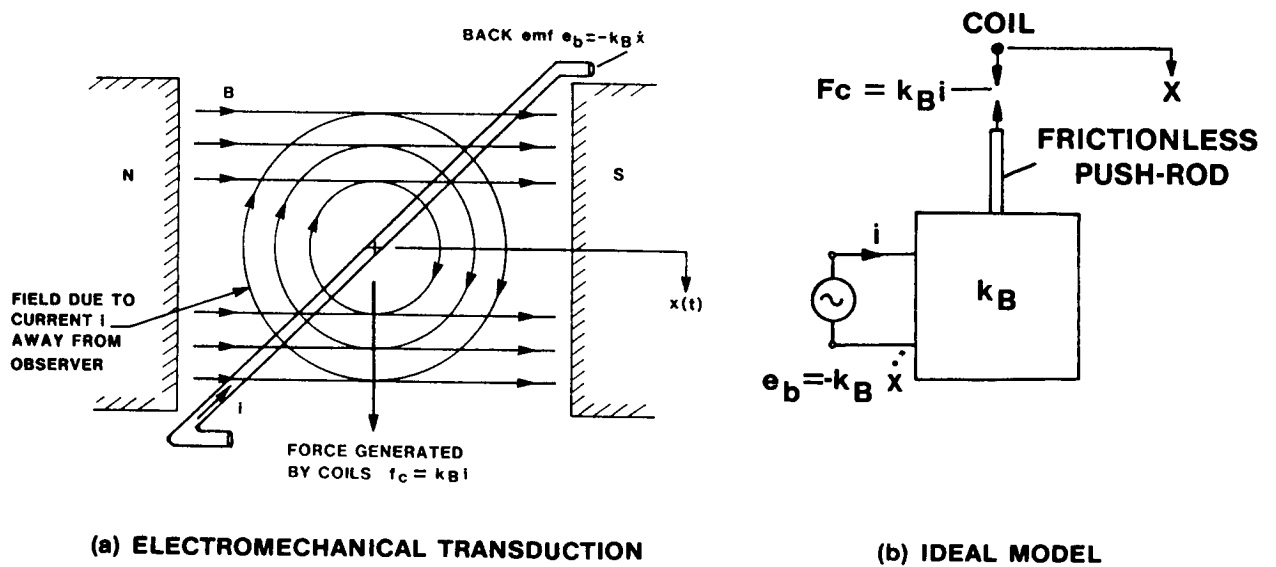
(b) IDEAL MODEL

Fig. 7 Ideal Electromechanical Transducer

STRUCTURE

k^*

m

FORCE
TRANSMITTED

X

m_a

≈ 0

ARMATURE

$k_B i$

i   R   L

$e_o \exp(j\omega t)$ $e_b = -k_B \dot{x}$ k_B

VOLTAGE IMPUTTED
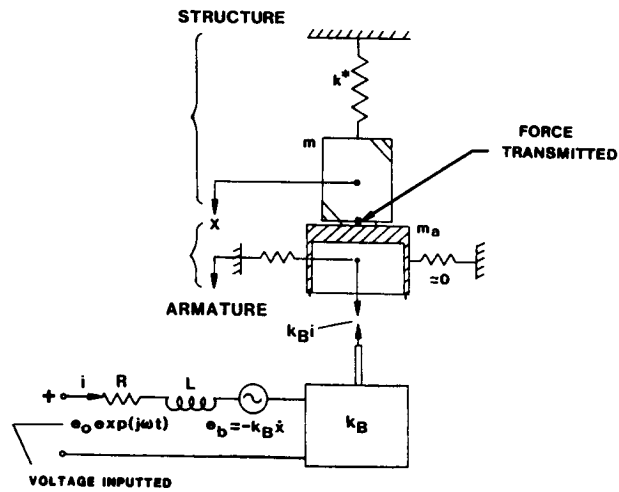
Fig. 8   Electromechanical Model of a Structure + Exciter

where x_o and i_o denote amplitudes of displacement and current that are obtained by solving (6) and f_c now denotes the force $k_B e_o/R$ transmitted into the structure at the zero frequency. The force drop-off now depends on two factors since

$$f_d = f_o(0) - f_o(\omega_N)$$

$$= [1 - \frac{1}{\sqrt{\{ (1-MC/K+C)^2 + (M+C/K)^2 \}}}] f_c \qquad (8)$$

251

Here C, called the <u>Electrical Resistance Factor</u>, quantifies nondimensionalized electrical damping whereas K, called the <u>Electrical Inductance Factor</u>, quantifies nondimensionalized electrical stiffness, both expressed relative to structural loss factor, and are defined by

$$C = \frac{(k_B{}^2/R)/\ /km}{\eta} = \frac{\text{elec. damping-to-str. crit. damping}}{\text{str. loss factor}} \qquad (9)$$

$$K = \frac{(k_B{}^2/L)/k}{\eta} = \frac{\text{elec. stiffness-to-str. stiffness}}{\text{str. loss factor}} \qquad (10)$$

Effect of Electromechanical Factors

Fig. 9 shows how the Electrical Resistance Factor C affects the force transmitted. It reveals that <u>lower</u> resistance can reduce the transmitted; it can also introduce unacceptable violent fluctuations in the phase. For example, for the parameters illustrated, the phase shows a <u>drop-rise-drop-rise</u> pattern over -180° to +180° between Peak and Notch. This is in contrast to the <u>drop-rise</u> pattern exhibited by the mechanical model as shown by Figs. 4 and 5.

Fig. 10 exhibits how electrical inductance factor K influences the force drop-off. This figure shows that a <u>larger</u> inductance can reduce the force transmitted and introduce unacceptable drop-rise-drop-rise fluctuations in the phase. These two figures re-emphasize the need for adequate frequency resolution to measure the phase of the force signal.

$$\frac{\omega}{\omega_N} = \frac{\text{EXCITATION FREQUENCY}}{\text{NATURAL FREQUENCY}}$$
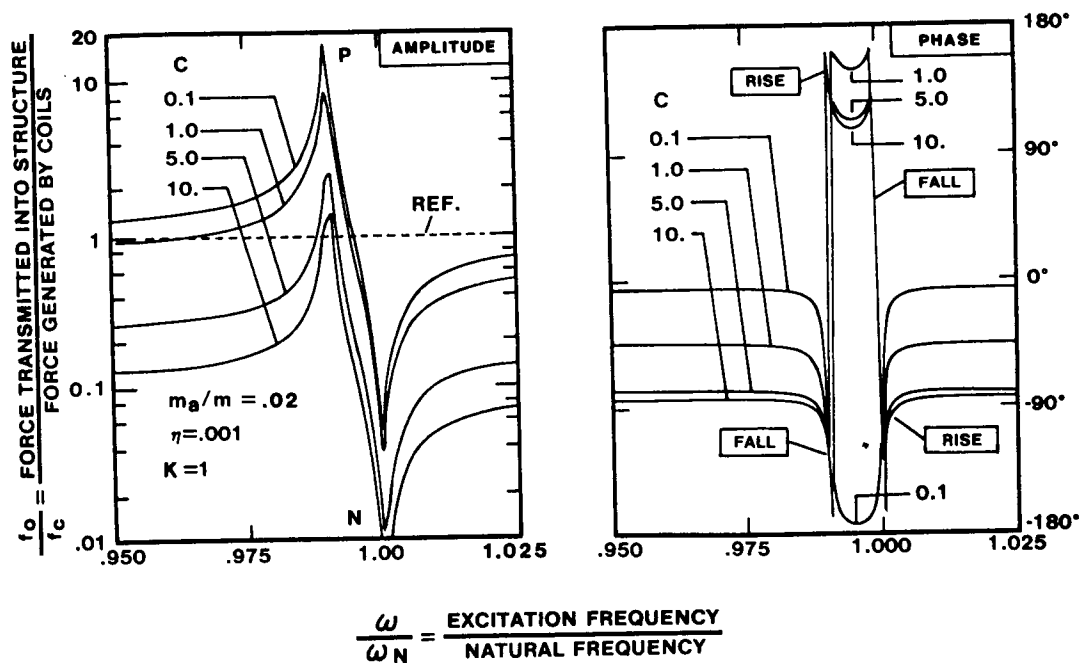
Fig. 9 Effect of Electrical Resistance Factor C on Force Transmitted

252
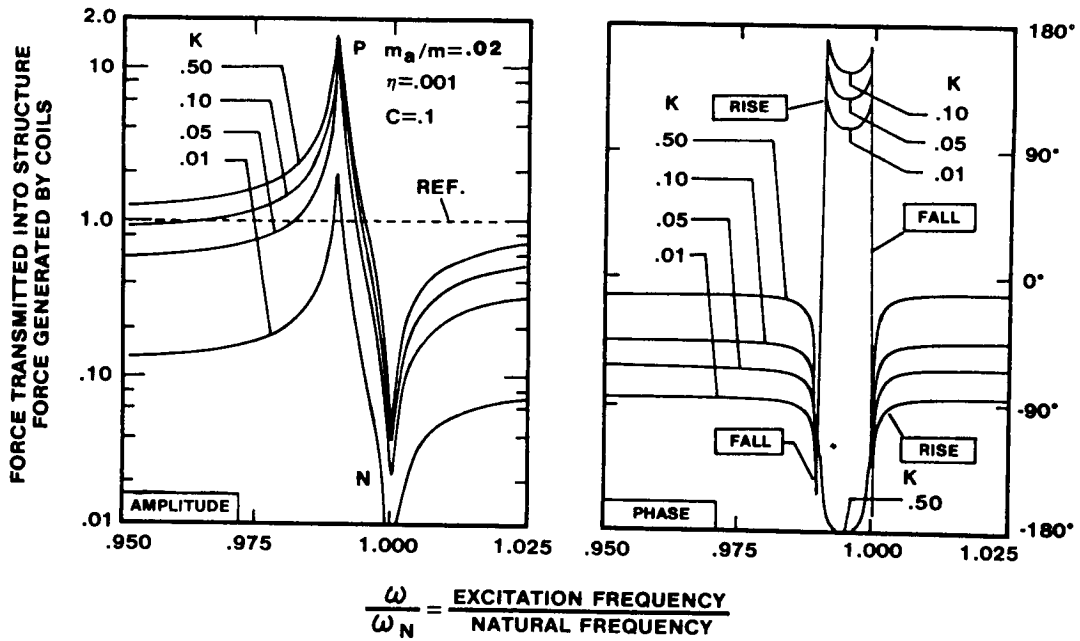
Fig. 10 Effect of Electrical Inductance Factor K on Force Transmitted.

The effect of Resistance Factor C on the force drop-off is revealed in Fig 11. This figure shows how a reduction in C value (i.e., increase in resistance) can eliminate the force drop-off. Similar effect can be obtained by increasing the K value (i.e., reducing the inductance) as shown in Fig. 12.

Thus, by a judicious choice of M, C and K values, we can control the force drop-off observed at the resonance frequency of the structure.
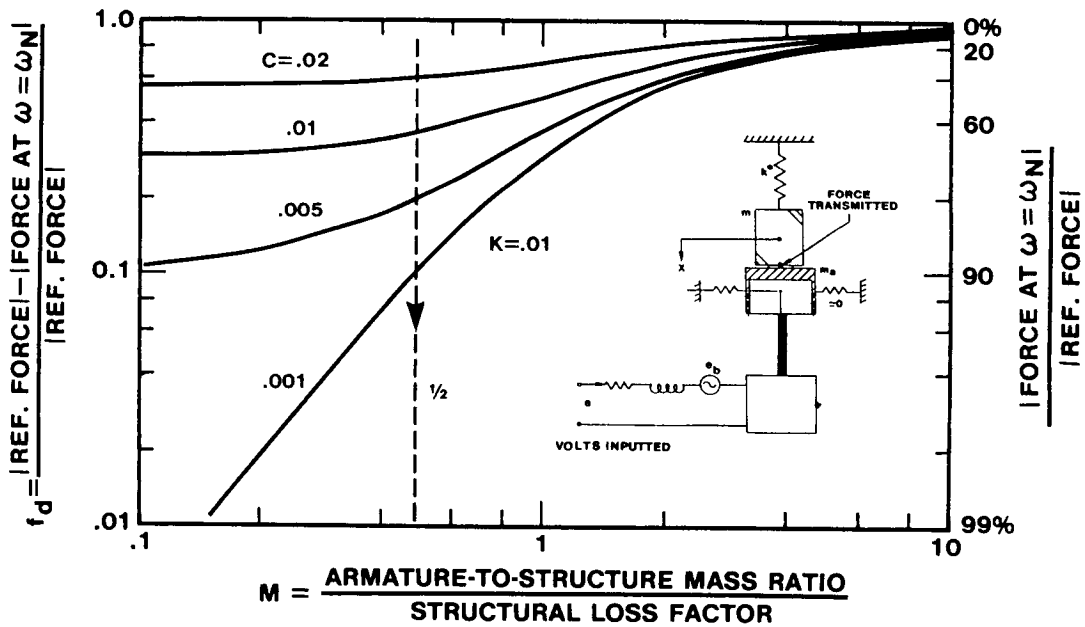
Fig. 11 Effect of Electrical Resistance Factor on Force Drop-off

253
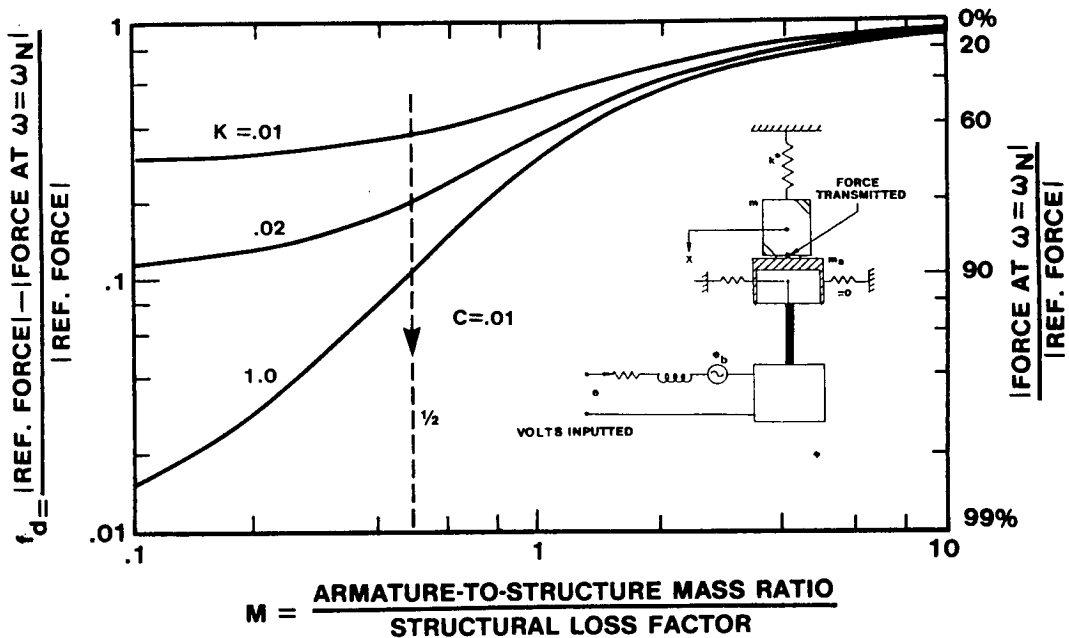
Fig. 12 Effect of Electrical Inductance Factor on Force Drop-off

CONCLUSIONS

The present paper identified three factors that affect the force transmitted by an electrodynamic exciter into a structure around the resonance frequency. This force transmitted is shown to depend on three factors. A purely mechanical factor, called Armature Mass Factor, describes the armature mass-to-structural mass ratio relative to the structural loss factor; it should be less than 1/2 to transmit more than 90% of force generated in the coils. The remaining two factors, called Electrical Resistance Factor C and Electrical Inductance Factor K describe the effect of coil resistance, inductance and magnetic field strength relative to structural damping and stiffness. Present analysis also revealed the phenomenon of phase-drop (in addition to the well-known phenomenon of force drop-off) that occurs around the resonance frequency. It also shows that the Electrical Resistance Factor should be decreased while Inductance Factor should be increased in order to reduce the force drop-off.

REFERENCES

1. D.J. Ewins, Modal Testing Theory and Practice. John Wiley Sons, 1984.

2. N. Granick and J.E. Stern, "Material Damping of Aluminum by a Resonant Dwell Technique," NASA TN D-2893, 1965.

3. W.F. Bangs, "Sinusoidal Vibration Testing of Nonlinear Spacecraft Structures," Shock, Vibration and Associated Environments, Bulletin No. 33, Part III, Mar. 1964, pp. 195-201.

4. D.K. Rao and D.I.G. Jones, "Investigation of Modes, Frequencies and Forced Response of a High Frequency Test System," Shock and Vibration Bulletin, No. 55, Part 2, pp. 27-38, June 1985.

5. D.K. Rao, "Electrodynamic Interaction Between a Resonating Structure and an Exciter," Proc. 5th Int. Conf. Modal Analysis, Apr. 1987, London.

6. S.H. Crandall, Dynamics of Mechanical and Electromechanical Systems,McGraw-Hill Book Co., 1968, p. 308.

7. G.R. Tomlinson, "A Simple Theoretical and Experimental Study for the Force Characteristics from Electrodynamic Exciters on Linear and Nonlinear Systems", Proc. 5th Int. Modal Anal. Conf., London, Vol. 2, pp. 1479-1486, Apr. 1987.

8. G.R. Tomlinson, "Force Distortion in Resonance Testing of Structures with electro-dynamic vibration Exciters", J. Sound and Vib., Vol. 63, No. 3, pp. 337-350, 1979.

9. N.L. Olsen, "Using and Understanding Electrodynamic Shakers in Modal Applications," Proc. 4th Int. Mod. Anal. Conf., Los Angeles, Vol. 2, pp. 1160-1167, Jan. 1986.

10. K. Unholtz, "Vibration Testing Machines", in Shock and Vibration Handbook, ed. by C.M. Harris and C.E. Crede, 1st ed., Vol. 2, pp. 25.1-25.74, McGraw-Hill Book Co., New York, 1961.

A System Identification Technique Based on the Random Decrement Signatures Part I: Theory and Simulation

Nabih E. Bedewi
Jackson C. S. Yang

Identification of the system parameters of a randomly excited structure may be treated using a variety of statistical techniques. Of all these techniques, the Random Decrement is unique in that it provides the homogeneous component of the system response. Using this quality, a system identification technique was developed based on a least-squares fit of the signatures to estimate the mass, damping, and stiffness matrices of a linear randomly excited system. In this part of the paper the mathematics of the technique is presented in addition to the results of computer simulations conducted to demonstrate the prediction of the response of the system and the random forcing function initially introduced to excite the system. Part II of the paper presents the results of an experiment conducted on an offshore platform scale model to verify the validity of the technique and to demonstrate its application in damage detection.

INTRODUCTION

In general, all system identification techniques begin by assuming a form for the equations describing the system, then attempt to identify the unknown parameters in that assumed system through prior knowledge of the actual response, and sometimes the input as well. For linear systems, the identification process could be conducted in two different ways depending on the available information. To describe the two methods, consider a multidegree-of-freedom system having the following set of differential equations:

$$[M]\ \ddot{X}\ +\ [K]\ X\ =\ F \tag{1}$$

where X is the response vector and F is the input loading vector. The response vector may further be viewed as the sum of the homogeneous solution vector X_h and the particular solution vector X_p, i.e.

$$X\ =\ X_h\ +\ X_p \tag{2}$$

PRECEDING PAGE BLANK NOT FILMED

The first way of identifying the system in Equation (1) is to measure the input into the system, **F**, and the response of the system, **X**. Then through the use of a curve fitting technique, matrices [M] and [K] may be identified [14,15]. The disadvantage of this method is that the input must either be of a type that could be measured, or it must be deliberately introduced into the system. Furthermore, if the system has N degrees-of-freedom and only M locations are monitored, where M < N, these monitored locations must be selected specifically to include all external loads into the system. Therefore, this method is impractical in applications where the system is naturally excited, such as offshore structures impacted by wave motion, and flight vehicles excited by turbulent air flow.

The other approach for identifying the system parameters is through the use of the system response only [2,7,8,9,12]. This leads to the identification of the eigenvalues and eigenvectors of Equation (1) as opposed to the mass and stiffness matrices.

Substituting Equation (2) into Equation (1) yields

$$[M] \; (\ddot{X}_h + \ddot{X}_p) \; + \; [K] \; (X_h + X_p) \; = \; F$$

which may be separated into two independent equations, namely

$$[M] \; \ddot{X}_p \; + \; [K] \; X_p \; = \; F \tag{3}$$

$$[M] \; \ddot{X}_h \; + \; [K] \; X_h \; = \; \{0\} \tag{4}$$

Equations (3) and (4) indicate that if **F** is not known, the system parameters may not be identified unless the homogeneous and particular solutions are separated. In practice, however, if the input spectral density is relatively flat over the range of the system frequencies, the ratios of the responses $x_i(t)$ at the different locations are taken in the frequency domain thus yielding the eigenvalues and the eigenvectors of Equation (4). If, on the other hand, the input spectral density has some mild fluctuations over the frequency range of the system, then taking the ratios of the responses could yield erroneous eigenvectors. In addition, if the system exhibits some damping, the modal damping ratios may not be identified correctly. This is mainly due to the fact that the frequency content of the particular component of the response may vary considerably at different locations in the system.

These problems may be overcome by employing the Random Decrement (Randomdec) and cross-Random Decrement (cross-Randomdec) techniques [3,4,5,6,10,11,13]. Given the response vector **X**, the Randomdec and corresponding cross-Randomdec signatures are calculated. Based on the results obtained in reference [1], the signatures should be interpreted as the homogeneous components of the response, namely X_h. With this being the case, the eigenvalues and eigenvectors of Equation (4) may be estimated accurately. The biggest advantage of this method is that the response need not be measured at the points where external loads are applied. Furthermore, modal damping may be evaluated accurately from the Randomdec signatures either in the time domain using the logarithmic decrement or in the frequency domain using the half power point (curve fitting could generally be used for close modes in both domains).

Although modal parameters might be sufficient for many applications, it is sometimes desirable, if not necesssary to have information reflecting the actual mass,

damping, and stiffness of the system. This could be the case in systems where damping is not proportional, or when the model is required for damage detection in which elements in the original matrices pertain to actual locations in the system. A technique is therefore proposed to estimate the [M], [C], [K] matrices of a linear system with the use of the Random Decrement technique.

PROPOSED SYSTEM IDENTIFICATION TECHNIQUE

Consider the linear set of equations

$$[M] \, \ddot{X} + [C] \, \dot{X} + [K] \, X = F \tag{5}$$

where [M] and [K] are real symmetric matrics and [C] is a nonproportional, real, symmetric damping matrix. Introducing matrix H_{pij} and vector Z_{pj}, where

$$H_{1ij} = [M] \qquad\qquad Z_{1j} = \ddot{X}$$

$$H_{2ij} = [C] \qquad\qquad Z_{2j} = \dot{X}$$

$$H_{3ij} = [K] \qquad\qquad Z_{3j} = X$$

Equations (5) may be rewritten in the form

$$\sum_{j=1}^{M} \sum_{p=1}^{3} H_{pij} Z_{pj} = F_i \qquad i = 1,2,\ldots,M \tag{6}$$

where M is the number of degrees-of-freedom in the system, and F_i symbolizes element i of vector F.

If Z_{pj} and F_i are composed of N discrete points in time, there should exist one equation similar to Equation (6) for every point k, where k = 1,2,...,N . Therefore, for one time step k

$$\sum_{j=1}^{M} \sum_{p=1}^{3} H_{pij} Z_{pjk} = F_{ik} \qquad \begin{matrix} i = 1,2,\ldots,M \\ k = 1,2,\ldots,N \end{matrix} \tag{7}$$

To identify the three matrices H_{pij}, a least squares scheme will be employed to obtain the best estimate for H_{pij} through minimizing the difference between the left and right sides of Equation (7). Therefore, defining an error index e_{ik} for each equation i at every time step k, Equation (7) may be rearranged as follows :

$$F_{ik} - \sum_{j=1}^{M} \sum_{p=1}^{3} \tilde{H}_{pij} Z_{pjk} = e_{ik} \qquad \begin{array}{l} i = 1,2,\ldots,M \\ k = 1,2,\ldots,N \end{array} \qquad (8)$$

where $\tilde{H}_{pij}$ is the best estimate for H_{pij}.

Adding the sum of the squares of Equation (8), the total error E in the system may be defined as

$$\sum_{i=1}^{M} \sum_{k=1}^{N} [\, F_{ik} - \sum_{j=1}^{M} \sum_{p=1}^{3} \tilde{H}_{pij} Z_{pjk} \,]^2 = \sum_{i=1}^{M} \sum_{k=1}^{N} e_{ik}^2 = E \qquad (9)$$

To minimize the error with respect to $\tilde{H}_{pij}$, the slope of Equation (9) relative to all the unknown parameters must be set to zero, i.e.

$$\frac{\partial E}{\partial \tilde{H}_{pij}} = 0 \qquad \begin{array}{l} p = 1,2,3 \\ i = 1,2,\ldots,M \\ j = 1,2,\ldots,M \end{array}$$

Therefore, taking the partial derivative of E with respect to $\tilde{H}_{pij}$ and noting that $\tilde{H}_{pij} = \tilde{H}_{pji}$ (symmetry condition), the following two equations result

$$\frac{\partial E}{\partial \tilde{H}_{pij}} = -2 \sum_{k=1}^{N} Z_{pik} [\, F_{ik} - \sum_{n=1}^{M} \sum_{q=1}^{3} \tilde{H}_{qin} Z_{qnk} \,] = 0 \qquad (10a)$$

for $i = j$, and

$$\frac{\partial E}{\partial \tilde{H}_{pij}} = -2 \sum_{k=1}^{N} \{ Z_{pjk} [\, F_{ik} - \sum_{n=1}^{M} \sum_{q=1}^{3} \tilde{H}_{qin} Z_{qnk} \,]$$

$$+ Z_{pik} [\, F_{jk} - \sum_{n=1}^{M} \sum_{q=1}^{3} \tilde{H}_{qin} Z_{qnk} \,] \} = 0 \qquad (10b)$$

for $i \neq j$.

Equations (10a) and (10b) form a set of $M(M+1)3/2$ linear simultaneous equations which may be solved either in closed form or by iteration. To use the latter, the partial derivatives must be taken of Equations (10a) and (10b) with respect to all the unknown parameters resulting in a constant Jacobian matrix, namely

$$\frac{\partial^2 E}{\partial \tilde{H}_{pij} \partial \tilde{H}_{ghl}} = 2 \sum_{k=1}^{N} Z_{pjk} Z_{glk}$$

for $i = j$, and

$$\frac{\partial^2 E}{\partial \tilde{H}_{pij} \partial \tilde{H}_{ghl}} = 2 \sum_{k=1}^{N} [Z_{pjk} Z_{glk} + Z_{pik} Z_{ghk}]$$

for $i \neq j$.

To obtain a solution in closed form, Equations (10a) and (10b) should be rewritten in the form

$$\sum_{k=1}^{N} \sum_{n=1}^{M} \sum_{q=1}^{3} \tilde{H}_{qin} Z_{pik} Z_{qnk} = \sum_{k=1}^{N} Z_{pik} F_{ik} \tag{11a}$$

for $i = j$, and

$$\sum_{k=1}^{N} \sum_{n=1}^{M} \sum_{q=1}^{3} [\tilde{H}_{qin} Z_{pjk} Z_{qnk} + \tilde{H}_{qjn} Z_{pik} Z_{qnk}] = \sum_{k=1}^{N} [Z_{pjk} F_{ik} + Z_{pik} F_{jk}]$$

$$\tag{11b}$$

for $i \neq j$, where the right side of Equations (11a) and (11b) contains the constant terms while the left side is a constant coefficient matrix premultiplied by a vector composed of the $M(M + 1)3/2$ unknown system parameters. This may be represented as follows:

$$[G] \mathbf{h} = \tilde{\mathbf{F}} \tag{12}$$

These equations can now be solved using any conventional linear equation solver.

It is apparent by inspection of Equation (12) that when the Random Decrement technique is applied, $\tilde{\mathbf{F}}$ reduces to zero , thus resulting in

$$[G] \mathbf{h} = \{0\}$$

or, in expanded form

$$
\begin{bmatrix}
g_{1,1} & g_{1,2} & \cdots\cdots\cdots & g_{1,\beta-1} & g_{1,\beta} \\
g_{2,1} & \cdots\cdots\cdots\cdots\cdots & & & g_{2,\beta} \\
\cdot & \cdot & & & \cdot \\
\cdot & & \cdot & & \cdot \\
\cdot & & & \cdot & \cdot \\
\cdot & & & & \cdot \\
\cdot & & & \cdot & \cdot \\
g_{\beta-1,1} & \cdots\cdots\cdots\cdots\cdots & & g_{\beta-1,\beta} \\
g_{\beta,1} & g_{\beta,2} & \cdots\cdots\cdots & g_{\beta,\beta-1} & g_{\beta,\beta}
\end{bmatrix}
\begin{bmatrix}
h_1 \\ h_2 \\ \cdot \\ \cdot \\ \cdot \\ \cdot \\ \cdot \\ h_{\beta-1} \\ h_{\beta}
\end{bmatrix}
=
\begin{bmatrix}
0 \\ 0 \\ \cdot \\ \cdot \\ \cdot \\ \cdot \\ \cdot \\ 0 \\ 0
\end{bmatrix}
\qquad (13)
$$

where $\beta = M(M + 1)3/2$. Equations (13) are in homogeneous form and therefore do not possess a unique solution for **h**.

On the other hand, if the rank of [G] is $\beta - 1$, and if one of the unknown parameters in **h** were indeed known, then a unique solution would exist. This may be proved by rearranging Equation (13) as follows :

$$
\begin{bmatrix}
g_{1,1} & g_{1,2} & \cdots\cdots & g_{1,\beta-1} \\
g_{2,1} & \cdots\cdots\cdots & & g_{2,\beta-1} \\
\cdot & \cdot & & \cdot \\
\cdot & & \cdot & \cdot \\
\cdot & & \cdot & \cdot \\
\cdot & & & \cdot \\
\cdot & & & \cdot \\
g_{\beta-1,1} & \cdots\cdots\cdots & & g_{\beta,\beta-1}
\end{bmatrix}
\begin{bmatrix}
h_1 \\ h_2 \\ \cdot \\ \cdot \\ \cdot \\ \cdot \\ \cdot \\ h_{\beta-1}
\end{bmatrix}
=
\begin{bmatrix}
-g_{1,\beta}h_{\beta} \\ -g_{2,\beta}h_{\beta} \\ \cdot \\ \cdot \\ \cdot \\ \cdot \\ \cdot \\ -g_{\beta-1,\beta}h_{\beta}
\end{bmatrix}
\qquad (14)
$$

where h_{β} was assumed to be the known parameter for convenience. Equation (14) may be set up for any known h_i by simply eliminating the ith row of [G] (since the partial derivative with respect to a constant is zero) then moving the ith column to the right side and multiplying it by the scalar $-h_i$. The only condition for selecting h_i is that the ith row must increase the rank of the system. With the aforementioned steps adhered to, Equation (14) will definitely have a unique solution.

If the rank of matrix [G] is less than $\beta - 1$, the solution of Equation (13) becomes more difficult to obtain. The linear dependency of the equations forming matrix [G] will require a greater effort to be eliminated, and, more parameters of vector **h** will have to be assumed. Therefore, if the rank is $\beta - 2$, two equations from Equations (13) must be removed and two parameters of vector **h** must be assumed. Calculating two or more parameters in many physical systems is extremely difficult, if not impossible. The examples used in the remainder of this paper are all of systems with a rank of $\beta - 1$.

The question to be raised then is how can the value of one of the parameters be known ?

Since **h** is composed of elements from the mass, damping, and stiff-ness matrices, it is physically immeasurable. Therefore, the best alternative would be to obtain a good estimate. The requirement imposed on the accuracy of the estimate depends greatly on the application for which the model is needed. If the model is to be used for damage detection, then knowing the absolute values of the [M], [C], [K] matrices is not essential, but rather, the ratio of the values of the elements at different instances in time. Therefore, assuming the order of magnitude of one of the elements in **h** should suffice as long as the same value is used every time. On the other hand, if the model is needed for simulation purposes, where one wishes to study the effect of different loading conditions on the response of the system, the absolute values are needed. In this case, the estimate for h_i may be obtained from either a finite element model, or by performing a simple static test on the system (if physically possible). The latter is carried out by applying a known static load at a point in the system and measuring the deflection at the same point or at any other point. These two values may then be used to scale the entire **h** vector (**h** must be already calculated by assuming the order of magnitude of h_i). The scaling procedure may be described by noting the static component of Equation (5), namely

$$[K] \ \mathbf{X} \ = \ \mathbf{F} \tag{15}$$

If [K] is separated into a scalar ε multiplying a matrix $[\tilde{K}]$, where $[\tilde{K}]$ is the estimated stiffness matrix using the proposed method, then Equation (15) becomes

$$\varepsilon \ [\tilde{K}] \ \mathbf{X} \ = \ \mathbf{F} \tag{16}$$

Since **F** and $[\tilde{K}]$ are known (**F** is the force applied during the static test) the system of equations

$$[\tilde{K}] \ \tilde{\mathbf{X}} \ = \ \mathbf{F}$$

may be solved to give $\tilde{\mathbf{X}}$, where

$$\tilde{\mathbf{X}} \ = \ \varepsilon \ \mathbf{X}$$

But, the response X_i at point i in the system was measured, therefore ε may be obtained by simply taking the ratio $\tilde{X}_i/X_i$. The value of ε may then be multiplied by the estimated mass, damping, and stiffness matrices $[\tilde{M}]$, $[\tilde{C}]$, and $[\tilde{K}]$ respectively to obtain [M], [C], and [K].

TESTS OF PROPOSED TECHNIQUE BY COMPUTER SIMULATION

To demonstrate the procedure for applying the proposed system identification technique, and to test its accuracy, a six degree-of-freedom model of a cantilever beam is used. Figure 1 shows the beam with the locations of the six points where the response is monitored. Using a finite element model (Reference [15]), the system matrices in Equation (5) were obtained.
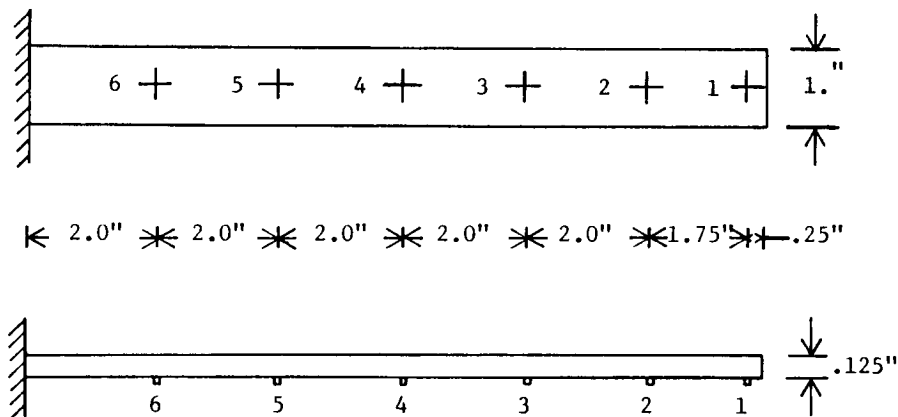
Figure 1 - Locations of monitored points on the cantilever beam

To distinguish between errors introduced by the system identification technique and the errors in the Randomdec signatures, two different scenarios were conducted. The technique was initially tested using exact free-decay response curves of the system and then tested using actual Randomdec signatures obtained from the random response of the system.

Case I: Exact Free-Decay Curves

A set of initial conditions was arbitrarily chosen for the six locations on the beam. Equation (5) was then solved numerically and the response vectors X, $\dot{X}$, and $\ddot{X}$ were recorded. The time step size was selected to insure that at least seven points were needed to construct one cycle of the highest frequency in the system. Solving for the eigen-values of Equation (5) the undamped natural frequencies of the system were found to be

f_1 =   25.908 Hz f_4 =   886.770 Hz

f_2 =   159.251 Hz f_5 = 1445.039 Hz

f_3 =   445.307 Hz f_6 = 2114.293 Hz

thus resulting in a step size of $\Delta T = 0.00007$ seconds. Furthermore, the number of time steps had to be selected to cover at least one cycle of the lowest frequency in the system. Therefore, 600 points were used.

One of the tests for the technique is its repeatability relative to different fixed parameters, i.e. as elements h_1 through h_{63} are in turn fixed. Since diagonal terms are more reliable than off-diagonal terms in the model, this test was strictly confined to the diagonal elements.

Equation (14) was solved eighteen times, each time fixing one of the diagonal elements in the [M], [C], [K] matrices. The fixed value was always taken as the actual value of the element to avoid scaling the $\mathbf{h}$ vector. After every evaluation of the $\mathbf{h}$ vector, the errors occurring in the diagonal terms, relative to their actual values, were calculated. Calculations were made of the errors in the mass, damping, and stiffness matrices as each diagonal element in the mass matrix was fixed. Similar results were obtained as each diagonal element in the damping and stiffness matrices was fixed, respectively. In all the cases, the average error occurring at every point on the beam was evaluated.

Following a careful inspection of the errors, two conclusions were made, viz. fixing the stiffness matrix gives better estimates of vector $\mathbf{h}$ than fixing the mass and damping matrices, and , due to the large variation in the error resulting from fixing different elements in the same matrix, the avarage value is probably a more consistent estimate. Therefore, based on these conclusions, and noting that fixing the stiffness matrix elements is the only case in which the average gives a better overall estimate than the individual estimates, it is further concluded that the best approach for estimating vector $\mathbf{h}$ is to take the average of the $\mathbf{h}$ vectors obtained by individually fixing the stiffness diagonal elements. In doing so, the $\mathbf{h}$ vectors must be scaled independently before the averaging process is carried out. Using this procedure, the system matrices were identified. These matrices were not identical to the actual system matrices; their validity to represent the system was checked by comparing the reponse to the same input. Therefore, a random input vector $\mathbf{F}$ with constant spectral density was simulated on the computer and used as input into Equation (5). This equation was solved using the actual and the estimated system matrices. Results were obtained for all the response points. Comparison of the actual and predicted responses at point 1 is shown in Figure 2. The responses of the two systems compare favourably.
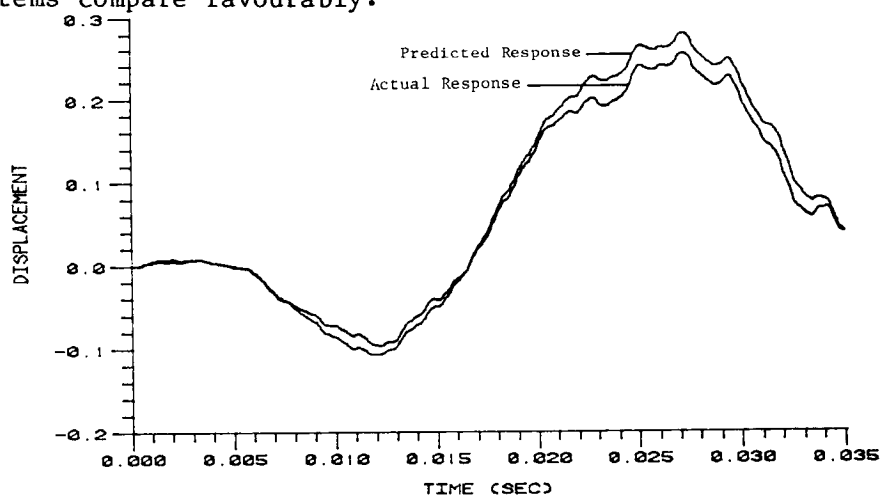
Figure 2 - Comparison of actual and predicted responses at point 1
(system identification from actual free-decay response)

265

Case II: Free-Decay Curves From Randomdec Signatures

To further evaluate the overall accuracy of the system identification technique, the technique had to be tested by incorporating Randomdec and cross-Randomdec signatures as opposed to actual free-decay response curves.

Two purely uncorrelated stationary, Gaussian, random records were used as input forces at points 2 and 4 on the cantilever beam. Equation (5) was solved and the response vector X recorded. Due to its high frequency content, station 6 was used as the triggering station with a trigger level of 0.0075. Five cross-Randomdec signatures (at stations 1 to 5), and one Randomdec signature (at station 6) were obtained for 600 lag points and 500 averaged segments. The cross-Randomdec signature for station 1 is shown in Figure 3. The first and second derivatives were then calculated for the six signatures using a finite difference scheme with an error on the order of ΔT^2.
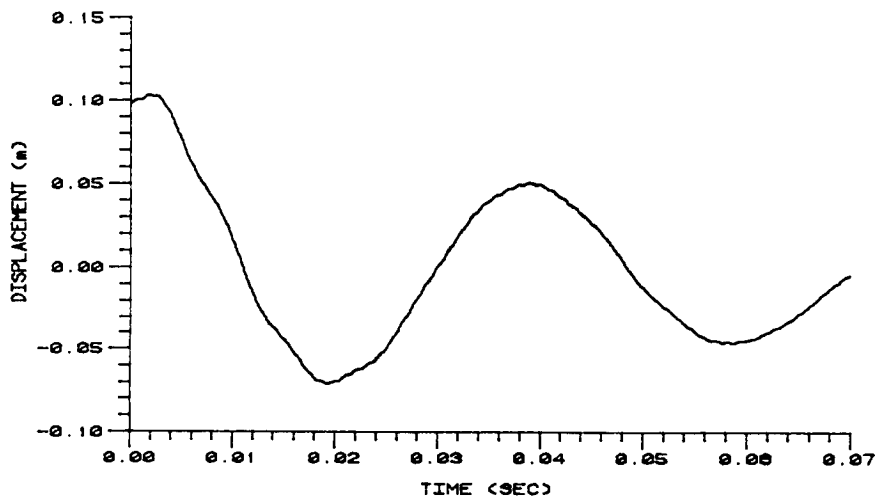
Figure 3 - Cross-Randomdec signature of time record at point 1

The procedure recommended in the previous section was used. Equation (14) was solved six times, each time fixing one of the diagonal elements in the stiffness matrix. K_{11} was fixed at 1000, K_{22} was fixed at 5000, and K_{33} through K_{66} were fixed at 10000. In each case, a load of 10 was applied at point 1 and, using the corresponding estimated stiffness matrix, the deflection at point 1 was calculated (since point 1 is the free end of the cantilever beam). The same procedure was followed using the actual stiffness matrix. The six h vectors were then scaled following the procedure outlined in the previous section, averaged, and rearranged in matrix form.

Again these matrices were not identical to the actual system matrices. To test their validity as a simulation tool, the estimated matrices were substituted into Equation (5). The force vector used to obtain the random records, from which the signatures were evaluated, was used as the input. Comparison of the calculated response versus the actual system response was obtained for all the stations. Results at stations 1 and 2 are shown in Figures 4 and 5. Once more, the results compare favourably.

266
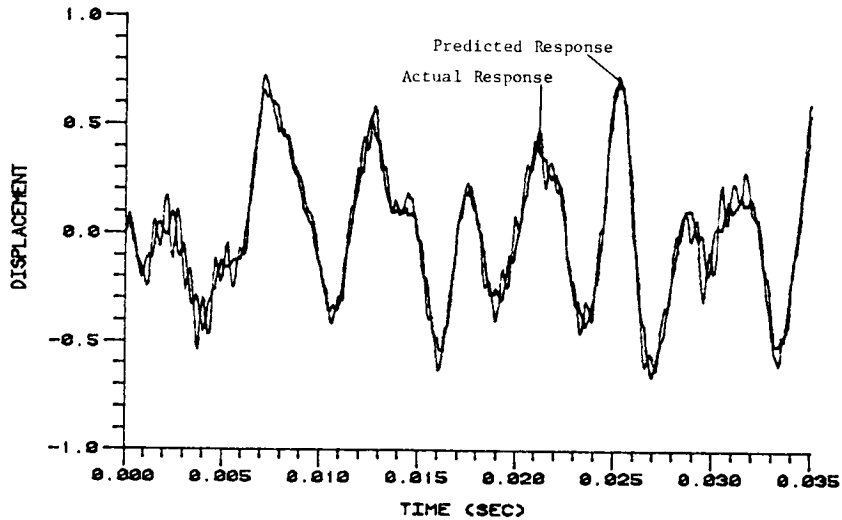
Figure 4 - Comparison of actual and predicted responses at point 1
(system identificatin from Randomdec signatures)

Figure 5 - Comparison of actual and predicted responses at point 2
(system identification from Randomdec signatures)

ESTIMATING THE INPUT INTO THE SYSTEM

An interesting application arises from the system identification technique by observing Equation (5). After estimating the mass, damping, and stiffness matrices, if the response vector X and its derivatives are substituted back into Equation (5), the outcome should be the force vector F.

Therefore, in a real application, the random response would be measured at several locations in the system. The signatures would then be obtained, their derivatives calculated, and Equation (14) used to estimate the [M], [C], [K] matrices following the procedure outlined in the previuos section. A direct substitution of the measured response and its derivatives into Equation (5) with the estimated matrices would result in a vector similar to the input vector. If the estimated mass, damping, and stiffness matrices were not scaled, the outcome of Equation (5) should be a scaled version of the input vector.

267

To demonstrate this approach, the example provided in the previous section was used. Results were obtained of the estimated input vector F versus the actual input. Since the forces were originally applied at locations 2 and 4 on the beam, the forces at locations 1, 3, 5, and 6 should be zero. These Results indicate that at the points where the loads were applied, the estimated input functions formed good approximations (see Figures 6 and 7). As for the unloaded points, the technique predicted forcing functions with relatively small magnitudes in comparison to the loaded points (see Figure 8).

Figure 6 - Comparison of actual and predicted force records
(record for location 2 - unfiltered response)
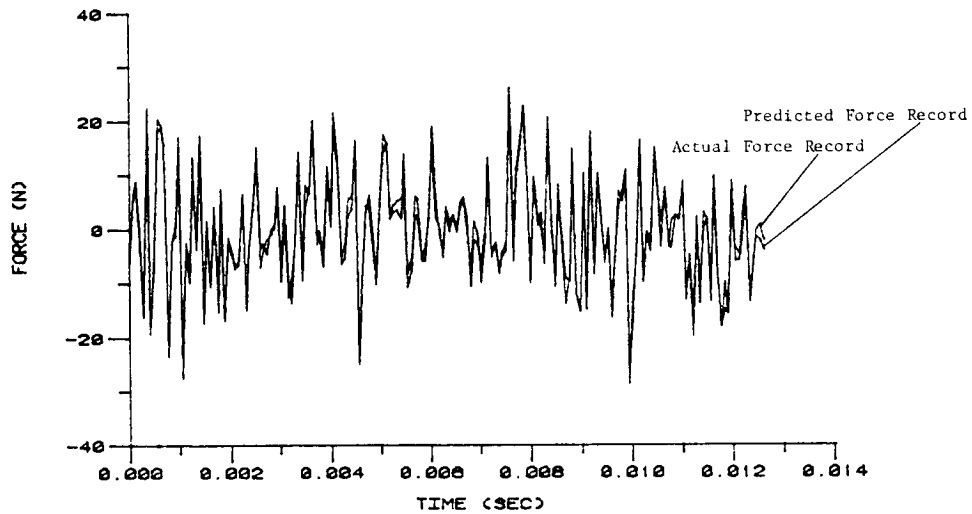
Figure 7 - Comparison of actual and predicted force records
(record for location 4 - unfiltered response)
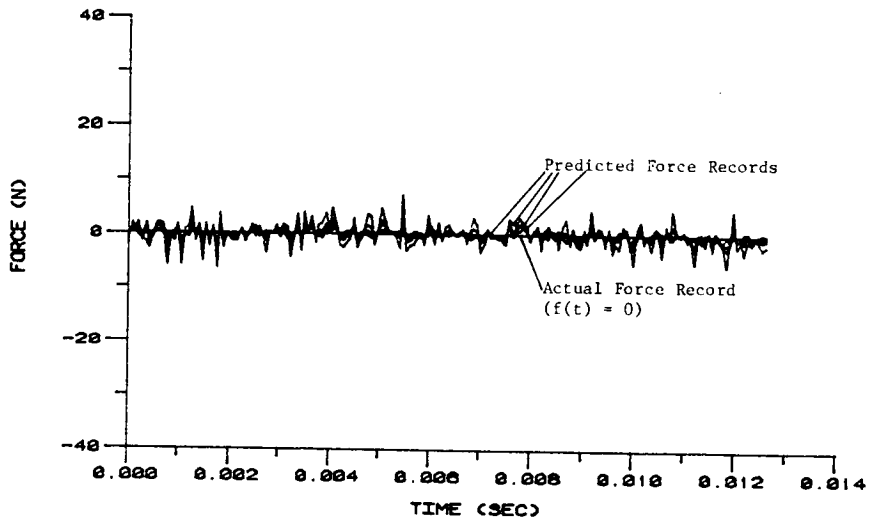
Figure 8 - Comparison of actual and predicted force records
(records for locations 1,3,5, and 6 - unfiltered)

Care must be excercised when employing filters in this technique. If the signatures are obtained after filtering the response record, the response vector X and its derivatives must also be fitered before substitution into Equation (5) . If this procedure is not followed, the estimated force vector F will also include the filtered modes of the system. This may be demonstrated using the same example. Studying the Fourier magnitude spectrums of the responses at points 1 and 6 and their derivatives , it was apparent that the lowest mode is quite dominant. Therefore, employing a high-pass filter at 80 Hz for the signatures, but not the response vector X, the resultant estimated inputs at points 2 and 4 are shown in Figures 9 and 10. The low mode is quite apparent in the estimated input records. This problem could also occur when calculating signatures from velocity and acceleration records since they usually tend to include a larger density of the higher frequency modes.

In addition to the aforementioned effects, the frequency content of the response records is a major cause for the dissimilarity between the identified system matrices and the actual matrices. This may be explained by considering the six degrees-of-freedom cantilever beam. If the beam were excited by a random force with a band-limited frequency range, where, for the sake of example, this range included only the lowest three modes, then the identified matrices will possess information concerning these three modes only. This would mean that the identified [M], [C], and [K] matrices would definitely be different from the actual matrices. Therefore, subjecting the predicted system to the actual input vector should result in a response very similar to the measured system response, whereas a force rich in the higher frequencies would yield different results. Hence, using the proposed technique for damage detection requires the frequency content of the input force to always be the same.

269
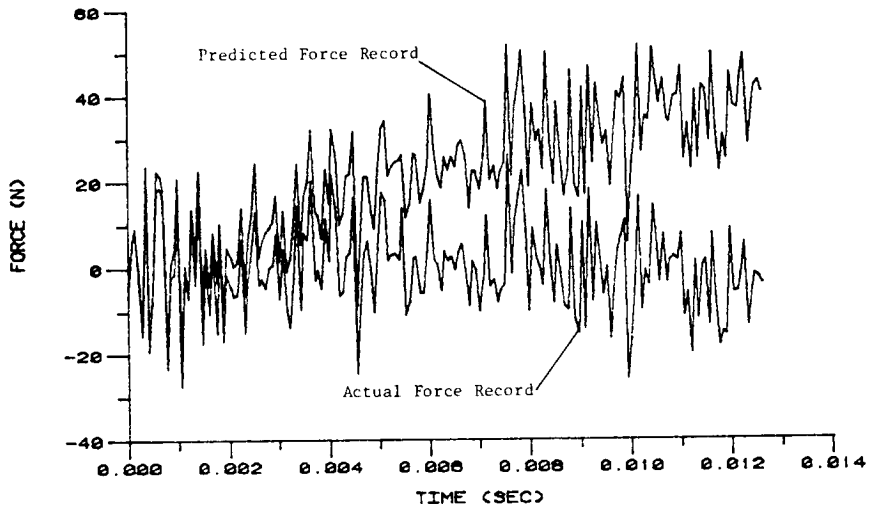
Figure 9 - Comparison of actual and predicted force records
(record for location 2 - filtered response)
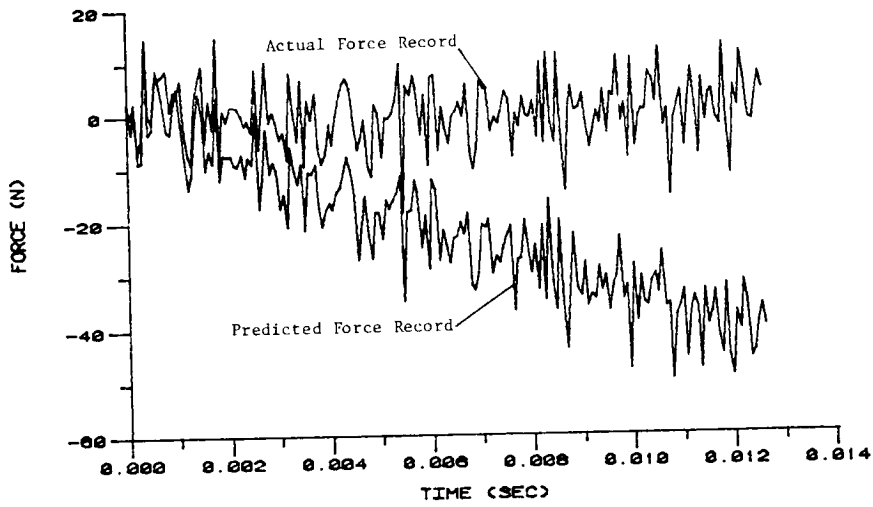
Figure 10 - Comparison of actual and predicted force records
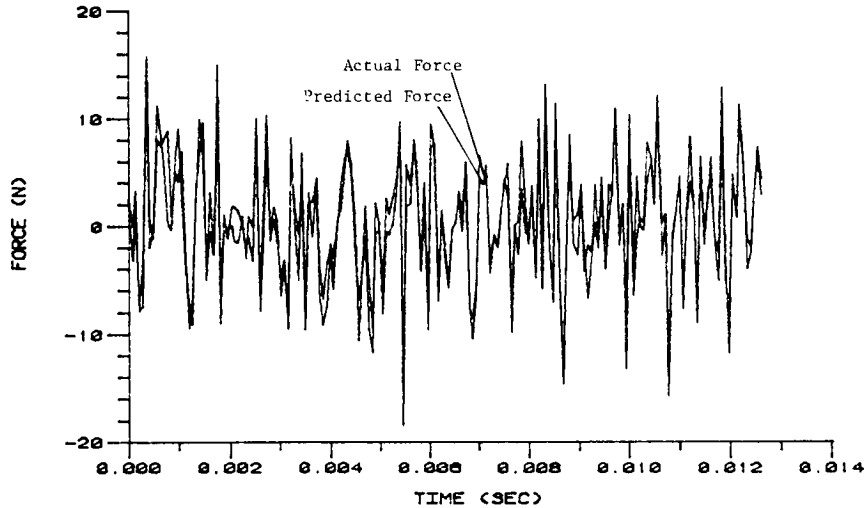(record for location 4 - filtered record)

CONCLUSIONS

A system identification technique was proposed based on a leastsquares fit of Randomdec and cross-Randomdec signatures to identifiy the mass, damping, and stiffness matrices of a linear multidegree-of-freedom system. Computer simulations carried out for a discretized finite element model of a cantilever beam proved the technique to be quite effective in predicting the response of the beam for a given frequency range of excitation. Furthermore, the proposed technique was demonstrated to be successful in predicting the random forcing function initially introduced to excite the system. The results of the simulation clearly indicated the importance of filtering the response of the beam and the effect it may have on the identified system.

NOMENCLATURE

$[A]$	flexibility matrix
$[C]$	damping matrix of multiple D.O.F. system
$[\tilde{C}]$	unscaled identified damping matrix
c_{ij}	element ij of damping matrix $[C]$
$\mathbf{F}$	input loading vector
$f_i(t)$	forcing function applied at point i
H_{pij}	system matrix to be identified
$\tilde{H}_{pij}$	estimated system matrix
$\mathbf{h}$	vector containing system parameters to be identified
h_i	element i of vector $\mathbf{h}$
$[K]$	stiffness matrix of multiple D.O.F. system
$[\tilde{K}]$	unscaled identified stiffness matrix
k_{ij}	element ij of stiffness matrix $[K]$
$[M]$	mass matrix of multiple D.O.F system
$[\tilde{M}]$	unscaled identified mass matrix
m_{ij}	element ij of mass matrix $[M]$
$[R]$	matrix containing ratio of flexibility matrices
r_{ij}	element ij of matrix $[R]$

t	time variable
X	response vector of multiple D.O.F. system
X_h	homogeneous response vector
X_p	particular response vector
X_i	system response at point i
$x(t), \dot{x}(t), \ddot{x}(t)$	position, velocity, and acceleration of variable x
z_{ij}	measured system response
β	number of system parameters to be identified
ϵ	scaling factor of identified system

REFERENCES

1. Bedewi, N.E., "The Mathematical Foundation of the Auto and Cross-Random Decrement Techniques and the Development of a System Identification Technique for the Detection of Structural Deterioration", Ph.D. Dissertation, University of Maryland, 1986.

2. Berman, A., "Parameter Identification Techniques for Vibrating Structures", The Shock and Vibration Digest, Vol. 11, No. 1, 1979, pp. 13-16.

3. Brignac, W.J., et al., "The Random Decrement Technique Applied to the YF-16 Flight Flutter Tests", AIAA/ASME/SAE 16th Structures Conf. Denver, Co., 1975.

4. Chang, C.S., "Study of Dynamic Characteristics of Aeroelastic Systems Utilizing Randomdec Signatures", NASA-CR 132563, 1975.

5. Cole, H.A., Jr., "Methods and Apparatus for Measuring the Damping Characteristics of a Structure", United States Patent No.3,620,069, Nov. 16, 1971.

6. Cole, H.A., Jr., "Failure Detection of a Space Shuttle Wing Flutter Model by Random Decrement", NASA TMX-62,041, May 1971.

7. Crandall, S.H., Mark, W.D., Random Vibration in Mechanical Systems, Academic Press, New York, 1963.

8. Gersch, W., Parameter Identification: Stochastic Process Techniques", The Shock and Vibration Digest, Vol. 7, No. 11, 1975, pp. 71-86.

9. Gersch, W. and Liu, R., "Time Series Methods for the Synthesis of Random Vibration Systems", ASME Journal of Appl. Mechanics, Vol. 43, 1976, pp. 159-165.

10. Hammond, C.E. and Dogget, R.V., Jr., "Determination of Subcritical Damping by Moving-Block/Randomdec Applications", Proc. of the NASA Symp. on Flutter Testing Techniques, Oct. 9-10, 1975.

11. Ibrahim, S.R. "Random Decrement Technique for Modal Identification of Structures", 18th Structures, Structural Dynamics, and Materials Conference, San Diego, CA., March 21-23, 1977.

12. Wang, Z. and Fang, T., "A Time-Domain Method for Identifying Modal Parameters", Journal of Appl. Mechanics, Vol. 53, March 1986, pp. 28-32.

13. Yang, J.C.S., Aggour, M.S., Dagalakis, N. and Miller, F., "Damping of an Offshore Platform Model by Randomdec Method", Proc. Second ASCE/EMD Specialty Conference on Dynamic Response of Structures, Atlanta, Georgia, January 1981.

14. Yang, J.C.S., Tsai, T., Tsai, W.H., and Chen, R.Z. "Detection and Identification of Structural Damage from Dynamic Response Measurements", 4th Int'l Symp. on Offshore Mechanics and Arctic Engr., Dallas, TX, February, 1985.

15. Yang, J.C.S, Tsai, T., Pavlin, V., Chen, J., and Tsai, W.H., "Structural Damage Detection by the System Identification Technique", 55th Shock and Vibration Bulletin, June 1985.

A System Identification Technique Based on the Random Decrement Signatures Part II: Experimental Results

Nabih E. Bedewi
Jackson C. S. Yang

Identification of the system parameters of a randomly excited structure may be treated using a variety of statistical techniques. Of all these techniques, the Random Decrement is unique in that it provides the homogeneous component of the system response. Using this quality, a system identification technique was developed based on a least-squares fit of the signatures to estimate the mass, damping, and stiffness matrices of a linear randomly excited system. In part I of this paper the mathematics of the technique was presented in addition to the results of computer simulations conducted to demonstrate the prediction of the response of the system and the random forcing function initilly introduced to excite the system. This part of the paper presents the results of an experiment conducted on an offshore platform scale model to verify the validity of the technique and to demonstrate its application in damage detection.

INTRODUCTION

A system identification technique was developed in part I of this paper for extracting meaningful information from randomly excited structures. This technique is based on the Random Decrement and cross-Random Decrement signatures of the structure [2,3,4,5]. Computer simulations performed using a linear system demonstrated the effectiveness of this technique in obtaining an accurate model of the system and in predicting the random forcing function introduced for excitation. The system identification technique is briefly desrcibed as follows:

Given a randomly excited linear multidegree-of-freedom system, response data is obtained at several locations. A model for the system is assumed in the form

$$[M] \ddot{X} + [C] \dot{X} + [K] X = F \tag{1}$$

where [M] and [K] are real symmetric matrices representing the mass and stiffness of the structure, [C] is a nonproportional , real, symmetric damping matrix, F is the forcing vector, and X and its time derivatives represent the response of the system. Random Decrement and cross-Random Decrement signtuares are then obtained from the response data thus forming the homogeneous components of the response. Substituting the signatures in Equation (1) and noting that vector F is zero, a least squares fit is then performed with the assumption that one of the elements in the system matrices is known. A detailed description of the constraints on the matrices and the least squares method is given in part I of this paper.

SCALE MODEL EXPERIMENT

A 1 : 13.8 scale model of an offshore platform structure was set up on outdoor earth ground. The base of the structure was welded to a steel (box type) frame, then both were lowered into a 6'x6'x3' pit hole. The pit was then filled with wet concrete up to the the base of the structure and left to cure.

The model structure consists of four legs made of 2" diameter, 0.25" wall, steel pipes. Figure 1 shows the configuration of the structure with its dimensions and labeled points. A pendulum was set up to provide random impact excitation at point 13. The responses at points 1 to 13 were monitored using accelerometers screwed into threaded aluminum blocks attached directly to the structure.
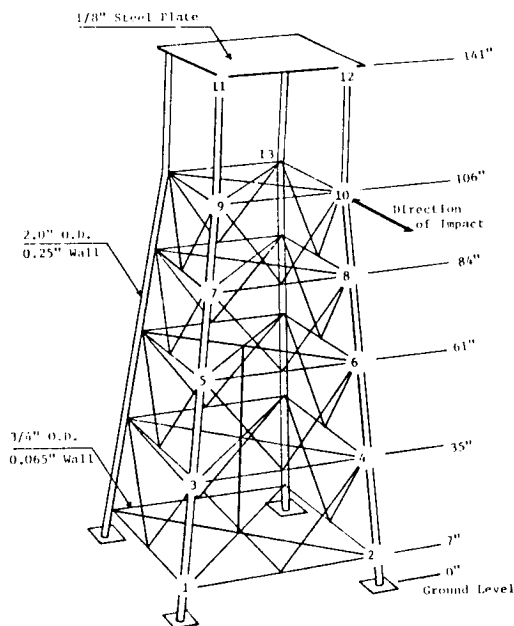
Figure 1 - Configuration of offshore platform scale model

VERIFICATION OF THE SYSTEM IDENTIFICATION TECHNIQUE

The first experiment was conducted to verify the reliability of the system identification technique in obtaining a model from Randomdec signatures. To accomplish this task, the response of the structure, as well as the input to the structure, had to be measured.

Four accelerometers were mounted at locations 4, 6, 8, and 13, and a load cell was firmly attached to the tip of the pendulum hammer. The structure was randomly impacted for 20 seconds while the output of the five transducers was recorded on analog tape simultaneously. The five channels were then digitized at a sampling rate of 1000 Hz after passing through a low pass filter set at 125 Hz. The cutoff frequency of the filter was selected based on a maximum system frequency of interest of 85 Hz.

The time record at location 13 was used for triggering the signatures. Figure 2 shows the Randomdec signature for location 13. The system identification technique was then employed in conjunction with the signatures to calculate the 30 unknown parameters in the [M], [C], [K] matrices. Four sets of matrices were initially calculated, each set corresponding to one fixed element in the stiffness matrix. The four sets of matrices were then averaged to obtain the best estimate for the model.
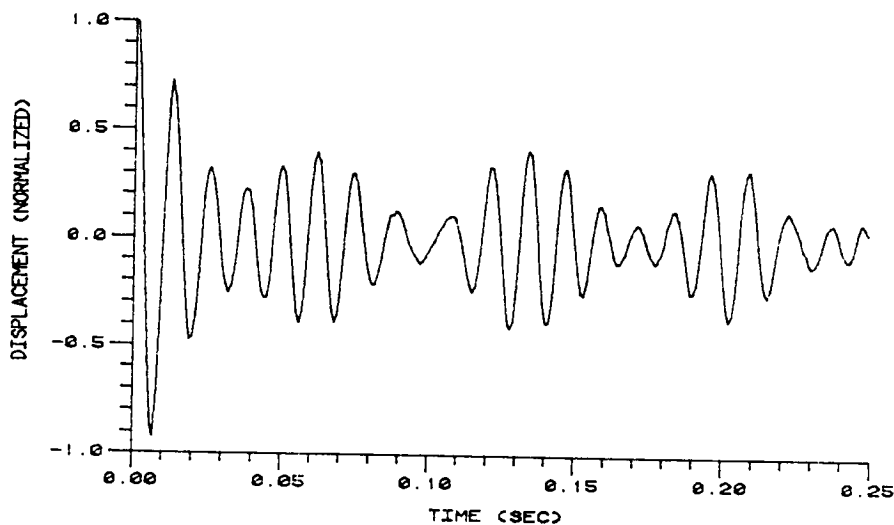
Figure 2 - Randomdec signature of time response at location 13

To confirm the accuracy of the established model, the three system matrices were substituted into the set of differential equations describing the system, Equation (1), and the second derivative of the load applied during the experiment introduced as input (the derivative is taken since the signatures were obtained from acceleration records). The initial conditions were extracted from the measured response of the system, and Equation (1) solved numerically. A step size of 0.001 sec. was used corresponding to the time step of the sampled data.

Since the estimated system parameters were not originally scaled to match the actual system in magnitude, the response had to be scaled to fascilitate the comparison. This was performed by multiplying the estimated reponses at the four points by the average of the ratios of the standard deviations of the measured responses to the standard deviations of the estimated responses. Furthermore, all the responses were multiplied by -1 since they appeared to be mirror images of the actual reponses about the time axis. This change in sign is a legitimate step since the same effect could have been achieved by scaling the system matrices by -1.

The results of the comparison at point 4 are shown in Figure 3. The plots indicate that the predicted system response is in good agreement with the actual response.
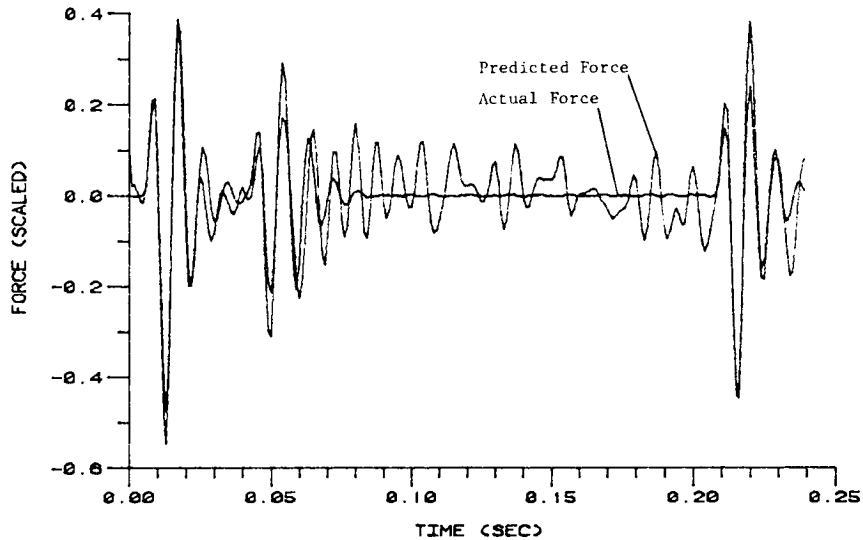
Figure 3 - Comparison of measured vs. predicted responses at point 4

Another approach to verify the accuracy of the model is to compare the measured force with the predicted force. Therefore, the measured system response was substituted in Equation (1) with the three estimated matrices and the force vector calculated. Again, the output was scaled for comparison. Figure 4 shows the predicted force time record and the second derivative of the measured force time record at location 13. The forces are in good agreement when a force is being applied, but some large oscillation exists in the predicted record when no force is actually being applied. Careful inspection of the figure reveals that the oscillations have a frequency of 125 Hz, correponding to the frequency of the filter. Figure 5 shows a comparison of the forces at locations 4, 6, and 8. The magnitude of the predicted forces is small relative to the force at point 13 (these records were already scaled using the scaling factor employed at point 13).
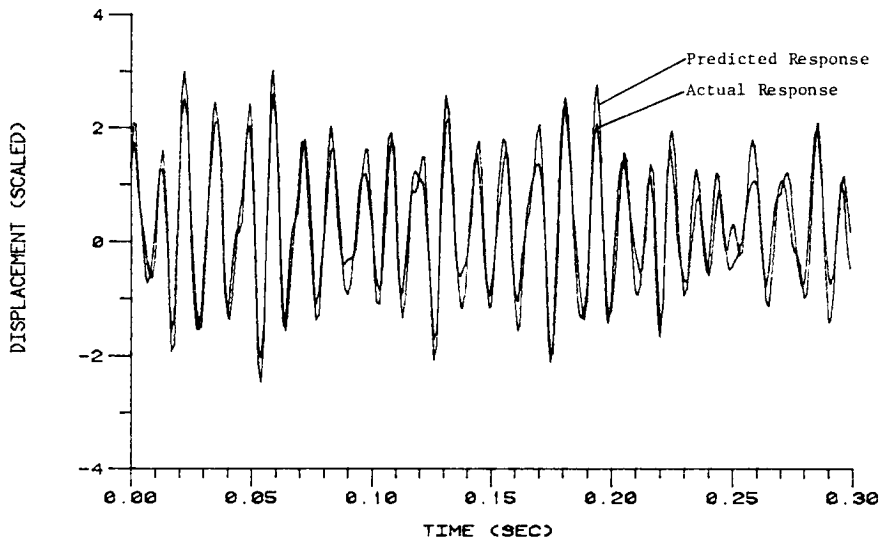
Figure 4 - Comparison of measured vs. predicted forces at point 13
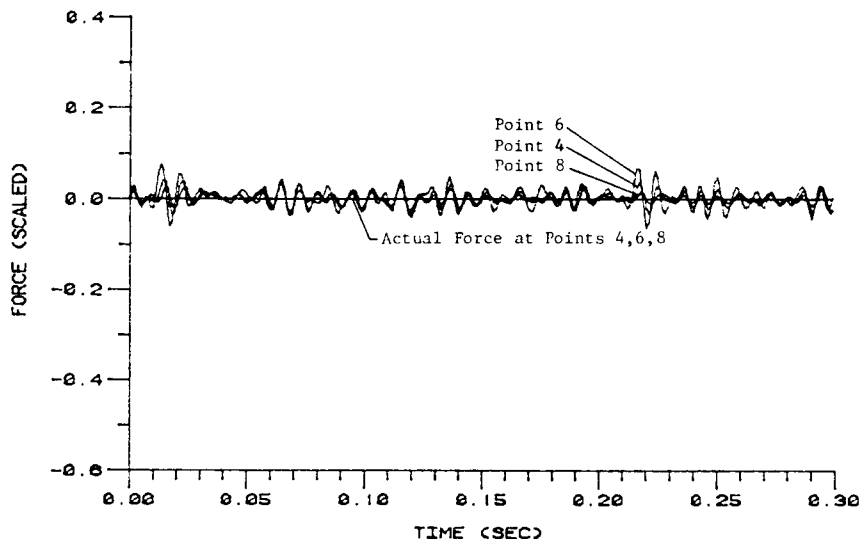
Figure 5 - Comparison of measured vs. predicted forces at points 4,6,& 8.

DAMAGE DETECTION

A useful application for the system identification technique is the detection of changes in the system parameters resulting from induced damage. A large crack in a structure would decrease the local stiffness, thus reducing one or more of its natural frequencies. On the other hand, a corroded section of the structure might reduce the localized mass as well as the stiffness. Therefore, by calculating the system matrices consistently and comparing them to the matrices of the originally perfect system, the occurance of a damage, and possibly its identity, might be detected.

Damage Detection Criterion

Although this approach is theoretically feasible and effective, it is not easy to implement in practice. The difficulty arises in interpreting the changes in the system model and in being able to connect the different changes with the types of damages that could have resulted in their occurrance. In addition, it is possible that some parameters are more meaningful than others in this application. For example, the diagonal elements in the mass matrix are more sensitive to changes in mass at their respective locations than the off diagonal elements.

The stiffness matrix is somewhat more difficult to analyze than the mass matrix. From the point of view of damage detection, it is more appropriate to observe changes in the flexibility matrix than the stiffness matrix. This can be easily verified by considering the static equations describing a multidegree-of-freedom system, namely

$$[K] \; X \; = \; F \tag{2}$$

Defining the flexibility matrix as $[A] = [K]^{-1}$, Equation (2) becomes

$$X \; = \; [A] \; F \tag{3}$$

279   C-4

Assuming the system to have three degrees-of-freedom, Equations (2) and (3) may be expanded as follows:

$$
\begin{aligned}
k_{11} x_1 + k_{12} x_2 + k_{13} x_3 &= f_1 \\
k_{21} x_1 + k_{22} x_2 + k_{23} x_3 &= f_2 \\
k_{31} x_1 + k_{32} x_2 + k_{33} x_3 &= f_3
\end{aligned}
\tag{4}
$$

and

$$
\begin{aligned}
x_1 &= a_{11} f_1 + a_{12} f_2 + a_{13} f_3 \\
x_2 &= a_{21} f_1 + a_{22} f_2 + a_{23} f_3 \\
x_3 &= a_{31} f_1 + a_{32} f_2 + a_{33} f_3
\end{aligned}
\tag{5}
$$

It is clear from Equations (4) that k_{ij} represents the force at point i when x_j = 1 and x_k = 0 where $k \neq j$. This is rather difficult to visualize in a complex system. On the other hand, it can be seen from Equation (5) that a_{ij} represents the deflection at point i when a unit load is applied at point j. Besides being more physically realizable, any element a_{ij} may be meaningfully treated separately.

The next issue to be addressed is the significance of the diagonal and off-digonal elements in the flexibility matrix. It has been traditionally accepted that only the diagonal terms need to be considered since they strongly reflect the absolute flexibility of their respective locations. This is not necessarily the most effective approach though. To demonstrate that off-diagonal elements are a better indication of the flexibility at a point, consider the system shown in Figure 6a. The beam is of length L and is rigidly attached at both ends. If three equidistant points are monitored on the beam, the resulting flexibility matrix could be found using simple "strength of materials" tables to be

$$
[A] = \begin{bmatrix} 2.197 & 2.604 & 1.058 \\ 2.604 & 5.208 & 2.604 \\ 1.058 & 2.604 & 2.197 \end{bmatrix} \frac{10^{-3} L^3}{EI}
$$

where E is Young's modulus of the material and I is the cross-sectional area moment of inertia of the beam. Now, taking the extreme case, suppose that the beam was cut at some point between locations 1 and 2, resulting in two cantilever beams of unequal lengths (Figure 6b). The new flexibility matrix of the damaged system is

$$
[A]^d = \begin{bmatrix} 5.208 & 0.000 & 0.000 \\ 0.000 & 41.667 & 13.020 \\ 0.000 & 13.020 & 5.208 \end{bmatrix} \frac{10^{-3} L^3}{EI}
$$
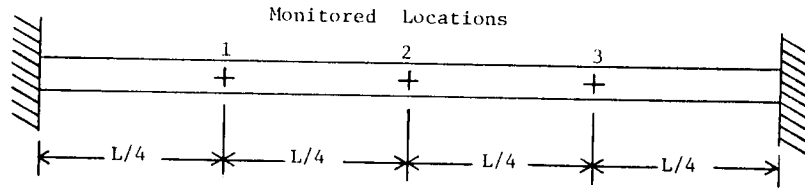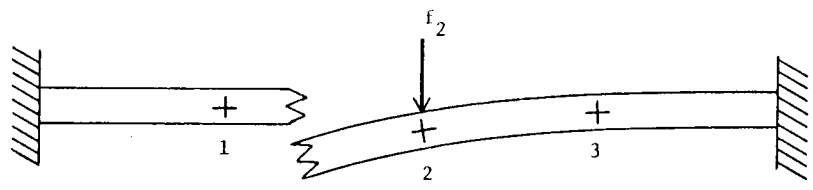
Figure 6 - a) Configuration of undamaged fixed-fixed beam
            b) Configuration of damaged fixed-fixed beam. Separation
               into two cantilever (fixed-free) beams.

A matrix [R] may now be constructed where each element r_{ij} is defined as

$$r_{ij} = \frac{a^d_{ij}}{a_{ij}}$$

namely

$$[R] = \begin{bmatrix} 2.371 & 0.000 & 0.000 \\ 0.000 & 8.000 & 5.000 \\ 0.000 & 5.000 & 2.371 \end{bmatrix}$$

Graphing the diagonal terms as a function of point location (Figure 7a), and noting
that the beam ends have a ratio of 1, it would be deduced that the damage occurred
at point 2 due to the symmetry. On the other hand, if the off-diagonal elements of
the adjacent points are plotted between the two points they represent (Figure 7b),
the damage would be correctly identified as being between 1 and 2. It is of vital
importance to note that for diagonal terms the steepest peak represents the damage

281

whereas for off-diagonal terms the steepest valley represents the damage. This is because a load applied at a point next to the damage would cause the point to deflect more than it did before the damage was introduced, whereas the point on the other side of the damage would deflect less than it did before the damage was introduced.

This example may be expanded intuitively to consider the intermediate event where the cut is not severe enough to separate the beam. If the beam is assumed to be composed of two springs, one represnting the portion to the left of the damage, and the other the portion to the right, then the deflection on either side of the damage would be in-directly proportional to its respective spring stiffness. In terms of the flexibility matrix ratio, this would mean that the terms which were zero would begin at 1 when no damage exists, then decrease as the damage size increases, until the limiting value of zero is reached when the cut goes all the way through the beam. Conversely, the off-diagonal terms larger than 1 would begin at unity for no damage and finally reach some finite limiting value for the through cut. Figure 7c depicts this process showing the direction of change in the off-diagonal elements. On the other hand, the ratio of the digonal elements would always result in a symmetric curve regardless of the severity of the damage (Figure 7d).

a) Plot of Flexibility Matrix Diagonal Elements

b) Plot of Flexibility Matrix Off-Diagonal Elements

c) Transition of Off-Diagonal Elements as Damage Increases

d) Transition of Diagonal Elements as Damage Increases
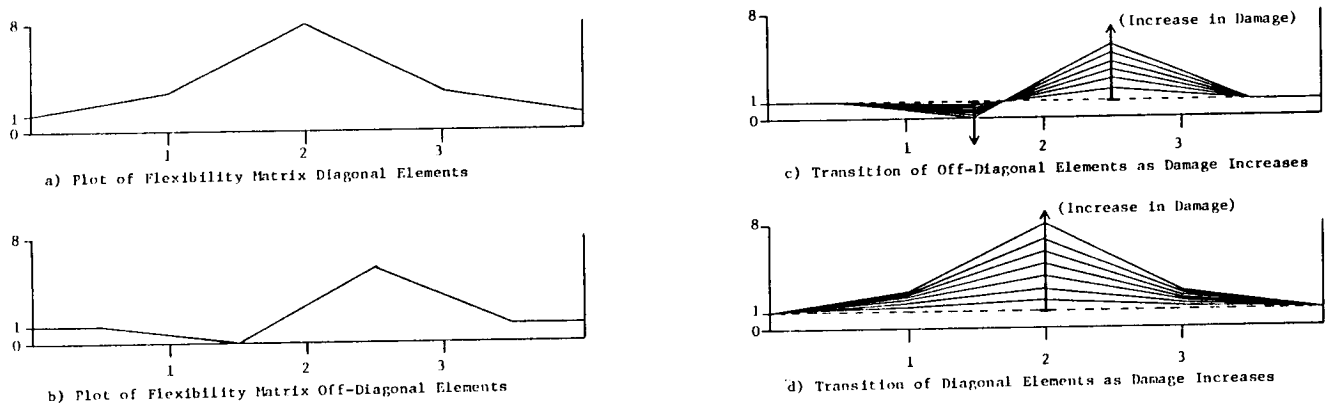
Figure 7

Experimental Implementation of Detection Criterion

An experiment was designed and conducted to verify the accuracy of the proposed damage detection criterion. The experiment was composed of two identical parts, one performed before the damage was induced, and the other afterward. To obtain the response of every labeled point on the structure, each part was actually carried out four times. Since four accelerometers were used, one accelerometer was kept at point

10 while the other three were moved to different locations for each run of the experiment. The four sets of monitored points were (1,2,3,10), (4,5,6,10), (7,8,9,10), and (11,12,13,10). The collected data were processed in the same fashion described earlier.

Since station 10 was common for all the sets, it was used for triggering while cross-Randomdec signatures were obtained for the other points. This resulted in four separate Randomdec signatures. The four signatures, shown in Figure 8, prove the repeatability of the technique.
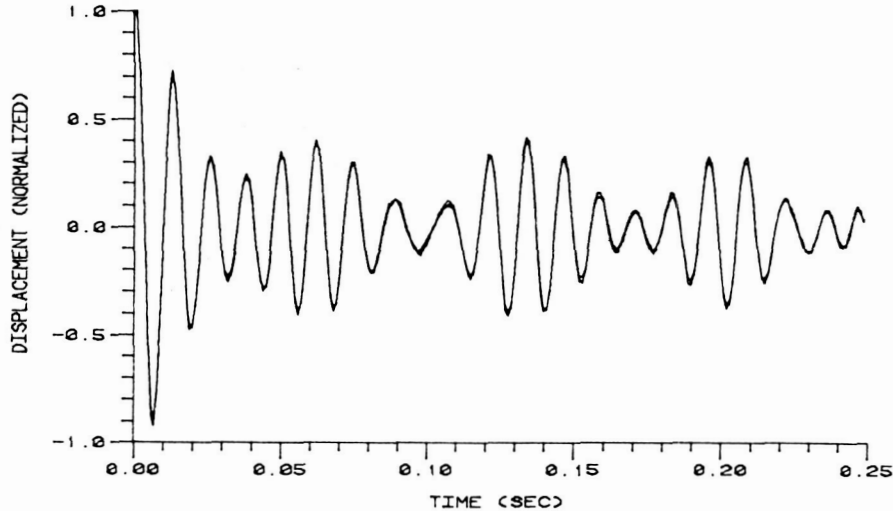
Figure 8 - Comparison of four independently obtained Randomdec
signatures at location 10
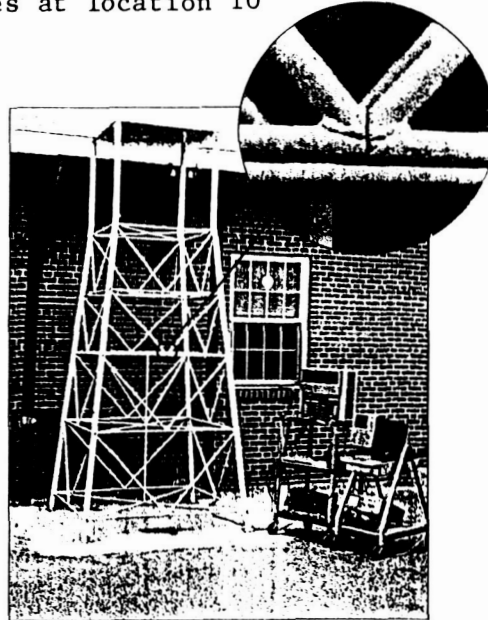
Figure 9 - Location of through cut on offshore platform model

A through cut was made with a hand saw at the cross member between points 5 and 6 (Figure 9). The same process was repeated and twelve cross-Randomdec signatures

calculated. Figure 10 shows the Randomdec signatures at location 10 before and after the damage was induced. The changes in frequency and phase are quite apparent.

The system identification technique was then used in conjunction with the two pairs of Randomdec signatures at point 10 and the two pairs of eleven cross-Randomdec signatures at points 1 to 9, 11, and 12 to obtain the system parameters before and after the damage. This resulted in two pairs of 12x12 [M], [C], and [K] matrices. The two stiffness matrices were inverted yielding two flexibility matrices, and the ratio of the respective elements taken. Table I shows the ratios of the diagonal elements and the off-diagonal elements representing adjacent points. Figure 11 shows the diagonal ratios plotted directly on the structure. It is not clear from the figure where the location of the damage is. The plot of the off-diagonal ratios on the structure is shown in Figure 12. Noting the fact that the lowest ratio indicates the location of the damage, it can be deduced from this figure and from Table I that the damage is residing somewhere between points 5 and 6.
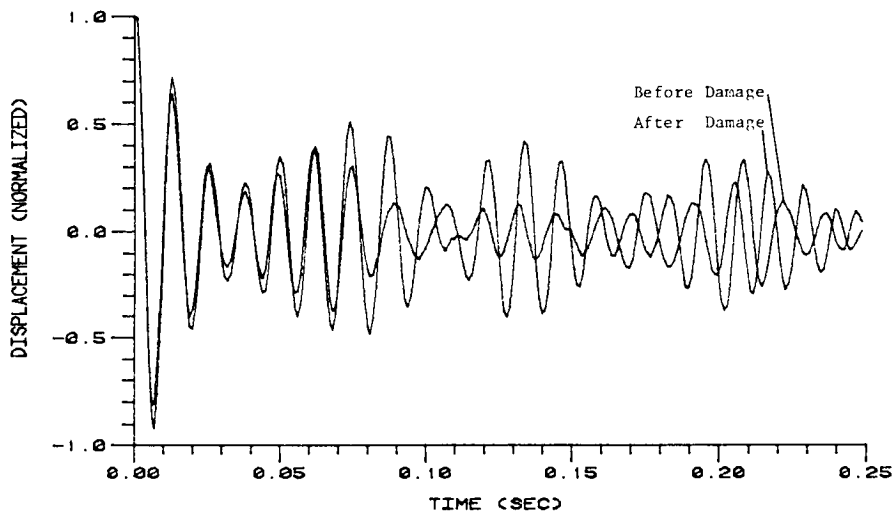
Figure 10 - Change in Randomdec signature at point 10 after damage

Table I - Ratios of flexibility matrix elements before and after damage

DIAGONAL ELEMENTS				OFF-DIAGONAL ELEMENTS					
LEG 1 POINTS		LEG 2 POINTS		LEG 1 MEMBERS		LEG 2 MEMBERS		INTERMEDIATE MEMBERS	
Point Number	Ratio	Point Number	Ratio	Member Number	Ratio	Member Number	Ratio	Member Number	Ratio
1	1.02	2	1.16	1,3	3.08	2,4	3.26	1,2	3.62
3	2.67	4	2.29	3,5	1.76	4,6	1.97	3,4	1.16
5	3.91	6	5.27	5,7	0.87	6,8	0.92	5,6	0.13
7	1.86	8	0.06	7,9	0.53	8,10	0.62	7,8	0.50
9	4.64	10	1.64	9,11	2.56	10,12	2.16	9,10	1.04
11	2.29	12	1.09	-	-	-	-	11,12	3.19

284
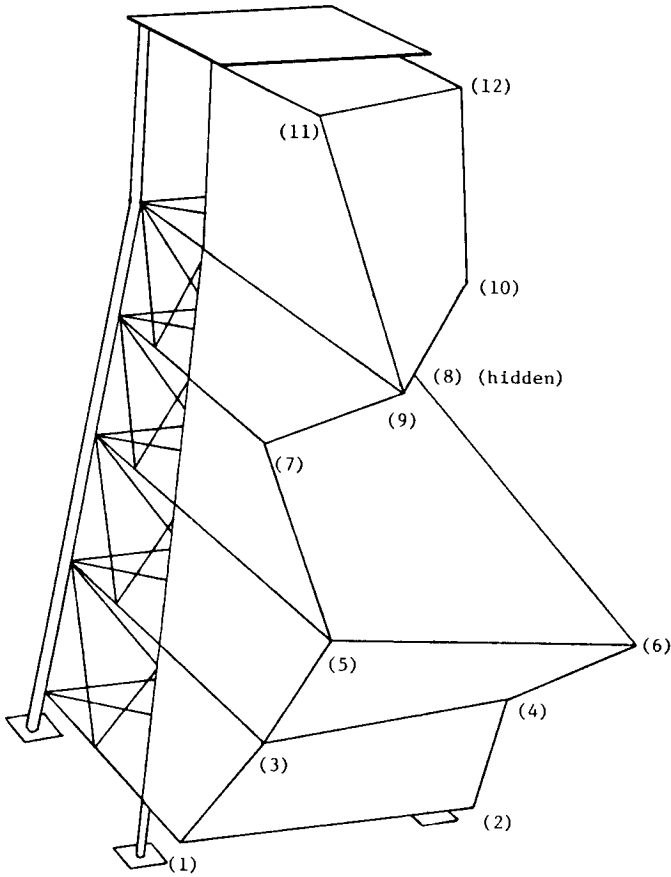
Figure 11 - Plot of flexibility matrix
diagonal elements on scale
model
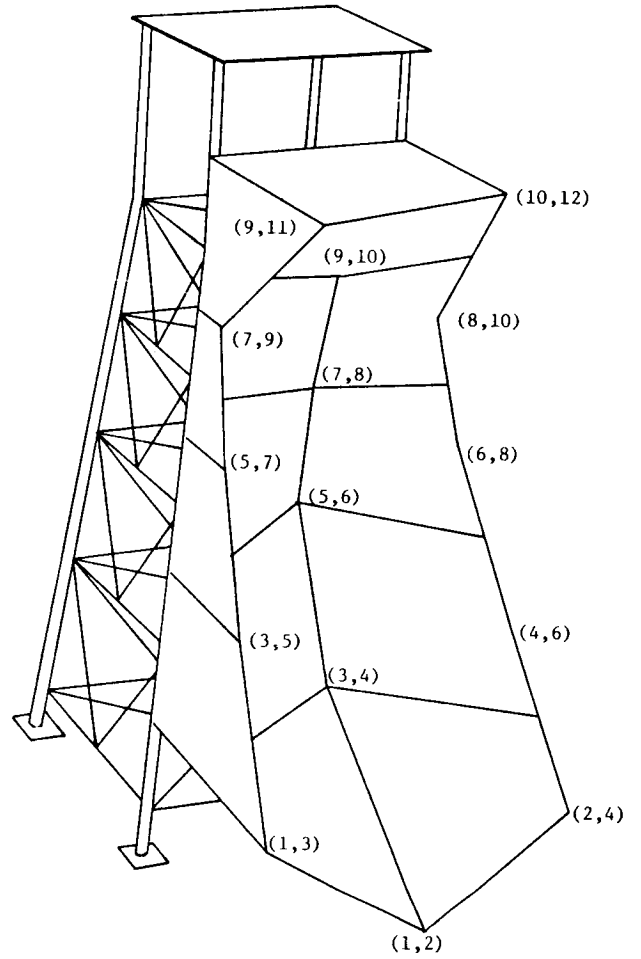
Figure 12 - Plot of flexibility matrix
off-diagonal elements on
scale model

CONCLUSIONS

An experiment was conducted on a scale model of an offshore platform structure to verify the applicability of the system identification technique introduced in part I of this paper. The technique was employed to obtain a mathematical model of the structure from the random response data. This model was then used to predict the response of the structure and the forcing function initially introduced to excite the structure. These results compared favorably with the measured data.

Finally, an approach to damage detection and location was demonstrated through the inversion and comparison of the stiffness matrix before and after the damage is introduced. The use of a simple example revealed that the off-diagonal elements are more effective in locating the damage than the diagonal elements. The experiment conducted on the scale model of the offshore platform confirmed these findings successfully.

NOMENCLATURE

$[A]$	flexibility matrix
a_{ij}	element ij of flexibility matrix
$[C]$	damping matrix of multiple D.O.F. system
E	Young's modulus
F	input loading vector
f_i	element i of forcing vector
I	area moment of inertia
$[K]$	stiffness matrix of multiple D.O.F. system
k_{ij}	element ij of stiffness matrix
$[M]$	mass matrix of multiple D.O.F system
$[R]$	matrix containing ratio of flexibility matrices
r_{ij}	element ij of matrix $[R]$
t	time variable
X	position vector of multiple D.O.F. system
x_i	element i of position vector
$\dot{X}$	velocity vector of multiple D.O.F. system
$\ddot{X}$	acceleration vector of multiple D.O.F. system

REFERENCES

1. Bedewi, N.E., "The Mathematical Foundation of the Auto and Cross-Random Decrement Techniques and the Development of a System Identification Technique for the Detection of Structural Deterioration", Ph.D. Dissertation, University of Maryland, 1986.

2. Cole, H.A., Jr., "Methods and Apparatus for Measuring the Damping Characteristics of a Structure", United States Patent No.3,620,069, Nov. 16, 1971.

3. Cole, H.A., Jr., "Failure Detection of a Space Shuttle Wing Flutter Model by Random Decrement", NASA TMX-62,041, May 1971.

4. Ibrahim, S.R. "Random Decrement Technique for Modal Identification of Structures", 18th Structures, Structural Dynamics, and Materials Conference, San Diego, CA., March 21-23, 1977.

5. Yang, J.C.S., Aggour, M.S., Dagalakis, N. and Miller, F., "Damping of an Offshore Platform Model by Randomdec Method", Proc. Second ASCE/EMD Specialty Conference on Dynamic Response of Structures, Atlanta, Georgia, January 1981.

6. Yang, J.C.S., Tsai, T., Tsai, W.H., and Chen, R.Z. "Detection and Identification of Structural Damage from Dynamic Response Measurements", 4th Int'l Symp. on Offshore Mechanics and Arctic Engr., Dallas, TX, February, 1985.

DYNAMIC TESTING

Structural Frequency Functions for an Impulsive, Distributed Forcing Function

Vesta I. Bateman

The response of a penetrator structure to a spatially
distributed mechanical impulse with a magnitude approaching
field test force levels (1-2 Mlb) was measured. The
frequency response function calculated from the response to
this unique forcing function is compared to frequency
response functions calculated from response to point forces
of about two thousand pounds and a hundred thousand pounds.
The results show that the strain gages installed on the
penetrator case respond similarly to a point, axial force and
to a spatially distributed, axial force. This result
suggests that the distributed axial force generated in a
penetration event may be reconstructed as a point axial force
when the penetrator behaves in a linear manner.

INTRODUCTION

Structural system response measured for the calculation of frequency response
functions is typically stimulated by a low-level force (100's of pounds) applied at
a point by an instrumented hammer. Often, in their intended use environment, the
systems encounter much higher service loads which are distributed over the
structure, and linearity of their responses under these conditions must be assumed.
This work describes the response of a structure to three different axial forcing
functions: a low-level (about two thousand pounds), point force generated by an
instrumented hammer; a high-level (about 100 klb), point force generated with a
Reverse Hopkinson Bar technique; and a high-level (1-2 Mlb), distributed force
generated with an explosive. The structure is an earth penetrator case whose design
is typical of those at Sandia National Laboratories and is shown in Figure 1. The
case is a hollow structure and does not include the internal components normally
present for a field test. The case material is steel (Type 4340) which has a yield
strength in excess of 170 ksi; the case was not noticeably deformed by any of the
tests described in this paper. These tests were undertaken to characterize the case
structural response to axial loads and to assess the effect of spatial distribution
of the axial load over the ogival nose. There were three goals initially defined
for this series of tests.
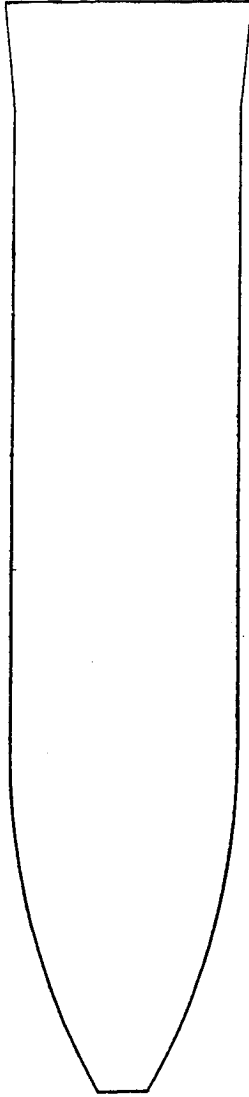
Figure 1:   Penetrator Case Used for Structural Response
Measurements with Three Axial Forcing Functions.

The first goal was to obtain good structural response measurements for the penetrator case by selection of optimum strain gage locations and by proper strain gage installation. Four axial locations, two on the interior and two on the exterior, were desired for the test series; each location had four gages spaced equidistantly around the circumference. Optimum locations were determined from the displacement mode shapes for one axial and three lateral modes which were identified in the 4096 Hz bandwidth for a modal analysis of the case performed by the Modal Testing Group at Sandia National Laboratories. The technique for inferring the strain mode shapes from modal data has recently been developed at Sandia [1] and will not be presented here. The locations chosen have good structural response for the axial and lateral modes below 4096 Hz and are: 7 in and 14 in from the case rear on the interior and 14 in and 24 in from the rear on the exterior. The gages installed on the case exterior required no special installation technique. The gages were installed on the interior with a fixture [2] which has been designed to insure consistent, accurate installation of four gages at an interior case location. The interior installation technique is also used to instrument penetrators for field test.

A second goal of these tests was to assess the structural response of the penetrator case to axial forcing functions spatially distributed on the penetrator ogival nose. The distributed forcing function was implemented with Deta Sheet explosive shaped into three different spatial distributions. The Deta Sheet configurations are described in "Explosive Loading Tests of Penetrator Unit" by Mr. John L. Cawlfield at this conference. Since the explosive forcing function time history can not be measured directly, the duration was limited to 20 μs so that the frequency content would be independent of the forcing function shape for frequencies 0-10 kHz. Consequently, only the force spatial distribution varied for the frequency range of interest, and the measured responses to the different force distributions could be compared over a frequency range of approximately 10 kHz. The multiple axial locations for the strain gages allowed an observation of how the structural response changes with axial location for a particular distributed force input.

The calculation of the structural frequency response functions for the penetrator case response at different locations was the third goal. Since the symmetric loading of the nose with the Deta Sheet configurations yields a net axial force (and resultant impulse), the structural frequency response functions for the distributed forcing function may be compared to the axial frequency response functions for the point axial forces at both high and low levels. The ultimate goal of this work is to reconstruct the force environment with a frequency response function and the structural response measured in a penetration event. The reconstructed force may be used to verify the computer models that are used for penetration design.

The method used for the structural frequency response function (FRF) calculation is the ratio of the response spectrum divided by the forcing function spectrum. A spectrum in this paper is the Fourier transform of a time history with a rectangular window. It is recognized that this results in leakage errors. The alternative was to use an exponential window which would reduce the leakage but increase the apparent damping of the structure. For this paper, the rectangular window was considered the better compromise.

The individual spectra for the force input and the measured response were combined to form the magnitude of the frequency response function which is defined as

$$H(j\omega) = \frac{O(j\omega)}{I(j\omega)}$$

where

$H(j\omega)$ = the structural frequency response function (FRF)
$O(j\omega)$ = the Fourier transform of the measured structural response
$I(j\omega)$ = the Fourier transform of the axial force input.

The division in the above equation is accomplished by a point-by-point complex division of the two spectra. This formulation represents a single input-single output linear system with no noise [3] and was chosen to facilitate the comparison of the transient responses to the three different transient forcing functions. Structural frequency response functions are often calculated with cross-spectrum and auto-spectrum functions from the average of many response measurements. Since multiple measurements with statistically meaningful characteristics were not possible for the high-level, point force and the distributive force, this simplified method for the FRF calculation was chosen.

All the FRFs in this paper are axial FRFs which means that four gage responses at the same distance from the rear of the penetrator case were combined to eliminate the lateral response. The lateral response for all the forcing functions was minimal and could not be distiguished from the noise level after it was separated from the axial response. For the purposes of force reconstruction, the FRF is not calculated beyond those frequencies for which the input forcing function spectrum has decreased by half its low frequency amplitude. Since the spectrum for the forcing function appears in the denominator of FRF calculation, the decreasing amplitude of the force spectrum will artificially amplify the higher frequencies of the structural response in the FRF.

A LOW-LEVEL, POINT FORCING FUNCTION TEST

The strain gage response to a point force of about 1900 lb was measured. This force was generated by an instrumented hammer with a metal tip and had a duration of about 300 μs. The strain gage response to the force was about $\pm$ 10 $\mu\epsilon$ which is a very low strain level. However, the response was sufficient to characterize the penetrator's structural response to the force. The measured force and strain gage response were used to calculate a frequency response function (FRF) shown in Figure 2. The FRF was calculated up to a frequency of 5400 Hz with a frequency resolution of 4 Hz and contains the first two axial modes of the penetrator case which are 2744 Hz and 5056 Hz. A third axial mode at 6976 Hz was determined from the spectrum of the strain gage time history. The FRF was not calculated for higher frequencies because the spectrum magnitude for the hammer impact had decreased by 50 percent at 5400 Hz. The FRF amplitude at frequencies above 5400 Hz was increasingly amplified by the decreased amplitude in the input force spectrum. As a consequence, both the second (since its frequency is so close to the upper frequency limit of 5400 Hz) and

Figure 2: Structural Frequency Response Function for a Penetrator Case with a 1900 lb, 300µs, Point Forcing Function at Measurement Point 14 in. from Rear, Interior (4 Hz Frequency Resolution).

third axial modes have higher amplitude than is characteristic of the structure. Therefore, this FRF would be useful for force reconstruction of axial structural response for only the first axial mode.

This low-level force test was performed to verify the dynamic response of the strain gages and to determine the axial modes of the penetrator case. The strain gage response was consistent for all the locations on the penetrator case. Only one location is shown here because all locations had essentially the same response to this low-level force. The response exhibited by the penetrator case at this low-level provided a basis of comparison for the remaining two tests.

A HIGH-LEVEL, POINT FORCING FUNCTION TEST

The high-level, point force input was generated in the Shock and Climatic Division shock lab with a test technique called the Reverse Hopkinson Bar [4]. This technique was developed to simulate the shock environment experienced by a vehicle during water impact at velocities as high as 600 ft/s and allows the independent control of the shock pulse amplitude and pulse duration. The Reverse Hopkinson Bar test creates a square-shaped forcing function and is configured as shown in Figure 3. An air gun is used to propel a steel bar (1 in diameter, 10 in long) toward the test structure. The force generated at the interface of the steel bar and the test structure is measured with strain gages installed at 2 in from the point of impact. Although these strain gages measure the correct amplitude of the elastic wave created by the impact, the gages do not record the correct duration because they are not at the point of impact. A method has been developed to correct the pulse duration and the corresponding spectrum [5]. The corrected spectrum for the Reverse Hopkinson Bar forcing function was used to calculate the FRF for this high-level, point force.

The dimensions of the Hopkinson Bar were chosen to generate a square pulse whose duration was about 100 μs. There appeared to be some reflections in the pulse from the penetrator case which extended the duration somewhat so that the spectrum for this high-level, point force was useable to about 7 kHz. A time history of the response to this high-level, point force is shown in Figure 4; it contains 8192 response points sampled at 50 kHz (20 μs per point). It is evident that the response was not measured for a sufficiently long period because the response amplitude is significant, about 25% of the peak amplitude, at the end of the record. The FRFs for this forcing function are shown in Figures 5-8; the FRF for each strain gage location is shown separately.

The amplitude of the peaks for the three axial modes vary for each location which is to be expected. However, the general magnitude of the FRF's is consistent for the four locations. Additionally, the frequencies for the three axial modes agree with the low-level force test measurements to within the frequency resolutions of the two calculations.

TEST ITEM

AIR
CHAMBER

TUBE

STRAIN
GAGE

BAR

REVERSE HOPKINSON
BAR
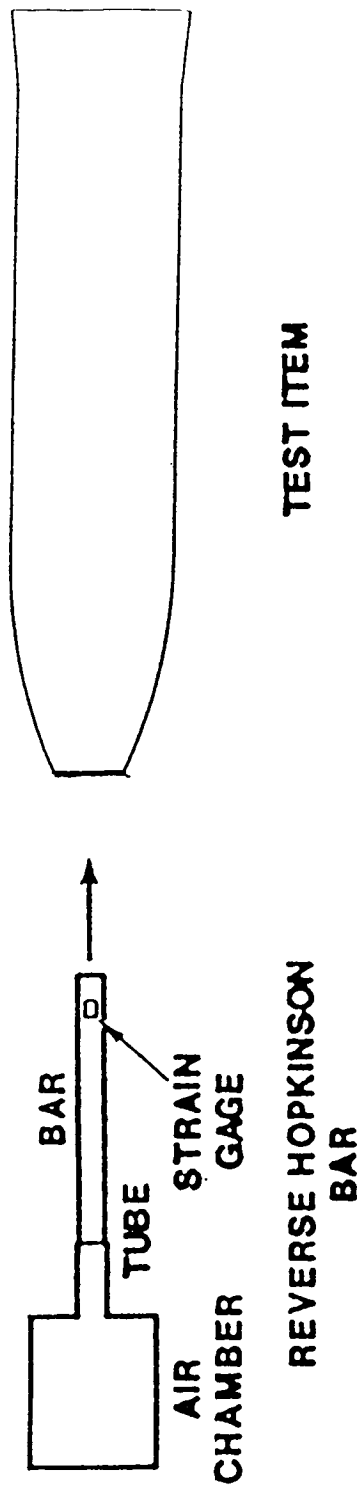
Figure 3: Reverse Hopkinson Bar Test Configuration
for a Penetrator Case and a 1 in Diameter,
10 in Long Hopkinson Bar.
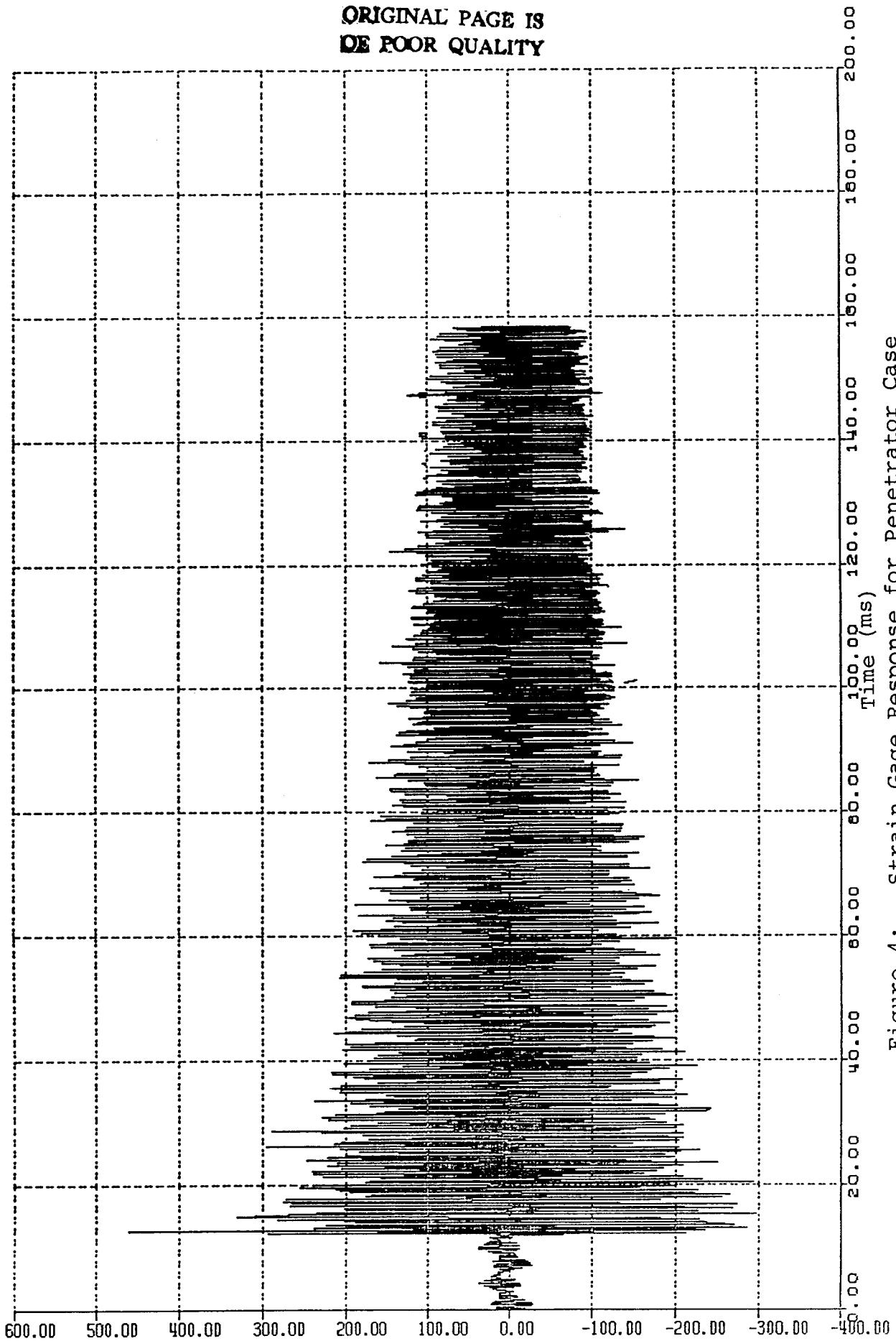
Figure 4:   Strain Gage Response for Penetrator Case
             with 100 klb, 100 µs Point Forcing Function
             (8k Sample Points, 20 µs per Point).

298
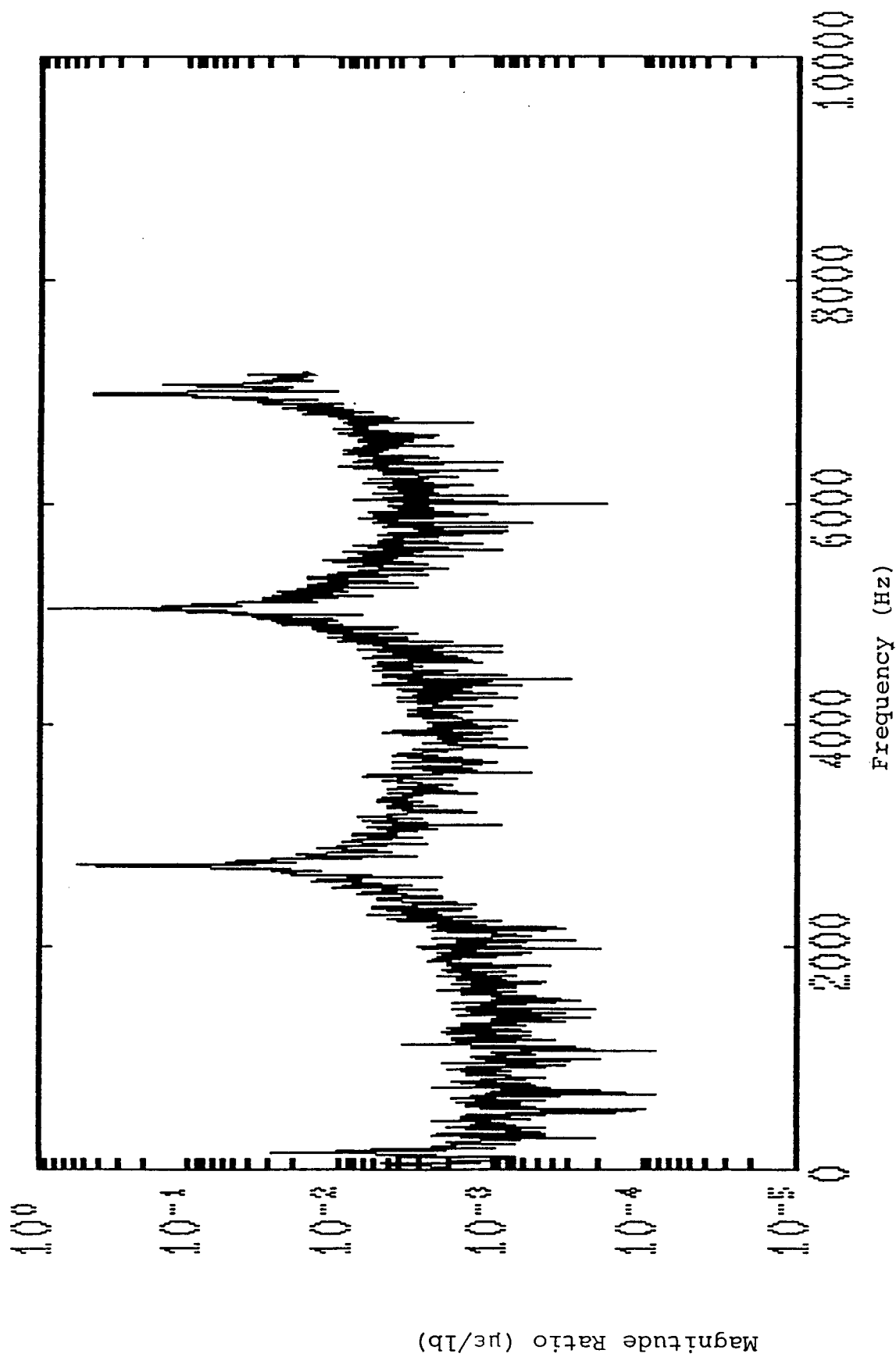
Figure 5: Structural Frequency Response Function for Penetrator Case with a 100 klb, 100 μs, Point Forcing Function at Measurement Point 7 in. from Rear, Interior (6 Hz Frequency Resolution).
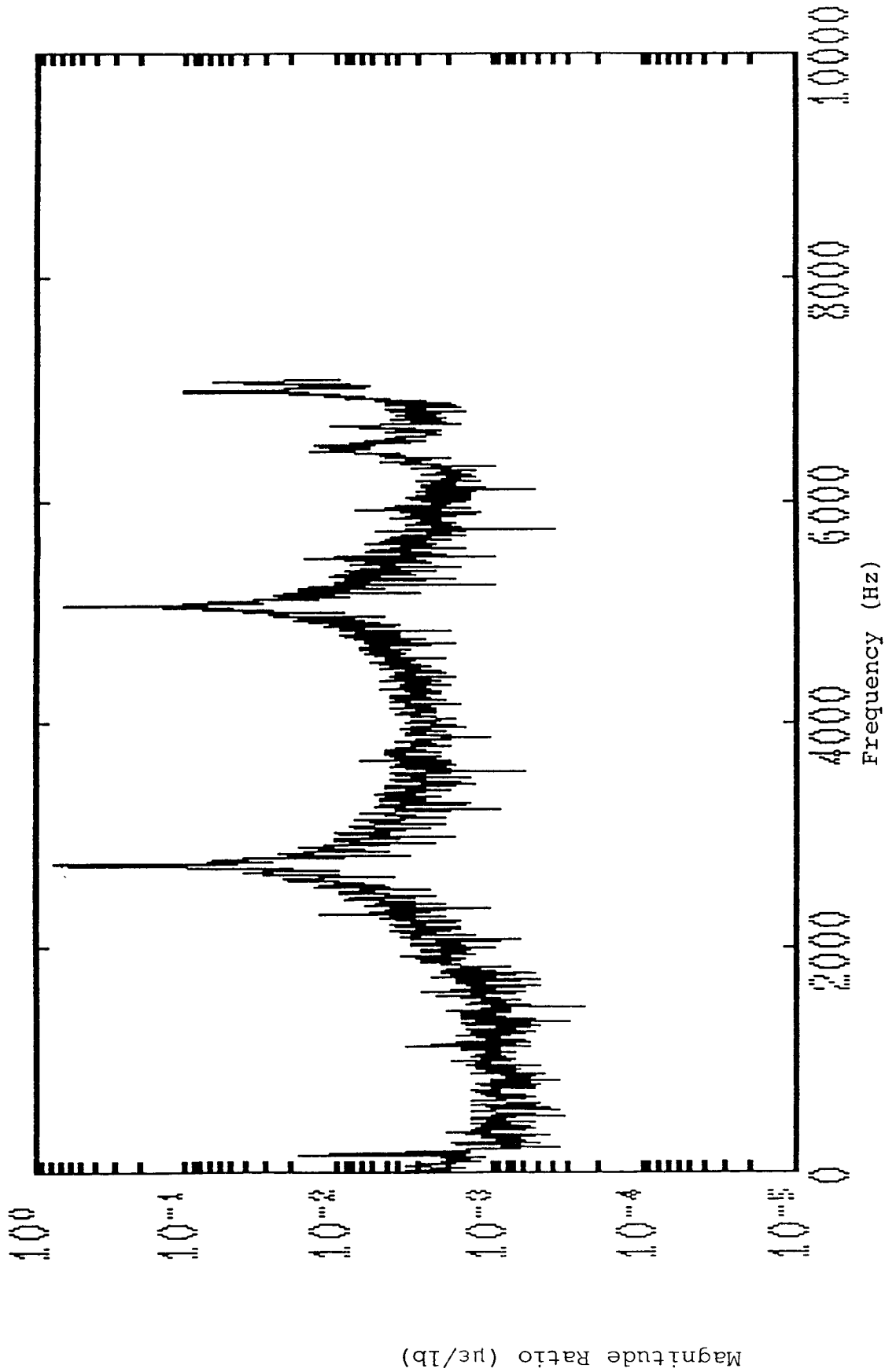
Figure 6: Structural Frequency Response Function for Penetrator Case with a 100 klb, 100 μs, Point Forcing Function at Measurement Point 14 in. from Rear, Interior (6 Hz Frequency Resolution).

ORIGINAL PAGE IS
OF POOR QUALITY

Magnitude Ratio ($\mu\varepsilon$/lb)
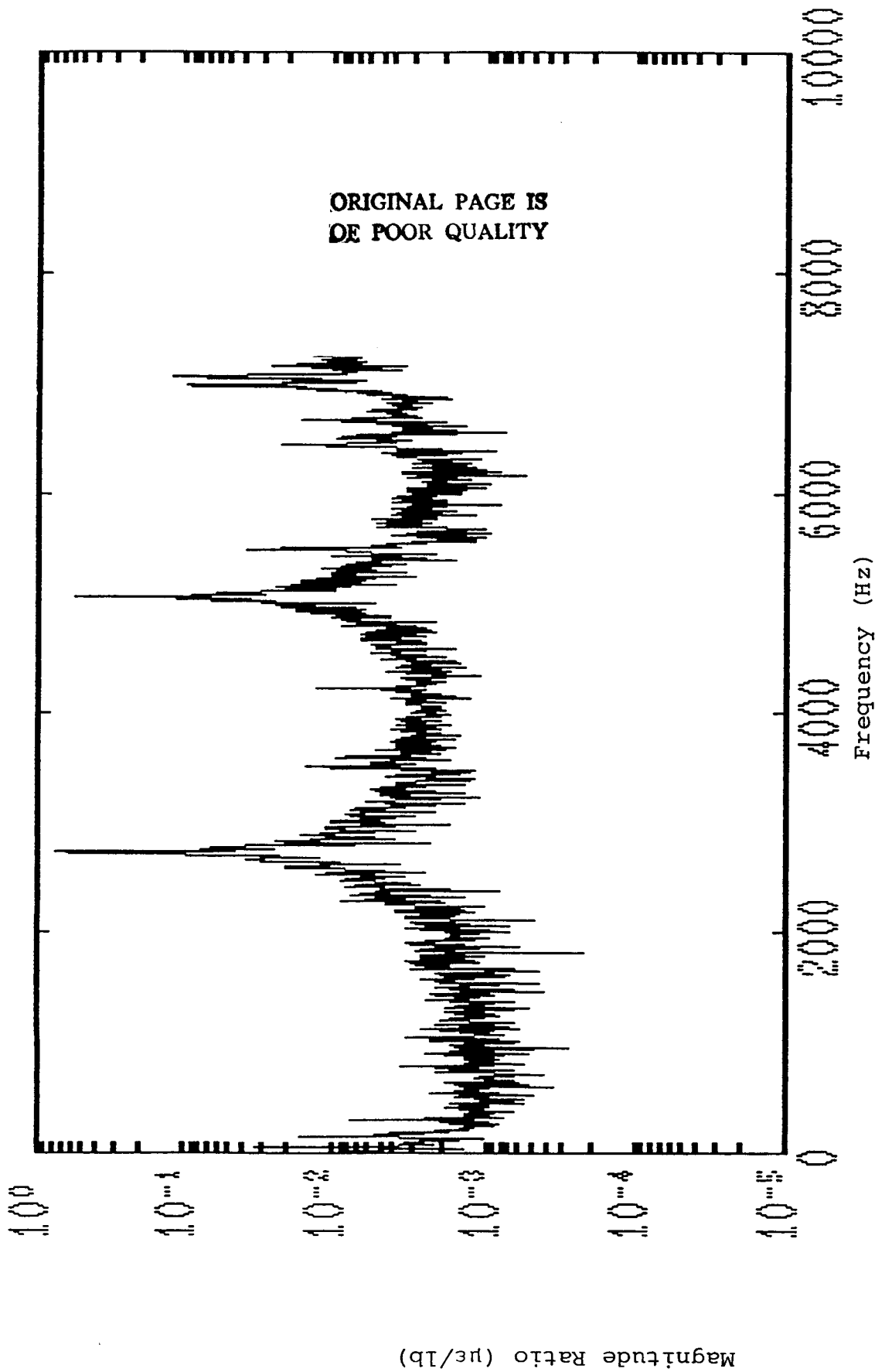
Frequency (Hz)

Figure 7:   Structural Frequency Response Function for
Penetrator Case with a 100 klb, 100 μs, Point
Forcing Function at Measurement Point 14 in.
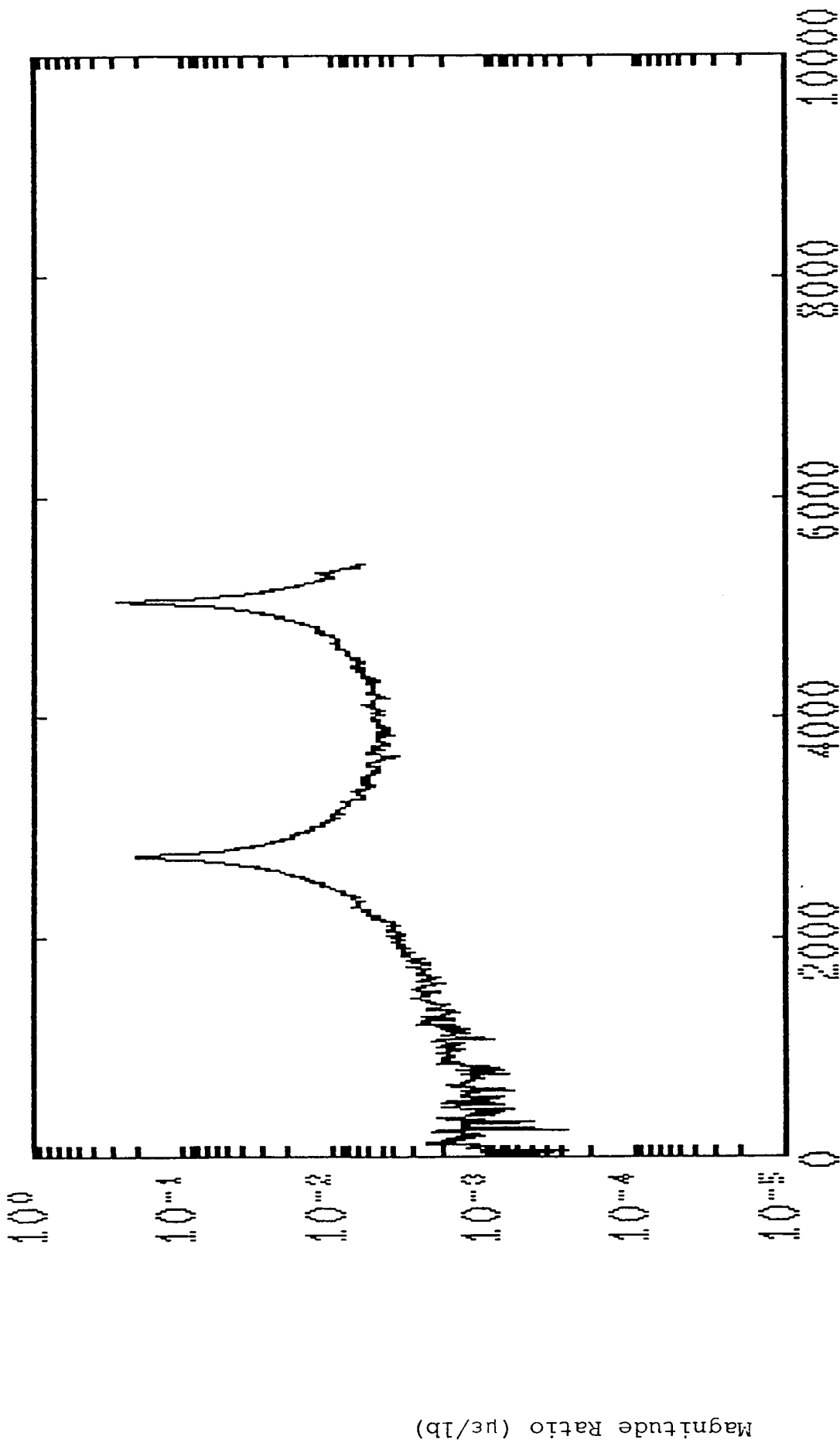from Rear, Exterior (6 Hz Frequency Resolution).

301
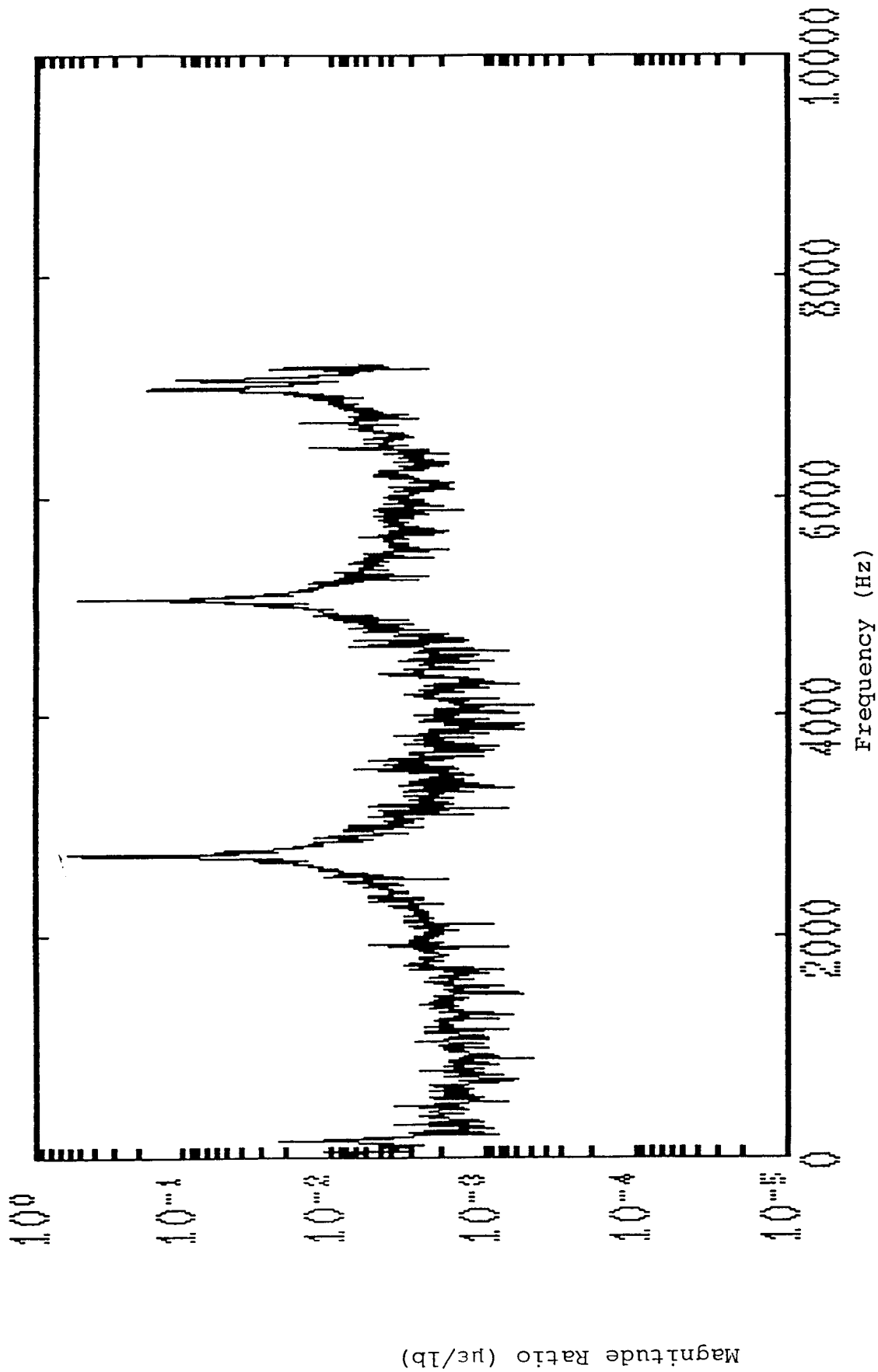
Figure 8:   Structural Frequency Response Function for
Penetrator Case with a 100 klb, 100 μs, Point
Forcing Function at Measurement Point 24 in.
from Rear, Exterior (6Hz Frequency Resolution).

302

A HIGH-LEVEL, DISTRIBUTED FORCING FUNCTION TEST

An impulsive, distributed forcing function was generated by three different explosive configurations. The three impulsive, distributed loads were designed to have approximately the same axial impulse of 20 lb-sec and a pulse duration of 20 μs or less. The pulse duration was chosen so that the frequency content in the forcing function would be essentially constant over the bandwidth of interest, 10 kHz. This unique forcing function simulates an ideal mechanical impulse at force levels which approximate the field conditions. The characteristics of the three distributed forcing functions are summarized in Table 1.

TABLE 1: CHARACTERISTICS OF THREE DISTRIBUTED,
IMPULSIVE FORCING FUNCTIONS.

Deta Sheet Layers	Distance along Penetrator Axis (in)*	Ogival Area Covered	Spectrum Decrease-10kHz
2	4.39	48.4 %	7 %
3	3.09	30.5 %	4 %
4	2.40	23.1 %	3 %

* The penetrator nose is solid for 3.20 in along its longitudinal axis.

Since the area of the explosive was limited by the restriction that the pulse duration be less than 20 μs, only one of the three distributed forces covered enough area to include a hollow portion of the penetrator case. Figure 9 is a typical time history of the strain gage response to a distributed forcing function. The 32768 sample points have been decimated to 1024 points for Figure 9 because the plotting device is restricted to 1024 points. However, the time history does show the general envelope of the structural response typically measured from the explosive forcing function. The large number of sample points (32768) was necessary in order to obtain a reasonable frequency resolution (15 Hz) with the sample period of 2 μs for the structural response.

In order to calculate a FRF for the explosive forcing function, three spectra were calculated for the theoretical prediction of the explosive time histories in Mr. Cawlfield's paper. These spectra have essentially constant magnitude for frequencies up to 10 kHz as shown by the values for percent magnitude decrease in Table 1; on the basis of the spectra, the distributed forcing functions may be considered mechanical impulses. The constant magnitude of the spectra means that all the structural frequencies were equally excited in the 10 kHz bandwidth which
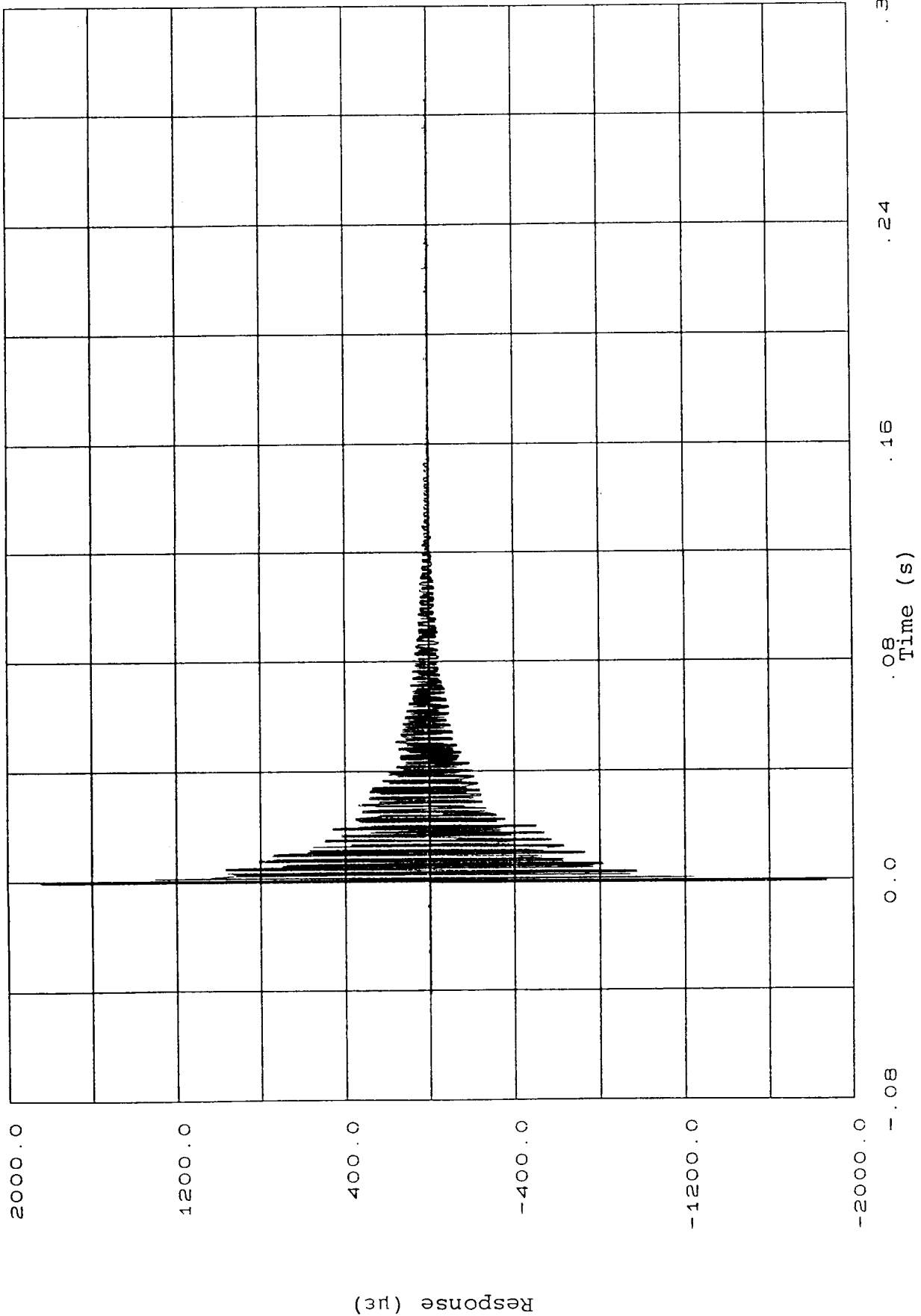
Figure 9: Strain Gage Response for Penetrator Case with a Distributed (30.5% of Ogival Area) Forcing Function (32768 Sample Points Decimated to 1024 Points).

was the motivation for restricting the explosive pulse duration to 20 μs. The spectra for the explosive forcing functions were interpolated so that the FRF's could be calculated.

The results of the FRF calculations for the distributed forcing function are shown in Figures 10-21. A FRF for each distributed force is presented for the four strain gage locations. The figures are grouped according to strain gage location so that the first three figures are for the location 7 in from the rear, interior. The FRFs for the other locations follow. All the FRFs were calculated for 10 kHz and show the same order of magnitude. The three axial modes present in the high-level, point force test are evident in all the FRFs; their frequencies agree with those of the other tests to within the frequency resolution of 15 Hz. The magnitude of the mode peaks varies according to location as expected. Additionally, there are some higher order modes between 8 and 10 kHz which have not been uniquely identified. The frequencies in the 8-10 kHz range are not noise because their amplitude is a decade above the noise floor which is less than 0.001 $\mu\epsilon$/lb and are consistently present in all the FRFs. These modes represent case motion in which all four strain gages at a location move together. This indicates that the modes may be either higher order axial modes or "breathing" modes of the penetrator case.
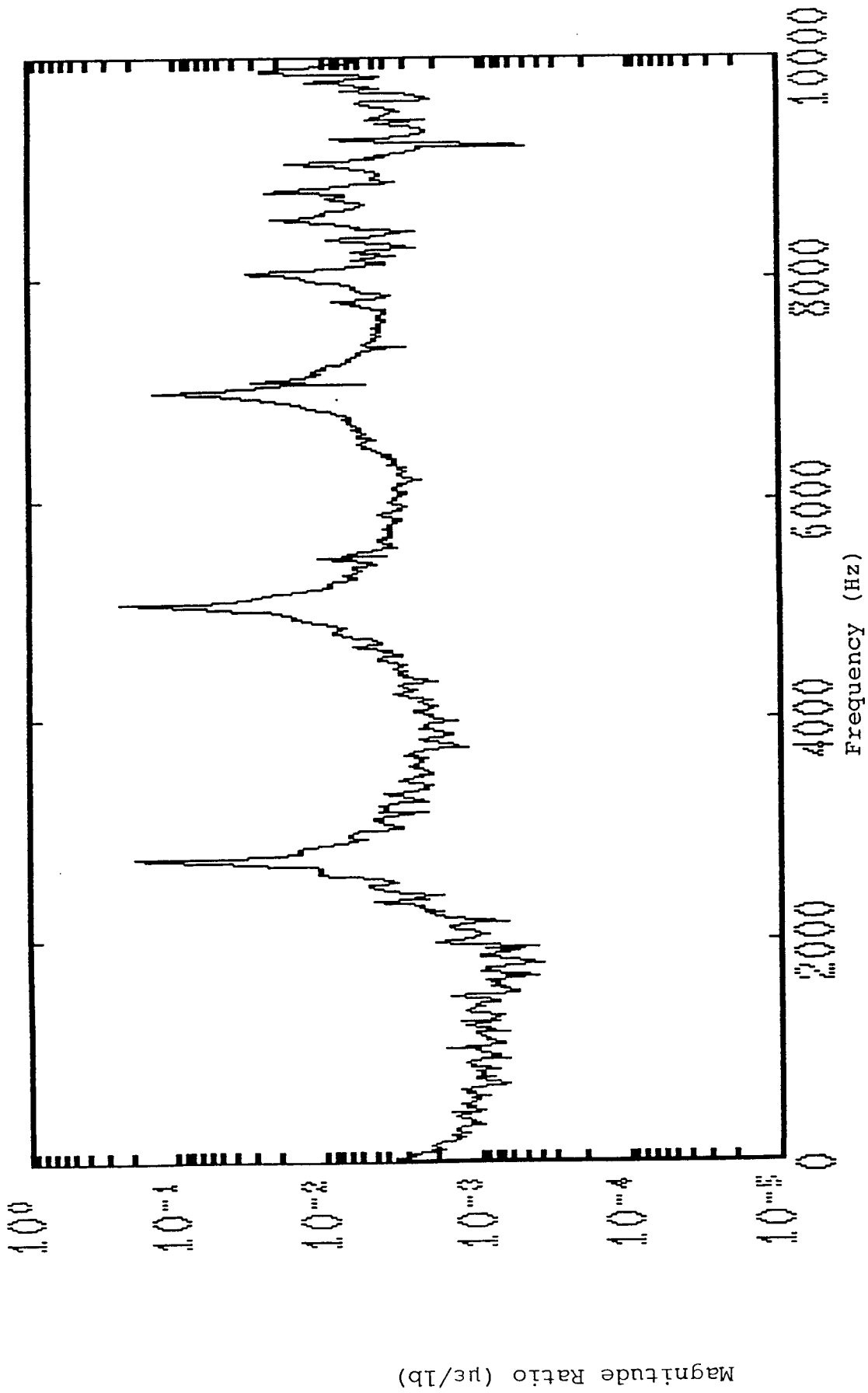
Figure 10: Structural Frequency Response Function for Penetrator Case with a Distributed (23.1% of Ogival Area) Forcing Function at Measurement Point 7 in. from Rear, Interior (15 Hz Frequency Resolution).
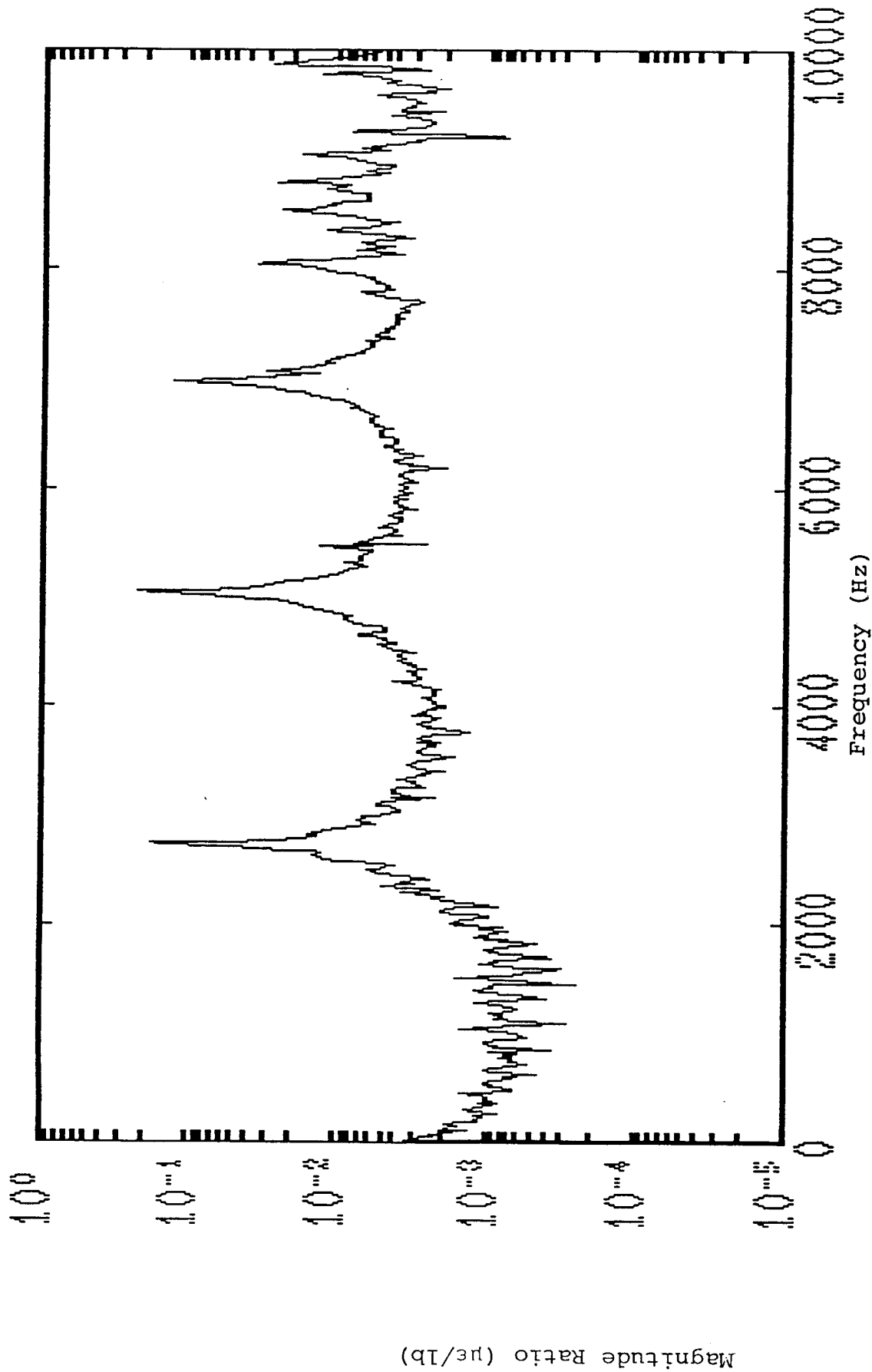
Figure 11: Structural Frequency Response Function for Penetrator Case with a Distributed (30.5% of Ogival Area) Forcing Function at Measurement Point 7 in. from Rear, Interior (15 Hz Frequency Resolution).
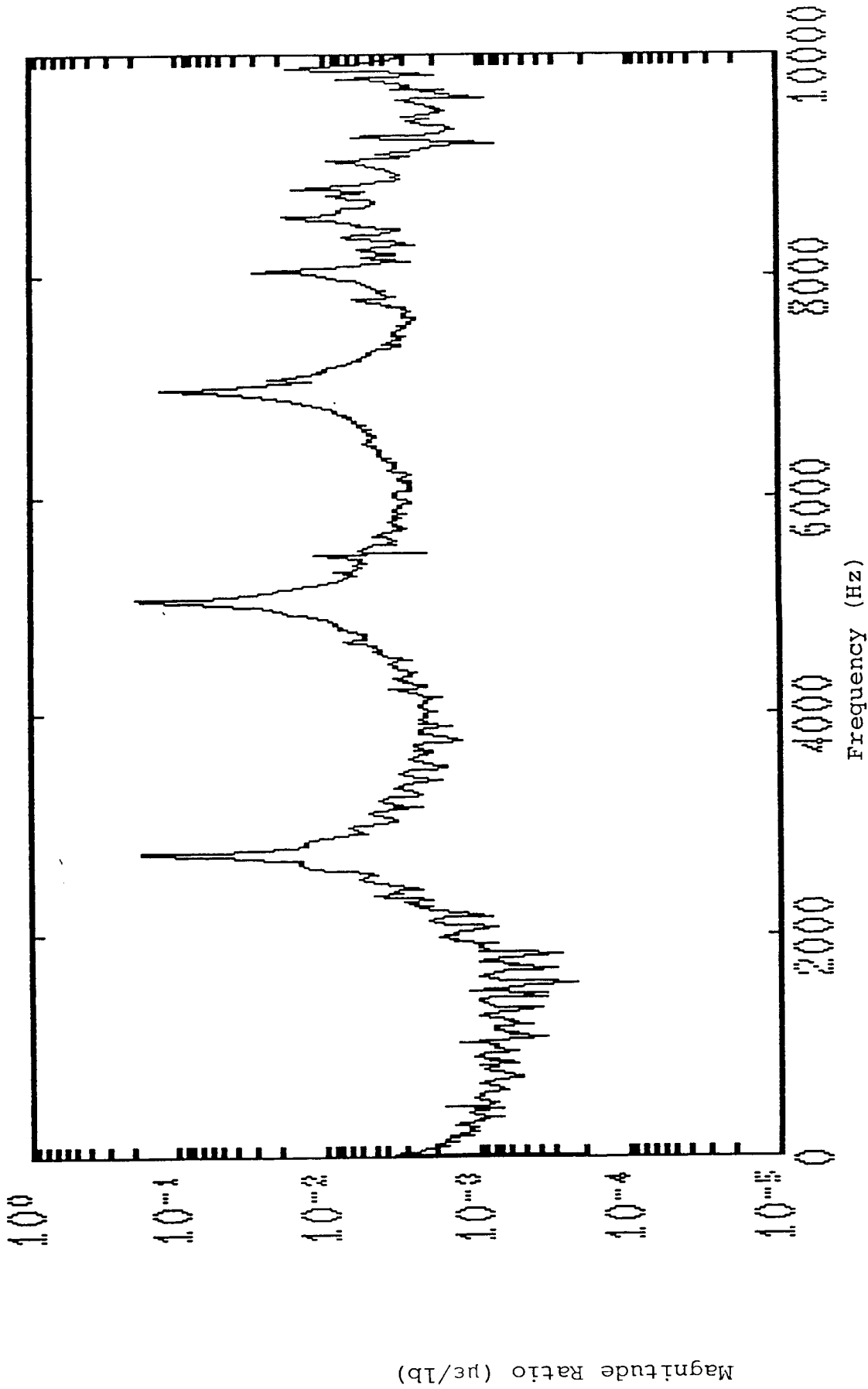
Figure 12:   Structural Frequency Response Function for
Penetrator Case with a Distributed (48.4%
of Ogival Area) Forcing Function at Measurement
Point 7 in. from Rear, Interior (15 Hz Frequency
Resolution).

308
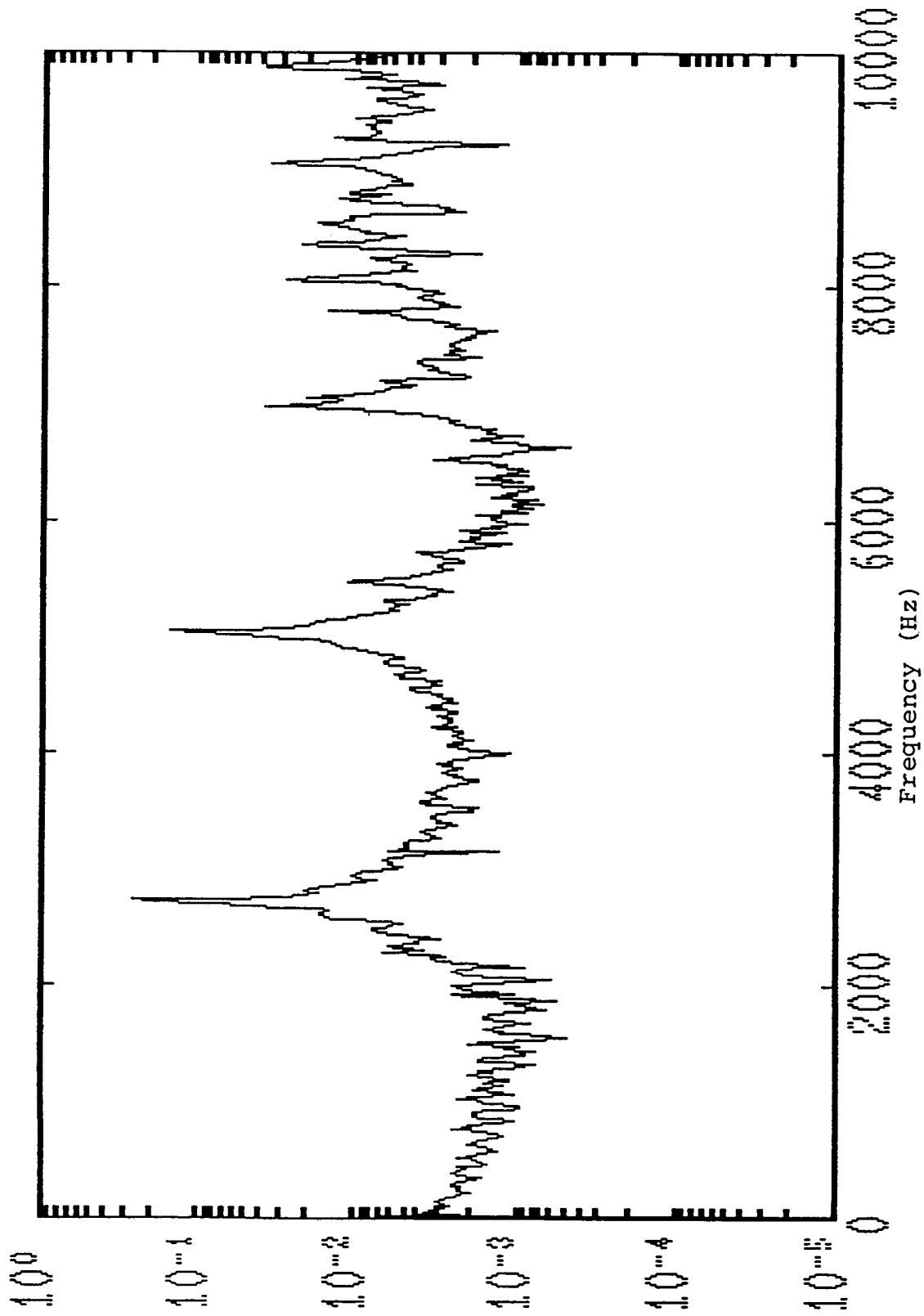
Figure 13: Structural Frequency Response Function for Penetrator Case with a Distributed (23.1% of Ogival Area) Forcing Function at Measurement Point 14 in. from Rear, Interior (15 Hz Frequency Resolution).

Frequency (Hz)

Magnitude Ratio (μέ/lb)
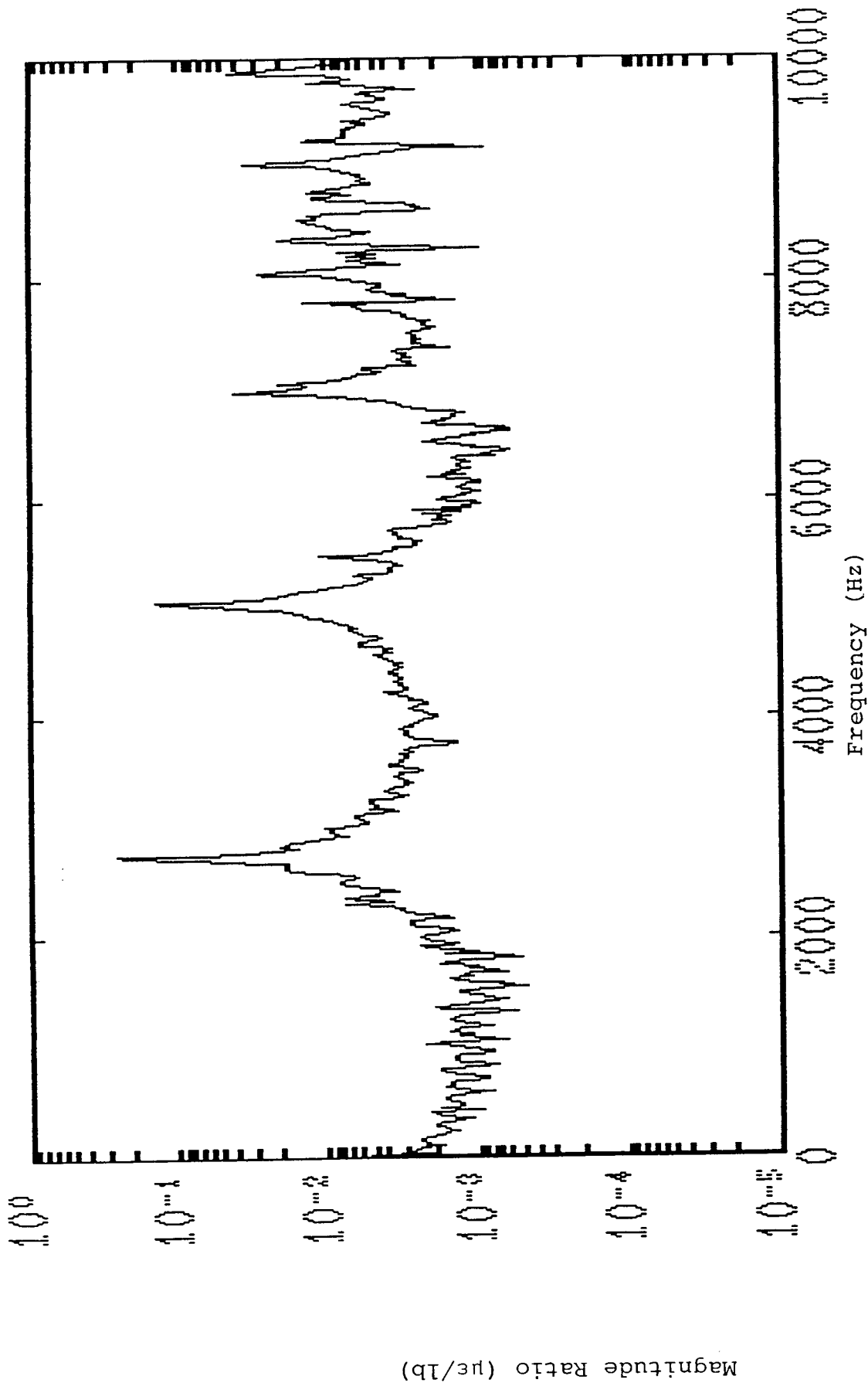
Figure 14: Structural Frequency Response Function for Penetrator Case with a Distributed (30.5% of Ogival Area) Forcing Function at Measurement Point 14 in. from Rear, Interior (15 Hz Frequency Resolution).
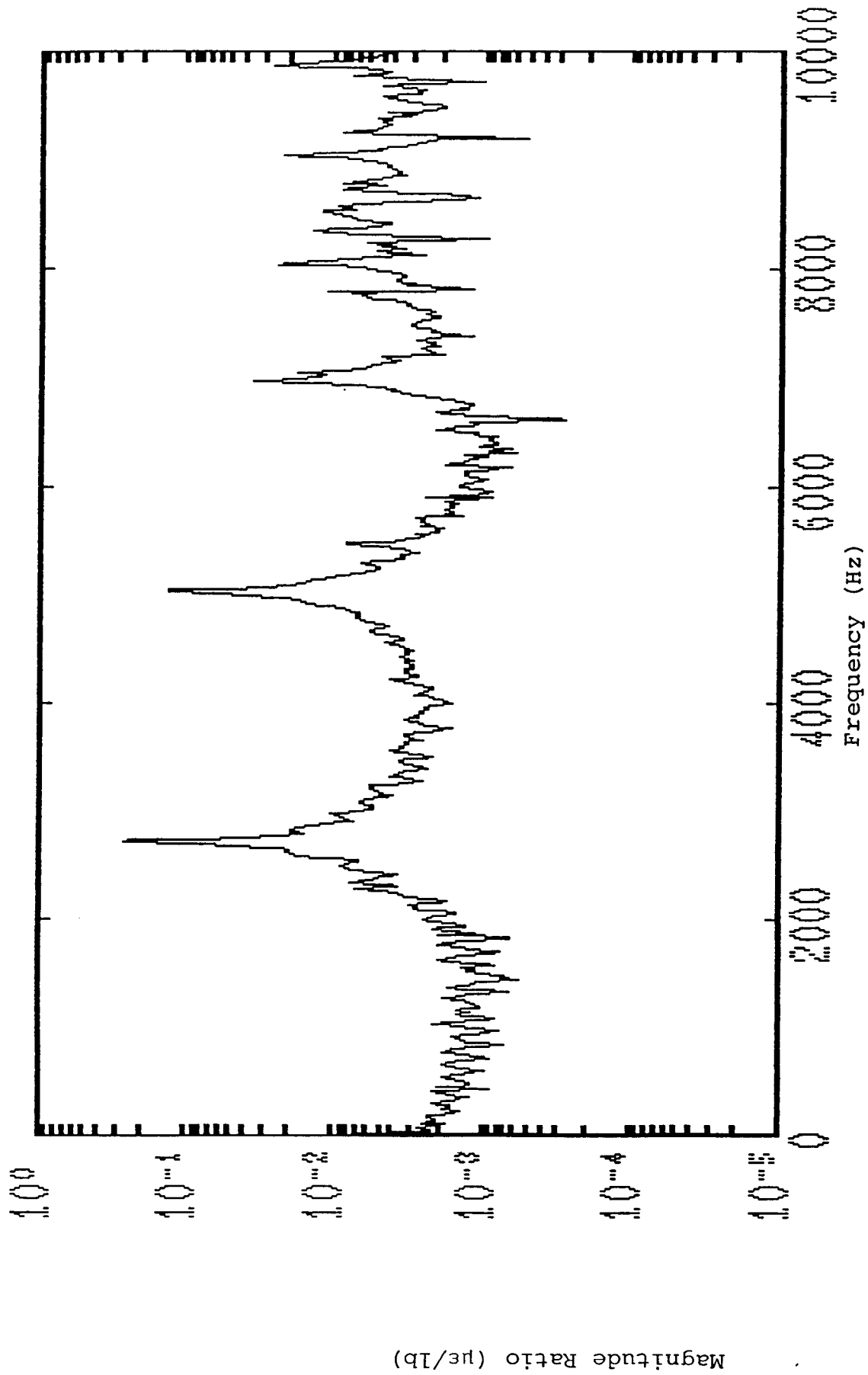
Figure 15: Structural Frequency Response Function for Penetrator Case with a Distributed (48.4% of Ogival Area) Forcing Function at Measurement Point 14 in. from Rear, Interior (15 Hz Frequency Resolution).

311
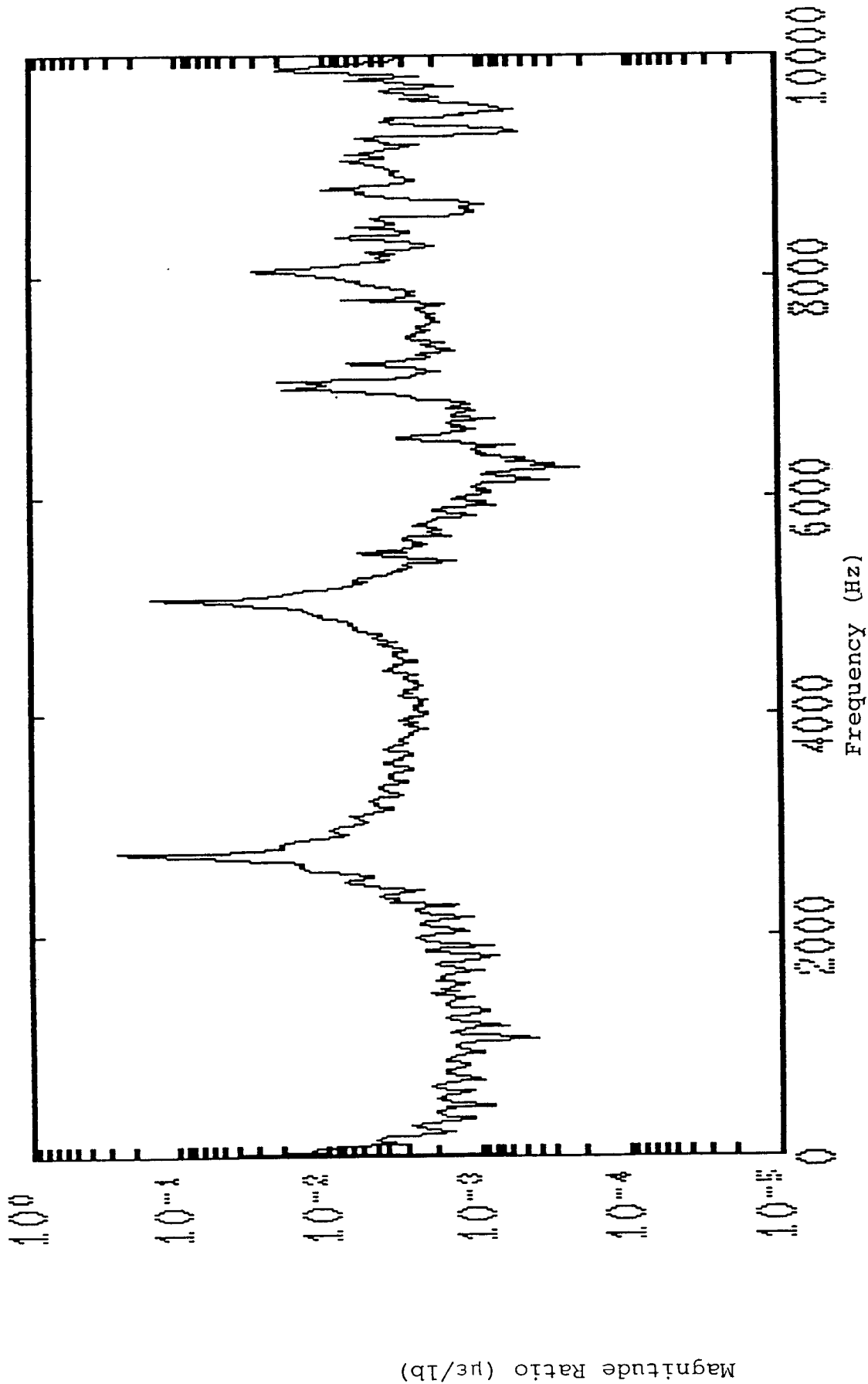
Figure 16: Structural Frequency Response Function for Penetrator Case with a Distributed (23.1% of Ogival Area) Forcing Function at Measurement Point 14 in. from Rear, Exterior (15 Hz Frequency Resolution).
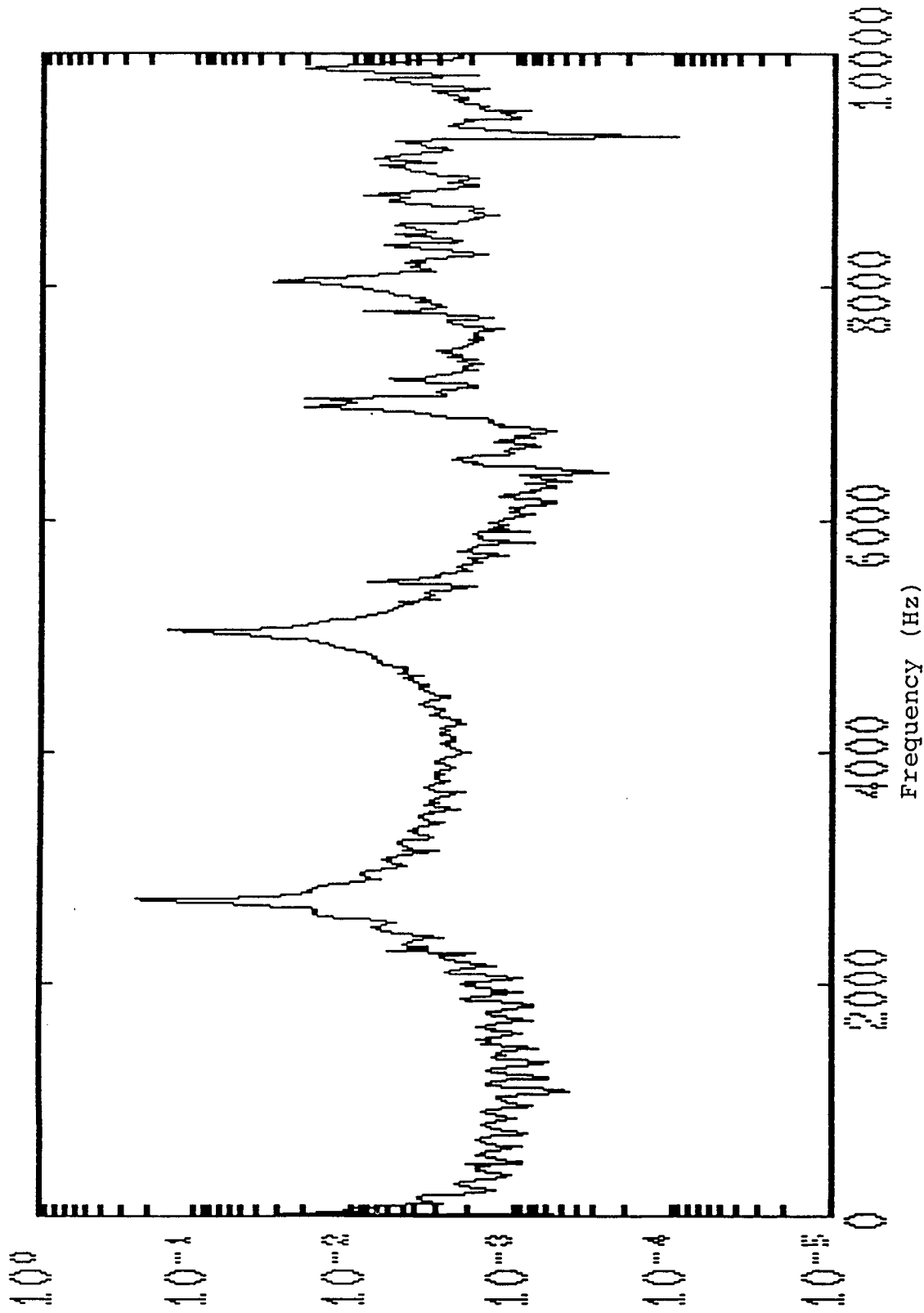
Figure 17: Structural Frequency Response Function for
Penetrator Case with a Distributed (30.5%
of Ogival Area) Forcing Function at Measurement
Point 14 in. from Rear, Exterior (15 Hz Frequency
Resolution).

313
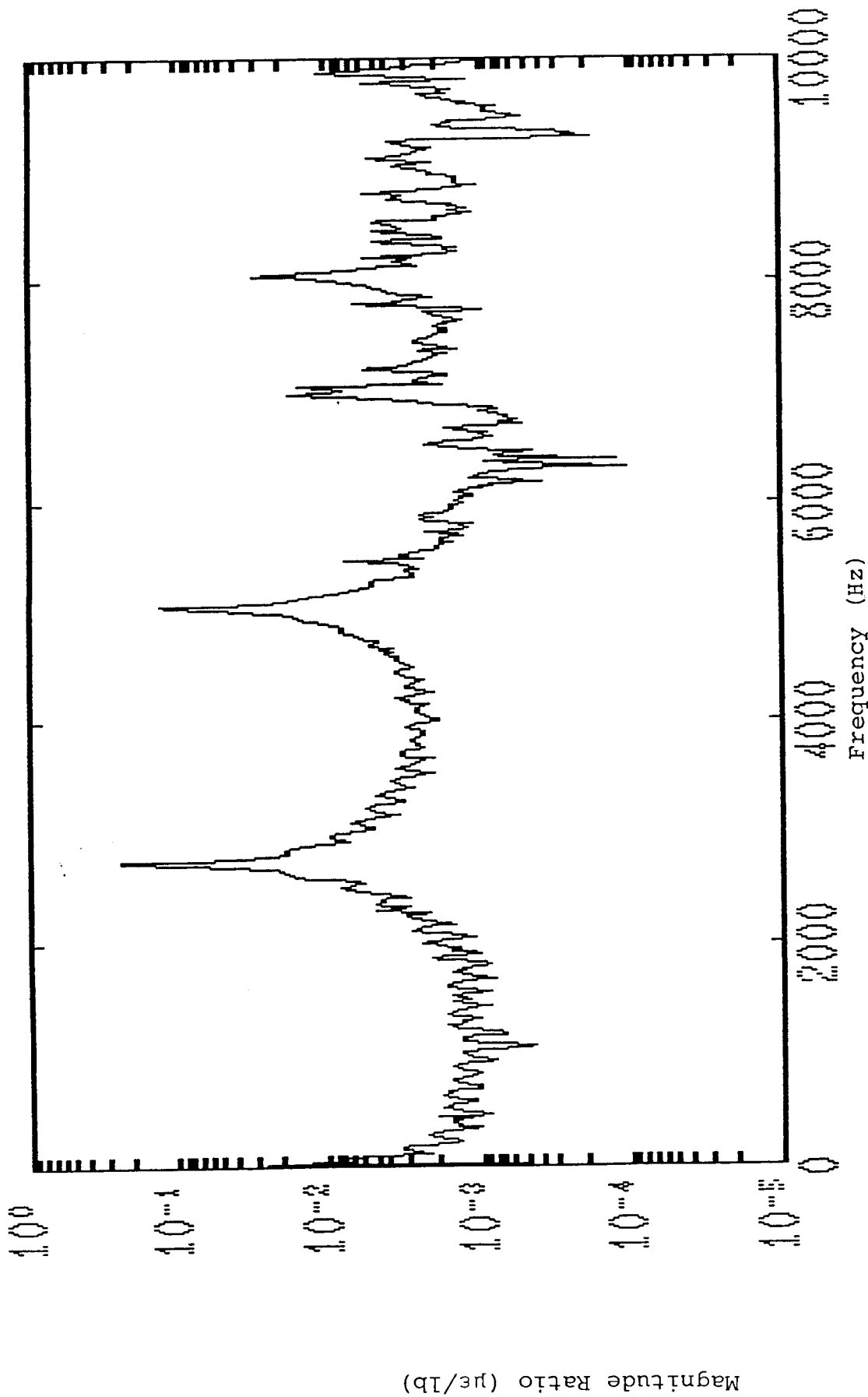
Figure 18: Structural Frequency Response Function for Penetrator Case with a Distributed (48.4% of Ogival Area) Forcing Function at Measurement Point 14 in. from Rear, Exterior (15 Hz Frequency Resolution).

Frequency (Hz)

Magnitude Ratio (με/1b)

314
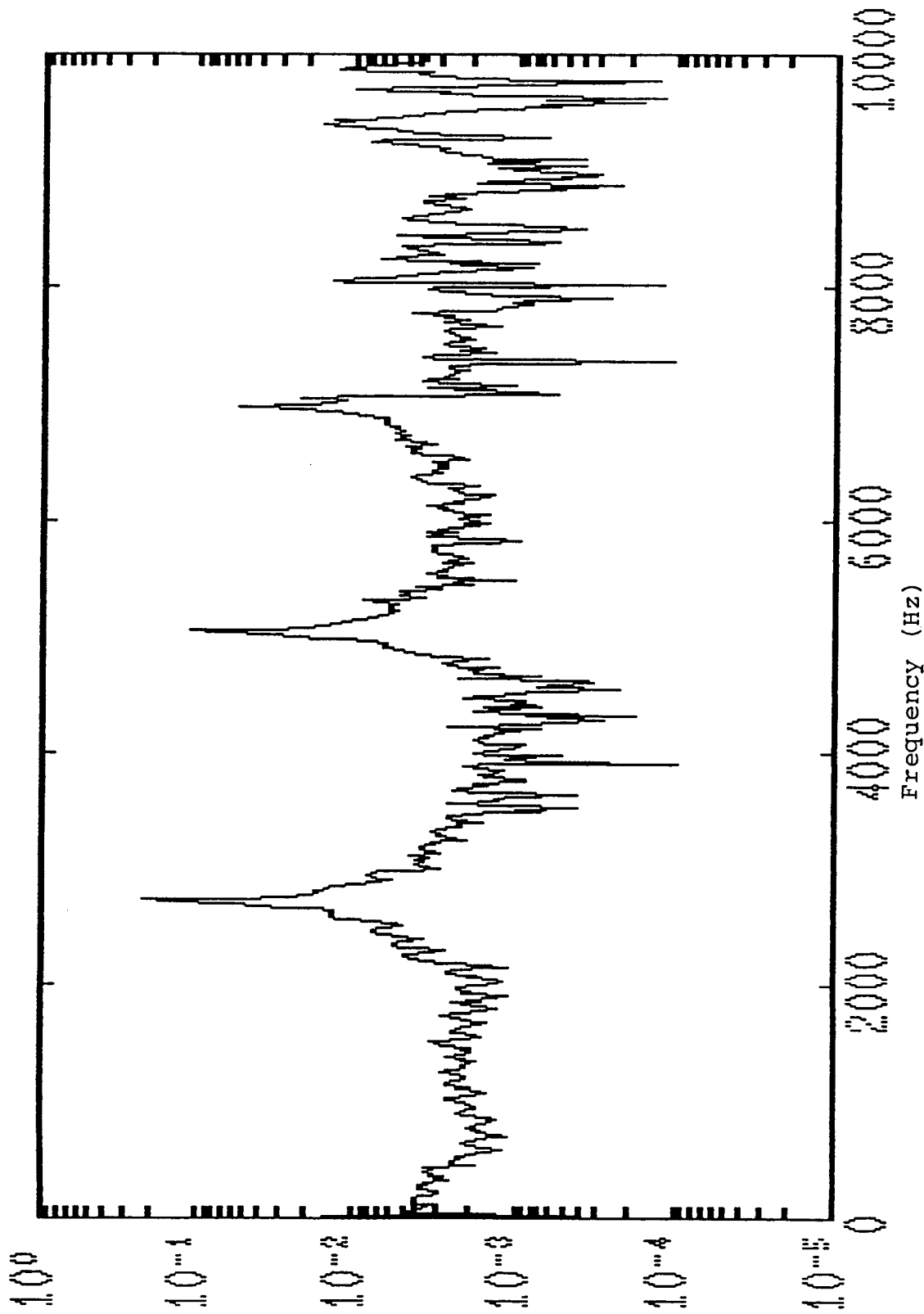
Figure 19: Structural Frequency Response Function for Penetrator Case with a Distributed (23.1% of Ogival Area) Forcing Function at Measurement Point 24 in. from Rear, Exterior (15 Hz Frequency Resolution).

315
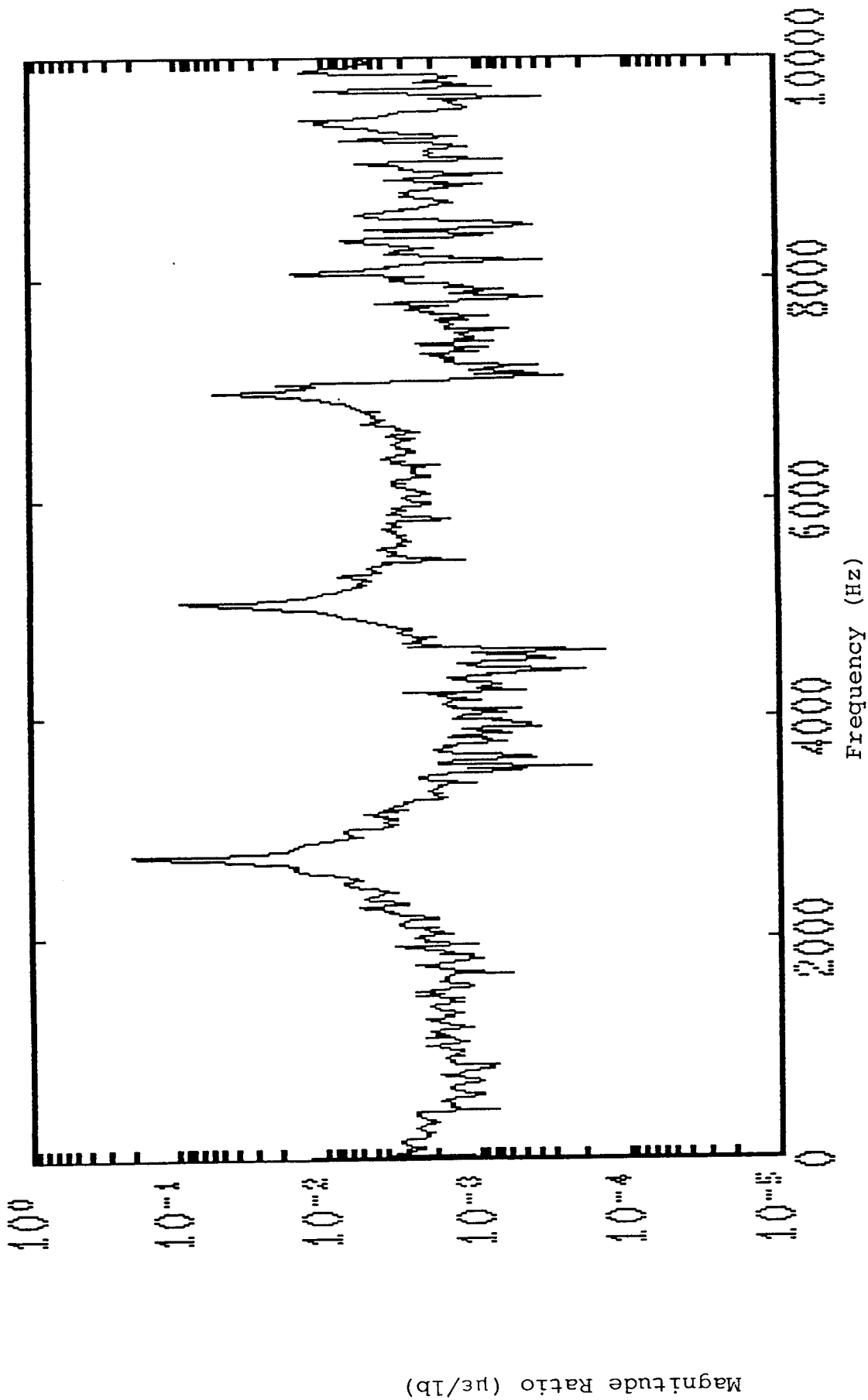
Figure 20: Structural Frequency Response Function for Penetrator Case with a Distributed (30.5% of Ogival Area) Forcing Function at Measurement Point 24 in. from Rear, Exterior (15 Hz Frequency Resolution).
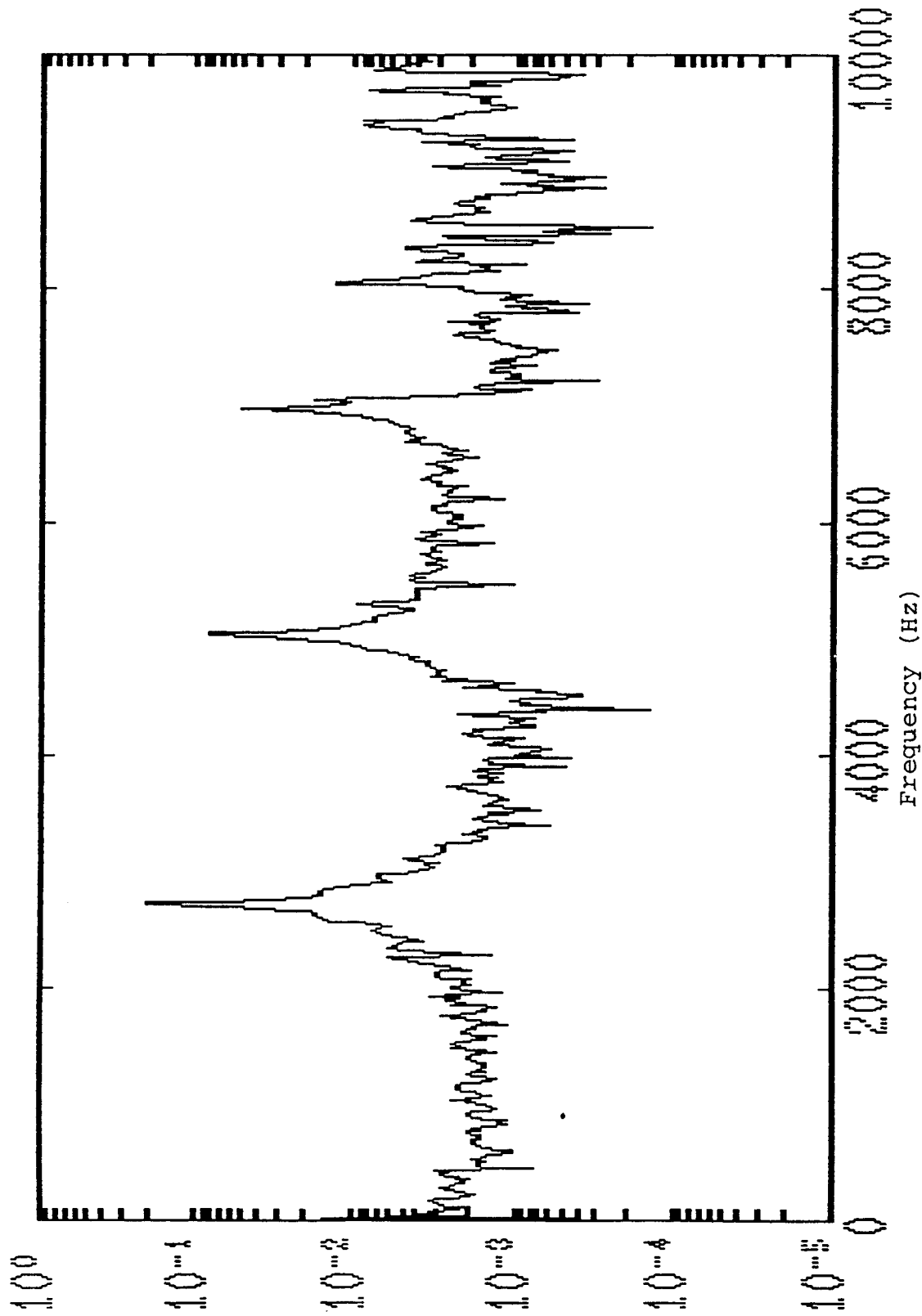
Figure 21: Structural Frequency Response Function for Penetrator Case with a Distributed (48.4% of Ogival Area) Forcing Function at Measurement Point 24 in. from Rear, Exterior (15 Hz Frequency Resolution).

CONCLUSIONS

A series of tests have been conducted to characterize the response of a penetrator case to axial forces. All three goals established prior to the tests have been accomplished. The FRFs for the penetrator case were calculated from responses at the four axial locations for three axial forcing functions. Good structural response measurements were obtained as demonstrated by the consistent structural characteristics in the FRFs. A spatially distributed load was successfully implemented with Deta Sheet in three configurations.

The parameters of the three forcing functions used to characterize the structural response of the penetrator case are summarized in Table 2. The frequency

TABLE 2: THREE AXIAL FORCING FUNCTIONS APPLIED
TO A PENETRATOR CASE.

Type	Force Level (lb)	Duration (μs)	Frequency Resolution	Impulse (lb-sec)
Instrumented Hammer	1.9 k	300	4 Hz	0.6
Reverse Hopkinson Bar	100 k	100	6 Hz	10
Distributed Impulsive	1-2 M	20	15 Hz	20

response functions for these forcing functions have been presented and show repeatable characteristics of magnitude and frequency content. The penetrator case exhibited linear behavior over the wide range of force magnitudes applied in this test series. The forcing functions included a mechanical impulse whose magnitude of 1-2 Mlb is the same order of magnitude force that the penetrator experiences in the field.

The structural response depicted in the FRFs indicates that the strain gages respond similarly to a point axial load and to a distributed axial load. There was no detectable difference in the shape or frequency of the first three axial modes of the penetrator case when they were excited by a 100 klb, point forcing function and by a 1 Mlb, distributed forcing function. This result suggests that the distributed axial force generated in a penetration event may be reconstructed as a point axial force when the penetrator behaves in a linear manner.

FUTURE WORK

The tests described in this paper will be used to characterize the lateral response of the penetrator case and the combined axial and lateral response of the penetrator unit with the internal components. The FRFs which result from these tests will indicate the linearity of the structure to lateral loads and to combined axial and lateral loads. The FRFs will also be used with field test response measurements to resolve the applied forces into point or distributed loads by various force reconstruction techniques.

ACKNOWLEDGEMENTS

REFERENCE

1. V. I. Bateman and P. L. Walter, "Instrumentation for the Measurement of Dynamic Response of Structural Systems," SAND87-0673, August 1987.

2. R. A. May, "Strain Gaging Earth Penetrators to Provide Dynamic Force Data," Proceedings of the 1987 SEM Spring Conference on Experimental Mechanics, Houston, Texas, June 14-19, 1987, pp. 108-113.

3. J. S. Bendat and A. G. Piersol, Random Data: Analysis and Measurement Procedures, Wiley Interscience, 1971, pp. 136-142.

4. W. K. Bell and N. T. Davie, "Reverse Hopkinson Bar Testing," Proceedings of the 33rd Annual Technical Meeting, Institute of Environmental Sciences, San Jose, CA, 4-8 May 1987.

5. V. I. Bateman, "A Comparison of Structural Frequency Response Functions Measured with Forces from 500 to 250,000 lb," SAND87-0632, August 1987.

SPACE SHUTTLE MAIN ENGINE VIBRATION

Fluid Mass and Thermal Loading Effects on the Modal Characteristics of Space Shuttle Main Engine Liquid Oxygen Inlet Splitter Vanes

H. V. Panossian

J. J. Boehnlein

Presented herein is an analysis and evaluation of experimental modal survey test data on the variations of modal characteristics induced by pressure and thermal loading effects. Extensive modal survey tests were carried out on a Space Shuttle Main Engine (SSME) test article using liquid nitrogen (LN_2) under cryogenic temperatures and high pressures. The results suggest that an increase of pressure under constant cryogenic temperature or a decrease of temperature under constant high pressure induces an upwards shift of frequencies of various modes of the structures.

INTRODUCTION

In many situations, structures that are surrounded by fluids display high amplitude resonant oscillations, especially when the fluid is in a dynamic flow condition. A known mechanism for this resonance is the periodic vortex shedding as the flow encounters the structure and separates into turbulent flow patterns. The vortices normally result in steady and unsteady drag forces parallel with the flow and unsteady lift forces perpendicular to the flow direction. When the internal damping of the structure is very low, resonant oscillations can be created that induce structure/wake unstable vibrations that take place in unison reinforcing each other at a frequency near one of the natural frequencies of the structure.

To evaluate such environmental effects, a test was designed using a Test Article that consisted of the Space Shuttle Main Engine (SSME) Liquid Oxygen (LOX) inlet line, inlet splitter vanes, and manifold welded to a forged base ring (Fig. 1 and 2). The inlet splitter vanes were instrumented with semiconductor strain gages and the leads were brought out through Conax fittings installed in an inlet adapter flange to a dummy Main Oxidizer Valve (MOV) connected to the LOX inlet line. External accelerometers were used on the inlet elbow to evaluate modal data on this component. Additionally, thermocouples were welded to the internal and external surface of the "tee" to allow monitoring of skin temperatures. This configuration allowed termination of the test item at boundaries considered to be realistic such that any measured response would be that expected to be seen in a complete engine. This hypothesis was evaluated by hanging test weights on the MOV inlet flange and evaluating response. These data comparisons are discussed later, but did show that the response changed.
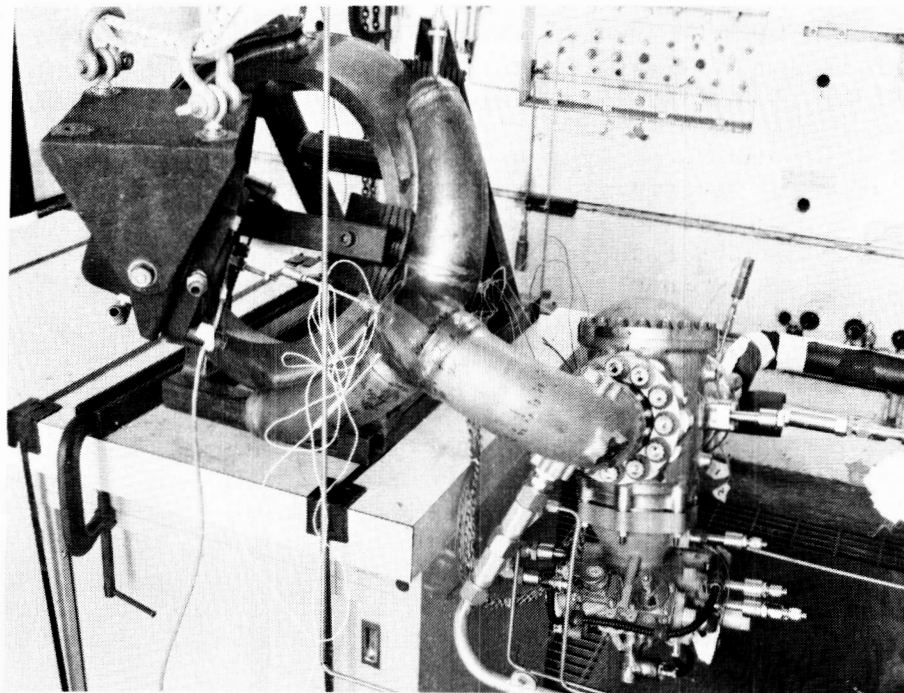
Fig. 1. Liquid Nitrogen Test Article

The results of these experiments that specifically addressed the issue of the effect of fluid pressure/mass and temperature variations on the frequencies of the SSME liquid oxygen inlet splitter vanes will be presented herein. The experiments consist of liquid nitrogen pressurization of the article from ambient to 4300 psi and under temperatures ranging from -40 to -240°F. Strain

324

gages located at various points on the splitter vanes recorded the strain levels under various pressure and temperature conditions (Fig. 2 and 3). Isoplots indicating vibration amplitudes versus frequency changes as a function of time will be presented and discussed. The influence of pressure variations under constant temperature and temperature variations under constant pressure on the natural frequency of modes between 3 to 5 kHz will be analyzed. Furthermore, a simple clamp was tightly attached to the LOX inlet elbow, near the splitter vane external edges, and its damping effect on the vane vibrations was analyzed through the strain gage data.
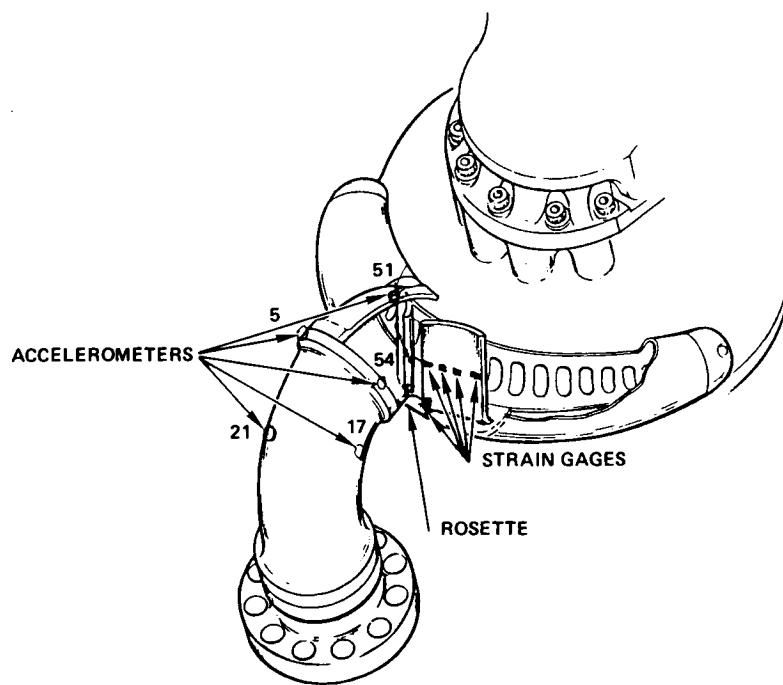
Fig. 2. SSME Main Injector LOX Inlet
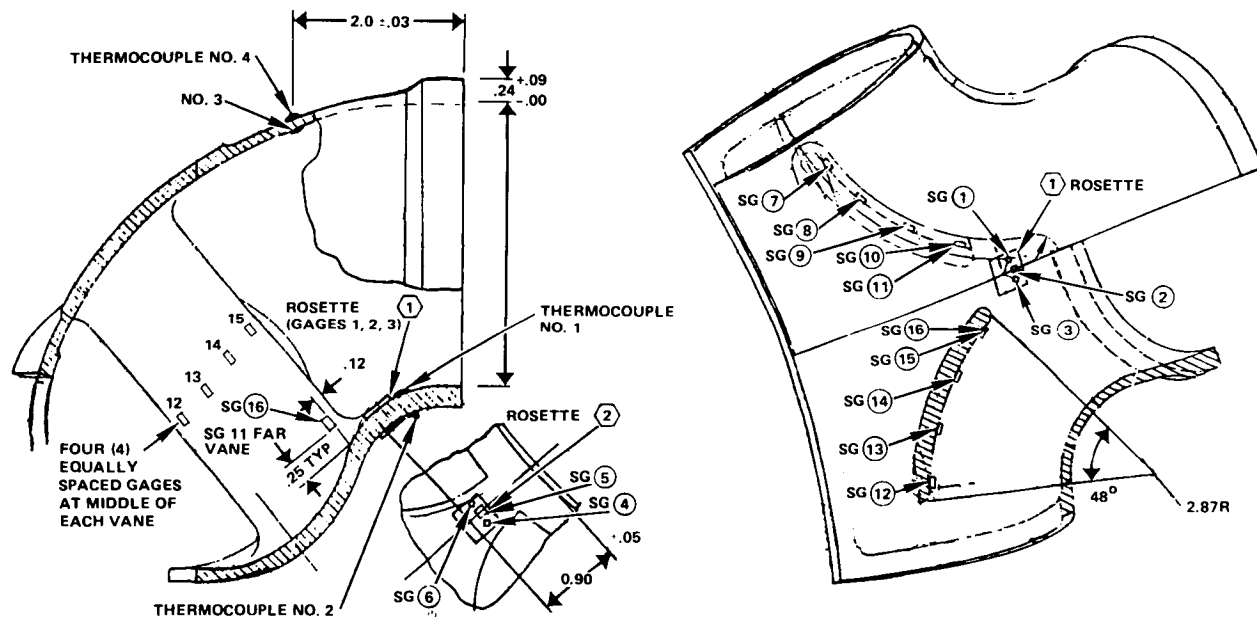
Fig. 3. Liquid Nitrogen Test Article Instrumentation Locations

The overall effect of increased pressure and/or decreased temperature was a shift of natural frequencies upwards--in some cases, significantly. Moreover, the presence of the clamp had the effect of damping out most of the vibrations of the splitter vanes and reducing their amplitudes appreciably. All indica-tions lead to the conclusion that there is a strong nonlinear behavior of the structure interacting with the fluid.

325

Vibration of structures in vacuum or air has been extensively studied. However, vibration of structures under the influence of a fluid medium has just recently raised the interest of researchers [1]. Whereas vibration of a metallic structure in air is virtually identical to that in vacuum, this is not the case with a structure that is in contact with a fluid. In the SSME, liquid oxygen enters the inlet tee (Fig. 2) at high velocity, high pressure, and cryogenic temperature, striking the splitter vanes and experiencing a division of main flow into the two sides of the tee into the injector. Thus, the splitter vanes are in the course of highly turbulent flow regimes. It is well known that in such severe environments, fluid/structure interaction can be potentially unstable and induce fluid-elastic instabilities [2].

The underlying objective of the present study program is to analyze the static effects of fluid pressure and thermal loadings on the splitter vane modal characteristics. Extensive experimental modal survey tests have been carried out at Rockwell International/Rocketdyne Division's Engineering Development Lab (EDL) regarding the static fluid mass, pressure, and thermal loading effects of various fluids under different temperature and pressure conditions on the modal characteristics of vibrating structures. The present article discusses the liquid nitrogen test results.

Theoretical Preliminaries

The liquid effect on natural frequencies of a structural vibration mode can be evaluated as the sum of fluid dynamic pressure distribution and the forces exerted by the structural surfaces. The elastic and acoustic problems are coupled by a feedback loop due to the influence of the radiation loading exerted by the fluid. This modifies the force that excites the structural vibrations, while the structural response changes, in turn, the radiation loading. This radiation loading sometimes takes the form of inertial forces and is comparable in magnitude to the inertia and elastic vibration forces in the structure [3].

The equation of motion for fluid/structure interaction problems can be derived from the Lagrangian [4]

$$L = (T_s + T_L) - (U + W) \tag{1}$$

where T_s is the kinetic energy of the structure, T_L is the kinetic energy of the fluid, U is the strain energy of the structure, and W is the potential energy of the applied loads. The potential function of an incompressible, nonviscous fluid must satisfy Laplace's equation

$$\nabla^2 \phi = 0 \tag{2}$$

where ∇^2 is the Laplacian operator, t is time, and ϕ is the potential function. The velocity vector of the fluid is given by

$$(\nu_x, \nu_\theta, \nu_r) = \left(-\frac{\partial \phi}{\partial x}, -\frac{1}{r}\frac{\partial \phi}{\partial \theta}, -\frac{\partial \phi}{\partial r} \right) \tag{3}$$

Under appropriate conditions, the velocity potential function can be approximated by

$$\phi = \phi(r) \sin(m\pi x/L) \cos n\theta \, e^{iwt} \qquad (4)$$

where w is the frequency, m is the number of axial half-waves, and n is the number of circumferential waves [3]. Under these assumptions and additional simplifications, it is possible to derive analytical approximation to the vane frequencies in the LOX inlet tee shell as a function of fluid pressure, temperature, and other structural parameters. Herein, we will not be concerned about the analytical developments. The interested reader can consult the references cited for details. The intent here is to present the experimental results and comment on their significance. The theoretical developments and predictions will be treated in a separate paper.

PROCEDURES AND APPROACH

The usual procedure of setting up and testing a structure was followed during the SSME Test Article modal survey experiments. The Test Article was appropriately isolated and measurements of strains and accelerations were taken. The strain and acceleration signals were processed through existing curve-fitting codes, and the results were then presented in various plots in the form of frequency response functions, power spectra, etc.

Instrumentation

Instruments utilized during the liquid nitrogen pressurization and low temperature tests consisted of:

1. A Genrad Micromodal Analyzer No. 2510 with appropriate signal conditioning devices, FM tape recorder, hybrid disk memory, and signal processor

2. A Goodman 5-lb high-frequency (300 to 5000 Hz) shaker with an appropriate connective quill (stinger) for steady-state, flat-random inputs, signal-input amplifiers, and filters (LP, BP, HP)

3. Twelve strain gages placed on four equidistant locations on the midspan of each vane, two at the bottom leading edge of each vane, in addition, two three-directional rosettes were placed externally on the top and bottom of the duct tee on the shell at the vane/shell interface (the strain gages were from Micromeasurements with model Numbers WK-062 RB)

4. Six 2E-3 piezoelectric accelerometers (Unholtz-Dickie) with charge amplifiers and signal conditioners) were placed on the elbow and the duct shell externally at locations 5, 17, 21, 51, and 54, respectively (Fig. 2, and 3)

5. Thermocouples

6. Pressure gages

7. Load cell

8. Miscellaneous filters, amplifiers, and other related equipment

Software

Several software routines were utilized during the modal survey tests. MODAL-PLUS by Structural Dynamics Research Corporation (SDRC) is a modal

analysis package that furnishes modal displacements, frequencies, and damping ratios, as well as other relevant data. Rocketdyne's EDL has Versions 7 and 9.2. The latter version is on the VAX computer system and has the advantage of speed and performance over Version 7.

Data acquisition software available at EDL consists of (1) Interactive Signal Analysis Package (ISAP) produced by Genrad, Inc., and DATUM put out by SDRC. The first program is useful in spectral analysis, cross- and auto-correlation, averaging time histories, as well as in generating transfer functions. Its resolution level involves 4096 lines/frame, which translates into 1600 frequency lines.

Data Reduction

The principal task that an analyzer performs is essentially _estimating_ the Fourier transform or the spectral densities of signals in the time domain that are supplied as inputs. The process involves expressing a periodic time function as an infinite sum of sinusoidal functions with discrete frequencies. In each case, the inputs are digitized (by an A-D converter) and recorded as a collection of discrete values evenly spaced in the measurement period T.

There are a number of concerns that the engineer has to properly deal with in every modal survey test data reduction process. These are, in general, related to discretization approximation, and the fact that time histories are not infinite. Some of the abovementioned problems are referred to as aliasing (whereby high frequency signals are misinterpreted as low frequency signals due to insufficient sampling rate), leakage (whereby a single frequency signal might be interpreted as a multiple frequency, one due to finite length of time history), and zoom (whereby only a certain frequency range is analyzed, which can cause aliasing and other problems). The engineer has to make sure that these problems are avoided or minimized and a good coherence level is obtained during the modal survey tests.

One additional problem that is encountered during modal survey testing is the random nature of vibration signals and, consequently, estimation of approximate spectral densities and correlation functions. Generally, it is very important that averaging be performed on several individual time histories, or samples, before a result with a high confidence level is obtained.

All of the abovementioned considerations have been undertaken in the SSME liquid nitrogen tests.

Test Procedure

A high frequency shaker was utilized to excite the structure throughout the duration of the modal tests. Flat-random input loads on the LOX inlet tee generated transfer functions relating the ratio of the response output (from the strain gages on the vanes) over the input force (from the shaker) versus the frequency range of interest (in this case, 3000 to 6000 Hz). These curves were plotted on a log-linear scale and the resonant peaks were indicative of the dominant strain modes. In a similar manner, variation (in time) of the Frequency Response Functions (frf) were plotted consecutively as the liquid nitrogen pressure was slowly increased to 4300 psi and the temperature was ramped down to -240°F. These so called "isoplots" gave a relatively clear indication of the frequency shifts of various strain modes as the test conditions were varied.

The Test Article was appropriately supported on soft material to simulate a "free" condition while the exciter was suspended and acted on the Test Article via a quill and a load cell attached to the end of the stinger. Strain gage and accelerometer data were recorded under three different test conditions and two different excitation point locations. Namely: (1) baseline, (2) with a clamp tied onto the elbow around the splitter vane/shell interface, and (3) with weights (two weights = 21.5 lb each and two weights = 15 lb each) added on the MOV. The excitation points were on the LOX inlet tee and on the elbow near the shell/vane interface.

Two different test regimes were followed: (1) the pressure was ramped up to 4300 psi during the time interval of 80 to 120 seconds, while the temperature was lowered to $-240°F$ in the time interval between 80 and 500 seconds into the test (Fig. 4) and (2) the temperature was asymptotically ramped down from -90 to $-255°F$ between 60 and 900 seconds (Fig. 5), while the pressure was ramped from 0 to 2000 psi during the first 90 seconds and raised linearly during 90 to 860 seconds time intervals up to 4200 psi (Fig. 6).
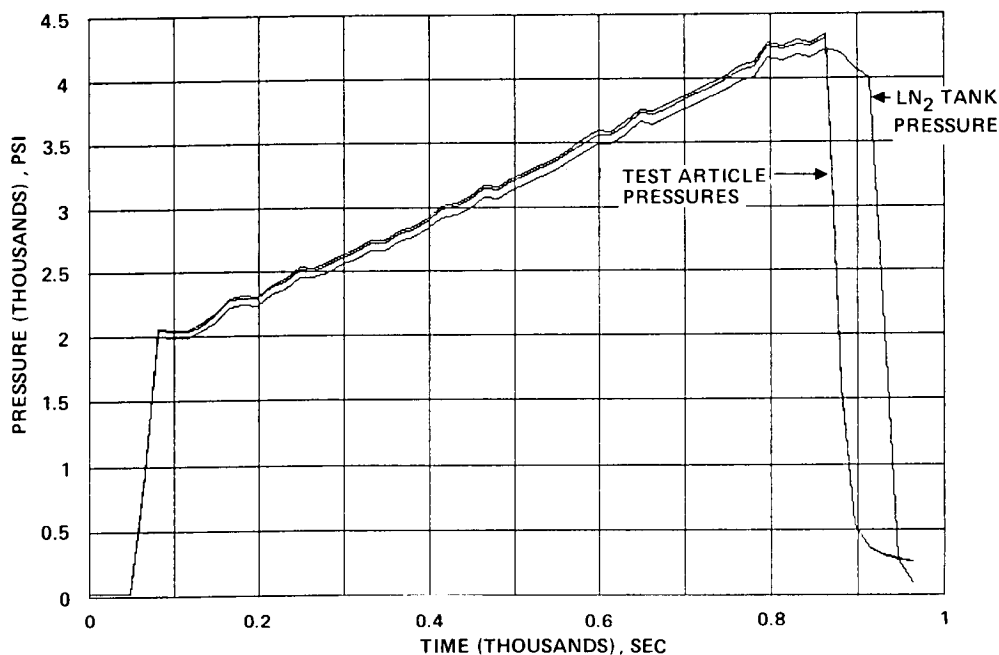
Fig. 4. Pressure vs Time (4000 Hz)

DATA ANALYSIS AND EVALUATION

In all experimental modal survey tests, data analysis is a fundamental part of the structural dynamic analysis and test evaluation. Data acquisition (collection, recording, transmission, storage, preparation, and qualification), data reduction via appropriate computer software, and functional representation of the test results by means of plots (that are generated by various curve-fitting techniques) all play important roles in the data analysis and evaluation process.

The data gathered during the liquid nitrogen tests are quite extensive. Moreover, the evaluation of such massive data in a scientific manner is a challenge; since approximations and qualitative judgements will have to be
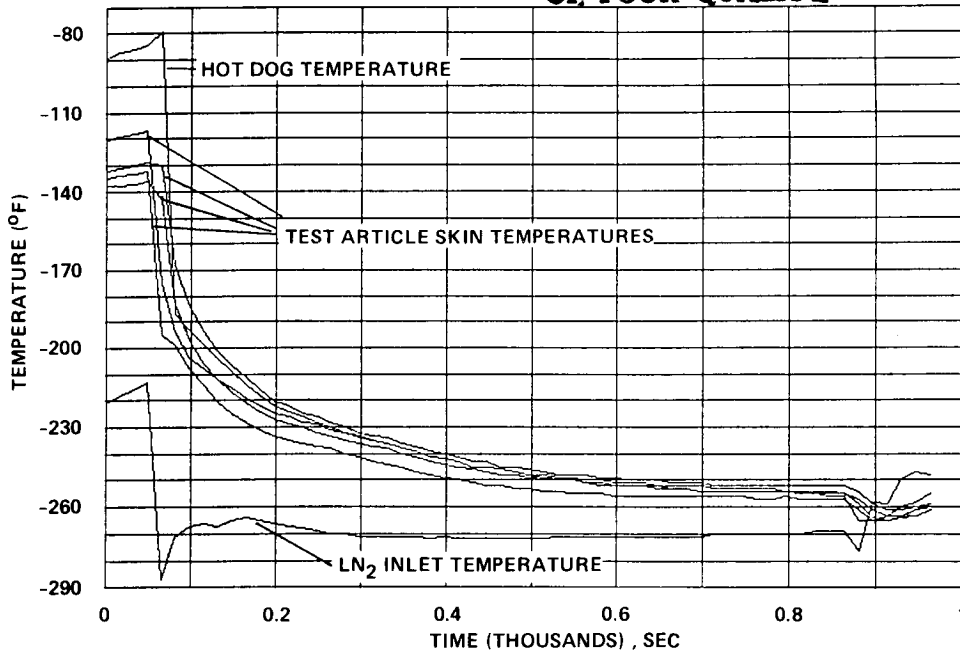
Fig. 5. Temperature vs Time (4000 Hz)
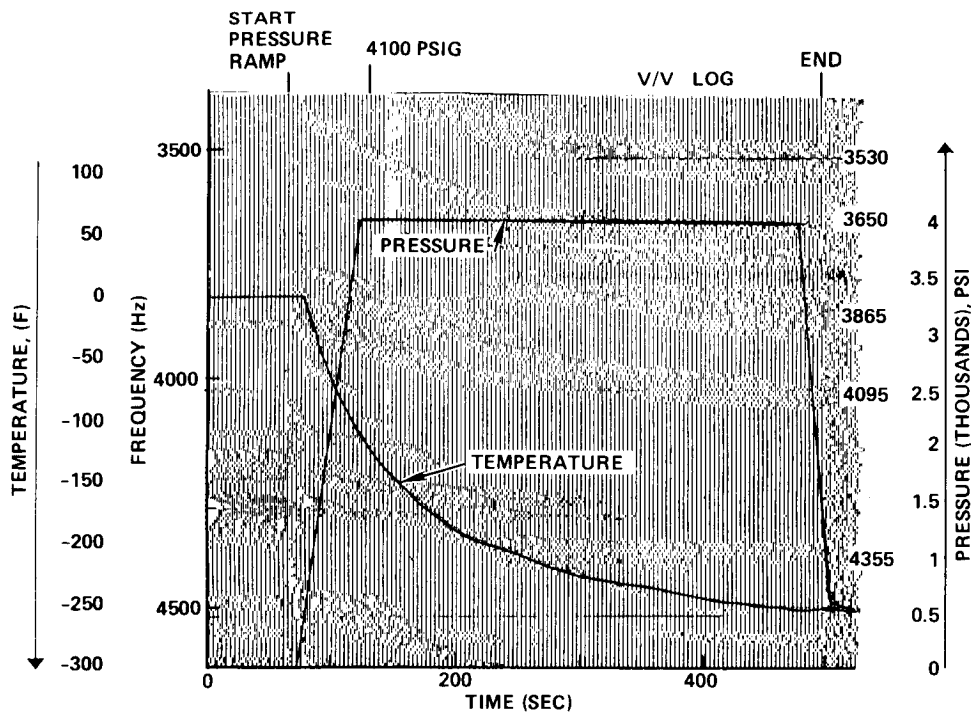
Fig. 6. Liquid Nitrogen Test Article Strain Gage Data
(Right Vane Trailing Edge)

utilized in order to draw meaningful conclusions. Under this light, the modal
survey test results, from strain gage measurements of the SSME LOX inlet
splitter vanes, provide significant information regarding the shifts of fre-
quencies of various vane modes under different temperatures and pressures.

330

Baseline

The degree of frequency shifts upwards, due to pressurization and cooling effects, of the splitter vane modes is seemingly a function of frequency. Thus, modes with frequencies in the 3900 to 4100 Hz region experience less shift (less than 300 Hz) as compared to modes at a higher or at a lower frequency (as high as 1000 Hz). Moreover, whether the pressure is slowly increased while ramping the temperature down to -240°F (in about 100 seconds), or the temperature is lowered (exponentially) while the pressure is ramped up, does not change the behavior of the modes, as indicated in the isoplots (Fig. 6 and 7). Reference point frequency response functions from an accelerometer at the shell/vane interface location (Fig. 2) shows the general behavior of modes under baseline conditions as the pressure is increased at low cryogenic temperatures (Fig. 8). Once again, the overall behavior is that modes near 4000 Hz have less of a shift than those at lower or higher frequencies. Furthermore, it is interesting to note that some modes are amplified by increase of pressure while others are completely attenuated, and still others start exhibiting their resonant peaks at higher pressures. All the measurement locations show a response at 4025 Hz frequency starting at around 4000 psi pressure (Fig. 8). These types of behavior might be an indication of nonlinearity (perhaps due to fluid/structure interaction).

3000   4000   5000   6000
FREQUENCY (HZ)
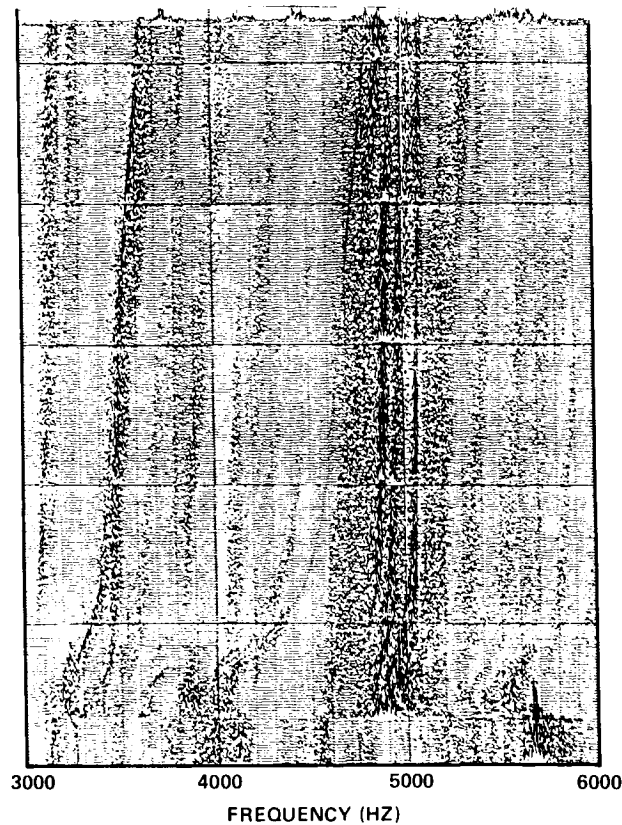
Fig. 7. Liquid Nitrogen Test Article Strain Gage Data
(Right Vane Trailing Edge - 0 Weights)

Quadrature plots (Fig. 9) indicate the phase relationship at each measurement location on the vanes, thus indicating the type of modes that are excited and various frequencies. The 4025-Hz mode seems to be a weak "twisting" mode, whereby the vane free edges move opposite in direction normal to the vane surface. Also, frfs of vanes all exhibit the abovementioned frequency.

3677　3848　3971 4025 4040　4259　4478

DB
LOG

4069　　　4232

3375　　　　　　　　　　　　　　　　4625

FREQUENCY (HZ)
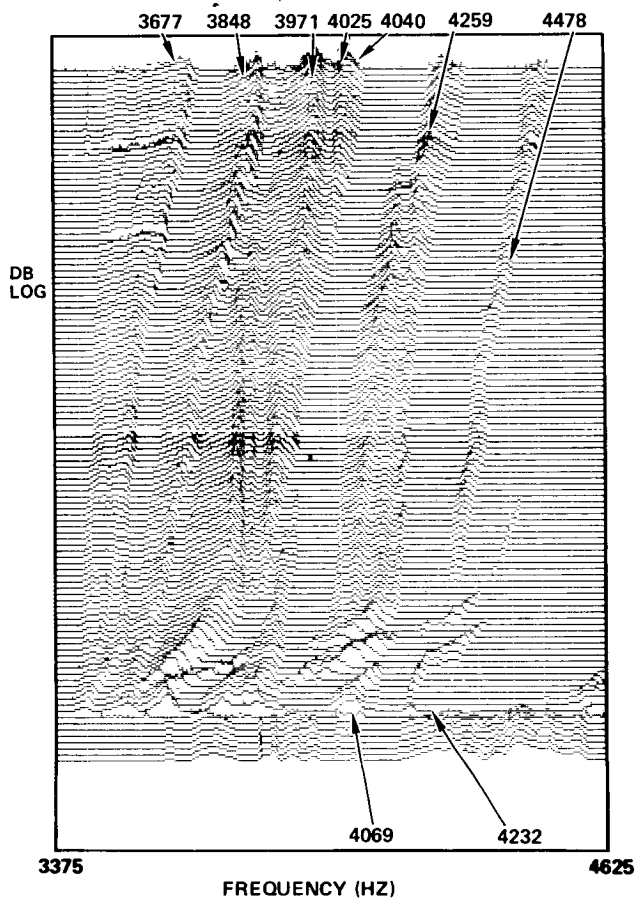
**Fig. 8. Liquid Nitrogen Test Article Accelerometer Data
(On the Shell Near Vanes - Al No Clamp**

2.50E+00

67X　　　　70 X　　　67X　　　4025 TWIST BEND

67X　　　　　　　　67X　　　　　　　67X

68X　　　　68X &　　　　　67X
　　　　　70X

AMPLITUDE

68X

70X　　　　　67X

NOTE: 67X, 68X, AND 70X REFER TO LOCATIONS
　　　7,8, AND 10 ONFIG.3

-2.50E+00
3.50E+03　　　　　　　　　　　　　　　　4.50E+03

FREQUENCY (HZ)
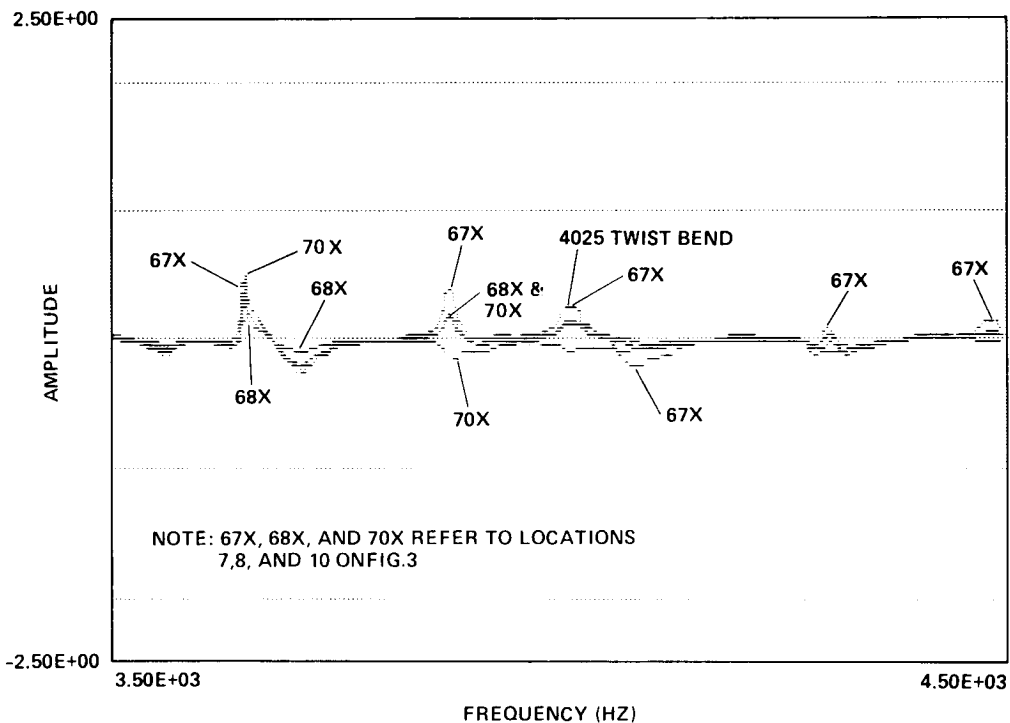
**Fig. 9. Imaginary Plots of frf Under Baseline Conditions
(No Weights, No Clamp)**

332

Several weights were added on the main oxidizer valve of the SSME Test Article (Fig. 1) to study the effects and changes that realistic hardware conditions would have on the modal behavior of the LOX inlet splitter vanes. The weights were added in three steps: Two weights of 21.5 lb each at first, then a third weight of 15 lb, and lastly, a fourth weight of 15 lb. The effect of the weight on the modal frequencies and amplitudes are shown in the isoplots (Fig. 10).
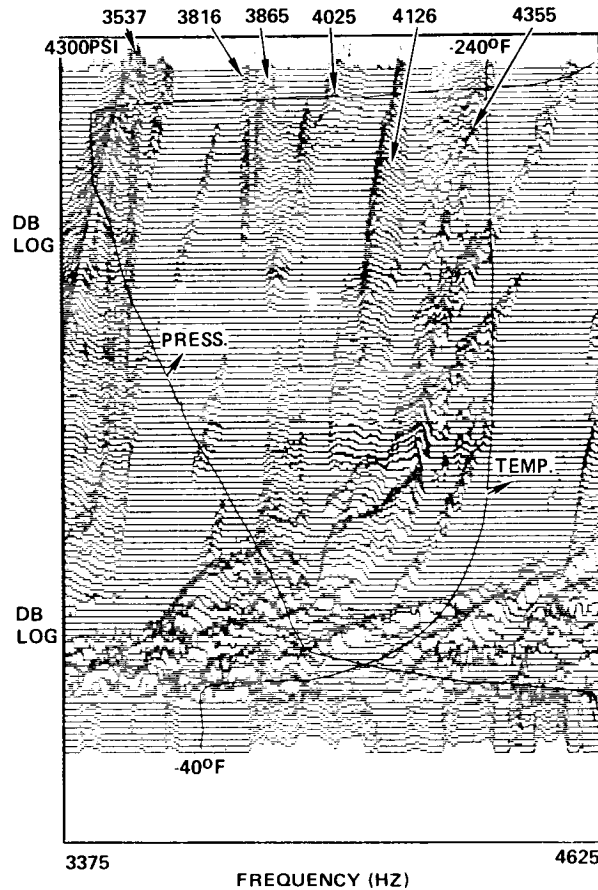
Fig. 10. Liquid Nitrogen Test Article Strain Gage Data
(Right Vane Trailing Edge - 4 Weights, No Clamp)

Once again the frequency shifts are upwards, similar to the previous case. However, many additional modes are excited with the weight on relative to the baseline situations. Moreover, the 4025-Hz frequency is still there with a little higher amplitude again appearing at around 4000 psi pressure. The case of three weights or two weights being somewhat similar to the four weights case; only the latter isoplot is included.

Clamp On

A simple clamp was attached around the splitter vanes on the shell to study the effect of preloading on the vane modal characteristics. Both without weights and with weight cases were considered and isoplots, as well as frfs, were generated for all cases. The general trend of frequency shifts was still prevailing relative to the baseline case, and the frequency shifts upward were

very similar to the previous cases—although with reduced amplitudes (Fig. 11). Specifically, Fig. 11 shows the effect that the clamp has on the isoplots. The 4025-Hz mode is still shown to be there at around 4000 psi pressure. The quadrature plots (Fig. 12) show this mode to be a weak bending mode.
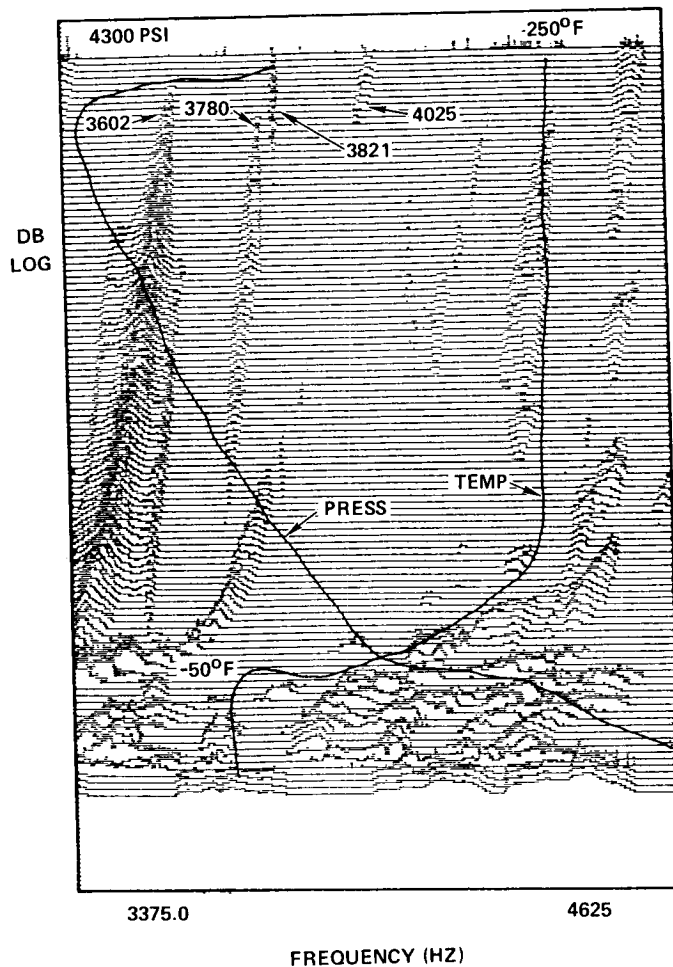
Fig. 11. Liquid Nitrogen Test Article Strain Gage Data
(Right Vane Trailing Edge - 4 Weights, Clamp On)

The overall effect of the clamp is reduction of the amplitudes of vibrations as well as reduction of the response excitation of some dominant modes. The significance of such a fixture is the stiffening effect and damping induced by the clamp on the external shell, which is obviously transmitted to the vanes. The reason for such an experiment was to evaluate the vibration suppression induced by external measures that are simple to implement.

CONCLUSIONS

Pressurization and cooling of metal shells induce frequency shifts upwards (opposite to the influence of wetting the shell from inside). The shifts are a function of frequencies. Preloading, and straining effects also cause variations in the modal behavior, however, the frequency shifts due to the pressure and thermal loading are similar to the baseline case.
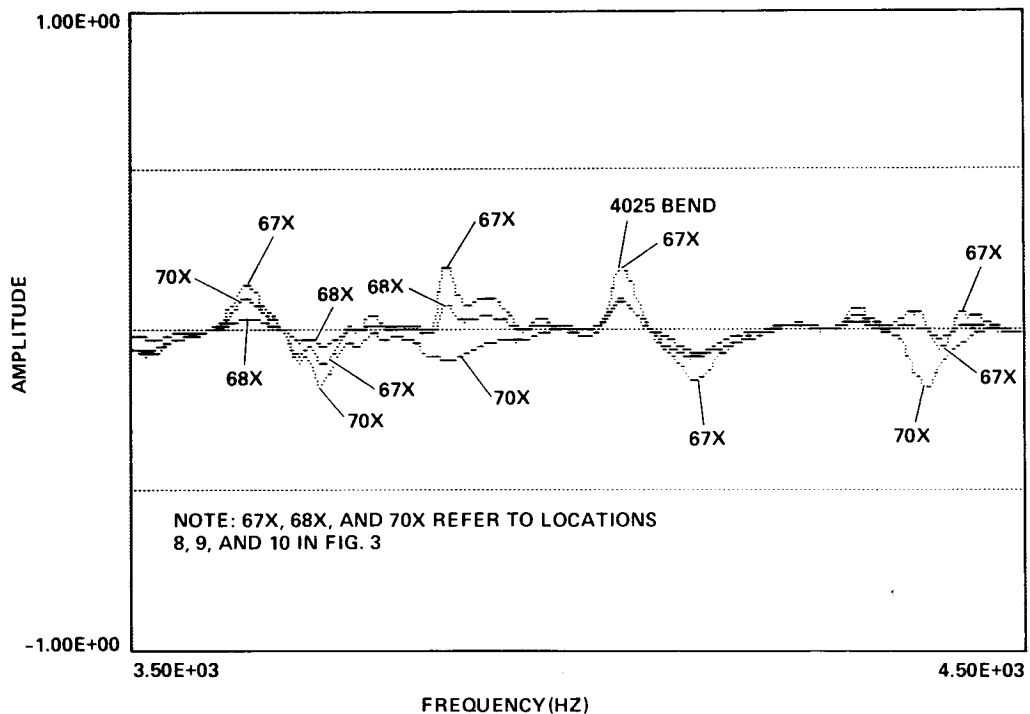
Fig. 12. Liquid Nitrogen Test Article Strain Gage Imaginary Plots
(4 Weights, Clamp On)

Attachment of a clamp around the shell reduces the overall amplitudes of vibration while keeping the frequency shifts virtually constant.

Further studies are needed to correlate the effect of wetting, with those of pressurization and cooling, upon the modal characteristics of metal shells and splitter vanes located in the shells.

REFERENCES

1. S. J. Brown, "A survey of Studies into the Hydrodynamic Response of Fluid-Coupled Circular Cylinders," ASME Journal of Pressure Vessel Technology, Vol. 104, pp. 2-19, 1982.
2. R. D. Blevins, Flow-Induced Vibrations, Van Nostrand, Reinhold, New York, 1977.
3. P. B. Gonzales and R. C. Batista, "Frequency Response of Cylindrical Shells Partially Submerged or Filled With Liquid," J. of Sound and Vibration. Vol. 113, No. 1, pp. 59-70, 1987.
4. C. Lanczos, , The Variational Principles of Mechanics, University of Toronto, Press, Toronto, Canada, 1970.

Incipient Failure Detection of Space Shuttle Main Engine Turbopump Bearings Using Vibration Envelope Detection

Charles B. Hopson

Rotor bearing defects are difficult to detect by traditional signal analysis techniques because the small amplitude, low frequency information is often masked by noise. This is especially true when trying to detect SSME turbopump damage from externally mounted accelerometer data. However, vibrations induced by defects often excite natural frequencies of neighboring structures, in effect, amplitude modulating the defect signature onto a structural resonance carrier frequency. By using a Vibration Envelope Detector to demodulate the information from the resonance carrier, a new low frequency spectrum can be obtained that may display an impact repetition rate, characteristic of the defect.

This paper discusses the results of an analysis performed on seven successive SSME static test firings, utilizing envelope detection of external accelerometer data. The results clearly show the great potential for using envelope detection techniques in SSME Incipient Failure Detection.

INTRODUCTION

High Pressure Oxygen Turbopump (HPOTP) bearing failure is a potentially catastrophic event capable of causing the loss of the Shuttle vehicle. Incipient Failure Detection (IFD) of HPOTP bearings must meet several requirements to be successful. It must be reliable and consistent for all engines and pumps. To insure bearing health during a flight, it must provide ample warning of bearing failure to allow safe engine shut-down. The technique should also have a minimum impact on cost and existing hardware. In addition to safety concerns, IFD would allow the maximum service of a turbopump before disassembly and inspection became necessary. IFD would also be a valuable tool in the improved design of turbopump components by monitoring the progression and characteristics of bearing degradation leading to failure.

The analysis of SSME turbopump data for indicators of bearing damage is difficult for several reasons. The severe noise environment makes the search for low amplitude, low frequency signatures nearly impossible with traditional techniques. Internal strain gages have proven to be very good for identification of

defects, but they are prone to failure and are not available on flight engines.

External accelerometers are common to both static and flight engines, however, the transmission of information from the bearings to the outside of the case is usually weak and buried in random noise. Additionally, the low pass filtering of the data during acquisition precludes the identification of higher frequency signatures such as inner and outer race defects.

This paper describes the results of an analysis conducted on seven successive SSME static test firings, using Vibration Envelope Detection (VED) to identify the bearing cage frequency of a HPOTP.

VIBRATION ENVELOPE DETECTION

The power spectrum of an accelerometer mounted on a rotor casing will ideally display a peak that is characteristic of a particular bearing defect. For example, an outer race defect will have a characteristic signature because of the repetitive impacting of balls on the defect. The impacting frequency is dependent upon the number of balls, the outer race diameter, rotational speed, etc. The signatures are difficult to detect because they are normally low frequency and low amplitude, often obscured by random noise. However, the impacting sometimes excites modes of neighboring structures, in effect, amplitude modulating the defect signature onto a modal resonance (carrier frequency). These carriers are higher in frequency that the defect frequency and two advantages are realized. Firstly, random noise is usually lower at high frequencies and secondly, for a fixed displacement, acceleration amplitude is proportional to the square of the frequency. To illustrate, assume a harmonic displacement of the form

$$x(t) = A \sin \omega t \tag{1}$$

where A is the peak amplitude and ω is the frequency. Differentiating twice results is an acceleration of the form

$$\ddot{x}(t) = -\omega^2 A \sin \omega t \tag{2}$$

Solving both equations for A sin ωt and equating,

$$\ddot{x}(t) = -\omega^2 x(t) \tag{3}$$

Hence, for a given displacement, acceleration is proportional to the square of the frequency.

Now assume that the amplitude of the defect signature is given by

$$V_D(t) = A_D \cos \omega_D t \tag{4}$$

where A_D is the peak amplitude and ω_D is the impacting frequency due to the defect. The amplitude of the structural resonance carrier can be described by

$$V_R(t) = A_R \cos \omega_R t \tag{5}$$

338

where A_R is the peak amplitude of the resonance and ω_R is the carrier frequency. Excitement of the structural mode by the impacting causes the resonance carrier amplitude to vary with the instantaneous magnitude of the defect signature.

Therefore, the instantaneous carrier amplitude becomes

$$A_C(t) = A_R + A_D \cos \omega_D t \qquad (6)$$

resulting in an amplitude modulated (AM) wave given by

$$V_{AM}(t) = (A_R + A_D \cos \omega_D t) \cos \omega_R t$$

$$= A_R(1 + m \cos \omega_D t) \cos \omega_R t \qquad (7)$$

where $m \equiv A_D/A_R$ is the depth of modulation. Equation (7) can also be expressed as

$$V_{AM}(t) = A_R \cos \omega_R t + \tfrac{1}{2} m A_R(\omega_R + \omega_D)t + \tfrac{1}{2} m A_R(\omega_R - \omega_D)t \qquad (8)$$

So the AM wave spectrum contains peaks at the structural resonance carrier frequency and at the difference frequencies $\omega_R + \omega_D$ and $\omega_R - \omega_D$ (upper and lower side frequencies). Thus, the spectrum contains the defect signature information, but centered around a higher frequency determined by the resonance of the excited structural mode.

The VED technique uses a band pass filter, centered around the resonance carrier, to filter out everything except the carrier and side frequencies, then outputs the envelope of this signal (the demodulated signal), resulting in a new low frequency spectrum containing the defect signature, free of the obscuring noise.

It should be understood that the enhanced spectrum will still contain the noise not filtered out before enveloping, but it will be much less than that in the original unprocessed spectrum. Ideally, the band pass filtered signal should contain the carrier and both sidebands. This means that the filter bandwidth must be twice that of the defect frequency of interest. A smaller bandwidth will attenuate the sidebands, decreasing the effectiveness of the technique. A bandwidth larger than twice the modulating impact frequency will allow excessive noise into the envelope detector. Noise between the side frequencies and the carrier will be introduced in either case, as will noise outside of the band due to finite filter roll off.

In this analysis a B&K constant percentage bandwidth tracking filter was used in conjunction with a Shaker Research Model 223A Vibration Envelope Detector.

DATA DESCRIPTION AND OBJECTIVE

This study was conducted on SSME Static Tests 406, 407, 408, 409, and 410 on the A2 Test Stand and Tests 283 and 284 on the A3 Test Stand. These tests were chosen because HPOTP #0307 was used on all seven firings and a high 2X cage frequency became apparent on Test 410. Internal strain gages installed on the pump,

failed before Test 283; however, the data acquired previous to Test 283 were useful for verifying that the cage signatures extracted by envelope detection were, in fact, real. In other words, when the VED technique extracted cage signatures that were not seen in the original spectra, the frequencies from the internal strain gage spectra and the VED spectra matched, thereby confirming that the technique was not producing false data.

The objective of the study, though, was to investigate the feasibility of using VED on external accelerometers. Considerable time was spent on Test 410 because it was known to have a high 2X cage signature. If a procedure could be found to extract the cage signature from Test 410 using VED, then the same procedure would be used on tests prior and subsequent to Test 410. A further objective, assuming a consistent procedure could be developed, was to determine if the amplitude of the cage signature or its harmonics would be useful in tracking the bearing degradation with time.

Before the study began, it was believed that the best measurement for analysis would be accelerometer PBP RAD 135-2: a radial accelerometer on the preburner pump. Experience later proved this assumption to be correct. PBP RAD 135-2 data are recorded at 60 ips and have a cut-off frequency of 2.5 kHz. For VED analysis, the frequency range must be at least twice as high as the defect frequency of interest. This fact alone precluded the search for inner and outer race defects. In fact, the frequency range should be upwards of 40 kHz to expect the successful detection of race defects. The cage signature, however, is much lower (~205 Hz); so this became the frequency of interest. It should be noted that even though PBP RAD 135-2 is filtered at 2.5 kHz, the rolloff is shallow enough that higher frequencies can be analyzed, although this ability diminishes rapidly.

Unfortunately, after Test 410, HPOTP #0307 was installed on an engine at the A3 Test Stand. This made comparison more difficult because the engine characteristics are somewhat different and it was discovered that the data filter rolloffs are considerably different making amplitude comparisons of peaks above 2.5 kHz disagree between test stands.

While this analysis could never be expected to detect all bearing defects (due to the limitations in the data recordings), it was hoped that it would demonstrate the feasibility of the VED technique and warrant further study.

DISCUSSION OF ANALYSIS PROCEDURE

The analysis began by reviewing the analog tape recording of PBP RAD 135-2 on Test 410, since it was known to contain a high 2x cage frequency. The tape output was connected to the constant percentage bandwidth tracking filter and the output of the filter was then fed into the Vibration Envelope Detector for demodulation. This envelope was then displayed on a spectrum analyzer. The bandwidth of the tracking filter was adjusted during the analysis so that it would be at least equal to but not much greater that 420 Hz (two times the cage frequency). As stated before, this allows the AM wave to be enveloped but keeps the noise to a minimum. As the tape was shuttled back and forth, the spectrum analyzer was monitored for cage signatures as the tracking filter was swept through the frequency range of the measurement.

As the analysis progressed, strong cage and cage harmonic peaks appeared on the spectrum analyzer when the center frequency of the filter got to around 6700 Hz. This indicated that the cage signatures were being carried on a signal in this frequency range. By increasing the tracking filter bandwidth, cage multiples out to the seventh harmonic were observed. The 6700 Hz frequency range then became the focus during the remainder of the analysis. Figure 1 shows the basic flow and a comparison of an original unprocessed spectrum and a VED enhanced spectrum. Note the absence of cage signatures in the original spectrum, while the enhanced spectrum contains the cage frequency plus the second and third harmonics.
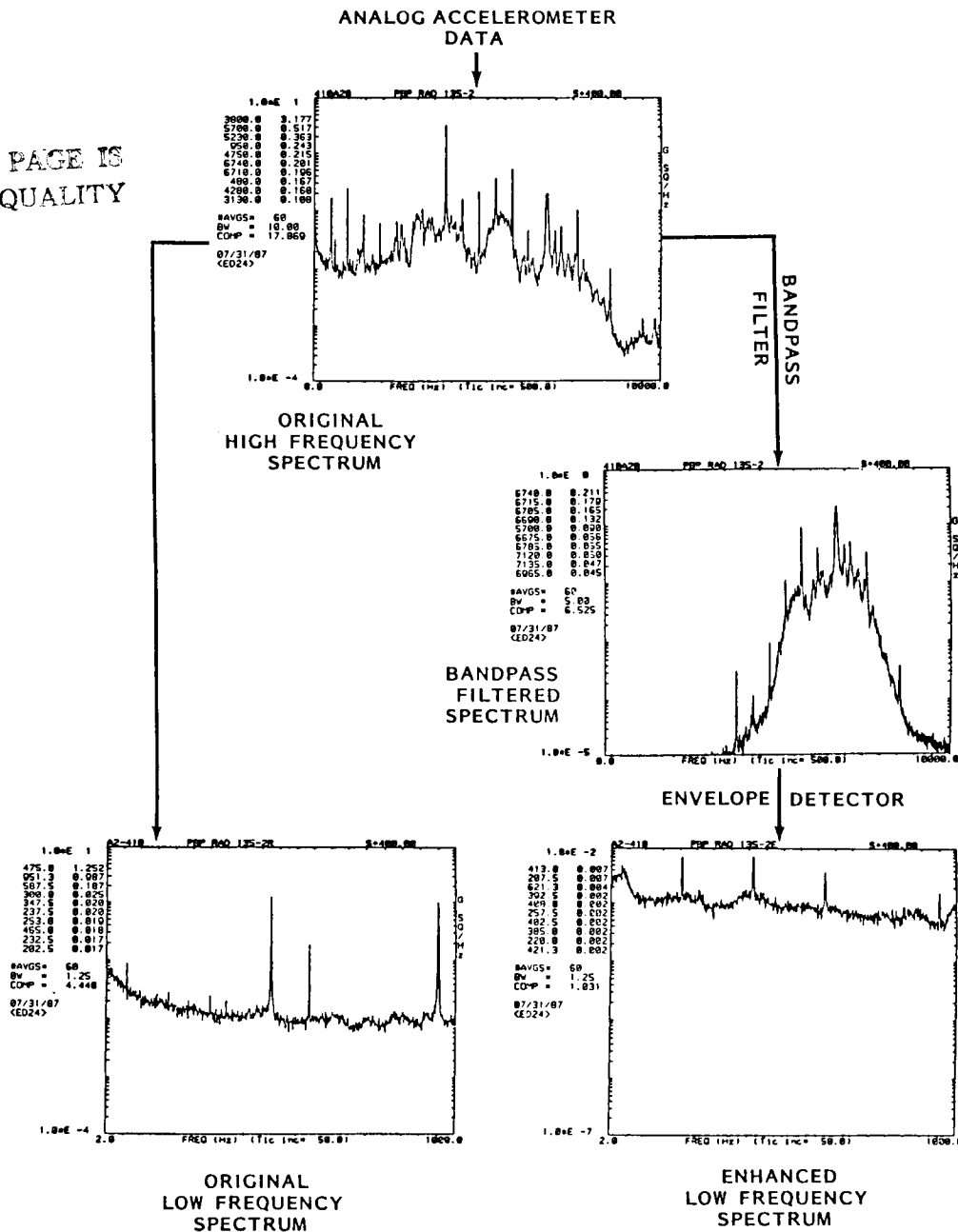
FIGURE 1   ENVELOPE DETECTION FLOW DIAGRAM

After the cage signature was extracted from the 6700 Hz carrier, a comparison was made between spectra from Tests 406 and 410. Since Test 406 was the first analyzed, it was used to baseline the characteristics of an undamaged bearing. When compared, a large anomalous peak can be seen on the spectrum of Test 410 that is absent on Test 406. This comparison is shown in Figure 2. In the PSD from Test 410, an upper side frequency corresponding to the fundamental cage is also clearly observed.

Figure 3 shows a summary of the spectra from Tests 407 through 410, analyzed using a 1500 Hz bandpass filter centered at 6750 Hz. The plots on the left are the original spectra from each test averaged over the time that the engine was running at 104% of the Rated Power Level (RPL). The plot to the right of each spectrum is the corresponding enhanced spectrum. Each pair of spectra was processed identically except that the enhanced spectra were processed after the signal was filtered, enveloped, and passed through an adaptive filter. The adaptive filter provides spectral line enhancement by adaptively building narrow bandpass digital filters around each line, reducing random noise. The adaptive filter was utilized in this study for peak identification, but was not used for amplitude analyses.

FIGURE 2 POWER SPECTRAL DENSITY COMPARISON OF TESTS 406 AND 410

The original spectra show the HPOTP synchronous frequency peak and harmonics, however peaks at the bearing cage frequency are not observed. Because of the enhancement, though, the cage signature becomes apparent. The spectra of subsequent tests show the cage signature increasing as bearing degradation advances. The cage harmonics become pronounced on Test 408 and increase in amplitude on Tests 409 and 410.

It was determined, after experimentation, that the optimum filter bandwidth for the analysis was around 1 kHz. This bandwidth allowed the cage and second harmonic to be demodulated with a minimum amount of noise introduced into the detector. This bandwidth, centered at 6750 Hz, was then used for the detailed analysis of all seven tests.

The VED analysis was conducted only during periods of constant engine power level so that amplitude and frequency comparisons could be made. Figure 4 is the time history of the HPOTP synchronous frequency over all seven tests. HPOTP speed changes are observed even at constant power level, due to LOX venting. Also, note that the synchronous frequency during Tests 283 and 284 is higher than on the previous five tests due to the different SSME on which the HPOTP was installed.

ORIGINAL RAW SPECTRA   VED ENHANCED SPECTRA
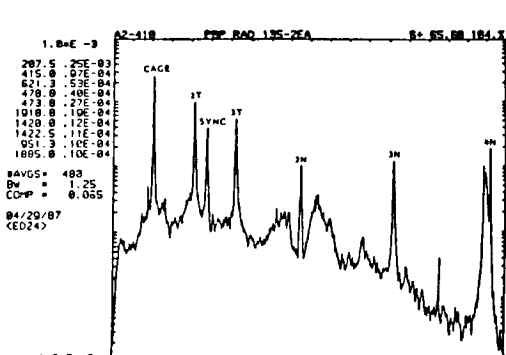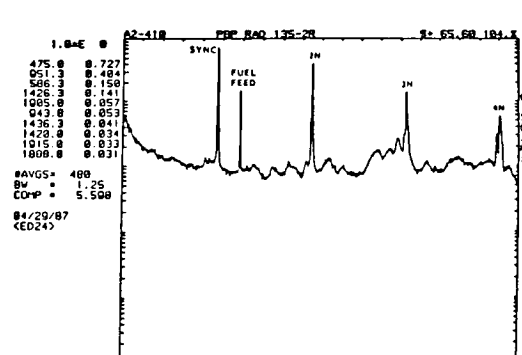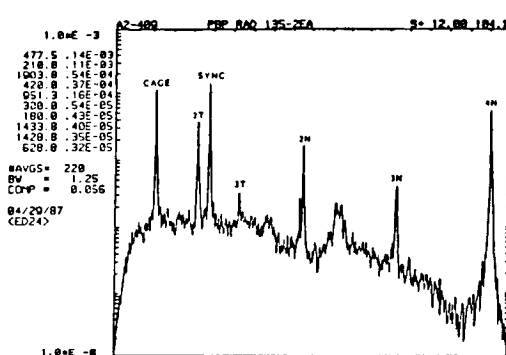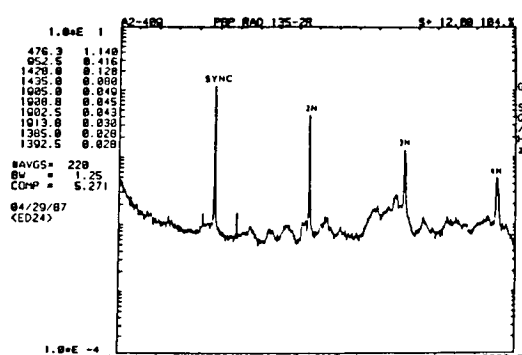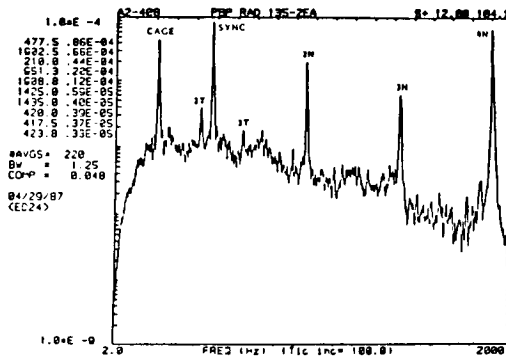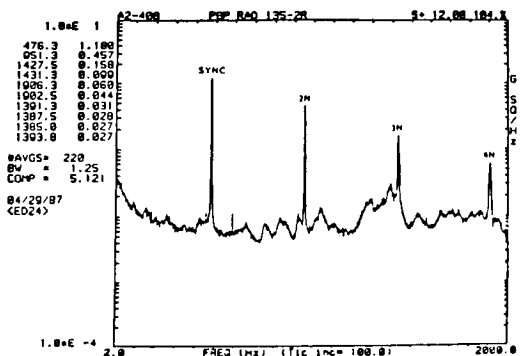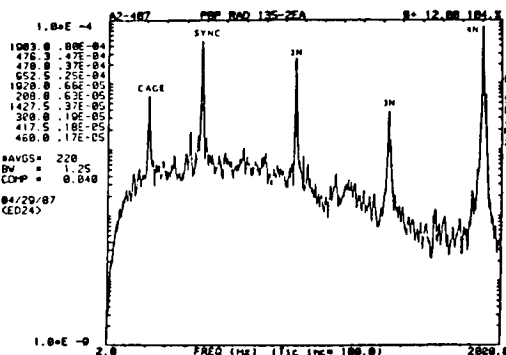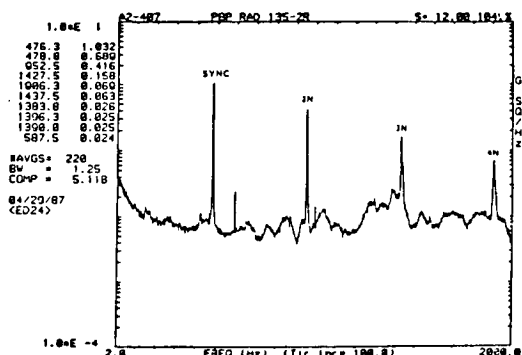
FIGURE 3   COMPARISON OF ORIGINAL SPECTRA AND
VED ENHANCED SPECTRA

343

Figure 5 is the time history of the anomalous carrier frequency. Observe that the frequency varies in correspondence to the synchronous frequency, indicating that it is not a resonance at all, but a response dependent on pump speed. Figure 6 is the time history of the ratio of the anomalous carrier to synchronous frequency. The ratio is shown to wander somewhat with changes in synchronous speed, however, it is in the vicinity of 14.2 times synchronous.

The anomalous carrier frequency abruptly disappeared seventy seconds into Test 283, and the ability to extract cage signatures by VED was lost. The source of the anomalous frequency has not been determined; however, it is nearly in the range where one might expect to find the second harmonic of an inner race defect signature. In fact, in the spectral analysis, there was an indication of a fundamental peak around 7.1 times synchronous which appeared to be related to the anomalous frequency; however, it was weak and sporadic. Actually, an inner race defect on a HPOTP bearing would be expected to be around 7.4 times synchronous and the disappearance of the anomalous frequency makes it even more puzzling.
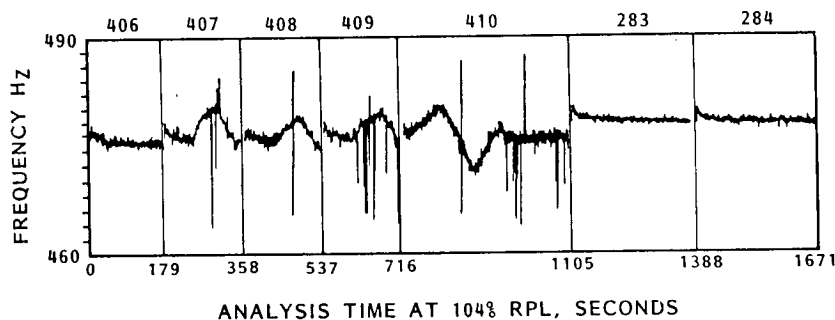
FIGURE 4   TIME HISTORY OF SYNCHRONOUS FREQUENCY
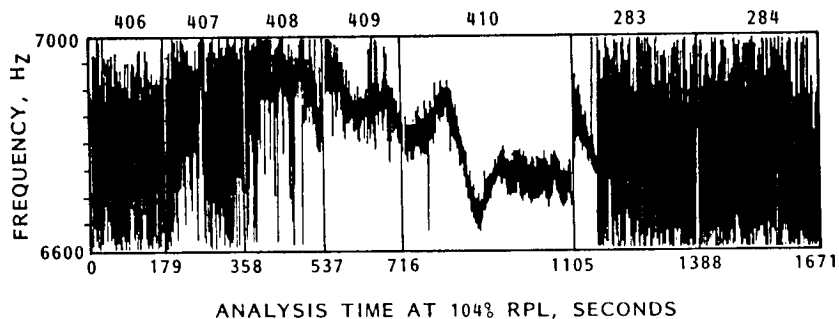
FIGURE 5   TIME HISTORY OF ANOMALOUS CARRIER FREQUENCY
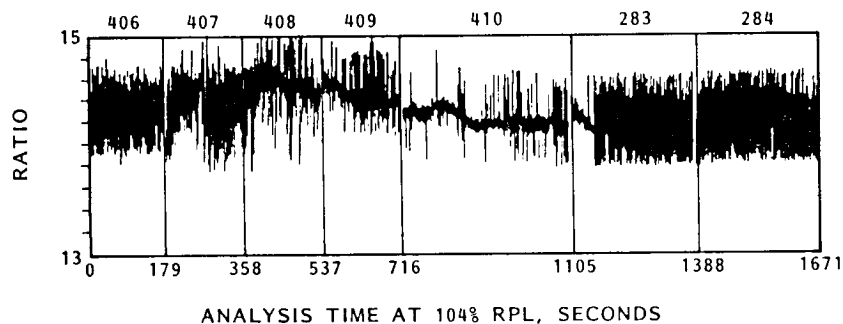
FIGURE 6   RATIO OF ANOMALOUS CARRIER FREQUENCY
TO SYNCHRONOUS FREQUENCY

344

Routine data processing procedures had not revealed the anomalous frequency, probably because it is in a frequency range not observed in routine data analysis. The event during Test 283 which caused the disappearance of the anomalous frequency has not been identified and without speculating on the cause, results from the VED analysis will be discussed here.

Referring back to Figure 6, note that although the ratio wanders during changes in pump speed, it is otherwise steady. The only exception is just before the anomalous event during Test 283. Here it is shown to decrease even though the pump speed was constant, possibly indicating the onset of a failure.

Figure 7 shows the time history of the anomalous frequency amplitude. Note how the amplitude increases as bearing degradation advances until the anomalous event, when the peak completely disappears.
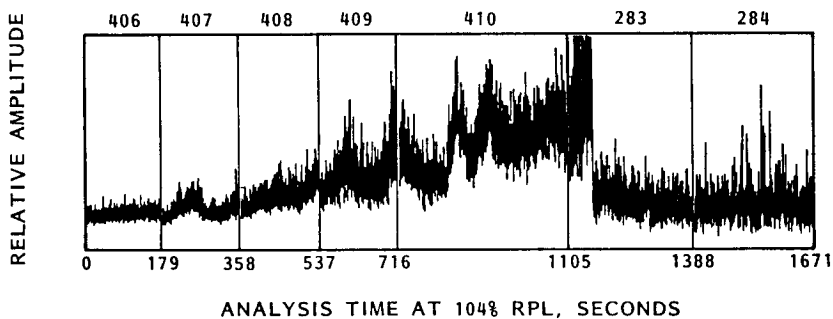
FIGURE 7   RELATIVE AMPLITUDE OF ANOMALOUS FREQUENCY
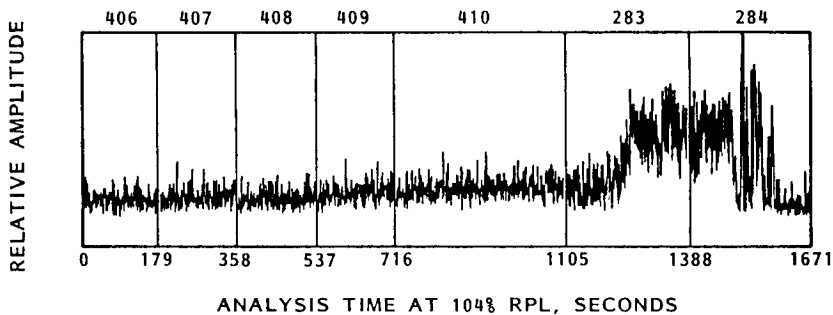
FIGURE 8   RELATIVE AMPLITUDE OF 2X CAGE FREQUENCY
(ORIGINAL SIGNAL)
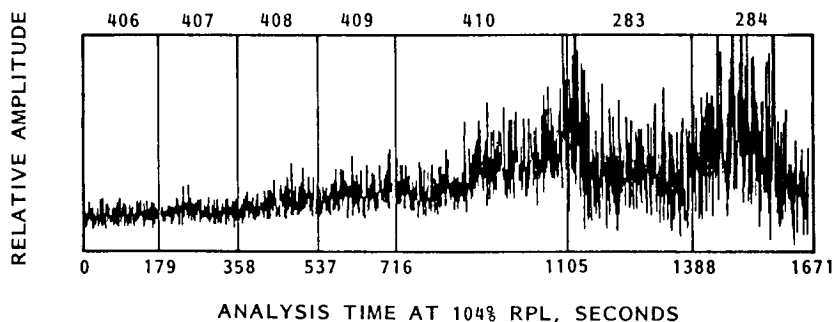
FIGURE 9   RELATIVE AMPLITUDE OF 2X CAGE FREQUENCY
(ENHANCED SIGNAL)

345

Figure 8 shows the time history of the second cage harmonic amplitude. During the first five tests, the amplitude is constant because the low amplitude cage signal is buried beneath the random noise. However, after the anomalous event, the amplitude increases dramatically, possibly caused by the event. Also note that the harmonic disappeared during Test 284. The rapid disappearance, indicating a significant event had occurred, prompted the disassembly and inspection of the pump.

The inspection revealed severe ball wear and pitting. The cage was almost completely destroyed and the unconfined balls showed signs of violent impacting. The bearing also showed signs of heavy side loads and outer race spinning.

Figure 9 is the time history of the second cage harmonic amplitude processed from the VED enhanced signal. Observe the steady increase in amplitude with time. This plot is very encouraging, because while the anomalous frequency may be an effect from some other problem and probably not always indicative of bearing failure, the 2x cage signature may be an accurate measure of a cause. Note that Figures 8 and 9 were constructed using identical processing parameters, except that the signal was sent through the filter and detector before it was digitized for Figure 9. Figure 8 gives no indication of bearing failure until about 1250 seconds into the analysis, while the amplitude is seen to begin increasing hundreds of seconds earlier in Figure 9, because of the great increase in signal-to-noise ratio due to VED.

CONCLUSIONS

The results presented in this paper are encouraging and support the theory that Vibration Envelope Detection may be a feasible diagnostic method for incipient failure detection of SSME turbopump bearings. The VED method revealed evidence of HPOTP bearing degradation in a series of static test firings much earlier than did routine data analysis, utilizing data from the same existing external accelerometer. While the success in this case was dependent upon an anomalous frequency of unknown origin, the tremendous amount of additional information contained in the data was clearly demonstrated and further study is therefore justified.

RECOMMENDATIONS

This study has clearly demonstrated the ability to retrieve useful diagnostic information by using VED; however, the potential for greater success is dependent upon the frequency range of the data. VED is a procedure that works best on high frequency resonances. For example, it is possible to detect very small displacements by enveloping the impact excited resonance of an accelerometer in the 50 kHz range. The only consistent, reliable IFD technique would be the use of VED on a resonance which not only contains the defect information, but which is also assured of being uniform in frequency and character. By increasing the frequency range of the data to 80 kHz, an exhaustive investigation could be initiated possibly leading to a real-time monitoring system. Until the frequency range is increased the capabilities of VED will not be realized.

ACKNOWLEDGEMENTS

REFERENCES

1   Operation Manual, Vibration Envelope Detector Model 223A, Shaker Research Corporation, Latham, New York.

2   Swanson, W. L., "Waveform and FFT of Radially Loaded Ball Bearings with Nonuniform Ball Wear", Technical Memorandum, TM-68101-1, Wyle Laboratories, Huntsville, Alabama, April 1987.

High Frequency Data Acquisition System for Space Shuttle Main Engine Testing

Pat Lewallen

Through advancement of high speed analog to digital con-
verters, fast I/O throughput of Winchester disk drives, and
CPU multi-tasking, it is now possible to digitize analog data
at very high sample frequencies for long periods of time.
This advancement makes it possible to provide high frequency
engineering data real time and eliminates some of the
dependency on analog tapes. This paper discusses the high
frequency data acquisition system developed for the SSME
single engine test facility at the National Space Technology
Laboratories (NSTL).

INTRODUCTION

Throughout the history of the Space Shuttle Main Engine (SSME) static testing
program, engineers have been responsible for reporting on the dynamic characteristics
of the engine and its components. However, the task of processing high frequency
data has always been based on the existence and manipulation of analog tapes,
resulting in time consuming techniques for providing engineering data. The complex-
ity of the SSME, along with more aggressive test schedules, have defined a need for a
better mechanism for processing dynamic data. Through the advancement of computer
technology, it is now possible to digitally acquire (digitize) large amounts of
analog data at high sample rates. Also, with the use of array processors, the time
required to convert time domain data to the frequency domain by use of the Fast
Fourier Transform (FFT) has been greatly reduced.

There are several benefits of acquiring high frequency data real time. There
is no need for any tape head misalignment or tape speed compensation since analog
tapes are not involved. The lengthy process of dubbing and shipping analog tapes is
eliminated. By automating the acquisition/FFT process, the programs can operate with
relatively few operator interventions. However, it is important to note that for
dynamic data, analog tapes should not be eliminated as the primary recording device.
For research and anomaly investigations, it is necessary to constantly change the
analog/digital (A/D) parameters as well as input signal conditioning. In order to
accomplish this, the tape must be replayed over and over. Some examples are input

adaptive filtering, looking at very high or very low frequency components, and electronic envelope detection.

Since much of dynamic data evaluation is done in the frequency domain, a data acquisition system must be able to not only acquire data but efficiently FFT the data. For a real time data acquisition system, it is not necessary to FFT the data "on the fly," since a large amount of time is being saved simply by not having to deal with analog tapes. However, the system must be able to compute FFT's utilizing some sort of firmware to facilitate a quick, efficient data transform process. The system developed for NSTL does this.

THE SPACE SHUTTLE MAIN ENGINE

The Space Shuttle propulsion system consists of two Solid Rocket Boosters and three SSME's. The SSME's are reusable, high performance, hydrogen/oxygen propellent rocket engines. The engines can be throttled over a thrust range of 50 to 111 percent of the designed thrust level. Each engine weighs approximately 7,000 pounds and can produce a sea-level thrust of 394,000 pounds. The engine operates at a chamber pressure of approximately 3,000 psia and has a design life of 27,000 seconds. The engines can be gimballed to provide pitch, yaw, and roll control during the orbiter boost phase.

Of primary concern to dynamicists is the health monitoring of the high pressure and low pressure turbopumps located on the engine. The high pressure fuel turbopump operates at 35,000 rpm providing over 63,000 horsepower. The high pressure oxygen turbopump operates at 28,500 rpm and delivers over 24,000 horsepower. The operating environment of the engine hardware makes it necessary to routinely analyze frequencies as high as 5 kHz in order to quantify the health status of the various engine components.

SSME SINGLE ENGINE TEST PROGRAM

SSME's have been undergoing static firings since 1975. Currently, there are three test stands active. Two stands are located at NSTL, Mississippi, approximately 50 miles due east from New Orleans, Louisiana, while the third is located at the Santa Susanna Flight Laboratory in California near Los Angeles. Two test stands are in development: B1 at NSTL and the technology test bed at Marshall Space Flight Center in Alabama. Over the past seven months, 85 static firings have occurred. These tests can last up to 750 seconds with a recent milestone achieved of a 1,000-second test.

Following each engine test (usually within 48 hours), engineers responsible for the monitoring of each engine subsystem meet together and present the data evaluation results. This input is used for component health evaluation as well as pre-test criteria for the next test. Some of the areas represented at the data reviews are: Combustion devices, turbomachinery, rotordynamics, systems performance, and dynamics.

For static firings, the engine is heavily instrumented, both with performance and dynamic measurements. Approximately 300 static measurements are active and are digitally acquired at 50 samples per second. From 90 to 160 high frequency measurements are active and are recorded on analog tapes. There are approximately 50 high frequency measurements which are critical to the data evaluation/review process.

DATA ACQUISITION AND PROCESSING
PREVIOUS METHOD

For each engine test, all dynamic measurements are recorded on analog tapes. In the previous method for dynamic data processing, duplicates of these tapes were transferred to the NASA computer complex at Slidell, LA. There, the data were digitized for the entire test duration at 5,120 samples per second and stored on disk using a Hewlett-Packard 5451C Fourier Analyzer. The data were recalled in blocks of 2,048 points, converted to the frequency domain using the Fast Fourier Transform (FFT), then squared to form the power spectral density (PSD). Each PSD was written to magnetic tape, then transferred to Slidell's UNIVAC 1100/90 series mainframe. From the UNIVAC, users from MSFC in Alabama and Rocketdyne in California could access the data, producing various forms of plotted and tabulated output.

This system was the first step in providing a mechanism for the full test duration digitization of a measurement, thereby eliminating repetitive use of the analog tapes. However, due to limited performance on the 5451C, only 6 measurements could be processed at one time. For a 500-second test, it required 3 hours to acquire/FFT a 6 measurement data set. Also, Slidell had to wait for the analog tape duplicates to arrive from the various test facilities (NSTL is only 20 miles away; however, the A3 California test stand must ship the tapes by commercial air). The sample rate limited the frequency analysis to 2.5 kHz and the PSD format, while providing for all analysis necessary for data review purposes, prevented the use of special purpose signal processing techniques (i.e., cross correlation, transfer function, etc.). Finally, due to the large amount of time required to convert a measurement from the time domain to the frequency domain, only 15 to 25 of the more than 100 measurements could be processed in time for data evaluation/review support. The remaining measurements were processed by Rocketdyne at their Canoga Park facility on a time delayed basis.

In order to support the resumption of Space Shuttle flights, the engine program has adopted an aggressive testing schedule. The goal is to conduct 12 tests per month (in the past, the test rate was approximately 9 tests per month). This schedule mandated the development of a system to acquire high frequency data real time to circumvent the time consuming task of handling/processing analog tapes. This type of system would allow dynamicists the necessary time to complete the data analysis required for each post-test data review.

REAL TIME SOLUTION

The data acquisition system at NSTL is built around a Harris MCX super microcomputer. The CPU system base is also known as a MASSCOMP 5700. It contains two

Motorola 68020 CPU's residing on two multi-buses with 4 Mbytes of memory. It has two data acquisition processors (DA/CP's), which output digitized data through a custom written FORTRAN 77 queued transfer program to Fujitsu Eagle (387 Mbyte) disk drives. Through UNIX multi-tasking, each DA/CP can operate simultaneously, utilizing its own disk controller, thereby doubling the throughput of a single DA/CP system. Because of higher disk write throughput capability, the input sample frequency can be increased to 10,240 samples per second. Each DA/CP can acquire up to 48 measurements through its own sample and hold front end cards. This provides a real time test throughput of 96 measurements. Also, due to the large amount of disk storage available, test durations of any length can be supported.

Once the data have been digitized, the data are recalled and transformed using the FFT. This is done rapidly on the MCX due to the presence of a vector accelerator (array processor). The VA-1, as it is called, can compute a 1024 point FFT in 2.5 milliseconds. Also, the VA-1 can overlap DMA array transfers into and out of itself with mathematical operations on resident arrays. This is necessary due to the limited memory resident on the VA-1 (32k floating point words). By taking advantage of this overlap, the VA-1 can be kept constantly busy computing FFT's as well as transferring data back and forth from program memory. For a test duration of 500 seconds, it takes less than 30 minutes to complete the FFT transformation of 48 measurements (over 60,000 FFT's). Also, the MCX has two VA-1's present, and again with UNIX multi-tasking, data from both DA/CP's can be processed simultaneously effectively processing 96 measurements in the same amount of time as 48.

The front end of the real time system consists of DIFA anti-aliasing low pass filters. These filters have a cutoff frequency rolloff of 135 dB/octave. The filter programming chassis contains an RS-232 interface which allows the MCX to remotely set the anti-aliasing filter values. To prevent any DC override of the A/D converter, all inputs to the filters are AC coupled.

A high speed data transmittal network is becoming operational to transfer the FFT data from NSTL to host computers at MSFC and Canoga Park, CA (Rocketdyne). This system utilizes NASA's Program Support Communication Network (PSCN) and can operate up to 1.344 Mbaud. Also important is the fact that from NSTL, the PSCN can broadcast the data to MSFC and Canoga Park simultaneously. Current time estimates for the transmittal of high frequency data is 2 to 3 hours. This means that the real time system can complete 96 measurements before the previous analog tape method can complete 6.

CONCLUSION

By developing a real time data acquisition system, NASA has eliminated the time consuming, logistics laden task of handling/processing analog tapes for SSME single engine test dynamic data processing. The real time system will provide engineering data for a complete set of SSME instrumentation (approximately 100 measurements) within 4 hours following engine cutoff, a decrease of over 48 hours from the previous analog tape based system.

Space Shuttle Main Engine Vibration Data Base

Pat Lewallen

N88-13631

In order to evaluate Space Shuttle Main Engine (SSME)
vibration data without having to constantly replay analog
tapes, the SSME Vibration Data Base was developed. This data
base contains data that have been digitized at a high sample
rate for the entire test duration. It provides quick and
efficient recall capabilities for numerous computation and
display routines. This paper describes the data base
components as well as some of the computation and display
features.

INTRODUCTION

The Space Shuttle Main Engine (SSME) single engine test program has been active
since 1975. Following each test, engineers have been responsible for reporting on
the dynamic characteristics of the engine and its components. Since 1983, the SSME
Vibration Data Base has been online to assist in the day-to-day data evaluation as
well as diagnostic problem definition and solution.

The primary objective of the SSME Vibration Data Base is to make available to
the dynamicist, in an efficient, systematic, and timely manner, data analysis
techniques which can be used in the evaluation of the operational integrity of the
SSME turbomachinery. The vast majority of the evaluations can be performed with
conventional power spectral density (PSD) and root-mean-square (RMS) time history
analysis. For those cases where these types of analyses are not adequate or where
failures or major incidents occur, the analog magnetic tapes are available for more
detailed and elaborate analysis.

DATA BASE COMPONENTS

The SSME Vibration Data Base consists of three components: (1) Power Spectral
Density (PSD) Isospectral Data Base, (2) Diagnostic Data Base, and (3) Anomalous
Frequency Data Base. The Isospectral and Diagnostic Data Bases will be described in

this paper. Each data base is a self-contained software system, with the Diagnostic Data Base receiving its data values directly from the Isospectral Data Base through electronic transfer.

ISOSPECTRAL DATA BASE

The Isospectral Data Base is housed on the UNIVAC 1100/90 series mainframe computer at NASA's Slidell Computer Complex, Slidell, LA. The basic unit of this data base is the power spectral density. For routine single engine tests, all of the necessary analysis required for data review reporting can be derived from PSD formatted data. Since the data are in the frequency domain, any discrete frequency can be easily detected and classified in terms of its speed and amplitude. Each measurement contained in the data base consists of contiguous PSD's over the entire test duration. The PSD frequency range can be up to 5 kHz; however, most of the data to date are good to 2.5 kHz.

By maintaining dynamic data in PSD form and contiguous over the entire single engine test duration, several techniques can be utilized to extract information from the data. Since its inception, many algorithms have been developed to provide analysis insight into SSME dynamic data. Some of these algorithms are: Shaft speed tracking filter for fundamental and harmonic discrete frequency tracking, classification of discrete frequencies not related to shaft speed, and turbopump speed histograms. Also available are several display programs. These include: PSD ensemble average, 3-dimensional water fall "isoplots," and floating average summary table of measurement amplitudes. Because these data are digitized once and subsequently data based, the need for constant use of analog tapes is eliminated. This provides quick turnaround for all of the above analysis procedures.

The Diagnostic Data Base consists of summarized RMS amplitudes computed for a select group of engine instrumentation. These values can be displayed in tabular or graphic form and are primarily used for overall description of pump health as well as trend analysis. A powerful statistics routine has been developed to provide statistical models which characterize normal and abnormal behavior and establish and update engine redline cutoff values.

ISOSPECTRAL ALGORITHMS AND DISPLAY ROUTINES

Synchronous Speed Tracking

For each SSME component (specifically the high and low pressure turbopumps), the shaft rotation frequency can be identified within the PSD's through a speed detection algorithm. Given the operating power level of the engine, the algorithm computes a predicted shaft speed. It then operates on a spatial average across all measurements within a given component (this reduces background noise and enhances discrete frequencies). From the spatial average, the discrete peak associated with the shaft rotation can be easily identified. This allows the program to track not only the fundamental frequency, but also its harmonics. For routine analysis, the first 4 harmonics are analyzed and data based. Also important is the fact that

certain "anomalous" frequencies (those not associated with any shaft rotations) can be easily detected and their amplitude tracked as well.

Display Routines

Several display routines are available in the data base. Most are menu driven and can be manipulated to suit most any need. Ensemble average PSD's can be displayed for any frequency range, starting at any time in the test and averaging for any period of time. Also available is a three-dimensional "waterfall" plot, or an isoplot. This plot displays frequency in the x-axis, time in the y-axis, and amplitude in the z-axis. It utilizes hidden line computations to display the 3-D effect. This display is perfect for identifying the presence of discrete frequencies present during a test. An example display is shown in Figure 1.

An amplitude versus time plot package is available for many types of time domain plotting. RMS time histories are displayed in this package, as well as the turbopump speed trace (Figure 2). This routine can be used to plot RMS amplitudes versus the turbopump speed to detect certain types of pump responses to critical operating speeds.

The data base can recall the turbopump speed trace and calculate/plot a speed histogram. This plot annotates the length of time the pump was operating at each encountered speed. This display is useful in defining the amount of time spent at potentially detrimental speeds.

Last, a summarized RMS table can be displayed, which defines a single value (in units RMS) to characterize each measurement response at each power level. This routine was designed to simulate the engineering judgment used in extracting these summary RMS levels. The table is produced by an algorithm which computes a running 11 point average across each power level duration. The values computed by this algorithm are used in each post-test data review and are the primary input for the Diagnostic Data Base.

DIAGNOSTIC DATA BASE FEATURES

The diagnostic data base is primarily used for test-to-test trend analysis and statistical amplitude definition for pump and engine lifetimes. The data base is housed on a TransEra 6040 40 Mbyte Winchester disk which interfaces to a Tektronix 4054 microcomputer. Summarized RMS values are contained for 16 accelerometer measurements, 8 on the high pressure fuel pump and 8 on the high pressure oxygen pump. The data base has recently been modified to house additional measurements located on the two low pressure pumps. For each single engine test or Space Transportation System (STS) flight, several other parameters are stored. These parameters include the power profile (engine thrust versus time), serial numbers of the various engine components, and the rotating shaft speed at each analysis power level.

A parameter search file is maintained for the data base which allows quick recall of any and all tests associated with certain engine hardware. The parameters housed in this file are: High pressure oxygen and fuel turbopump serial numbers, engine serial number, and the high pressure oxygen turbopump configuration build number. For any processing option in the master menu, data can be recalled using any

TEST 7500290   HPFP RAD   0 ACC   (5B- 9)   071287
TIME INC= 1.2 SEC XINC= 50.(HZ)   MAX= 30.0 LOG/10.%
BU= 50., 650.
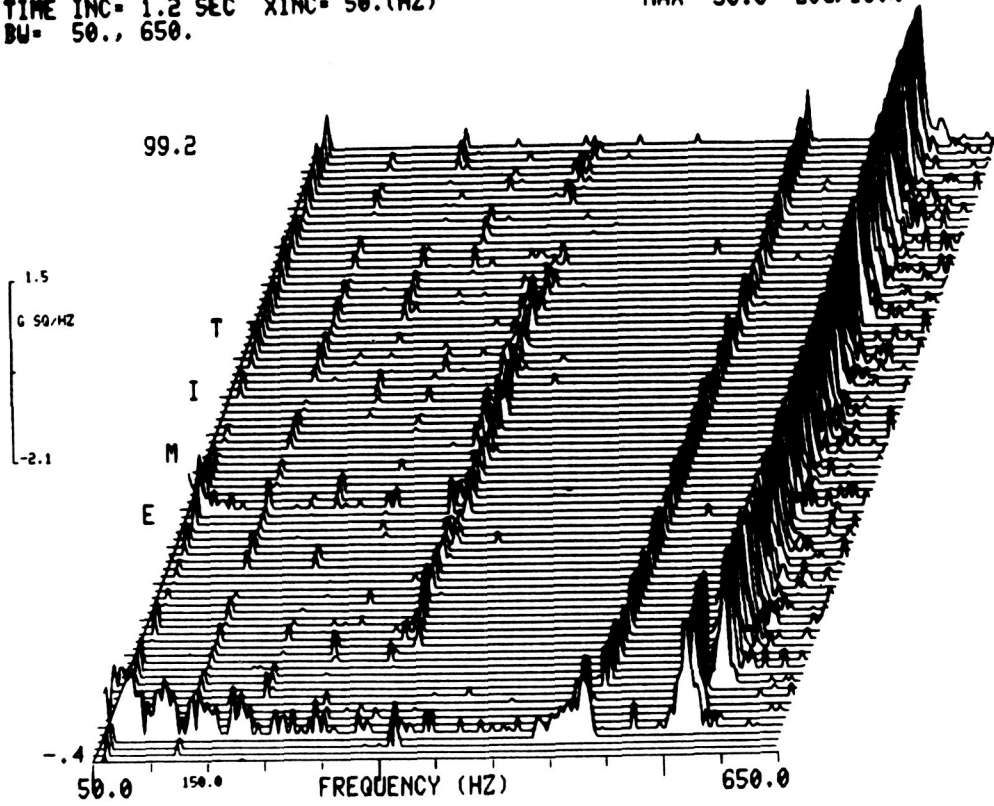
Fig. 1   Isospectral Display

ORIGINAL PAGE IS
OF POOR QUALITY
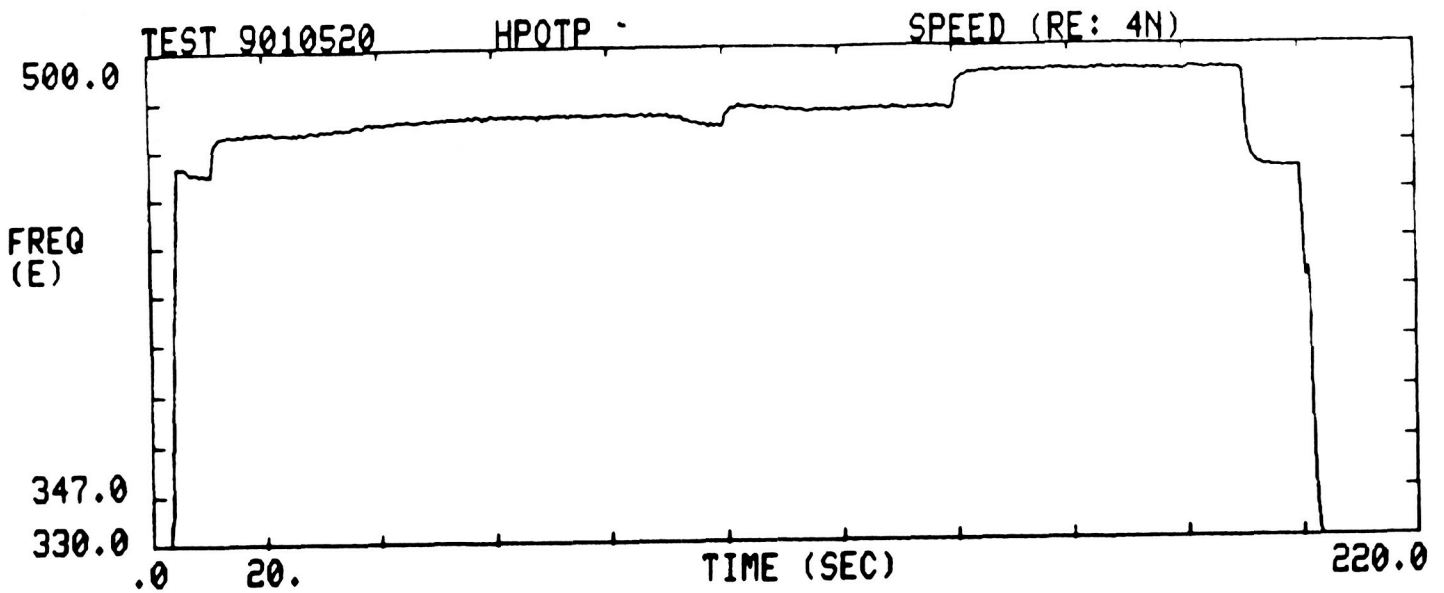
Fig. 2   SSME Component Speed Trace

of the above parameters. For example, a statistics package can be run on a particular oxygen turbopump and compared to the entire test program statistics output.

Processing Options

The Diagnostic Data Base can produce several types of tabulated and plotted information. One processing option available lists the run time activity in seconds at each engine power level for any search file component (Figure 3). This has been helpful in determining the current lifetime on pump bearings. It also provides a quick recall of a pump or engine's previous history for comparison to current activity. Another processing option plots the summarized RMS values versus their respective test numbers (Figure 4). This output once again can be limited to a specified engine component through use of the search file. This display is helpful in that it highlights any trends which may be present in the data.

The most powerful processing option in the data base is the statistical package. This option computes several statistical functions over any desired tests. One of the primary outputs of this package is a table which denotes for each measurement the sample size, mean G RMS level, maximum G RMS level, and the standard deviation (Figure 5). The values are broken down by each of the three active SSME test stands. The second output consists of a probability distribution or probability density plot (Figure 6). These plots can be configured by the user to overlay classical statistical functions, such as the normal or gamma curve, on the actual data. The use of these classical functions provide a continuous definition and enhance data characterization. The statistical package has been used extensively in the definition of engine redline, or cutoff, levels.

SUMMARY

The SSME Vibration Data Base has been the major force in automating dynamic data processing for SSME hot firings. It has demonstrated the feasibility of storing high sample rate data for long time periods and is the primary data evaluation tool for SSME dynamic data analysis. The continuing development of sophisticated computation, tracking, and display software will provide engineers with deeper insight and more complete information as to the dynamic environment of the SSME and its components.

| TEST # | SER# | DUR | >>>>>>>>>>>>>>> RUN SECONDS AT <<<<<<<<<<<<<< | | | | | | | | | |
			65%	90%	100%	102%	104%	106%	109%	111%	OTHER	RAMP
A3-277	0210	200	0	0	11	0	184	0	0	0	0	6
A3-278	0210	200	0	0	11	0	184	0	0	0	0	6
A3-279	0210	200	0	0	11	0	184	0	0	0	0	6
A3-280	0210	200	0	0	11	0	184	0	0	0	0	6
A3-281	0210	200	0	0	11	0	184	0	0	0	0	5
A3-282	0210	200	0	0	11	0	184	0	0	0	0	6
A3-283	0210	300	0	0	10	0	284	0	2	0	0	6
A3-284	0210	300	0	0	11	0	284	0	2	0	0	6
A3-285	0210	223	0	0	5	0	0	0	212	0	0	6
A3-286	0210	300	0	0	11	0	284	0	0	0	0	6
A3-287	0210	300	10	0	11	0	266	0	0	0	0	14
A3-289	0210	300	0	0	11	0	284	0	0	0	0	5
A3-290	0210	300	0	0	11	0	284	0	0	0	0	5
TOTAL			10	0	132	0	2790	0	212	0	0	79

TOTAL OPERATIONAL TIME = 3223 SECONDS

Fig. 3 Engine Lifetime Activity Table

Synchronous @104% Power Level

| | LOX PBP RAD 45 | | | | LOX PBP RAD 135-1 | | | | LOX PBP RAD 135-2 | | | |
Test Stand	# Tests	C̄ rms	Sig	Max C rms	# Tests	C̄ rms	Sig	Max C rms	# Tests	C̄ rms	Sig	Max C rms
A1	73	2.4	1.2	6.8	32	2.4	1.4	8.2	71	2.5	1.2	7.6
A2	87	2.1	1.1	6.2	49	2.3	1.5	7.9	81	2.0	1.2	8.4
A3	53	2.8	2.6	8.6	24	4.5	2.6	9.1	46	2.7	2.3	8.3
Combined	213	2.4	1.7	8.6	105	2.9	2.0	9.1	198	2.3	1.5	8.4

STATISTICAL SUMMARY OF SSME VIBRATION DATA   7 JUL 87

Synchronous @104% Power Level

| | LOX PBP RAD 180 | | | | LOX PBP RAD 225 | | | | LOX TURB RAD 45 | | | |
Test Stand	# Tests	C̄ rms	Sig	Max C rms	# Tests	C̄ rms	Sig	Max C rms	# Tests	C̄ rms	Sig	Max C rms
A1	10	2.9	2.3	7.8	70	2.7	1.4	8.8	19	1.0	0.5	2.5
A2	17	3.0	1.3	6.2	77	1.9	1.1	7.8	17	1.1	0.5	2.6
A3	25	4.1	2.4	7.8	28	1.7	1.7	6.9	18	1.2	0.7	2.4
Combined	52	3.5	2.1	7.8	175	2.2	1.4	8.8	54	1.1	0.6	2.6

TEST #'S A1300-533, A2200-428, A3200-290.

Fig. 4. Statistical Tabulation

Mean = 2.30
Std dev = 1.54

Step size = 0.5

Bin Sums

(0 5) · 76 114 135
(2 5) 85 54 36 20
(4 5) ·9   6   5   6
(6 5)   6   7   8   4
(8 5)   2   2

LOX PBP RAD 45
LOX PBP RAD 135-2
LOX PBP RAD 225

ORIGINAL PAGE IS
OF POOR QUALITY

Gamma Curve (0.1)

MSE=11.26 MAE=1.86

G rms

Fig. 5 Probability Distribution

SP AVG(FUEL PUMP RAD 0, FUEL PUMP RAD 90)

SSME DIAGNOSTIC DATA BASE   POWER LEVEL= 100%

*=HPFP4105
#=HPFP5302--
+=HPFP2614--
X=HPFP6101
Z=HPFP9411--

S
y
n
c
h
r
o
n
o
u
s

G
R
M
S

AAAAAAAA AAAAAAAA AAAAAAA AAAAAA AAAAA
11111111 11111222 1113333 222222 32333
-------- -------- ------- ------ -----
55555555 55555444 4552222 444444 23222
22333233 22222222 9228889 222222 69888
89013742 42356678 5016790 301245 47345
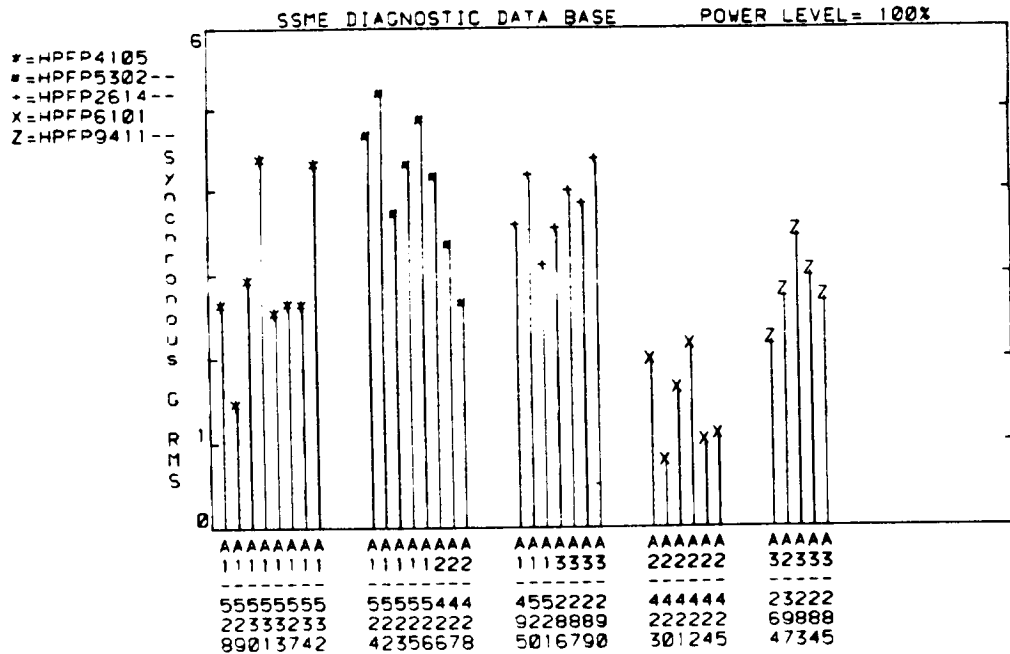
Fig. 6 Plot of RMS Amplitudes for Several Fuel Turbopumps

359

Exact Finite Element Method Analysis of Viscoelastic Tapered Structures to Transient Loads

Constantine Chris Spyrakos

N88-13632

A general method is presented for determining the dynamic torsional/axial response of linear structures composed of either tapered bars or shafts to transient excitations. The method consists of formulating and solving the dynamic problem in the Laplace transform domain by the finite element method and obtaining the response by a numerical inversion of the transformed solution. The derivation of the torsional and axial stiffness matrices is based on the exact solution of the transformed governing equation of motion, and it consequently leads to the exact solution of the problem. The solution permits treatment of the most practical cases of linear tapered bars and shafts, and employs modelling of structures with only one element per member which reduces the number of degrees of freedom involved. The effects of external viscous or internal viscoelastic damping are also taken into account.

INTRODUCTION

The static dynamic and stability analysis of nonuniform structures composed of tapered beams and/or bars has attracted considerable attention (Chu et. al. 1970; Kounadis 1975; Sato 1980). A thorough presentation of developments pertinent to the dynamic behavior of tapered beams/bars has been presented by Kolousek (1973). Lately, GangaRao and Spyrakos (1986) determined the static and dynamic response of tapered flexural/axial members through an analytical technique applicable to the wide class of initial-boundary value problems governed by linear differential operators with variable coefficients. Besides analytical methods restricted to limited cases due to the involved equations of motion and the associated conditions, numerical methods such as the Finite Difference Method (FDM) (Liable 1985) and especially the Finite Element Method (FEM), have been successfully employed (Gallagher et al. 1970; Rough et al. 1979). The FEM appears to be more popular than the FDM since it presents several organizational advantages and handles boundary conditions easier. Use of the FEM has been primarily based on the approximate lumped or consistent mass representation and on displacement functions which are solutions of the static governing equations (Beaufait et al. 1970; Gupta 1985). Tapered members are considered as an assembly of uniform elements with known stiffnesses which are super-imposed to construct the stiffness of the

PRECEDING PAGE BLANK NOT FILMED

member. This stepped representation requires a relatively large number of elements to accurately determine the dynamic response. In the case of linearly tapered members, an alternative approach would be the use of exact stiffness matrices developed from the solution of the static governing equation of axial/flexural deformation (Just 1977; Holzer 1986). Recently, Banerjee and Williams (1986) developed exact dynamic stiffness matrices for the axial, torsional, and flexural vibration of tapered beams to harmonically varying forces. The approximate as well as the exact stiffness matrices developed by Banerjee can be used in a conventional modal analysis formulation to provide the response of tapered structures. Such an analysis, however, requires prior determination of the natural frequencies and nodal shapes that can be obtained by solving the free vibration problem (Bathe 1982). Alternative highly accurate and efficient FEM formulations, based on transformed dynamic stiffness matrices, have been successfully employed by Spyrakos and Beskos, (1982) and Tamma et. al. (1987) for the dynamic analysis of frameworks modelled with uniform elements and subjected to general transient forces. In their analysis, the transformed dynamic stiffness matrices were developed through application of either Fourier or Laplace transform with respect to time on the equation of motion of a beam element. The structural response in the time domain is obtained from the transformed stiffness equation and a numerical inversion. Therefore, such an approach retains the advantages of the direct stiffness method eliminating the need for prior solution of an eigenvalue problem.

In this paper, the dynamic response of structures composed of tapered bars and shafts to transient axial and/or torsional forces is determined. The formulation considers the most practical cases of cross-sections and types of taper, and includes effects of both external viscous and internal viscoelastic damping. The analysis employs the FEM with dynamic stiffness matrices expressed in the Laplace transform domain. The derivation of the stiffness matrices is based on the exact solution of the axial or torsional tapered element governing equations expressed in terms of Bessel functions. Thus, modelling of the structure requires only one element per member which reduces the number of degrees of freedom involved and simplifies the modelling of the configuration. Furthermore, evaluation of the response from the stiffness equation leads to the "exact" solution of the problem. A numerical Laplace transform based on Durbin's algorithm (Durbin 1974) is then used to determine the structural response in the time domain. Durbin's algorithm was chosen since it allows an efficient and accurate direct and inverse numerical Laplace transform of general forcing functions (Beskos et al. 1983).

FORMULATION OF THE PROBLEM

Consider the general tapered bar element a-b with a straight centroidal axis and directions of the principal axes being the same for all cross sections as shown in Figure 1. The variation of the cross-sectional area A(x) and polar second moment of area J(x) may be represented as

$$A(x) = A_a \left(1 + r \frac{x}{L}\right)^m$$

and $\qquad$ (1)

$$J(x) = J_a (1 + r \frac{x}{L})^{m+2},$$

where L is the length of the element and A_a, J_a denote the values of the cross-sectional area and polar second moment of area, respectively, at the cross-section a in Figure 1. Given the geometrical properties of the element at the end sections (a and b), the positive constants r and m can be evaluated from the expressions

$$r = \left(\frac{A_a J_b}{A_b J_a} \right)^{1/2} - 1$$

and

$$m = 2 \ln\left(\frac{A_b}{A_a} \right) / \left(\ln \frac{J_b A_a}{J_a A_b} \right)^{-1} \qquad (2)$$
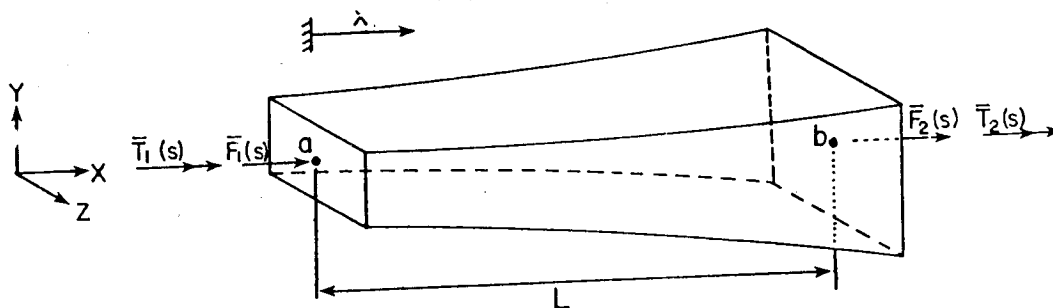
Figure 1. Geometry and sign convention of a general bar/shaft element

Even though the developments presented in the following sections are valid for any value of m from equation (2), special emphasis will be placed on the practical cases of linear taper with m=1 and m=2. The case of m=1 corresponds to rectangular and I-sections, while m=2 pertains to circular as well as I-sections (Gupta 1985).

Axial Vibration

The equation of motion for a small amplitude, free axial vibration of a linear elastic tapered bar (m=1) is

$$\frac{\partial}{\partial x} [EA(x) \frac{\partial u}{\partial x}] - \rho A(x) \frac{\partial^2 u}{\partial t^2} = 0, \qquad (3)$$

where $u = u(x,t)$ is the axial displacement of the bar and E, ρ are the modulus

of elasticity and the mass density of the bar, respectively. Expressing, $A(x)$ in terms of $\xi = 1 + r \frac{x}{L}$ equation (3) takes the form

363

$$\frac{\partial^2 u}{\partial \xi^2} + \frac{m}{\xi} \frac{\partial u}{\partial \xi} - \frac{\rho L^2}{Er^2} \frac{\partial^2 u}{\partial t^2} = 0 \qquad (4)$$

The Laplace transform $\bar{y}$ (s) of a function y(t) is defined by

$$\bar{y}(s) = \int_0^{\infty} y(t) \, e^{-st} dt \qquad (5)$$

where s is, in general, a complex number. Application of the Laplace transform with respect to time on equation (4), under the assumption of zero initial conditions, yields

$$\xi^2 \bar{u}'' + m \xi \bar{u}' - s^2 \frac{\rho L^2}{Er^2} \xi^2 \bar{u} = 0, \qquad (6)$$

where primes indicate differentiation with respect to the spatial variable ξ. The general solution of equation (6) can be obtained on the basis of the procedure indicated by Myers (1971). The resulting expression contains Bessel functions of the second kind with complex kernels which are not readily applicable for a concise development of an element stiffness matrix. Thus, after some algebraic manipulations and use of properties of Bessel functions (Abramovitz et al. 1965), one can arrive at the following concise form of the general solution:

$$\bar{u}(s) = \xi^k \{ C_1 I_k (\frac{sL}{r} (\frac{\rho}{E})^{1/2} \xi) + C_2 K_k (\frac{sL}{r} (\frac{\rho}{E})^{1/2} \xi) \}, \qquad (7)$$

where C_1 and C_2 are constants and $k = \frac{1-m}{2}$.

Adapting as positive directions of the nodal displacements and forces the ones shown in Figure 1, the evaluation of the axial stiffness matrix for the bar element a-b can be obtained by relating the axial displacements at the nodes a and b to the axial forces

$$\bar{F}_1(s) = -(EA_a \frac{r}{L}) \frac{d\bar{u}}{d\xi} \Big|_{\xi=1} \quad \text{and} \quad \bar{F}_2(s) = (EA_b \frac{r}{L}) \frac{d\bar{u}}{d\xi} \Big|_{\xi=1+r}$$

through the displacement function $\bar{u}(s)$ given by equation (7) (Spyrakos et al. 1982). An entry $\bar{k}_{ij}$, through Laplace transformed stiffness matrix, is defined as the transformed force at the ith degree of freedom due to a unit transformed displacement at the jth degree of freedom while all the other transformed displacements are zero. Thus, with the sign convention of Figure 1, the following element transformed nodal force-displacement relationship in terms of the dynamic stiffness influence coefficients $\bar{k}_{ij}$ coefficients can be obtained

$$\left\{ \begin{array}{c} \bar{F}_1(s) \\ \bar{F}_2(s) \end{array} \right\} = \left[\begin{array}{cc} \bar{k}_{11} & \bar{k}_{12} \\ \bar{k}_{21} & \bar{k}_{22} \end{array} \right] \left\{ \begin{array}{c} \bar{u}_1 \\ \bar{u}_2 \end{array} \right\}, \qquad (8)$$

where

$$\bar{k}_{11} = -H \{ I_k(b) K_n(a) + I_n(a) K_k(b) \}$$

$$\bar{k}_{12} = \bar{k}_{21} = \frac{H}{a(1+r)^k} \qquad (9)$$

$$\bar{k}_{22} = -H (1+r)^m \{ I_n(b) K_k(a) + I_k(a) K_n(b) \}$$

with A, a, b and n given by

$$n = -\frac{1}{2}(1+m), \quad H = \frac{EA_a}{B} s(\rho/E)^{1/2}, \quad a = \frac{sL}{r}(\rho/E)^{1/2}$$

$$b = (1+r)a, \quad B = I_k(a) K_k(b) - I_k(b) K_k(a) \qquad (10)$$

For the case $m = 2$, the stiffness influence coefficients can be expressed in terms of hyperbolic functions through the relationships (Abramovitz et al. 1965)

$$I_{-1/2}(z) = (2/\pi z)^{1/2} \cosh z$$

$$K_{-1/2}(z) = e^{-z}(\pi/2z)^{1/2} \qquad (11)$$

Thus, after some computational effort, equations (9) take the form

$$\bar{k}_{11} = -\bar{H} \{ \cosh(ar) + a^{-1} \sinh(ar) \}$$

$$\bar{k}_{12} = \bar{K}_{21} = \bar{H}(1+r) \qquad (12)$$

$$\bar{k}_{22} = -\bar{H}(1+r)^2 \{ \cosh(ar) - b^{-1}\sinh(ar) \},$$

where

$$\bar{H} = \frac{EA_a}{\bar{B}} s(\rho/E)^{1/2} \text{ and } \bar{B} = -\sinh^{-1}(ar) \qquad (13)$$

It should be noted that the dynamic stiffness influence coefficients $\bar{D}_{ij}$

presented by Beskos and Narayanan (1983) for a uniform bar element can be easily deduced from equations (12) and (13) for a=b and r tending to zero.

Torsional Vibration

The equation of motion for free tortional vibration of a linear elastic tapered shaft with circular cross-sections is

$$\frac{\partial}{\partial x}\{ GCJ(x) \frac{\partial \phi}{\partial x} \} - \rho J(x) \frac{\partial^2 \phi}{\partial t^2} = 0, \qquad (14)$$

365

where $\phi(x,t)$ is the angular displacement, G is the shear modulus, and C, which is equal to one for circular cross-sections represents the torsional rigidity of the cross-section. When C is given appropriate values, equation (14) can also be utilized to approximate the torsional response of a number of other cross-sections. Substituting $J(x)$ given by equation (2) and expressing x in terms of ξ, equation (14) results

$$\frac{\partial^2 \phi}{\partial \xi^2} + \frac{m+2}{\xi} \frac{\partial \phi}{\partial \xi} - \frac{\rho L^2}{CGr^2} \frac{\partial^2 \phi}{\partial t^2} = 0 \qquad (15)$$

Application of Laplace transform on equation (15) leads to

$$\xi^2 \overline{\phi}'' + (m+2) \xi \overline{\phi}' - s^2 \frac{\rho L^2}{CGr^2} \xi^2 \overline{\phi} = 0 \qquad (16)$$

Observing the similarity between the equations of motion (6) and (16) and following the procedure employed for the treatment of the axial vibration, one can obtain the tortional stiffness equation

$$\begin{bmatrix} \overline{T}_1(s) \\ \overline{T}_2(s) \end{bmatrix} = \begin{bmatrix} \overline{k}_{11} & \overline{k}_{12} \\ \overline{k}_{21} & \overline{k}_{22} \end{bmatrix} \begin{Bmatrix} \overline{\phi}_1 \\ \overline{\phi}_2 \end{Bmatrix} , \qquad (17)$$

where the dynamic stiffness influence coefficients $\overline{k}_{ij}$ can be determined from equation (9) by replacing the variables m, a, b and H with ℓ, α, β and D, respectively, given by

$$\ell = m+2, \quad \alpha = \frac{sL}{r} \left(\frac{\rho}{CG} \right)^{1/2}$$

$$\beta = (1+r)\alpha, \quad D = CGJ_a \ s \left(\frac{\rho}{CG} \right)^{1/2} /B \qquad (18)$$

The positive directions of the nodal torsions and angular displacements are depicted in Figure 1.

For the case $m = 2$, the dynamic stiffness influence coefficients $\overline{k}_{ij}$ can be expressed in terms of hyperbolic functions with the aid of expressions (11). Thus,

$$\overline{k}_{11} = - \overline{D} \{ \sinh(\alpha r) [\frac{3}{\alpha} - \frac{1}{\beta} - \frac{3}{\alpha^2 \beta}] + \cosh(\alpha r) [1 + \frac{3}{\alpha^2} - \frac{3}{\alpha \beta}] \}$$

$$\bar{k}_{12} = \bar{D} (1 + r)^2 \tag{19}$$

$$\bar{k}_{22} = -\bar{D} (1 + r)^4 \{ \sinh(\alpha r) [\frac{1}{\alpha} - \frac{3}{\beta} + \frac{3}{\alpha \beta^2}] + \cosh(\alpha r) [1 - \frac{3}{\beta^2} - \frac{3}{\alpha \beta}] \},$$

where

$$\bar{D} = \frac{CGJ_a}{(\rho/CG)^{1/2}} [(\frac{1}{\alpha \beta} - 1) \sinh(\alpha r) - \frac{r}{\beta} \cosh(\alpha r)] \tag{20}$$

It is of interest to note that the torsional dynamic stiffness influence coefficient $\bar{D}_{ij}$, which are presented by Beskos et al. (1983) for a uniform element, can be deduced as a particular case of the $\bar{k}_{ij}$ given by equation (19) for $\alpha = \beta$ and r tending to zero.

EFFECT OF DAMPING

Both internal and external viscous damping can be accounted for by the transformed dynamic stiffness influence coefficients. For reasons of simplicity, the material of the bar is assumed to be a Kelvin solid obeying the constitutive law (Flugge 1967)

$$\sigma = W (\varepsilon + f \frac{d\varepsilon}{dt}), \tag{21}$$

where σ is the stress, ε is the strain, W represents either the modulus of elasticity E or the shear modulus G, and f is the damping coefficient. Equation (21) in the Laplane transform domain takes the form

$$\bar{\sigma} = W (1 + fs) \bar{\varepsilon} \tag{22}$$

which implies that internal viscous damping can be considered by replacing W with W(1+fs) in equations (6) and (15), respectively.

When external viscous damping is present, the additional damping force, R, is introduced in the equations of motion. Denoting with c the coefficient of damping, R can be expressed as

$$R = -c \frac{du}{dt} \tag{23}$$

Application of Laplace transform on equation (17) yields

$$\bar{R} = -cs\bar{u} \tag{24}$$

Expressions (22) and (24) indicate that equations (8) and (17) can account for combined external viscous and internal viscoelastic damping by replacing the variables a and α with a and α , respectively, where

$$a = \frac{sL}{r} \left(\frac{\rho}{E(1+fs)} \right)^{1/2} + cs \quad , \quad \alpha = \frac{sL}{r} \left(\frac{\rho}{CG(1+fs)} \right)^{1/2} + cs \tag{25}$$

In contrast to the conventional way of accounting for damping as a percentage of the critical damping either in a mode superposition analysis or in a direct integration procedure, the present formulation allows the assignment of different damping properties for each individual structural member. As a result, the dynamic behavior of linear structures can be efficiently simulated in a more rational way.

FORMULATION OF THE PROBLEM

Once the dynamic stiffness coefficients are defined, the dynamic problem of a bar/shaft can be formulated in the following static-like form in the Laplace transform domain

$$\{\bar{F}(s)\} = [\bar{k}(s)] \{\bar{u}(s)\}, \tag{26}$$

where $\{\bar{F}(s)\}$ and $\{\bar{u}(s)\}$ represent the Laplace transformed axial/torsional dynamic load and displacement vectors, respectively. After the transformed boundary conditions are applied, $\{\bar{u}(s)\}$ can be obtained from equation (26) by a matrix inversion of the dynamic stiffness matrix for a sequence of values of s. Then the response $\{u(t)\}$ in the time domain can be determined by a numerical inversion of the Laplace transformed displacement vector. The response $\{u(t)\}$ is the exact solution of the dynamic problem, since the dynamic stiffness matrices have been developed from the exact solutions of the transformed equations of motion.

The numerical algorithm adopted herein to invert the transformed response has been developed by Durbin (1974). It combines both finite Fourier cosine and sine transforms and operates with complex values of s. Thus, it is more time consuming than other algorithms operating with real data. Nevertheless, Durbin's algorithm has been chosen since it provides higher accuracy than real data algorithms, a feature which is crucial in dynamic problems involving excitations of a transient time variation.

The above formulation is based on the assumption of zero initial conditions. However, consideration of non-zero initial conditions does not present any difficulty. In this case, the Laplace transform of equation (4) yields

$$\xi^2 \bar{u}'' + m \xi \bar{u}' - \xi^2 \frac{\rho L^2}{Er^2} s^2 \bar{u} = \bar{q} (x,s),$$

$$\bar{q} (x,s) = - \frac{\rho L^2}{Er^2} \xi^2 [s u(x,o) + \dot{u}(x,o)], \tag{27}$$

where u(x,o) and u(x,o) are the initial axial displacement and velocity of the axial element, respectively. Thus, the initial conditions in the Laplace transform domain can be represented by a load distributed along the length of the element. The distributed load can be converted to a vector of equivalent nodal forces $\{\overline{f}_i(s)\}$, i = 1,2, through standard finite element procedures (Davies 1980).

NUMERICAL EXAMPLES

This section presents the solutions of numerical examples in order to illustrate the method and demonstrate its merits. The numerical computations where performed on a IBM 3081-D computer.

EXAMPLE 1

Consider the structural system in figure 2 which consists of one tapered and one uniform bar with rectangular cross-sections having a constant width b. The numerical data pertaining to this system is L = 10 in (25.4 cm), b = 1.0 in (2.54
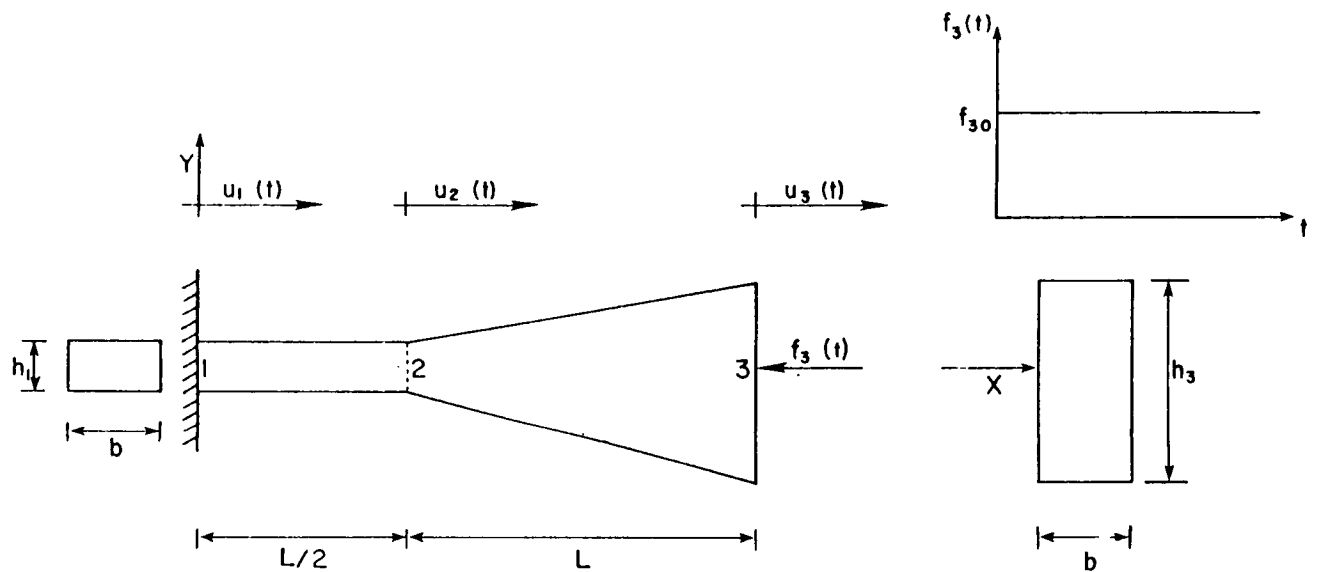
Fig. 2 Geometry and loading of the structural system of example 1

cm), h_1 = h_2 = 0.5 in (1.27 cm), h_3 = 2.5 in (6.35 cm), ρ = 0.002 lb-sec^2/in^4 (0.0214 kg/cm^3), E = 10^7 lb/in^2 (6.89x10^5 N/mm^2), and f_{30} = 10^6 lb (4.448x10^6 N). The values of the subscript i = 1,2,3 denote the element nodes as shown in figure 2. With the aid of the k_{ij} and the dynamic stiffness influence coefficients for a uniform bar (Beskos et al, 1983), $\overline{D}_{ij}$, the equilibrium equations in the frequency domain can be written in the form

$$\left\{ \begin{array}{c} \bar{f}_1(s) \\ 0 \\ -\bar{f}_3(s) \end{array} \right\} = \left[\begin{array}{ccc} \bar{D}_{11} & \bar{D}_{12} & 0 \\ \bar{D}_{21} & \bar{D}_{22} + \bar{K}_{22} & \bar{K}_{12} \\ 0 & \bar{K}_{21} & \bar{K}_{22} \end{array} \right] \left\{ \begin{array}{c} 0 \\ \bar{u}_2(s) \\ \bar{u}_3(s) \end{array} \right\} \qquad (28)$$

Equation (29) solved for $\bar{u}_3(s)$ yields

$$\bar{u}_3(s) = -\bar{f}_3(s) \, [\bar{K}_{22} - \frac{(\bar{K}_{12})^2}{\bar{K}_{11} + \bar{D}_{22}} \,]^{-1} \, , \qquad (29)$$

where

$$\bar{D}_{22} = h_1 bEw/tanh \quad \frac{wL}{2} \qquad (30)$$

with $\quad w = \dfrac{\rho s^2}{E}^{1/2}$

Evaluation of the Bessel functions appearing in the $\bar{k}_{ij}$ stiffness coefficients involve complex kernels with s ranging from very small to very large arguments. Thus, accurate evaluation of the $\bar{k}_{ij}$ requires use of appropriate assymptotic expansions of the modified Bessel functions $I_k(s)$ and $K_k(s)$ (Watson 1966).

The response $u_3(t)$ in the time domain is obtained by a numerical inversion using Durbin's algorithm and is plotted in figure 3. The total CPU time, including the formulation of equation (28), was only 0.14 secs. In order to establish the accuracy of the method, the $u_3(t)$ is also determined by the NASTRAN computer code using a mesh of twenty equal elements for the tapered bar and ten for the uniform member. The total CPU time required by NASTRAN was 26.87 secs. The present method required considerably less CPU time than NASTRAN, since it modelled the structure with one element per member. As shown in figure 3 the results obtained by NASTRAN and the present method are almost identical.
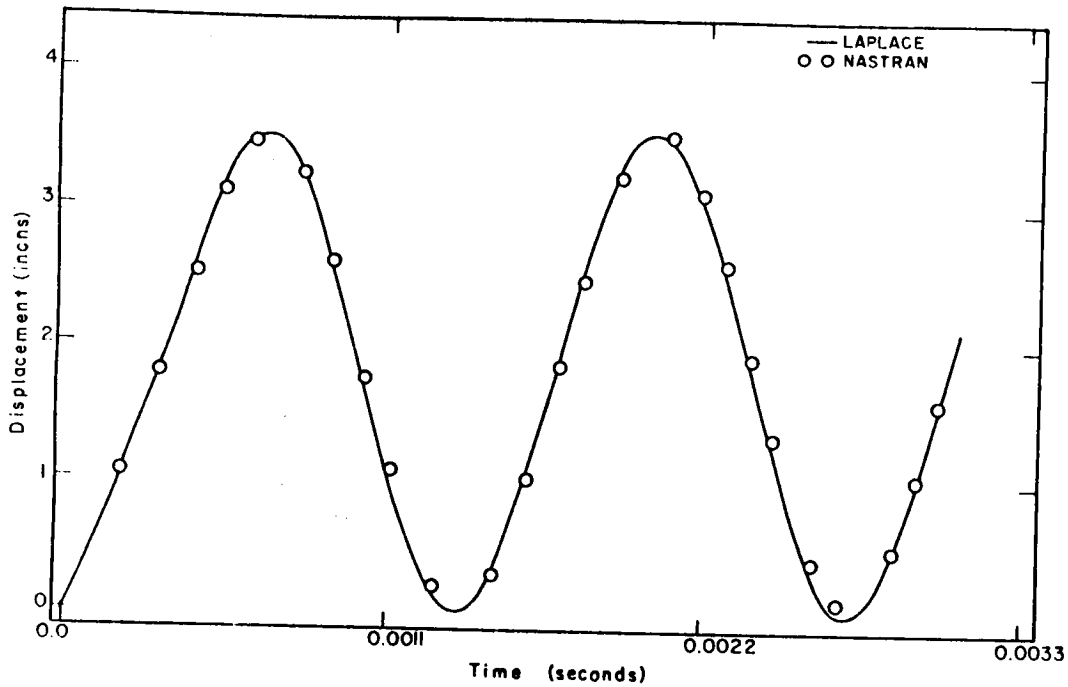
Fig. 3 Axial response $u_3(t)$ vs time of example 1

EXAMPLE 2

Consider the structural system of figure 4 that is composed of one tapered and one uniform shaft with circular cross-sections and subjected to a concentrated step torque of magnitude $T_{30} = 10^6$ lb-in (11.29×10^6 N-cm). The geometry of the structure is described by the parameters $L = 10$ in (25.4 cm), $R_1 = R_2 = 0.3989$ in (1.013 cm), $R_3 = 0.8921$ in (2.266 cm), $q = 0.002$ lb-sec^2/in^4 (0.0214 kg/cm^3) and $E = 10^7$ lb/in^2 (6.89×10^5 N/mm^2). The torque $-\bar{T}_3(s)$ acting at node 3 causes the torsional deformation $\bar{\Phi}_3(s)$ which can be evaluating from

$$\bar{\Phi}_3(s) = -\bar{T}_3(s) \left[\bar{K}_{22} - \frac{(\bar{K}_{12})^2}{\bar{K}_{11} + \bar{D}_{22}} \right]^{-1} , \qquad (31)$$

where

$$\bar{D}_{22} = J_1 \quad GW \, [\tanh \, (\frac{WL}{2})]^{-1} \qquad (32)$$

with

$$W = \frac{\rho s^2}{2\pi R_1^2 G}^{1/2}$$

371
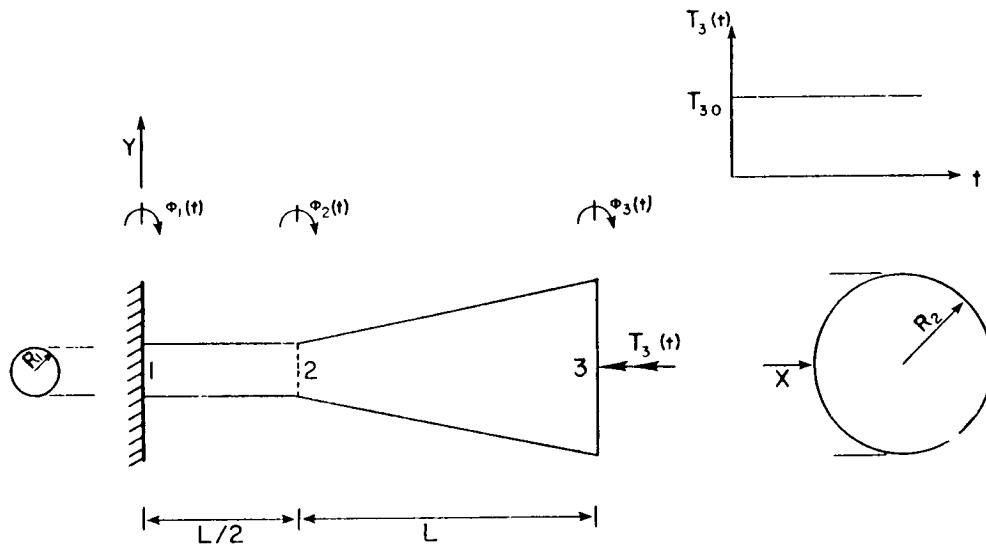
Fig. 4 Geometry and loading of the structural system of
         example 2

In equations (32) the subscript 1 pertains to node 1 of the uniform shaft element.   Figure 5 shows the angular response $\Phi_3(t)$ in the time domain obtained by numerical inversion of $\bar{\Phi}_3(s)$.   The same figure also portrays results obtained by NASTRAN for a discretization of forty elements for the tapered shaft and ten for the uniform member.   The total CPU time required by NASTRAN was 38.23 secs, while the present method required only 0.09 secs. Evaluation of the angular response $\Phi_3(t)$ by the present method required less computational time than the evaluation of the axial response $u_3(t)$ in the first example.   This can be primarily attributed to the functional form of the $\bar{k}_{ij}$ and $\bar{k}_{ij}$ stiffness coefficients of equations (29) and (31), respectively.   The former are expressed in terms of Bessel functions, while the latter consists of hyperbolic functions.   It should be mentioned that results obtained by NASTRAN for a twenty element discretization of the tapered member did not provide sufficient accuracy.
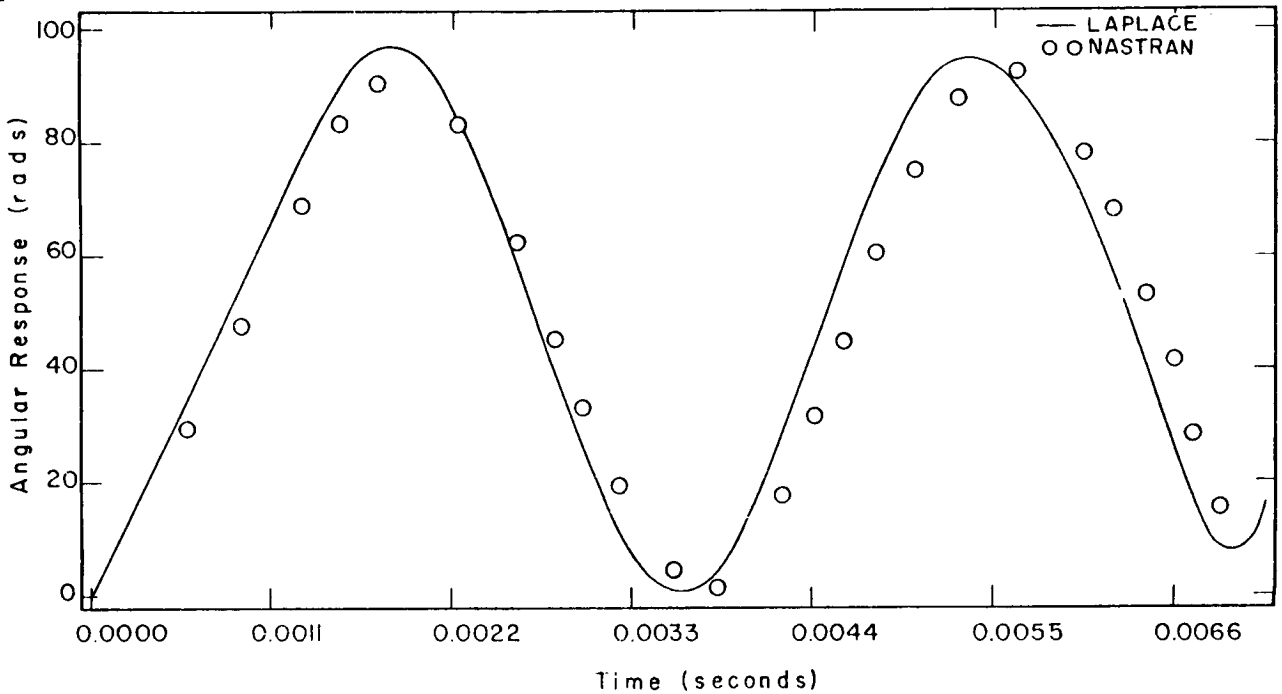
Fig. 5 Angular response $\Phi_3(t)$ vs time of example 2

CONCLUSIONS

In this work, the exact dynamic stiffness matrices of viscoelastic tapered bar and shaft elements are developed. These matrices can be incorporated in a finite element formulation to determine the response of structural systems to dynamic forces of a transient time variation. The formulation is performed in the Laplace transform domain resulting in a static-like relationship between the force and displacement vectors. The dynamic response is then obtained in the frequency domain numerically, and is subsequently evaluated in the time domain by a numerical inversion. Although the geometries and loading of the example problems presented are simple, the present method is general and applies to complicated situations.

Within the realm of assumptions and limitations of linear theories, the $\bar{k}_{ij}$ and $\bar{k}_{ij}$ dynamic stiffness coefficients lead to the "exact" solution of the problem, since they have been developed from the exact solutions of the transformed equations of motion. Thus, results obtained by the present method can be used to compare the accuracy of other numerical methods such as conventional finite element and finite differences methods.

Use of the $\bar{k}_{ij}$ and $\bar{k}_{ij}$ coefficients accounts for the inertia and stiffness properties of the system members accurately, through a modelling that requires only one element per member. This is a significant advantage of the proposed method over conventional finite element methods employing a lumped or a consistent mass representation. Further, the method does not require the evaluation of nodal shapes or eigenvectors. Any inaccuracy of results can be primarily attributed to the accuracy of the numerical inversion algorithm used.

The $\bar{k}_{ij}$ and $\bar{k}_{ij}$ coefficients permit consideration of different levels of external or internal viscoelastic damping at each one of the axial/torsional members, the supports and the joints. Thus, one can control the response through a more rational estimation of the damping attributed to the individual structural members.

REFERENCES

Abramowitz, M., and Stegan, I.E. (1965). Handbook of Mathematical Functions National Bureau of Standards, Washington, D.C.

Banerjee, J.R., and Williams R.W. (1986). "Exact Bernouli-Euler Dynamic Stiffness Matrix for a Range of Tapered Beams." International Journal for Numerical Methods in Engineering, Vol. 21, 2289-2302.

Bathe, K.J. (1982). Finite Element Procedures in Engineering Analysis. Prentice Hall, New Jersey.

Beaufait, F.W., Rowan, W.H. Hoadley, P.G., and Hackett, R.M. (1970) Computer Methods of Structural Analysis. Prentice Hall, New Jersey.

Beskos, D.E., and Narayanan, G.V. (1983). "Dynamic Response of Frameworks by Numerical Laplace Transform." Computer Methods in Applied Mechanics and Engineering, Vol. 37, 289-307.

Chu, F.H., and Pilkey, W.D. (1979). "Transient Analysis of Structural Members by the CSDT Riccati Transfer Matrix Method." Computers and Structures, Vol. 10, 599-611.

Davies, A.J. (1980). The Finite Element Method: A First Approach. Oxford University Press, London.

Durbin, F. (1974). "Numerical Inversion of Laplace Transform: An Efficient Improvement of Dudner and Abate's Method." The Computer Journal, Vol. 17, 371-376.

Flugge, W. (1967). Viscoelasticity. Blonsdell Publishing Company, Massachusetts.

Gallager, R.H., and Lee, C.H. (1970). "Static Dynamic and Stability Analysis with Non-Uniform Elements." International Journal for Numerical Methods in Engineering, Vol. 2, 265-275.

GangaRao, H.V.S., and Spyrakos, C.C. (1986). "Closed Form Series Solutions of Boundary Value Problems with Variable Properties." Computers and Structures, Vol. 23, No. 2, 211-215.

Gupta, A.K. (1985). "Vibration of Tapered Beams." Journal of the Engineering Mechanics Division, ASCE, Vol. 111, 19-36.

Holzer, S.M. (1985). Computer Analysis of Structures: Elsevier, New York.

Just, D.J. (1977). "Plane Frameworks of Tapering Box and I-section." Journal of the Structural Division, ASCE, Bol. 103, 71-86.
Kolonsek, V. (1973). Dynamics in Engineering Structures. Butterworths, London.

Kounadis, A.N. (1975). "Beam Columns of Varying Cross-section Under Lateral Harmonic Loads." Ingenieur-Archiv., Vol. 44, 43-51.

Liable, J.P. (1985). Structural Analysis. CBS College Publishing, New York.

Myers, J.E. (1971). Analytical Methods in Conduction Heat Transfer. McGraw-Hill, New York.

Rough, K.E., and Kao, J.S. (1979). "A Tapered Beam Finite Element for Rotor Dynamics." Journal of Sound and Vibration, Vol. 66, 119-149.

Sato, K. (1980). "Transverse Vibrations of Linearly Tapered Beams with Ends Restrained Elastically Against Rotation Subjected to Axial Force." International Journal of Mechanical Science, Vol. 22, 109-115.

Spyrakos, C.C., and Beskos, D.E. (1982). "Dynamic Response of Frameworks by Numerical Laplace Transform." Computers and Structures, Vol. 15, 495-505.

Tamma, K.K., Spyrakos, C.C., (1987) and Lambi, M.A. (1987). "Thermal/Structural Dynamic Analysis via a Transform Method Based Finite Element Approach." Journal of Spacecrafts and Rockets, AIAA, Vol. 24, No. 3, 219-226.

Watson, G.N. (1966). A Treatice on the Theory of Bessel Functions. Cambridge University Press, London.

ISOLATION AND DAMPING

Optimal Shock Isolation with Minimum Settling Time

W. D. Pilkey
T. W. Lim

N88-13633

The computationally-determined limiting performance of shock isolation systems has been a useful tool in providing characteristics of optimal shock isolation. The limiting performance is defined as the minimum peak value of certain responses while other system responses are constrained. As is the case with most optimization problems, the "trajectory" in reaching the minimum performance index (peak response values) is unique, as is the minimum performance index itself. However, the responses of the system after the minimum performance index is achieved are not single-valued. This paper shows how unique isolator forces and corresponding responses can be chosen by superimposing a minimum settling time onto the limiting performance of the shock isolation system. Basically, this means that the system which has reached the peak value of the performance index is "settled" to rest in minimum time.

INTRODUCTION

The limiting performance of a system is its absolute optimal response characteristics. It is computed by replacing those portions of a system being designed by active generic isolator forces. These isolator forces are then obtained so as to minimize a given performance index while typically satisfying bounding constraints on response variables or isolator force magnitudes. Since isolator forces are not restricted to represent any particular design elements during the optimization procedure, the resulting limiting performance response is optimal over all possible design configurations. No conditions are placed on the number or type of elements which are replaced by isolators; they may be active, pasive, or nonlinear. For the class of problems treated in this paper, the performance index and the constraints are linear combinations of system response variables and isolator forces. Also, the equations of motion are linear, so that it is possible to formulate the optimization procedure as a linear programming problem.

The limiting performance may be illustrated graphically by plotting the performance versus a constraint bound. If the performance index is chosen to minimize the maxmum response of a system subject to a prescribed constraint, the resulting tradeoff curve depicted in Fig. 1 gives the limiting performance of the system. The limiting performance charateristics are of considerable value to the mechanical system designer. First of all, they indicate from the design specifications alone whether a proposed design is feasible. Second, during the design cycle, they provide a measure of the success of the design configurations under consideration. Reference [1] describes limiting performance as applied shock isolation systems. Steady state systems [2], techniques for using general purpose

PRECEDING PAGE BLANK NOT FILMED

structural analysis computer programs to generate the equations of motion for limiting performance studies [3], and the use of limiting performance characteristics in identifying the optimum design of suspension systems for rotating shafts [4] have been treated.
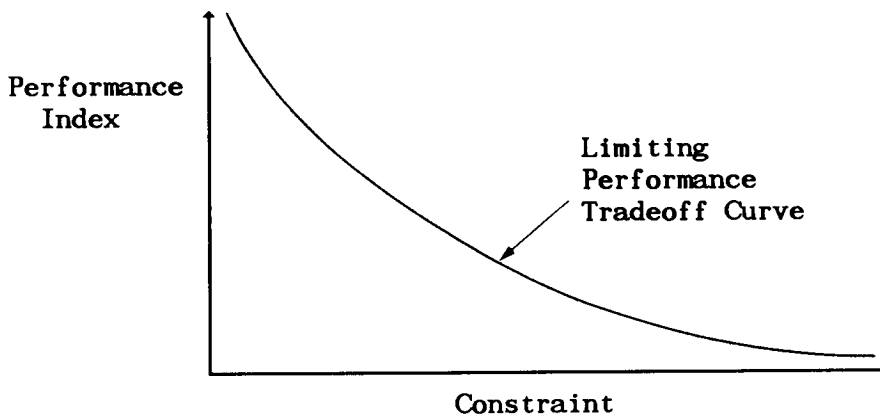
Fig. 1 Limiting Performance Characteristics

Although the limiting performance provides useful information, it has been noticed that the min-max norm of the limiting performance gives a unique solution only until the peak value of the performance index is achieved. A non-unique solution occurs after the peak value. For the tradeoff studies, the response after the peak is of little importance as long as the unique performance index is obtained. However, rapid settling of the disturbed system due to the external disturbance is often desired. Therefore, it is necessary to impose an additional measure of performance to obtain a unique solution after the peak value of the performance index is achieved. The response after the peak is selected to achieve the minimum settling time. Two different approaches can be used to achieve this goal [5]. This paper deals with the formulation using the performance index and its application to the shock isolation problems.

PROBLEM STATEMENT

A linear vibrating system with n degrees of freedom subject to arbitrary external excitations $\underline{f}(t)$ and isolator forces $\underline{u}(t)$ is expressed in the first order system of differential equations

$$\underline{s}(t) = A\underline{s}(t) + B\underline{u}(t) + C\underline{f}(t) \tag{1}$$

where $\underline{s}(t)$ is an n-dimensional state vector and A, B, and C are n x n, n x nu and n x nf constant coefficient matrices. The quantities nu and nf are the number of isolator forces and excitations, respectively. Constraints are imposed on the dynamic system under study. The format of the constraints is

$$\underline{y}_L \leq Q_1\underline{s} + Q_2\underline{u} + Q_3\underline{f} \leq \underline{y}_U \qquad \text{for } t_o \leq t \leq t_f \tag{2}$$

where $\underline{y}_L$ and $\underline{y}_U$ are nc-dimensional lower and upper constraint vectors; Q_1, Q_2, and Q_3 are nc x n, nc x nu, and nc x nf constant coefficient matrices; and t_o and t_f

380

are the given initial and final times.

The problem is to find an optimal isolator force $\underline{u}(t)$ which will transfer an initial state $\underline{s}(t_o) = \underline{s}_o$ to a desired final state $\underline{s}(t_f) = \underline{s}_f$ in the minimum time while extremizing a given performance index of the form

$$\text{Minimize } J = \{t_o \overset{\max}{\leq} t \leq t_f | \underline{p}_1^T \underline{s} + \underline{p}_2^T \underline{u} + \underline{p}_3^T \underline{f} | \} \tag{3}$$

where $\underline{p}_1$, $\underline{p}_2$, and $\underline{p}_3$ are given n, nu, and nf constant coefficient vectors. Since the min-max norm of the limiting performance gives a unique solution only until the peak value of the performance index is achieved, an additional measure of performance is desired to obtain a unique solution after the peak value. The resulting unique solution is referred to as limiting-performance/minimum-time (LP/MT) solution.

LINEAR PROGRAMMING FORMULATION

To obtain the LP/MT solution, the performance index given in Eq. (3) is modified. Two sets of performance indices are considered. One set of them, referred to as the transient performance index, is given by

$$J_t = t_o \overset{\max}{\leq} t < t_t | \underline{p}_1^T \underline{s} + \underline{p}_2^T \underline{u} + \underline{p}_3^T \underline{f} | \tag{4}$$

where t_t is the time limit for the transient period. The other set, referred to as the steady-state performance index is defined as

$$J_s = t_t \leq t \leq t_f | \underline{p}_1^T \underline{s} + \underline{p}_2^T \underline{u} + \underline{p}_3^T \underline{f} | \tag{5}$$

Now, the "global" performance index is defined by

$$J = J_t + J_s \tag{6}$$

Note that the vectors $\underline{p}_1$, $\underline{p}_2$, and $\underline{p}_3$ are not changed in Eqs. (4) and (5).

To place the optimization procedure into the standard linear programming form, the system in Eq. (1) is discretized using uniform time intervals to obtain a set of state difference equations

$$\underline{s}(k+1) = G\underline{s}(k) + H[B\underline{u}(k) + C\underline{f}(k)] \tag{7}$$

where $\underline{s}(k)$ = state vector at time $t = t_k$

$\underline{u}(k)$, $\underline{f}(k)$ = isolator force and external excitation vector at $t = t_k$, assumed to be constant over the interval $t_k \leq t < t_{k+1}$

$G = e^{Ah}$

$H = \int_o^h e^{A(h-\tau)} d\tau$

$$h = \text{time step} = t_{k+1} - t_k \quad (k=1, 2, \ldots, N-1)$$

The state vector, at any time $t = t_k$, can be expressed as a function of the initial state $\underline{s}(1)$ and the isolator force history $\underline{u}(1), \underline{u}(2), \ldots, \underline{u}(N-1)$ and the external excitation $\underline{f}(1), \underline{f}(2), \ldots, f(N-1)$. For $k = 1, 2, \ldots, N-1$

$$\underline{s}(k+1) = G^k \underline{s}(1) + \sum_{j=1}^{k-1} G^{k-j} H[B\underline{u}(j) + C\underline{f}(j)] + H[B\underline{u}(k) + C\underline{f}(k)] \qquad (8)$$

The constraints in Eq. (2) are discretized similarly

$$\underline{y}_L(k) \leq Q_1 \underline{s}(k) + Q_2 \underline{u}(k) + Q_3 \underline{f}(k) \leq \underline{y}_U(k) \quad \text{for } k = 1, 2, \ldots, N-1 \qquad (9)$$

The objective functions of Eqs. (4) and (5), which reflect the min-max norm, are discretized and converted into a constraint set. Since J_t is the maximum value of $|p_1^T \underline{s} + p_2^T \underline{u} + p_3^T \underline{f}|$ for $t_o \leq t < t_t$ and so is J_s for $t_t \leq t \leq t_f$.

$$|p_1^T \underline{s}(k) + p_2^T \underline{u}(k) + p_3^T \underline{f}(k)| \leq J_t \quad \text{for } t_o \leq t < t_t$$

$$|p_1^T \underline{s}(k) + p_2^T \underline{u}(k) + p_3^T \underline{f}(k)| \leq J_s \quad \text{for } t_t \leq t \leq t_f \qquad (10)$$

To place this optimization problem into a standard linear programming form, define

$$\underline{z} = \begin{bmatrix} J_t \\ J_s \\ \underline{u} \end{bmatrix} \qquad (11)$$

where $\underline{u} = [\; \underline{u}(1)^T \; \underline{u}(2)^T \; \ldots \; \underline{u}(N-1)^T \;]^T$ \qquad (12)

and

$$\underline{c}^T = [\; 1 \quad 1 \quad 0 \; \ldots \; 0 \;] \qquad (13)$$

Then the linear programming problem is to minimize

$$J = \underline{c}^T \underline{z} \qquad (14)$$

subject to the constraints

$$H\underline{z} \leq \underline{b} \qquad (15)$$

where H and $\underline{b}$ represent constraints of Eqs. (9) and (10).

The minimum time (t_{min}) is the smallest time which will make the global performance index of Eq. (6) stay within a desired value. Since the performance index can be computed for each iteration, an interpolation method such as the

secant method or simple bisection method [6] can be employed to find t_{min} efficiently.

NUMERICAL EXAMPLES

Example 1: A Single DOF System Subject to a Shock Velwave

A single degree-of-freedom (DOF) system composed of a mass m and supporting structure (Fig. 1) is subject to the horizontal shock velwave of Fig. 2.
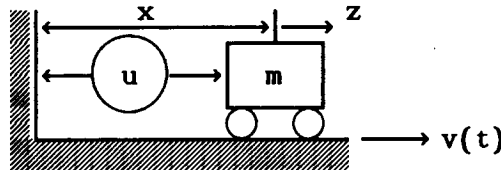
Fig. 1 A Single DOF Syatem
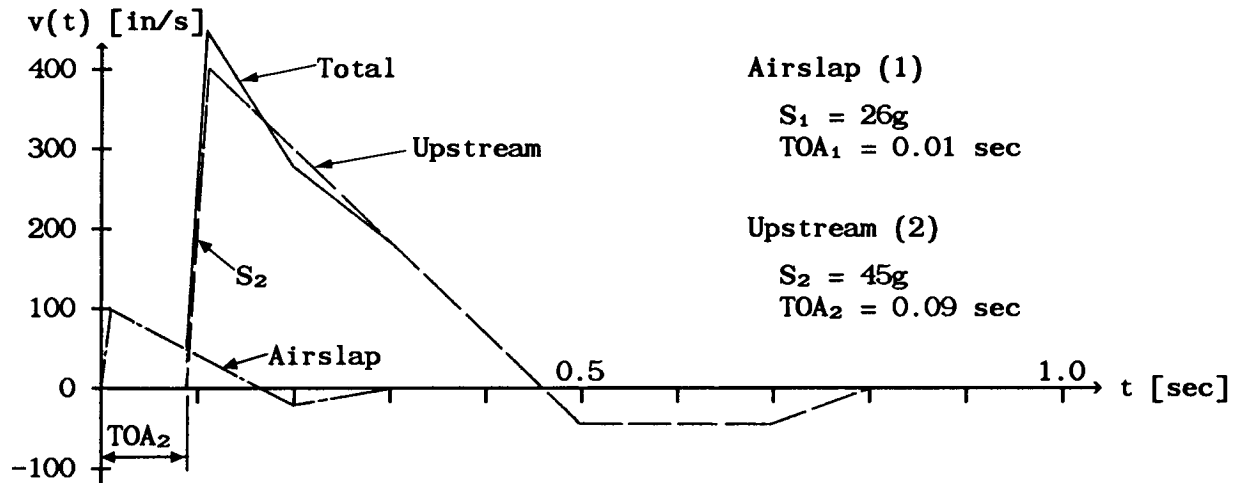
Note: Slope (S), Time of Arrival (TOA), and Total = 1 + 2

Fig. 2 Shock Velwave

Suppose the acceleration of the mass is to be limited to 15g (g = acceleration of gravity). The optimal isolator force $u^*(t)$ which minimizes the rattlespace between the mass and the supporting structure is desired.

The equation of motion is

$$\ddot{z} = u/m = U \tag{16}$$

The system is assumed to be at rest initially. The performance index to be minimized is

$$\max |z - y| \tag{17}$$

383

where

$$y = \int_{t_o}^{t_f} v(t) \, dt \tag{18}$$

and the constraint on the peak acceleration would be

$$|\ddot{z}| \leq 15g \tag{19}$$

Define a state vector

$$\underline{s} = [\ z \ \ \dot{z} \ \ y\ ]^T \tag{20}$$

The problem can now be transformed into the standard LP/MT isolator problem format described previously. The optimal isolator is sought, which will reduce the disturbed rattlespace to zero in minimum time while minimizing the performance index and satisfying the constraints. The resulting time responses are shown in Fig. 4. The performance index is 0.914 in and the minimum time is 0.17 sec.

Example 2: Two DOF Model of a Flexible Package Structure

A two mass model of a flexible package structure with a rigid base is shown in Fig. 5.
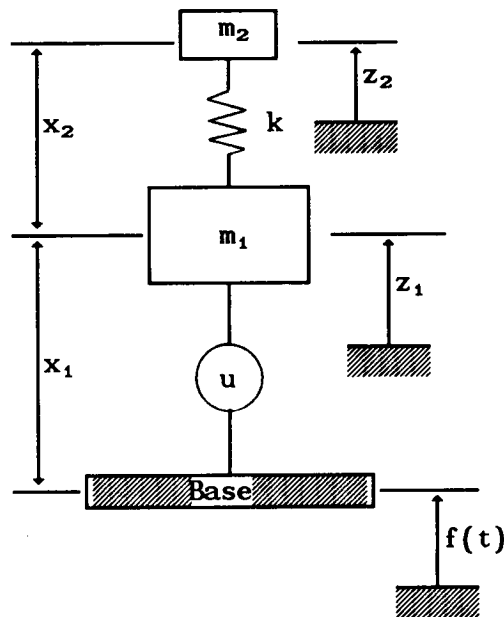
Fig. 5 Two DOF Flexible Package Model

The base is subject to external displacement which is described by

$$f(t) = 12t^2 e^{-t} \ \text{[in]} \tag{21}$$

The optimal isolator force is sought which will reduce the absolute displacement of

m_2 (z_2) within 5% of the peak value of the external disturbance $f(t)$ in minimum time.
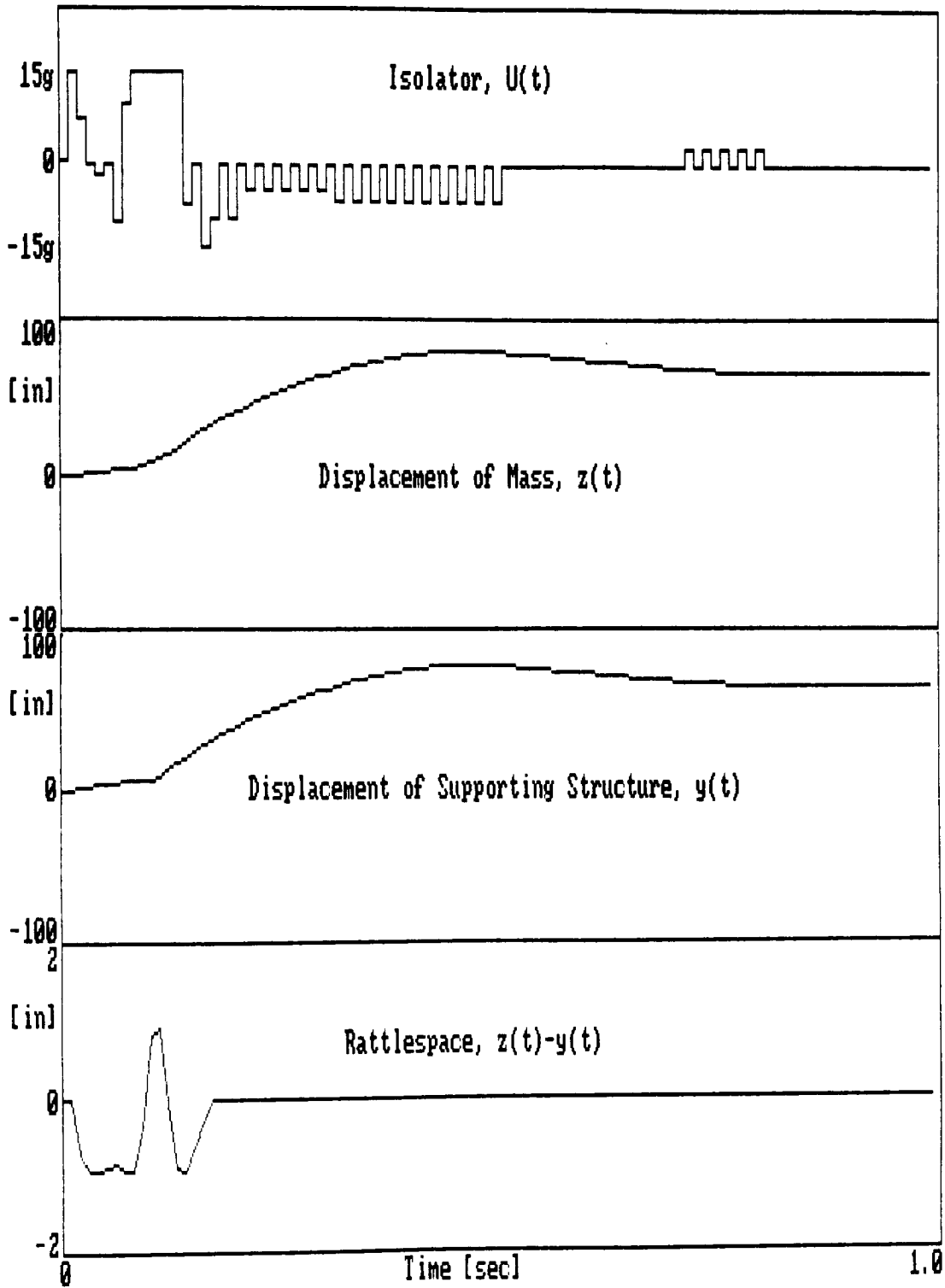
Fig. 4 Resulting Time Responses for Example 1

The performance index is to minimize

$$J = \max_t |z_2(t)|$$

(22)

while satisfying prescribed constraints

$$|U| = |u/m_2| \leq U_{max}$$
$$|x_2| = |z_2 - z_1| \leq X_{2max}$$
$$|x_1| = |z_1 - f| \leq X_{1max}$$

(23)

The equations of motion can be written as

$$\mu \ddot{z}_1 + \lambda(z_1 - z_2) = U$$

$$\ddot{z}_2 + \lambda(z_1 - z_2) = 0$$

(24)

where

$$\mu = m_1/m_2$$
$$\lambda = k/m_2$$

(25)

Let

$$\underline{s} = [z_1 \ \dot{z}_1 \ z_2 \ \dot{z}_2]^T$$

(26)

Then the equations of motion, the performance index, and the constraints as given by Eqs. (24), (22), and (23), respectively, can be converted into the standard LP/MT format. Choose U_{max} = 2g [in/sec^2], X_{1max} = 2 [in], X_{2max} = 1 [in], μ = 100, and λ = 6.28 [rad/sec^2]. The solution for the optimal LP/MT isolator shows that the performance indices are J_t = 5.729 [in] and J_s = 0.099 [in], and the minimum time is t_{min} = 12.0 [sec]. Figure 6 shows the time responses.

CONCLUSIONS

The objective of this study was to show how unique isolator forces and corresponding responses could be chosen by superimposing a minimum settling time onto the limiting performance of the shock isolation systems. The limiting performance / minimum time characteristics were computed by linear programming. It was demonstrated that the superimposition of minimum settling time provided not only the value of the optimal performance index but also the minimum settling time which, in turn, gives unique solutions for shock isolation problems. The optimal LP/MT isolator characteristics can be used to check the feasibility of proposed design requirements and to measure the success of a given design during the design process by comparing the response of the designed system with that of LP/MT characteristics. Furthermore, the LP/MT charateristics would provide with a designer an insight to build a near optimal shock isolation system.
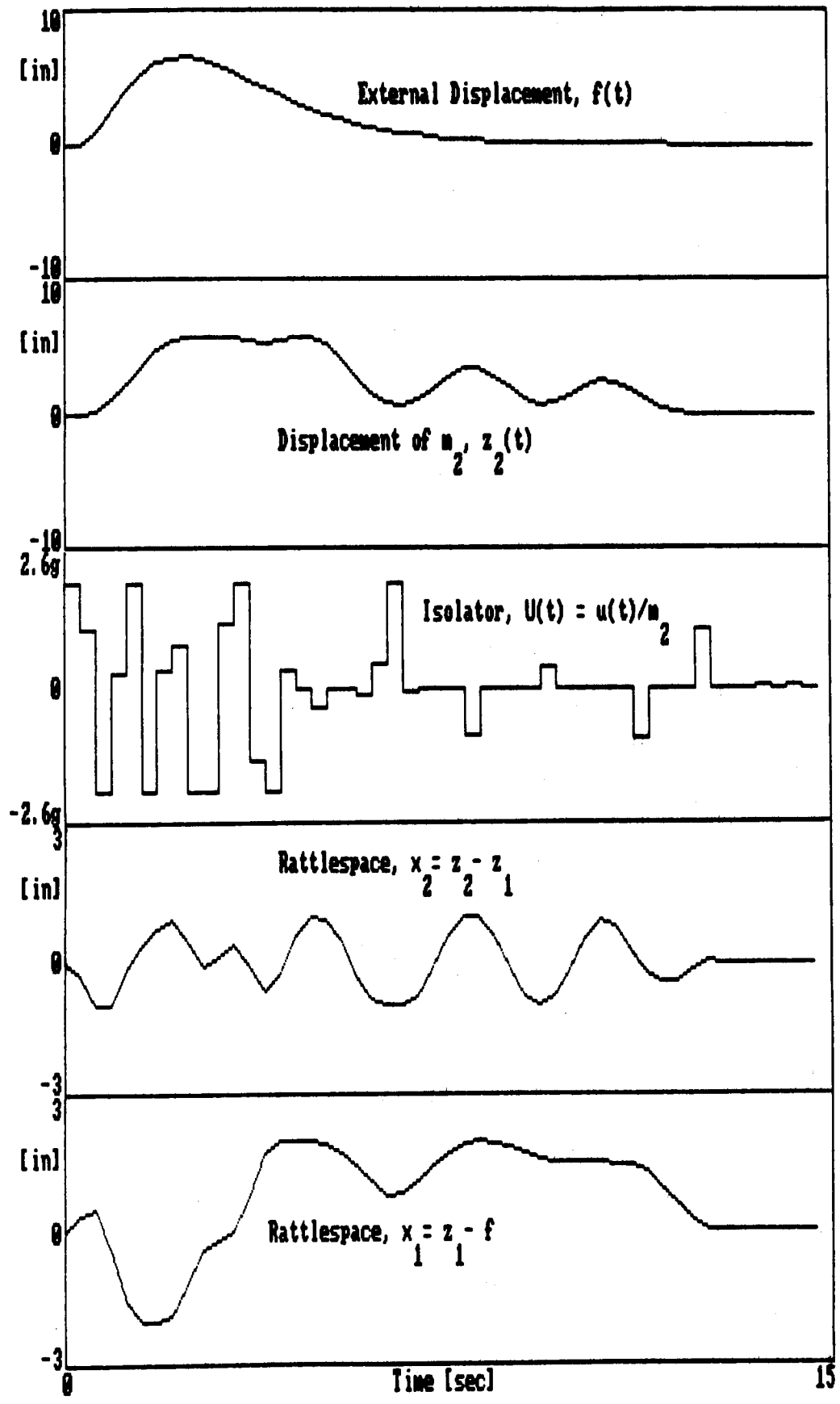
Fig. 6   Resulting Time Responses for Example 2

REFERENCES

1. E. Sevin and W. D. Pilkey, Optimum Shock and Vibration Isolation, The Shock and Vibration Information Center, Washington, D.C., 1971

2. B. P. Wang and W. D. Pilkey, "Limiting Performance Characteristics of Steady State Systems", ASME J. Appl. Mech., 41, pp. 721-726, 1975

3. W. D. Pilkey, Y. H. Chen, and A. J. Kalinowski, "The Use of General Purpose Computer Programs to Derive Equations of Motion for Optimal Isolation Studies", Shock Vib. Bull., No. 46, pp. 269-276, 1976

4. W. D. Pilkey, B. P. Wang, and D. Vannoy, "Efficient Optimal Design of Suspension Systems for Rotating Shafts", ASME J. Eng. Indus., 98, No. 3, 1976

5. J. K. Haviland, T. W. Lim, W. D. Pilkey, and H. Politansky, "The Control of Linear Dampers for Large Space Structures", AIAA Guidance, Navigation, and Control Conference, Monterey, CA, Aug. 1987

6. J. M. Ortega and W. G. Poole, Jr., An Introduction to Numerical Methods for Differential Equations, pp. 124-128, Pitman Publish. Inc., MA, 1981

An Efficient Frequency Response Solution for Nonproportionally Damped Systems

Paul Conti
William K. Rule

Recent advances in computer technology have made it possible to use large finite element models for shock and vibration analyses. One type of dynamic analysis is the calculation of responses and loads in the frequency domain for steady-state operating conditions. If substantial nonproportional damping levels are generated by energy dissipative components, such as bearings or hydraulic cylinders, then the calculation of accurate frequency domain results can be computationally intensive for large models. To reduce the computational effort, it is common to assume that damping is proportional to the mass and stiffness of the system. This proportional damping approximation can lead to significant errors in the frequency domain results. A method has been developed to produce very accurate results for this type of model without the large computational burden of a traditional nonproportional damping analysis.

INTRODUCTION

Recent advances in computer technology have made it possible, but not always practical, to use large finite element models for shock and vibration analyses. At one time, refined models were used only for linear static stress and deflection analyses which are less computationally demanding. Dynamic analyses were generally limited to smaller lumped parameter or coarse finite element models. However, today's more aggressive design goals are promoting lighter weight structures that must operate effectively in higher performance environments. To help achieve these goals, dynamic analyses of refined finite element models are becoming a more accepted part of the design process.

One type of dynamic analysis is the calculation of vibration responses and loads in the frequency domain for steady-state operating conditions. When damping levels are low and energy dissipation is well distributed throughout the system, proportional or modal damping approximations usually produce sufficiently accurate results with a relatively modest computational effort.

On the other hand, if substantial levels of nonproportional damping are generated by energy dissipative components, such as bearings or hydraulic cylinders, then the calculation of accurate frequency domain results can be computationally intensive for large models. To reduce this effort, it is common to assume that damping is proportional to the mass and stiffness of the system. However, in this case, the proportional damping approximation can produce significant errors in the frequency domain results. A method has been developed to calculate very accurate results for this type of model without the large computational burden of a traditional nonproportional damping analysis.

THEORETICAL BACKGROUND

Finite element models can be used to represent the vibration behavior of structural systems in a steady-state operating condition. In matrix form, the system of N equations of motion can be written as follows:

$$\left(-\omega^2[M] + j\omega[C] + j[H] + [K]\right)_{N \times N} \{u\}_{N \times 1} = \{F\}_{N \times 1} \tag{1}$$

where $[M], [C], [H], [K]$ are the physical mass, viscous damping, hysteretic damping, and stiffness matrices, respectively and $\{u\}$, $\{F\}$ are the physical displacement and force vectors, respectively. The variable ω is the frequency (rad/sec) and $j = \sqrt{-1}$.

When the finite element model represented by Eq. (1) exceeds several hundred degrees of freedom, the system is usually reduced prior to direct frequency domain calculations. A popular reduction method is to use M real normal modes of the system that span the frequency range of interest to create a transformation matrix and constraint relationship as follows:

$$\{u\}_{N \times 1} = [\Psi]_{N \times M} \{\gamma\}_{M \times 1} \tag{2}$$

where $M \ll N$ and the M columns of $[\Psi]$ are the real normal mode shape vectors and $\{\gamma\}$ is the modal displacement vector. By substituting Eq. (2) into Eq. (1) and premultiplying both sides of the resultant equation by $[\Psi]^T$, we have:

$$\left(-\omega^2 \lceil m \rfloor + j\omega[\,c\,] + j[\,h\,] + \lceil k \rfloor\right)_{M \times M} \{\gamma\}_{M \times 1} = \{f\}_{M \times 1} \tag{3}$$

where:

$$
\begin{array}{lll}
\lceil m \rfloor & = [\Psi]^T [M] [\Psi] & \text{diagonal modal mass matrix} \\
[\,c\,] & = [\Psi]^T [C] [\Psi] & \text{modal viscous damping matrix} \\
[\,h\,] & = [\Psi]^T [H] [\Psi] & \text{modal hysteretic damping matrix} \\
\lceil k \rfloor & = [\Psi]^T [K] [\Psi] & \text{diagonal modal stiffness matrix} \\
\{f\} & = [\Psi]^T \{F\} & \text{modal force vector}
\end{array}
$$

The reduced system represented by Eq. (3) is an approximation to the original system in Eq. (1). The modal displacement vector $\{\gamma\}$ becomes the new set of independent coordinates and the original physical displacement vector $\{u\}$ is back-calculated through the mode shape matrix in Eq. (2). The modal displacements in Eq. (3) can be calculated at each frequency of interest through a frequency-dependent matrix inversion in this way:

$$\{\gamma\} = \left(-\omega^2 \lceil m \rfloor + j\omega [c] + j[h] + \lceil k \rfloor\right)^{-1} \{f\} \tag{4}$$

In the reduced system of Eq. (3) and Eq. (4), the modal mass and stiffness matrices are diagonal, but the damping matrices can have large off-diagonal terms requiring a fully populated complex matrix inversion for each solution frequency. Although the system has been reduced, a large number of retained modes and/or large number of frequency steps can produce a computationally intensive solution. If a proportional damping approximation is made at this stage, the off-diagonal terms in the damping matrices are ignored and the resultant equations of motion are then fully uncoupled. In this case, the frequency domain solution in Eq. (4) becomes very efficient because a scalar, rather than matrix, inversion is required at each frequency of interest. Neglecting the effects of these off-diagonal coupling terms in the damping matrices, however, can generate substantial errors in the frequency response and load calculations.

The presence of discrete damper components in the model does not usually influence all of the system modes to a significant extent. Only those modes that have a substantial amount of relative motion across the dampers will be strongly affected by their energy dissipative properties. When little relative motion exists across the dampers for a given mode, the dampers are not effectively exercised and little energy dissipation is produced for that mode. Therefore, Eq. (3) can be partitioned so that modal coordinates corresponding to the modes that significantly exercise damper components are separated from the other modal coordinates in this way:

$$\left(-\omega^2 \begin{bmatrix} \lceil m_{nn} \rfloor & 0 \\ 0 & \lceil m_{pp} \rfloor \end{bmatrix} + j\omega \begin{bmatrix} c_{nn} & c_{np} \\ c_{pn} & c_{pp} \end{bmatrix} \right.$$
$$\left. + j \begin{bmatrix} h_{nn} & h_{np} \\ h_{pn} & h_{pp} \end{bmatrix} + \begin{bmatrix} \lceil k_{nn} \rfloor & 0 \\ 0 & \lceil k_{pp} \rfloor \end{bmatrix}\right) \left\{ \begin{matrix} \gamma_n \\ \gamma_p \end{matrix} \right\} = \left\{ \begin{matrix} f_n \\ f_p \end{matrix} \right\} \tag{5}$$

where the subscripts n, p denote the 'nonproportionally' and 'proportionally' damped partitions, respectively.

The new analysis technique presented in this paper is a hybrid of the traditional proportional and nonproportional damping solution methods. The off-diagonal terms in the c_{pp} and h_{pp} quadrants of the damping matrices in Eq. (5) should be small compared to the diagonal terms of their respective quadrants. Ignoring these off-diagonal terms and replacing those quadrants with diagonal or proportionally damped matrices is a small approximation. The larger off-diagonal terms in the c_{nn}, c_{np}, c_{pn}, h_{nn}, h_{np}, h_{pn} quadrants are retained to represent the significant nonproportional damping effects. This approximation becomes the basis for a condensation of $\{\gamma_p\}$ onto the $\{\gamma_n\}$ modal coordinates which eventually creates a more efficient method of solving Eq. (3) with a small loss of accuracy. The concept of partitioning and condensing is similar to the Guyan reduction technique [1] although the present application is very different.

The new hybrid formulation begins with the expansion of Eq. (5) for the pn and pp quadrants as follows:

$$\left(-\omega^2 \lceil m_{pp} \rfloor + j\omega \lceil c_{pp} \rfloor + j \lceil h_{pp} \rfloor + \lceil k_{pp} \rfloor\right) \{\gamma_p\} = \{f_p\} - \left(j\omega [c_{pn}] + j [h_{pn}]\right) \{\gamma_n\} \tag{6}$$

where $\lceil c_{pp} \rfloor$, $\lceil h_{pp} \rfloor$ are the diagonal (proportionally damped) approximations to the original damping matrix quadrants. From Eq. (6), the vector $\{\gamma_p\}$ can be expressed in terms as $\{\gamma_n\}$ as follows:

$$\{\gamma_p\} = \lceil D_{pp} \rfloor^{-1} (\{f_p\} - (j\omega [c_{pn}] + j [h_{pn}]) \{\gamma_n\}) \qquad (7)$$

where

$$\lceil D_{pp} \rfloor = \left(-\omega^2 \lceil m_{pp} \rfloor + j\omega \lceil c_{pp} \rfloor + j \lceil h_{pp} \rfloor + \lceil k_{pp} \rfloor\right)$$

By substituting Eq. (7) into the expansion of the nn and np quadrants of Eq. (5), we have:

$$[D_{nn}] \{\gamma_n\} + (j\omega [c_{np}] + j [h_{np}]) \lceil D_{pp} \rfloor^{-1} (\{f_p\} - (j\omega [c_{pn}] + j [h_{pn}]) \{\gamma_n\}) = \{f_n\} \qquad (8)$$

where

$$[D_{nn}] = \left(-\omega^2 [m_{nn}] + j\omega [c_{nn}] + j [h_{nn}] + [k_{nn}]\right)$$

Eq. (8) can be simplified and inverted to solve for $\{\gamma_n\}$ as follows:

$$\{\gamma_n\} = \left[\tilde{D}_{nn}\right]^{-1} \left\{\tilde{f}_n\right\} \qquad (9)$$

where

$$\begin{aligned}
\left[\tilde{D}_{nn}\right] = & \left([D_{nn}] + \omega^2 [c_{np}] \lceil D_{pp} \rfloor^{-1} [c_{pn}]\right. \\
& + \omega [c_{np}] \lceil D_{pp} \rfloor^{-1} [h_{pn}] + w [h_{np}] \lceil D_{pp} \rfloor^{-1} [c_{pn}] \\
& \left. + [h_{np}] \lceil D_{pp} \rfloor^{-1} [h_{pn}]\right)
\end{aligned}$$

and

$$\left\{\tilde{f}_n\right\} = \{f_n\} - (j\omega [c_{np}] + j [h_{np}]) \lceil D_{pp} \rfloor^{-1} \{f_p\}$$

The calculation of $\{\gamma_n\}$ through the hybrid solution in Eq. (9) provides an accurate, but more efficient, alternative to the traditional nonproportional damping solution in Eq. (4). The hybrid system matrix, $\left[\tilde{D}_{nn}\right]$ although fully populated, is usually significantly smaller than the modal system matrix in Eq. (4). Because the number of calculations required for the inversion of fully populated matrices increases cubically with the matrix order, substantial savings can be gained through order reductions. Additional effort, of course, is required for the calculation of $\left[\tilde{D}_{nn}\right]$ and $\left\{\tilde{f}_n\right\}$ at each solution frequency and offsets some of the computational savings gained from the matrix inversion of a smaller system. However, the small approximation of replacing a nearly-diagonal $[D_{pp}]$ with a diagonal $\lceil D_{pp} \rfloor$ matrix quadrant makes these additional calculations for the generation of $\left[\tilde{D}_{nn}\right]$ quite manageable.

Once $\{\gamma_n\}$ has been determined for each frequency using Eq. (9), the remainder of the modal displacements $\{\gamma_p\}$ can be calculated using Eq. (7). Finally, the physical displacements $\{u\}$ of the original dynamic system can be calculated using Eq. (2) thus completing the frequency domain solution of Eq. (1).

APPLICATION

Recently, the authors performed an evaluation of a rotating equipment design intended for marine application. This evaluation included a frequency response analysis using a very large

finite element model of the system where more than 200 resonant modes were needed to span the frequency range of interest. The solution was to be calculated at more than 1500 spectral lines to provide the desired resolution over the frequency range of interest. Because significant levels of nonproportional damping were present in the model and accurate results were required, a traditional nonproportional damping analysis was attempted. Using MSC/NASTRAN software on a CRAY mainframe computer system, a partial solution over a narrow frequency range was performed. The CPU time used for each frequency step of solution was linearly extrapolated to estimate the time for a complete solution. The required CRAY CPU time was estimated to exceed 40,000 seconds and the solution was judged to be impractical using conventional approaches. As a result, the alternative method presented in this paper was developed.

The new hybrid method was first applied to another large finite element model whose size and construction was similar to the model previously discussed. The 71,000 degree of freedom model was divided into six substructures where each substructure was generated using the Craig-Bampton formulation [2]. The residual system of assembled substructures consisted of 4,300 degrees of freedom. It was dynamically reduced prior to frequency response solution using 123 real normal modes that spanned the frequency range of interest as outlined in Eqs. (1), (2), and (3). Viscous damper and hysteretic damper elements were used to represent the energy dissipative effects of fluid-film bearings and elastomeric mounts, respectively. The modal damping matrices were nearly fully populated with large off-diagonal terms indicating that significant levels of nonproportional damping were present in the system model.

The frequency response solution of the reduced system with 123 modal coordinates was calculated at 400 spectral lines for each of the three methods discussed in this paper which include:

- Method 1: Traditional nonproportional damping solution

- Method 2: Traditional proportional damping solution

- Method 3: New hybrid solution

Figure 1 presents a comparison of calculated frequency responses for each of the three solution methods evaluated at the same structural location. Method 1 results are 'exact' and differ substantially from the approximate results of Method 2. The computational time required for the accurate results of Method 1, however, was 52 times greater than the approximate Method 2 solution. On the other hand, Method 3 results from the hybrid solution compare favorably with the 'exact' solution from Method 1, but required only 8% of the computational time needed for that solution.

For this particular hybrid solution, the reduced system matrix in Eq. (5) was partitioned into 31 'nonproportionally-damped' and 92 'proportionally-damped' modal degrees of freedom. In other words, 31 real modes were judged to be significantly influenced by the discrete damper elements in the model. The remaining 92 real modes were not significantly affected and were subsequently approximated with 92 'proportionally-damped' modes, thus producing an efficient solution with little sacrifice in accuracy.

The matrix partitioning process outlined in Eq. (5) was not a straight forward task. As more modes are included in the 'nonproportionally-damped' partition, the accuracy as well as the computational expense will increase and eventually converge to the traditional nonproportional

damping solution. Several partitioning schemes were developed and studied based on the relative magnitudes of off-diagonal to diagonal terms in the damping matrices. In the future, more sophisticated partitioning algorithms are expected to generate even more economical solutions.

ACCELERATION (dB)

+++++++ Method 1: Nonproportional Damping Solution (CPU = 52X)
++++++ Method 2: Proportional Damping Solution (CPU = 1X)
oooooo Method 3: Hybrid Solution (CPU = 4X)
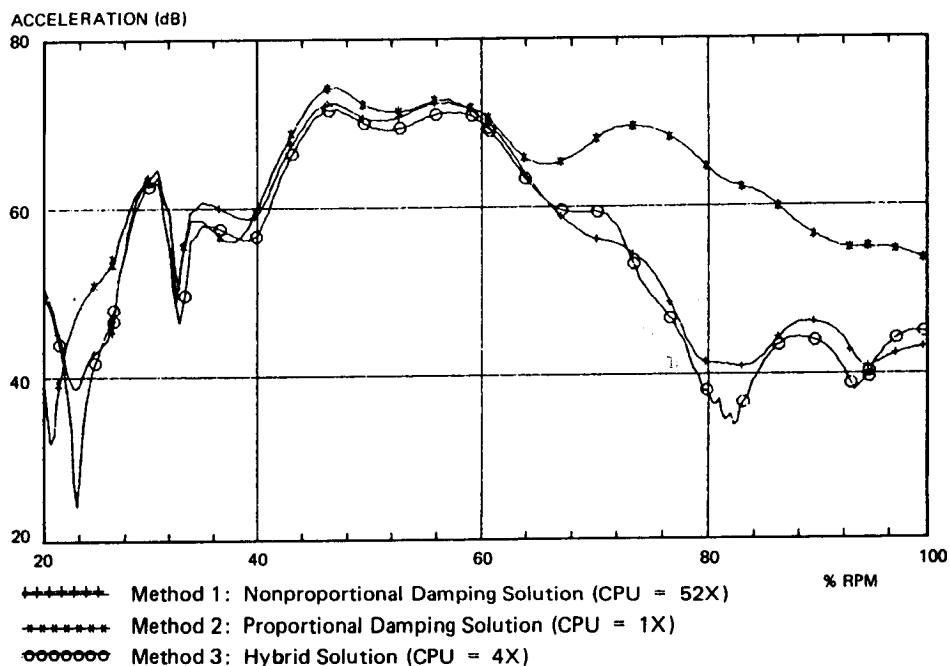
Figure 1
Comparison of Frequency Response Calculations for Different Solution Methods

CONCLUSIONS

A method has been presented to accurately and economically calculate steady-state frequency responses based on the analysis of large finite element models with nonproportional damping effects. The new method is a hybrid of the traditional nonproportional and proportional damping solution methods. It captures the advantages of each conventional approach without the burden of their respective shortcomings, as demonstrated with comparative analyses performed on a large finite element model.

REFERENCES

1. Guyan, R.J., "Reduction of Stiffness and Mass Matrices", AIAA Journal, Vol. 3, No. 2, pp. 380, February, 1965.

2. Craig, R.R., Jr., and Bampton, M.C.C., "Coupling of Substructures for Dynamic Analysis", AIAA Journal, Vol. 6, No. 7, pp. 1313-1319, July, 1968.

Shape Optimization of Damping Layers

T.-C. Lin
R. A. Scott

N88-13635

Shape optimization of unconstrained and constrained damping
layers is treated. The specific problem analyzed is a
cantilever beam loaded at its tip by a harmonic force.
Finite element modeling and mathematical programming
techniques are used to obtain the solution. Performance
measures are taken to be reduction of maximum displacement
and increase in fatigue lifetime. Results include the
improvement, over the uniform treatment case, of these
measures when the profile of the damping layer is optimized.

INTRODUCTION

Treatment of vibration problems by damping layers, both constrained and uncon-
strained is quite common. Early work in the field can be found in Ross, Ungar and
Kerwin [1]. More recently, finite element techniques have been used to address the
problem. Papers relevant to the present work are those of Johnson, Kienholz and
Rogers [2], Johnson and Kienholz [3], Soni and Bogner [4], and Soni [5].

Advances have also been made recently on the structural optimization front.
Improvements in design sensitivity analysis were given by Kim, Anderson and
Sandstrom [6]. Shape optimization techniques using pure finite element modeling
were presented by Kikuchi, Chung, Torigaki and Taylor [7]. Of note is the work of
Niordson [8], who showed the importance of imposing a slope constraint in the opti-
mum design of elastic plates. Viscoelastic materials have also been treated. A
study quite closely related to the theme of the present paper was given by Lekszycki
and Olhoff [9], who analyzed shape optimization of an elastic beam covered by an
unconstrained viscoelastic layer. Using calculus of variation techniques, they
obtained an explicit optimality condition, which was solved in an iterative fashion.

Here shape optimization is considered for both constrained and unconstrained
layers on a beam. A key question addressed is, for a given volume of material,
how much improvement can be obtained, over the uniform treatment case, if the profile
of the damping layer is allowed to vary and be optimized. The specified problem
treated involves a cantilever beam loaded at its tip by a time harmonic force.
Performance measures are taken to be reduction in maximum displacement, and improve-
ment in fatigue lifetime. Finite element modeling, together with numerical
approaches to the complex eigenvalue problem and mathematical programming techniques
are used to obtain the solution.

It should be noted that complete details are not presented in the paper (these
can be found in [10]). The work focuses on the essential ideas and on the results.

Only a single constrained layer is treated here and the basic configuration is sketched in Fig. 1. The mechanical modeling used is traditional. The basic
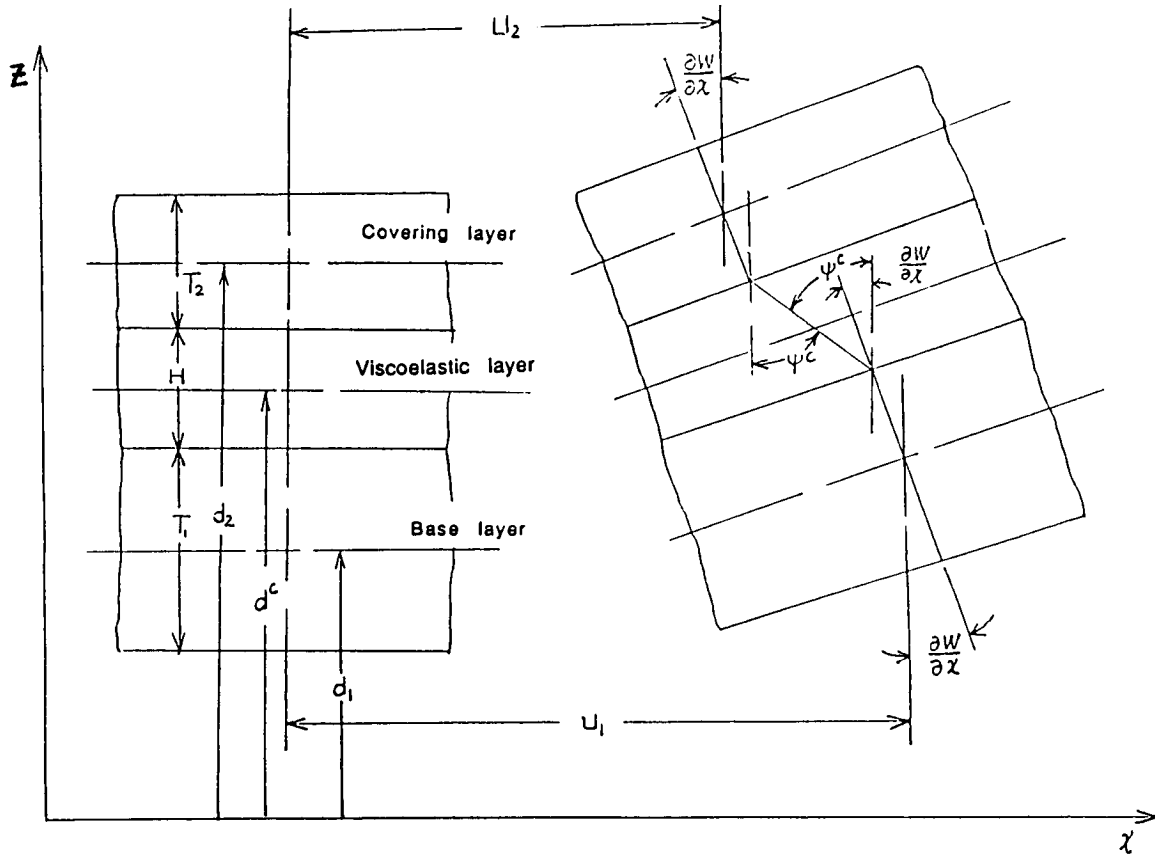
Figure 1. Basic Configuration of a Three-Layered Beam

beam and constraining layer are taken to be Euler-Bernoulli beams and the damping layer, for which shear is important, is treated as a Timoshenko beam. Perfect bonding is assumed. With this modeling, the displacement components are given by

$$\bar{U}(x,z,t) =$$

$$U_1(x,t)-(z-d_1)W_{,x}(x,t), \quad d_1-T_1/2 \le z \le d_1+T_1/2, \text{ base layer} \tag{1}$$

$$U_2(x,t)-(z-d_2)W_{,x}(x,t), d_2-T_2/2 \le z \le d_2+T_2/2, \text{ covering layer} \tag{2}$$

$$U^c(x,t)-(z-d^c)\psi^c(x,t), \quad d^c-H/2 \le z \le d^c+H/2, \text{ damping layer} \tag{3}$$

$$\bar{W}(x,z,t) = W(x,t) \tag{4}$$

$$U^c(x,t) = (1/2)(U_1(x,t)+U_2(x,t))+(1/4)(T_2-T_1)W_{,x} \tag{5}$$

$$\psi^c(x,t) = (1/H)(U_1(x,t)-U_2(x,t))-(1/2H)(T_1+T_2)W_{,x} \tag{6}$$

In the above, U_1, U_2, and U^c are the midplane longitudinal displacements of the base beam, covering layer and core, respectively.

The relevant, non-zero strains are

$$\varepsilon_{x1} = U_{1,x} - (z-d_1)W_{,xx} \tag{7}$$

$$\varepsilon_{x2} = U_{2,x} - (z-d_2)W_{,xx} \tag{8}$$

$$\varepsilon_x^c = (U_{1,x}+U_{2,x})/2+(T_1-T_2)W_{,xx}/4 + (z-d_c)[U_{2,x}-U_{1,x})/H + (T_1+T_2)W_{,xx}/2H] \tag{9}$$

$$\gamma_{xz}^c = -\psi^c + W_{,x} \quad,d^c-H/2\leq z\leq d^c+H/2 \tag{10}$$

For the base beam and covering layer, the stress strain relations are

$$\sigma_{x1} = E_1\varepsilon_{x1} \tag{11}$$

$$\sigma_{x2} = E_2\varepsilon_{x2} \tag{12}$$

where E denotes Young's modulus. The damping layer is treated as a Kelvin solid, for which the stress-strain relations are

$$\sigma_x^c = E^c\varepsilon_x^{\ c} + \zeta_1^c\ \dot{\varepsilon}_x^{\ c} \tag{13}$$

$$\sigma_{xz}^{\ c} = G^c\gamma_{xz}^c + \eta_1^{\ c}\ \dot{\gamma}_{xz}^c \tag{14}$$

where G^c stands for the shear modulus of the core and $\zeta_1^{\ c}$, $\eta_1^{\ c}$ are material parameters characterizing the viscoelasticity. For harmonic loading, such as is being considered here, the complex modulus approach is adopted. Then

$$\sigma_x^{\ c} = E^*\dot{\varepsilon}_x^{\ c} \tag{15}$$

$$\sigma_{xz}^{\ c} = G^*\gamma_{xz}^c \tag{16}$$

where

$$G^* = \text{complex shear modulus of the damping layer}$$
$$= G^c(1+i\eta^c) \tag{17}$$

$E^* =$ complex Young's modulus of the damping layer

$$= E^c(1+i\zeta^c) \qquad (18)$$

where η^c and ζ^c are the loss factors for the damping material. For harmonic motion of frequency ω, the relationships between the Kelvin parameters and the loss factors are

$$G^c = E^c/(2(1+\nu^c)) \qquad (19)$$

$$\eta^c = \eta_1^c \, \omega/G^c \qquad (20)$$

$$\zeta^c = \zeta_1^c \, \omega/E^c \qquad (21)$$

In the sequel, following Nashif, Jones and Henderson [11], Poisson's ratio ν^c is taken to be a constant.

Equations (1) through (21) essentially set forth the mechanical modeling. The procedure then is straightforward. The principle of virtual work states:

$$\int_V (\sigma_x \delta\varepsilon_x + \sigma_{xz}\delta\gamma_{xz})dv + \delta V_I - \delta V_s = 0 \qquad (22)$$

where δV_I and δV_s denote virtual work by the inertia forces and surface tractions, respectively. Using eqs. (1) through (21) in eq. (22) leads to an integral expression involving the "degrees of freedom" U_1, U_2, W, $\partial W/\partial x$. This expression is then discretized using a finite element method. Note that similar modeling can be done for an arbitrary number of layers.

FINITE ELEMENT MODELING

Using eqs. (1) through (6), it can be shown that the volume integrals in eq. (22) reduce to line integrals in the x-direction. These integrals are then discretized using finite elements of length L_e. Rod elements are used for axial displacements. Specifically, the shape functions are given by:

$$U_i(x) = [(1-x/L_e) \quad x/L_e][(U_i^1 \quad U_i^2)]^T \qquad (23)$$

where $i = 1, 2$ indicate base beam and covering layer, respectively, and U_i^1, U_i^2 are nodal displacements. Beam elements are used to handle the transverse deformations, with shape functions given by

$$W(x) = [N_1 \ N_2 \ N_3 \ N_4][W^1 \ \theta^1 \ W^2 \ \theta^2]^T \qquad (24)$$

where $\theta \equiv \dfrac{\partial W}{\partial x}$, and

$$N_1 = 1 - 3x^2/L_e^2 + 2x^3/L_e^3$$

$$N_2 = x - 2x^2/L_e + x^3/L_e^2$$

$$N_3 = 3x^2/L_e^2 - 2x^3/L_e^3$$

$$N_4 = - (x^2/L_e - x^3/L_e^2) \tag{25}$$

Again in eq. (24), superscripts indicate nodal quantities.

Standard finite element methodology now applies. For harmonic forcing the procedure ultimately leads to, on assembling the various element matrices,

$$- \omega^2 [M] \, \underline{X} + i[C] \, \underline{X} + [K] \, \underline{X} = \underline{F} \tag{26}$$

where $\underline{X}$ is a vector of nodal parameters and $\underline{F}$ is a vector of nodal forces (magnitudes). The stiffness, mass and damping matrices, $[K]$, $[M]$, and $[C]$ are lengthy, but straightforward expressions and will not be reproduced here. Note that the form $i[C]$ for the damping matrix, which is frequency dependent, arises from use of the complex modulus approach.

FATIGUE LIFE TIME CALCULATIONS

Here the approach set forth in the SAE document, Ref. [12] is followed. In reality localized plastic flow occurs in fatigue and the nominal stresses and strains, σ and ε, should be replaced by the actual quantities S and e. Neuber introduced the following empirical rule

$$e = \frac{\sigma_{max}^2}{SE} \tag{27}$$

This equation has two unknowns, e and S, and the other needed relationship is the cyclic stress-strain curve for the material, which is curve-fitted by

$$e = \frac{S}{E} + (\frac{S}{K'})^{\frac{1}{n'}} \tag{28}$$

where K' and n' are material parameters. Eqs. (27) and (28) are then solved iteratively to obtain S_{max}. The number of cycles to failure N_f is calculated from another empirical relationship, namely:

$$S_{max} = \sigma_f' (2N_f)^b \tag{29}$$

where σ_f' and b are material parameters. Later in the paper an aluminum alloy (AL3015) is studied and for this material the parameters are

399

$$E = 1.0 \times 10^4 \text{ ksi}$$

$$K' = 28.6 \text{ ksi}$$

$$n' = 0.093$$

$$\sigma_f' = 38.4 \text{ ksi}$$

$$b = -0.088$$

OPTIMIZATION PROBLEM

The optimization task is to find a vector b of design variables H_i, $i = 1,2..$ $...n$, where H_i is the thickness of the damping layer in the ith finite element, which will minimize the objective function f, here taken to be:

$$f: \quad \min \ (\max |R_j|) \qquad j = 1,2,.....N,$$

where R_j represents the deflection response at node j, subject to the constraints:

volume constraint of damping layer $\quad V_0 - V = 0$

and inequality constraints:

$$H_i \geq 0$$

$$H_i^u - H_i \geq 0, \text{ where } H_i^u \text{ is an upper bound for } H_i:$$

slope constraints:

$$H_v - \left| \frac{\partial H_i}{\partial x} \right| \geq 0, \ H_v \text{ a specified constant.} \tag{30}$$

The constraint on the gradient in eq. (30) needs some explanation. The idea was introduced by Niordson [8] in a study on optimization of elastic plates. He pointed out that without it, exotic shapes (tending towards ribbed structures, with extremely thin stiffeners) would be generated. Apart from the practicality of such structures, the underlying theory (Kirchoff plate theory) is not valid for such rapidly varying shapes. To preserve the underlying theory, he restricted the design space to plates of slowing varying thickness, by means of a slope constraint.

In the current work, the numerical approach requires that the constraints be differentiable. Hence the slope constraints are replaced by the equivalent statements:

$$H_v + \frac{\partial H_i}{\partial x} \geq 0 \qquad\qquad (31)$$

$$H_v - \frac{\partial H_i}{\partial x} \geq 0 \qquad\qquad (32)$$

One remark should be made. For some unconstrained layers, it was found that the slope constraints were not necessary to obtain smooth shapes. However, the constraints were found to be essential for constrained layers.

Mathematical programming techniques are used here to obtain the solution. A proven, reliable technique is employed. Belegundu and Arora [13] showed that the program SUMT has these features. Moreover, a listing is available in Kuester [14].

To use the program, sensitivity derivatives $\underline{U}_i(\underline{b}_o)$ are required, where

$$\underline{U}_i(\underline{b}_o) = \left. \frac{\partial \underline{X}}{\partial b_i} \right|_{\underline{b} = \underline{b}_o} , \quad i = 1,2,\ldots\ldots \qquad\qquad (33)$$

Partial differentiation of eq. (26) can be shown to give

$$\{- \omega^2 [M] + i [C] + [K]\}\underline{U}_i = \underline{R}_p \qquad\qquad (34)$$

where

$$\underline{R}_p \equiv \omega^2 \frac{\partial [M]}{\partial b_i} \underline{X} - i \frac{\partial [C]}{\partial b_i} \underline{X} - \frac{\partial [K]}{\partial b_i} \underline{X} \qquad\qquad (35)$$

Note that in the present problems, [M], [K], and [C] have known analytical forms and the derivatives in eq. (35) can be carried out explicitly. Then eq. (34) has the same structure as eq. (26) and can be solved in the same fashion once the latter has been solved.

The constraint equations in problem are simple algebraic expressions and their sensitivity derivatives can also be readily obtained.

NUMERICAL STRATEGY

Eigenvalue extraction was done by means of a subspace iteration technique together with Jacobi's method for matrix diagonalization. Response was calculated using a Gaussian direct elimination method, modified for complex equations. Design sensitivity coefficients were calculated as discussed in connection with eq. (35). Their magnitudes are then fed into the optimization scheme SUMT.

PROGRAM VALIDATION AND RESULTS

To check the accuracy of the finite element modeling, several calculations were done to determine the natural frequencies and loss factors and compared with results of Soni [5]. The comparisons involved a cantilever aluminum beam (7 inches long, .5 inches wide and .06 inches deep) with .06 inches thick aluminum face sheets. The material constants used were $E = 1.0 \times 10^7$ psi and $\rho = 0.1$ lb/in^3. The core

401

material was ISD468. For this material, the behavior of G^c and η^c with frequency is known. Poisson's ratio ν^c was taken to have the constant value 0.35. It was assumed (also assumed throughout the paper) that the loss factor is the same in dilation and shear, so that $\zeta^c = \eta^c$. Tables 1 and 2 give comparisons of the first six undamped natural frequencies and the ratio $\eta_2^{(r)}/\eta^c$, $\eta_2^{(r)}$ being the modal loss factor, respectively. Overall, quite good agreement is seen, lending confidence to the numerical procedures.

Table 1. Comparison of Natural Frequencies

Mode Number	M. L. Soni [5] (hz)	Present Result (hz)
1	64.70	64.13
2	298.00	296.80
3	748.20	745.80
4	1409.50	1403.70
5	2305.00	2296.00
6	3447.00	3400.00

Table 2. Comparison of the Ratio $\eta_2^{(r)}/\eta^c$

Mode Number	M. L. Soni [5]	Present Result
1	0.2725	0.2840
2	0.2401	0.2450
3	0.1531	0.1560
4	0.0878	0.0896
5	0.0560	0.0572

The optimization phase of the program was checked on the following test problem given by Rosenbrock (see [14]): minimize the objective function f, where

$$f = -x_1 x_2 x_3, \text{ subject to}$$

constraints:

$$0 \le x_i \le 42$$

$$0 \le (x_1 + 2x_2 + 2x_3) \le 72$$

Rosenbrock gave the solution: f = -3456.0, x_1 = 24, x_2 = 12, x_3 = 12. The present method gave f = -3453.8, x_1 = 23.4, x_2 = 12.2, x_3 = 12. Very good agreement is seen. This, and the fact that the trends in Lekszycki and Olhoff's [9] work were

reproduced accurately (as will be seen shortly) led to the conclusion that the program was accurate.

Results for unconstrained layers will now be given.

The first material studied is the one used in [9], for which the parameters are: $E^c = 0.1 \times 10^8$ lb/in^2, $\eta^c = 0.5$, $\rho^c = 0.035$ lb/in^3 and for the base layer $E_1 = E^c$, $\rho = 0.1$ lb/in^3. The dimensions are: $T_1 = 0.06$ inches, B (width) = 0.5 inches, L = 7 inches (Soni's example).

Note that this damping material has quite large moduli (perhaps unrealistically so). Moreover, note that, as in Ref. [9], the effects of shear are neglected.

A harmonic force is applied at the tip. The thickness constraint H_i^u is taken to be 0.32 inches. The initial amount of damping material must be specified. A percentage measure is used, namely:

$$\% \text{ volume of damping material} = \frac{\text{volume of damping material}}{\text{volume of base layer}}$$

Figure 2 shows a result for 100% damping using the present methodology, but ignoring shear effects. A symmetric configuration is used with equal amounts of damping material on the top and bottom of the beam. Only the upper layer is shown in the figure. In fact without a constraining layer, shear effects in the core are quite small and can always be neglected so that in effect an Euler-Bernoulli beam is used. The first bending frequency of the composite beam is $\omega_n = 595$ rad/sec and the excitation frequency is $\omega = 20$ rad/sec, so that we have a case of low
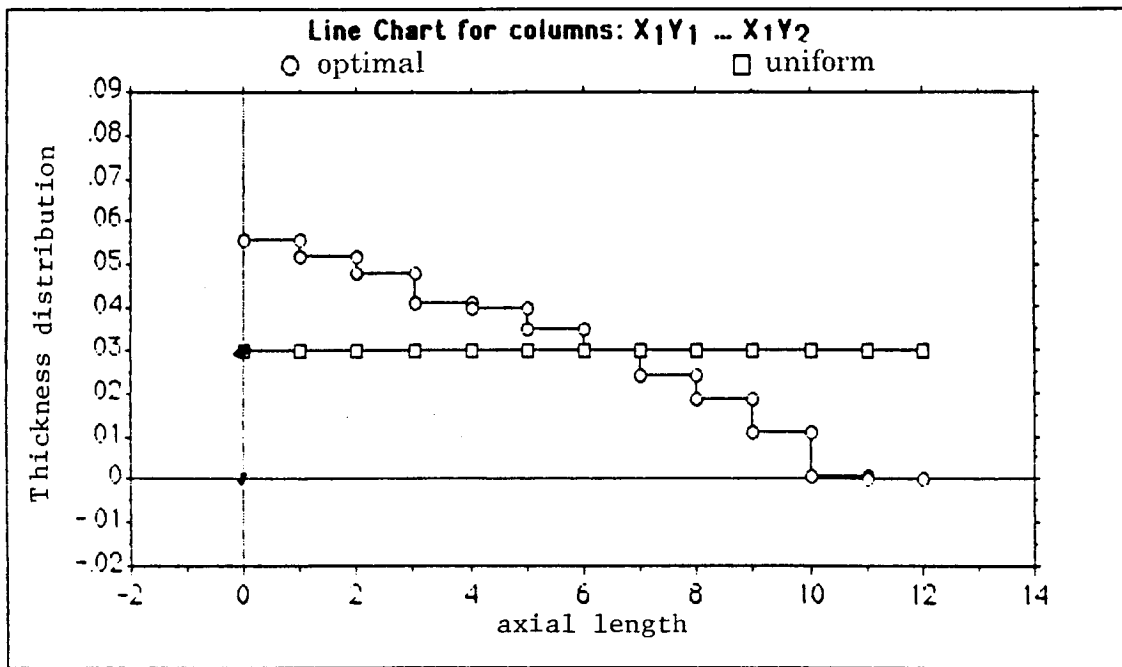
Figure 2. Optimal Shape for High Modulus Material

frequency excitation. The same trend as in Ref. [9] is seen. It is interesting that the present results were obtained without having to specify a constraint on the slope (true for all the results on the unconstrained layers). It was also found that the thickness constraint (0.32 inches) was not active.

Table 3 shows the improvements that can be obtained for various damping treatments. Two kinds of percent reduction in responses are defined by:

$$RRU = \frac{\text{Max. response of bare beam} - \text{max. response with uniform damping}}{\text{Max. response of bare beam}}$$

$$RRO = \frac{\text{Max. response of bare beam} - \text{max. response with optimal damping}}{\text{Max. response of bare beam}}$$

Table 3. Performance Improvements

% Volume	RRU %	RRO %	Fatigue Life Uniform	Fatigue Life Optimal
100.0	88.6	93.0	0.1775×10^5	0.8764×10^5
66.6	79.9	87.4	0.6722×10^4	0.4270×10^5
33.3	59.4	72.7	0.235×10^4	0.909×10^4
16.6	38.1	58.3	0.129×10^4	0.5994×10^4

Optimization would seem to be worth the trouble. For example, for 33.3% damping an improvement (RRO-RRU) of 13.3% is seen. For 100% damping the improvement is 4.4%. Better fatigue performance is also seen. Optimization led to 39.4%(log value) improvement for 33% damping and 74% improvement for 100% damping.

High frequency excitation was also studied (not treated in Ref. [9]). Figure 3 shows the optimum shape for ω = 750 rad/sec and 100% damping. It is interesting to note that the optimum profile has the opposite trend to that for the low frequency profile.

As a next step in the study, a more realistic material was chosen, namely LORD-400. This is a medium shear modulus material with parameters obtained from Ref. [11]. The natural frequency now is ω_n = 220 rad/sec (based on 100% damping).

The optimal shape for a low frequency excitation (ω = 20 rad/sec) is shown in Figure 4, for a 100% damping material and a bound on thickness of 0.24 inches. Note that the same shape trend is seen, as for the high shear modulus. The thickness changes in Figure 4 are severe and one may question the use of Euler-Bernoulli beam theory. A smaller upper bound on the thickness constraint was used, namely 0.15 inches. The result is shown in Figure 5. A different, smoother shape is seen. This shape dependence on the thickness constraint was not observed for the high modulus material.
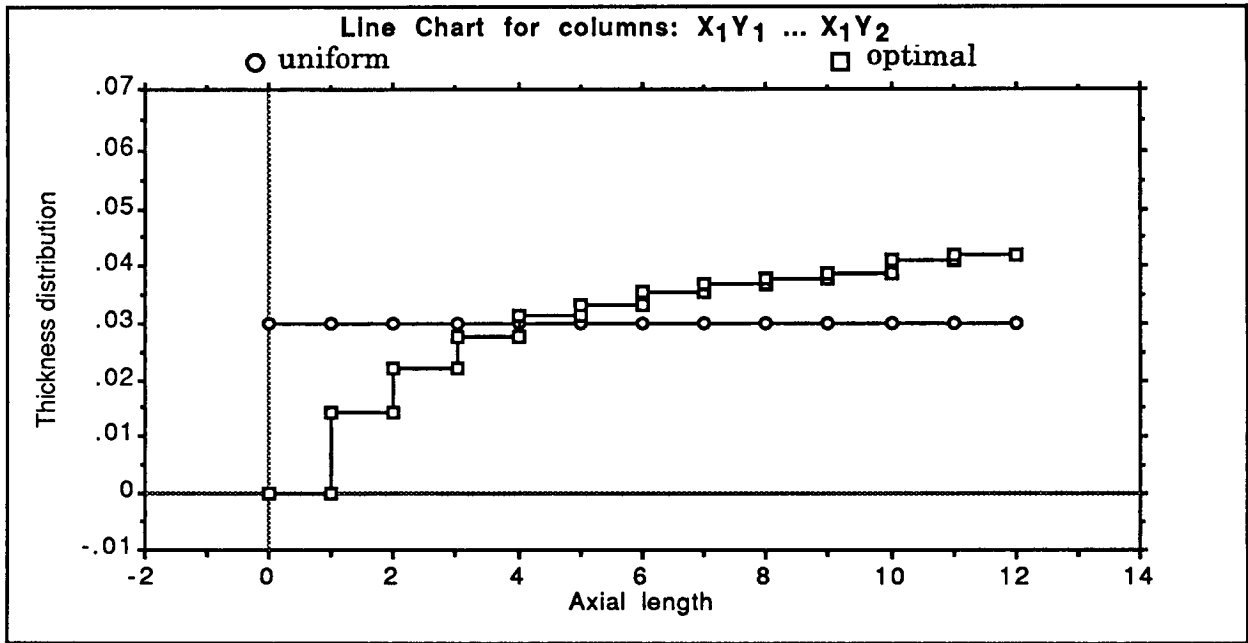
Figure 3. Optimal Shape at High Frequency
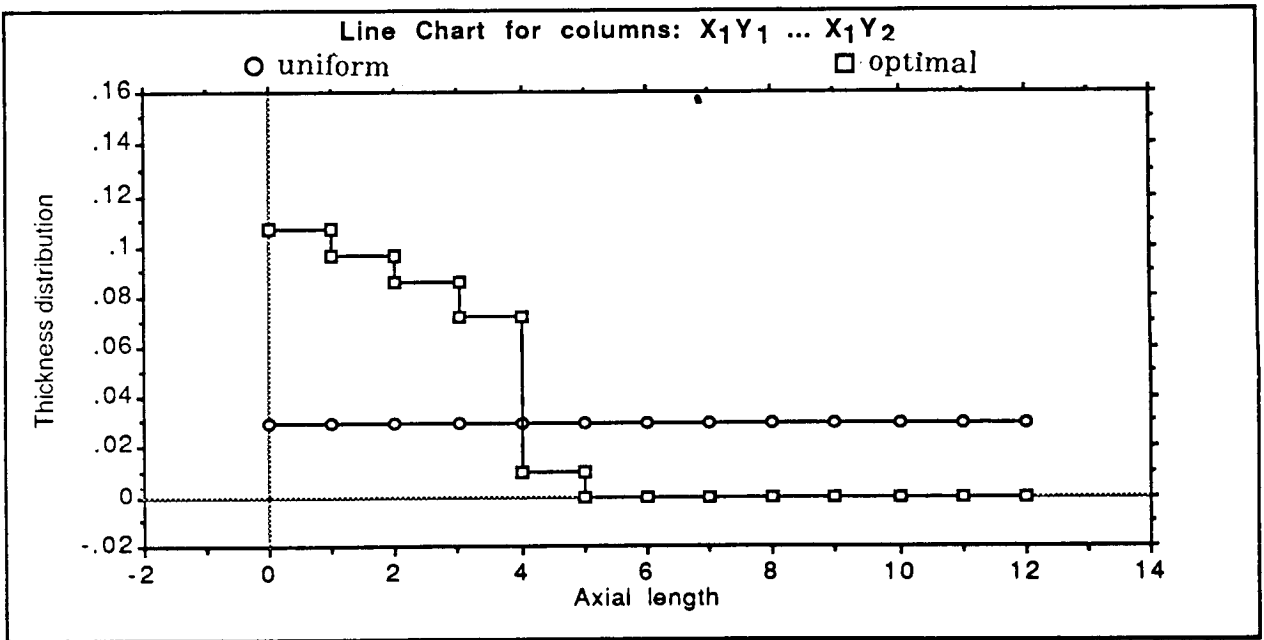
Figure 4. Optimal Shape (LORD-400) for Large Upper Bound
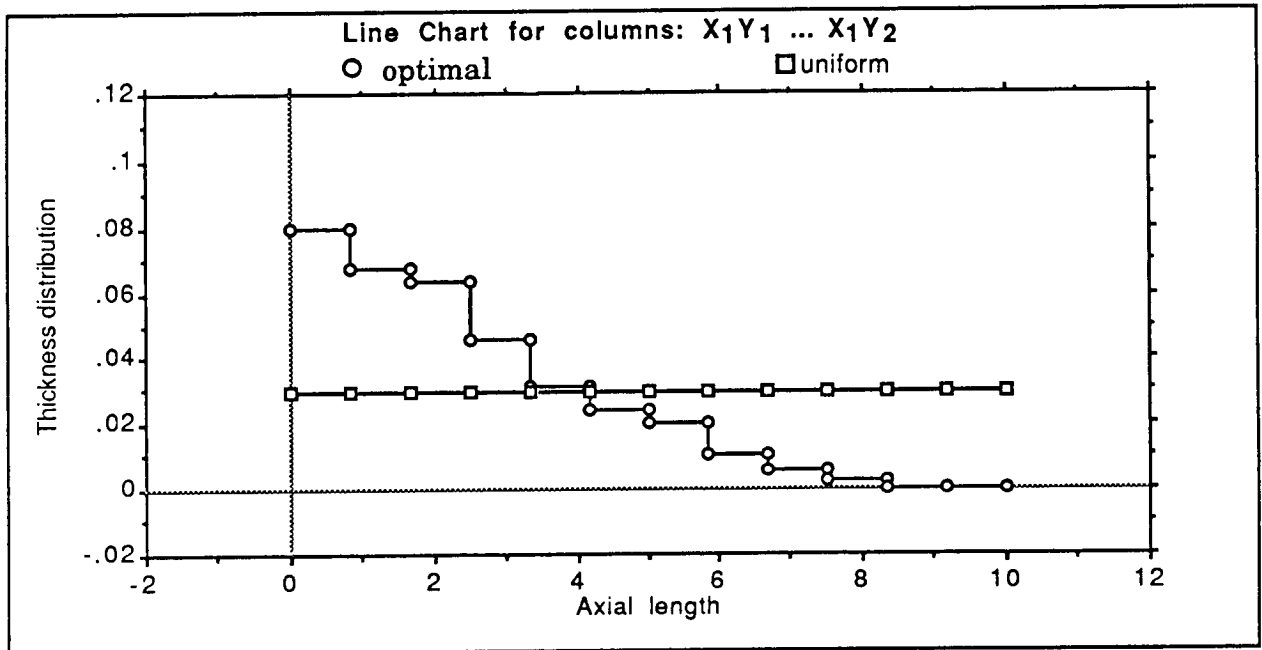
Figure 5. Optimal Shape (LORD-400) for Small Upper Bound

Using the lower upper bound, the following values were found for performance improvement: at 100% damping, RRU = 9.0%, RRO = 19.0%; at 66.6% damping RRU = 4.7%, RRO = 12.1%; at 33.3% damping, RRU = 2.4%, RRO = 7.0%. Results on fatigue are: at 33.3% and 100% damping, the improvements are 5% and 12%, respectively. Though the gains are not as large as for the high modulus material, optimization still seems attractive.

A typical result for high frequency excitation (ω = 240 rad/sec) is shown in Figure 6, for a thickness upper bound of 0.15 inches and 33% damping.

Note that the same shape reversal as was seen for the high modulus material is found. RRO has the value 24.5% so optimization is also worthwhile at high frequencies.

Constrained layers will now be treated (for LORD-400). The first item that should be mentioned is that now a slope constraint is required. Figure 7 shows a shape obtained without such a constraint. Large oscillations in the profile are seen (as was seen by Niordson [8] in his work on elastic plates). Such shapes are not acceptable within the framework of the current mechanical modeling. It was discovered, like Niordson that a slope constraint led to smoother profiles. A slope constraint was imposed at the element level in the form

$$\left| H_{i+1} - H_i \right| < .25 \, H_o \qquad i = 1, 2, \ldots\ldots N-1$$

where H_o is the thickness of the original uniform damping layer. The thickness of the covering layer is taken to be 10% of the thickness of the damping layer. Only symmetric configurations are considered. A thickness bound of .15 inches was used.

406
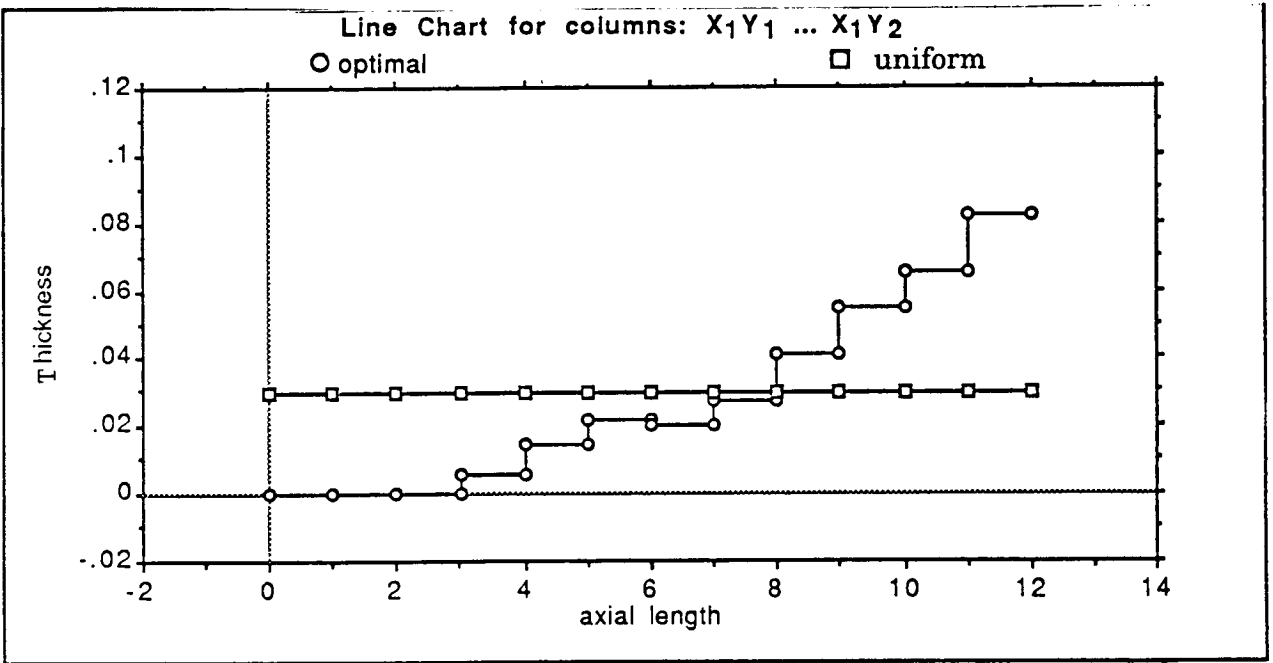
Figure 6.   Optimal Shape (LORD-400) for High Frequency Excitation
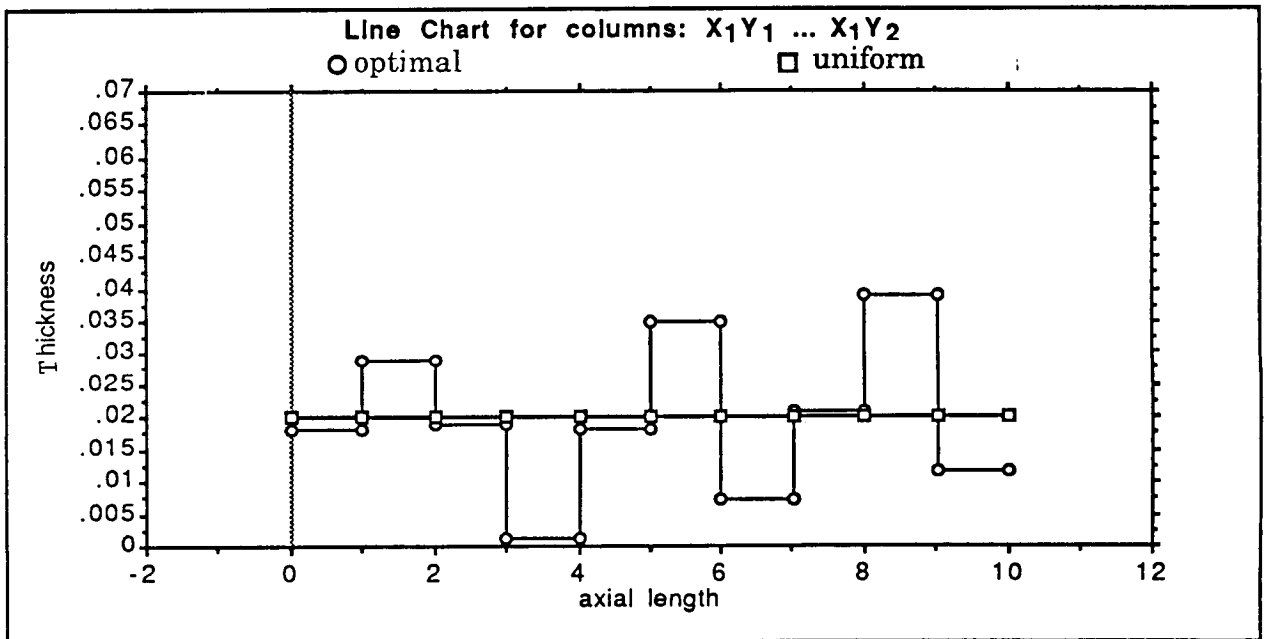
Figure 7.   Optimum Shape With No Slope Constraint

An optimum shape for low frequency excitation (ω = 20 rad/sec), is shown in Figure 8 for 100% damping. Comparing this with Figure 5, it is seen that the optimum profiles have opposite trends. One should not anticipate the same trend in both cases. The basic stress at work in the unconstrained damping layer is the bending stress σ_x^c, whereas it is the shear stress σ_{xz}^c in the constrained case.

The improvement in performance (RRO) at 100% damping was found to be 53%. This should be compared with the 19% improvement noted for the unconstrained layer (with the smaller thickness bound). It can be concluded that constrained layers lead to significant improvement in performance.
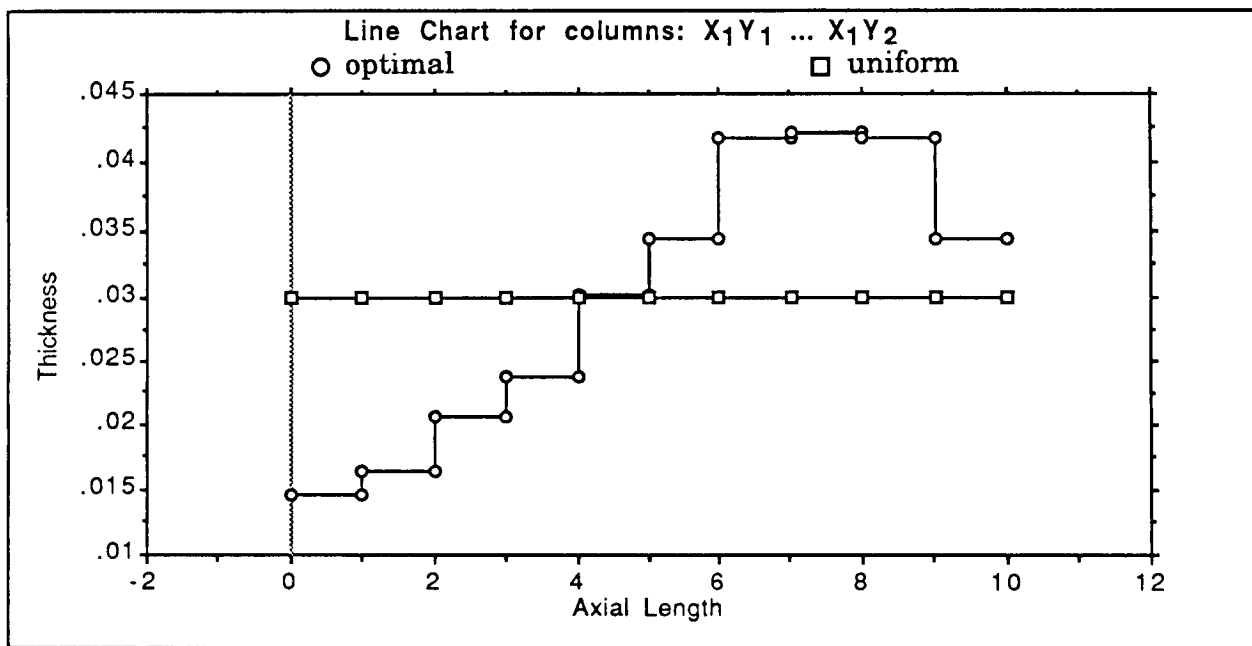
Figure 8. Optimum Shape of a Constrained Damping Layer

REFERENCES

1. D. Ross, E. E. Ungar and E. M. Kerwin, Jr., Damping of Plate Flexural Vibrations by Means of Viscoelastic Laminae, Section 3, ASME Monograph on Structural Damping, 1959.

2. C. D. Johnson, D. A. Kienholz and L. C. Rogers, "Finite Element Prediction of Damping in Beams with Constrained Viscoelastic Layers," Shock Vib. Bull., Vol. 51, Pt. 1, pp. 71-81, May 1981.

3. C. D. Johnson and D. A. Kienholz, "Finite Element Prediction of Damping Layers," AIAA J., Vol. 20, No. 9, pp. 1284-1290, Sept. 1982.

4. M. L. Soni and F. K. Bogner, "Finite Element Vibration Analysis of Damped Structures," AIAA J., Vol. 20, No. 5, pp. 700-707, May 1982.

5. M. L. Soni, "Finite Element Analysis of Viscoelastically Damped Sandwich Structures," Shock. Vib. Bull., Vol. 51, Pt. 1, May 1981.

6. K. O. Kim, W. J. Anderson and R. E. Sandstrom, "Nonlinear Inverse Perturbation Method in Dynamic Analysis, " _AIAA J._, Vol. 21, No. 9, pp. 1310-1316, Sept. 1983.

7. N. Kikuchi, K. Y. Chung, T. Torigaki and J. E. Taylor, "Adaptive Finite Element Methods for Shape Optimization of Linearly Elastic Structures," _Comp. Meth. Appl. Mech. Eng._, Vol. 57, pp. 67-89, 1986.

8. F. Niordson, "Optimal Design of Elastic Plates with a Constraint on the Slope of Thickness Function," _Int. J. Sol. Struct._, Vol. 19, pp. 141-151, 1983.

9. T. Lekszycki and N. Olhoff, "Optimal Design of Viscoelastic Structures Under Forced Steady-State Vibrations," _J. Struct. Mech._, Vol. 9, pp. 363-387, 1981.

10. T.-C. Lin, _Optimal Design of Viscoelastic Structures_, Ph.D. Dissertation, Mechanical Engineering, University of Michigan. Submitted, August 1987.

11. A. D. Nashif, D.I.G. Jones and J. P. Henderson, _Vibration Damping_, John Wiley and Sons, New York, 1985.

12. SAE Standard J1099, pp. 3.59-3.66, 1976.

13. A. D. Belegundu and J. S. Arora, "A Study of Mathematical Programming Methods for Structural Optimization - Part II. Numerical Results," Int. J. Num. Meth. Engng., Vol. 21, pp. 1601-1523, 1985.

14. J. L. Kuester, "Optimization Techniques With Fortran," McGraw-Hill, 1973.

A Passive Vibration-Cancelling Isolation Mount

Alan O. Sykes

N88-13636

Machines operating at constant rpm are found in many industrial, domestic, and military applications. For those machines which generate single-frequency vibration, a conceptual alternative to a system of conventional (KR) or compound (CD) mounts is a system of passive vibration-cancelling (VC) mounts.

This paper presents an analysis of an idealized passive vibration-cancelling two-terminal mount with one degree-of-freedom at each mechanical terminal isolating a nonrigid machine from a nonrigid foundation. To evaluate the VC mount, its effectiveness as a function of frequency is compared with the effectivenesses of both KR and CD mounts isolating a _rigid_ machine from a nonrigid foundation. The comparisons indicate that a carefully designed and manufactured VC mount should provide substantially greater vibration reduction at its cancellation frequency than either a KR or CD mount having the same low frequency stiffness, i.e. stiffness at the natural frequency of the machine-mount system.

Although there are a number of practical problems to be solved before VC mounts can become a reality, and some additional analytical work should be done to "fine tune" their design, there appears to be nothing of a technical nature to preclude their successful development.

INTRODUCTION

Common engineering practice for reducing machine-excited structural vibration is to interpose vibration isolation mounts between the machine and the supporting structure. For many vibration problems, conventional vibration mounts provide adequate vibration reduction; however, if the reduction provided by conventional mounts is insufficient, more elaborate isolation mounts or mount systems are required. A compound mounting system may be employed in which the machine is attached to a stiff massive platform by one set of isolation mounts, the platform to the supporting structure by a second. Alternately, the machine may be supported by a system of compound mounts, each of which consists conceptually of two damped springs connected together by a rigid mass [1].

For single frequency single degree-of-freedom vibration reduction, or for vibration reduction when the vibratory output of a machyine is dominated by vibration at a single frequency in a single degree-of-freedom, an alternative to either a set of conventional(KR) or compound (CD) mounts is a set of vibration-cancelling (VC) mounts.

A passive-vibration cancelling mount consists of a compound mount paralleled by a third resilient element, the stiffness and loss factor of which are chosen such that the forces transmitted from the machine through the two mechanically paralleled paths are equal in magnitude and opposite in phase, so that when superposed, they cancel.

VC MOUNT ANALYSIS AND ITS SPECIALIZATION TO INCLUDE KR AND CD MOUNTS

The analysis of the VC mount will be carried out using the simple model in Fig.1 in which the CD mount consisting of z_1, z_2, and M_1, is paralleled by a third mechanical element z_3.

Terminal
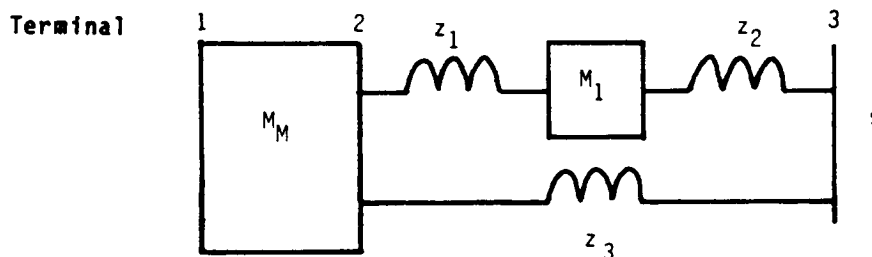
Fig. 1 Model of a Nonrigid Machine M_M Isolated from a Nonrigid Supporting Structure s by a Vibration-Cancelling Mount Consisting of Four Elements z_1, z_2, z_3, and M_1.

The analysis will assume steady-state sinusoidal vibration, that the vibratory input at Terminal 1 of the machine can be characterized as a force rather than a motion, and that the structure of the mount is such that the left terminals of z_1 and z_3 undergo the same motion, and the right terminals of z_2 and z_3 undergo the same motion*. The phasor of the vibratory velocity of the supporting structure will be obtained by two applications of a mechanical version of the Thevenin Electrical Network Theorem [2]. (A different statement of the Thevenin Theorem is required if motion rather than force is specified at Terminal 1 of the machine.) The analysis will make use of a two-terminal version of multiterminal network theory derived in [2], in which each two-terminal mechanical element is characterized by two point and two point-to-point (transfer) free admittances or blocked impedances.

Vibratory Velocity of the Supporting Structure

Let $f_{2,2\beta}$ be the phasor of the force at Terminal 2 of the machine with Terminal 2 blocked. By Thevenin's Theorem [2], the phasor $x_{2,3\beta}$ of the velocity at Terminal 2 of the VC mount when Terminal 3 is blocked is given by

$$x_{2,3\beta} = \frac{f_{2,2\beta}}{z_M + z_{CD22} + z_{(3)22}} ,$$

(1)

where:

z_M is the impedance of the machine at Terminal 2 with Terminal 1 free;

z_{CD22} is the impedance at Terminal 2 of the CD section of the mount with Terminal 3 blocked; and

---

*Different fonts are used for text and equations; however, the meaning of literal symbols is the same in both fonts.

412

$z_{(3)22}$ is the impedance at terminal 2 of the mechanical element z_3 with Terminal 3 blocked.

To calculate the velocity at Terminal 3 when the mount is connected to the supporting structure by Thevenin's Theorem, it is first necessary to calculate the phasor $f_{3,3\beta}$ of the blocked force at Terminal 3. By superposition, the blocked force at Terminal 3 is the sum of the forces transmitted through the CD and paralleled sections of the mount and applied to the blocking structure. The phasors of these forces can be obtained by calculating the phasors of the forces applied to the two sections of the mount at Terminal 2, and by multiplying these forces by the negatives of their force transmissibilities T_{CDf32} and $T_{(3)32}$.

Let $f_{2CD,3\beta}$ be the phasor of the force applied at Terminal 2 of the CD section of the mount, and $f_{2(3),3\beta}$ be the phasor of the force applied at Terminal 2 of the paralleled section, both with Terminal 3 blocked.

By superposition,

$$f_{3,3\beta} = T_{CDf32}\, f_{2CD,3\beta} + T_{(3)f32}\, f_{2(3),3\beta} \cdot \tag{2}$$

Since

$$f_{2CD,3\beta} = z_{CD22}\, x_{2,3\beta}, \quad \text{and} \tag{3}$$

$$f_{2(3),3\beta} = z_{(3)22}\, x_{2,3\beta}, \tag{4}$$

then

$$f_{3,3\beta} = \left[T_{CDf32}\, z_{CD22} + T_{(3)f32}\, z_{(3)22} \right] x_{2,3\beta} \cdot \tag{5}$$

Substituting for $x_{2,3\beta}$ from Eq.(1), Eq.(5) becomes

$$f_{3,3\beta} = T_{CDf32}\, z_{CD22} + T_{(3)f32}\, z_{(3)22}\, \frac{f_{2,2\beta}}{z_M + z_{CD22} + z_{(3)22}} \cdot \tag{6}$$

By Thevenin's Theorem, the phasor x_{3VC} of the velocity of the supporting structure when machine, mount, and supporting structure are connected is given by

$$x_{3VC} = \frac{f_{3,3\beta}}{z_{VCM} + z_S} = \frac{\left[T_{CDf32}\, z_{CD22} + T_{(3)f32}\, z_{(3)22} \right]}{z_M + z_{CD22} + z_{(3)22}}\, \frac{f_{2,2\beta}}{z_{VCM} + z_S}, \tag{7}$$

where

z_{VCM} is the impedance at Terminal 3 of the VC mount with Terminal 2 of the mount attached to the machine, with Terminal 1 of the machine free.

From Appendix 1, z_{VCM} is given by

$$z_{VCM} = (z_{CD33} + z_{(3)33})\, \frac{[(1/y_{(3)22}) + (1/y_{CD22})] + z_M}{z_{CD22} + z_{(3)22} + z_M}, \tag{8}$$

413

where:

$z_{(3)33}$ is the impedance at Terminal 3 of the mechanical element z_3 with Terminal 2 blocked;

$y_{(3)22}$ is the admittance of z_3 at Terminal 2 with Terminal 3 free; and

y_{CD22} is the admittance of the CD section of the mount at Terminal 2 with Terminal 3 free.

Substituting for z_{VCM} from Eq.(8) into Eq.(7), the phasor x_{3VC} of the velocity of the supporting structure when machine, mount, and supporting structure are connected is given by

$$x_{3VC} = \left[\frac{(T_{CDf32}\, z_{CD22} + T_{(3)f32}\, z_{(3)22})}{z_M + z_{CD22} + z_{(3)22}} \right] \frac{f_{2,2\beta}}{(z_{CD33} + z_{(3)33}) \left[\frac{(1/y_{(3)22}) + (1/y_{CD22}) + z_M}{z_{CD22} + z_{(3)22} + z_M} + z_s \right]} . \qquad (9)$$

The equation for the phasor x_{3CD} of the velocity at Terminal 3 with z_3 removed and the CD section remaining can be obtained from Eq.(9) by making the substitutions $T_{(3)f32} = z_{(3)22} = 1/[y_{(3)22}] = z_{(3)22} = 0$.

$$x_{3CD} = \frac{T_{CDf32}}{z_M + z_{CD22}} \frac{z_{CD22}}{z_{CD33} \frac{(1/y_{CD22}) + z_M}{z_{CD22} + z_M} + z_s} f_{2,2\beta} . \qquad (10)$$

The equation for the phasor x_{3KR} of the velocity at Terminal 3 with the CD section of the mount removed and only z_3 remaining can be obtained from Eq.(9) by making the substitutions $T_{CDf32} = z_{CD22} = 1/(y_{CD22}) = z_{CD33} = 0$.

$$x_{3KR} = \frac{T_{CDf32}}{z_M + z_{(3)22}} \frac{z_{(3)22}}{z_{(3)33} \frac{(1/y_{(3)22}) + z_M}{z_{(3)22} + z_M} + z_s} f_{2,2\beta} . \qquad (11)$$

When z_3 is a massless spring-dashpot mount, so that $1/[y_{(3)22}] = 0$, Eq. (11) can be further simplified to

$$x_{3KR} = \frac{f_{2,2\beta}}{z_M + z_s + \frac{z_M\, z_s}{z_{(3)22}}} . \qquad (12)$$

414

Requirements for Vibration Cancellation

It can be seen from Eq.(9) that the condition for vibration cancellation, namely that the forces transmitted to the supporting structure via the two paths in the VC mount be equal in magnitude and opposite in phase, is equivalent to requiring that the phasor x_{3vc} of the velocity of the supporting structure be zero, i.e. that

$$T_{CDf32} \, z_{CD22} + T_{(3)f32} \, z_{(3)22} = 0 \; . \tag{13}$$

This section of the paper will determine the relationships that must be established between the properties of the components of the CD and paralleled paths to achieve cancellation when z_1, z_2, and z_3 are massless spring-dashpots, and M_1 is a rigid mass.

Given that:

$$z_1 = R_1 - j(K_1/w) \; ; \tag{14}$$

$$z_2 = R_2 - j(K_2/w) \; ; \tag{15}$$

$$z_3 = R_3 - j(K_3/w) \; ; \tag{16}$$

$$z_M = jwM_1 \; ; \tag{17}$$

then:

$$T_{CDf32} = \frac{R_2 - j\frac{K_2}{w}}{R_2 + j(wM_1 - \frac{K_2}{w})} \; ; \tag{18}$$

$$z_{CD22} = \frac{[R_1 - j\frac{K_1}{w}] \; [R_2 + j \; (wM_1 - \frac{K_2}{w})]}{R_1 + R_2 + j \; [wM_1 - \frac{(K_1 + K_2)}{w}]} \; ; \tag{19}$$

$$T_{(3)f32} = 1 \; ; \tag{20}$$

$$z_{(3)22} = R_3 - j\frac{K_3}{w} \; ; \tag{21}$$

where:

$\qquad M_1 \quad$ is the mass of the inertial element in th CD section of the mount;

$R_1, R_2, R_3 \quad$ are the mechanical resistances of z_1, z_2, z_3, respectively;

$K_1, K_2, K_3 \quad$ are the stiffnesses of z_1, z_2, z_3, respectively;

$$w = 2\pi f \; , \tag{22}$$

$\qquad$ f being the frequency in Hertz.

Substituting from Eqs.(18) – (21) into Eq. (13), the cancellation condition for a VC mount constructed from ideal mechanical elements (massless spring-dashpots and rigid lossless masses) becomes

$$\frac{(R_1 - j\frac{K_1}{w})(R_2 - j\frac{K_2}{w})}{R_1 + R_2 + j\,[wM_1 - \frac{(K_1 + K_2)}{w}]} + R_3 - j\frac{K_3}{w} = 0 . \tag{23}$$

Eq.(23) is complex, and for it to be zero, both real and imaginary parts must be zero. Collecting real and imaginary parts, equating both to zero, defining the loss factors of r_1, r_2, r_3,

$$r_1 = \frac{wR_1}{K_1} , \tag{24}$$

$$r_2 = \frac{wR_2}{K_2} , \tag{25}$$

$$r_3 = \frac{wR_3}{K_3} , \tag{26}$$

and solving the resulting pair of equations simultaneously, one can show that to achieve cancellation at the circular frequency w_c

$$w_c = 2\pi f_c , \tag{27}$$

where f_c is the cancellation frequency, r_3 and M_1 must have the magnitudes:

$$r_3 = \frac{r_1K_1\,(1+\frac{K_2}{K_3}) + r_2K_2\,(1+\frac{K_1}{K_3})}{\frac{K_1K_2}{K_3}\frac{(1-r_1r_2)}{2} + \left[\,[\frac{K_1K_2(1-r_1r_2)}{K_3\quad 2}]^2 - [r_1K_1+r_2K_2][r_1K_1(1+\frac{K_2}{K_3})+r_2K_2(1+\frac{K_1}{K_3})]\,\right]^{1/2}} ; \tag{28}$$

$$M_1 = \frac{1}{w_c^2}\left[\frac{K_1+K_2+K_1K_2}{K_3}\frac{(1-r_1r_2)}{2} + \left[\frac{K_1K_2(1-r_1r_2)}{K_3\quad 2}\right]^2 - [r_1K_1+r_2K_2][r_1K_1(1+\frac{K_2}{K_3})+r_2K_2(1+\frac{K_1}{K_3})]\right]^{1/2} . \tag{29}$$

From Eqs. (28) and (29), r_3 and M_1 depend on the stiffnesses of the resilient elements in both the CD and paralleled (KR) sections of the mount, and on the loss factors in the CD section.

In the next section of the paper, formulae will be developed for calculating the effectivenesses of VC, CD, and KR mounts.

416

MOUNT EFFECTIVENESS

Definition

For steady-state sinusoidal machine-excited supporting structure vibration, mount effectiveness is defined as the ratio of the phasor of the velocity of the supporting structure when the machine is directly attached to it, to the phasor of the velocity of the supporting structure when the machine is attached to it by an isolation mount.

Velocity of the Supporting Structure with the Machine Directly Attached

Let $f_{2,2\beta}$ be the phasor of the force at Terminal 2 of the machine with Terminal 2 blocked. Let x_2 be the phasor of the supporting structure velocity with the machine directly attached to it.

By Thevenin's Theorem, x_2 is given by

$$x_2 = \frac{f_{2,2\beta}}{z_M + z_S} . \tag{30}$$

Effectiveness Equations for VC, CD, and KR Mounts

By the definition above, the effectiveness, E_{VC}, of the VC mount is given by the ratio

$$E_{VC} = \frac{x_2}{x_{3VC}} ; \tag{31}$$

the effectiveness, E_{CD}, of the CD mount by the ratio

$$E_{CD} = \frac{x_2}{x_{3CD}} ; \tag{32}$$

and the effectiveness, E_{KR}, of the KR mount by the ratio

$$E_{KR} = \frac{x_2}{x_{3KR}} . \tag{33}$$

From Eqs. (9) and (30),

$$E_{VC} = \frac{[z_{CD33} + z_{(3)33}] [(1/y_{CD22}) + (1/y_{(3)22}) + z_M] + z_S [z_M + z_{CD22} + z_{(3)22}]}{[z_M + z_S] [T_{CDf32} z_{CD22} + T_{(3)f32} z_{(3)22}]} . \tag{34}$$

417

From Eqs. (10) and (30),

$$E_{CD} = \frac{z_{CD33} \, [(1/y_{CD22}) + z_M] + z_s \, [z_M + z_{CD22}]}{[z_M + z_s] \, T_{CDf32} \, z_{CD22}} \, . \tag{35}$$

From Eqs. (12) and (30),

$$E_{VC} = \frac{z_M + z_s + \dfrac{z_M \, z_s}{z_3}}{[z_M + z_s]} \, . \tag{36}$$

Eqs. (34) and (35) are quite broad in applicability. Eq. (34) gives the effectiveness of two arbitrary mechanical elements in parallel in isolating a nonrigid machine from a nonrigid supporting structure; Eq. (35), the effectiveness of a single arbitrary mechanical element in isolating a nonrigid machine from a nonrigid supporting structure.*

Note that zeros for undamped systems, and minima for damped systems occur in the denominators of E_{VC}, E_{CD}, and E_{KR} at the frequency at which the reactive components of z_M and z_s are equal in magnitude and opposite in phase, a condition under which, in the absence of an isolation mount, the machine resonates with the supporting structure.

In the next section of the paper, effectiveness equations will be obtained for CD and VC mounts constructed from idealized mechanical elements.

Effectiveness Equations for CD and VC Mounts Constructed from Ideal Mechanical Elements

From Eqs. (14) – (17):

$$z_{CD33} = \frac{[R_2 - j\frac{K_2}{w}] \quad [R + j \, (wM_1 - \frac{K_1}{w})]}{R_1 + R_2 + j \, [wM_1 - \frac{(K_1 + K_2)}{w}]} \, ; \tag{37}$$

$$y_{CD22} = \frac{R_1 + j(wM_1 - \frac{K_1}{w})}{(R_1 - j\frac{K_1}{w}) \, j \, wM_1} \, ; \tag{38}$$

---

*Consider two arbitrary mechanical elements constrained so that their input terminals both experience the same motion $x_1(t)$, and their output terminals the same motion $x_2(t)$. By definition, elements constrained in this manner are said to be mechanically in parallel.

$$z_{(3)33} = R_3 - j\frac{K_3}{w} ; \tag{39}$$

$$y_{(3)22} = \frac{1}{0} = \infty ; \tag{40}$$

$$z_M = jwM_M ; \text{ and} \tag{41}$$

$$z_S = R_S + jX_S ; \tag{42}$$

where:

M_M is the mass of the machine;

R_s and X_s are the mechanical resistance and reactance of the supporting structure, respectively.

From Eqs. (14) – (21), (24) – (26), and (37) – (43), it can be shown that E_{CD} and E_{VC} can be written in nondimensional form as:

$$E_{CD} = \frac{N_1 + N_2 + N_3}{D_1} ; \tag{43}$$

$$E_{VC} = \frac{N_1 + N_2 + N_3 + N_4 + N_5}{D_1 D_2} ; \tag{44}$$

where:

$$N_1 = \left[\frac{M_1}{M_M} + \frac{r_1 + j\left[\left(\frac{w}{w_1}\right)^2 - 1\right]}{r_1 - j} \right] j \left(\frac{w}{w_{OCD}}\right)^2 ; \tag{45}$$

$$N_2 = \left[\frac{r_2 + j\left[\left(\frac{w}{w_2}\right)^2 - 1\right]}{r_2 - j} \right] \frac{w}{w_{OCD}} \ z'_s ; \tag{46}$$

$$N_3 = \left[\frac{\frac{b}{b+1} r_1 + \frac{r_2}{b+1} + j\left[\left(\frac{w}{w_{12}}\right)^2 - 1\right]}{(r_1-j)\ (r_2-j)} \right] j \left(\frac{w}{w_{OCD}}\right)^2 \frac{w}{w_{OCD}} \ z'_s ; \tag{47}$$

$$N_4 = \frac{b+1}{bk_2} \left[\frac{(r_3-j)\left(\frac{b}{b+1} r_1 + \frac{r_2}{b+1} + j\left[\left(\frac{w}{w_{12}}\right)^2 - 1\right]\right)}{(r_2-j)} \right] \left[\frac{1}{r_1 + j\left[\left(\frac{w}{w_1}\right)^2 - 1\right]} \frac{M_1}{M_M} + \frac{1}{r_1-j} \right] j \left(\frac{w}{w_{OCD}}\right)^2 ; \tag{48}$$

$$N_5 = \frac{b+1}{bk_2} \ \frac{r_3-j}{r_1-j} \left[\frac{\frac{b}{b+1} r_1 + \frac{r_2}{b+1} + j\left[\left(\frac{w}{w_{12}}\right)^2 - 1\right]}{(r_2-j)} \right] \frac{w}{w_{OCD}} \ z'_s ; \tag{49}$$

$$D_1 = j \left(\frac{w}{w_{OCD}}\right)^2 + \frac{w}{w_{OCD}} \ z'_s ; \tag{50}$$

$$D_2 = 1 + \frac{b+1}{bk_2} (r_3-j) \left[\frac{\frac{b}{b+1} r_1 + \frac{r_2}{b+1} + j\left[\left(\frac{w}{w_{12}}\right)^2 - 1\right]}{(r_1-j)\ (r_2-j)} \right] ; \tag{51}$$

420

$$b = K_1/K_2 \; ; \qquad (52)$$

$$j = (-1)^{1/2} \; ; \qquad (53)$$

$$k_2 = K_2/K_3 \; ; \qquad (54)$$

$$r_1 = wR_1/K_1 \; ; \qquad (55)$$

$$r_2 = wR_2/K_2 \; ; \qquad (56)$$

$$r_3 = wR_3/K_3 \; ; \qquad (57)$$

$$w = 2\pi f = 2\pi \text{ (frequency in Hertz)} \; ; \qquad (58)$$

$$w_1^2 = K_1/M_1 \; ; \qquad (59)$$

$$w_2^2 = K_2/M_1 \; ; \qquad (60)$$

$$w_{12}^2 = (K_1 + K_2)/M_1 \; ; \qquad (61)$$

$$w_{OCD}^2 = [K_1K_2/(K_1+K_2)]/M_M \; ; \qquad (62)$$

$$z_s' = w_{OCD} \, z_s/[K_1K_2/(K_1+K_2)] \; . \qquad (63)$$

In these equations:

  w_{OCD} is the natural frequency of the machine M_M on the CD mount — or CD section of the VC mount — neglecting the reactance of M_1;

  z_s' is the ratio of the complex supporting structure impedance z_s to $w_{OCD}K_1K_2/(K_1+K_2)$, the magnitude of the stiffness reactance of the CD mount (or the CD section of the VC mount), neglecting the reactance of M_1.

The loss factor r_3 and the mass ratio M_1/M_M in Eq. (43) and (44) — See Eqs. (45) - (63)— can be obtained from Eqs. (28) and (29), or in terms of the parameters b and k_2 from the equations:

$$r_3 = \frac{r_1b+r_2 + bk_2(r_1+r_2)}{bk_2\frac{(1-r_1r_2)}{2}+\left[\left[bk_2\frac{(1-r_1r_2)}{2}\right]^2-[r_1b+r_2][r_1b+r_2+bk_2(r_1+r_2)]\right]^{1/2}} \; ; \qquad (64)$$

$$\frac{M_1}{M_M} = (b+1)k_2\left(\frac{w_{OVC}}{w_c}\right)^2\left[\frac{b+1 + bk_2(1-r_1r_2)+\left[\left[bk_2\frac{(1-r_1r_2)}{2}\right]^2- [r_1b+r_2][r_1b+r_2+bk_2(r_1+r_2)]\right]^{1/2}}{1+b(1+k_2)}\right] \; ; \qquad (65)$$

where

$$w_{OVC} = 2\pi f_{OVC} \; , \qquad (66)$$

f_{OVC} being the natural frequency of the machine M_M on the VC mount, neglecting the reactance of M_1.

$$w_{OVC}^2 = [K_3 + K_1K_2/(K_1+K_2)]/M_M \; ; \qquad (67)$$

and

$$w_c = 2\pi f_c \ , \tag{68}$$

f_c being the frequency at which cancellation occurs.

Effectiveness Calculations

Mount effectiveness is a complex quantity having a magnitude and phase. Its magnitude is a measure of the isolation provided by a vibration mount.

Curves giving the magnitudes in dB of the effectivenesses, $E_{KR}(dB)$, $E_{CD}(dB)$, and $E_{VC}(dB)$, for spring-dashpot (KR), compound (CD), and vibration-cancelling (VC) mounts vs. frequency ratio w/w_{OKR} (or w/w_{OCD}) for resistive, masslike, and springlike supporting structures are presented in Figs. (2) – (10)*. In these figures, the ratio of the supporting structure impedance (whether resistive or reactive) to the mount impedance at the natural frequency of the machine-mount system on an infinite impedance supporting structure is taken as a parameter.

Figs. (2) – (4) compare KR and CD mounts; Figs. (5) – (7) compare KR and CD mounts; and Figs. (8) – (10) compare CD and VC mounts.

The calculations were performed for CD-VC mount pairs for which the CD mount and the CD section of the VC mount were identical. A result of this procedure is that the natural resonant frequency of a rigid machine on the VC mount is always somewhat higher than that of the machine on the CD mount. Such a procedure is justified if the the VC mount is to be constructed from commercially-available isolation mounts, but is less than ideal for CD and VC mount comparison in that the improvement in the performance of the VC mount over that of the CD mount in the frequency band about the cancellation frequency is less than if the two natural frequencies were the same. However, since the difference in natural frequencies is small, the difference in the relative performance of the CD and VC mounts near the cancellation frequency is also small.

For the KR effectiveness curves,

$$w_{OKR}^2 = K_3/M_M \ , \tag{69}$$

where:

K_3 is the stiffness (spring constant) of the mount;
M_M is the mass of the machine; and
z_s' is the nondimensional supporting strucure impedance defined as

$$z_s' = w_{OKR} z_s / K_3, \tag{70}$$

---

*The effectiveness of a mount in dB is defined by the equation

$$E(dB) = 20 \log |E| \ . \tag{71}$$

422

Fig.2 – Mount Effectiveness in dB for KR and CD Mounts; Resistive Supporting Structure.

423
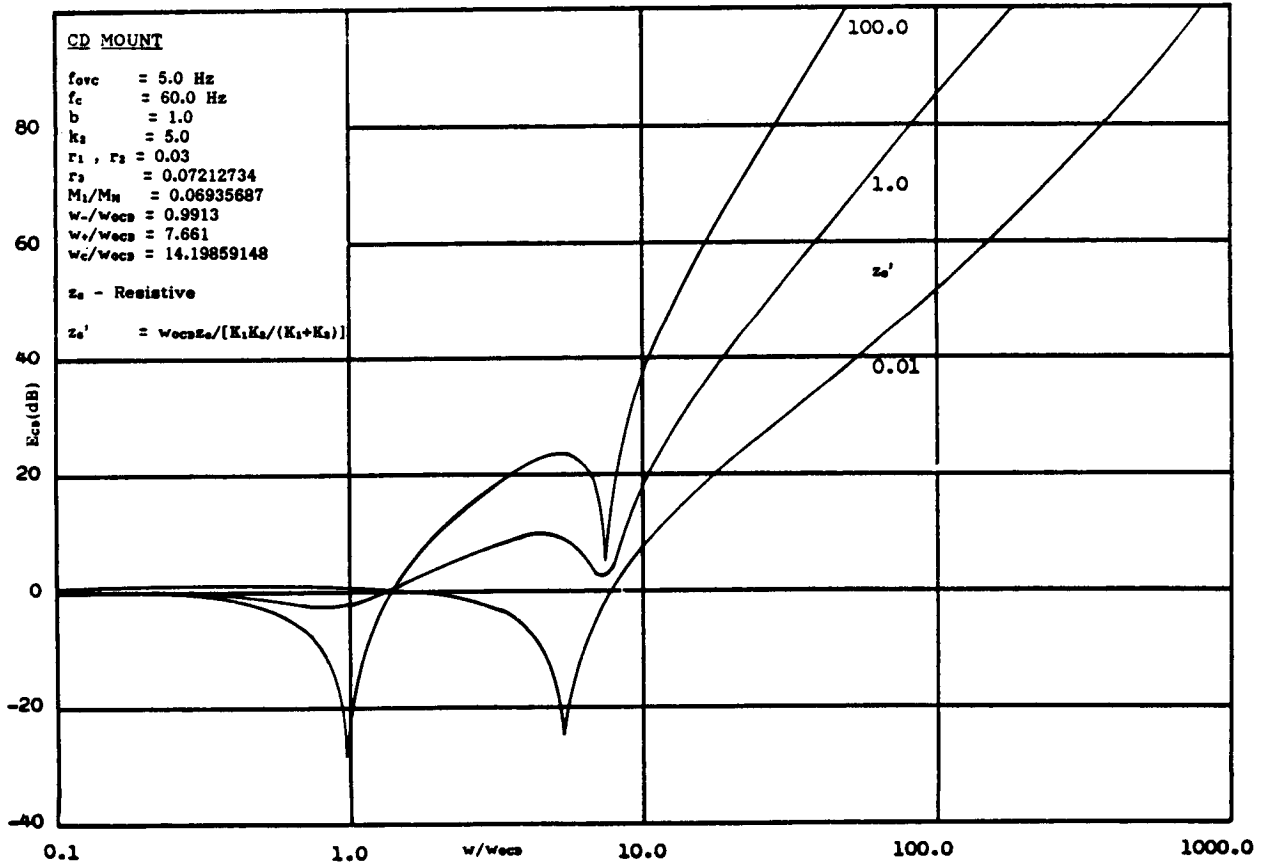
Fig.3 – Mount Effectiveness in dB for KR and CD Mounts; Masslike Supporting Structure.

SPRING–DASHPOT (KR) MOUNT

r_3 = (wR_3/K_3) = 0.03

z_s – Springlike

z_s' = $w_{oss}z_s/K_3$

$E_{ss}(dB)$

z_s'
–j100.0
–j10.0
–j1.0
–j0.1
–j0.01

w/w_{oss}
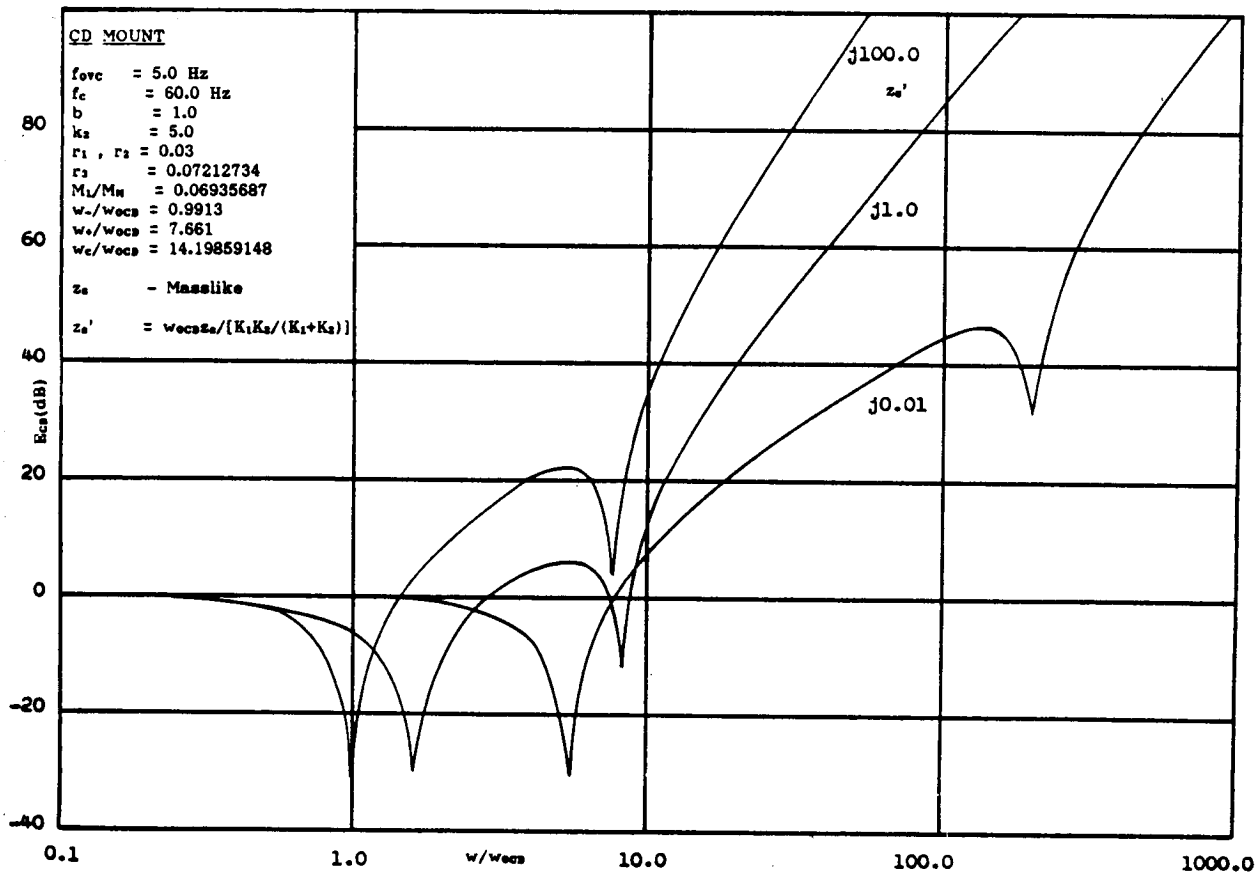
Fig.4 – Mount Effectiveness in dB for KR and CD Mounts; Springlike Supporting Structure.

CD MOUNT

f_{ovc} = 5.0 Hz
f_c = 60.0 Hz
b = 1.0
k_2 = 5.0
r_1 , r_2 = 0.03
r_3 = 0.07212734
M_L/M_M = 0.06935687
w_-/w_{ocs} = 0.9913
w_o/w_{ocs} = 7.661

z_s – Springlike

z_s' = $w_{ocs}z_s/[K_1K_2/(K_1+K_2)]$

$E_{cs}(dB)$

–j100.0
z_s'
–j1.0
–j0.01

w/w_{ocs}

425

Fig.5 - Mount Effectiveness in dB for KR and VC Mounts; Resistive Supporting Structure.

SPRING-DASHPOT (KR) MOUNT

$r_3 = (wR_3/K_3) = 0.03$

z_s - Resistive

$z_s' = w_{oxz}z_s/K_3$

VC MOUNT

f_{ovc}	= 5.0 Hz
f_c	= 60.0 Hz
b	= 1.0
k_2	= 5.0
r_1, r_2	= 0.03
r_3	= 0.07212734
M_1/M_N	= 0.06935687
w_-/w_{ocs}	= 0.9913
w_+/w_{ocs}	= 7.661
w_c/w_{ocs}	= 14.19859148

z_s - Resistive

$z_s' = w_{ocs}/[K_1K_2/(K_1+K_2)]$

426

SPRING–DASHPOT (KR) MOUNT

r_3 = (wR_3/K_3) = 0.03

z_s — Masslike

z_s' = $W_{om}z_s/K_3$

z_s'

j100.0

j10.0

j1.0

j0.1

j0.01

E_{ss}(dB)

80

60

40

20

0

-20

-40

0.1   1.0   w/w$_{om}$ 10.0   100.0   1000.0
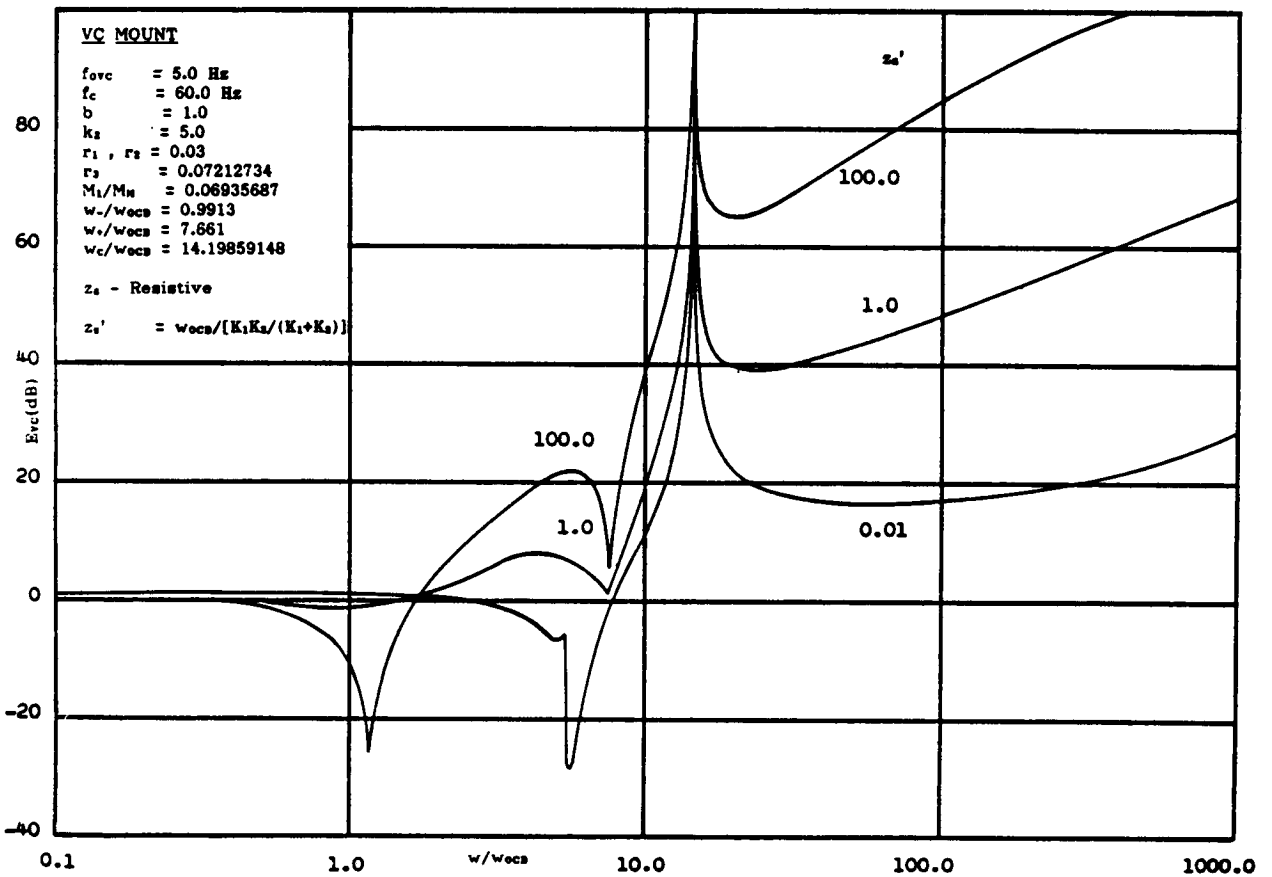
Fig.6 - Mount Effectiveness in dB for KR and VC Mounts; Masslike Supporting Structure.

VC MOUNT

f_{ovc} = 5.0 Hz
f_c = 60.0 Hz
b = 1.0
k_2 = 5.0
r_1 , r_2 = 0.03
r_3 = 0.07212734
M_1/M_N = 0.06935687
w_-/w_{ocs} = 0.9913
w_+/w_{ocs} = 7.661
w_c/w_{ocs} = 14.19859148

z_s — Masslike

z_s' = $w_{ocs}z_s/[K_1K_2/(K_1+K_2)]$

z_s'

j100.0

j1.0

j100.0

j1.0

j0.01

E_{vc}(dB)

80

60

40

20

0

-20

-40

0.1   1.0   w/w$_{ocs}$ 10.0   100.0   1000.0

427

SPRING-DASHPOT (KR) MOUNT

$r_3 = (wR_3/K_3) = 0.03$

z_s – Springlike

$z_s' = w_{oxz}z_s/K_3$

z_s': −j100.0, −j10.0, −j1.0, −j0.1, −j0.01

E$_{ss}$(dB)

w/w$_{ocs}$
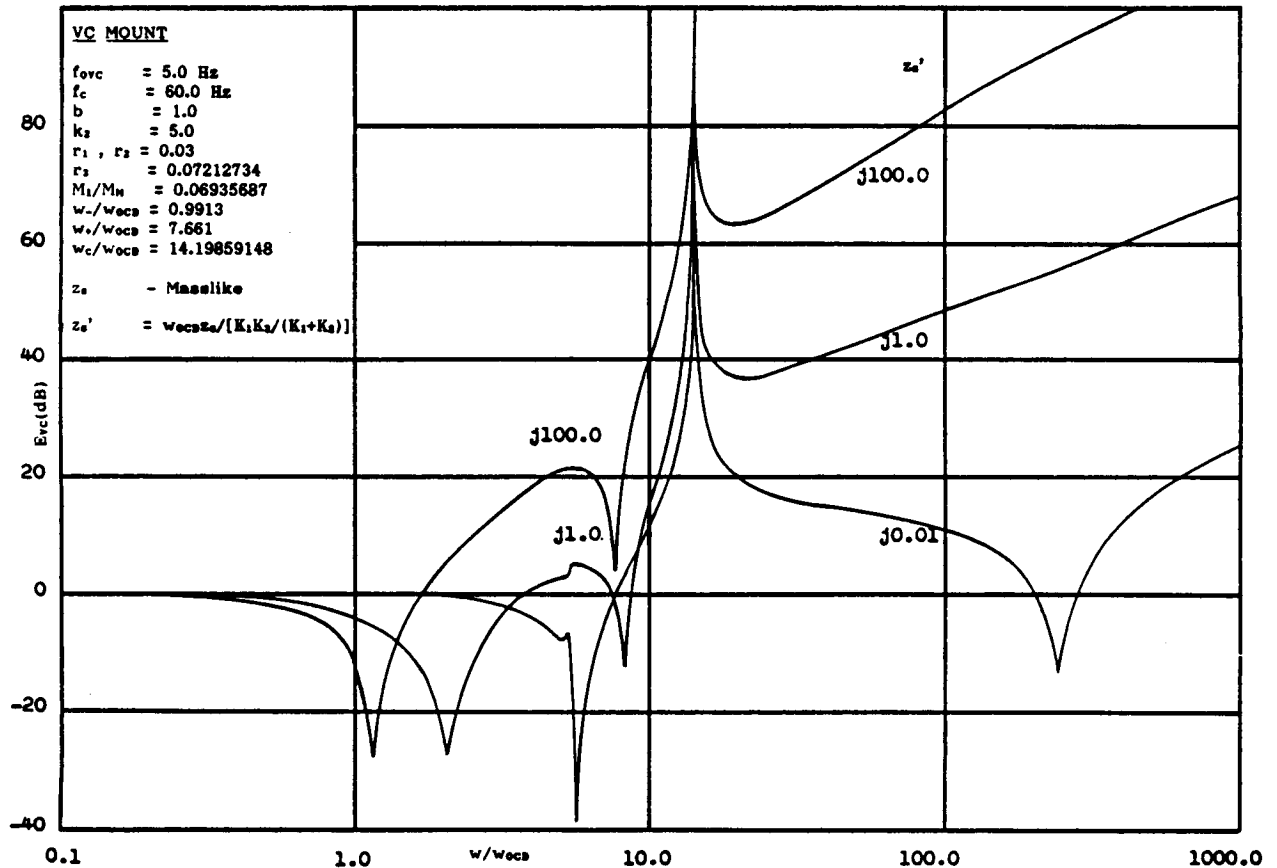
Fig.7 – Mount Effectiveness in dB for KR and VC Mounts; Springlike Supporting Structure.

VC MOUNT

$f_{ovc} = 5.0$ Hz
$f_c = 60.0$ Hz
$b = 1.0$
$k_2 = 5.0$
$r_1 , r_2 = 0.03$
$r_3 = 0.07212734$
$M_1/M_n = 0.06935687$
$w_-/w_{ocs} = 0.9913$
$w_+/w_{ocs} = 7.661$
$w_c/w_{ocs} = 14.19859148$

z_s – Springlike

$z_s' = w_{ocs}z_s/[K_1K_2/(K_1+K_2)]$

z_s': −j100.0, −j1.0, −j0.01

−j100.0, −j1.0

E$_{vc}$(dB)

w/w$_{ocs}$

428

CD MOUNT

f_{ovc} = 5.0 Hz
f_c = 60.0 Hz
b = 1.0
k_2 = 5.0
r_1, r_2 = 0.03
r_3 = 0.07212734
M_1/M_N = 0.06935687
w_-/w_{ocs} = 0.9913
w_o/w_{ocs} = 7.661
w_c/w_{ocs} = 14.19859148

z_s - Resistive
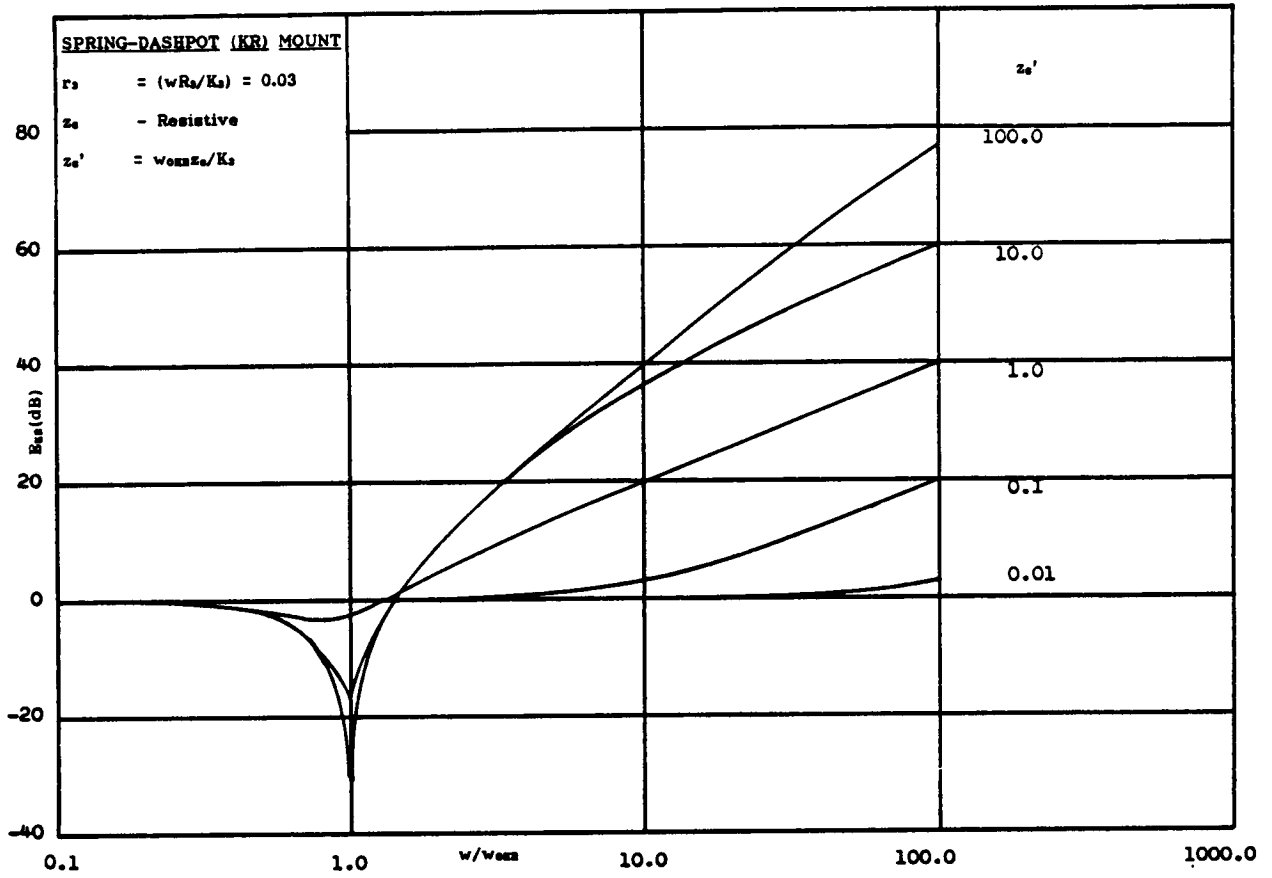
z_s' = $w_{ocs}z_s/[K_1K_2/(K_1+K_2)]$
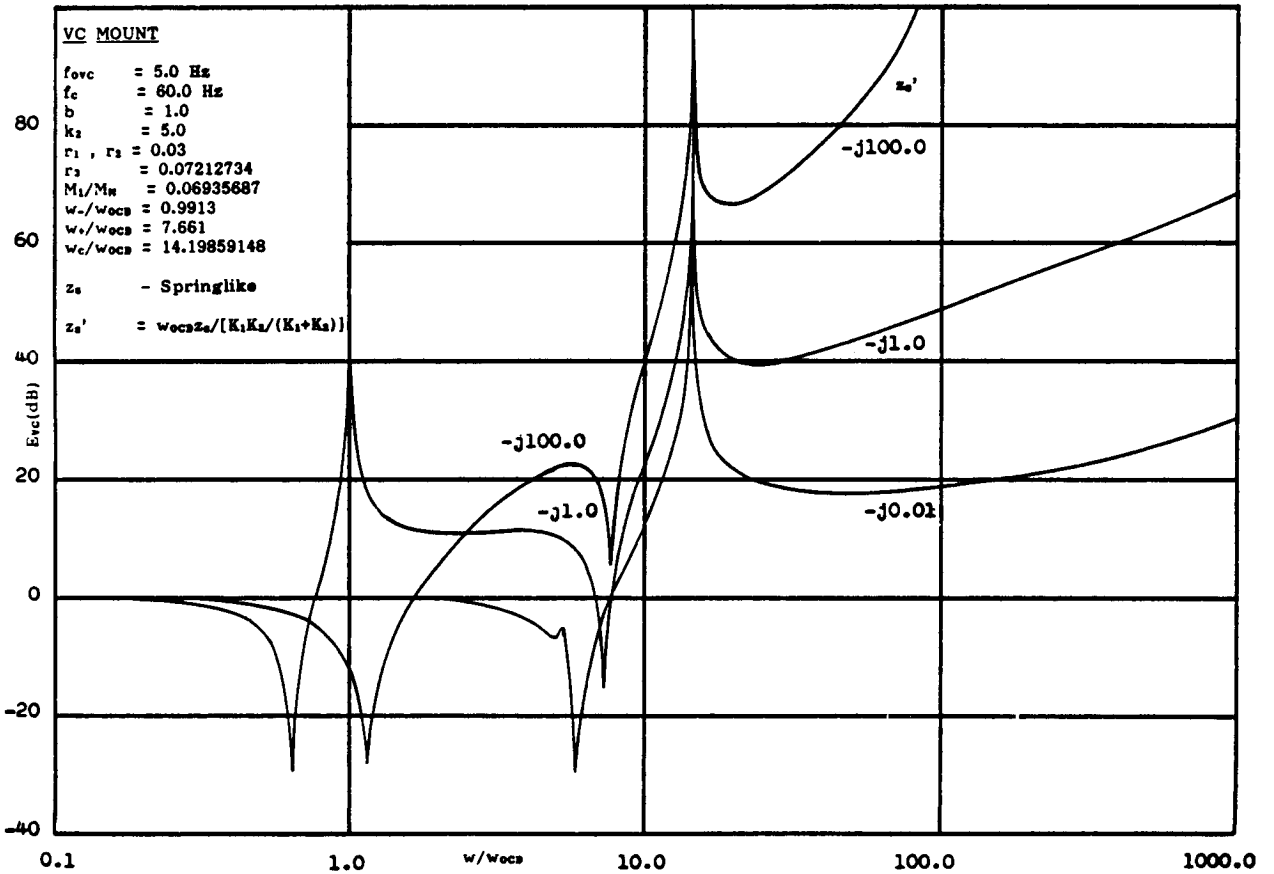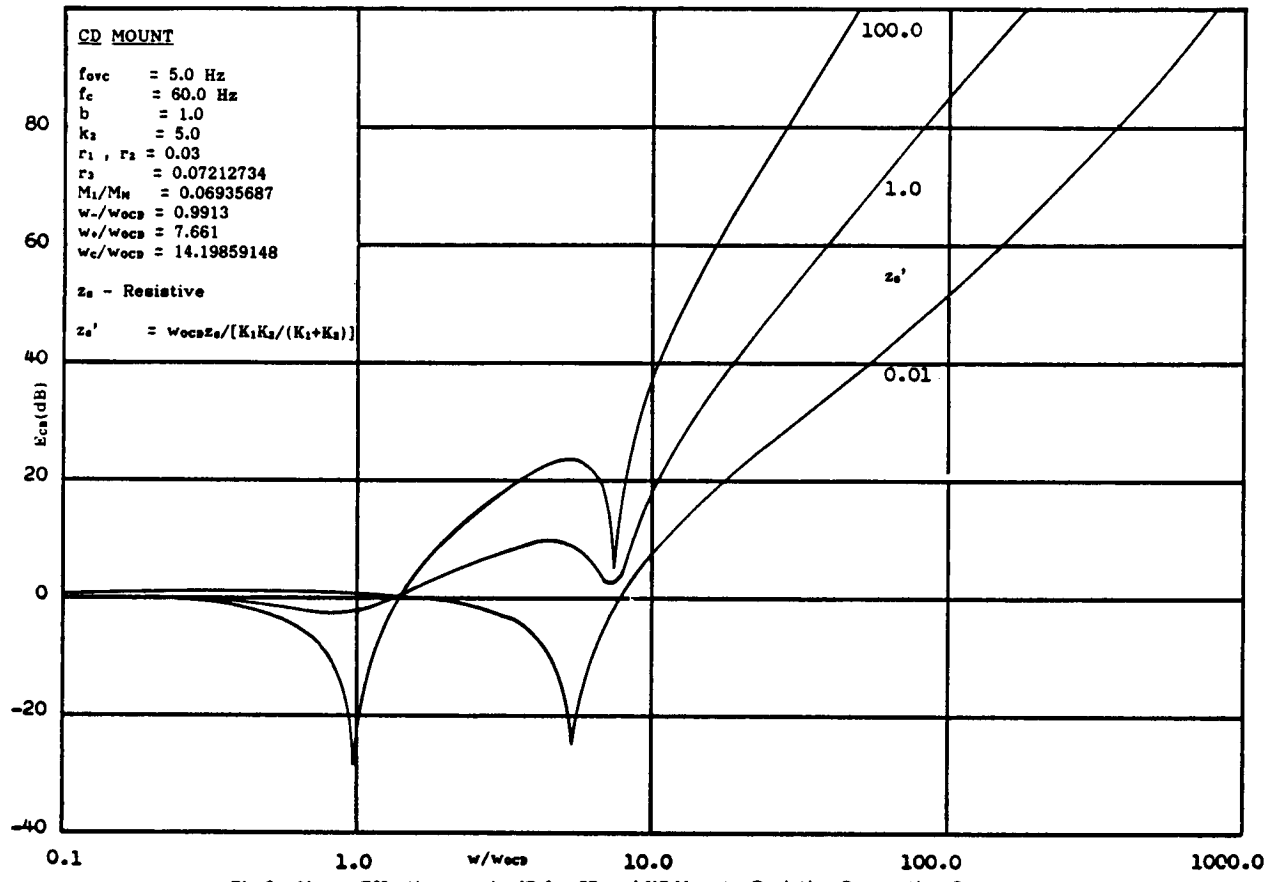
Fig.8 - Mount Effectiveness in dB for CD and VC Mounts; Resistive Supporting Structure.

VC MOUNT

f_{ovc} = 5.0 Hz
f_c = 60.0 Hz
b = 1.0
k_2 = 5.0
r_1, r_2 = 0.03
r_3 = 0.07212734
M_1/M_N = 0.06935687
w_-/w_{ocs} = 0.9913
w_o/w_{ocs} = 7.661
w_c/w_{ocs} = 14.19859148

z_s - Resistive

z_s' = $w_{ocs}/[K_1K_2/(K_1+K_2)]$

429

CD MOUNT

f_{ovc} = 5.0 Hz
f_c = 60.0 Hz
b = 1.0
k_2 = 5.0
r_1 , r_2 = 0.03
r_3 = 0.07212734
M_1/M_N = 0.06935687
w_-/w_{ocs} = 0.9913
w_+/w_{ocs} = 7.661
w_c/w_{ocs} = 14.19859148

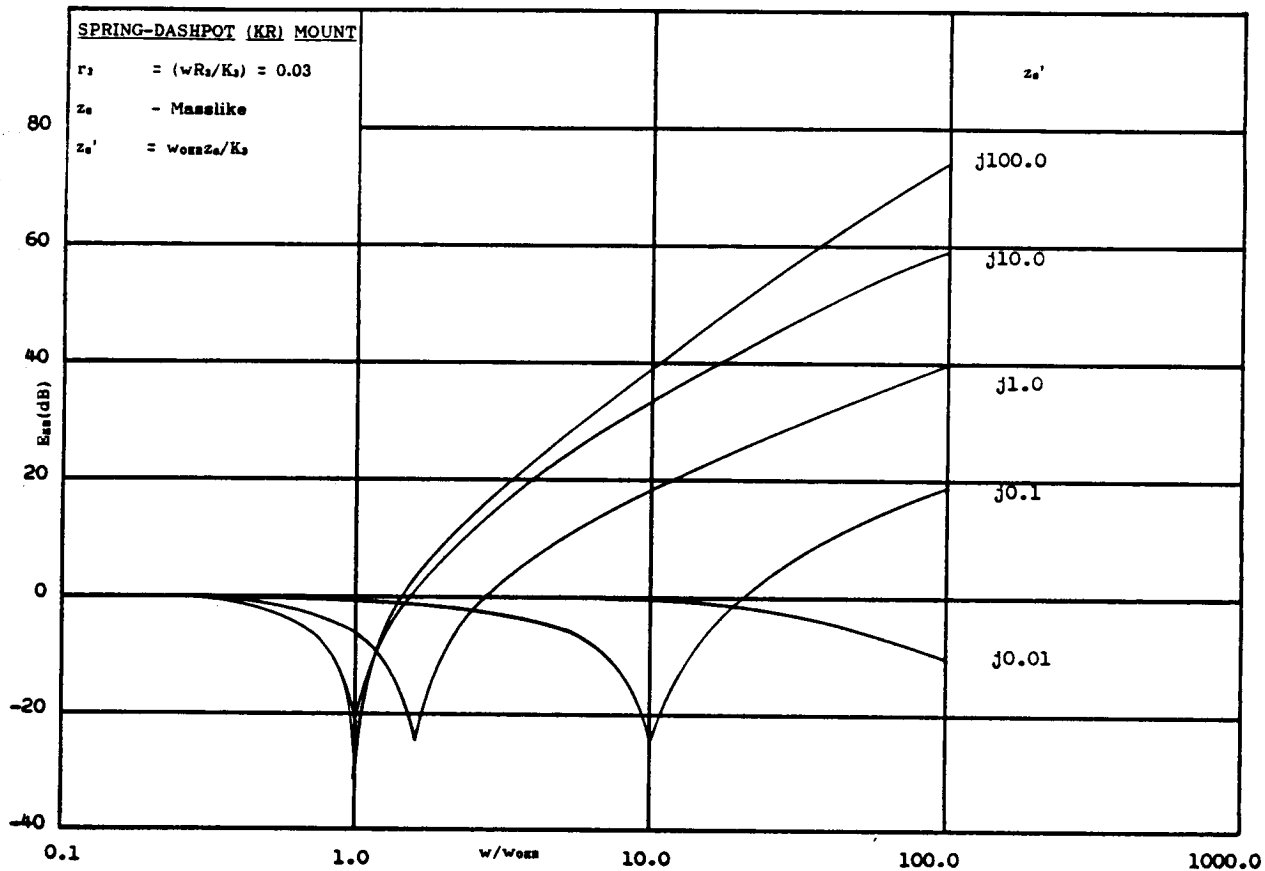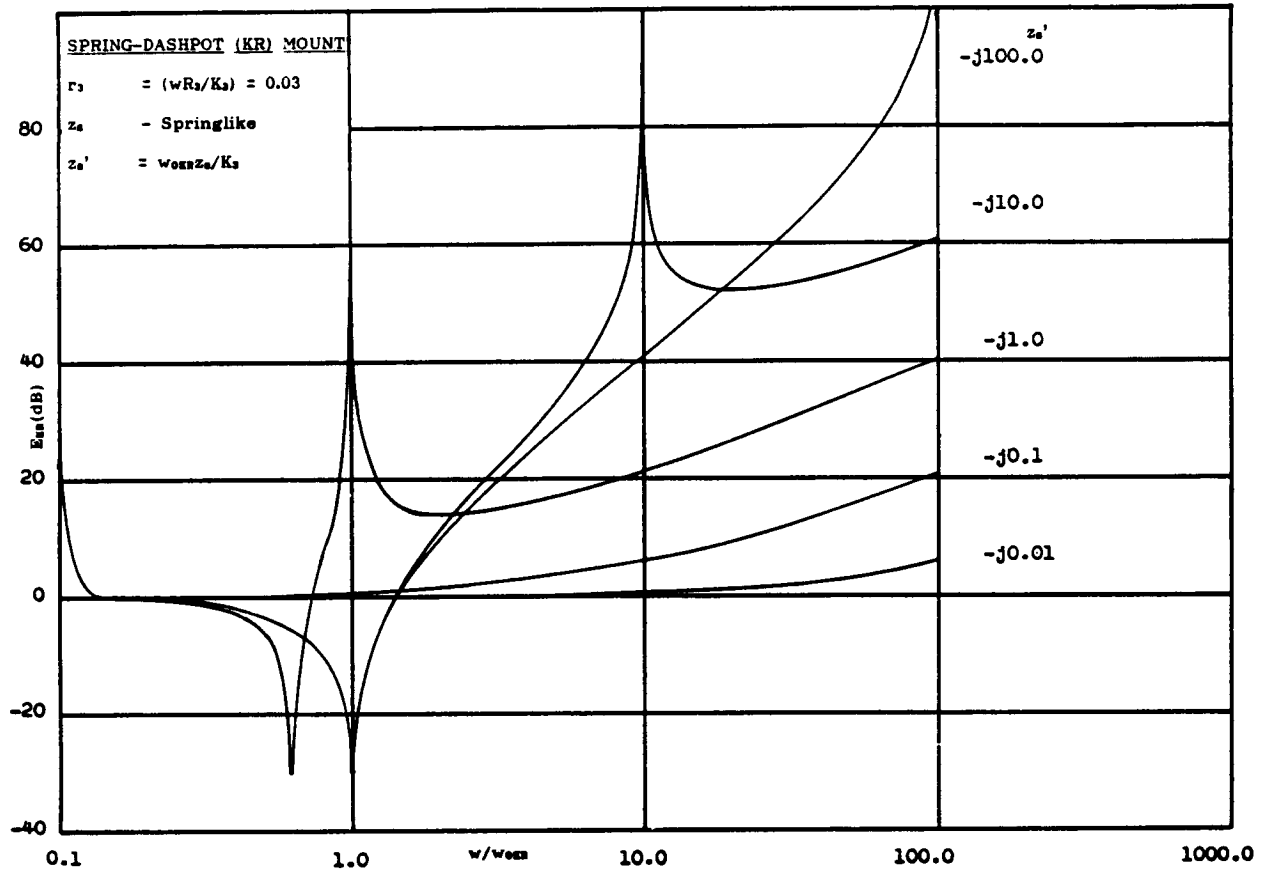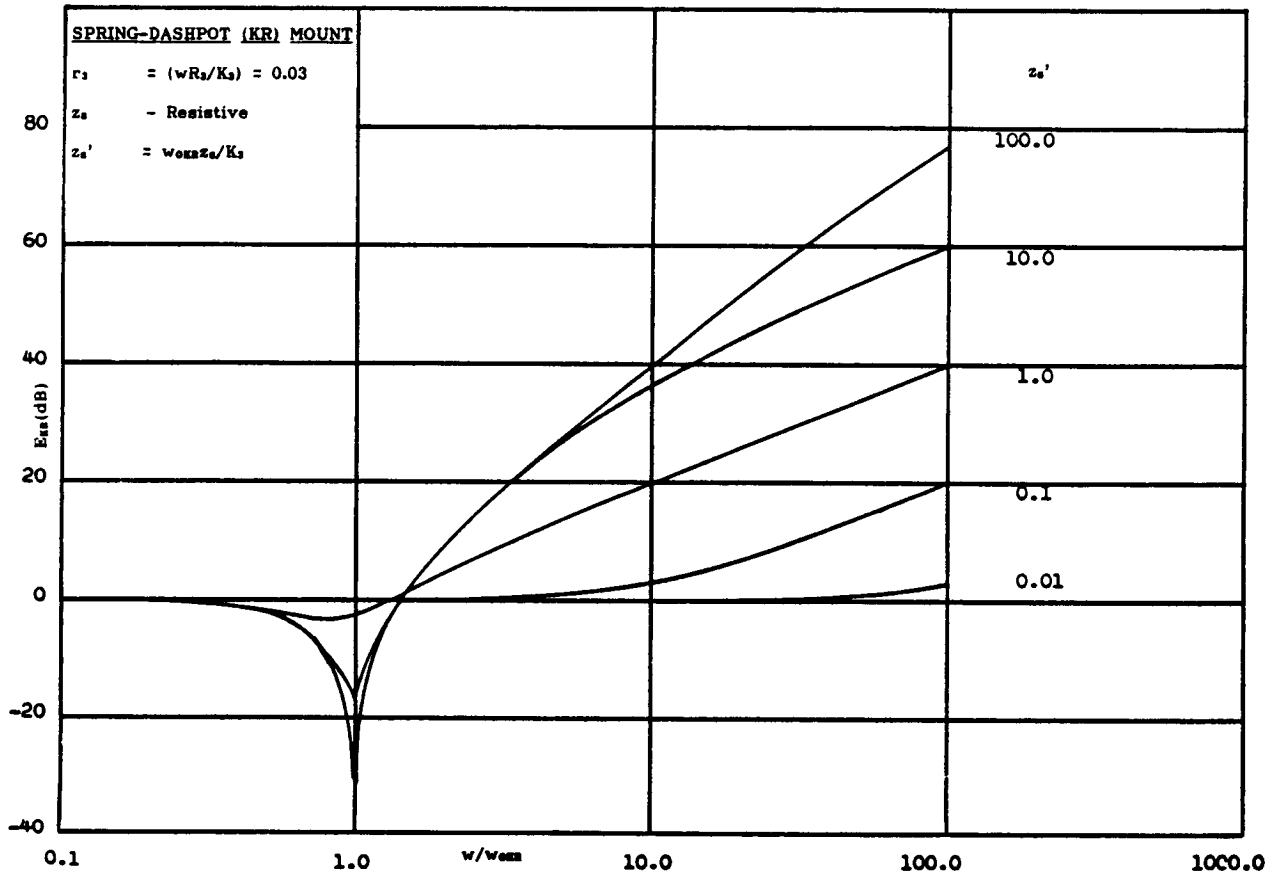z_s — Masslike

z_s' = $w_{ocs}z_s/[K_1K_2/(K_1+K_2)]$
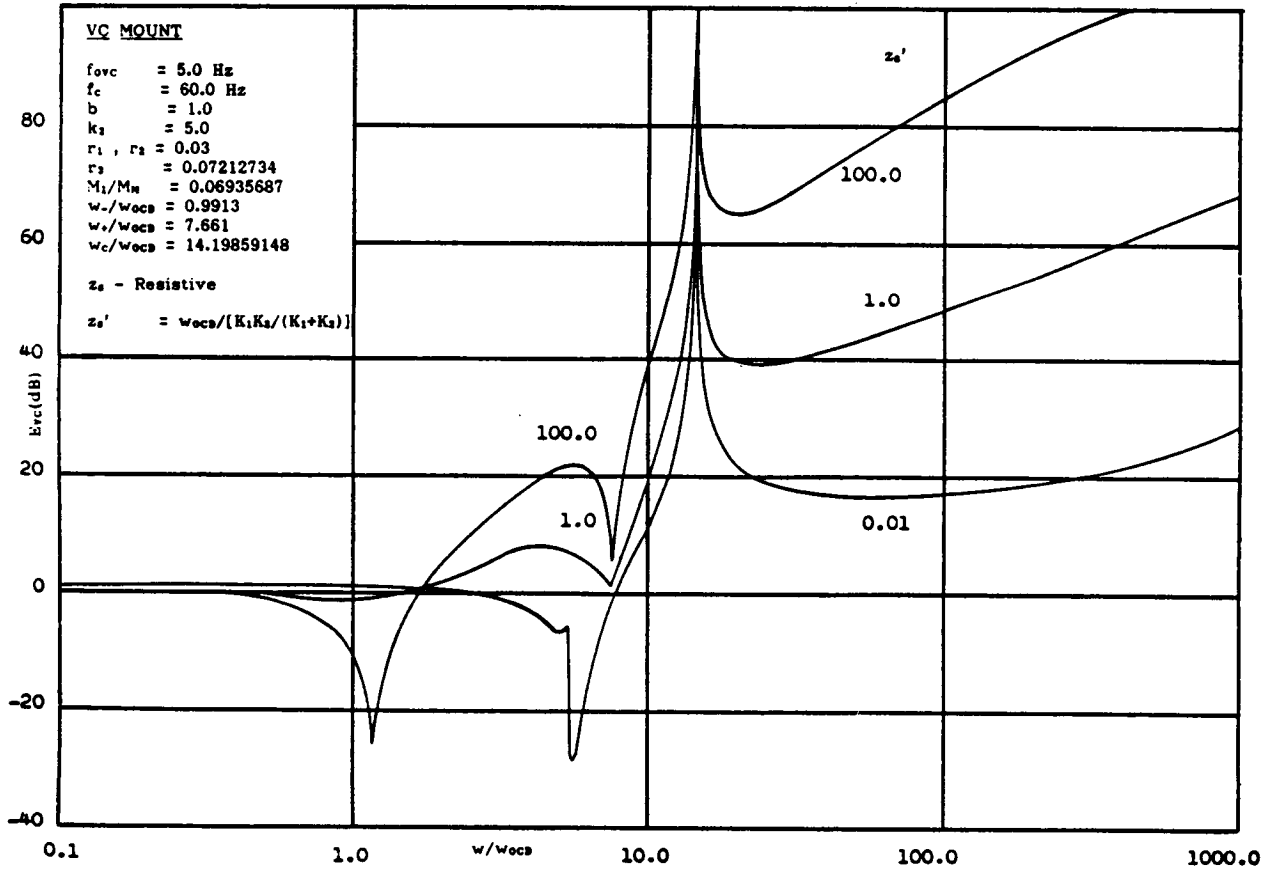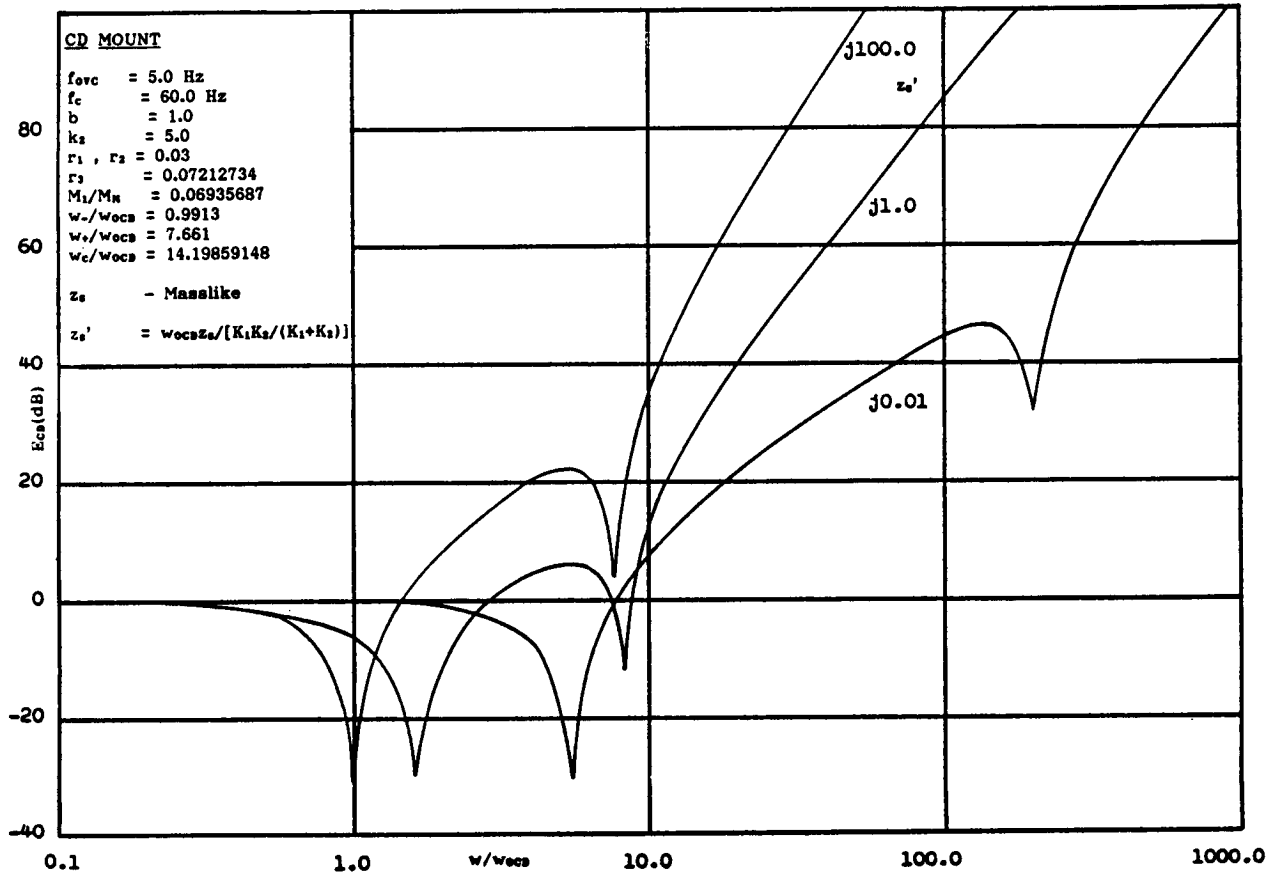
Fig.9 – Mount Effectiveness in dB for CD and VC Mounts; Masslike Supporting Structure.

VC MOUNT

f_{ovc} = 5.0 Hz
f_c = 60.0 Hz
b = 1.0
k_2 = 5.0
r_1 , r_2 = 0.03
r_3 = 0.07212734
M_1/M_N = 0.06935687
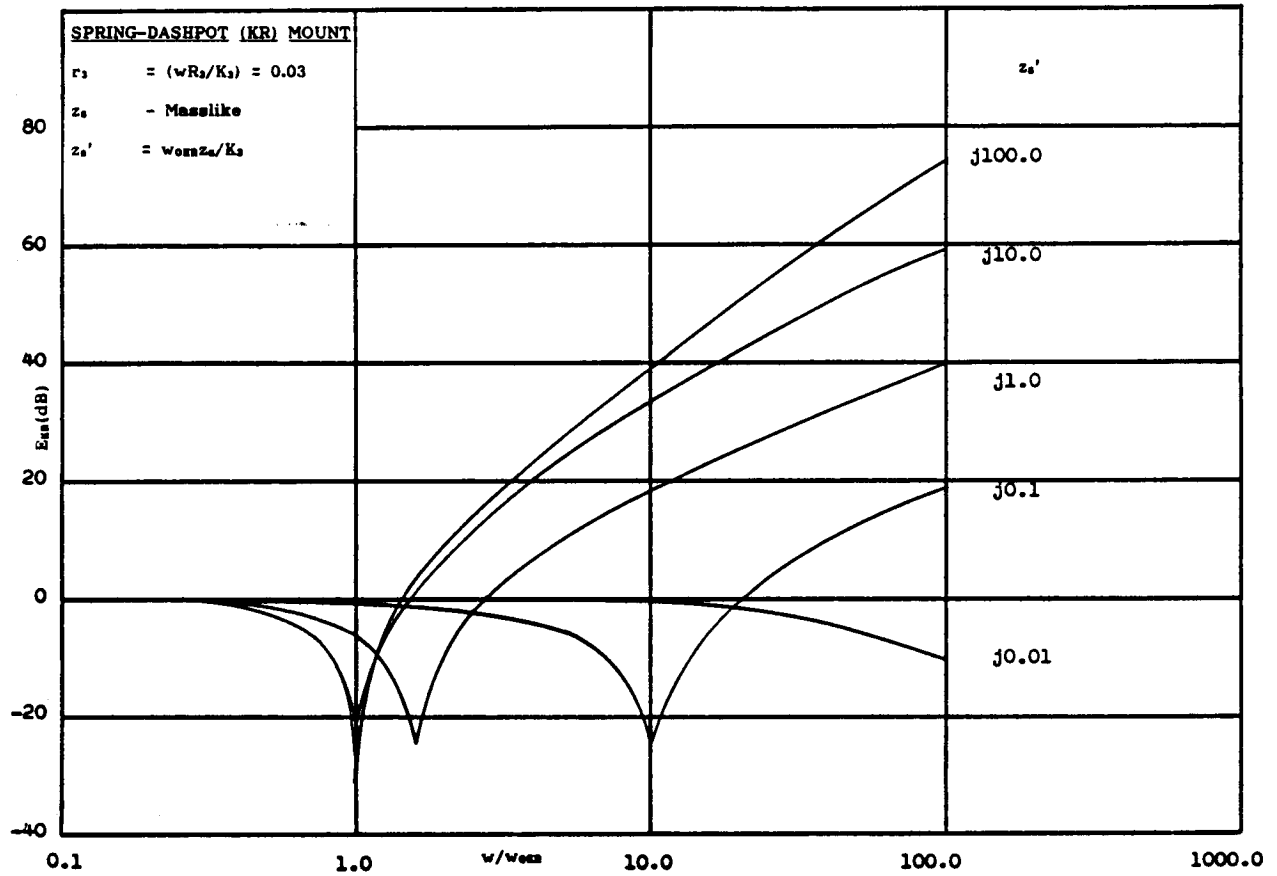w_-/w_{ocs} = 0.9913
w_+/w_{ocs} = 7.661
w_c/w_{ocs} = 14.19859148

z_s — Masslike

z_s' = $w_{ocs}z_s/[K_1K_2/(K_1+K_2)]$

430

CD MOUNT

f_{ovc} = 5.0 Hz
f_c = 60.0 Hz
b = 1.0
k_2 = 5.0
r_1 , r_2 = 0.03
r_3 = 0.07212734
M_1/M_N = 0.06935687
w_-/w_{ocs} = 0.9913
w_+/w_{ocs} = 7.661

z_s — Springlike

z_s' = $w_{ocs}z_s/[K_1K_3/(K_1+K_3)]$
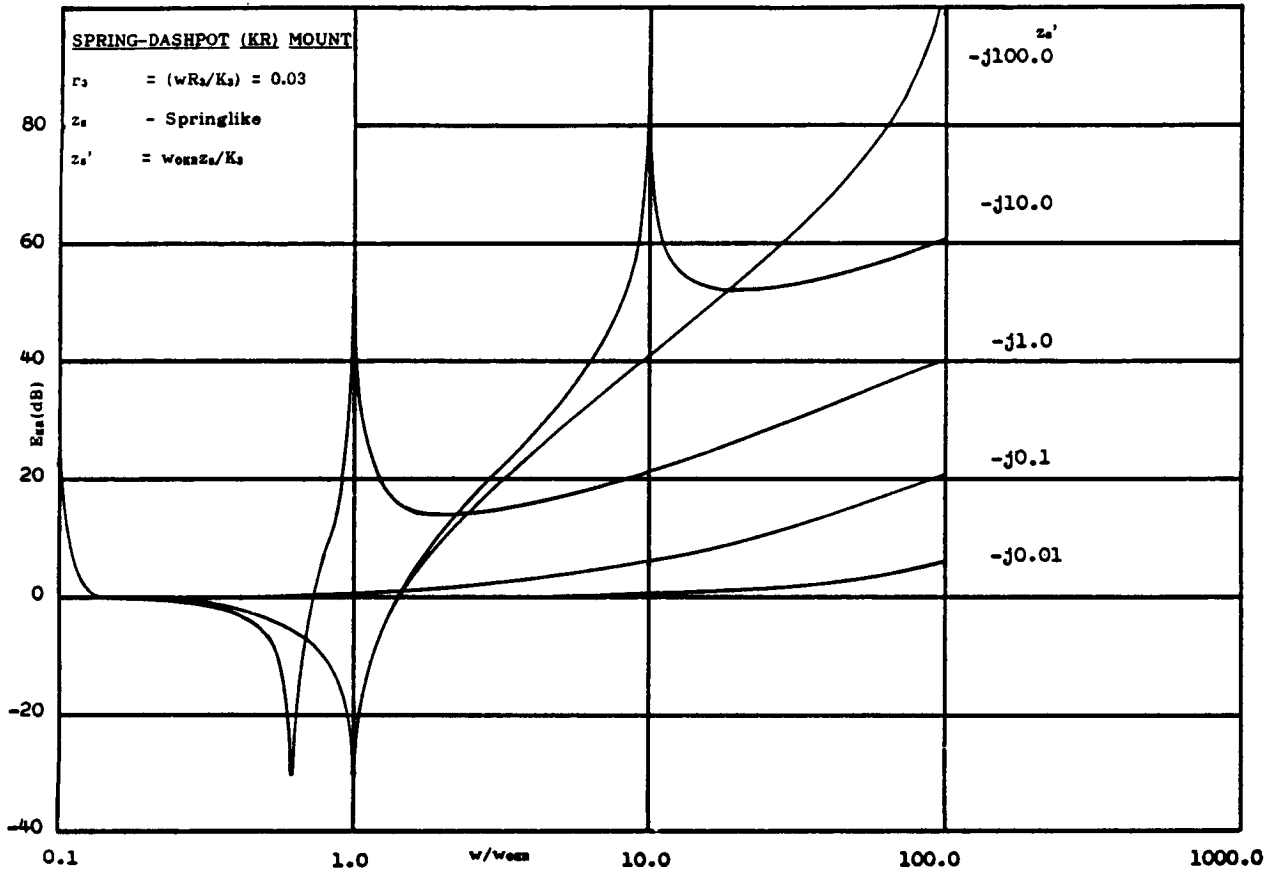
$-j100.0$

z_s'

$-j1.0$

$-j0.01$
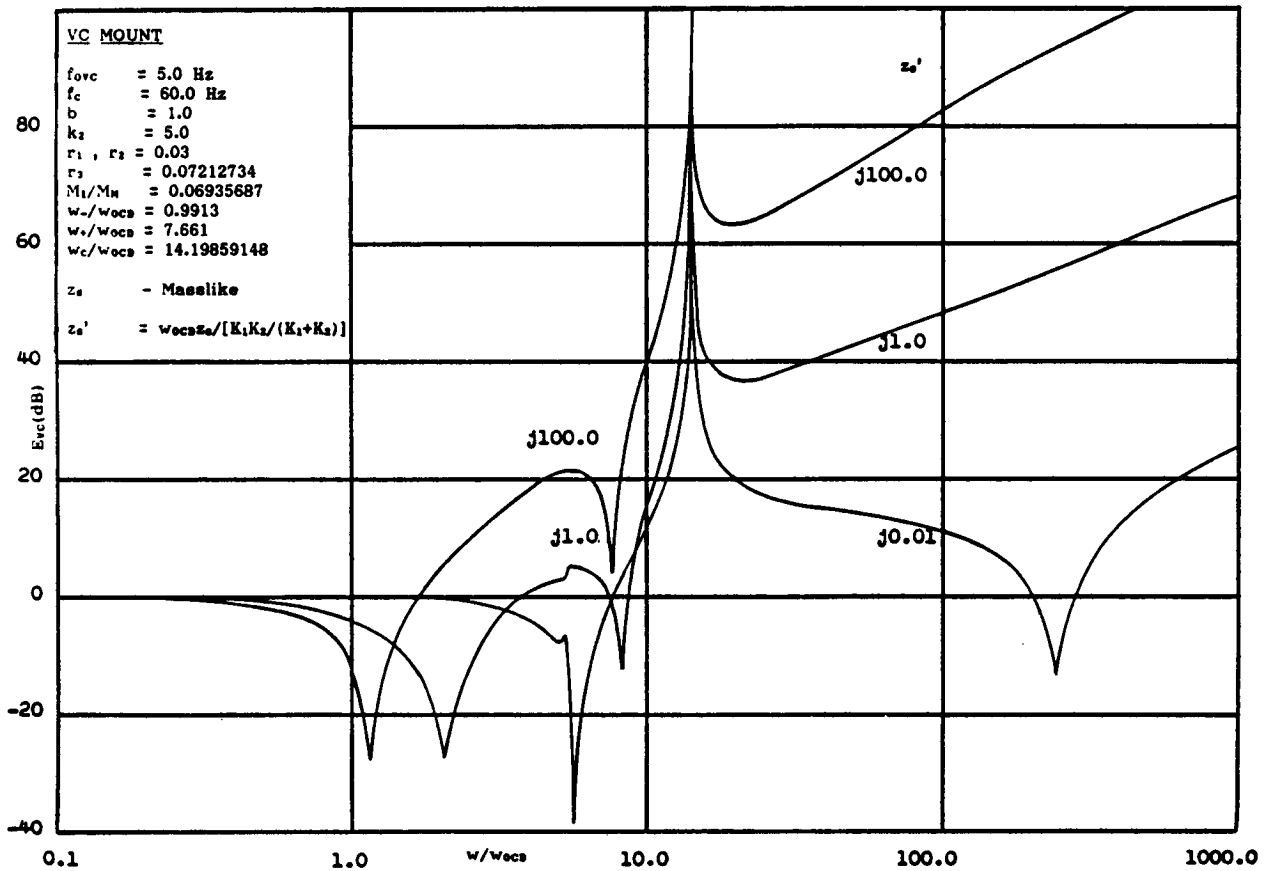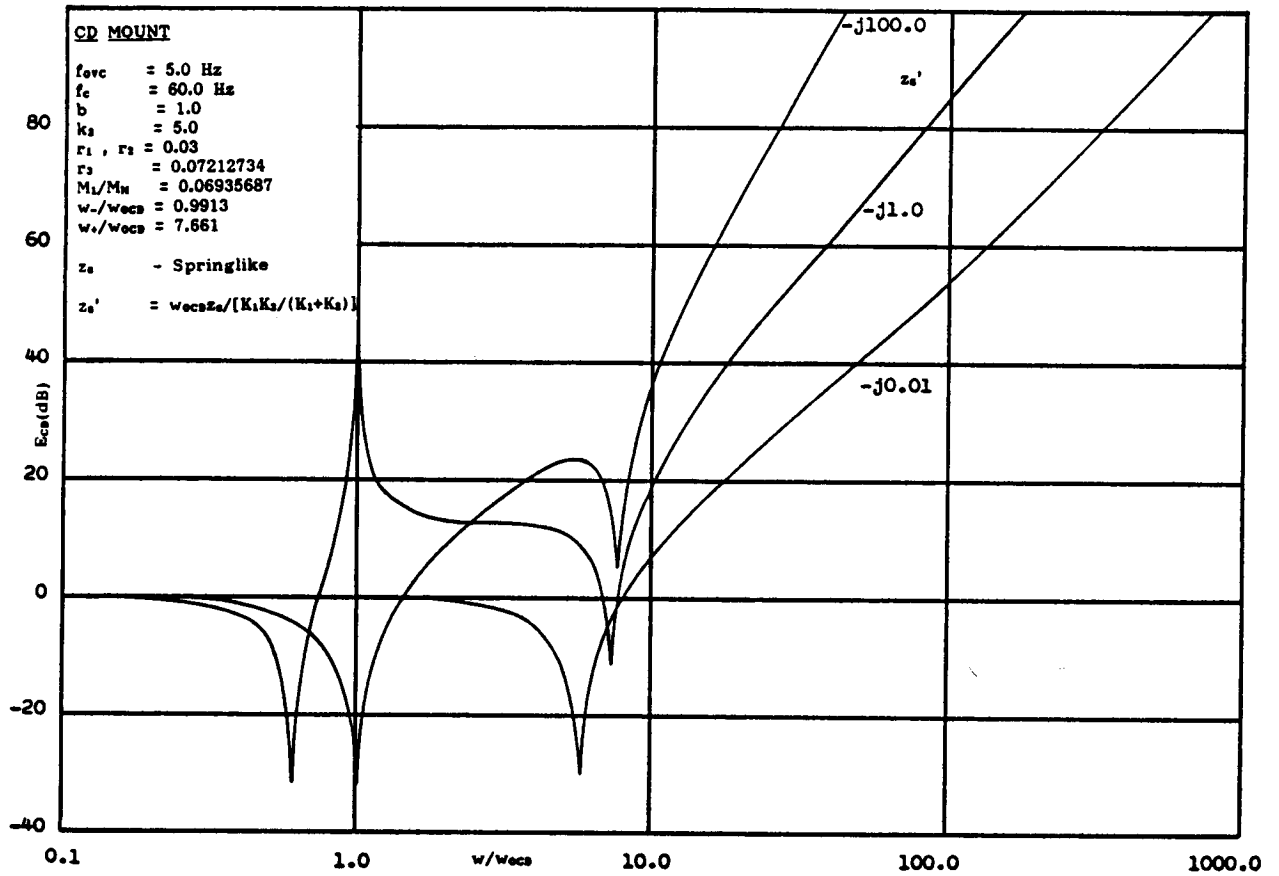
Fig.10 – Mount Effectiveness in dB for CD and VC Mounts; Springlike Supporting Structure.

VC MOUNT

f_{ovc} = 5.0 Hz
f_c = 60.0 Hz
b = 1.0
k_2 = 5.0
r_1 , r_2 = 0.03
r_3 = 0.07212734
M_1/M_N = 0.06935687
w_-/w_{ocs} = 0.9913
w_+/w_{ocs} = 7.661
w_c/w_{ocs} = 14.19859148

z_s — Springlike

z_s' = $w_{ocs}z_s/[K_1K_3/(K_1+K_3)]$

z_s'

$-j100.0$

$-j1.0$

$-j100.0$

$-j1.0$

$-j0.01$

431
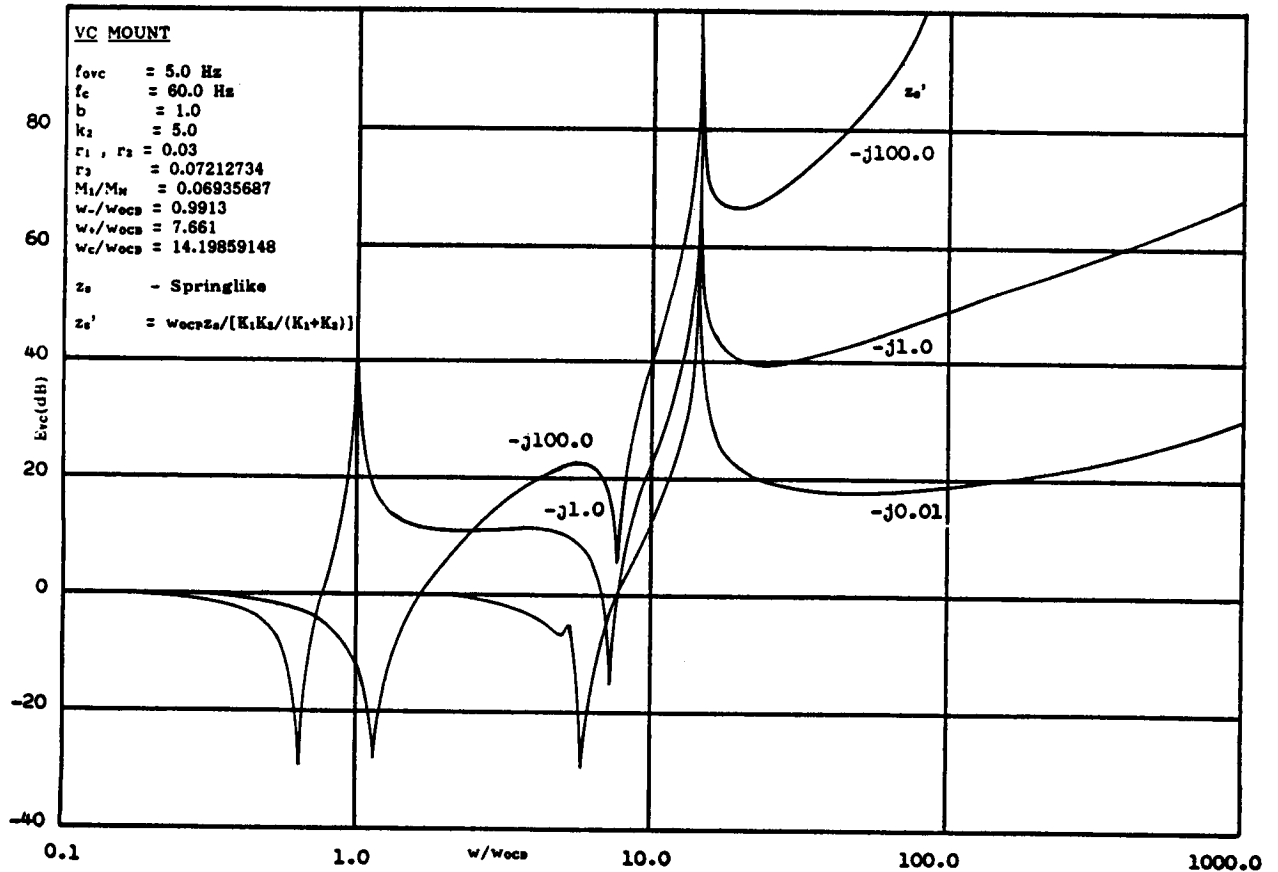
where z_s is the supporting structure impedance.

For the CD and VC mount effectiveness curves,

$$w_{OCD}^2 = [K_1 K_2/(K_1+K_2)]/M_M = [bK_2/(b+1)]/M_M , \qquad (72)$$

where:

K₁   is the stiffness of the resilient element in the CD mount (CD section of the VC mount) attached to the machine;

K₂   is the stiffness of the resilient element in the CD mount (CD section of the VC mount) attached to the supporting structure;

M$_M$ is th mass of the machine;

$$b = K_1/K_2; \qquad (73)$$

$$z_s' = w_{OCD}[(K_1+K_2)/K_1 K_2] z_s = w_{OCD}[(b+1)/bK_2] z_s . \qquad (74)$$

The example chosen for the calculations is the isolation of a machine by a VC mount, the natural frequency f_{OVC} of the machine on the mount being 5.0 Hz, the cancellation frequency f_c being 60.0 Hz. The mount parameters chosen for the calculation were: b = 1.0 ; k_2 = 5.0 ; and r_1 = r_2 = 0.03 .

Given these data, r_3 and M_1/M_M were calculated from Eqs. (64) and (65). From these equations: r_3 = 0.07212734 ; M_1/M_M = 0.06935687.

The effectiveness calculations for the CD and VC mounts were made by substituting Eqs. (45)-(51) into Eqs. (43) and (44) for E_{CD} and E_{VC}, and then expressing $(w/w_1)^2$, $(w/w_2)^2$, $(w/w_{12})^2$ in terms of $(w/w_{OCD})^2$ by means of the relationships:

$$(w/w_1)^2 = (M_1/M_M)[1/(b+1)](w/w_{OCD})^2 ; \qquad (75)$$

$$(w/w_2)^2 = (M_1/M_M)[b/(b+1)](w/w_{OCD})^2 ; \qquad (76)$$

$$(w/w_{12})^2 = (M_1/M_M)[b/(b+1)^2](w/w_{OCD})^2 . \qquad (77)$$

The compound section of the VC mount is treated as the compound mount, the effectiveness of which is to be compared with that of th KR and VC mounts. Using the relationships

$$w_{OVC}^2 = (2\pi f_{OVC})^2 = [K_3 + K_1 K_2/(K_1 + K_2)]/M_M , \tag{78}$$

where w_{OVC}^2 is the square of the natural circular frequency of the machine on the VC mount, and Eq. (72) where w_{OCD}^2 is the square of the natural circular frequency of the machine on the CD section of the mount, one can find the relationship between w_{OCD} and w_{OVC}.

$$w_{OCD} = [bk_2/(b+1+bk_2)]^{1/2} w_{OVC} . \tag{79}$$

Given that $b = 1.0$, $k_2 = 5.0$, and $f_{OVC} = 5.0$ Hz, from Eq. 79, $f_{OCD} = 4.22$ Hz.

The frequency f_{12} at which M_1 resonates with K_1 and K_2, with the input terminal of K_1 and the output terminal of K_2 blocked, can be calculated from Eqs. (61) and (78):

$$w_{12} = 2\pi f_{12} = [(b+1)^2/(b+1+bk_2)]^{1/2} [M_M/M_1]^{1/2} w_{CVC} ; \tag{80}$$

hence, $f_{12} = 32.09$ Hz.

Comparison of the Effectivenesses of KR, CD, and VC Mounts as a Function of Frequency, and Supporting Structure Resistance or Masslike or Springlike Reactance

From Figs. 2 – 10, the effectivenesses of KR, CD, and VC mounts are strongly dependent on supporting structure impedance. At frequency ratios less than about 10, for nondimensional impedance ratios $z_s' = 0.01$, 1.0 , 100.0 , the simple KR mount is more effective than either the CD or VC mount; however, at frequency ratios greater than 10, for $z_s' = 1.0$ or greater, both CD and VC mounts have greater effectivenesses than the KR mount. In the frequency range from about 10 – 20, the VC mount has significantly higher effectiveness than the CD mount, and this increase in effectiveness would be even greater were the VC and CD mounts to have the same stiffness, i.e., were the natural frequencies of the machine on the two mounts to be the same. The effectiveness of the VC mount at the frequency ratio 14.2, which corresponds to the cancellation frequency, is infinite and independent of the supporting structure and machine impedances. Variations in source frequency of as much as + 5% can be tolerated without reducing the effectiveness of the VC mount below that of KR or CD mounts of the same stiffness because of the relatively broad frequency ratio band over which appreciable cancellation occurs.

For masslike supporting structures, for which $z_s' << j1.0$, a third minimum in effectiveness occurs for both CD and VC mounts at a frequency at which the impedance "looking back" into the mount at Terminal 3 is springlike and of equal magnitude to the supporting structure impedance, e.g., at $(w/w_{OCD}) = 200$ for $z_s' = j\,0.01$ in Figs. 7 and 8. (Whether such minima will occur at high frequency ratios is dependent on the losses -- the mechanical resistance -- of the supporting structure.)

For springlike supporting structures, a maximum in effectiveness occurs at a frequency ratio corresponding to the frequency at which the masslike reactance "looking back" into the machine is equal in magnitude and opposite in sign to the springlke reactance of the supporting structure, e.g., at $(w/w_{OCD}) = 1.0$ for $z_s' = -j\,1.0$, and for $(w/w_{OCD}) = 100$ for

$z_s' = -j\,100.0$ in Figs. 9 and 10. The maximum in effectiveness occurs because introducing a mount between machine and supporting structure eliminates the resonance that occurs in its absence.

VC MOUNT DESIGN

A straightforward procedure has been developed for the design of VC mounts. It is assumed that:

1. The natural frequency f_{ovc} of the machine of mass M_M is specified on the basis of static loading, shock, or other considerations;

2. M_M is known;

3. Appropriate materials and techniques are available for constructing resilient elements z_1 , z_2 , z_3 having specified stiffnesses K_1 , K_2 , K_3 and loss factors r_1 , r_2 , r_3 ;

4. The stiffness ratio $b = K_1/K_2$ is specified;

5. The cancellation-frequency f_c is specified.

The stiffness K_T of a VC mount with M_1 having negligibly small impedance compared with that of M_M at w_{ovc} is given by -- see Fig. 1 --

$$K_T = K_3 + \frac{K_1 K_2}{K_1 + K_2} \, . \tag{81}$$

The stiffnesses K_1 , K_2 , K_3 of resilient elements z_1 , z_2 , z_3 can be calculated from b, k_2 , and K_T which can be determined from $w_{ovc} = 2\pi f_{ovc}$ and M_M.

$$K_T = w_{OVC}^2 \, M_M. \tag{82}$$

From Eq. (81) :

$$K_1/K_T = [b+1]k_2/[b+1+bk_2] \; ; \tag{83}$$

$$K_2/K_T = [b+1]k_2/[b+1+bk_2] \; ; \tag{84}$$

$$K_3/K_T = [b+1]/[b+1+bk_2] \; . \tag{85}$$

The loss factor r_3 for resilient element z_3 , and the mass M_1 required in the compound section of the mount for cancellation at the frequency $f_c = w_c/2\pi$ can be calculated from w_{ovc} , w_c , b , k_2 , r_1 , and r_2 from Eqs. (64) and (84) below:

$$r_3 = \frac{r_1 b + r_2 + bk_2(r_1+r_2)}{bk_2\dfrac{(1-r_1r_2)}{2} + \left[\left[bk_2\dfrac{(1-r_1r_2)}{2}\right]^2 - [r_1b+r_2][r_1b+r_2+bk_2(r_1+r_2)]\right]^{1/2}} ; \qquad (64)$$

$$M_1 = (b+1)k_2\left(\frac{w_{ovc}}{w_c}\right)^2\left[\frac{b+1 + bk_2\dfrac{(1-r_1r_2)}{2} + \left[[bk_2\dfrac{(1-r_1r_2)}{2}]^2 - [r_1b+r_2][r_1b+r_2+bk_2(r_1+r_2)]\right]^{1/2}}{1+b(1+k_2)}\right]M_M . \qquad (86)$$

Eqs. (64) and (83) – (86) can be used to calculate VC mount design curves which show the variation of K_1/K_T , K_2/K_T , M_1/M_M and r_3 as a function of k_2 with f_{ovc} , f_c , b , r_1 and r_2 as parameters. A sample set of curves for $f_{ovc} = 5.0$ Hz, $f_c = 60.0$ Hz, $b = 1.0$, $r_1 = r_2 = 0.03$ is presented in Fig. 11. Such curves are useful, not so much for detailed design, but for selecting ranges of acceptable values of M_1/M_M , r_3 , K_1/K_T , $K_2//K_T$, and K_3/K_T for specified values of f_{ovc} , b , r_1 , r_2 , and f_c .

From Fig. (11), for the specified values of f_{ovc} , b , r_1 , r_2 , and f_c , resilient material considerations suggest that acceptable mount designs might have stiffness ratios k_2 in the range 0.1 – 2.0 , mass ratios M_1/MM in the range 0.015 – 0.25 , and loss factors r_3 in the range 0.06 – 0.12.

As an example of the use of the curves, for $k_2 = 1.0$: $(M_1/M_M) = 0.014$; $r_3 = 0.12$; K_1/K_T , K_2/K_T , $K_3/K_T = 0.67$.

CONCLUSION

An analysis of a single–frequency vibration–cancelling (VC) isolation mount, and calculations of its effectiveness as well as those of conventional (KR) and compound (CD) mounts have been presented.

The VC mount, at and near its cancellation frequency, provides substantially greater vibration reduction than either a KR mount, or a CD mount having the same intermediate mass as the CD section of the VC mount, both the KR and CD mounts having the same low frequency stiffness as the VC mount. At its cancellation frequency, its performance is independent of the natural frequency of the machine /mount system, which suggests that single–frequency vibration reduction should be possible with relatvely stiff VC mounts, an advantage for many applications. Its performance at its cancellation frequency is also independent of both machine and supporting structure impedance.

Conceptually, whether a VC , CD , or KR mount should be selected for a particular application depends on the vibration spectrum of the source, and on the machine and supporting structure impedances at the source frequencies. For a complex source spectrum, a careful analysis is required before a selection can be made, but for certain simple source spectra, the advantage of one or another of the three mounts is clear.

For a stable single–frequency source, or a source the spectrum of which is dominated by a single–frequency component, the VC mount is the best choice since its effectiveness at its cancellation frequency, if perfectly designed and manufactured, is infinite.

For a source with a broadband output spectrum, a compound mount is the best choice if the intermediate mass in the mount can be large enough that the higher normal mode
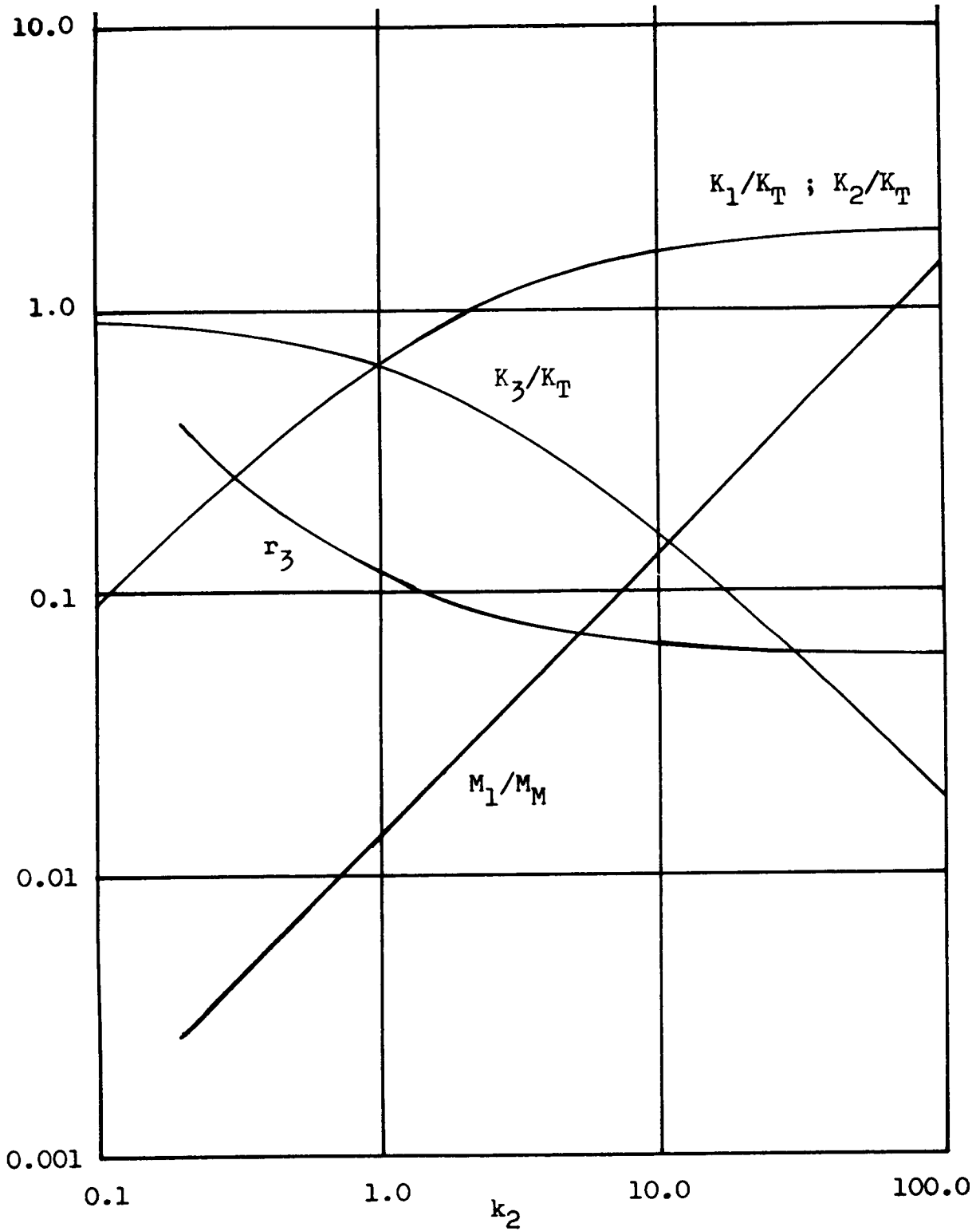
Fig.11 – VC Mount Design Curves. K_1/K_T , K_2/K_T , K_3/K_T , r_3 , and M_1/M_M vs. k_2.
$f_{ovc} = 5.0$ Hz ; $f_c = 60.0$ Hz ; b = $(K_1/K_2) = 1.0$; $r_1 = r_2 = 0.03$; $k_2 = K2/K_3$;
$K_T = [K_1K_2/(K_1+K_2)] + K_3$.

436

frequency of the machine/mount system, when attached to an infinite impedance supporting structure, is below the frequencies of any important components in the source output spectrum. If restrictions on the size of the intermediate mass place the higher normal mode frequency above the frequencies of important components in the source spectrum, a KR mount may be the best choice.

REQUIREMENTS FOR ADDITIONAL WORK

Although the analysis and calculations presented here establish the feasibility of the VC mount concept for reducing single-frequency vibration, additional analytical and experimental studies are required to facilitate its development for practical applications.

Analytical studies are required to determine:

1. How errors in mount parameters influence mount cancellation-frequency, and effectiveness at and near cancellation frequency;

2. Whether the ideal-element VC mount model is adequate for enginneering purposes, or a more sophisticated model taking account of resilient element mass and intermediate mass compliance is required;

3. The feasibility of multifrequency VC mounts;

4. How the ratio of the stiffnesses of the resilient elements in the CD section of the mount, their loss factors, the natural frequency of the machine/mount system, and the cancellation frequency influence the mass ratio required for cancellation, the normal mode frequencies of the machine/mount system both for low and high supporting structure impedances, and the loss factor for the paralleled section of the mount.

Experimental studies are required to:

1. Test and validate the single-frequency single-degree-of-freedom VC mount concept;

2. Evaluate various concepts for two and three degree-of-freedom VC mounts;

3. Determine how closely the stiffness and loss factors of resilient elements can be predicted and controlled, what variations in the properties of resilient elements can be expected as functions of time, temperature, temperature gradient, and from element-to-element and batch-to-batch. (These studies will determine whether VC mounts can mass-produced, or will require a mount-by-mount "tuning" process.

References

1. John C. Snowdon, Vibration Isolation: Use and Characterization, NBS Handbook 128. U.S. Government Printing Office, Washington, DC 20402. Stock No. 003-003-02065-6, 1979.
2. Alan O. Sykes, "Application of Admittance and Impedance Concepts in the Synthesis of Vibrating Systems", Synthesis of Vibrating Systems, American Society of Me chanical Engineers, United Engineering Center, 345 East 47th Street, New York, 1971.
3. Alan O. Sykes, " The Effects of Machine and Foundation Resilience and of Wave Propagation on the Isolation Provided by Vibration Mounts", SAE Transactions 66, 532, 1958.

Bibliography

1. Alan O. Sykes, "Vibration Cancelling Isolation Mounts", Abstract, 65th Meeting of the Acoustical Society of America, May 1963.
2. Alan O. Sykes, Vibration Cancelling Isolation Mount, Patent No. 3,128,978.

Appendix 1 – The Admittance and Impedance of Two Arbitrary Two-Terminal Mechanical Elements in Tandem

$$\frac{f_1}{x_1} \rightarrow \quad \boxed{\quad s \quad \Big|\ \overset{f_2}{\underset{x_2}{\longleftarrow}}\quad g \quad}$$
$$\quad 1 \qquad 2$$
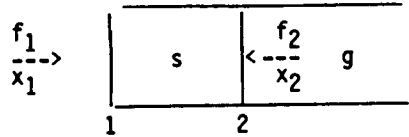
The equation of motion for small amplitude vibration for the arbitrary two-terminal s can be written in phasor form either as:

$$x_1 = y_{s11}f_1 + y_{s12}f_2 \quad ; \tag{A-1}$$

$$x_2 = y_{s21}f_1 + y_{s22}f_2 \quad ; \tag{A-2}$$

or as

$$f_1 = z_{s11}f_1 + z_{s12}f_2 \quad ; \tag{A-3}$$

$$f_2 = z_{s21}f_1 + z_{s22}f_2 \quad . \tag{A-4}$$

Noting from Newton's law of action and reaction that

$$-f_2 = z_g x_2 \quad , \tag{A-5}$$

and substituting from Eq. (A-5) into Eq. (A-4),

$$x_2 = -\frac{z_{s21}}{z_{s22} + z_g} x_1 \quad . \tag{A-6}$$

Substituting from Eq. (A-6) into Eq. (A-3),

$$f_1 = z_{s11} - \frac{z_{s21}z_{s12}}{z_{s22} + z_g} \; x_1 \; ; \tag{A-7}$$

hence, the drive-point impedance $z_{d.p.}$ at Terminal 1 for s and g in tandem is given by

$$z_{d.p.} = z_{s11} - \frac{z_{s21}z_{s12}}{z_{s22} + z_g} \; . \tag{A-8}$$

Rearranging terms,

$$z_{d.p.} = \frac{z_{s11}(z_{s22} + z_g) - z_{s21}z_{s12}}{z_{s22} + z_g} = z_{s11} \frac{(z_{s22} - z_{s21}z_{s12}/z_{s11}) + z_g}{z_{s22} + z_g} \; . \tag{A-9}$$

Noting from Eqs. (A-1) – (A-4) that

$$z_{s22} - z_{s21}z_{s12}/z_{s11} = 1/y_{s22} \; , \tag{A-10}$$

Eq. (A-9) can be written

$$z_{d.p.} = z_{s11} \frac{(1/y_{s22}) + z_g}{z_{s22} + z_g} \; . \tag{A-11}$$

 A similar derivation based on Eqs. (A-1) and (A-2) will show that the drive-point admittance $y_{d.p.}$ at Terminal 1 for s and g in tandem is given by

$$y_{d.p.} = y_{s11} \frac{(1/z_{s22}) + y_g}{y_{s22} + y_g} \; . \tag{A-12}$$

Eqs. (A-11) and (A-12) are particularly useful because drive-point impedance and impedance can be calculated without knowledge of point-to-point impedance or admittance. They also provide insight into how the mass of real resilient elements and the stiffness of real masses influence drive-point impedance and admittance.

439

Measurement of Suspension and Ride Characteristics of the M1 Main Battle Tank

Bobby E. Reed
Billy Palmertree
C. W. Bobbitt

Personnel operating the M1 tank are subjected to an extremely harsh vibrational environment as the vehicle traverses rough terrain and performs the severe maneuvers which are a routine part of its operational function. When this environment exists at a high level for an extended period of time, the effectiveness of the tank personnel can be severely diminished, even to the point of inability to function at all. Means have been developed to measure the effect of this vibration on human subjects so as to determine the limits to which they may be taken in terms of operating effectiveness and also in terms of physical well being. This paper describes (1) improved hardware for making these measurements, (2) a method for relating tank hull input forces to ride quality, and (3) installation and calibration of instrumentation to measure the hull forces.

INTRODUCTION

The US Army's M1 Main Battle Tank (Figure 1) is a very heavy vehicle which is required to operate in a wide variety of difficult cross-country terrains. At a weight of 65 tons, the tank's top speed of 41 mph can give rise to vibrational environments containing large amplitude components over a wide frequency range from 1 Hz or less to the high frequencies associated with shock forces of the suspension system "bottoming out." These vibrations are imposed on both the tank hull and its occupants. The hull design allows the tank to withstand a higher level of vibration than can be tolerated by the crew members, so human response limits the severity of the conditions under which the vehicle can operate. Because of this limit, it is necessary first of all to establish the ranges of vibrational environments over which the human operator can function effectively, and secondly, to devise some means of characterizing this environment in a readily measurable way. Both of these requirements have been met to a degree by a large amount of experimental research and development over the past two decades, but there still remains some lack of agreement as to the level of vibration in a given frequency range that the human body can safely tolerate and continue to function effectively, and there is always room for improvement in devices designed to give a measure of ride quality based on vibrational amplitudes and frequencies.

In addition to experimental research aimed at established human limits, it is also desirable to relate this ride quality to the input forces transmitted to the tank hull through the suspension system. By correlating these forces with the ride quality, the various computer models of the tank (which are used in design and analysis studies) can be made to output a ride quality indication from any and all scenarios of tank operation. This will provide a relatively inexpensive means of, for example, a parametric study of tank suspension as it relates to operator effectiveness. The correlation of input forces with ride quality must come from field testing in which both quantities are measured simultaneously. To this end, the Instrumentation Services Division (ISD) of the Waterways Experiment Station (WES) has designed and constructed an improved ride meter which quantifies ride quality and has instrumented and calibrated the suspension system of an M1 tank in order to measure hull input forces. The remainder of this paper will describe these two activities in detail.

Figure 1. M1 Tank

It is noted that ISD performed this work for the Mobility Systems Division (MSD) under the sponsorship of the US Army Corps of Engineers and the US Army Tank-Automotive Command (TACOM).

RIDE QUALITY MEASUREMENT

In the effort to provide a manageable quantity which indicates ride quality, two basic methods have emerged over the years as being most indicative of ride quality. Both of these methods weigh amplitude of vibration as a function of frequency so that those frequencies which are most harmful to the human body (through visceral resonances, for example) are assigned a higher weight and thereby contribute more substantially to the output of the method, which in both cases is a single number which reflects the severity of the ride. Since both methods employ a weighted frequency spectrum, they give comparable assessments of ride quality, but there is still some discussion as to which is the better indicator.

The weighting functions for these methods are shown in Figure 2. Note that the quantity being weighted is a signal from an accelerometer located at some point on the tank hull usually on the seat of an occupant. The figure shows two smooth curves and a set of discrete points. The discrete points represent center frequencies of the 1/3-octave filters. The rms acceleration of the output of each filter is determined and used as a measure of ride quality. This is the International Standards Organization (ISO) standard for describing human response to whole-body vibration. In practice, ISO prefers to have the measured rms level at each 1/3-octave center frequency compared with recommended values, but for complex vibrations it is desirable to have a single number representing the overall weighted rms acceleration. To this end, the Society of Automotive Engineers (SAE) had a ride meter constructed with a smooth filter indicated by the solid curve of Figure 2. Note that this curve essentially passes through the center frequencies of the 1/3-octave filters. The remaining curve, shown by the broken line, is the standard filter for ride meters used by the US Army to evaluate vehicle ride quality. The major differences in these two smooth curves can be seen to be the frequency of maximum weighting and the frequency spread. While the SAE/ISO meter outputs a single number representing a rms acceleration, the WES ride meter, using the Army standard filter, gives an overall value of mean-square acceleration which represents vibrational power. Thus, the output of the WES ride meter is considered to be proportional to the power absorbed by the human body and is therefore referred to as an absorbed power meter. With proper scaling, this output can be specified directly in watts of absorbed power. This provides a simple yet powerful measure of ride quality, since it is readily compared to the presently accepted value of six watts as an upper bound to crew effectiveness.
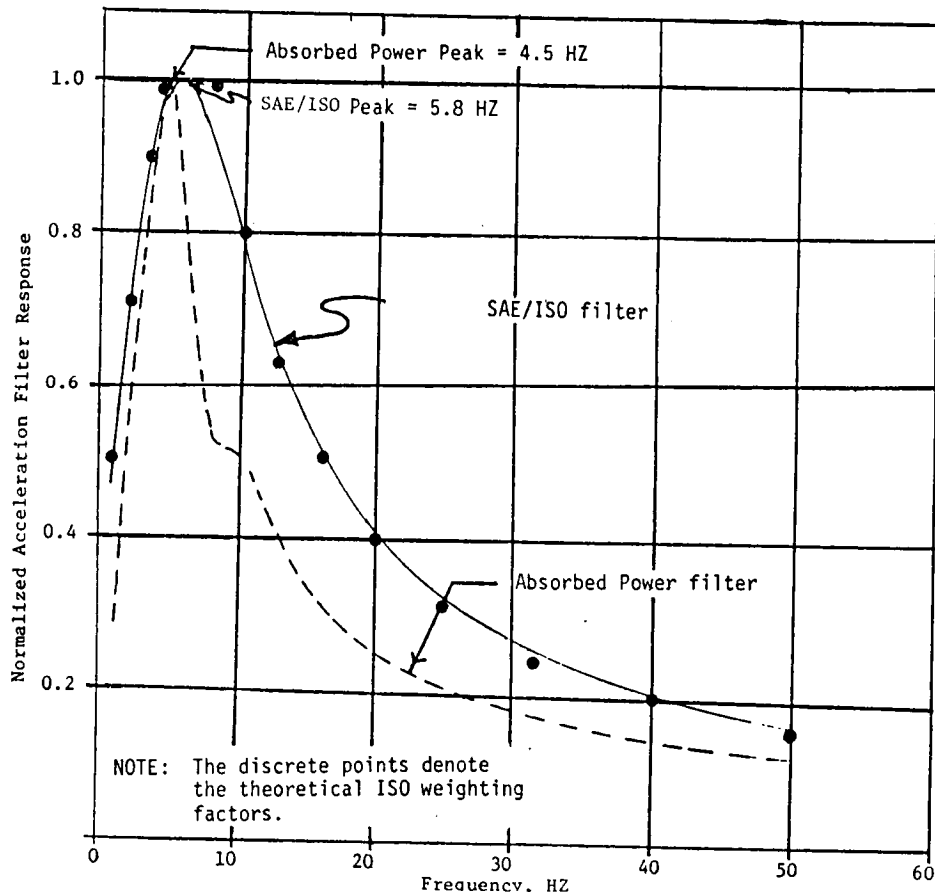

Figure 2   Normalized filter responses

Human Body Vibration Response Curves

The information on the ride meter given above was taken for the most part from a WES technical report by Murphy and Ahmad[1]. This report has several references on human body response which are included here as a bibliography.

DEVELOPMENT OF THE WES RIDE METER

At the request of the Mobility Systems Division, ISD designed and constructed a ride meter whose function was to measure the absorbed power weighted according to the Army standard filter characteristics. This system is shown in Figure 3 and includes the ride meter, the output indicator with clipboard for recording data, and the input accelerometer in its mounting case. As a matter of interest, an identical servo-accelerometer is included in the photograph. Figure 4 is a close-up view of the ride meter with top cover removed showing power and accelerometer inputs through the cables on the left, the function selector switch on the operator panel, and the several PC boards containing ride meter circuitry. The panel also contains an off-on switch and reset button for manually controlling the time interval over which the accelerometer signal is processed. A close-up of the output indicator and clipboard is shown in Figure 5. Here it is seen that any of three display positions can be selected and read out on the digital voltmeter. At the conclusion of a test run, the ride meter contains information on the total time of the run and on the number indicating absorbed power. Both of these pieces of information are in the form of a voltage which is the output of an operational amplifier connected as an integrator. Time is obtained by integrating a constant; absorbed power is obtained by sequentially passing the accelerometer signal through a 30 Hz low pass filter, the Army standard weighting filter, a squaring circuit, and the integrator. These quantities are read out in turn on the digital indicator and recorded on the data sheet. Thereafter, the value of absorbed power in watts is obtained by hand calculation.

Although this initial design ride meter functioned very well, and is currently being used in several applications, it was found desirable to design and construct a new model which had expanded capabilities and performed its functions automatically.

Unlike the original design, which was completely analog in operation, the new design combines analog and digital operations and is consequently referred to as the WES Hybrid Ride Meter. In this design, the system remains analog in nature from the input through the integrator of the weighted acceleration signal, then is converted to digital for further processing and storage in memory.

A block diagram of the hyrid ride meter is shown in Figure 6. The input signal is first passed through a 30 Hz low pass filter because the higher frequencies with corresponding lower amplitudes do not contribute significantly to decreased operator effectiveness. The signal is then scaled appropriately and fed to parallel paths which produce both the absorbed power value and tne ISO rms acceleration value. The output of the integrating amplifiers are monitored and provision is made to avoid saturation of the amplifiers within a microprocessor program.
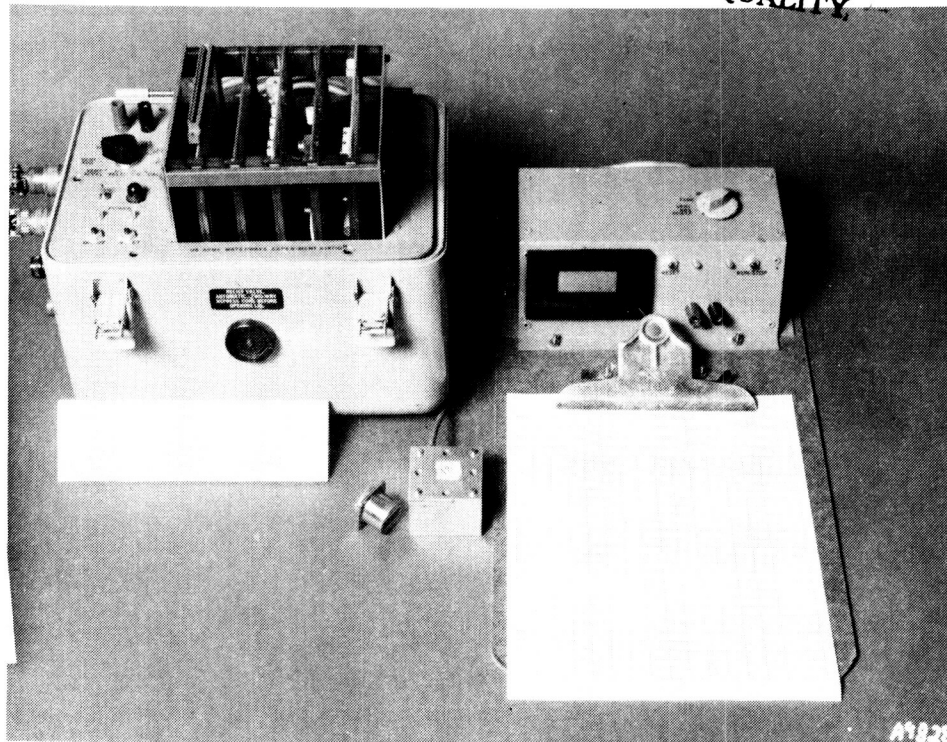
Figure 3.   Absorbed Power Ride Meter

Figure 4.   Meter Electronics and Control Module
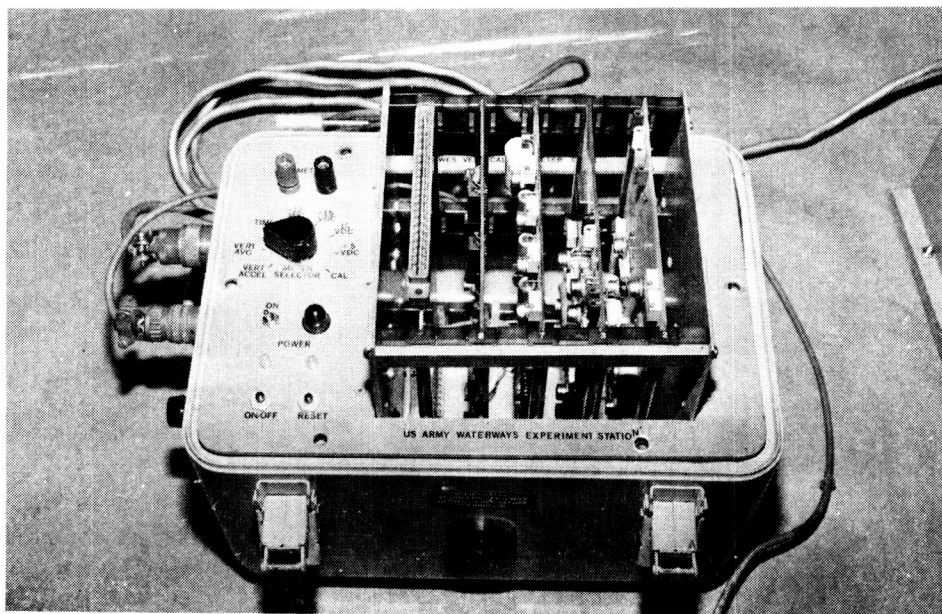
445

Figure 5. Data Readout and Log Sheet
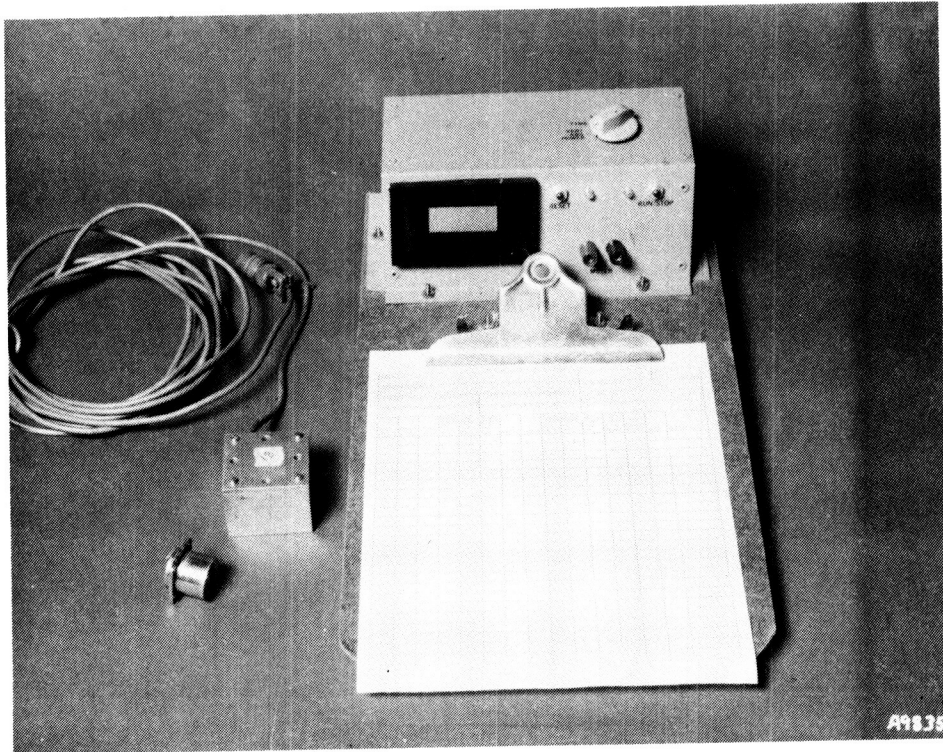

K_{Abs} = Absorbed Power Weighting Factor
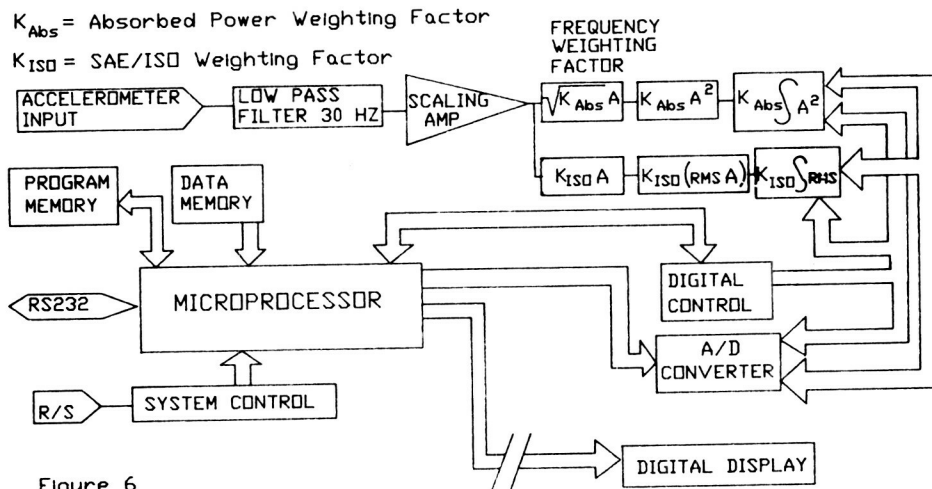
K_{ISO} = SAE/ISO Weighting Factor

Figure 6

Block Diagram of Micro Based Ride Meter

446

The hybrid ride meter will allow data to be taken and processed in several different modes so that data acquisition can be tailored to the demands of a particular test program. This is accomplished by controlling the meter operation with a microprocessor and providing memory for the data storage. This memory space is sufficient for 785 tests or continuous recording for up to 12 or 13 hours which provides much greater flexibility than has been heretofore possible. Typically, the accumulated test values are transferred to a computer where they can be formatted and further processed as desired. The WES Hybrid Ride Meter is pictured in Figure 7 with its input accelerometer and a lap-top computer. A close up of the face plate is shown in Figure 8. The ride meter with top removed, Figure 9, shows the internal components. In this view, the right hand slot holds the microprocessor board, shown beside a pen in Figure 10 for size comparison.

This new hybrid ride meter was designed for use in a wide variety of test and measurement situations. Because of the importance of the concept of a single number indicator of ride effect on the human operator and because of the great versatility of the hybrid ride meter, its several functions will be described here in detail.
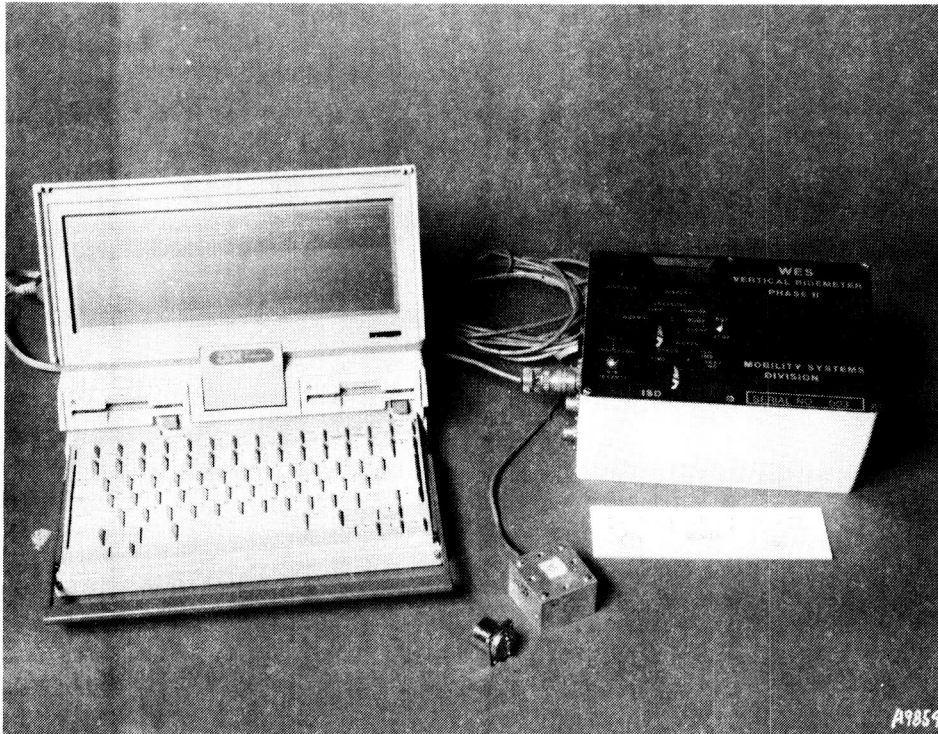
Figure 7. Hybrid Ride Meter System
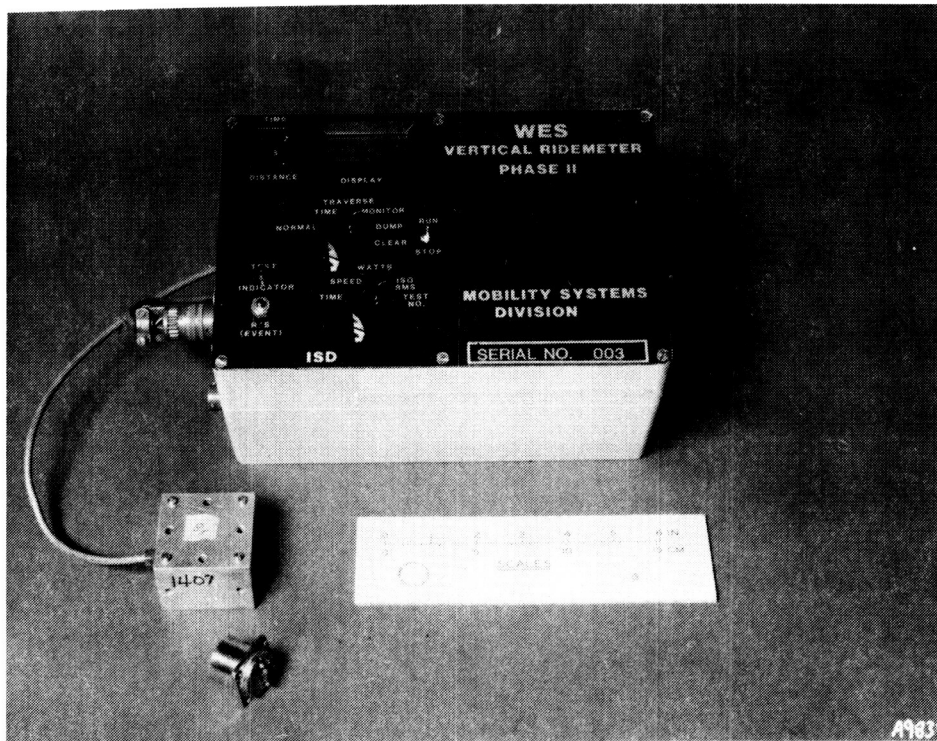
Figure 8. Ride Meter Display and Control Unit with
Accelerometer Attached

Figure 9. Hybrid Analog and Digital Electronics
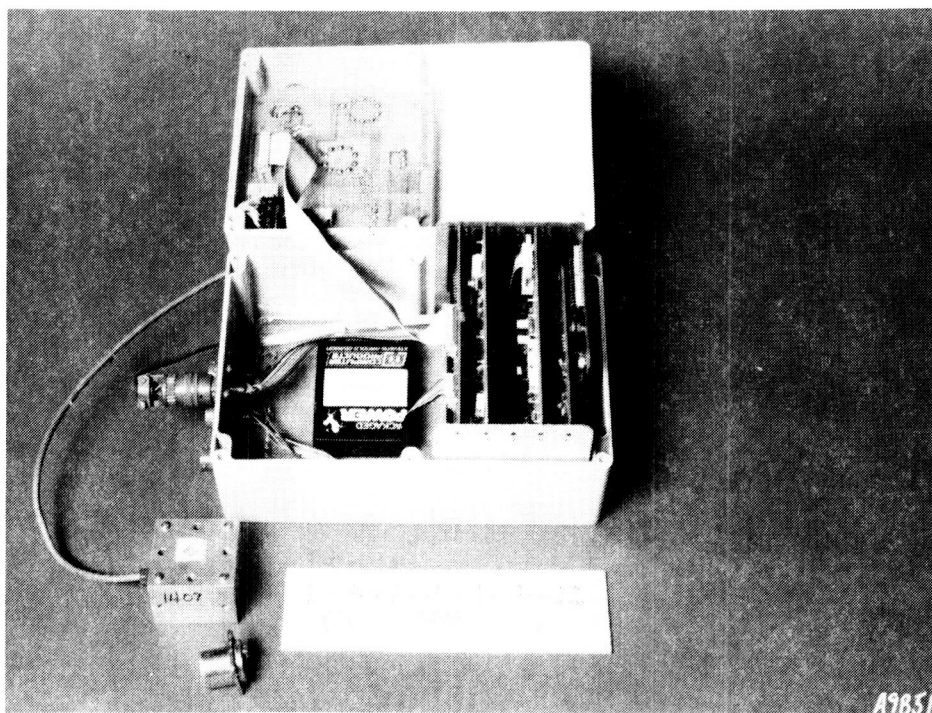
448

Figure 10. Microprocessor with A/D, Digital IO, and Memory

        Figure 11 shows a computer drawing of the face plate with the various
switches and controls clearly indicated. The mode selector control and the
run-stop switch are located directly below the digital read-out indicator.
Below these two controls is a data selector switch which chooses the quantity
to be displayed on the indicator when the mode switch is in the MONITOR
position. In the lower left corner is the R/S event switch. Pressing this
button when the run-stop switch is in the run position causes an interrupt to
be sent to the microprocessor commanding it to begin data collection.
Pressing R/S again commands the microprocessor to stop data collection. The
control in the upper left hand corner is a thumbwheel which selects a number
between 0-15 in the display window. With the mode selector set in the NORMAL
position, the displayed number represents distance in hundreds of feet. This
is the selected course length. Pressing the R/S button begins a test which is
terminated by pressing the R/S button when the vehicle has traversed the
chosen test length. This course length is compared with time to calculate an
average speed through course.

        In the TIME position of the mode selector switch, the thumbwheel display
number gives a chosen time of test in tens of seconds; that is, a test time of
from 10 to 150 seconds can be chosen, in increments of ten seconds. A test is
initiated by pressing the R/S button, in which case the test data are based on
the actual time of test. In either case, the microprocessor resets the system
and starts another test automatically. This operation will continue until the
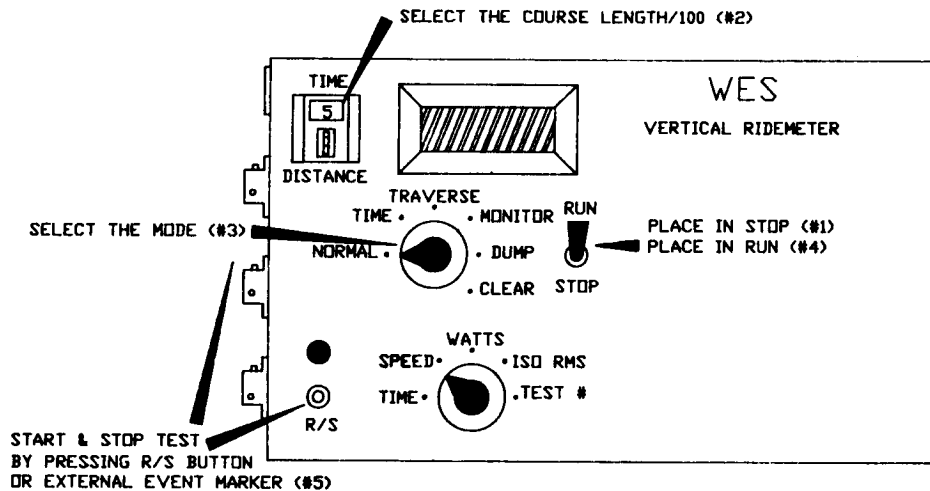Run/Stop switch is placed in the stop position.

Figure 11.
Hybrid Meter Controls

In addition to the NORMAL and TIME modes, a TRAVERSE data collecting mode is provided. In the traverse mode, the operator will start the system when entering a predetermined course and will activate the event switch at the end of each subcourse segment until the full course has been traversed at which time the stop switch is activated.

The data collected and stored for all three modes are time, absorbed power in watts, and ISO rms acceleration in g's. In addition, speed and distance traveled are collected and stored in the NORMAL mode, and in the other modes if wheel pips are available.

An operator can examine the data at any time by placing the mode selector in the MONITOR position and using the data selector switch. Because the ride meter memory usually contains the results of many individual tests, a means is provided for selecting the desired test number. Placing the data selector in TEST # position produces a display of the most recently completed test numbers. The desired test number is obtained by pressing the R/S button, which causes the displayed test numbers to be incremented or decremented by one, according as the thumbwheel display number is set to 1 (increment) or 0 (decrement). Upon arriving at the chosen test number, the data selector is used to display time, speed, absorbed power, or ISO rms acceleration. When the mode selector is moved off the MONITOR position, the microprocessor will return to the correct test number.

The DUMP postiion of the mode selector switch allows the operator to transfer all test data in the ride meter to a computer file that is LOTUS compatible software. The ride meter is connected to the computer through an RS232 cable, and utilizes a communication software package such as CROSSTALK or MIRROR to effect the transfer. In the DUMP mode, the microprocessor displays a menu to guide the operations. For all modes of operation, the Run/Stop switch is placed in the Stop position before selecting the modes. After setting the mode selector, placing the Run/Stop switch in the run position commands the microprocessor to select the chosen mode.

The final position of the mode selector is CLEAR, which clears all data memory in the ride meter.

The single number ride meter output is desired from an input acceleration signal which is weighted and integrated. To relate this number to operator effectiveness, it is necessary that the acceleration signal reflect as closely as possible the motion experienced by the operator and for this reason, the input signal usually is from an accelerometer fixed to the driver's seat and oriented to sense the vertical component of acceleration. In Figure 12, the position of the accelerometer relative to the driver's body is indicated. This location is deemed to give a reasonable measure of the acceleration felt by the driver. For purposes of comparison, an identical accelerometer is fastened rigidly to the tank floor adjacent to the driver's seat. This can be seen as the small square shape immediately to the right of the seat in Figure 13. A comparison of the ride quality given by these two accelerometers gives a measure of the effectiveness of the seat in protecting the driver from the vibrations felt by the tank hull.

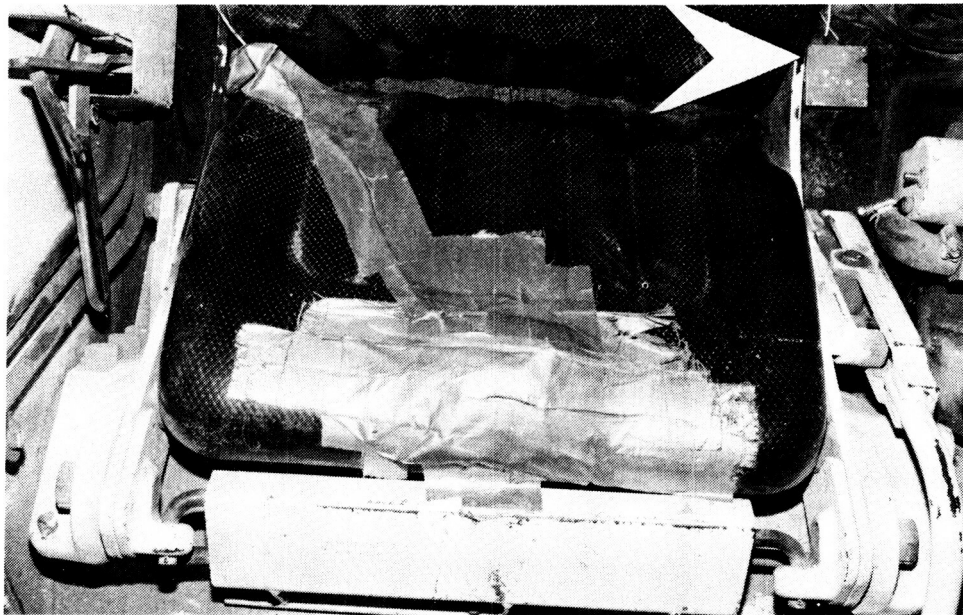Figure 12. Driver Seat Accelerometer

Figure 13. Floor Mounted Accelerometer at Driver Seat

In the design of the vehicle suspensions, it has been found useful to obtain ride quality numbers from sensors located at the center of gravity of the vehicle. Figure 14 shows the CG installation of a single axis accelerometer sensing vertical acceleration and Figure 15 shows a triaxial installation at the CG. In some tests, the three outputs of the triaxial ride numbers are combined and used to obtain an overall ride quality number for absorbed power and ISO rms acceleration.

In addition to the accelerometers at the driver location and the CG packages, an accelerometer is mounted at the roadwheel axle on the roadwheel suspension (road arm) to sense acceleration in the direction perpendicular to the road arm. The sensor complement is completed by roll and pitch gyros located reasonably close to the center of gravity as shown in Figure 15.

In any specific test run of the M1 tank, it is desirable to have ride quality numbers derived from each of the sensors on the vehicle. This is readily accomplished by recording all signals on magnetic tape and subsequently playing them back through the ride meter in the laboratory. In this way, correlations can be made between the ride quality numbers from the various sensors, and this information can be expected to contribute to improved suspension designs as well as to refined measures of crew effectiveness in relation to the vibration environment.
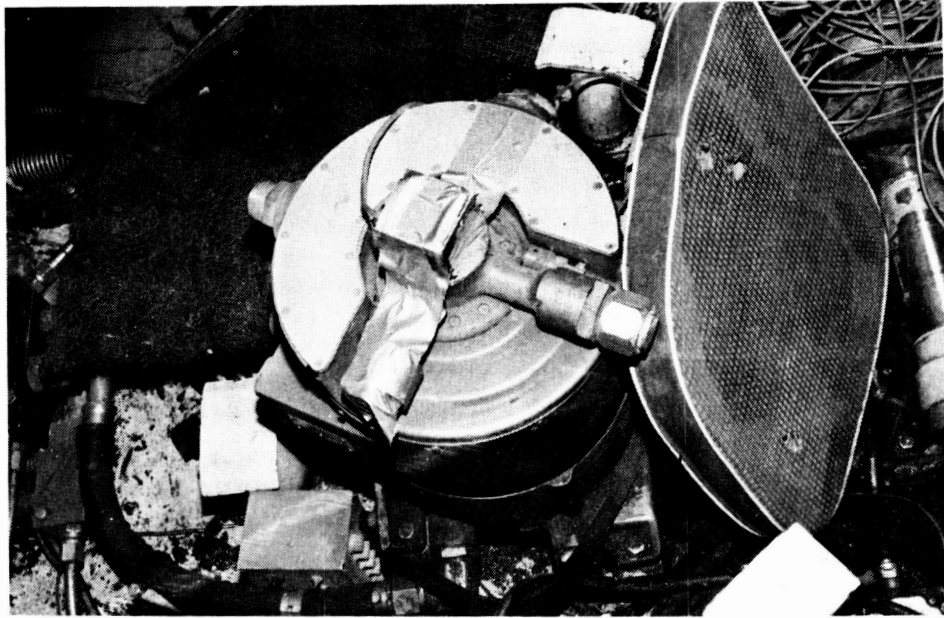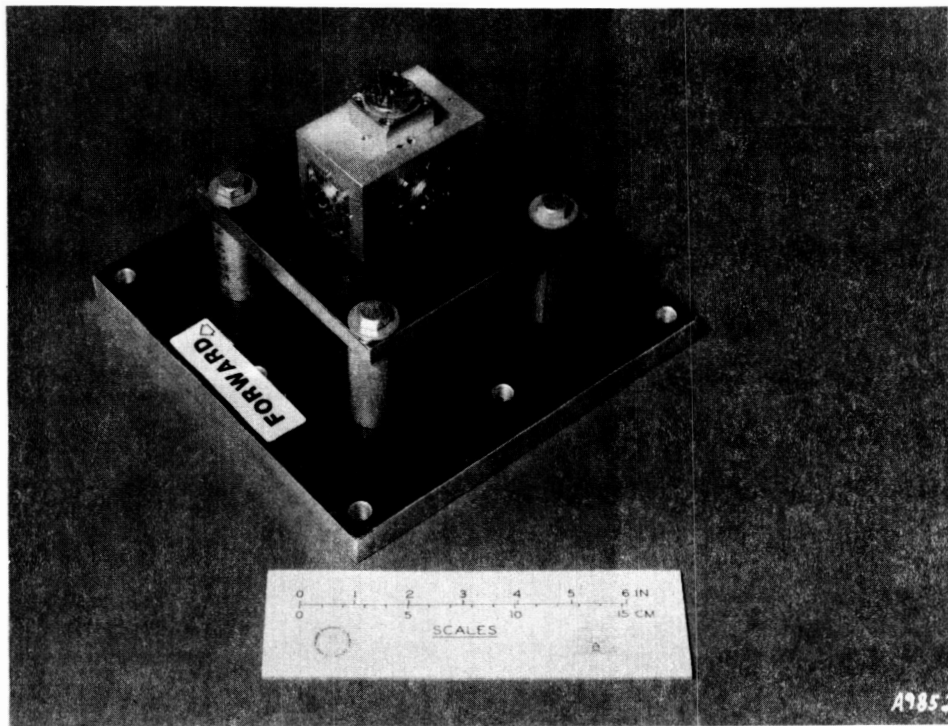
Figure 14. C.G. Vertical Accelerometer

Figure 15. Triaxial Accelerometer Mount for C.G.

Finally, the ride quality numbers will be used to compare the relative merits of two suspension systems designed for the M1. These are the conventional torsion bar suspension (with fluid dampers on road arms 1, 2, and 7), and the hydro-pneumatic suspension. Some indication of the external differences of these suspensions can be found in Figure 16 (torsion bar) and Figure 17 (hydro-pneumatic). A detailed contrast of these two systems will be deferred to a later report after significant comparison testing has been done. For the present, a description of the method of measurement of hull forces on the torsion bar suspension system will be given.
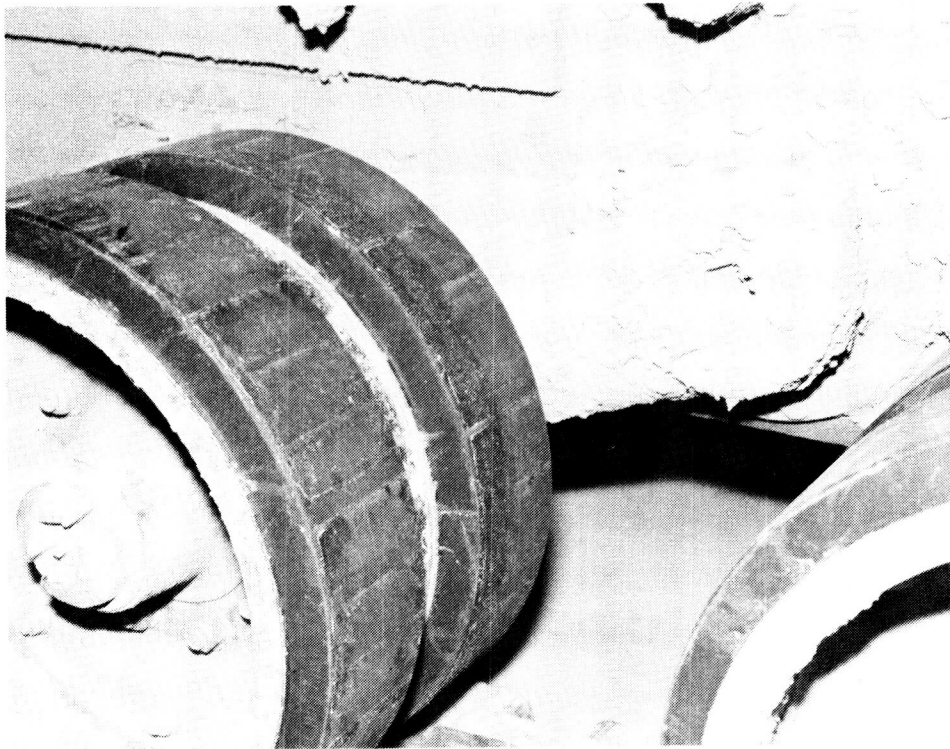

Figure 16. Standard Torsion Bar Suspension

Figure 17. Hydro-pneumatic Suspension

MEASUREMENT OF HULL FORCES

From the preceding discussion, it is clear that the ride meter outputs
from the diverse sensor locations will provide a good basis for comparison of
the two types of suspension provided for the M1 tank. By the same token,
however, the single number indicator does not give any useful information on
how the forces of the surroundings are put into the vehicle. A knowledge of
these forces is desirable because computer models of the vehicle can take
representations of these forces as input and produce, among other things, the
ride quality number that is given in an actual test by the ride meter. If the
computer model is reliable and the input forces are accurate, various test
scenarios can be simulated on the computer instead of actually being carried
out in the field. The cost savings of such a procedure are immediately
apparent.

To accomplish these purposes, it is necessary to build a data base of
hull input forces under various field conditions. The torsion bar suspension
design gives rise to input torques as well as input forces at each road arm
station, so provision must be made to measure these quantities. These
measurements will be made only on the vehicle with torsion bar suspension;
there are no present plans to instrument the hydro-pneumatic suspension
system.

455

The M1 tank rides on seven roadwheels per side, numbered 1-7 front to back. The number 1, 2, and 7 roadwheels are supported by torsion bars and fluid dampers, the others are supported only by torsion bars. The design of the suspension is such that only torque is transmittted through the torsion bars, while torque and force (notably, vertical force) are transmitted through the load-carrying elements associated with the damper. Both torque and force are measured with strain gage bridges.

The torsion bar is a thick-walled cylinder approximately 2.5 inches in diameter and 86 inches long which extends from the roadwheel to a point of attachment on the opposite side of the tank. The torsion bridge on this member was placed at a convenient location and presented no special problems. Gaging the rotary damper, however, was somewhat more involved. The road arm is rigidly fixed to a large tubular shaft which is keyed to the rotor of the damper. This same shaft, through bearings, supports the weight of the tank and transmits any other road forces to the hull. In carrying these forces, the shaft behaves as a beam, so that the magnitude of the forces can be measured by gaging the beam in a bending mode. At the same time, an additional bridge is attached to the shaft to sense torque due to the damping force in the rotary shock absorber. Some difficulty was encountered in the force measurement because the angular orientation of the bending gages changed with changing road arm angle, but this problem was resolved with careful laboratory calibration. A photograph of the bending and torsion gage shows their locations on the shaft in Figure 18. Note that the shaft is shown attached to the ride meter road arm through splines. The shaft is also welded to the road arm on the outside face. The splines on the other end of the shaft engage the damper rotor.
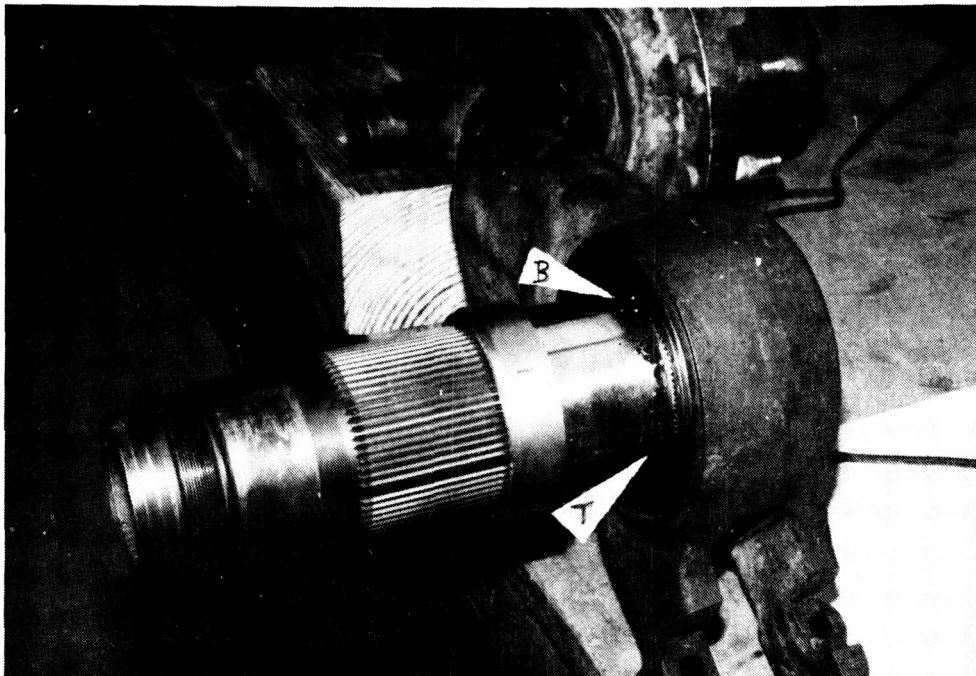

Figure 18. Road Arm Torsion and Bending Strain Gage Locations

Details of the calibration procedures and comparative test data between the two systems will be discussed completely in a later report when sufficient test data for meaningful conclusions will be available. These tests are scheduled for the month of August 1987 but will not be completed in time for inclusion here.

CONCLUSION

Interest in vehicle ride quality and its measurement has been growing steadily over the past two decades. Its importance to the military establishment with its great variety of surface vehicles is obvious, but ride quality is becoming a factor of increasing importance in the transportation industry, to manufacturers of all types of aircraft, farm machinery, earth-moving and construction equipment, and others. At the present time, it cannot be said that there is general satisfaction with commonly used indicators of ride quality, nor is there complete agreement as to the level of vibration, and to the frequency weighting functions which accurately assess limits of operator effectiveness and well being. However, experimental activity in this area is growing, and there will be reliable standards for evaluating the effect of vibrational environment on the human operator. Once this is established, it should be possible to effect significant improvements in suspension design.

REFERENCES

Murphy, Newell R., Jr., and Ahmad, Falih H., 1986. "Comparison of Measures of Vibration Affecting Occupants of Military Vehicles," Technical Report GL-86-13, US Army Engineer Waterways Experiment Station, Vicksburg, Mississippi.

BIBLIOGRAPHY

Pradko, F., Lee, R., and Kaluza, V., 1966. "Theory of Human Vibration Response," presented at the Winter Annual Meeting and Energy Systems Exposition of the American Society of Mechanical Engineers, New York.

Berry, L. G., 1975. "Advanced Concept Vehicle - Cargo," MASSTER Test Report GM 265A, Headquarters, Modern Army Selected Systems Test, Evaluation and Review, Fort Hood, Texas.

International Standards Organization (ISO), 1968. "Guide for the Evaluation of Human Exposure to Whole-Body Vibration," 2d ed., Publication ISO 2631.

Allen, G. R., 1975. "Ride Quality and International Standard ISO 2631 (Guide for the Evaluation of Human Exposure to Whole-Body Vibration)," 1975 Ride Quality Symposium, NASA TM X-3295/DOT-TSC-OST-75-40.

Osborne, D. J., 1983. "Whole-Body Vibration and International Standard ISO 2631: A Critique," The Human Factors Society, Inc.

Barton, J. C., 1976. "Whole-Body Vibration Levels: A Realistic Baseline for Standards," Society of Automotive Engineers, Earthmoving Industry Conference.

Van Deusen, B. "A Statistical Technique for the Dynamic Analysis of Vehicles Traversing Rough Yielding and Non-Yielding Surfaces. Report for NASA Contract NASW-1287, May 1966.

Advanced Joining Concepts for Passive Vibration Control

Jacky C. Prucz
Constantine Spyrakos

PRECEDING PAGE BLANK NOT FILMED

Passively damped joints, in which the conventional adhesives are replaced by high damping viscoelastic materials, have the potential of being effective practical means for passive vibration control. However, this potential cannot be materialized unless the associated structural penalties are reduced to acceptable limits. The paper describes a rational methodology for the development of advanced joining concepts for structural and mechanical systems, capable of providing enhanced dissipation of vibrational energy without serious penalties in strength, stiffness or weight characteristics. One such configuration is that of a rhombic-type joint, that provides a beneficial deformation coupling between the direction of load transfer and less critical offset directions. A comprehensive parametric study has been carried out in order to establish design guidelines for favorable tradeoffs between damping benefits and the associated stiffness, strength and weight penalties in a rhombic joint. The results are compared with the corresponding tradeoffs for a double-lap joint made of the same materials.

INTRODUCTION

Artificial damping devices are the most powerful means of energy dissipation available to the designer for passive vibration control. They may include damping layers applied over large areas or local dampers attached to problem components. Layer treatments usually rely upon material damping mechanisms [1], whereas common types of local damping treatments are dynamic absorbers, dashpots [2], inertial [3], friction [4], tuned and broad-band viscoelastic [3] dampers. Although the dominant contribution of joints and supports to structural damping is well recognized, past investigations have been focused on friction associated with interfacial slip [5]. Despite an early analysis of the damping benefits achievable by incorporating viscoelastic materials in structural supports of beams and plates [6], no systematic research efforts have pursued this approach so far. Elastomeric materials, like rubber or synthetic rubberlike products are occasionally used in mechanical couplings or bridge bearings to allow higher flexibility of such connections, along with a certain reduction in vibration levels. Only limited applications of elastomeric bearings for vibration control can be found so far, mainly in base-isolation systems for earthquake protection of buildings and bridges [7].

Renewed interest in utilizing viscoelastic materials in structural joints has been spawned recently by technological developments that have increased the need for effective vibration control on one hand, and have improved the engineering properties of viscoelastic materials on the other hand. Both the damping and the general structural analysis of viscoelastic materials have been placed on a sound mathematical basis, especially in regard with the linear viscoelastic behavior. The most popular modeling approaches are based on the complex modulus concept [8] and numerical algorithms either in the transform or time domains [9]. General analysis methods of viscoelastic damping have been proposed recently by using a "fractional calculus" [10] or an integro-differential formulation of the equations of motion.

Passively damped joints, in which high damping viscoelastic materials are incorporated, usually as a replacement to conventional adhesives, have the potential to be an effective means of passive vibration control over a broad frequency band. This potential is indicated by recent theoretical and experimental investigations of passively damped joints based on the double [11,12] or single [13] lap configurations. It cannot materialize, however, unless a "designed-in" approach is adopted for the development of joint configurations that provide favorable tradeoffs between damping enhancement and associated structural penalties. Passively damped lap joints dissipate mechanical energy when worked in the axial direction, due to shear deformation of the viscoelastic layers. Consequently, their damping properties in the 0.1-100 Hz frequency range can be as much as one order of magnitude higher than those of similar joints with conventional elastic adhesives [11]. However, the associated penalty in axial stiffness is about 80%, even if the designed-in approach is adopted. The addition of elastic connection elements between the members of the joint can reduce the stiffness penalty to only 60%, but then the damping enhancement may drop to less than one-half of that achievable without the elastic links. It is difficult to attain favorable tradeoffs between damping and stiffness in passively damped lap joints since high damping requires high shear deformation of the adhesive layers which, in turn, requires large relative displacements between the adherends along the axial direction. Moreover, the lap configuration implies also an adverse relationship between the damping and strength characteristics of the joint since the shear deformation of the viscoelastic layers is part of the load transfer process through the joint.

This paper presents a theoretical performance analysis of a different configuration for passively damped joints, that can possibly be used as an alternative to the conventional double-lap configuration. It is based on a rhomb-like geometry where the viscoelastic adhesive is enclosed by the elastic joint members in an arrangement as shown in Fig. 1. The tradeoffs achievable with such a configuration between damping benefits and associated structural penalties may be superior to those of double-lap joints since large shear deformation of the adhesive can be obtained by displacement coupling between the x and y directions (Fig. 1). The paper includes numerical results from parametric studies of a rhombic joint configuration and a comparative evaluation with a double lap passively damped joint (Fig. 2).
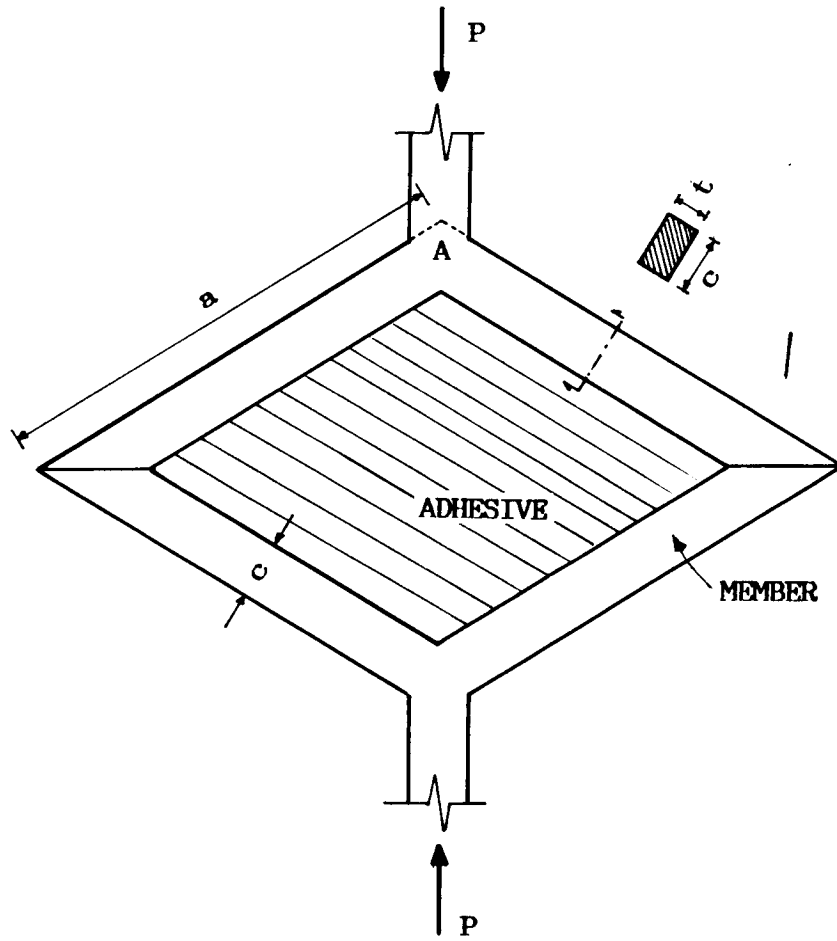
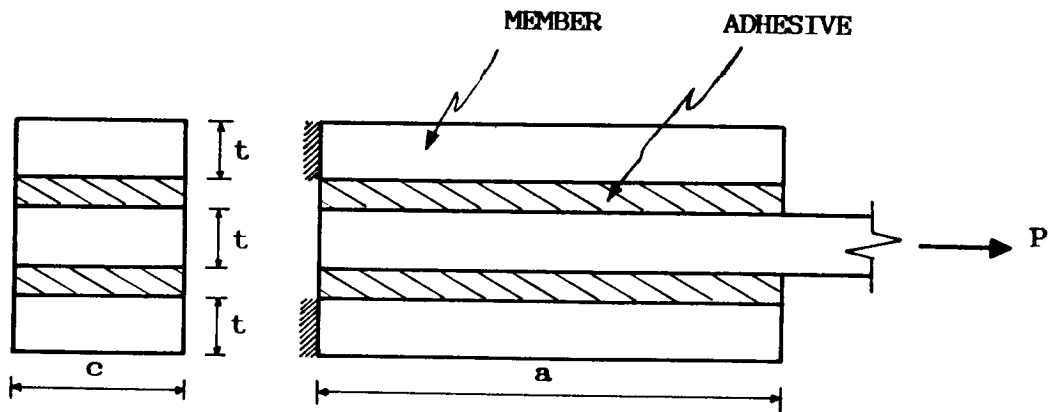FIG.1 - PHYSICAL MODEL OF RHOMBIC JOINT

FIG.2 - PHYSICAL MODEL OF DOUBLE-LAP JOINT

461

The major objective of this section is to describe a rational methodology for predicting the effects of structural interactions between various constituents of a passively damped rhombic joint on some of its performance characteristics like weight, damping, strength and stiffness in the load transfer direction. The model employed for this purpose is focused, therefore, on elastic stress analysis rather than the viscoelastic behavior of the adhesive. Besides elastic strength and stiffness, it predicts only the relative energy dissipation with respect to variations in geometric parameters and stiffness ratio between the adhesive and the adherend. The adhesive loss factor is not included explicitly in the model, but it is not expected to change the predicted effects of the above design parameters on the overall joint damping. For a given viscoelastic material, it may be regarded as a factor independent of the joint configuration that determines the actual level of dissipated energy when multiplied by the corresponding values of relative energy dissipation provided by this analysis. A similar approach has been employed in Ref. [14] for a double lap joint and has been validated, subsequently, by comparison with an equivalent viscoelastic investigation [12].

The underlying assumptions of such an approach are that the joint is subjected to oscillatory loading and the viscoelastic adhesive behaves similarly to a Voigt solid at any one frequency, so that its constitutive description can rely on the complex modulus concept [8]:

$$G_a = G_1 (1 + i\eta) \tag{1}$$

If inertia effects are ignored, these assumptions lead to a quasi-static analysis, in which the material properties may change from one frequency [11] or temperature [15] to an other, but the form of the governing elasticity equations remains unchanged. Effectiveness investigations of constrained layer damping treatments are commonly confined to quasi-static models, which are sufficiently accurate for low frequency vibrations [1].

In accordance with the above assumptions, the total mechanical energy dissipated per cycle by the viscoelastic adhesive can be evaluated as follows [1]

$$D = \pi G_1 \eta \int_{V_a} |\gamma|^2 \, dV_a \tag{2}$$

If the adhesive is assumed to be the only source of energy dissipation in a passively damped joint, the parameter D is a direct measure of the overall joint damping. Eq. (2) shows that for a given viscoelastic material, at given frequency and temperature conditions, the damping characteristics are determined by the magnitude of shear strains induced in the adhesive. This observation is consistent with the well known finding that the major mechanism of viscoelastic energy dissipation is cyclic shear, rather than extensional, deformation [16].

The above discussion supports the approach of employing a fully elastic model in order to evaluate the effect of structural interactions between the constituents of a passively damped joint on the amount of energy dissipated by its viscoelastic adhesive. For a certain loss factor of the viscoelastic material, the joint damping may be considered to be proportional to the elastic distortional (octahedral) energy

stored in the adhesive during a loading cycle. If the plane stress assumption is adopted for the stress analysis of a rhombic joint, this octahedral energy is expressed as [17]:

$$U_d = \frac{1}{12G_1} \int_{V_a} \left[(\sigma_{xx} - \sigma_{yy})^2 + \sigma_{yy}^2 + \sigma_{xx}^2 + 6\sigma_{xy}^2 \right] dV_a \qquad (3)$$

where the stress components in Eq. (3) correspond to the amplitude value of the external oscillatory load on the joint. The damping assessment in the present work relies, therefore, on the approximation

$$D \approx C * U_d \qquad (4)$$

where "C" is a proportionality constant that depends on the loss factor of the viscoelastic adhesive.

A plane stress quasi-static analysis has been conducted on a rhombic joint configuration by using an "in-house" boundary element program. Consequently, only the rhombic frame formed by the elastic members of the joint has to be discretized, whereas a continuum solution for the stress and deformation fields in the adhesive can be obtained from the integral equations of the boundary element method [18]. Displacement continuity conditions are imposed in all directions along the adhesive-adherend interfaces, so that no debonding and microslip effects are included in this investigation. The boundary element program had been previously validated by application to several test cases.

The stress and deformation results provided by this program for the loading case shown in Fig. 1 have been utilized to predict the following three performance characteristics of a rhombic joint:

1. Damping - by calculating U_d from Eq. (3).

2. Stiffness - by calculating the ratio between the applied load and the corresponding elastic deformation.

$$K = P/u_y \text{ (A)} \qquad (5)$$

3. Strength - by calculating the minimum value of P at which shear-induced debonding may occur at the adhesive-adherend interface.

Each of the above properties, along with weight characteristics, have been evaluated over a broad range of design parameters in an effort to identify design configurations that yield favorable tradeoffs between damping benefits on one hand and stiffness, strength and weight penalties on the other hand. Selected numerical results are presented in the following section and compared with those corresponding to a double lap joint.

NUMERICAL RESULTS

An extensive parametric study has been conducted on the joint model shown in Fig. 1, by following the procedure outlined in the previous section. Its major results are depicted, in non-dimensional form, in Figs. 3-5. Constant values have been selected in all these figures for the following design parameters:

Dimensions: a = 3.0 in., t = 0.25 in.

Material Properties: $E_m = 10^7$ psi, $\nu_m = 0.3$, $\nu_a = 0.45$

$\rho_m = 0.1$ lb/in^3, $\rho_a = 0.036$ in/in^3

The normalizing factors used for the selected performance characteristics are listed below:

1. Damping – the total strain energy, U, stored in the joint for the corresponding design configuration.

2. Stiffness – an arbitrary value of 1,250,000 lb/in, that may correspond to the extensional stiffness of a 6 x 3 x 0.25 in. aluminum prismatic bar.

3. Strength – an arbitrary value of 30,000 lb for P, that may correspond to a shear bond strength of 2,000 psi and a uniform shear stress distribution over a bond area of 15 in^2.

4. Weight – an arbitrary value of 0.225 lb, that may correspond to the weight of a 6 x 1.5 x 0.25 prismatic bar made of aluminum.

All the calculations covering the parameter ranges shown in Figs. 3-5 have revealed that the octahedral strain energy, U_d, is an approximately constant percentage, of about 90%, of the total strain energy stored in the adhesive of a rhombic joint. The damping performance of the joint, which is measured by U_d in this analysis, is determined, therefore, by the distribution of strain energy between the adhesive and the adherends.

The effect of the stiffness level of the adhesive on the joint damping and stiffness characteristics, is illustrated in Fig. 3 for $\theta = 20°$ and c/a = 0.1. This effect is much more pronounced on damping than on stiffness, especially for values of G_a/E_m below 0.001, which may represent most viscoelastic adhesives available today [11]. It indicates the importance of selecting stiffer adhesives not only to improve the stiffness of the joint, but also its damping by increasing the strain energy share of the adhesive.

Figure 4 shows the effect of the geometric parameter c/a on all the performance characteristics selected for this investigation, for $\theta = 20°$ and $G_a/E_m = 0.005$. This parameter does not appear to have a significant effect on the strength of the joint, but it has opposite effects on damping and weight on one hand and stiffness on the other hand. A light weight slender member, that may correspond to c/a = 0.1 for example, will provide higher damping but lower stiffness, whereas a "bulkier" member, that may correspond to c/a = 0.2, can provide a better tradeoff between damping and stiffness, but at the expense of higher weight.

The opening angle of the rhomb, θ, has a significant effect on the joint properties, as depicted in Fig. 5 for c/a = 0.1 and $G_a/E_m = 0.005$. While damping considerations would demand for a value of θ about 30-50 degrees, this range should be avoided from the strength and stiffness standpoints. A small value of θ, about 10-20 degrees, appears to be preferable for overall performance optimization of such a joint configuration.
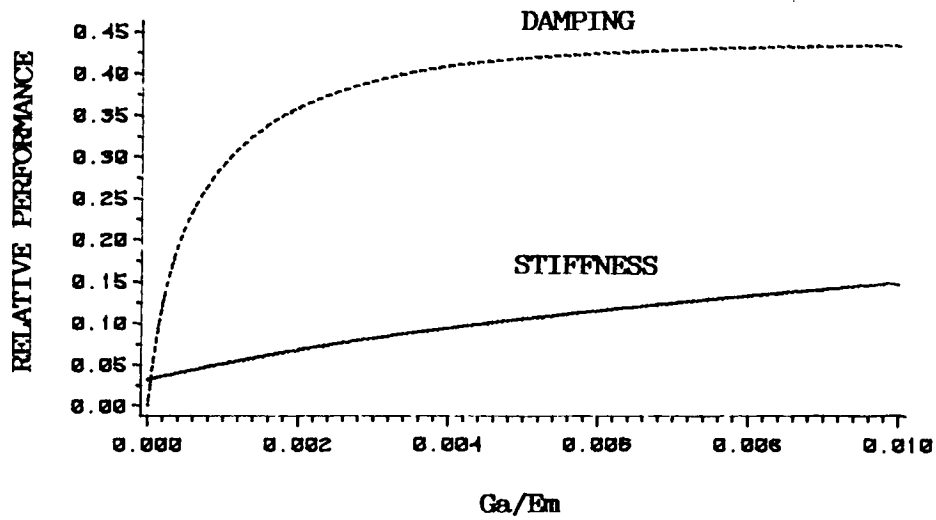
FIG.3 - RELATIVE PERFORMANCE CHARACTERISTICS OF
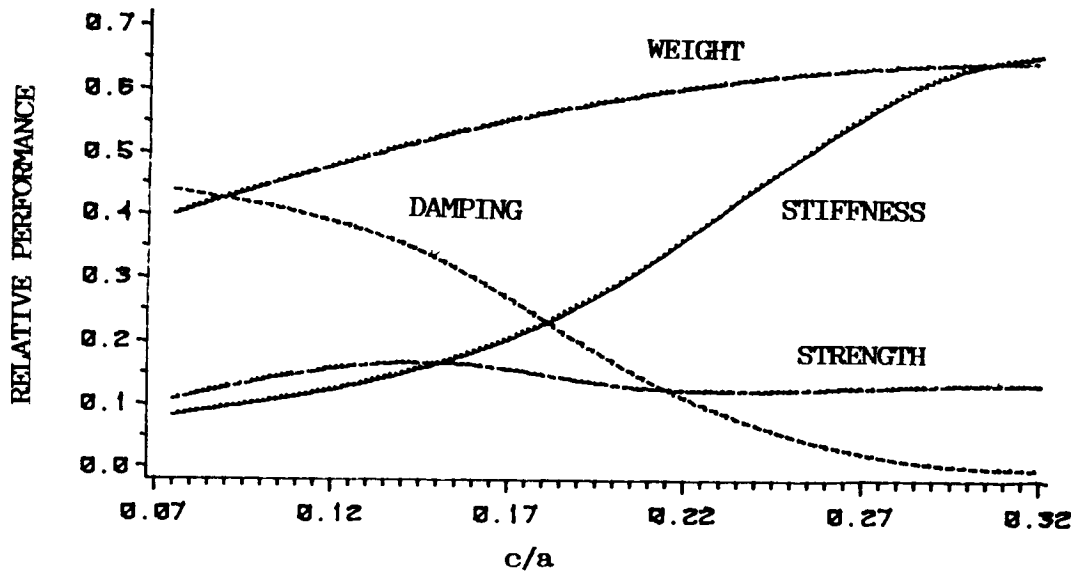RHOMBIC JOINT AS FUNCTIONS OF MATERIAL
MODULI OF ITS CONSTITUENTS

FIG.4 - EFFECT OF MEMBER DIMENSIONS ON
RELATIVE PERFORMANCE CHARACTERISTICS
OF RHOMBIC JOINTS

The above performance characteristics of a rhombic joint have been compared with the corresponding properties of a passively damped joint of double lap configuration, whose physical model is shown in Fig. 2. A plane strain finite element analysis has been conducted on the double lap joint in order to predict its damping, stiffness and strength characteristics, by following the same procedure as for the rhombic joint. The results of this comparison are summarized, in non-dimensional form, in Figs. 6-8. The same constant parameters and normalizing factors used for Figs. 3-5 have been retained in Figs. 6-8, both for the rhombic and double lap configurations. An adhesive layer thickness of 0.02 in. has been assumed for the double lap joint.

Figure 6 illustrates the stiffness penalties of the two joint configurations as functions of the adhesive stiffness, for $c/a = 0.2$ and $\theta = 20°$. The "stiffness penalty" parameter is defined as follows:

$$SP = \frac{K_o - K}{K_o} \qquad (6)$$

where the reference stiffness K_o is selected as the joint stiffness in the particular case when $G_a/E_m = 0.5$, both for the rhombic and double lap configurations. The rhombic joint is evidently superior to the double lap in the small values range of the G_a/E_m ratio, that covers most adhesives available today, but this conclusion is reversed in the less practical case of $G_a/E_m > 0.0005$.

A similar comparison between the two joint configurations is shown in Fig. 7 in regard with damping. The "damping benefit" parameter displayed in this figure is defined as follows:

$$DB = \frac{U_d - U_{do}}{U} \qquad (7)$$

where U_{do} is the octahedral strain energy in the adhesive in the particular case when $G_a/E_m = 0.5$, both for the rhombic and double lap configurations. The use of soft adhesives is desirable in double lap joints from the damping standpoint, but not in rhombic joints where the associated damping benefit is less significant. Stiff adhesives appear to provide better damping performance in rhombic, rather than double lap, joints.

Strenght and weight comparisons between rhombic and double lap joints are illustrated in Fig. 8 for $G_a/E_m = 0.005$ and $\theta = 20°$. The predicted strength of the rhombic joint is about one order of magnitude higher than that of the double lap joint. This indicates the practical potential of achieving significant improvements in the load transfer efficiency through structural joints by using rhombic configurations, which are not associated with high free-edge stress concentrations. Because of their different geometry, the weight of a double lap joint appears to be more sensitive than the weight of a rhombic joint to variations of the (c/a) parameter.

CONCLUSIONS

Passively damped joints based on a rhombic configuration have the potential of providing better tradeoffs between their damping, stiffness, strength and weight characteristics than the conventional double lap configuration. The strength properties, in particular, appear to be significantly higher, which indicates the
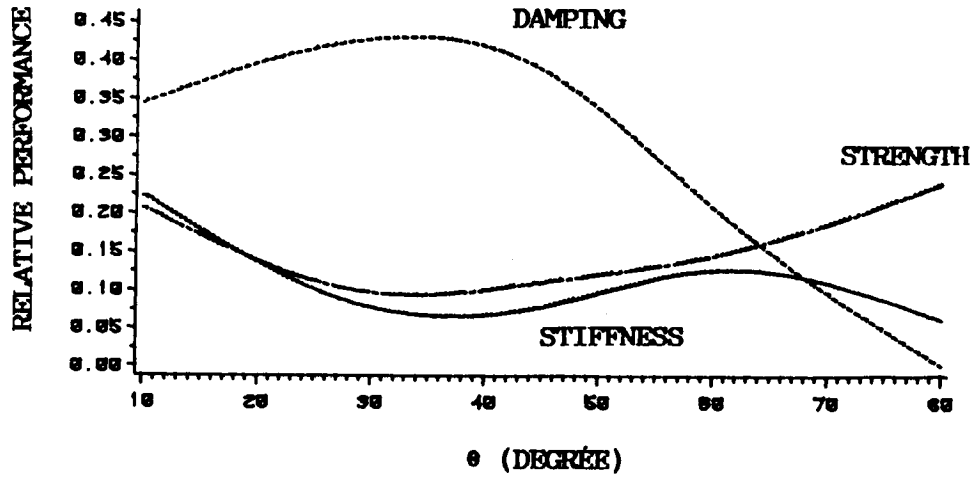
FIG.5 - EFFECT OF OPENING ANGLE ON RELATIVE
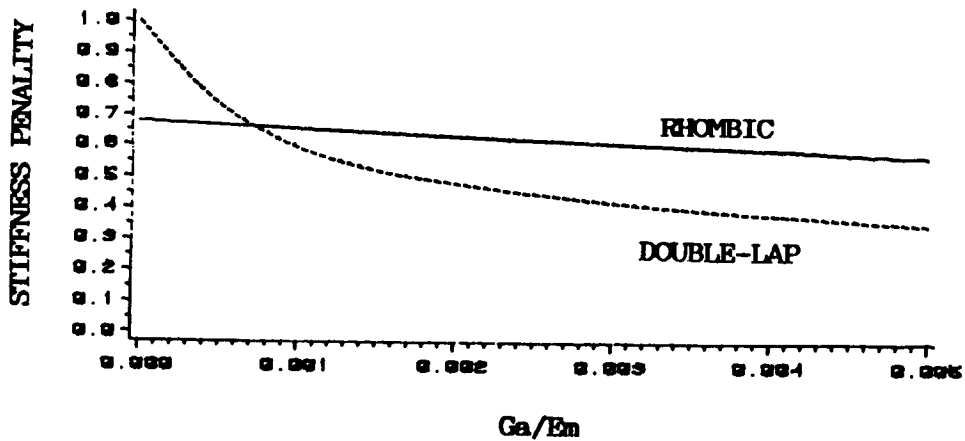PERFORMANCE CHARACTERISTICS OF
RHOMBIC JOINTS

FIG.6 - COMPARISON BETWEEN STIFFNESS PENALTIES
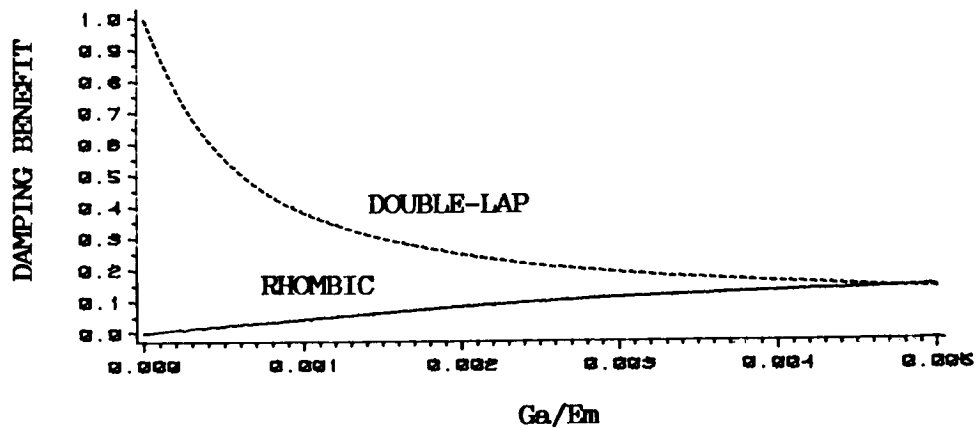FOR RHOMBIC AND DOUBLE-LAP JOINT
CONFIGURATIONS

FIG.7 – COMPARISON BETWEEN DAMPING BENEFITS
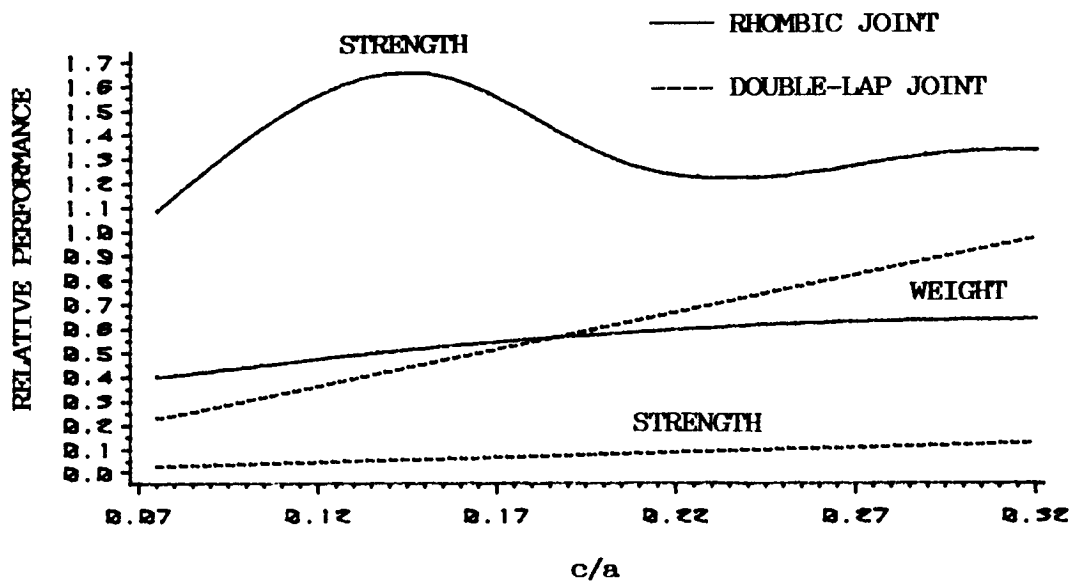FOR RHOMBIC AND DOUBLE-LAP JOINT
CONFIGURATIONS

FIG.8 – STRENGTH AND WEIGHT COMPARISONS
BETWEEN RHOMBIC AND DOUBLE-LAP JOINT
CONFIGURATIONS

possibility of enhancing load transfer efficiencies by employing rhombic joints. Proper matching between the stiffness levels of the adhesive and the adherend appears to be a dominant factor in establishing the resultant damping-stiffness tradeoff of the joint.

This paper illustrates the importance of modeling and understanding structural interactions among the various components of passively damped joints. It presents a simple, but useful methodology for predicting overall performance parameters of such joints and conducting a systematic quantitative analysis for their enhancement. Although this analysis procedure does not include explicitly the viscoelastic behavior of the adhesive, it is an expedient tool for preliminary design studies of passively damped joints.

NOMENCLATURE

a	Length of joint member (Figs. 1 and 2)
c	Width of joint member (Figs. 1 and 2)
D	Energy dissipated per cycle
E_m	Young modulus of joint member
G_a	Adhesive shear modulus
G_1	Storage shear modulus of adhesive
i	Imaginary unit (i = $\sqrt{-1}$)
K	Joint stiffness along loading direction
P	Amplitude of external oscillatory load
t	Thickness of joint member (Figs. 1 and 2)
$u_y(A)$	Displacement of point A (Fig. 1) along y-direction
U_d	Distortional strain energy in adhesive
U	Total strain energy in the joint
V_a	Volume of adhesive material
γ	Shear strain in adhesive
η	Adhesive loss factor
ν_m, ν_a	Poisson ratio of member and adhesive, respectively
ρ_m, ρ_a	Mass density of member and adhesive, respectively
θ	Opening angle of rhombic joint (Fig. 1)
$\sigma_{xx}, \sigma_{yy}, \sigma_{xy}$	Cartesian stress components

REFERENCES

1. Torvik, P. J., "The Analysis and Design of Constrained Layer Damping Treatments," Damping Applications for Vibration Control, Torvik, P. J., ed., ASME/Applied Mechanics Division, AMD-Vol. 38, 1980, pp. 85-112.

2. Horner, G. C., "Optimum Damper Locations for a Free-Free Beam," Large Space Systems Technology - 1980, Vol. II, Kopriver, F., ed., NASA Conference Publication 2168, November 1980, pp. 5-16.

3. Hobbs, G. K., Kuyper, D. J., and Brooks, J. J., "Response Analysis of a System with Discrete Dampers," Shock and Vibration Bulletin, Bulletin 46, Part 4, August 1976, pp. 137-152.

4. Plunkett, R., "Friction Damping," Damping Applications for Vibration Control, Torvik, P. J., ed., ASME Winter Annual Meeting, Chicago, 1980, pp. 65-74.

5. Beards, C. F., "Damping in Structural Joints," Shock and Vibration Digest, Vol. 11, No. 9, September 1979, pp. 35-41.

6. Mentel, T. J., "Vibrational Energy Dissipation at Structural Support Junctions," Section Four, Structural Damping, Ruzicka, J. E., ed., ASME Annual Meeting in Atlantic City, NJ, 1959.

7. Eighth World Conference on Earthquake Engineering, "Base Isolation and Mechanical Systems for Response Reduction," Proceedings 8th WCEE, Vol. V, Section 7.5, San Francisco, CA, July 1984, pp. 925-1070.

8. Bert, C. W., "Material Damping: An Introductory Review of Mathematical Models, Measures and Experimental Techniques," Journal of Sound and Vibration, Vol. 29, No. 2, 1973, pp. 129-153.

9. Spyrakos, C. C. and Beskos, D. E., "Dynamic Response of Frameworks by Fast Fourier Transform," Computers & Structures, Vol. 15, No. 5, 1982, pp. 495-505.

10. Bagley, R. L. and Torvik, P. J., "On the Fractional Calculus Model of Viscoelastic Behavior," Journal of Rheology, Vol. 30, No. 1, 1986, pp. 133-155.

11. Prucz, J., Reddy, A. D., Rehfield, L. W., and Trudell, R. W., "Experimental Characterization of Passively Damped Joints for Space Structures," Journal of Spacecraft and Rockets, Vol. 23, No. 6, November-December 1986, pp. 568-575. Also presented as Paper 85-0756 at the 26th AIAA/ASME/ASCE/AHS Structures, Structural Dynamics and Materials Conference, Orlando, FL, April 15-17, 1985.

12. Prucz, J., "Analysis of Design Tradeoffs for Passively Damped Structural Joints," Journal of Spacecraft and Rockets, Vol. 23, No. 6, November-December 1986, pp. 576-584. Also presented as Paper 85-0780 at the 26th AIAA/ASME/ASCE/AHS Structures, Structural Dynamics and Materials Conference, Orlando, FL, April 15-17, 1985.

13. Gunawan, S. and Gibson, R. F., "Analytical and Experimental Characterization of Extensional Damping in Single Lap Viscoelastic Adhesive Joints," AIAA Paper No. 87-0886-CP, Presented at the AIAA/ASME/ASCE/AHS 28th Structures, Structural Dynamics and Materials Conference, Monterey, CA, April 6-8, 1987.

14. Trudell, R. W., Rehfield, L. W., Reddy, A., Prucz, J., and Peebles, J., "Passively Damped Joints for Advanced Space Structures," Proceedings of Vibration Damping 1984 Workshop, Sponsored by the Air Force Wright Aeronautical Laboratories, Long Beach, CA, February 27-29, 1984, AFWAL-TR-84-3064, pp. DDD-1-DDD-29.

15. Prucz, J., Smith, P., Rehfield, L. W., and Reddy, A. D., "Influence of Temperature on Structural Joints with Designed-in Damping," Proceedings of "Damping 1986" Workshop, held March 5-7 in Las Vegas, NV, Air Force Wright Aeronautical Laboratories, AFWAL-TR-86-3059, Vol. 1, pp. CF-1-CF-37.

16. Lazan, B. J., Damping of Materials and Members in Structural Mechanics, Pergamon Press, Inc., 1968.

17. Ugural, A. C. and Fenster, S. K., Advanced Strength and Applied Elasticity, The SI Version, Elsevier Science Publishing, 1984, pp. 31-53.

18. Brebbia, C. A., ed., New Developments in Boundary Element Methods, Proceedings of the Second International Seminar on Recent Advances in Boundary Element Methods, held at the University of Southampton, March 1980, CML Publications.

ANALYTICAL METHODS

Dynamic Response of Laminated Composite Plates Using a Three-Dimensional Hybrid-Stress Finite-Element Formulation

W. J. Liou

C. T. Sun

In this paper a method of analysis of dynamic response of laminated composite plates is presented. The analysis is carried by using a hybrid-stress finite-element numerical technique established by the authors in their earlier publication. By using this approach the response of simply supported laminated plates subject to sinusoidal loading are investigated. For the solution of the finite-element equations of motion of free vibrations and dynamic response problems, two effective methods of solution, the space iteration method and the Newmark direct integration method are used. These two methods are discussed in this paper.

INTRODUCTION

Since Pian [1] first established the assumed stress hybrid finite element model and derived the corresponding element stiffness matrix in 1964, the hybrid stress model has been shown highly accurate, and easy to fulfill the compatibility condition of the finite element method. Laminated thick plate element has been developed by Mau et al. [2] by using hybrid stress method. In the comparison of results with elasticity solution [3,4], they observed excellent accuracy in predicting both displacements and stresses. In their assumption for the stress field, transverse normal stress was not included. Constant transverse displacement through the laminate thickness was also assumed. These assumptions did not agree well with the actual mechanism of deformation of laminated plates in bending. Spilker [5] developed an eight-node isoparametric multilayer plate element for the analysis of thin to thick fiber-reinforced composite plates. This model has the generality in describing laminate response and can be easily used to implement to attack complex laminated plate problems, but the assumption of constant transverse displacement through laminate thickness still remains.

The hybrid stress model is based on the modified complementary energy principle. An optimum choice of the number of the assumed stress modes for given boundary displacement approximation can be made, which give greater flexibility in the descriptions of the stress field. The detail of the development of this method is documented in [6].

In the present investigation, a three-dimensional eight-node hybrid stress element has been developed to analyze free vibrations of laminated plates. All six stress components are included and assumed independently within each layer through stress polynomials with 55 unknown stress parameters. The stress field within each layer satisfies the dynamic equilibrium equations of free vibration. The interface traction continuity and laminate upper/lower surface traction-free conditions are also enforced. The displacement field is interpolated in terms of

nodal displacements through shape functions. The displacements (u,v,w) are assumed to vary linearly through the thickness of each lamina.

To solve the governing finite element equations of motion for a linear dynamic analysis without damping the well-known Newmark direct integration method [7] will be used to integrate the following equation

$$[M]\{\ddot{q}\} + [k]\{q\} = [Q]$$

step by step.

The dynamic response of simply supported laminated composite plates under a dynamic sinusoidally distributed load

$$Q = Q_o \sin \frac{\pi x}{a} \sin \frac{\pi y}{b} H(t)$$

is analyzed. Numerical results of [90/0] antisymmetric cross-ply laminate and [0/90/0] symmetric cross-ply laminate are presented. Center deflection, bending stresses σ_x, σ_y, transverse shear stresses τ_{xz} and τ_{yz} and normal stress σ_z for both laminates are plotted as a function of time. Fast convergence is observed .

SUBSPACE ITERATION METHOD

the free vibration finite element equations of motion with damping neglected are

$$M \ddot{q} + K q = 0 \tag{1}$$

where K is the structure stiffness matrix and M is the structure mass matrix. Equation (1) can be solved by expressing the field variable as

$$q = \phi e^{i\omega t} \tag{2}$$

where ϕ is a nodal vector of order n, t the time variable, and ω the natural frequency of vibration of the plate in the mode described by the vector ϕ. Substituting equation (2) into Equation (1) yields the generalized eigenvalue problem

$$K \phi - \omega^2 M \phi = 0 \tag{3}$$

from which ϕ and ω can be determined. For matrices of dimension n x n, there will be n eigensolutions (ω_1^2, ϕ_1), (ω_2^2, ϕ_2),......., (ω_n^2, ϕ_n), An important property of the eigenvectors is that they satisfy the orthogonality conditions, i.e.

$$\phi_i^T M \phi_j = \delta_{ij}$$

$$\phi_i^T K \phi_j = \omega_i^2 \delta_{ij} \tag{4}$$

and $0 < \omega_1^2 < \omega_2^2 \dots\dots < \omega_n^2$

There are many different techniques existing for the solution of eigenvalue problems. Since the procedures for the eigenvalues problems are time consuming, the choice of an appropriate and effective method is an important factor for the general application, especially in the large eigenvalue problem. The subspace iteration method suggested by Bathe [8] will be adopted to conduct the investigation. This method has been used extensively in a number of general-

purpose finite element analysis programs and has proven cost-effective and reliable. In structure analysis, the lowest few eigenvalues (natural frequencies) are the main concern of investigators. The basic objective in the subspace iteration method is to solve for the p smallest eigenvalues and corresponding eigenvectors, which satisfy

$$K \phi = M \phi \Lambda \tag{5}$$

where $\phi = [\phi_1, \phi_2, \ldots\ldots, \phi_p]$

and Λ is a diagonal matrix of ω_i^2 and the eigenvector ϕ_i also satisfies the orthogonality conditions (Equation (4)).

The subspace iteration method consists of three steps [8]:
1. Establish q starting iteration vectors; q > p, q = min(2p, p+8) is a proper selection, where p is the number of eigenvalues and eigenvectors to be calculated.
2. Use simultaneous inverse iteration on the q vectors and Ritz analysis to extract the "best" eigenvalue and eigenvector approximations from the q iteration vectors.

For k = 1, 2,....,

$$K \overline{X}_{k+1} = M X_k \tag{6}$$

where X_1 is the starting iteration vector.

Find the projections of the operators K and M,

$$K_{k+1} = \overline{X}_{k+1}^T K \overline{X}_{k+1}$$

$$M_{k+1} = \overline{X}_{k+1}^T M \overline{X}_{k+1} \tag{7}$$

Solve for the eigensystem of the projected operators,

$$K_{k+1} Q_{k+1} = M_{k+1} Q_{k+1} \Lambda_{k+1} \tag{8}$$

Find an improved approximation to the eigenvectors,

$$K_{k+1} = \overline{X}_{k+1} Q_{k+1} \tag{9}$$

As $k \to \phi$

$$\Lambda_{k+1} \to \Lambda \text{ and } X_{k+1} \to \phi \tag{10}$$

3. After iteration convergence, use the Sturm sequence check to verify that the required eigenvalues and corresponding eigenvectors have been calculated.

Reference [8] has presented very detailed descriptions about the subspace iteration method and is a good reference to use to become familiar with this method.

The governing finite element equations of motion for a linear dynamic analysis are

$$M \ddot{q} + K q = 0 \tag{11}$$

where M and K are the mass and stiffness matrices, q and $\ddot{q}$ are the nodal displacement and acceleration vector, and Q is the load (nodal force) vector of the finite element system. In finite element analysis, there exist many effective numerical procedures to solve the linear differential equations, Equation (11). Basically, they can be divided into two methods of solution: the direct integration method and the mode superposition method. In the present study, the Newmark direct integration method [7] will be followed to integrate Equation (11) step by step. The following assumptions are made in the numerical analysis:

$$\dot{q}_{n+1} = \dot{q}_n + [(1-\delta)\ddot{q}_n + \delta\ddot{q}_{n+1}]\Delta t \tag{12}$$

$$q_{n+1} = q_n + \dot{q}_n\Delta t + [(\frac{1}{2}-\alpha)\ddot{q}_n + \alpha\ddot{q}_{n+1}]\Delta t^2 \tag{13}$$

where Δt is the time step size, n is the step number, and the parameters δ and α control integration accuracy and stability. At time $t_{n+1} = (n+1)\Delta t$, the finite element equations of motion (Equation (11)) are described as:

$$M \ddot{q}_{n+1} + K q_{n+1} = Q_{n+1} \tag{14}$$

Solving from Equation (13) for $\ddot{q}_{n+1}$ in terms of q_{n+1}, and then substituting into Equation (14) and rearranging the terms transforms the equations to the form

$$\hat{K} q_{n+1} = \hat{Q}_{n+1} \tag{15}$$

where

$$\hat{K} = a_0 M + K \tag{16}$$

$$\hat{Q}_{n+1} = Q_{n+1} + M(a_0 q_n + a_1 \dot{q}_n + a_2 \ddot{q}_n)$$

and

$$a_0 = 1/\alpha(\Delta t)^2$$

$$a_1 = 1/\alpha(\Delta t) \tag{17}$$

$$a_2 = (1 - 2\alpha)/2\alpha$$

Once the displacements q_{n+1} at time step n+1 are known from Equation (15), the velocities and accelerations can be computed by using Equations, (12) and (13) and expresses as

$$\ddot{q}_{n+1} = a_0(q_{n+1} - q_n) - a_1\dot{q}_n - a_2\ddot{q}_n \tag{18}$$

$$\dot{q}_{n+1} = \dot{q}_n + a_3\ddot{q}_n + a_4\ddot{q}_{n+1} \tag{19}$$

where

$$a_3 = (1 - \delta)(\Delta t) \tag{20}$$

$$a_4 = \delta(\Delta t)$$

A special scheme originated by Newmark with $\delta = 0.5$ and $\alpha = 0.25$ is used here to integrate the equations step by step. These values correspond to the constant-average-acceleration method, which gives an unconditionally stable numerical scheme [7].

DYNAMIC RESPONSE OF A SIMPLY SUPPORTED LAMINATED SQUARE PLATE

The dynamic response of simply supported laminated plates is presented in this section. The laminates are subjected to suddenly applied sinusoidally distributed pulse loading,

$$q(x, y, t) = (q_0 \sin \pi x/a \, \sin \pi y/b) H(t) \tag{21}$$

where $H(t)$ is the Heavyside step function. The following two laminated plates are considered:

1. A two-layer anti-symmetric cross-ply (90/0) square laminate with layers of equal thickness.

2. A three-layer symmetric cross-ply (0/90/0) square laminate with layers of equal thickness.

In both problems, the same material properties as in Putcha and Reddy [9] are employed for each individual layer.
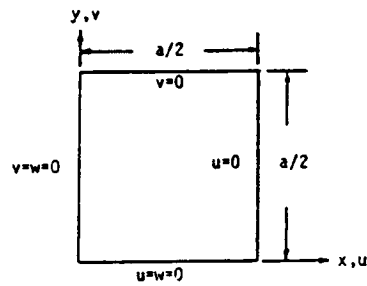
$$E_L = 525 \text{ GPa}$$

$$E_T = 21 \text{ GPa}$$

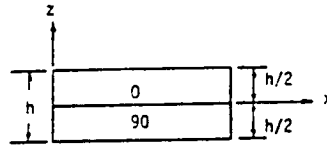$$G_{LT} = G_{TT} = 10.5 \text{ GPa} \tag{22}$$

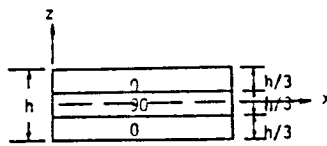$$\nu_{LT} = \nu_{TT} = 0.25$$

$$\rho = 0.8 \text{ g/cm}^3$$

Owing to the biaxial symmetry of the laminate geometry, only one quadrant of the laminate is analyzed. The geometry configurations and boundary conditions of the finite element model are shown in Figure 1.

(a) Top view and boundary conditions of laminate

(b) Two-layer anti-symmetric laminate

(c) Three-layer symmetric laminate

Figure 1   Laminate geometry configurations and boundary conditions

The normalized deflection and stresses are described as

$$\bar{w} = 1000E_T h^3 w/q_o a^4$$

$$(\bar{\sigma}_x, \bar{\sigma}_y) = 10(\sigma_x, \sigma_y)/q_o S^2 \tag{23}$$

$$(\bar{\sigma}_z, \bar{\tau}_{xz}, \bar{\tau}_{yz}) = 10(\sigma_z, \tau_{xz}, \tau_{yz})/q_o S$$

$$S = a/h \qquad \bar{z} = z/h$$

In the present study q_o is taken to be 100 and the time step size is equal to 5 microseconds. The normalized central transverse deflection, $\bar{w}(a/2, a/2, 0)$, as a function of time for a two-layer anti-symmetric simply supported cross-ply square laminate under sinusoidal loading is shown in Figure 2. Throughout Figures 3, 4, 5 and 6, the stresses with respect to time for a two-layer laminate are plotted. In Figures 3 and 4, it is observed that the normalized normal stress $\bar{\sigma}_x$ at center top surface of the laminate is close to the normalized normal stress $\bar{\sigma}_y$ at center bottom surface of the laminate, except $\bar{\sigma}_x$ is in tension and $\bar{\sigma}_y$ is in compression. As shown in Figure 5, the variation of normalized shear stress $\bar{\tau}_{xz}$ is similar to $\bar{\tau}_{yz}$. From the plots, it is seen that the periods of the transient response for $\bar{w}$, $\bar{\sigma}_x$, $\bar{\sigma}_y$, $\bar{\tau}_{xz}$, and $\bar{\tau}_{yz}$ are very closely related. This fact agrees with the results of Putcha and Reddy [9]. The period for the normalized transverse normal stress $\bar{\sigma}_z(a/2, a/2, h/2)$, is much shorter when compared with others. A shorter time step size ($\Delta t = 1$ microsecond) is employed to observe the periodic response of the normalized transverse normal stress $\bar{\sigma}_z$ as shown in Figure 6.
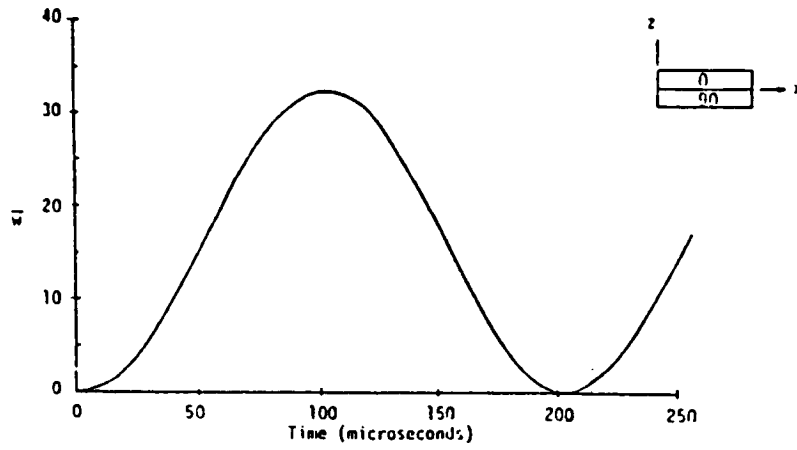
Figure 2   Center deflection versus time for a 2-layer cross-ply (90/0) simply
            supported square laminate under suddenly applied sinusoidal loading
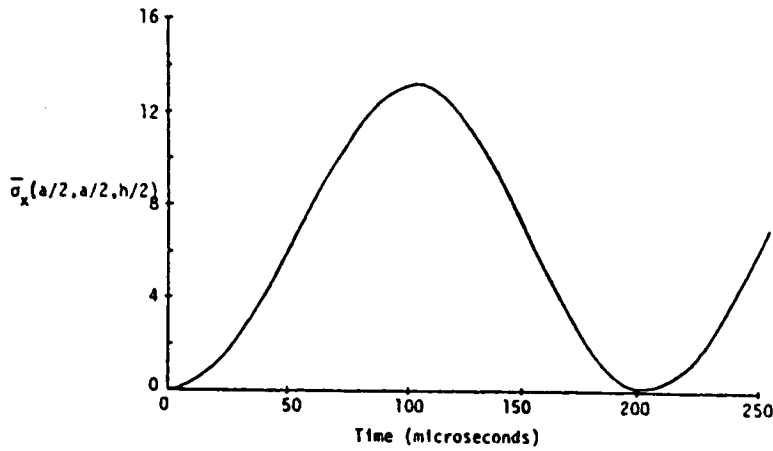

Figure 3   Normal stress versus time for a 2-layer (90/0) laminate under suddenly
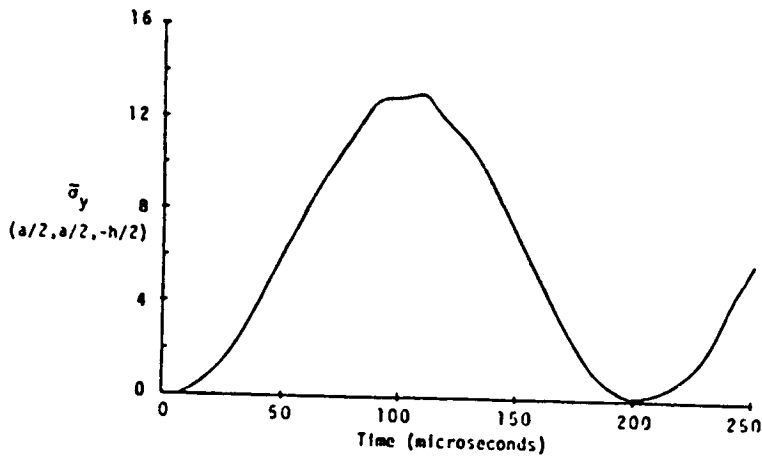   applied sinusoidal loading

Figure 4   Normal stress versus time for a 2-layer (90/0) laminate under suddenly
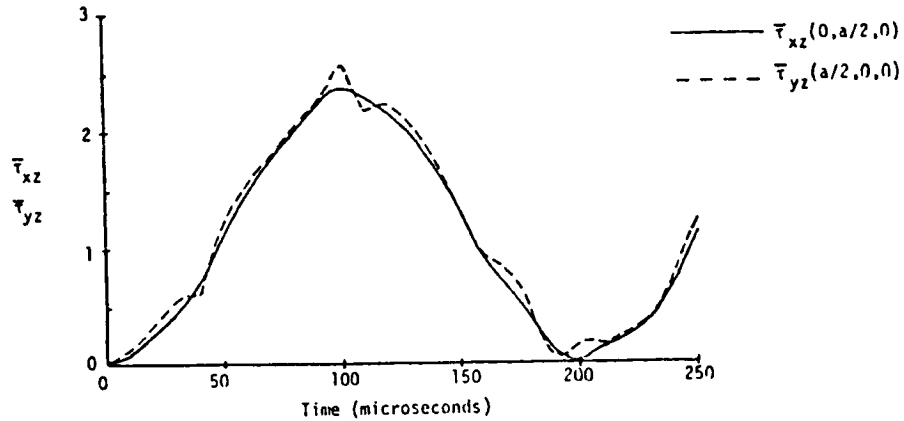   applied sinusoidal loading

481

Figure 5   Transverse shear stresses versus time for a 2-layer (90/0) laminate under suddenly applied sinusoidal loading
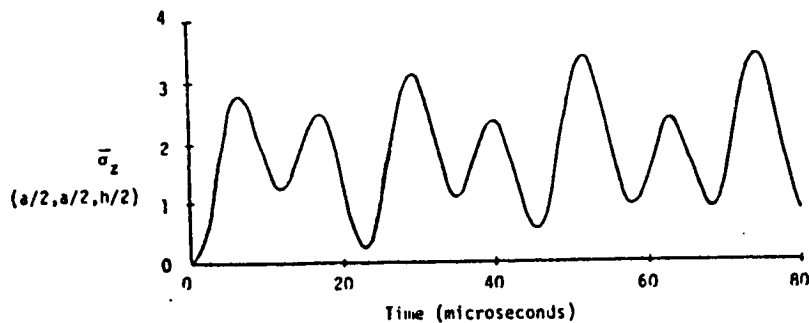

Figure 6   Transverse normal stress versus time for a 2-layer (90/0) laminate under suddenly applied sinusoidal loading

The normalized central transverse deflection with respect to time for a three-layer simply supported cross-ply (0/90/0) square laminate under sinusoidal loading is shown in Figure 7. Figure 8 contains the normalized maximum normal stresses, $\bar{\sigma}_x$ and $\bar{\sigma}_y$, as a function of time. The normalized shear stresses, $\bar{\tau}_{xz}$ and τ_{yz}, are shown in Figure 9. The periods for the normalized deflection and stresses are similar. In Figure 9, the amplitude of the response is larger for $\bar{\tau}_{xz}$ than for $\bar{\tau}_{yz}$; it is because the bending stiffness is higher in the x-direction than in the y-direction for a three-layer (0/90/0) laminate with layers of equal thickness. The normalized central normal stress distribution, $\bar{\sigma}_x$, through the thickness of the laminate for time from 20 to 80 microseconds is shown in Figure 10.

In the present study, a four-node isoparametric plate element with 48 assumed stress parameters for each lamina is used. Fast convergence is observed; only a 5 x 5 mesh is modeled in a quadrant of the laminate.

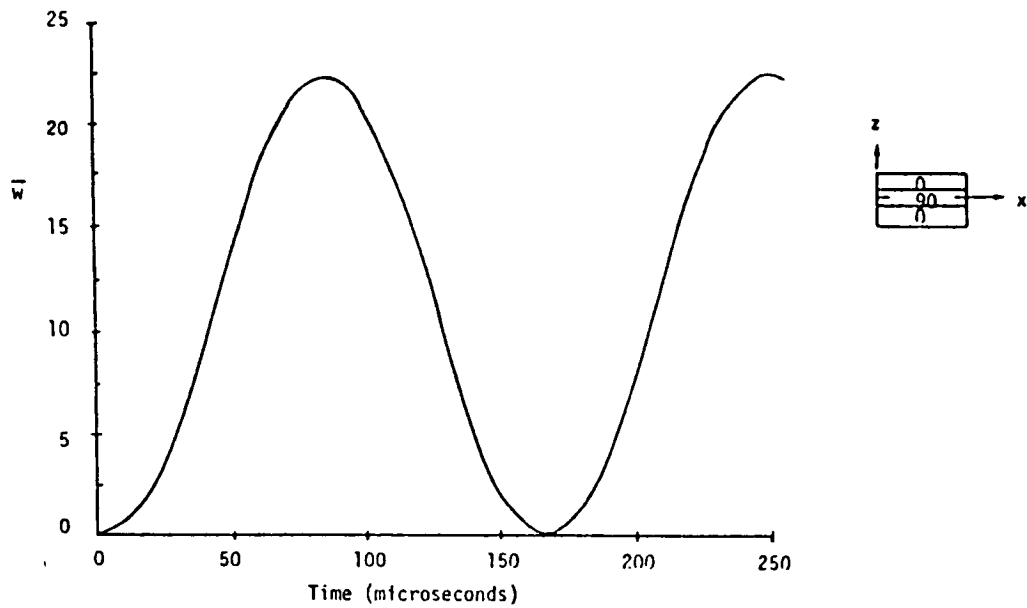**Figure 7** Center deflection versus time for a 3-layer cross-ply (0/90/0) laminate under suddenly applied sinusoidal loading
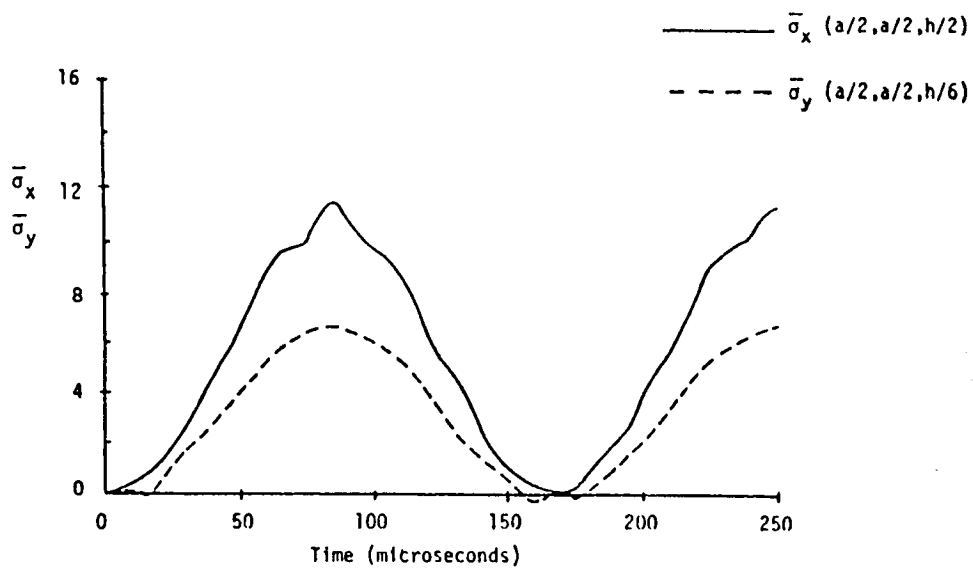

Figure 8 Normal stresses versus time for a 3-layer (0/90/0) laminate under suddenly applied sinusoidal loading
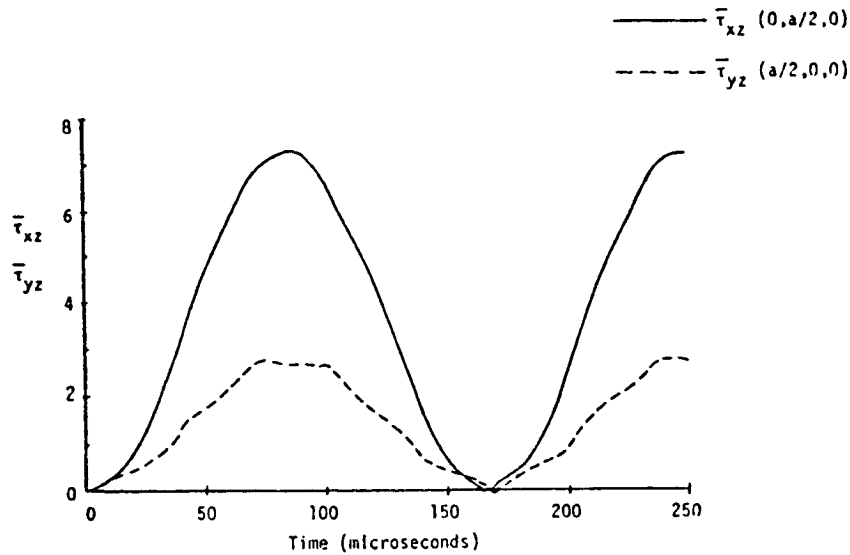
483

Figure 9   Transverse shear stresses versus time for a 3-layer (0/90/0) laminate
             under suddenly applied sinusoidal loading
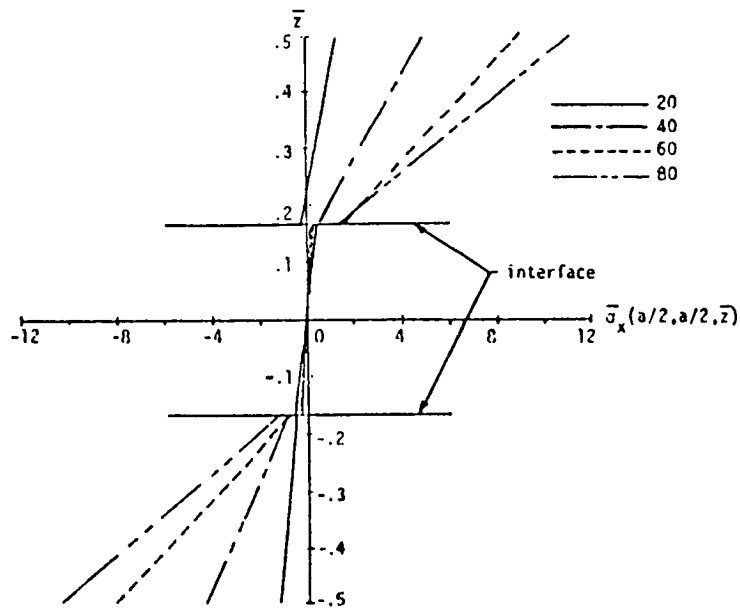

Figure 10   Through-thickness center normal stress versus $\bar{z}$ for a 3-layer
             (0/90/0) laminate under suddenly applied sinusoidal loading
             for time from 20 to 80 microseconds

CONCLUDING REMARKS

The proposed three-dimensional hybrid stress finite element method in conjunction with the Newmark's direct integration method seems to be a powerful technique for analyzing laminated composite plates under dynamic loading. By using this approach the transverse deflection, the in-plane bending stresses and the interlaminar shear stresses and normal stress can be evaluated very easily without consuming too much computation time. This method can also be used to analyze forced vibration problems of laminated composite under impact loading. The result will be published in the near future.

REFERENCES

1. Pian, T. H. H., "Derivation of Element Stiffness Matrices by Assumed Stress Distribution," _AIAA J_. Vol. 2, pp. 1333-1336, 1964.

2. Mau, S. T., Tong, P., and Pian, T. H. H., "Finite Element Solutions for Laminated Thick Plates," _J. Composite Materials_, Vol. 6, pp. 304-311.

3. Reissner, E., and Stavsky, Y., "Bending and Stretching of Certain Types of Heterogeneous Allotropic Elastic Plates," _J. Applied Mechanics_, Vol. 28, pp. 402-408, 1961.

4. Whitney, J. M., and Panago, N. J., "Shear Deformation in Heterogeneous Anisotropic Plates," _J. Applied Mechanics_ Transactions, ASME, 92, pp. 1031-1036, 1970.

5. Spilker, R. L.,, "A Hybrid-Stress Finite Element Formulation for Thick Multilayer Laminates," _Computer and Structures_, Vol. 11, pp. 507-514, 1980.

6. Sun, C. T., and Liou, W. J., "A Three-Dimensional Hybrid Stress Isoparametric Element for the Analysis of Laminated Composite Plates," _Computer and Structures_ Vol. 25, No. 2, pp. 241-249, 1987.

7. Newmark, N. M., "A Method of Computation for Structural Dynamics," ASCE _J. Engineering Mechanics Division_, 85, pp. 67-94, 1959.

8. Balke, K. J., _Finite Element Procedures in Engineering Analysis_, Prentice-Hall, Englewood Cliffs, New Jersey, 1982.

9. Putcha, N. S., and Reddy, J. N., "On Dynamics of Laminated Anisotropic Plates Using a Refined Mixed Plate Element" ASME Winter Annual Meeting, New Orleans, La. pp. 161-169, 1984.

Dynamic Behavior of Dissymmetric Rotor Bearings Modelled With a Periodic Coefficient Large System

P. M. Guilhen

P. Berthier

G. Ferraris

M. Lalanne

This work is concerned with the instability and unbalance response of dissymmetric rotor-bearing systems containing periodic coefficients when modeling produces matrices with a large number of degrees of freedom. It is important to solve the equations and then to predict the dynamic behavior of the system. This can be done knowing the instability areas, and the unbalance response in the stable areas. One deals here with a large number of equations and a reduction of the number of degrees of freedom of the system is achieved through a pseudo modal method. This method is shown to give satisfactory results.

INTRODUCTION

It is now more and more necessary to predict accurately the dynamic behavior of rotor bearings systems : natural frequencies as a function of the speed of rotation which gives the critical speeds and instability zones and response to unbalance and nonsynchronous forces.

For most of rotors containing a large number of degrees of freedom, calculations do not pose any problem today. Many authors, as [1], [2], [3], [4], have shown that, using a method based either on substructuring or on a modal reduction, the number of degrees of freedom can be lowered significately and the results are without significant loss of accuracy.

For dissymmetric rotors, it happens sometimes that the equations lead to periodic coefficients. In this case, some authors, as [5], [6], [7], [8] give methods to detect instability zones (mainly transfer-matrix or infinite determinant methods) and to calculate step by step the unbalance response. But usually, these methods are applied on systems having a few degrees of freedom (up to 20). The purpose of this study is to develop for large periodic systems, a method which can be used to obtain the dynamical behavior of the systems. In a first part, a pseudo-modal method adapted to the resolution of periodic differential equations is presented. In a second part an industrial application containing 96 degrees of freedom is considered. The influence of the number of modes on the results, and the accuracy of the methods are discussed.

PSEUDO-MODAL METHOD

The systeme to be solved can be written as :

$$M X^{\bullet\bullet} + A(t) X^{\bullet} + K(t)X = F(t) \qquad\qquad (1)$$

M, A, K are n order matrices and it has been shown [8] that $A(t)$ and $K(t)$ can be written as :

$$A(t) = A_o + A_1 \sin 2\Omega t + A_2 \cos 2\Omega t \qquad (2)$$

$$K(t) = K_o + K_1 \sin 2\Omega t + K_2 \cos 2\Omega t \qquad (3)$$

The pseudo-modal method consists in using a "modal" base of the system

$$M \, X^{\bullet\bullet} + \overline{K} \, X = 0 \qquad (4)$$

The modal base is calculated from the system at rest ($\Omega = 0$) and at the initial instant ($t = 0$). In these conditions, there are neither periodic coefficients, nor gyroscopic effects. Furthemore, the damping of the bearings is omited, and the non symmetric terms of the stiffness matrix K are symmetrised :

$$K = K_o + K_2 \qquad (5)$$

$$\overline{K} = \text{sym } (K) \qquad (6)$$

The modal base ϕ is built with the lowest ℓ modes of (4), ($\ell \ll n$). The relation between the degrees of freedom of the system and the modal parameters is :

$$X = \phi \, q \qquad (7)$$

Equation (1) with (2), (3) and (7) leads to :

$$M \phi \, q^{\bullet\bullet} + (A_o + A_1 \sin 2\Omega t + A_2 \sin 2\Omega t) \phi \, q^{\bullet} + (K_o + K_1 \sin 2\Omega t$$
$$+ K_2 \cos 2\Omega t) \phi \, q = F \qquad (8)$$

and premultiplying by ϕ^t, (8) can be written as :

$$m \, q^{\bullet\bullet} + (a_o + a_1 \sin 2\Omega t + a_2 \cos 2\Omega t) q^{\bullet} + (k_o + k_1 \sin 2\Omega t + k_2 \cos 2\Omega t) q = f \quad (9)$$

with

$$m = \phi^t M \phi \; ; \; a_o = \phi^t A_o \phi \; ; \; a_1 = \phi^t A_1 \phi \; ; \; a_2 = \phi^t A_2 \phi$$
$$k_o = \phi^t K_o \phi \; ; \; k_1 = \phi^t K_1 \phi \; ; \; k_2 = \phi^t K_2 \phi \; ; \; f = \phi^t F \qquad (10)$$

SOLUTION OF THE EQUATIONS

Instabilities and unbalance response come from the reduced system (9), and from (7). The method used is that detailed in [8]. Here the basic principles are shown.
  * Instabilities are found with the resolution of :

$$m \, q^{\bullet\bullet} + a \, q^{\bullet} + kq = 0 \quad \text{with :} \qquad (11)$$

$$a = a_o + a_1 \sin 2\Omega t + a_2 \cos 2\Omega t \qquad (12)$$

$$k = k_o + k_1 \sin 2\Omega t + k_2 \cos 2\Omega t \qquad (13)$$

(11) is transformed into :

$$\frac{dp}{dt} = B p \tag{14}$$

with

$$p = \begin{vmatrix} q \\ q^\bullet \end{vmatrix} \tag{15}$$

and

$$B = \begin{vmatrix} O & I \\ -m^{-1}k & -m^{-1}a \end{vmatrix} \tag{16}$$

B is a periodic matrix, of period T. The period T of the periodic coefficients is divided in s intervals of length $h = T/s$. System (14) is considered to be constant on each interval and a matrix T_i connecting displacements and velocities at the instants ih and (i-1)h can be calculated. The general matrix connecting q and $q^\bullet$ over a period T is obtained by the product of matrices :

$$T_f = T_{s-1} \quad \cdots \quad T_j \cdot T_{j-1} \quad \cdots \quad T_1 \cdot T_o \tag{17}$$

and

$$p(T) = T_f p(O) \tag{18}$$

The $2.\ell$ complex eigenvalues of T_f are representative of the stability of the system. If they are all less than unity the system is stable. Here each matrix T_j is calculated with a Newmark formulation and the expression of T_j is given below.

$$T_j = \begin{vmatrix} D^{-1} F & D^{-1} E \\ \frac{2}{h}(D^{-1}F-I) & \frac{2}{h}D^{-1}E- I \end{vmatrix} \tag{19}$$

with

$$D = \frac{4m}{h^2} + \frac{2c_{j+1}}{h} + k_{j+1} \tag{20}$$

$$E = \frac{4m}{h} + c_{j+1} - c_j \tag{21}$$

$$F = \frac{4m}{h^2} + \frac{2c_{j+1}}{h} - k_j \tag{22}$$

Instability zones are obviously the same as those which would be obtained from (1).

* Unbalance response is the solution of (9). Numerical resolution is made with a Newmark formulation and the initial conditions are chosen as :

$$t = O \quad q(O) = O \tag{23}$$

489

$$q^{\bullet}(0) = 0 \qquad (24)$$

$$q^{\bullet\bullet}(0) = m^{-1} f(0) \qquad (25)$$

APPLICATION

A rotor of a 220 KW Steam Compressor, (Fig.1) is studied. The rotor contains symmetric shaft and disks, and dissymmetric bearings. Calculations are at first made in a fixed reference frame where equations have constant coefficients and are obtained with a finite element model and are easily solved [9]. Then, calculations are made in a rotating reference frame : the equations have periodic coefficients and are also obtained with a finite element model. The comparison of the results in the two different frames shows the interest of the method proposed.
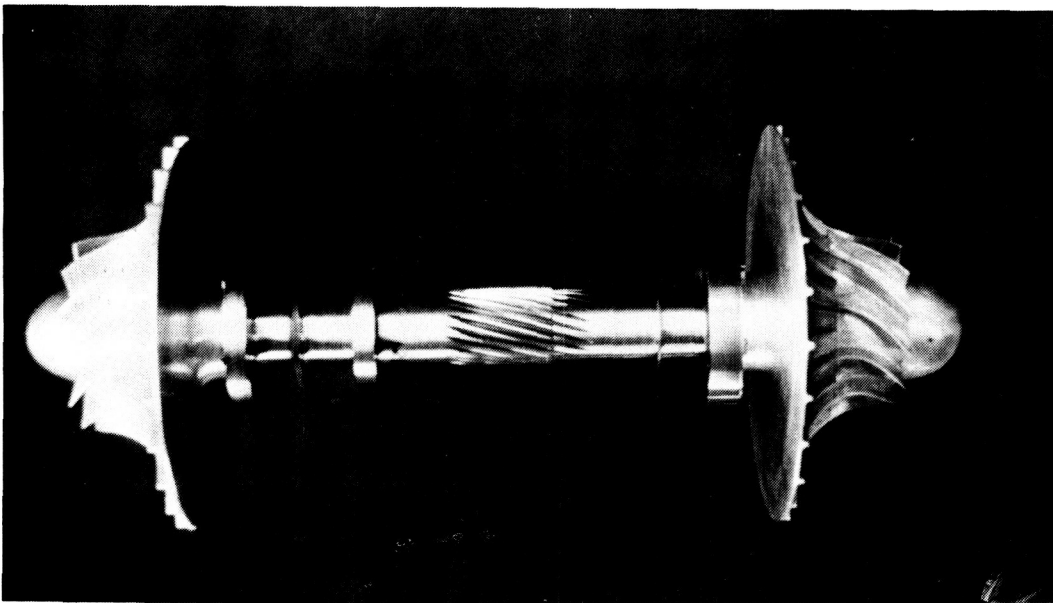

Fig. 1 : 220 KW Steam Compressor Rotor

1 - Description of the model

The rotor is modeled with 23 finite elements, as shown in Fig.2. Two calculations are made with different materials for the disks. They are in Aluminium for rotor A, and in steel for rotor B.
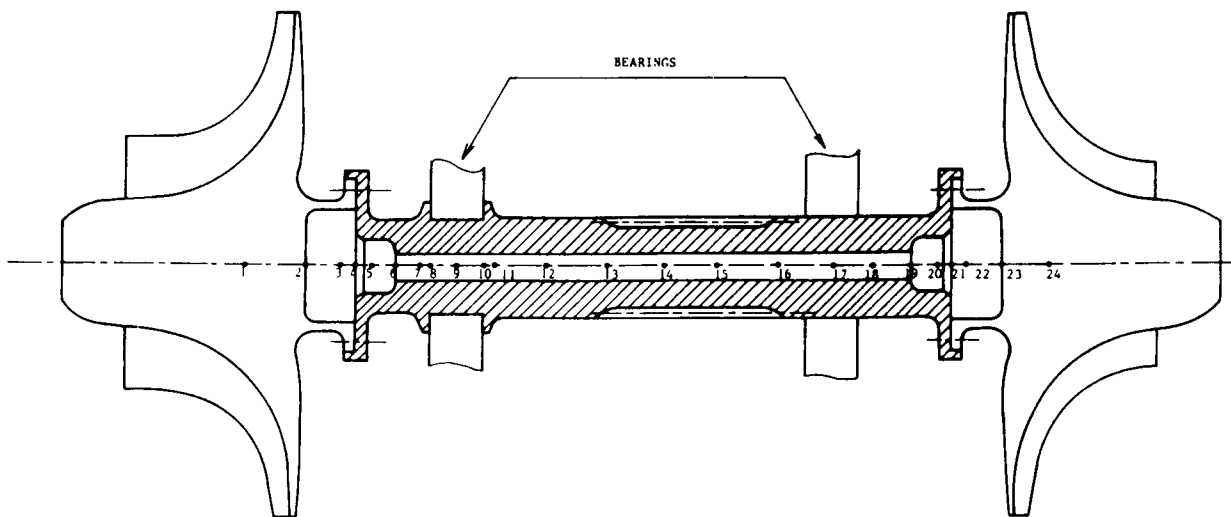
Fig. 2 : Modelisation of the rotor

2 - Calculations

The two rotors are used for different purposes. For rotor A (aluminium disks) the unbalance response can be performed over 4 critical speeds because the motion is always stable in the operating range (0 - 60000 RPM). For rotor B, instabilities appear near 20.000 RPM. So the two configurations will provide satisfactory tests both for instabilities and unbalance response.

3 - Results

* Instabilities

They appear at 21300 RPM in the fixed reference frame. In the rotating one the instability with 14 modes appears at 19700 RPM.

* Unbalance response

Fig. 3, 4, 5 represent the maximum of the unbalance response at node 1. Different number of modes (6-10-14) are considered, and compared to the results in the fixed-reference frame. The resolution in the rotating reference frame with reduced coordinates introduces a slight gap in the frequencies. This creates differences in the amplitude to up to 10 % in the critical frequencies zones. Only the permanent solution is compared, and the number of rotations of the rotor necessary to obtain the permanent solution depends a lot on its rotating speed.

CONCLUSION

The dynamic behavior of periodic coefficient large system is predicted here with a pseudo modal method, using a significant reduction of the number of degrees of freedom.

Differences which are shown in the industrial example presented may be inherent to the numerical calculations.
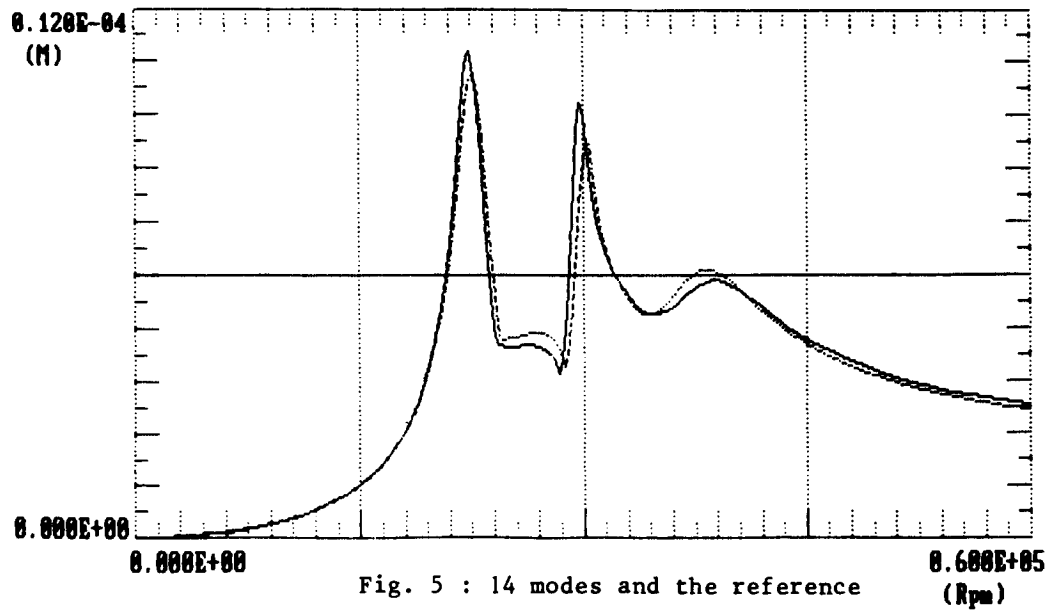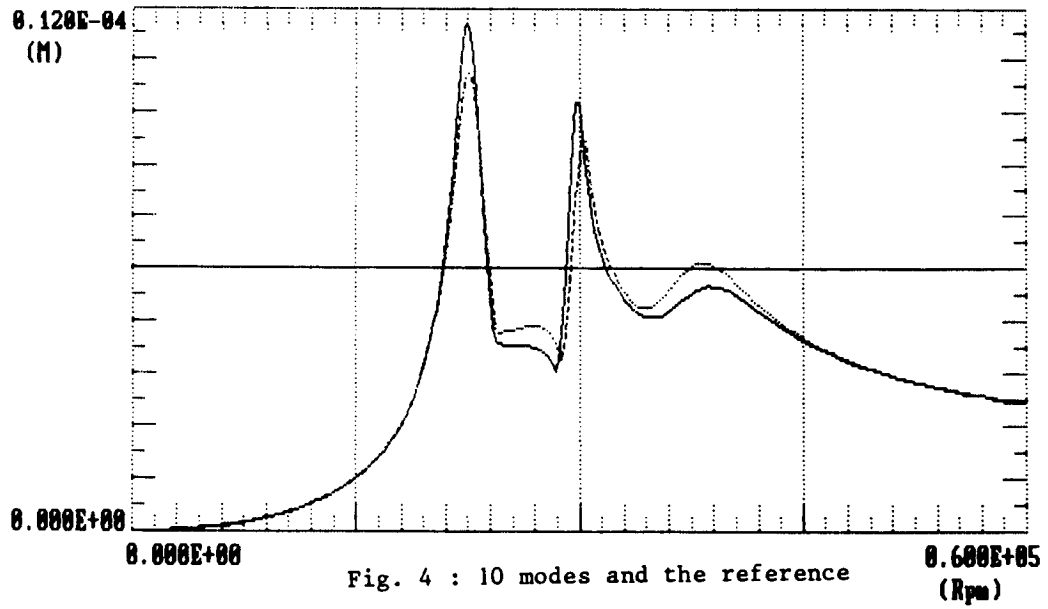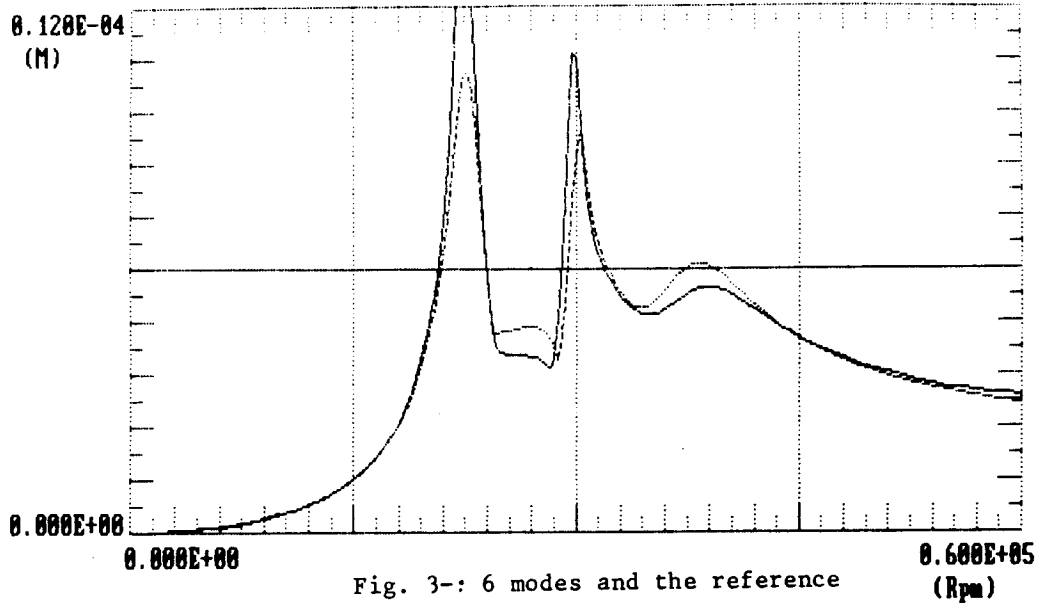
Fig. 3-: 6 modes and the reference

Fig. 4 : 10 modes and the reference

Fig. 5 : 14 modes and the reference

492

REFERENCES

1. D.W. Childs, J.B. Bates, "Residual-flexibility corrections for transient modal rotordynamic models", Trans. A.S.M.E., J. Mech. Design, April 1978, vol.100/251-256.
2. E.J. Gunter, K.C. Choy, P.E. Allaire P.E., "Modal analysis of turbo-rotors using planar modes-theory", Journal of the Franklin Institute, vol.305, n°4, April 1978.
3. D.A. Glasgow, H.D. Nelson, "Stability analysis of rotor bearing systems using component mode synthesis", Trans. A.S.M.E., J. Mech. Design, vol.102, n°2, April 1980/352-359.
4. P. Berthier, G. Ferraris, J. Der Hagopian, M. Lalanne, "Application d'une méthode pseudo-modale à la détermination du comportement dynamique des monorotors et des multirotors coaxiaux", 7th Worl congress on the theory of machines and mechanisms, Seville, sept.87.
5. E. Anton, H. Ulbrich, "Active control of vibration in the case of asymmetrical high speed rotors by using magnetic bearings", A.S.M.E. Paper n°85 DET 28.
6. S.T. Noah, G.R. Hopkins, "A generalized Hill's method for the stability analysis of parametrically excited dynamic system", Trans. A.S.M.E., J. App. Mech., vol.49, March 1982/217-223.
7. S. Zhou, N.F. Rieger, "Instability analysis procedure for 3 level multi bearing rotor foundation systems", NTIS-HC A21/NFAD1, Instability in rotating machinery, Symposium, Carson City, June 1985.
8. P.M. Guilhen, P. Berthier, G. Ferraris, M. Lalanne, "Instability and unbalance response of dissymmetric rotor bearings systems", Accepted A.S.M.E. Conf. Boston, 1987, and Trans. A.S.M.E.
9. P. Berthier, G. Ferraris, M. Lalanne, "Prediction of critical speeds, unbalance and nonsynchronous forced response of rotors". 53th Shock and Vib. Bull., 1983.

NOMENCLATURE

A	"Damping" matrix $[n.n]$ containing periodic coefficients
a	modal damping matrix $[\ell.\ell]$
B	matrix which transforms a $[\ell.\ell]$ second order differentiel system into in $[2\ell.2\ell]$ first order differential system
E	Young modulus (N/m^2)
F	unbalance force vector
h	time interval $h = T/s$
I	unity matrix
K	"stiffness" matrix $[n.n]$ containing periodic coefficients
k	modal stiffness matrix $[\ell.\ell]$
ℓ	number of modes taken into acount
M	mass matrix $[n.n]$
m	modal mass matrix $[\ell.\ell]$
n	number of degrees of freedom
P	vector $[2\ell]$ containing modal displacements and vitess
q	modal displacement vector $[\ell]$
s	number of intervals in a period T
T	period of coefficients of differential equations

T_f transfer matrix over one period T

X^f displacements vector $[n]$

b   modal base built with the first ℓ modes

Ω rotation speed of the rotor

ρ volumic mass (Kg/m^3)

ν Poisson coefficient

$\cdot$ d/dt

$\cdot\cdot$ d^2/dt^2

Significance of Foundation-Soil Separation in Dynamic Soil-Structure Interaction

C. C. Spyrakos
P. N. Patel

The dynamic response of flexible surface strip-foundations allowed to uplift is numerically obtained for externally applied forces of a transient time variation. The soil medium is represented by an isotropic, homogeneous and linear elastic half-space. The soil is treated by a time domain Boundary Element Method, while the flexible founadtion is treated by the Finite Element Method. In order to effectively simulate soil-foundation separation, thin-layer FEM interface elements are used at the contact area. The numerical procedure of determining the area of contact by solving the nonlinear equations of motion is based on the BEM and FEM appropriately combined through equilibrium and compatibility considerations. For various relative stiffnesses between the foundation and soil the system is subjected to a concentrated impulse force and/or moment acting on the surface foundation. It is observed that separation significantly affects the foundation response, and should be considered in the analysis for a range of relative stiffness between the foundation and the soil.

INTRODUCTION

Most soil-structure interaction problems are treated under the assumption of complete bond between the foundation and the soil [1-3]. However, for a given eccentricity and intensity of external dynamic forces, a foundation will partially separate from the underlying soil, as tension is incompatible with the constitutive laws of soils. Recently, some attention has been directed towards the study of the effects that partial foundation-soil separation may cause on the structure response [4-6]. These studies have been initiated from observations during strong ground motions, actual performance of structures during earthquakes and laboratory tests [7-10]. Both analytical studies and numerical investigations demonstrated that uplift may have controversial effects on structural behavior. Factors such as slenderness ratio, foundation to superstructure mass ratio, eigen properties of the structure,

type and duration of the exciting disturbance may have either benevolent or malevolent effects on the structure response.

The methods of non-linear analysis usually employed to obtain the structure response can be classified into three categories: a. Employment of discrete systems idealizing the foundation in a small number, usually two, of elasto-plastic springs and ignoring both the radiation damping and the coupling between the soil-foundation contact stresses at the time of separation [11]; b. Simulation of the soil behavior by either a damped Winkler foundation or a foundation supported on two elastic spring-dampers attached at the ends [4,5,12]; c. Employment of a finite difference [8] or finite element method (FEM) of analysis [13,14] to model soil media leading to a large system of equations. Recently, Wolf et al. [15,16] determined the response of a typical nuclear-reactor building modeled by a single degree of freedom in the vertical direction supported by a rigid circular foundation subjected to vertically incident seismic waves. Their formulation is based on a time domain indirect boundary element formulation (BEM) employing an inverse Fourier transform on the level of the individual boundary elements.

In this paper, the dynamic response of massless flexible surface strip-foundations allowed to uplift is numerically obtained for externally applied forces of a transient time variation. The soil medium is represented by a homogeneous and linear elastic half-space. The soil is treated by the BEM, while the foundation and the interface are treated with the aid of FEM. The numerical procedure of determining the area of contact by solving the nonlinear equations of motion is based on the BEM and FEM appropriately combined through equilibrium and compatibilty considerations. Thus, the formulation does not require the adoption of frequency independent compliances needed for the solution of nonlinear dynamic soil-structure interaction problems. The primary contributions of this work are the development of a methodology that allows a rigorous treatment of the separation effects on soil-structure interaction problems as well as a thorough investigation of the influence of uplift on the response of flexible surface strip-foundations.

METHODOLOGY

Consider the soil-structure system of figure 1, which is allowed to oscillate with unilateral contact. The foundation and the interface are treated with the aid of FEM, while the soil is treated by the BEM. The two domains are appropriately combined through equilibrium and compatibility considerations at the soil-foundation interface. The interface is modeled with thin-layer elements of negligible influence on the system response. The treatment of the thin-layer elements simulating the interface behavior is discussed in the next section. In the following, the treatment of the soil and the foundation is briefly discussed.

Under the assumptions of zero initial conditions and zero body forces, the BEM formulation is developed through a numerical treatment of the integral equation governing the soil motion at the soil-foundation interface having the form [17,18]

$$\tfrac{1}{2}u_\beta(\xi,t)=\int_s \{v_{\alpha\beta}[x,t;\xi/t_{(\tilde n)\alpha}(x,t)] -$$

$$-\sigma_{(\tilde n)\alpha\beta}[x,t;\xi/u_\alpha(x,t)]\}ds(x), \qquad (1)$$

where s denotes the soil-foundation interface as well as a portion of the free surface around it, and the tensors $v_{\alpha\beta}$ and $\sigma_{(\tilde n)\alpha\beta}$ represent the fundamental solution pair of the infinite space under conditions of plane strain.
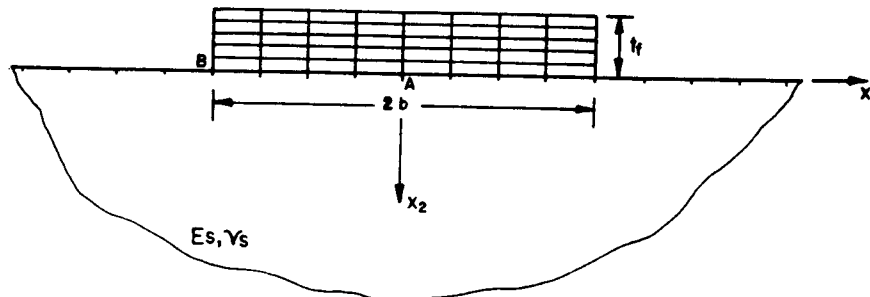

Fig. 1 Soil-structure modelling

The numerical treatment of the boundary integral equation (1) involves both time and spatial discretization. Thus, the time variation of $t_{(\tilde n)}(x,t)$ is approximated as a sequence of rectangular impulses of equal duration Δt. The soil-foundation interface, as well as a part of the surrounding free soil surface are dicretized into Q elements of equal length L. The foundation response at time $t=N\Delta t$ due to a sequence of impulses initiating at time $m\Delta t$ can be determined from

$$\tfrac{1}{2}u^{Np}=\sum_{q=1}^{Q}\sum_{n=m}^{N}([\int_{\Delta s}G^{lq}ds]\{t^{N-l+1}\} -$$

$$-[\int_{\Delta s}F^{lq}ds]\{u^{N-l+1}\}), \qquad (2)$$

where G^{lq} and F^{lq} are the discretized kernel functions

$$v_{\alpha\beta}[x,t;\xi/t_{(\tilde n)\alpha}(x,t)] \quad \text{and} \quad \sigma_{(\tilde n)\alpha\beta}[x,t;\xi/u_\alpha(x,t)]$$

respectively, $n=1,2,\ldots,N$, $l=N+n-1$, $q=1,2,\ldots,Q$, and $p=1,2,\ldots,Q$.

The other component of the system, the flexible foundation is analyzed through standard finite element procedures. The discretization is carried out using four node rectangular isoparametric plane-strain finite elements. The dynamic equation of the foundation motion is given by

$$[M_f]\{\ddot q_t\}+[C_t^f]\{\dot q_t\}+[K_t^f]\{q_t\}=\{R_t\}-\{P_t\} \qquad (3)$$

where $[M_f]$ is the mass matrix, $[C_t^f]$ and $[K_t^f]$ are the time

dependent damping and stiffness matrices respectively, the vectors $\{\ddot{q}_t\}$, $\{\dot{q}_t\}$ and $\{q_t\}$ are the nodal acceleration, velocity and displacement vectors, respectively, the vectors $\{R_t\}$ and $\{P_t\}$ are the nodal external forces and nodal forces associated with the contact stresses. The matrices $[C_t^I]$ and $[k_t^I]$ are time dependent because they contain the terms pertaining to thin-layer interface elements. The propertiese of the thin-layer elements are dependent on the contact area which is a function of time.

Equation (2) relates the average vertical displacements at the center of each element to the contact stresses developed over the elements of the soil-foundation interface. Equation (3), relates the vertical nodal displacement to the nodal forces associated with the contact stresses developed at the ends of the FEM elements at the interface. In order to introduce compatibility between the deflection of the foundation and the soil motion at the interface, the average displacement over an element q is approximated by the mean value of the nodal displacements at the ends of the element q. Similarly, compatibility of forces can be established if each contact force P_t applied at a node i is approximated by the mean value of the two resultant forces R_t associated with the contact stresses that develop over two successive elements joined at the common node i. Thus, for the whole interface region the compatibility relationships can be expressed as

$$\{q_t\}=[T]\{u_t\}$$
and $\quad\quad\quad\quad\quad\quad\quad\quad\quad\quad\quad\quad\quad\quad\quad\quad$ (4)
$$\{P_t\}=[T]^T\{R_t\}$$

where the entries of matrix $[T]$ are either 0 or 1/2. The order of matrix $[T]$ is $Q \times (Q+1)$.

Combination of equations (2), (3) and (4) results in a system of nonlinear equations of motion

$$[M]\{\ddot{q}_t\}+[C_t]\{\dot{q}_t\}+[K_t]\{q_t\}=\{F_t\}-\{P_t\} \quad\quad\quad (5)$$

All quantities in equation (5) are known at a given time. Equation (5) is solved iteratively to satisfy the time dependent boundary conditions at the soil-foundation interface. The contact area at the beginning of each time step is known from the iterative solution of the previous time step. Thus equation (5) at time $t+\Delta t$, where Δt is a small time increment, can be written as

$$[M]\{\Delta\ddot{q}_t^{\,i+1}\}+[C_t]\{\Delta\dot{q}_t^{\,i+1}\} +$$
$$+ [k_t]\{\Delta q_t^{\,i+1}\}=\{\Delta R_t\}+\{R_t^{\,n,i}\} \quad\quad (6)$$

where $\quad\quad\quad \{q_{t+\Delta t}\}=\{q_t\}+\{\Delta q_t\},$

$\quad\quad\quad\quad\quad [K_{t+\Delta t}]=[K_t]+[\Delta K_t],$ etc.

and $\{\Delta R_t^{\,n,i}\}$ is the unknown nonlinear load vector corresponding to the time increment Δt to be determined by iteration and i is the number of iteration within the same time step. The vector $\{\Delta R_t^{\,n,i}\}$

is given by

$$\{\Delta R_t^{n,i}\} = -[\Delta C_t^i]\{\dot{q}_{t+\Delta t}^i\} - [\Delta K_t^i]\{q_{t+\Delta t}^i\} \qquad (7)$$

An unconditionally stable scheme of direct integration based on Wilson θ method is used in the time domain. At the desired time $t+\Delta t$ the accelerations, velocities and displacements are given by the linear acceleration assumptions:

$$\{\ddot{q}_{t+\Delta t}\} = (1-1/\theta)\ddot{q}_t + (1/\theta)\ddot{q}_{t+\tau} \qquad (8)$$

$$\{\dot{q}_{t+\Delta t}\} = \dot{q}_t + (\Delta t/2)(\ddot{q}_t + \ddot{q}_{t+\Delta t}) \qquad (9)$$

$$\{q_{t+\Delta t}\} = q_t + \Delta t \dot{q}_t + (\Delta t^2/6)(\ddot{q}_{t+\Delta t} + 2\ddot{q}_t) \qquad (10)$$

where τ is given by $\tau = \theta \Delta t$. When $\theta = 1.0$ the algorithm reduces to the standard linear acceleration method. A stability analysis reported by Wilson, Farhoomand and Bathe [19] shows that the scheme is unconditionally stable provided $\theta \geq 1.37$.

THIN-LAYER INTERFACE ELEMENTS

In order to simulate unilateral contact at the soil foundation interface, the interface is modeled with the aid of FEM thin-layer elements of negligible influence on the system response. The interface element can undergo four basic modes of deformation. (1) Stick or no-slip, (2) slip or sliding, (3) separation or debonding; and (4) rebonding. An interface element is in stick mode when there is no relative motion between the adjoining bodies. If a relative movement takes place while maintaining the contact between the adjoining bodies, the slip or sliding is said to occur. Separation or debonding takes place when the bodies open up due to contraints of unilateral contact. If the interface element in separation mode returns to stick mode in subsequent loading, rebonding takes place.

The interface element described above has been successfully used for solution of a number of static as well as dynamic two-demensional problems where all domains are discretized with the aid of FEM [14,20]. In this study, the equations of the interface elements are derived separately and then added to those of the foundation prior to establishing the compatibility and equilibrium criteria with the soil BEM modeling described in the previous section.

The primary reason for resorting to interface elements at the interface is to facilitate the computation of the contact area prior to each time step. The interface element when in stick mode is essentially treated like any other plane strain element with the soil elastic modulus, E_s, and Poisson ratio, v_s. In the present study, the concept of sliding is not addressed. In debonding mode of a given interface element, the elastic modulus is assigned a value of zero. This in essence creates a void element with no stiffness. Within a given cycle of iterations in a time step, if rebonding is detected through interpenetration, the forces associated with the contact stresses are applied to the

penetrating node. Thus stick mode of a previously defined void element can be stimulated without modification to the global stiffness matrix $[K_t^I]$. The interface element thickness plays an important role in the convergence of the solution as reported by several researchers [14,20]. In this study the ratio between the thickness of the interface element, and the thickness of its neighbouring FEM element is taken as 0.01.

NUMERICAL EXAMPLES

The combined time domain BEM-FEM technique described above is employed here to determine the dynamic response of a flexible massless strip-footing subjected to externally applied loads. The dynamic behavior of undamped flexible footing depends on the special distribution of the externally applied forces and by the material properties of the elastic footing. Therefore, the footing and the supporting elastic medium are analyzed in this work for three sets of elastic contstants and two types of exernal forces (figure 2). The parameter characterizing the flexibility of the soil-foundation system is the relative stiffness defined by

$$K_r = D_f . D_s \qquad (11)$$

where $D_f = E_f t_f^3 / (1-v_f^2)$ and $D_s = 2(1-v_s)/(E_s b^3)$ (12)

and where the subscript f and s denotes the footing and the soil, respectively, E and v represent modulus of elasticity and poisson's ratio, respectively, and t_f is the thickness of the footing.

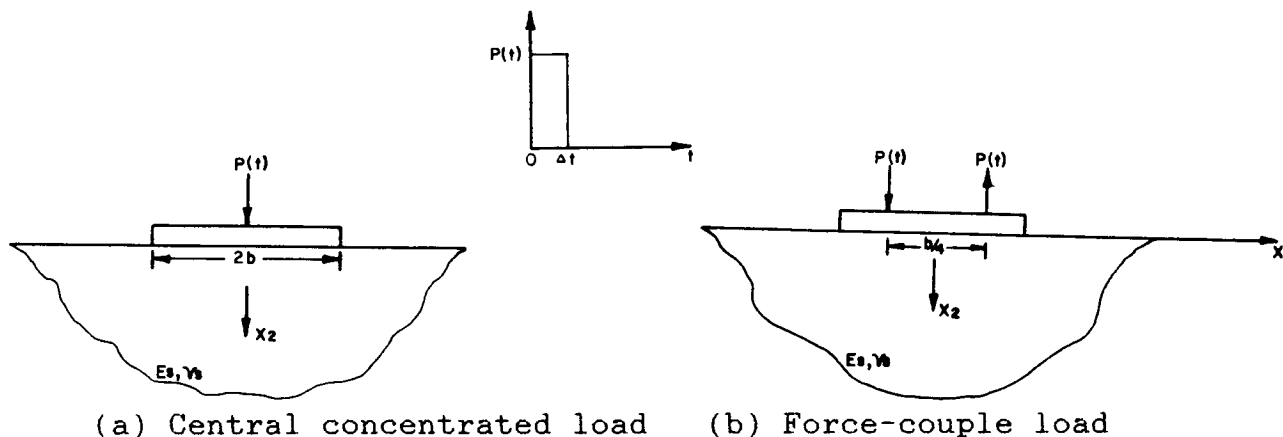(a) Central concentrated load   (b) Force-couple load

Fig. 2 Loadings considered

The soil is discretised into 16 BEM elements and the foundation is discretised into 40 FEM elements as shown in figure 1. Figure 2 shows the two types of external loadings considered, the point force and a moment applied as a force couple of two equal, opposite point forces. The duration of both impulse forces is $\Delta t = 0.16 \times 10^{-4}$ sec, and the relative stiffness considered are $K_r = 0.3$, $K_r = 3.0$ and $K_r = 30.0$. The response of the center point A, and edge point B of figure 1 are plotted in figure 3 through 5. All responses are compared with the corresponding solution of the complete bond case, i.e. uplift not permitted.
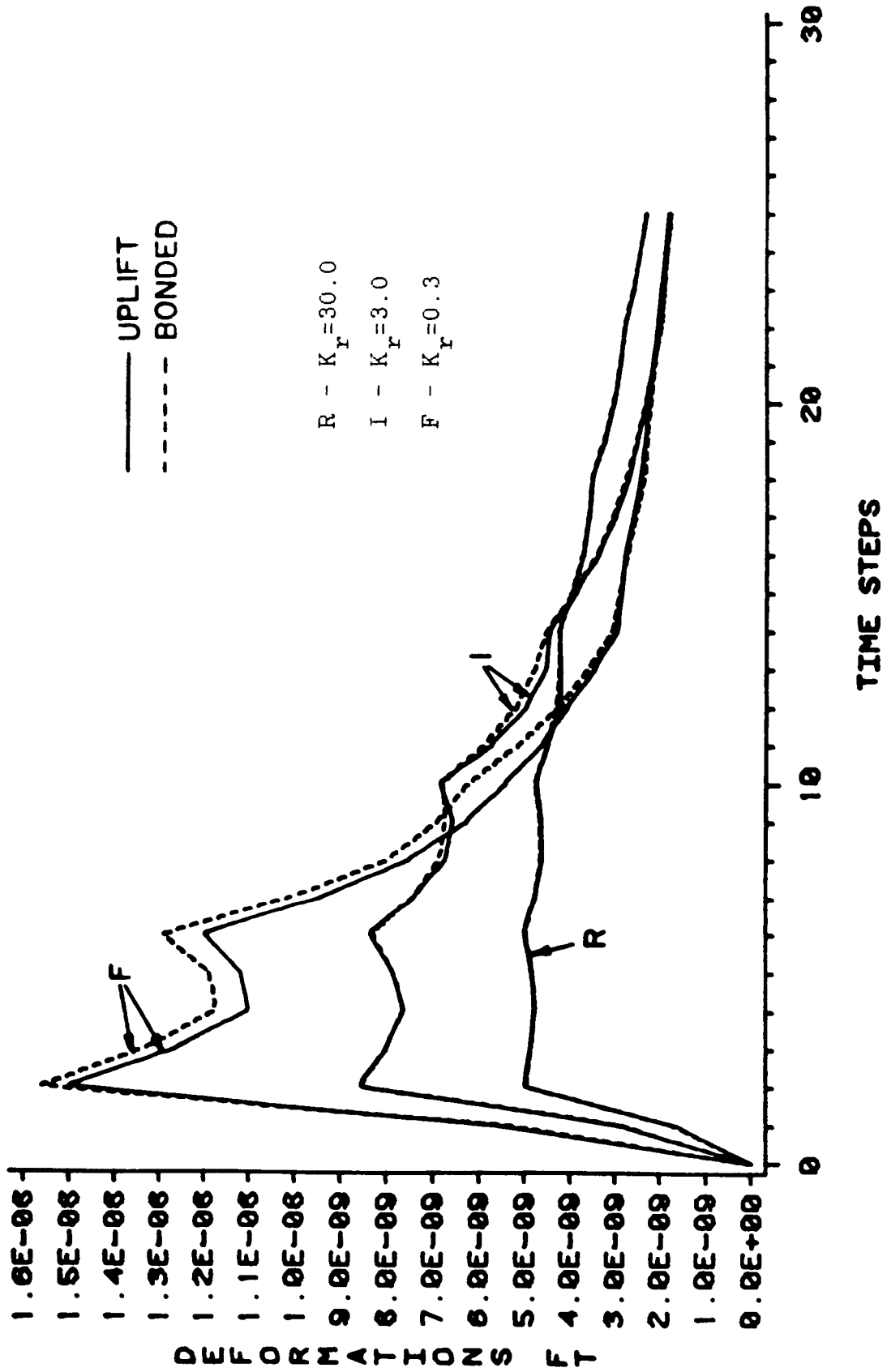
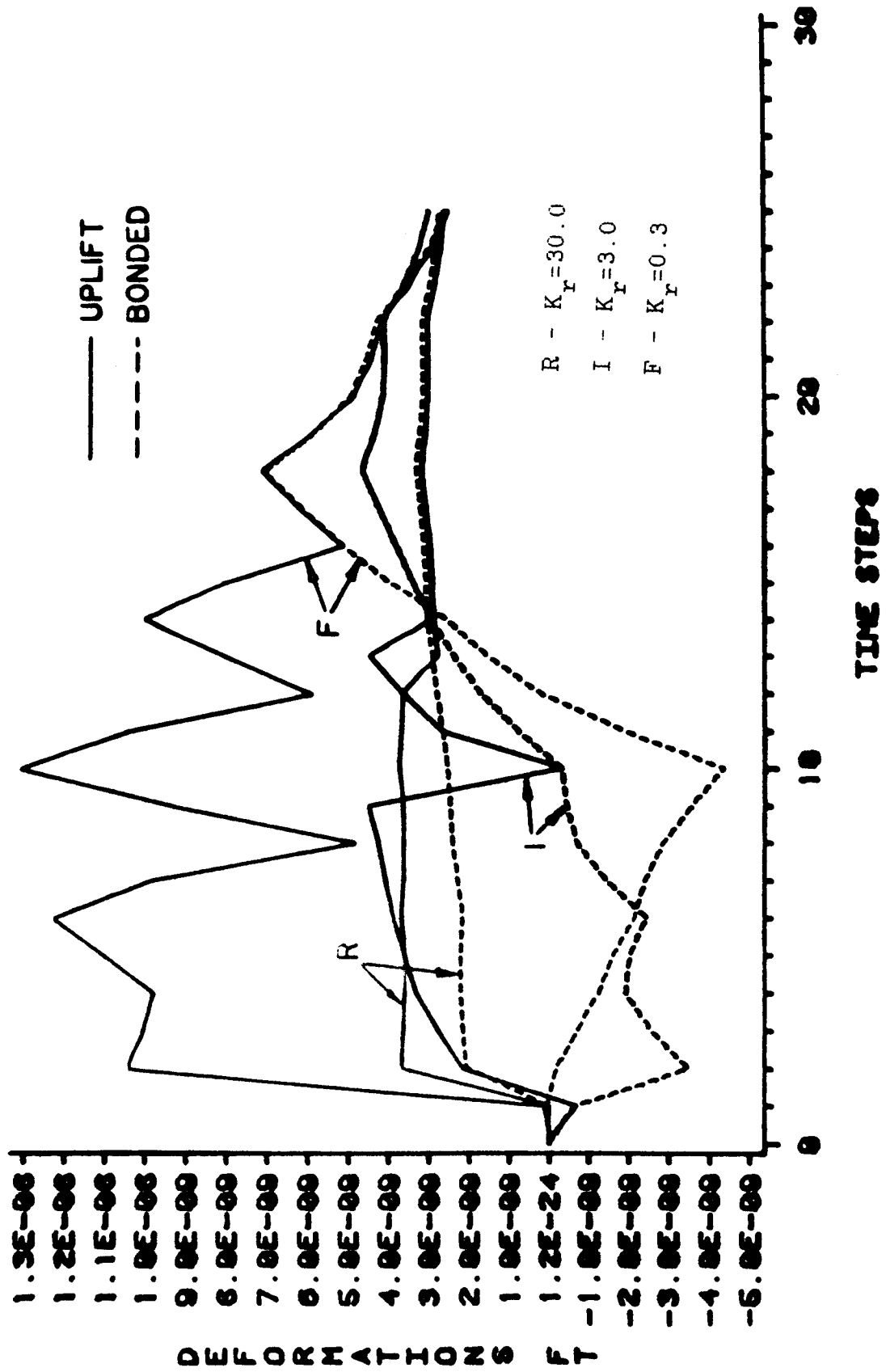Fig. 3   Midpoint Deflection due to central concentrated load

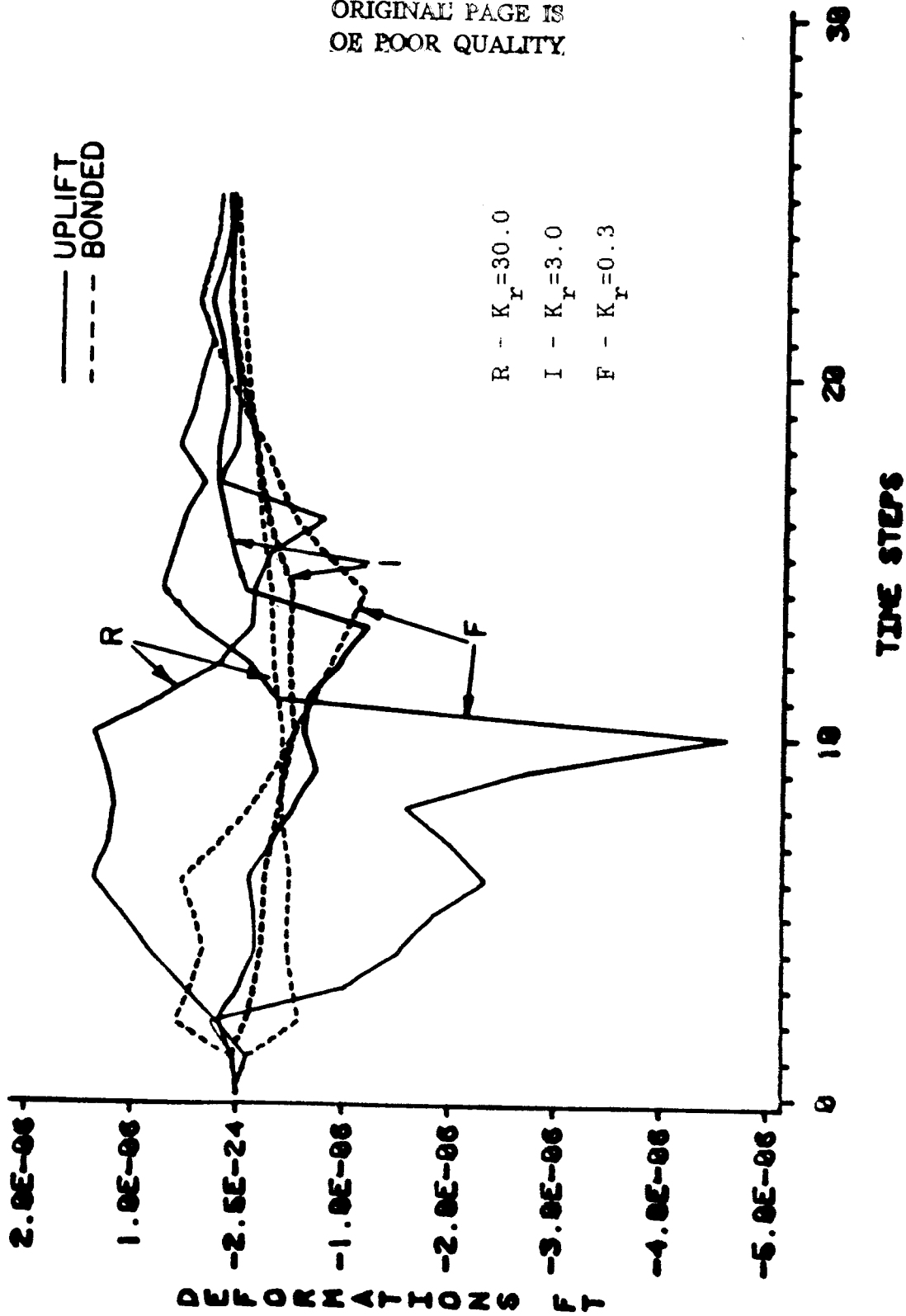Fig. 4 Edgepoint deflection due to central concentrated load

Fig. 5   Edgepoint deflection due to force-couple load

503

The responses at the midpoint A and the edge point B of figure 1 due to a vertcal concentrated rectangular impulse load at midpoint A are plotted for unilateral and bilateral contact for various relative stiffnesses (K_r=0.3, 3.0, 30.0). As seen from figure 3, the response at the center for the unilateral contact is higher then the corresponding bilateral contact case. Figure 4 shows that the deformations at the edge point to be significantly higher for the case of unilateral contact then that for the bilateral case. The deformations are in the opposite sense because the foundation is not held back as tension is incompatible with the assumed constitutive laws of the soil (unilateral contact). At both, the center point and edge point locations the differences between the unilateral and bilateral contact conditions decreases with increasing foundation stiffness.

In the case of force couple loading, the softer foundation K_r=0.3 and stiffer foundation K_r=30.0 undergo higher deformation differences than the intermediate stiffness K_r=3.0 as shown in figure 5. The deformations become identical with the passage of time as seen for the concentrated load case.

CONCLUSIONS

It can be concluded that intermediate relative stiffness leads to moderate deformations when uplift is permitted. Very flexible footings produces higher deformations in unilateral contact compared to bilateral contact, and thus should be considered in their design. Unilateral contact does not significantly increase deformations for stiff footings subjected to concentrated central loading. However, relatively large deformation differences occur when the loading is eccentric necessitating consideration of uplift in their design.

REFERENCES

1. Wolf, J.P., Dynamic Soil-Structure Interaction, Prentice Hall, Englewood Cliffs, New Jersey, 1985.

2. Spyrakos, C.C., Patel, P.N. and Beskos, D.E., "Dynamic Analysis of Flexible Embedded Foundations: Plane Strain Case," Proc. 3rd Int. Conv. Compt. Meth. Exper. Meas., Porto Corras, 1986.

3. Spyrakos, C.C. and Antes, H.m "Time Domain Boundary Element Approaches in Elastodynamics: A Comparative Study," Comp. Struct., Vol. 24, No.4, pp 529-535, 1986.

4. Yim, S. C.-S. and Chopra A., "Simplified Earthquake Analysis of multistory Structure with foundation uplift," ASCE Journal of Structural Engineering, Vol. 111, No. 12, pp. 2708-2731, 1985.

5. Koh, A.-S., Spanos P.D. and Roesset, J.M., "Harmonic Response of Rigid Block on Flexible Foundation," ASCE Journal of the Engineering Mechanics Division, Vol. 112, No. 11, Nov. 1986.

6. Spyrakos, C.C., "Dynamic Behavior of Foundations in Bilateral

and Unilateral Contact," _Shock and Vibration Digest_, (submitted).

7. Rotenberg, A., Jennings, P.C. and Housner, G.W., "The Response of Veteran's Hospital Building 41 in the San Fernando Earthquake," Report No. EERL 80-03, Earth. Engng. Research Lab., California Institute of Technology, Pasedena, California.

8. Vaughn, D.K., and Isenberg, J., "Non-linear Rocking Response of Model Containment Structure," _Earth. Engng. Struct. Dyn._, Vol.11, 1983.

9. Housner, G.W., "The Behavior of Inverted Pendulum Structures During Earthquakes," Bull. Seis. Soc. Amer., Vol.53, 1963.

10. Huckelbridge, A.A. Jr. and Clough, R.W, "Seismic Response of Uplifting Building Frame," Proc. ASCE, ST8, 1978.

11. Kennedy, R.P., Short, S.A., Wesley, D.A. and Lee, T.H., "Effect of Nonlinear Soil-Structure Interaction Due to Base Slab Uplift on the Seismic Response of a High-Temperature Gas-Cooled Reactor (HTGR)," _Nuclear Engng. Design_, Vol. 38, 1976.

12. Psycharis, J.N., "Dynamic Response of Rocking Structures Allowed to Uplift," Report No. EERL 81-02, Earth. Engng. Research Lab., California Institute of Technology, Pasedena, California, 1981.

13. Roesset, J.M. and Tassoulas, J.L., "Nonlinear Soil-Structure Interaction: An Overview," Winter Annual Meeting, ASME, Phoenix, Arizona, 1984.

14. Zaman, M.M., Desai, C.S. and Drumm, E.C., "Interface Model for Dynamic Soil-Structure Interaction," _ASCE Journal of Geotechnical Engineering_, Vol.110, pp. 1257-1273, 1984.

15. Wolf, J.P. and Obernhuber, P., "Non-linear Soil-Structure Interaction analysis Using Green's Function of Soil in the Time Domain," _Earth. Engng. Struct. Dyn._, Vol. 13, pp. 213-223, 1985.

16. Wolf, J.P. and Darbre, G.R., "Non-linear Soil-Structure Interaction Analysis Based on the Boundary Element Method in the Time Domain with Application to Embedded Foundation," _Earth. Engng. Struct. Dyn._, Vol. 14, 1986.

17. Spyrakos, C.C. and Beskos, D.E., "Dynamic Response of Rigid Strip Foundations by a Time Domain Boundary Element Method," _Int. J. Num. Meth. Engng._, Vol.23, pp. 1547-1565, 1986.

18. Spyrakos, C.C. and Beskos, D.E., "Dynamic Response of Flexible Strip Foundations by Boundary and Finite Elements," _Soil Dyn. Earth. Engng._, Vol. 5, No. 2, pp. 84-96, 1986.

19. Wilson, E.L., Farhoomand I. and Bathe, K.J., "Nonlinear Dynamic Analysis of Complex Structures," _Earthquake Engineering and Structural Dynamics_, Vol. 1, pp. 241-252, 1973.

20. Chen, R.-J., "Finite Element Modeling of Interface Behavior in Geologic Media," Thesis presented to the West Virginia University, at Morgantown, W.V., in 1985, in partial fufillment of the requirements for the degree of Doctor of Philosophy.

1. REPORT NO. NASA CP-2488	2. GOVERNMENT ACCESSION NO.	3. RECIPIENT'S CATALOG NO.
4. TITLE AND SUBTITLE 58th Shock and Vibration Symposium		5. REPORT DATE October 1987
		6. PERFORMING ORGANIZATION CODE
7. AUTHOR(S) Walter and Barbara Pilkey, Compilers		8. PERFORMING ORGANIZATION REPORT #
9. PERFORMING ORGANIZATION NAME AND ADDRESS George C. Marshall Space Flight Center Marshall Space Flight Center, Alabama 35812		10. WORK UNIT NO. M-571
		11. CONTRACT OR GRANT NO.
		13. TYPE OF REPORT & PERIOD COVERED
12. SPONSORING AGENCY NAME AND ADDRESS National Aeronautics and Space Administration Washington, D.C. 20546 and The Department of Defense Washington, D.C.		Conference Publication
		14. SPONSORING AGENCY CODE
15. SUPPLEMENTARY NOTES Co-sponsored by the Department of Defense and co-hosted by the Marshall Space Flight Center and the U. S. Army Missile Command. Formerly sponsored by The Shock and Vibration Information Center.		

16. ABSTRACT

This NASA Conference Publication contains the proceedings of the 58th Shock and Vibration Symposium, held in Huntsville, Alabama, October 13-15, 1987. Previous Shock and Vibration Symposia were organized by the Shock and Vibration Information Center. The papers are grouped in the categories: mechanical shock, dynamic analysis, space shuttle main engine vibration, isolation and damping, and analytical methods.

17. KEY WORDS Shock Vibration Symposium		18. DISTRIBUTION STATEMENT Unclassified-Unlimited Subject Category: 39
19. SECURITY CLASSIF. (of this report) Unclassified	20. SECURITY CLASSIF. (of this page) Unclassified	21. NO. OF PAGES 518 22. PRICE A22